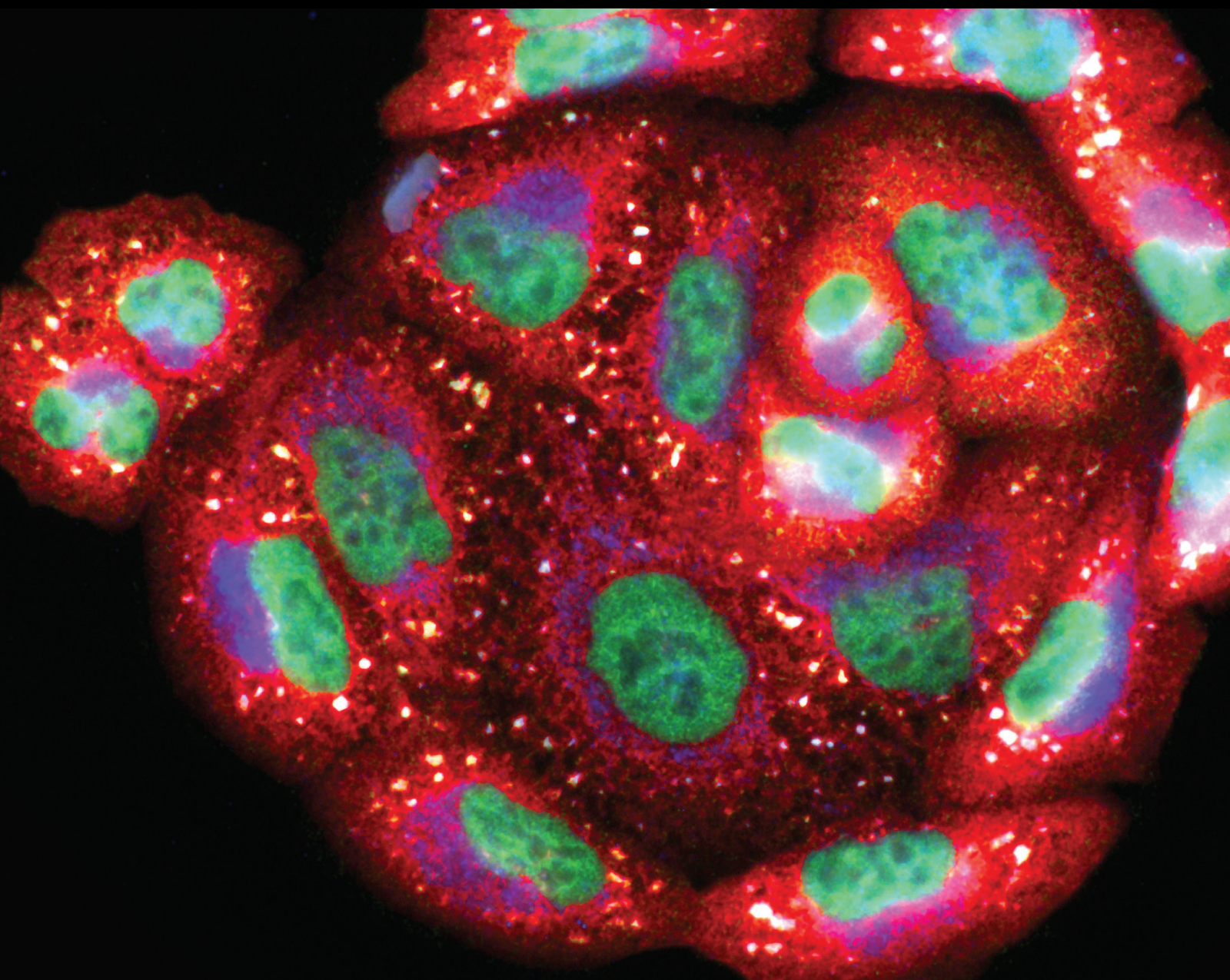# Role of Redox Homeostasis in Cancer Biology and Anticancer Therapy

Lead Guest Editor: Qiang Tong
Guest Editors: Xiangmin Lv, Li Yang, Bin Duan, and Yadan Wang

Role of Redox Homeostasis in Cancer Biology and Anticancer Therapy

Role of Redox Homeostasis in Cancer Biology and Anticancer Therapy

Lead Guest Editor: Qiang Tong
Guest Editors: Xiangmin Lv, Li Yang, Bin Duan, and Yadan Wang

Tim Hofer, Norway
John D. Horowitz, Australia
Silvana Hrelia, Italy
Dragan Hrncic, Serbia
Zebo Huang, China
Zhao Huang, China
Tarique Hussain, Pakistan
Stephan Immenschuh, Germany
Norsharina Ismail, Malaysia
Franco J. L, Brazil
Sedat Kacar, USA
Andleeb Khan, Saudi Arabia
Kum Kum Khanna, Australia
Neelam Khaper, Canada
Ramoji Kosuru, USA
Demetrios Kouretas, Greece
Andrey V. Kozlov, Austria
Chan-Yen Kuo, Taiwan
Gaocai Li, China
Guoping Li, USA
Jin-Long Li, China
Qiangqiang Li, China
Xin-Feng Li, China
Jialiang Liang, China
Adam Lightfoot, United Kingdom
Christopher Horst Lillig, Germany
Paloma B. Liton, USA
Ana Lloret, Spain
Lorenzo Loffredo, Italy
Camilo López-Alarcón, Chile
Daniel Lopez-Malo, Spain
Massimo Lucarini, Italy
Hai-Chun Ma, China
Nageswara Madamanchi, USA
Kenneth Maiese, USA
Marco Malaguti, Italy
Steven McAnulty, USA
Antonio Desmond McCarthy, Argentina
Sonia Medina-Escudero, Spain
Pedro Mena, Italy
Víctor M. Mendoza-Núñez, Mexico
Lidija Milkovic, Croatia
Alexandra Miller, USA
Sara Missaglia, Italy

Premysl Mladenka, Czech Republic
Sandra Moreno, Italy
Trevor A. Mori, Australia
Fabiana Morroni, Italy
Ange Mouithys-Mickalad, Belgium
Iordanis Mourouzis, Greece
Ryoji Nagai, Japan
Amit Kumar Nayak, India
Abderrahim Nemmar, United Arab Emirates
Xing Niu, China
Cristina Nocella, Italy
Susana Novella, Spain
Hassan Obied, Australia
Pál Pacher, USA
Pasquale Pagliaro, Italy
Dilipkumar Pal, India
Valentina Pallottini, Italy
Swapnil Pandey, USA
Mayur Parmar, USA
Vassilis Paschalis, Greece
Keshav Raj Paudel, Australia
Ilaria Peluso, Italy
Tiziana Persichini, Italy
Shazib Pervaiz, Singapore
Abdul Rehman Phull, Republic of Korea
Vincent Pialoux, France
Alessandro Poggi, Italy
Zsolt Radak, Hungary
Dario C. Ramirez, Argentina
Erika Ramos-Tovar, Mexico
Sid D. Ray, USA
Muneeb Rehman, Saudi Arabia
Hamid Reza Rezvani, France
Alessandra Ricelli, Italy
Francisco J. Romero, Spain
Joan Roselló-Catafau, Spain
Subhadeep Roy, India
Josep V. Rubert, The Netherlands
Sumbal Saba, Brazil
Kunihiro Sakuma, Japan
Gabriele Saretzki, United Kingdom
Luciano Saso, Italy
Nadja Schroder, Brazil

Anwen Shao (iD), China
Iman Sherif, Egypt
Salah A Sheweita, Saudi Arabia
Xiaolei Shi, China
Manjari Singh, India
Giulia Sita (iD), Italy
Ramachandran Srinivasan (iD), India
Adrian Sturza (iD), Romania
Kuo-hui Su (iD), United Kingdom
Eisa Tahmasbpour Marzouni (iD), Iran
Hailiang Tang, China
Carla Tatone (iD), Italy
Shane Thomas (iD), Australia
Carlo Gabriele Tocchetti (iD), Italy
Angela Trovato Salinaro, Italy
Rosa Tundis (iD), Italy
Kai Wang (iD), China
Min-qi Wang (iD), China
Natalie Ward (iD), Australia
Grzegorz Wegrzyn, Poland
Philip Wenzel (iD), Germany
Guangzhen Wu (iD), China
Jianbo Xiao (iD), Spain
Qiongming Xu (iD), China
Liang-Jun Yan (iD), USA
Guillermo Zalba (iD), Spain
Jia Zhang (iD), China
Junmin Zhang (iD), China
Junli Zhao (iD), USA
Chen-he Zhou (iD), China
Yong Zhou (iD), China
Mario Zoratti (iD), Italy

Contents

Contents

Retraction

Retracted: Stearoyl-CoA Desaturase 1 Potentiates Hypoxic plus Nutrient-Deprived Pancreatic Cancer Cell Ferroptosis Resistance

Oxidative Medicine and Cellular Longevity

Oxidative Medicine and Cellular Longevity has retracted the article titled "Stearoyl-CoA Desaturase 1 Potentiates Hypoxic plus Nutrient-Deprived Pancreatic Cancer Cell Ferroptosis Resistance" [1] due to concerns with figure duplications in Figure 1(b) as originally noted on PubPeer [2]. Specifically, the DMSO Nor panel is duplicated with the DMSO H/NS panel, and the Erastin Nor+Fer-1 panel is duplicated with the SAS Nor+Fer-1 panel. In both cases, the field of view is different between the panels. The author responded to explain that the duplications were introduced due to an error when preparing their manuscript, however, this did not satisfy the concerns of the editorial board and the article is retracted due to concerns with the reliability of the data.

The authors do not agree to the retraction.

References

[1] J. Gao, Z. Zhang, Y. Liu et al., "Stearoyl-CoA Desaturase 1 Potentiates Hypoxic plus Nutrient-Deprived Pancreatic Cancer Cell Ferroptosis Resistance," *Oxidative Medicine and Cellular Longevity*, vol. 2021, 14 pages, 2021.

[2] 2021, https://pubpeer.com/publications/0E8247FC6B3045A767D1AB34FB4BB5.

Erratum

Erratum to "Berbamine Suppresses the Progression of Bladder Cancer by Modulating the ROS/NF-*κ*B Axis"

Chenglin Han [iD],[1] **Zilong Wang,**[1] **Shuxiao Chen,**[2] **Lin Li,**[3] **Yingkun Xu,**[1] **Weiting Kang** [iD],[1] **Chunxiao Wei,**[4] **Hongbin Ma,**[5] **Muwen Wang** [iD],[1,4] **and Xunbo Jin** [iD][1,4]

[1]*Department of Urology, Shandong Provincial Hospital, Cheeloo College of Medicine, Shandong University, Jinan, Shandong 250021, China*
[2]*Department of Vascular Surgery, Shandong Provincial Hospital, Cheeloo College of Medicine, Shandong University, Jinan, Shandong 250021, China*
[3]*Department of Orthopedics, Shandong Provincial Hospital, Cheeloo College of Medicine, Shandong University, Jinan, Shandong 250021, China*
[4]*Department of Urology, Shandong Provincial Hospital Affiliated to Shandong First Medical University, Jinan, Shandong 250021, China*
[5]*Department of Hepatobiliary, The First Affiliated Hospital of Harbin Medical University, Harbin, Heilongjiang 150000, China*

Correspondence should be addressed to Muwen Wang; docwmw1@163.com and Xunbo Jin; jxb@sdu.edu.cn

Received 19 November 2021; Accepted 19 November 2021; Published 14 December 2021

In the article titled "Berbamine Suppresses the Progression of Bladder Cancer by Modulating the ROS/NF-*κ*B Axis" [1], the incorrect figure files were used during the production process. The figures should be corrected as follows:

(a)

(b)

(c)

Figure 2: Continued.

(d)

FIGURE 2: Berbamine induced S-phase arrest in bladder cancer cells. (a, b) Representative images and quantitative cell cycle distribution was detected by flow cytometry. (c, d) The protein levels of a cell cycle regulator involving P21, P27, CyclinD, CyclinA2, and CDK2 were examined by western blotting, and ImageJ analyzed relative expression levels. Values are represented (all dates are expressed) as the mean ± SD. The experiment was repeated at least three times. Statistical significance was determined using two-tailed Student's t-test or one-way ANOVA. $^{*}p < 0.5$; $^{**}p < 0.01$; $^{***}p < 0.001$.

(a)

(b)

(c)

Figure 6: Continued.

(d)

(e)

(f)

(g)

(h)

Figure 6: Berbamine exerted antitumor activity against bladder cancer cells by modulating the ROS/NF-κB axis. 5637 and T24 cells were treated with 32 μM berbamine in the presence or absence of 10 mM NAC. (a, b) Representative images of the ROS generation level were captured using a fluorescence microscope. (c, d) Flow cytometry was performed to measure cell apoptosis. (e, f) The levels of Bcl-2 and Bax proteins were measured by western blotting. (g, h) The levels of P65 and P-P65 proteins were measured by western blotting. Values are represented (all dates are expressed) as the mean ± SD. The experiment was repeated at least three times. Statistical significance was determined using two-tailed Student's t-test or one-way ANOVA. $^{*}p < 0.5$; $^{**}p < 0.01$; $^{***}p < 0.001$; $^{\#}p < 0.5$; $^{\#\#}p < 0.01$.

References

[1] C. Han, Z. Wang, S. Chen et al., "Berbamine Suppresses the Progression of Bladder Cancer by Modulating the ROS/NF-κB Axis," *Oxidative Medicine and Cellular Longevity*, vol. 2021, Article ID 8851763, 21 pages, 2021.

Research Article

Construction of Potential Gene Expression and Regulation Networks in Prostate Cancer Using Bioinformatics Tools

Heyu Liu,[1] **Lirong Li,**[2] **Yuan Fan,**[3] **Yaping Lu** ,[3] **Changhong Zhu,**[1] **and Wei Xia** [1]

[1]*Institute of Reproductive Health, Tongji Medical College, Huazhong University of Science and Technology, Wuhan 430030, China*
[2]*Department of Urology, Union Hospital, Tongji Medical College, Huazhong University of Science and Technology, Wuhan 430030, China*
[3]*Sinopharm Genomics Technology Co., Ltd., Wuhan 430030, China*

Correspondence should be addressed to Yaping Lu; luyaping@sinopharm.com and Wei Xia; tjxiawei@hust.edu.cn

Objective. To identify the key genes involved in prostate cancer and their regulatory network. *Methods*. The dataset of mRNA/miRNA transcriptome sequencing was downloaded from The Cancer Genome Atlas/the Gene Expression Omnibus database for analysis. The "edgeR" package in the R environment was used to normalize and analyze differentially expressed genes (DEGs) and miRNAs (DEmiRNAs). First, the PANTHER online tool was used to analyze the function enrichment of DEGs. Next, a protein-protein interaction (PPI) network was constructed using STRING and Cytoscape tools. Finally, miRNA-gene regulatory networks were constructed using the miRTarBase. *Results*. We identified 4339 important DEGs, of which 2145 were upregulated (Up-DEGs) and 2194 were downregulated (Down-DEGs). Functional enrichment analysis showed that the Up-DEGs were related to the immune system and the cell cycle in prostate cancer, whereas the Down-DEGs were related to the nucleic acid metabolic process and metabolism pathways. Twelve core protein clusters were found in the PPI network. Further, the constructed miRNA-gene interaction network showed that 11 downregulated miRNAs regulated 16 Up-DEGs and 22 upregulated miRNAs regulated 22 Down-DEGs. *Conclusion*. We identified 4339 genes and 70 miRNAs that may be involved in immune response, cell cycle, and other key pathways of the prostate cancer regulatory network. Genes such as BUB1B, ANX1A1, F5, HTR4, and MUC4 can be used as biomarkers to assist in the diagnosis and prognosis of prostate cancer.

1. Introduction

Prostate cancer (PCa) is one of the most common malignant tumors in urology. Its incidence has been increasing in recent years, and it has now become the leading cause of cancer-related deaths among middle-aged men [1]. Androgen deprivation therapy using surgical or chemical castration is the standard treatment for all stages of PCa [2]. However, patients ultimately tend to develop castration-resistant PCa, which requires further treatment. The treatment of PCa is limited by the low selectivity of medication and drug resistance encountered in all radiotherapy, chemotherapy, and immunotherapy. Thus, the reduction of multidrug resistance and identification of a clear molecular target would significantly improve the efficacy of therapeutic inter-

ventions for PCa. With the development and clinical application of molecule-targeted drugs, the molecule-targeted treatment of tumors has been widely accepted. However, there is currently a lack of precise and effective indicators to predict the efficacy of chemotherapy and targeted drug therapy. Therefore, there is an urgent need to find new indicators to indicate the use of correct drugs and improve patient survival and quality of life [3]. These new indicators or tumor molecular markers would be helpful in the diagnostic and prognostic evaluation of PCa.

With the development of high-throughput gene chip and sequencing technology, it is possible to rapidly study the gene expression profile of PCa, thereby identifying the gene expression and key gene expression changes in PCa tissues and cells under specific conditions. Bioinformatics involves

gene chip data analyses. It uses sequence alignment, statistical analysis, visual mapping, biological clustering, biological molecular network, and pathway analysis to mine the massive and complex bioinformatics data generated by gene chip technology to enable more systematic study and comprehensive treatment of diseases [4]. In recent years, large-scale genome sequencing and gene chip detection approaches have been used in cancer research. The Cancer Genome Atlas (TCGA) database contains the global gene chip dataset. As the largest cancer gene information database available at present, the TCGA database includes rich and standardized clinical data on many cancer types and multiple groups, including data on gene expression, miRNA expression, copy number variation, DNA methylation, and single nucleotide polymorphism, based on large sample sizes for each cancer type. Thus, this database can be used for the search for cancer biomarkers using bioinformatics tools.

miRNAs are evolutionarily conserved short (approximately 18–22 nucleotides long) noncoding single-stranded RNA molecules that function as posttranscriptional gene regulators [5]. A large body of evidence has proven that the occurrence and development of cancer is often accompanied by the abnormal expression of some miRNAs [6]. Studies on lung cancer and breast cancer have shown that miRNAs can be used as biological targets for cancer treatment [7, 8]. Therefore, it is meaningful to use miRNAs as biomarkers for the early diagnosis and prognosis of cancer, but this use is limited as several functions and biological processes of miRNAs remain unidentified. In this study, differentially expressed genes (DEGs)/miRNAs were extracted from the microarray transcriptome data of PCa in TCGA/ the Gene Expression Omnibus (GEO) database. Physiological functions and signal transduction pathways related to the DEGs were then obtained by Gene Ontology (GO) enrichment and Kyoto Encyclopedia of Genes and Genomes (KEGG) pathway analyses. Further, the protein-protein interaction (PPI) network and prostate-specific gene coexpression network were analyzed to identify the core protein clusters and key genes. Finally, the miRNA-gene interaction network was constructed. This process laid a foundation for the clinical diagnosis and prognosis of PCa.

2. Materials and Methods

2.1. RNA-Seq and miRNA-Seq Data.
The transcriptome profiling datasets were downloaded from the GDC data portal [9]. The RNA-Seq dataset was obtained by advanced search with strings "cases.project.project_id" in ["TCGA-PRAD"], "files.analysis.workflow_type" in ["HTSeq - Counts"], and "files.data_category" in ["transcriptome profiling"]. And the miRNA-Seq dataset was obtained by advanced search with strings "cases.project.project_id" in ["TCGA-PRAD"], "files.data_category" in ["transcriptome profiling"], and "files.data_type" in ["miRNA Expression Quantification"].

Both the RNA-Seq and miRNA-Seq datasets originated from a total of 499 clinical PCa samples, including white (413 cases), black or African American (58 cases), Asian (12 cases), American Indian or Alaska native (1 case), and race not reported (14 cases) patients, and 52 normal prostate

samples (race not reported). The patient age ranged from 41 to 78 years old.

For the RNA-Seq dataset, HTSeq-Count tables of the 499 tumor and 52 normal samples were merged to form a gene read count matrix. And for the miRNA-Seq dataset, the "read_count" columns in the quantification files were merged to form a miRNA count table.

2.2. Differential Expression Analyses.
The read count matrices of genes and miRNAs were, respectively, used to call differentially expressed genes (DEGs) and differentially expressed miRNAs (DEmiRNAs) between tumor and normal samples by the Bioconductor package "edgeR" in the R software (version 4.0.2). The edgeR programs including filtering, normalization, dispersion estimating, and quasilikelihood F-tests were performed. The cut-off we used to pick significant DEGs and DEmiRNAs was p value < 0.05, false discovery rate (FDR) < 0.05, and $|\log 2FC| > 1$. The logfold change against log-counts per million, with DEGs or DEmiRNAs highlighted, was plotted.

2.3. Gene Functional Enrichment Analyses.
The official Gene Ontology (GO) online tool (http://geneontology.org/) with human genes as the background was used to implement Gene Ontology enrichment. Ensemble gene lists of 2145 upregulated DEGs (Up-DEGs) and 2194 downregulated DEGs (Down-DEGs) were separately submitted to the web service powered by PANTHER. Overrepresentation tests (released 20200728) were performed with Fisher's exact test as the test type and the calculated false discovery rate as the correction method. The GO terms were sorted and filtered by FDR and fold enrichment. And the top 10 terms of the three GO domains (cellular component, biological process, and molecular function) were shown.

Kyoto Encyclopedia of Genes and Genomes (KEGG) pathway enrichment analyses were performed to reveal signaling pathways in prostate cancer. Firstly, ensemble IDs of DEGs were converted and filtered to 1481 Up-DEGs' symbols and 1961 Down-DEGs' symbols by the HGNC (HUGO Gene Nomenclature Committee) BioMart server. Then, the DEGs' symbols were called by the gene-list enrichment tool in KOBAS3.0 to do KEGG pathway enrichment with default parameters. The cut-off for significant pathways was set as corrected p value < 0.05, and the top 10 pathways were shown.

2.4. Construction of Protein-Protein Interaction (PPI) Networks.
Firstly, 1481 Up-DEGs' symbols and 1961 Down-DEGs' symbols were separately input to the Search Tool for the Retrieval of Interacting Genes/Proteins (STRING) online tool [10] to build PPI networks, with "the minimum required interaction score" set as "highest confidence (0.900)" and the "hide disconnected nodes in the network" option was checked. And the tabular text output PPI files were exported.

Secondly, the PPI files were imported into the Cytoscape 3.8.2 software [11]. The MCODE application was used to find clusters (highly interconnected areas) in the network, and the score of key PPI nodes was calculated using the k
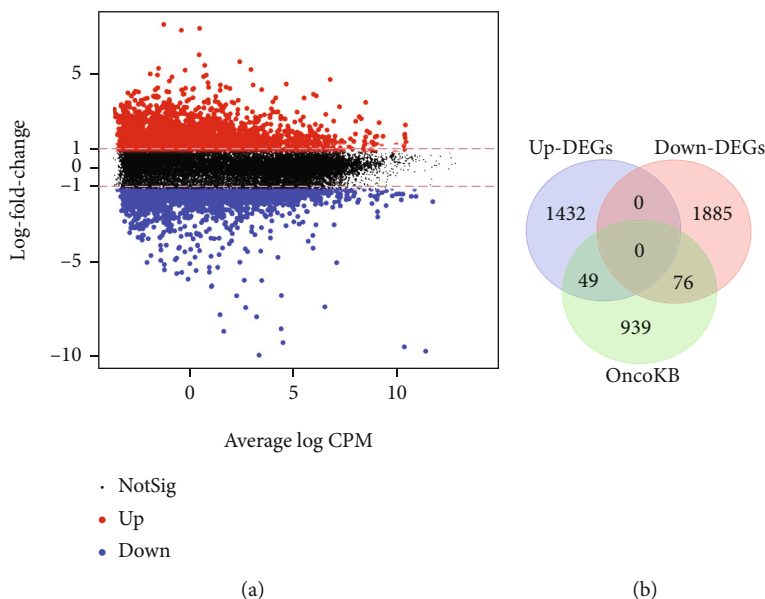
FIGURE 1: Differentially expressed genes (DEGs) between PCa and normal samples. (a) The MA plot of DEGs. (b) Venn diagram of DEGs overlapped with OncoKB cancer genes.

-core decomposition algorithm. The cluster finding parameters were node score cutoff, 0.2; haircut, true; fluff, false; k-core, 7; and max. depth from seed, 100. The score of nodes reflected the density of the nodes and the surrounding nodes. Linked proteins had the same score and formed core protein clusters.

Finally, to depict the PPI networks of the core protein clusters, yFiles Layout Algorithms in Cytoscape applications were used.

2.5. Profiling of miRNAs and Gene Regulation Networks. 50 upregulated DEmiRNAs (Up-DEmiRNAs) and 20 downregulated DEmiRNAs (Down-DEmiRNAs) were compared to PCa-related miRNAs in miRCancer (miRNA Cancer Association Database), and a Venn diagram was drawn.

The miRTarBase provides information about experimentally validated miRNA-target gene interactions [12, 13]. To obtain miRNA-gene interactions in PCa regulation, the 91 Up-DEGs from five upregulated and 137 Down-DEGs from seven downregulated core protein clusters were used to bait the corresponding miRNA regulators verified by comprehensive experiments.

To increase the reliability of miRNA-gene interactions in PCa, we selected the DEmiRNAs and the corresponding DEGs as high-confident regulation pairs. The experimentally validated high-confident regulation networks were constructed and displayed using the Cytoscape 3.8.2 software.

3. Results

3.1. Identification of DEGs in Prostate Cancer Response. To know how genes respond in prostate cancer, we collected RNA-Seq datasets from the TCGA-PRAD project, including 449 tumor samples and 52 normal samples, and performed transcriptome profiling.

Differential expression analyses uncovered DEGs either upregulated or downregulated in comparison between tumor and normal. In total, 4339 DEGs were identified, and the screening criteria were (1) $|logFC| > 1$, (2) $p < 0.05$, and (3) $FDR < 0.05$. The MA plot gives a quick overview of the 2145 upregulated DEGs (Up-DEGs) and 2194 downregulated DEGs (Down-DEGs) (Figure 1(a)).

The ensemble IDs of DEGs were converted and filtered to 1481 Up-DEGs' symbols and 1961 Down-DEGs' symbols, which were then compared with the OncoKB cancer gene list. 125 DEGs identified in this study were also found in OncoKB, but we also detected a large proportion of DEGs (96.4%, 3317/3442) that have potential to be actionable genes in prostate cancer (Figure 1(b)).

3.2. Enrichment of Gene Functions in Prostate Cancer. To reveal effective biological functions in prostate cancer, Gene Ontology (GO) enrichment analyses of DEGs are conducted. The GO enrichment analysis of the 2145 Up-DEGs showed that in biological processes, they were mainly enriched in complement activation, classical pathway, humoral immune response mediated by circulating immunoglobulin, complement activation, and immunoglobulin-mediated immune response; in molecular functions, mainly in antigen binding, immunoglobulin receptor binding, signaling receptor binding, and hormone activity; and in cellular components, mainly in immunoglobulin complex, DNA packaging complex, nucleosome, and chromatin (Figure 2(a)). The GO enrichment analysis of the 2194 Down-DEGs showed that in biological processes, they were mainly enriched in nucleobase-containing compound metabolic process, nucleic acid metabolic process, heterocycle metabolic process, and gene expression; in molecular functions, mainly in RNA binding, nucleic acid binding, heterocyclic compound binding, and organic cyclic compound binding; and in cellular
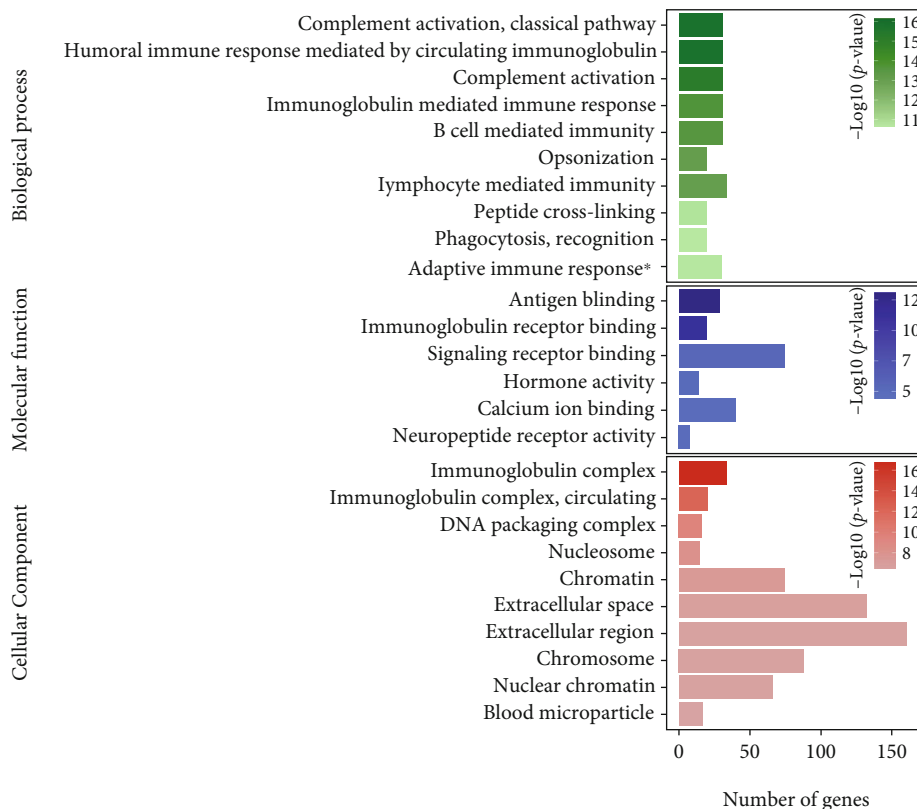
(a)
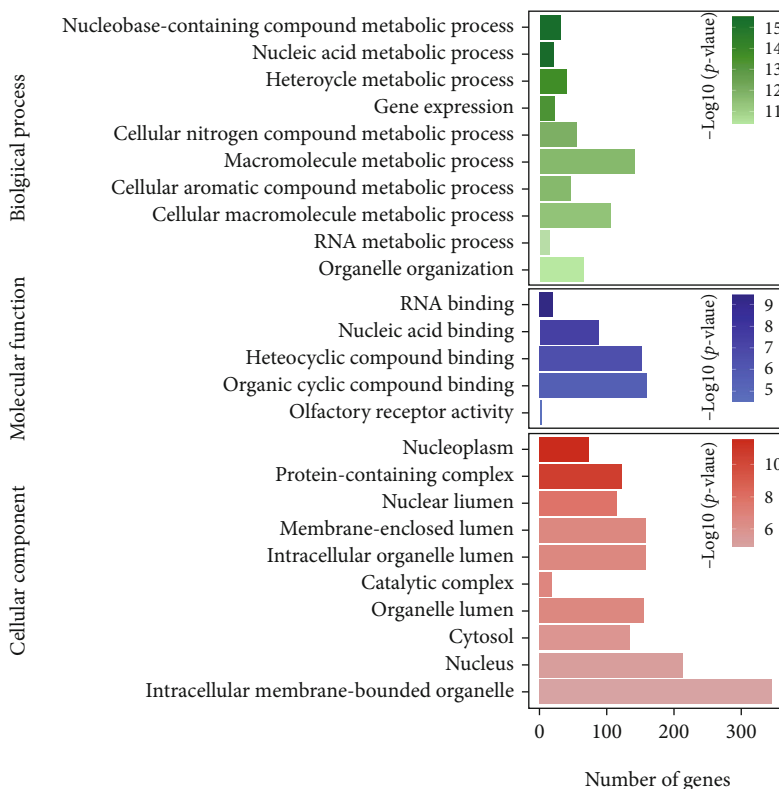
(b)

FIGURE 2: Enrichment of Gene Ontologies (GO) of Up-DEGs and Down-DEGs: (a) GO enrichment of Up-DEGs; (b) GO enrichment of Down-DEGs. The top 10 terms in the three GO domains (biological process, molecular function, and cellular component) are shown.
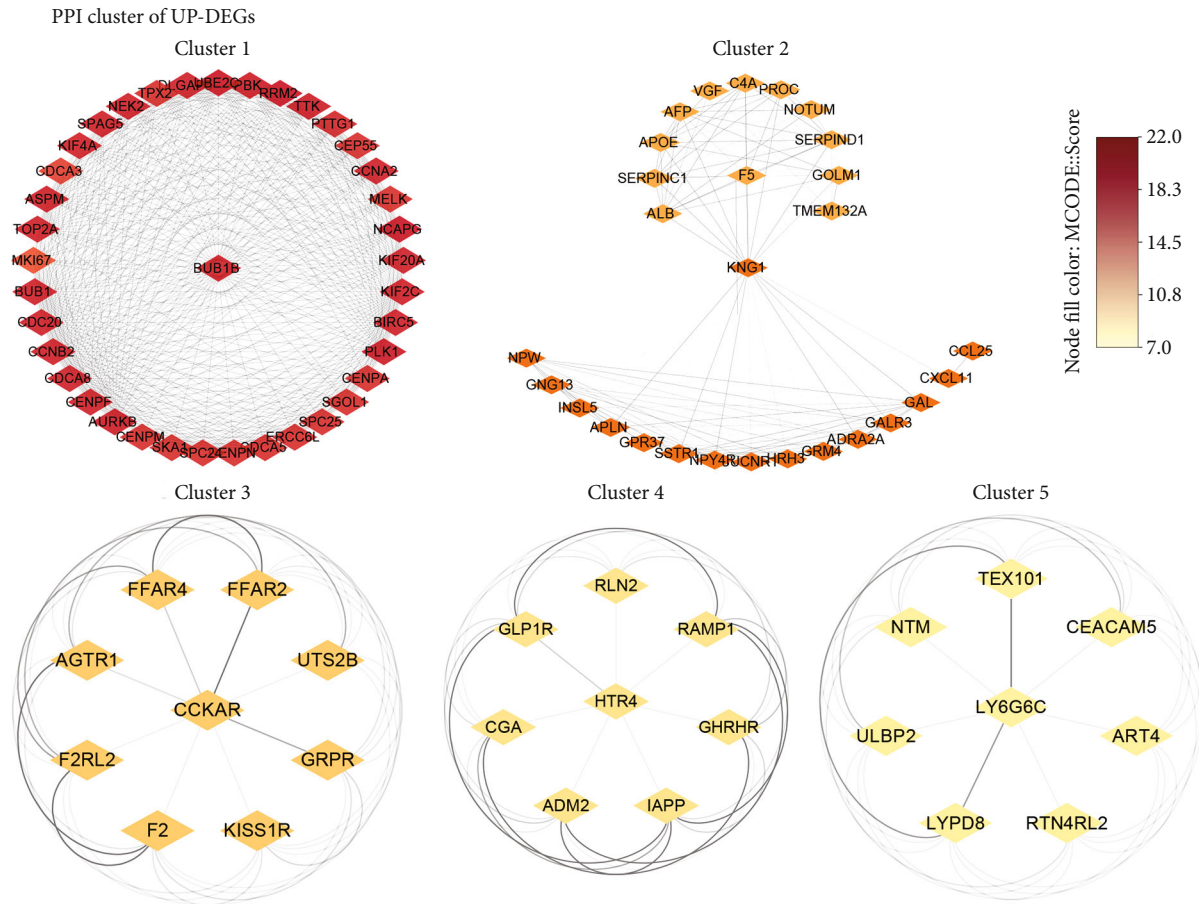
FIGURE 3: Core protein-protein interaction (PPI) networks of Up-DEGs. The network nodes are proteins. The edges represent the predicted functional associations. The node fill color mapped the MCODE score, reflecting the density of the nodes and the surrounding nodes. The edge transparency represents the combined interaction score between two nodes.

components, mainly in nucleoplasm, protein-containing complex, nuclear lumen, and membrane-enclosed lumen (Figure 2(b)).

To profile prostate cancer-responsive mechanisms, enrichment analyses of biological pathways defined by Kyoto Encyclopedia of Genes and Genomes (KEGG) were carried out. Most of the Up-DEGs were significantly enriched in the pathways termed as "neuroactive ligand-receptor interaction," "cell cycle," "complement and coagulation cascades," "oocyte meiosis," "maturity onset diabetes of the young," "nicotine addiction," "linoleic acid metabolism," and "bile secretion" (Supplementary Figure 1A), whereas the Down-DEGs were mainly involved in "calcium signaling pathway," "metabolic pathways," "neuroactive ligand-receptor interaction," "focal adhesion," "cAMP signaling pathway," "arrhythmogenic right ventricular cardiomyopathy (ARVC)," "dilated cardiomyopathy (DCM)," "hypertrophic cardiomyopathy (HCM)," "gastric acid secretion," and "PI3K-Akt signaling pathway" (Supplementary Figure 1B).

These results suggest the importance of these pathways in PCa medical mechanisms.

3.3. Core Protein-Protein Interaction (PPI) Networks in Prostate Cancer. To do further functional research of the

DEGs, the STRING database providing functional association networks was retrieved. First, the identified Up-DEGs and Down-DEGs were, respectively, submitted to the STRING database to construct PPI networks. And "the minimum required interaction score" was set to the "highest confidence (>0.9)" to filter high-confident interactions. Next, to discover core protein clusters hidden under the huge networks, MCODE clustering algorithms in Cytoscape 3.8.2 were applied. The score of key PPI nodes was calculated using the k-core decomposition algorithm, and the functional clusters with scores ≥ 7, referred to as the "core protein clusters," were screened out.

In the PPI network of the Up-DEGs, there are 907 nodes and 1307 edges retained, and the average node degree is 2.88. The expected number of edges is 497, and the network has significantly more interactions than expected (the PPI enrichment p value < 1.0e-16) (not shown). Finally, five core protein clusters of Up-DEGs were constructed (Figure 3). Cluster 1 has the maximum score 27.676, with 38 nodes and 512 edges, including known cancer-related genes, such as BUB1 (mitotic checkpoint serine/threonine-protein kinase BUB1), CDC20 (cell division cycle protein 20 homolog), and PLK1 (serine/threonine-protein kinase PLK1). Cluster 2 has 28 nodes and 198 edges, including proteins

PPI clusters of down-DEGs
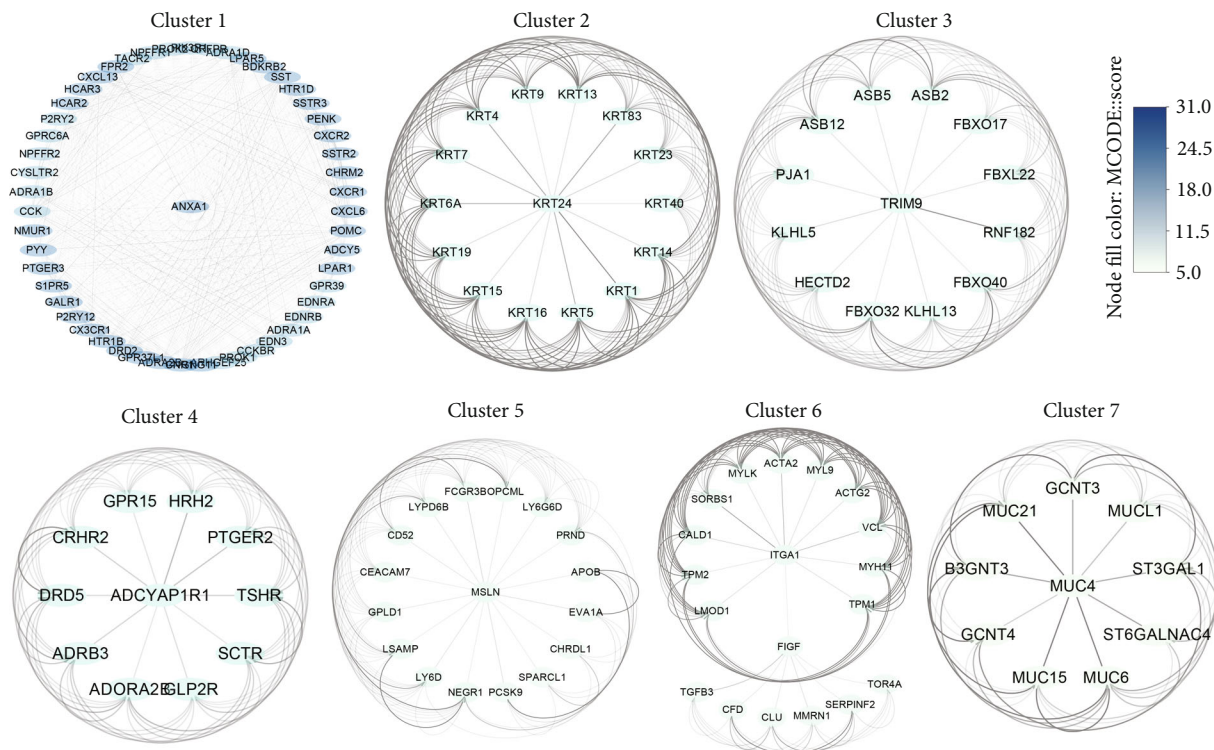
FIGURE 4: Core protein-protein interaction (PPI) networks of Down-DEGs. The network nodes are proteins. The edges represent the predicted functional associations. The node fill color mapped the MCODE score, reflecting the density of the nodes and the surrounding nodes. The edge transparency represents the combined interaction score between two nodes.

in the coagulation system, such as KNG1 (kininogen-1) and F5 (pronounced factor five). Cluster 3 has 9 nodes and 36 edges, including the GRPR (gastrin-releasing peptide receptor) which is known to be expressed in numerous cancers. Furthermore, there are 8 nodes and 8 edges in both cluster 4 and cluster 5.

In the PPI network of the Down-DEGs, 1668 nodes and 2524 edges were identified, and the average node degree is 3.03. The expected number of edges is 1389, and the network has significantly more interactions than expected (the PPI enrichment p value < 1.0e-16) (not shown). Finally, seven core protein clusters of Down-DEGs were constructed (Figure 4). Cluster 1 has the maximum score 32.549, with 52 nodes and 830 edges, including known cancer-related genes, such as ANXA1 (annexin A1) and SSTR2 (somatostatin receptor type 2). Cluster 2 has 15 nodes and 105 edges, including KRT (keratin) family proteins whose expression is helpful in determining the epithelial origin in anaplastic cancers. Cluster 3 has 13 nodes and 78 edges, including the FBXO32 (F-box only protein 32) which was reported to be associated with tumorigenesis. Further, there are 11 nodes and 55 edges in cluster 4, 17 nodes and 81 edges in cluster 5, 19 nodes and 88 edges in cluster 6, and 10 nodes and 40 edges in cluster 7.

The above results suggest that all of these PPI interactions in the core protein clusters play essential roles in prostate cancer regulation networks and deserved further research.

3.4. Well-Grounded miRNA-Gene Regulation Networks in PCa.
To explore how miRNAs respond in prostate cancer, we collected miRNA-Seq datasets from the TCGA-PRAD project, including 449 tumor samples and 52 normal samples, and performed miRNA-Seq analyses.

Firstly, differential expression analyses uncovered DEmiRNAs either upregulated or downregulated in comparison between tumor and normal. In total, 70 DEmiRNAs were identified, and the screening criteria were (1) |logFC | > 1, (2) $p < 0.05$, and (3) FDR < 0.05. The MA plot gives a quick overview of the 50 upregulated DEmiRNAs (Up-DEmiRNAs) and 20 downregulated DEmiRNAs (Down-DEmiRNAs) (Figure 5(a)).

Compared to PCa-related miRNAs in miRCancer (miRNA Cancer Association Database), 24 DEmiRNAs identified in this study were also found in miRCancer, but we also detected more than half of DEmiRNAs (65.7%, 46/70) that have potential to be actionable miRNAs in prostate cancer (Figure 5(b)).

Subsequently, the DEGs in the five upregulated core protein clusters and the seven downregulated core protein clusters were uploaded as "seeds" to the miRTarBase (experimentally validated miRNA-target interaction database), and the miRNA-DEG interaction network verified by comprehensive experiments was obtained. The results showed that in the core protein cluster, 91 Up-DEGs interacted with 829 miRNAs and 137 Down-DEGs interacted with 791 miRNAs.

(a) (b)
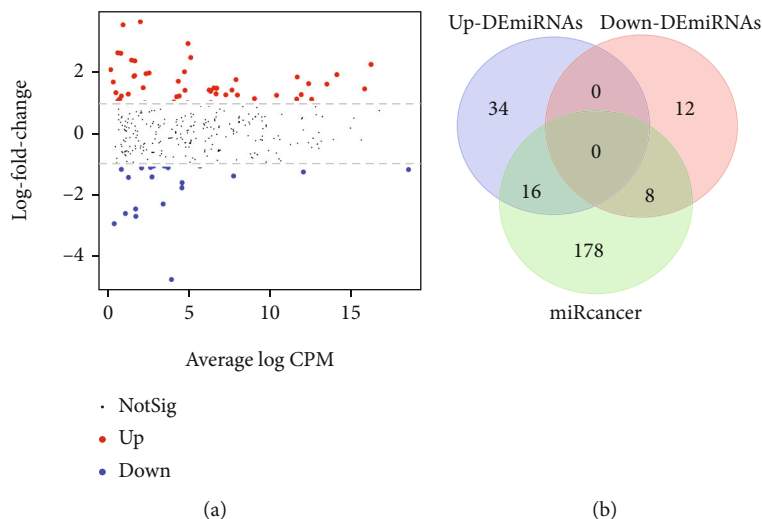
Figure 5: Differentially expressed miRNAs (DEmiRNAs) between PCa and normal samples. (a) The MA plot of DEmiRNAs. (b) Venn diagram of DEmiRNAs overlapped with PCa-related miRNAs in miRCancer.

Lastly, miRNAs are noncoding single-stranded small molecular RNAs that are highly conserved in evolution and regulate gene expression through translational inhibition. Therefore, the 791 miRNAs that were found to interact with the 137 downregulated "seeds" were crossed with the 50 Up-DEmiRNAs; this revealed 22 Up-DEmiRNAs (hsa-mir-500a, hsa-mir-17, hsa-mir-425, hsa-mir-20b, hsa-mir-508, hsa-mir-3074, hsa-mir-106a, hsa-mir-183, hsa-mir-25, hsa-mir-18a, hsa-mir-342, hsa-mir-20a, hsa-mir-93, hsa-mir-3653, hsa-mir-561, hsa-mir-200c, has-mir-96, has-mir-148a, has-mir-1304, has-mir-146b, has-mir-7-1, and has-mir-5586) that could predict the gene expression regulation in PCa (Figure 6(a)). Next, the 829 miRNAs that were found to interact with the 91 upregulated "seeds" were crossed with the 20 Down-DEmiRNAs; this revealed 11 Down-DEmiRNAs (hsa-mir-187, hsa-mir-1251, hsa-mir-889, hsa-mir-204, hsa-mir-222, hsa-mir-221, hsa-mir-23c, hsa-mir-143, hsa-mir-10a, hsa-mir-652, and hsa-mir-450b) that could predict the gene expression regulation in PCa (Figure 6(b)).

Taken together, we constructed the experimentally validated high-confident regulation networks of the DEmiRNAs and the corresponding DEGs in PCa, which indicate that these miRNA-Gene interactions play essential roles in PCa molecular regulation.

4. Discussion

In this study, we attempted to identify tumor microenvironment-related genes/miRNAs from the TCGA database that contribute to PCa occurrence and development. First, there were 2145 upregulated genes and 2194 downregulated DEGs between PCa and normal samples. Next, the DEGs, were subsequently subjected to GO and KEGG pathway enrichment analysis, which showed that these DEGs were significantly enriched in the functional modules and biological process of cancer development, and indicated some significant characteristics of PCa, such as

hyperactivity of immune response [14], hormone activity, diabetes [15, 16], and nicotine addiction [17]. Finally, the results of PPI network analysis and prostate tissue-specific gene coexpression network analysis revealed that six upregulated genes (BUB1B, F5, KNG1, CCKAR, HTR4, and LY6G6C) and eight downregulated genes (ANXA1, KRT24, TRIM9, ADCYAP1R1, MSLN, ITGA1, FIGF, and MUC4) were present as the core genes in the prostate tissue-specific gene coexpression network.

These genes play an important role in various human cancers, including prostate cancer. For example, Rajan et al. identified seven hub genes (ADAM7, fam72b, BUB1B, ccnb1, ccnb2, TTK, and cdk172) related to cell cycle in prostate biopsy tissues before and after docetaxel chemotherapy and androgen deprivation therapy in patients with advanced hormone-naive prostate cancer [18]. BUB1B also had differential expressions in our results. BUB1B is a key mitotic checkpoint kinase. Ding et al. identified BUB1B as the top-scoring kinase by RNA interference and bioinformatics analysis, which can monitor proper spindle microtubule attachment to the kinetochore, and it is knocked down inducing mitotic catastrophe and cell death in glioblastoma [19, 20]. The above research suggests that BUB1B has potential to be a novel antimitotic target in some cancers, including prostate cancer.

For another example, our study found that the expression of ANXIA1 is downregulated in prostate cancer, and the results are also proven in other literatures [21–23], which occurs in the early stage of cancer or intraepithelial tumor transformation of prostate cancer and becomes more prominent with the development of cancer. Inokuchi et al. proved that reducing the expression of ANXA1 can enhance the invasion of prostate cancer tumor by upregulating the expression and activity of IL-6 [24]. Therefore, the loss of ANXA1 may be a useful marker for the development and progression of prostate cancer. However, some studies have proven that the expression of ANXA1 is negatively

(a)

(b)
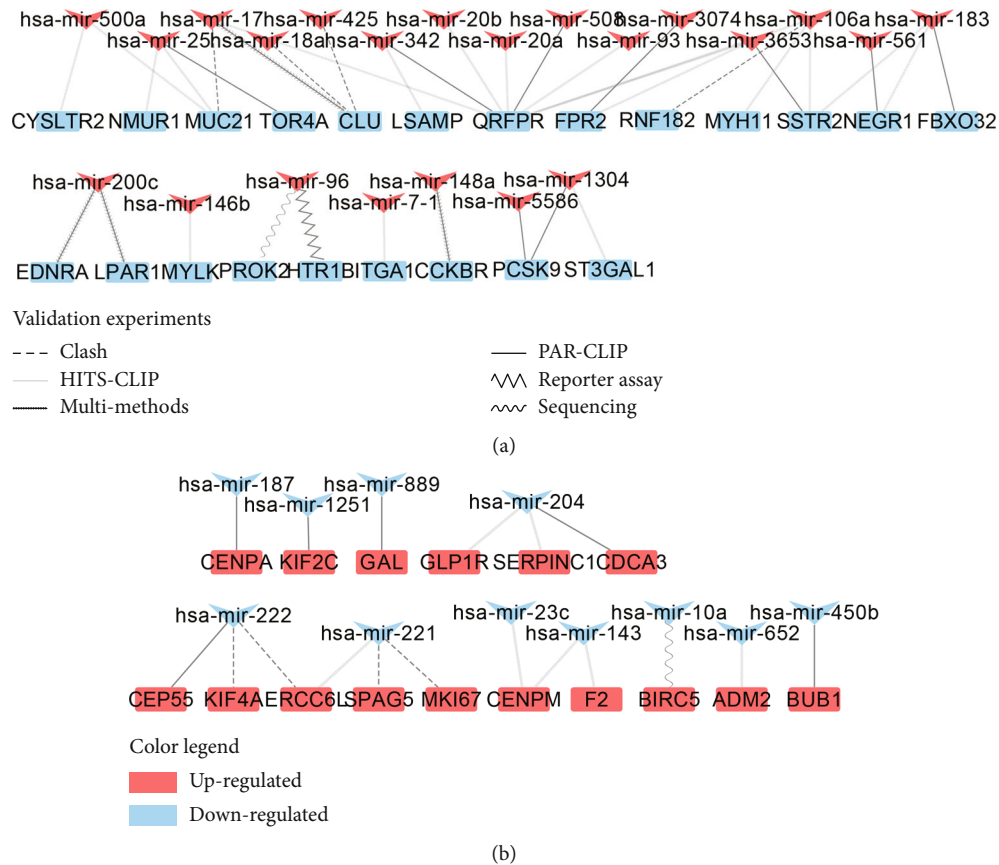
FIGURE 6: Experimentally validated DEmiRNA-DEG interaction networks: (a) Up-DEmiRNAs targeted Down-DEGs; (b) Down-DEmiRNAs targeted Up-DEGs. Line types indicate validation experiments of the interactions. "Multi-methods" includes luciferase reporter assay, qRT-PCR, and Western blot.

correlated with androgen receptor (AR), and the expression of ANXA1 increases after AR knockdown or AR antagonists are used, which accelerates the invasion and metastasis of advanced PCa [25, 26]. ANXA1 may act as a tumor inhibitor in the early stage of cancer, but in the late stage of cancer, it may play the opposite role. To sum up, as a "double-edged sword," the clinical research and treatment of using ANXA1 as tumor inhibitors should be cautious and limited.

The F5 gene, which is the most common genetic coagulation factor mutation, also increases the risk of thrombosis. Garber et al. found that F5 gene variation was associated with breast cancer. The F5 expression was enriched in breast cancer and was associated with overall survival [27]; moreover, the F5 gene was associated with the risk of thrombosis in cancer patients [28]. F5 is also associated with the risk of thrombosis in patients with metastatic androgen-dependent prostate cancer who undergo diethylstilbestrol and docetaxel chemotherapy [29]. This provides an interesting direction for further research to strengthen the relationship between cancer and coagulation.

MUC4 usually plays an important role in the pathogenesis of pancreatic, ovarian, and breast malignancies [30–32]. Through abnormal overexpression, MUC4 can interact with HER2 (a ligand-dependent receptor tyrosine kinase) physically and phosphorylated activate and stabilize HER2 to pro-

mote tumor invasion and metastasis. Our study has proven that MUC4 is downregulated in prostate cancer tissues, like other literatures [33, 34]. In line with our results, Dizeyi et al. found that the HTR4 expression was upregulated in prostate cancer [35]. They found that HTR4 is associated with the late progression of hormone refractory prostate cancer, possibly due to the paracrine/autocrine mechanism of HTR4-induced hormones or growth factors, and HTR4 is also associated with estrogen receptor α and estrogen receptor β. The overexpression of the receptor of the neuroendocrine cell product may be related to the occurrence of hormone refractory prostate cancer, which provides a new direction for the trigonometric relationship between cancer neuroendocrine sex hormones. Our study first described the upregulation of KNG1 and CCKAR in prostate cancer. Previous studies have described the presence of KNG1 and CCKAR as biomarkers of various types of cancer, such as thyroid cancer [36, 37], liver cancer [38], ovarian cancer [39], and cholangiocarcinoma [40]. In different stages of PCa development and progression, especially in the process of hormone-sensitive PCa progressing to castration-resistant PCa, the proteomic alterations and transcriptomic data have significant differences in changes [41]. By analyzing the microarray-based profiling data of isogenic prostate cancer xenograft models published by Chen et al. [42], we found that the differentially expressed genes of hormone-sensitive

PCa compared with castration-resistant PCa included BUB1B, ADCYAP1R1, HTR4, and LY6G6C, which was also proposed in our study. These results indicate that the core of this study has the potential to become a new biomarker of prostate cancer, especially for the prognosis evaluation of castration-resistant PCa.

In addition, our study also reported the full expression of microRNA in prostate cancer and predicted the micro-RNA/mRNA interaction network in a very reliable way. In this study, several microRNAs were first proposed to upregulate or downregulate differential expression in prostate cancer tissues. Some of them have been reported in the literature. For instance, Schaefer et al. found that 15 differentially expressed microRNAs were related to the diagnosis and prognosis of prostate cancer [43], of which the upregulated hsa-mir-183 and downregulated hsa-miR-222 overlap our results. hsa-mir-25 is related to the invasion of prostate cancer and may be a signaling mechanism of aurora kinase A or integrin [44]. Yang et al. found that hsa-mir-93 can act as a tumor promoter through the regulatory axis Dab2/AKT/ERK1/2 [45]. hsa-mir-200c can reverse the epithelial stromal transformation of prostate cancer [46]. hsa-mir-204 has been widely studied in prostate cancer, which is negatively related to the expression of UCA1 and plays a role in tumor metastasis and sensitivity to chemotherapy [47]. The functions of these miRNAs in prostate cancer deserve further investigation.

5. Conclusions

We constructed a series of functional networks centered on core genes involved in PCa. These networks provide new ideas for future research on the occurrence, development, and metastasis of PCa and also indicate potential new targets and biomarkers for its clinical treatment and diagnosis, respectively.

Data Availability

The datasets used and/or analyzed during the current study are available from the corresponding authors on reasonable request.

Conflicts of Interest

The authors declare that there are no conflicts of interest regarding the publication of this manuscript.

Authors' Contributions

LHY and LLR collected the data. LYP and FY conducted the statistical analysis. LHY and XW wrote the manuscript. ZCH and XW made appropriate modifications and suggestions on the manuscript. All authors read and approved the final manuscript. Heyu Liu and Lirong Li contributed equally to this work.

Supplementary Materials

Figure 1: KEGG pathway of DEGs in prostate cancer response mechanisms. (Supplementary Materials)

References

[1] R. L. Siegel, K. D. Miller, and A. Jemal, "Cancer statistics, 2019," CA: a Cancer Journal for Clinicians, vol. 69, no. 1, pp. 7–34, 2019.

[2] M. Gamat and D. G. McNeel, "Androgen deprivation and immunotherapy for the treatment of prostate cancer," Endocrine-Related Cancer, vol. 24, no. 12, pp. T297–T310, 2017.

[3] T. A. Yap, A. D. Smith, R. Ferraldeschi, B. Al-Lazikani, P. Workman, and J. S. de Bono, "Drug discovery in advanced prostate cancer: translating biology into therapy," Nature Reviews. Drug Discovery, vol. 15, no. 10, pp. 699–718, 2016.

[4] A. R. Jones and S. J. Hubbard, "An introduction to proteome bioinformatics," Methods in Molecular Biology, vol. 604, pp. 1–5, 2010.

[5] V. Ambros, "The functions of animal microRNAs," Nature, vol. 431, no. 7006, pp. 350–355, 2004.

[6] G. A. Calin, C. Sevignani, C. D. Dumitru et al., "Human microRNA genes are frequently located at fragile sites and genomic regions involved in cancers," Proceedings of the National Academy of Sciences of the United States of America, vol. 101, no. 9, pp. 2999–3004, 2004.

[7] J. Qi and D. Mu, "MicroRNAs and lung cancers: from pathogenesis to clinical implications," Frontiers in Medicine, vol. 6, no. 2, pp. 134–155, 2012.

[8] A. R. Halvorsen, Å. Helland, P. Gromov et al., "Profiling of microRNAs in tumor interstitial fluid of breast tumors - a novel resource to identify biomarkers for prognostic classification and detection of cancer," Molecular Oncology, vol. 11, no. 2, pp. 220–234, 2017.

[9] "The Cancer Genome Atlas Program," 2019, https://tcga-data.nci.nih.gov/docs/publications/tcga/.

[10] "STRING: functional protein association networks," 2019, https://string-db.org/.

[11] P. Shannon, A. Markiel, O. Ozier et al., "Cytoscape: a software environment for integrated models of biomolecular interaction networks," Genome Research, vol. 13, no. 11, pp. 2498–2504, 2003.

[12] D. Karagkouni, M. D. Paraskevopoulou, S. Chatzopoulos et al., "DIANA-TarBase v8: a decade-long collection of experimentally supported miRNA–gene interactions," Nucleic Acids Research, vol. 46, no. D1, pp. D239–D245, 2018.

[13] "miRTarBase update 2018: a resource for experimentally validated microRNA-target interactions," 2019, http://mirtarbase.mbc.nctu.edu.tw.

[14] J. Dai, Y. Lu, and H. Roca, "Immune mediators in the tumor microenvironment of prostate cancer," Chinese Journal of Cancer, vol. 36, no. 1, p. 29, 2017.

[15] P.-C. Hsu, W.-H. Lin, T.-H. Kuo, H.-M. Lee, C. Kuo, and C.-Y. Li, "A population-based cohort study of all-cause and site-specific cancer incidence among patients with type 1 diabetes mellitus in Taiwan," Journal of Epidemiology, vol. 25, no. 9, pp. 567–573, 2015.

[16] M. LaTayia, T. S. Aaron-Brooks, R. E. Vickman et al., "Hyperglycemia and T cell infiltration are associated with stromal and

epithelial prostatic hyperplasia in the nonobese diabetic mouse," *The Prostate*, vol. 79, no. 9, pp. 980–993, 2019.

[17] R. L. Prueitt, T. A. Wallace, S. A. Glynn et al., "An immune-inflammation gene expression signature in prostate tumors of smokers," *Cancer Research*, vol. 76, no. 5, pp. 1055–1065, 2016.

[18] P. Rajan, J. Stockley, I. M. Sudbery et al., "Identification of a candidate prognostic gene signature by transcriptome analysis of matched pre- and post-treatment prostatic biopsies from patients with advanced prostate cancer," *BMC Cancer*, vol. 14, no. 1, p. 977, 2014.

[19] M. Venere, "Mitotic control of cancer stem cells," *Cancer Discovery*, vol. 3, no. 2, pp. 141–144, 2013.

[20] D. Yu, C. G. Hubert, J. Herman et al., "Cancer-specific requirement for BUB1B/BubR1 in human brain tumor isolates and genetically transformed cells," *Cancer Discovery*, vol. 3, no. 2, pp. 198–211, 2013.

[21] C. P. Paweletz, D. K. Ornstein, M. J. Roth et al., "Loss of annexin 1 correlates with early onset of tumorigenesis in esophageal and prostate carcinoma," *Cancer Research*, vol. 60, no. 22, pp. 6293–6297, 2000.

[22] J. S. Kang, B. F. Calvo, S. J. Maygarden, L. S. Caskey, J. L. Mohler, and D. K. Ornstein, "Dysregulation of annexin I protein expression in high-grade prostatic intraepithelial neoplasia and prostate cancer," *Clinical Cancer Research*, vol. 8, no. 1, pp. 117–123, 2002.

[23] K. T. Patton, H. M. Chen, L. Joseph, and X. J. Yang, "Decreased annexin I expression in prostatic adenocarcinoma and in high-grade prostatic intraepithelial neoplasia," *Histopathology*, vol. 47, no. 6, pp. 597–601, 2005.

[24] J. Inokuchi, A. Lau, D. R. Tyson, and D. K. Ornstein, "Loss of annexin A1 disrupts normal prostate glandular structure by inducing autocrine IL-6 signaling," *Carcinogenesis*, vol. 30, no. 7, pp. 1082–1088, 2009.

[25] W. Yang, K. Wang, J. Ma et al., "Inhibition of androgen receptor signaling promotes prostate cancer cell migration via upregulation of annexin A1 expression," *Archives of Medical Research*, vol. 52, no. 2, pp. 174–181, 2021.

[26] F. Yang, J. Cai, H. Zhan et al., "Suppression of TRPM7 Inhibited Hypoxia-Induced Migration and Invasion of Androgen-Independent Prostate Cancer Cells by Enhancing RACK1-Mediated Degradation of HIF-1α," *Oxidative Medicine and Cellular Longevity*, vol. 2020, Article ID 6724810, 15 pages, 2020.

[27] M. Tinholt, B. Stavik, X. Tekpli et al., "Coagulation factor V is a marker of tumor-infiltrating immune cells in breast cancer," *Oncoimmunology*, vol. 9, no. 1, article 1824644, 2020.

[28] J. E. Garber, S. Halabi, S. M. Tolaney et al., "Factor V Leiden mutation and thromboembolism risk in women receiving adjuvant tamoxifen for breast cancer," *Journal of the National Cancer Institute*, vol. 102, no. 13, pp. 942–949, 2010.

[29] R. Bruce Montgomery, P. S. Nelson, D. Lin, C. W. Ryan, M. Garzotto, and T. M. Beer, "Diethylstilbestrol and docetaxel: a phase II study of tubulin active agents in patients with metastatic, androgen-independent prostate cancer," *Cancer*, vol. 110, no. 5, pp. 996–1002, 2007.

[30] S. Kaur and N. Sharma, "MUC4-mediated regulation of acute phase protein lipocalin 2 through HER2/AKT/NF-κB signaling in pancreatic cancer," *Clinical Cancer Research*, vol. 20, no. 3, pp. 688–700, 2014.

[31] M. P. Ponnusamy, A. P. Singh, M. Jain, S. Chakraborty, and N. Moniaux, "MUC4 activates HER2 signalling and enhances the motility of human ovarian cancer cells," *British Journal of Cancer*, vol. 99, no. 3, pp. 520–526, 2008.

[32] M. F. Mercogliano, M. De Martino, L. Venturutti et al., "TNFα-induced mucin 4 expression elicits trastuzumab resistance in HER2-positive breast cancer," *Clinical Cancer Research*, vol. 23, no. 3, pp. 636–648, 2017.

[33] A. P. Singh, S. C. Chauhan, S. Bafna et al., "Aberrant expression of transmembrane mucins, MUC1 and MUC4, in human prostate carcinomas," *The Prostate*, vol. 66, no. 4, pp. 421–429, 2006.

[34] S. Zhang, H. S. Zhang, V. E. Reuter, S. F. Slovin, H. I. Scher, and P. O. Livingston, "Expression of potential target antigens for immunotherapy on primary and metastatic prostate cancers," *Clinical Cancer Research*, vol. 4, no. 2, pp. 295–302, 1998.

[35] N. Dizeyi, A. Bjartell, P. Hedlund, K. A. Taskén, V. Gadaleanu, and P.-A. Abrahamsson, "Expression of serotonin receptors 2B and 4 in human prostate cancer tissue and effects of their antagonists on prostate cancer cell lines," *European Urology*, vol. 47, no. 6, pp. 895–900, 2005.

[36] J. Tang, D. Kong, Q. Cui et al., "Bioinformatic analysis and identification of potential prognostic microRNAs and mRNAs in thyroid cancer," *PeerJ*, vol. 6, article e4674, 2018.

[37] J. Yu, Y. Huang, C. Lin et al., "Identification of kininogen 1 as a serum protein marker of colorectal adenoma in patients with a family history of colorectal cancer," *Journal of Cancer*, vol. 9, no. 3, pp. 540–547, 2018.

[38] W. Jiang, L. Zhang, Q. Guo et al., "Identification of the pathogenic biomarkers for hepatocellular carcinoma based on RNA-seq analyses," *Pathology Oncology Research*, vol. 25, no. 3, pp. 1207–1213, 2019.

[39] J. Zhang, S. Huang, L. Quan et al., "Determination of potential therapeutic targets and prognostic markers of ovarian cancer by bioinformatics analysis," *BioMed Research International*, vol. 2021, Article ID 8883800, 13 pages, 2021.

[40] H.-L. Xu, "Variants in CCK and CCKAR genes to susceptibility to biliary tract cancers and stones: a population-based study in Shanghai, China," *Journal of Gastroenterology and Hepatology*, vol. 28, no. 9, pp. 1476–1481, 2013.

[41] S. Varambally, J. Yu, B. Laxman et al., "Integrative genomic and proteomic analysis of prostate cancer reveals signatures of metastatic progression," *Cancer Cell*, vol. 8, no. 5, pp. 393–406, 2005.

[42] C. D. Chen, D. S. Welsbie, C. Tran et al., "Molecular determinants of resistance to antiandrogen therapy," *Nature Medicine*, vol. 10, no. 1, pp. 33–39, 2004.

[43] A. Schaefer, M. Jung, H.-J. Mollenkopf et al., "Diagnostic and prognostic implications of microRNA profiling in prostate carcinoma," *International Journal of Cancer*, vol. 126, no. 5, pp. 1166–1176, 2010.

[44] E. Zoni and G. van der Horst, "miR-25 modulates invasiveness and dissemination of human prostate cancer cells via regulation of αv- and α6-integrin expression," *Cancer Research*, vol. 75, no. 11, pp. 2326–2336, 2015.

[45] K. Yang, Y.-W. Li, Z.-Y. Gao et al., "miR-93 functions as a tumor promoter in prostate cancer by targeting disabled homolog 2 (DAB2) and an antitumor polysaccharide from green tea (Camellia sinensis) on their expression," *International Journal of Biological Macromolecules*, vol. 125, pp. 557–565, 2019.

[46] S. Basu, A. Chaudhary, P. Chowdhury et al., "Evaluating the role of hsa-miR-200c in reversing the epithelial to mesenchymal transition in prostate cancer," *Gene*, vol. 730, article 144264, 2020.

[47] C. He, X. Lu, F. Yang et al., "LncRNA UCA1 acts as a sponge of miR-204 to up-regulate CXCR4 expression and promote prostate cancer progression," *Bioscience Reports*, vol. 39, no. 5, 2019.

Retraction

Retracted: Stearoyl-CoA Desaturase 1 Potentiates Hypoxic plus Nutrient-Deprived Pancreatic Cancer Cell Ferroptosis Resistance

Oxidative Medicine and Cellular Longevity

Oxidative Medicine and Cellular Longevity has retracted the article titled "Stearoyl-CoA Desaturase 1 Potentiates Hypoxic plus Nutrient-Deprived Pancreatic Cancer Cell Ferroptosis Resistance" [1] due to concerns with figure duplications in Figure 1(b) as originally noted on PubPeer [2]. Specifically, the DMSO Nor panel is duplicated with the DMSO H/NS panel, and the Erastin Nor+Fer-1 panel is duplicated with the SAS Nor+Fer-1 panel. In both cases, the field of view is different between the panels. The author responded to explain that the duplications were introduced due to an error when preparing their manuscript, however, this did not satisfy the concerns of the editorial board and the article is retracted due to concerns with the reliability of the data.

The authors do not agree to the retraction.

References

[1] J. Gao, Z. Zhang, Y. Liu et al., "Stearoyl-CoA Desaturase 1 Potentiates Hypoxic plus Nutrient-Deprived Pancreatic Cancer Cell Ferroptosis Resistance," *Oxidative Medicine and Cellular Longevity*, vol. 2021, 14 pages, 2021.

[2] 2021, https://pubpeer.com/publications/0E8247FC6B3045A767D1AB34FB4BB5.

Research Article

Stearoyl-CoA Desaturase 1 Potentiates Hypoxic plus Nutrient-Deprived Pancreatic Cancer Cell Ferroptosis Resistance

Jie Gao,[1] Zhengyang Zhang [ID],[1] Yanfang Liu,[2] Zining Zhang,[1] Ming Wang,[1] Aihua Gong,[2] Lin Xia,[3] Xiang Liao [ID],[1] Dongqing Wang [ID],[1] and Haitao Zhu [ID][1]

[1]*Department of Medical Imaging, The Affiliated Hospital of Jiangsu University, Zhenjiang, China 212001*
[2]*School of Medicine, Jiangsu University, Zhenjiang, China 212013*
[3]*International Genome Center, Jiangsu University, Zhenjiang, China 212013*

Correspondence should be addressed to Xiang Liao; liaoxiang025@126.com, Dongqing Wang; wangdongqing71@163.com, and Haitao Zhu; zhht25@163.com

Hypoxia and nutrient starvation (H/NS) microenvironment, a notable characteristic of pancreatic carcinoma, plays a critical role in cell death resistance and tumor recurrence. However, its role in ferroptosis remains to be classified. Here, we found that H/NS contributed to the pancreatic cancer cell ferroptosis resistance depending on the altered intracellular lipid compositions. Mechanistically, H/NS induced the upregulation of stearoyl-CoA desaturase 1 (SCD1), which promoted monounsaturated fatty acids (MUFAs) synthesis and protected against lipid peroxidation. Surprisingly, SCD1 showed a strong correlation with antiferroptosis gene expression. Moreover, short-hairpin RNA-based knockdown of SCD1 enhanced erastin-induced ferroptosis *in vitro* under H/NS. Finally, our results demonstrate the synergistic effect of erastin and A939572, a special SCD1 inhibitor, in dictating pancreatic carcinoma subcutaneous ferroptotic death. Taken together, our findings reveal a new role of the H/NS microenvironment against ferroptosis and suggest a potential therapeutic strategy for overcoming ferroptosis resistance in pancreatic cancer cells.

1. Introduction

Due to the imbalance of unlimited proliferation of cancer cells and poor supplement of blood vessels, hypoxia and nutrient starvation (H/NS) has been recognized as the most important characteristic of pancreatic carcinoma microenvironment [1, 2]. H/NS microenvironment is not only the driver of pancreatic cancer cell growth and metastasis but also inducing cancer cell death resistance, which ultimately results in therapy failure. Therefore, it is necessary to investigate the mechanisms underlying the H/NS microenvironment mediating the cancer cell death resistance.

Ferroptosis, a newly identified type of programmed cell death, is characterized by iron-dependent lipid peroxidation [3]. Recently, more and more researches demonstrated tumor microenvironment, and energy materials were also

critical regulators of ferroptosis [4, 5]. However, the exact mechanisms were still unclear. Under H/NS, cancer cells mostly depended on metabolism reprogramming, such as elevated de novo synthesis of fatty acids (FAs), for the sake of thriving [6, 7]. Extensive researches show that ferroptosis was tightly related to the FA balance. Polyunsaturated fatty acids (PUFAs) promote free radical generation and lipid peroxide accumulation, which act as a trigger for ferroptosis [8, 9]. Monounsaturated fatty acids (MUFAs) block the lipid ROS accumulation on the plasma membrane and further induce the ferroptosis-resistant state [10]. Stearoyl-CoA desaturase 1 (SCD1), a critical regulator of de novo synthesis, catalyzes the desaturation of saturated fatty acids (SFAs) to MUFAs [11]. These findings suggested that SCD1 may be involved in H/NS microenvironment-induced ferroptotic cell death resistance in cancer cells.

To test this hypothesis, we show that pancreatic cancer cells under H/NS condition are associated with the upregulation of SCD1 expression and ferroptosis inducer resistance. Silencing of SCD1 in H/NS cultured pancreatic cancer cells enhanced erastin induced ferroptosis *in vitro* and *in vivo*, which suggests a potential ferroptosis-based therapeutic strategy for pancreatic cancer.

2. Materials and Methods

2.1. Cell Culture. Human pancreatic cancer cell lines (BXPC3, SW1990, PANC1, and Patu8988) and mice pancreatic cancer cell line Panc02 were obtained from the Cell Bank of the China Academy of Sciences (Shanghai, China). Cells were cultured in high glucose Dulbecco's modified Eagle medium (DMEM) with 10% fetal bovine serum (FBS; ExCell FSP500) and antibiotics (100 units/mL penicillin, 100 mg/mL streptomycin) at 37°C in an incubator with a humidified atmosphere of 5% CO_2. Hypoxic (H) incubation was performed at 94% N_2, 5% CO_2, and 1% O_2. Nutrient starvation (NS) condition was performed in DMEM with 2% FBS and antibiotics (100 units/mL penicillin, 100 mg/mL streptomycin). H/NS condition was performed in DMEM with 2% FBS and antibiotics (100 units/mL penicillin, 100 mg/mL streptomycin) at 94% N_2, 5% CO_2, and 1% O_2 for the indicated time (6, 12, and 24 hours).

2.2. Reagents. Erastin (#HY-15763), (1S,3R)-RSL3 (RSL3; #HY-100218A), sulfasalazine (SAS, #HY-14655), oleic acid (OA; #HY-N1446), or ferrostatin-1(Fer-1; #HY-100579) were purchased from MedChemExpress (MCE, USA). BODIPY-C11 (#D2861) was obtained from Invitrogen. Propidium iodide (PI) was purchased from KeyGEN BioTECH.

2.3. Cell Viability Assay. Cell viability was measured using Cell Counting Kit-8 (CCK-8; Dojindo, #CK04). PANC1 and Patu8988 cells were seeded into 96-well plates overnight, then exposed to conditions, and treated with reagents as indicated at the indicated time (6, 12, and 24 hours). Subsequently, 10 μL of the CCK-8 solution with 90 μL DMEM was added to each well of the plate to replace the original medium, incubated for 1-4 h at 37°C, 5% CO_2. Then, the absorbance (OD value) at wavelengths of 450 nm was measured with a microplate reader (Biotek, #Epoch2).

Cells were seeded in 12-well plates at appropriate cell density and incubated overnight at 37°C containing 5% CO_2 and then exposed to conditions and treated with reagents as indicated. Cell death was analyzed by SYTOX green (Invitrogen) or PI staining (KeyGEN) with microscopy.

2.4. Lipid Peroxidation Assay. The relative MDA level in cells or tumor issues lysates was measured using a Lipid Peroxidation (MDA) Assay Kit (Abcam, ab118970), and the experiments were carried out as described previously [12]. Cells or tumor tissues were homogenized with lysis buffer and the MDA in samples reacts with thiobarbituric acid (TBA) to generate an MDA-TBA adduct which can be quantified colorimetrically (OD = 532 nm).

C11-BODIPY imaging assay was performed to evaluate lipid peroxidation in cells. Briefly, cells were collected and stained with 5 μM of BODIPY-C11 dye and 5 μg/ml of DAPI.

Pictures were photographed with a fluorescent microscope (Nikon, Japan).

2.5. Western Blot. Cells were lysed on ice for 30 min and centrifuged at 12,000×g for 10 min at 4°C. Protein concentrations were quantified using the bicinchoninic acid (BCA) assay (Invitrogen, #23225). Western blot assay was performed as described previously [13]. Antibodies were as follows: anti-human GPX4 (Abcam, #ab41787, 1 : 1000), anti-human SCD1 (Abcam, #ab19862, 1 : 1000), anti-human ACSL4 (Proteintech, #22401-1-AP, 1 : 1000), anti-human FTH1 (CST, #4393, 1 : 1000), anti-human NRF2 (CST, #12721, 1 : 1000), and anti-human β-tubulin (Abcam, #ab6046, 1 : 1000). Secondary antibody (either anti-rabbit or anti-mouse) was purchased from Thermo Fisher Scientific (Invitrogen). The blots were analyzed using the software ImageJ (Version 1.80, NIH, USA).

2.6. Quantitative Real-Time Polymerase Chain Reaction Assay (qRT-PCR). Total RNA was extracted using RNAiso Plus (Takara) according to the manufacturer's instructions. For mRNA analysis, cDNA was synthesized from 1 μg total RNA using the RevertAid First-Strand cDNA Synthesis Kit (Thermo, #K1622). The experiment was performed for reverse transcription according to the manufacturer's instructions. Subsequently, SYBR Green-based real-time PCR was performed in triplicate using SYBR Green master mix (Vazyme) on a QuantStudio 3 real-time PCR machine (Invitrogen). For analysis, the threshold cycle (Ct) values for each gene were normalized to expression levels of ACTB. Analysis was performed using the QuantStudio Design and Analysis Software. The primers, which were synthesized and desalted from Genscript, are shown in Table 1.

2.7. RNAi and Gene Transfection. Cancer cells were seeded in 6-well plates to achieve a confluence of 40-50% overnight. To generate knockdown cells, cells were infected with lentivirus carrying shRNA followed by puromycin (1 μg/ml) selection for 10-14 days. These established stable cell lines were maintained in DMEM containing 10% FBS and puromycin (0.75 μg/ml) for further experiments. The specific shRNA sequences are listed in Table 2.

2.8. ELISA Assay. To measure the content of MUFAs, pancreatic cancer cells were seeded in 6 cm dishes to achieve a confluence of 40-50% overnight and then incubated in indicated conditions. Cells were collected and MUFA concentrations were measured using the Human MNSFA ELISA KIT (Fankewei, #F10525, Shanghai, China) according to the manufacturer's instructions.

2.9. Xenograft Tumor Models. Animal studies were approved by the Committee on the Use of Live Animals for Teaching and Research of Jiangsu University. Five-week-old female C57BL/6 mice were obtained from GemPharmatech Company and maintained under standard conditions in the Animal Center of Jiangsu University.

Panc02 cells (5×10^5) were injected subcutaneously into the right dorsal flanks of C57BL/6 mice. When tumors

TABLE 1: Sequences of primers used for qRT-PCR.

Name	Direction	Sequence (5′-3′)
SCD1-human	Forward	CCTGGTTTCACTTGGAGCTGTG
	Reverse	TGTGGTGAAGTTGATGTGCCAGC
FTH1-human	Forward	TCCTACGTTTACCTGTCCATGT
	Reverse	GTTTGTGCAGTTCCAGTAGTGA
ACSL4-human	Forward	GCTATCTCCTCAGACACACCGA
	Reverse	AGGTGCTCCAACTCTGCCAGTA
NRF2-human	Forward	CACATCCAGTCAGAAACCAGTGG
	Reverse	GGAATGTCTGCGCCAAAAGCTG
GPX4-human	Forward	ACAAGAACGGCTGCGTGGTGAA
	Reverse	GCCACACACTTGTGGAGCTAGA
ACTB-human	Forward	CACCATTGGCAATGAGCGGTTC
	Reverse	AGGTCTTTGCGGATGTCCACGT

TABLE 2: Sequences of shRNAs.

Name	Sequence (5′-3′)
SCD1-shRNA1	CCGGCGTCCTTATGACAAGAACATTCTCGAGAATGTTCTTGTCATAAGGACGTTTTTG
SCD1-shRNA2	CCGGCTACGGCTCTTTCTGATCATTCTCGAGAATGATCAGAAAGAGCCGTAGTTTTTG
GPX4-shRNA	GATCGTGGATGAAGATCCAACCCAACTCGAGTTGGGTTGGATCTTCATCCAC TTTTTG

reached a volume of 50-100 mm^3, the mice were randomly divided into four groups (five mice per group) and treated with DMSO (control), erastin (20 mg/kg), A939572 (1 mg/kg), or erastin (20 mg/kg) + A939572 (1 mg/kg) every two days for two weeks. The tumor volume and growth speed were monitored every two days until the end point at day 14.

2.10. Patient Selection. To determine the expression of SCD1 in pancreatic cancer tissues and normal tissues, the datasets in GEO (GSE16515) concluding 52 samples were adopted. The Cancer Genome Atlas (TCGA) database (https://tcga.xenahubs.net/download/TCGA.PAAD.sampleMap/HiSeqV2.gz) including those from 183 pancreatic carcinoma patient specimens were utilized to further analyze the association of SCD1 expression level with overall survival and disease-free survival rate. High and low groups were defined as above and below the quartile, respectively.

2.11. Statistical Analysis. All data are presented as the mean ± standard error of the mean (SEM). Statistical analysis was performed using Prism 8 software. The differences between groups were analyzed using Student's t-tests, one-way analysis of variance (ANOVA), or two-way ANOVA. $P < 0.05$ was considered to reflect a statistically significant difference. All the experiments were repeated at least three times.

3. Results

3.1. Hypoxic and Nutrient-Deprived Condition Protects Pancreatic Cancer Cells from Ferroptosis. Hypoxia combination nutrient starvation (H/NS) is a notable characteristic of pancreatic carcinoma microenvironment and facilitates cancer cell death resistance. We firstly access the role of H/NS on pancreatic cancer cell ferroptosis. Ferroptosis inducer can be divided into system Xc⁻ inhibitors (such as erastin, sorafenib, or sulfasalazine) and GPX4 deletion or inactivation (such as RSL3). Erastin, sulfasalazine, and RSL3 could induce PANC1 and Patu8988 cancer cell death, which could be rescued by ferrostatin-1 (Fer-1), a ferroptosis inhibitor (Figure S1A). To mimic the H/NS condition, PANC1 and Patu8988 cancer cells were cultured with 2% FBS in a hypoxia chamber with 1% O$_2$ and then treated with various ferroptosis inducers. Compared to normal culture condition (control), PANC1 and Patu8988 cancer cells cultured in H/NS condition were more resistant to the ferroptosis inducer for the indicated time (6 h, 12 h, and 24 h), which is similar to the presence of Fer-1 (Figures 1(a) and 1(b), Figure S1B and S1C). Due to GPX4 is a critical regulator of ferroptosis, we constructed a stable GPX4 knockdown PANC1 cell line (Figure S1D) and further evaluated the cell viability under normal and H/NS condition. Compared to parental cancer cells, the cell viability of GPX4-knockdown cancer cell was decreased under normal condition, while little change under H/NS condition (Figure 1(c)). Given that lipid peroxidation is one of the most crucial features in ferroptosis, we next evaluated intracellular malondialdehyde (MDA) levels, an end product of lipid peroxidation. Ferroptosis inducers (erastin, sulfasalazine, or RSL3) increased the MDA levels, which can be abolished under the H/NS condition (Figure 1(d)). The results indicated that H/NS condition rescued ferroptosis inducers or GPX4 depletion induced ferroptosis.

3.2. SCD1 Expression Is Positively Related to Pancreatic Cancer H/NS Condition and Progression. Monounsaturated fatty acids (MUFAs) could block the lipid ROS accumulation
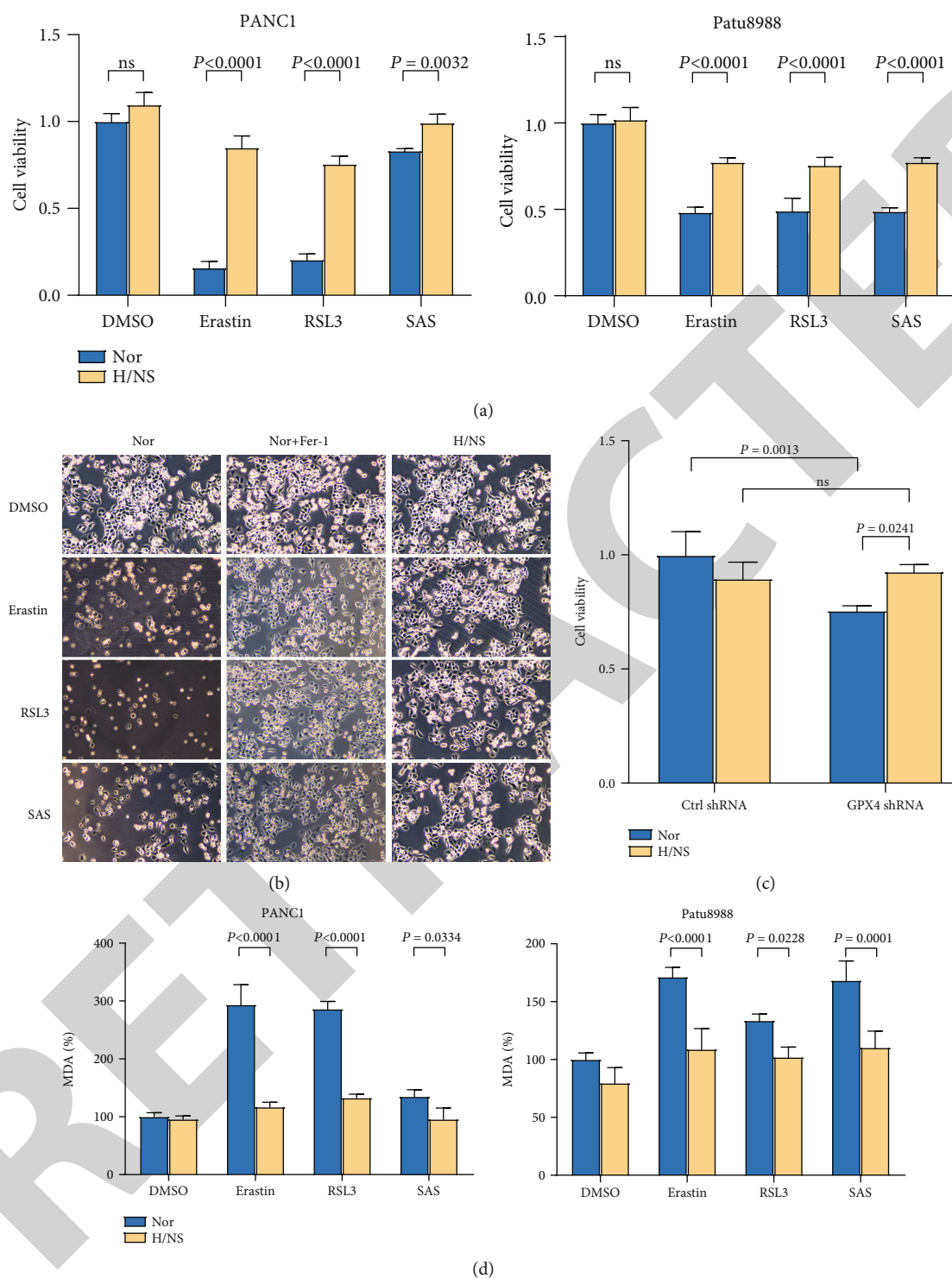
FIGURE 1: H/NS condition protects pancreatic cancer cells from ferroptosis. (a) PANC1 and Patu8988 cells were treated with erastin ($5\,\mu M$ for PANC1 and $40\,\mu M$ for Patu8988), RSL3 ($3\,\mu M$ for PANC1 or $5\,\mu M$ for Patu8988), or sulfasalazine ($2\,mM$) cultured in normal or H/NS condition for 24 hours. Cell viability was measured using a CCK8 kit. (b) Representative images showing the induction of cell death in PANC1 cells treated with erastin ($5\,\mu M$), RSL3 ($3\,\mu M$), or sulfasalazine ($2\,mM$) cultured under normal or H/NS condition with or without Fer-1 for 24 hours. (c) Cell viability was measured in Ctrl shRNA and GPX4 shRNA PANC1 cells cultured in normal or H/NS condition for 24 h. (d) PANC1 and Patu8988 cells were treated with DMSO (control), erastin ($5\,\mu M$ for PANC1 and $40\,\mu M$ for Patu8988), RSL3 ($3\,\mu M$ for PANC1 or $5\,\mu M$ for Patu8988), and sulfasalazine ($2\,mM$) in normal or H/NS condition for 24 hours. The levels of MDA were assayed. SAS represents for sulfasalazine; RSL3 represents for (1S,3R)-RSL3; Fer-1 represents for ferrostatin-1; GPX4 represents for glutathione peroxidase 4; Nor represents for normal condition. H/NS represents for hypoxia combination with nutrient starvation condition. Experiments were repeated three times and the data are expressed as the mean ± SEM. $^{*}P < 0.05$. $^{**}P < 0.01$. $^{***}P < 0.001$. $^{****}P < 0.0001$.

on the plasma membrane and induce a ferroptosis-resistant state in cells, especially in the hypoxia and H/NS condition [14, 15]. SCD1 is an endoplasmic reticulum enzyme that catalyzes the rate-limiting step in the formation of MUFAs. Therefore, we hypothesize that SCD1 is involved in H/NS condition rescued cancer cell ferroptosis. Kaplan–Meier analysis of the TCGA data showed a trend of that high SCD1 expression associated with low disease-free survival and overall survival rate (Figure 2(a)). Analysis of a gene expression database in Gene Expression Omnibus (GSE16515) indicated that SCD1 was upregulated in pancreatic cancer tissues compared with normal pancreatic tissues (Figure 2(b)).

To further explore the role of SCD1 in H/NS cultured pancreatic cancer cell ferroptosis, we firstly detected basal SCD1 expression under normal and H/NS conditions in PDAC cell lines Patu8988, PANC1, BXPC3, and SW1990, with relatively high SCD1 expression in PANC1 and Patu8988 cells, which were chosen for the further research (Figure 2(c)). Following cultured PANC1 and Patu8988 cells under H/NS condition for the indicated time, there was a significant upregulation of SCD1 in protein- and mRNA-expression levels (Figures 2(d)–2(e), Figure S1E). As the primary function of SCD1 is to regulate the production of MUFAs, we also tested the concentration of intracellular MUFAs in H/NS cultured cancer cells, and a higher concentration of MUFAs was observed (Figure 2(f)). Altogether, these findings suggested that SCD1 is closely correlated to the pancreatic carcinoma malignancy and H/NS microenvironment.

3.3. SCD1 Is a Suppressor of Ferroptotic Pancreatic Cancer Cell Death under H/NS.
To further explore the role of SCD1 in H/NS involved pancreatic cancer cell ferroptosis, two stable knockdown cell clones (SCD1 shRNA1 and shRNA2) were established with high silencing efficiency verified by Western Blot and qRT-PCR (Figures 3(a) and 3(b)).

Compared to the control group, erastin could significantly induce the SCD1 knockdown pancreatic cancer cell death under H/NS condition (Figure 3(c)). Also, the cell viability of SCD1-knockdown cells under H/NS condition was decreased upon erastin treatment, which was reversed in the presence of oleic acid (OA) or Fer-1 (Figure 3(d)). Furthermore, knockdown of SCD1 significantly increased MDA production in H/NS cultured PANC1 and Patu8988 in the presence of erastin (Figure 3(e)). Given that MUFAs, products of SCD1-catalyzed reaction, negatively regulate ferroptosis, we therefore asked whether MUFA concentration was altered in SCD1 shRNA groups. ELISA assay results showed a marked decrease in MUFA concentration occurred in SCD1 shRNA groups under H/NS condition (Figure 3(f)).

TCGA database analysis also showed that SCD1 expression correlated with the expression of ferroptosis-resistant markers (ACSL3, SLC7A11, and NQO1) in pancreatic cancer (Figure 3(g)). Together, these results revealed that SCD1-mediated MUFA formation precipitates ferroptosis resistance under H/NS.

3.4. Inhibition of SCD1 Activity Sensitizes Pancreatic Cancer Ferroptosis In Vitro and In Vivo.
Next, we test whether SCD1 inhibitor, A939572, may have a synergistic effect on inducing ferroptosis. As expected, pretreatment with A939572 productively sensitized pancreatic cancer cells to erastin induced cell death (Figures 4(a) and S2A), which could be rescued in the presence of Fer-1. Furthermore, MDA production and lipid ROS level were significantly increased under A939572 and erastin combination treatment, consistent with an increased feature of ferroptosis (Figures 4(b) and 4(c)). Moreover, the expression level of FTH1 and NRF2 increased, while no significantly changed of ACSL4 in cells treated with A939572 and erastin under H/NS (Figure S2B-F).

We next investigated whether A939572 and erastin have synergistic ferroptosis-inducing effect *in vivo*. Administration of A939572 and erastin reduced the size of Panc02 subcutaneous tumors in C57BL/6 mice by 26.5% and 35.6%, respectively, and the combination therapy further reduced the size by 80.3%, compared with vehicle-treated tumors at day 14 (Figures 4(d)–4(f)). Moreover, combination treatment of A939572 and erastin also significantly augmented MDA levels in tumor tissues (Figure 4(g)) and had little impact on GPX4 protein expression (Figure S2G). This data suggested that pharmacological inhibition of SCD1 enhanced ferroptosis in pancreatic cancer *in vitro* and *in vivo*.

4. Discussion

In the present study, we provided evidence that H/NS results in SCD1 high expression in PDAC cells. Furthermore, SCD1-mediated accumulation of MUFAs is involved in protecting PDAC cells from ferroptosis under H/NS condition. Importantly, combining ferroptosis inducers with SCD1 inhibitor showed a synergistic effect *in vitro* and *in vivo*.

As one of the most aggressive malignancy, PDAC therapy has no significantly breakthrough until now. The tumor microenvironment has been considered a crucial component of therapy resistance [16]. Hypoxia and nutrient deprivation are the two most striking features in the solid tumor microenvironment. Our results show that pancreatic cancer cells under H/NS condition were significantly resistant to the ferroptosis inducers, a novel form of tumor-suppressor function for cancer therapy. Cells adapt to the H/NS microenvironment depending on metabolism reprogramming [17]. Since hypoxia restrains glucose-based acetyl-CoA generation, cancer cells rely on glutamine or acetate as alternative substrates for acetyl-CoA generation to fuel their elevation of FA synthesis pathway [7, 18, 19]. Also, cancer cells mainly depend on the uptake of exogenous unsaturated FAs in the absence of oxygen [20, 21] and facilitate increased endogenous FA desaturation via upregulation of SCD1 expression in low-serum condition [22]. Expression of SCD1 and endogenous MUFA production increased under such H/NS condition according to our results. SCD1 plays a critical role in the de novo synthesis of FAs, catalyzing the conversion of saturated fatty acids (SFAs) into Δ9-monounsaturated fatty acids (MUFAs). Our data emphasized the essential role of SCD1 mediated MUFA production in such H/NS condition of PDAC, and this protective effect of SCD1 is

(a)

(b)

(c)

(d)

Figure 2: Continued.

(e)

(f)
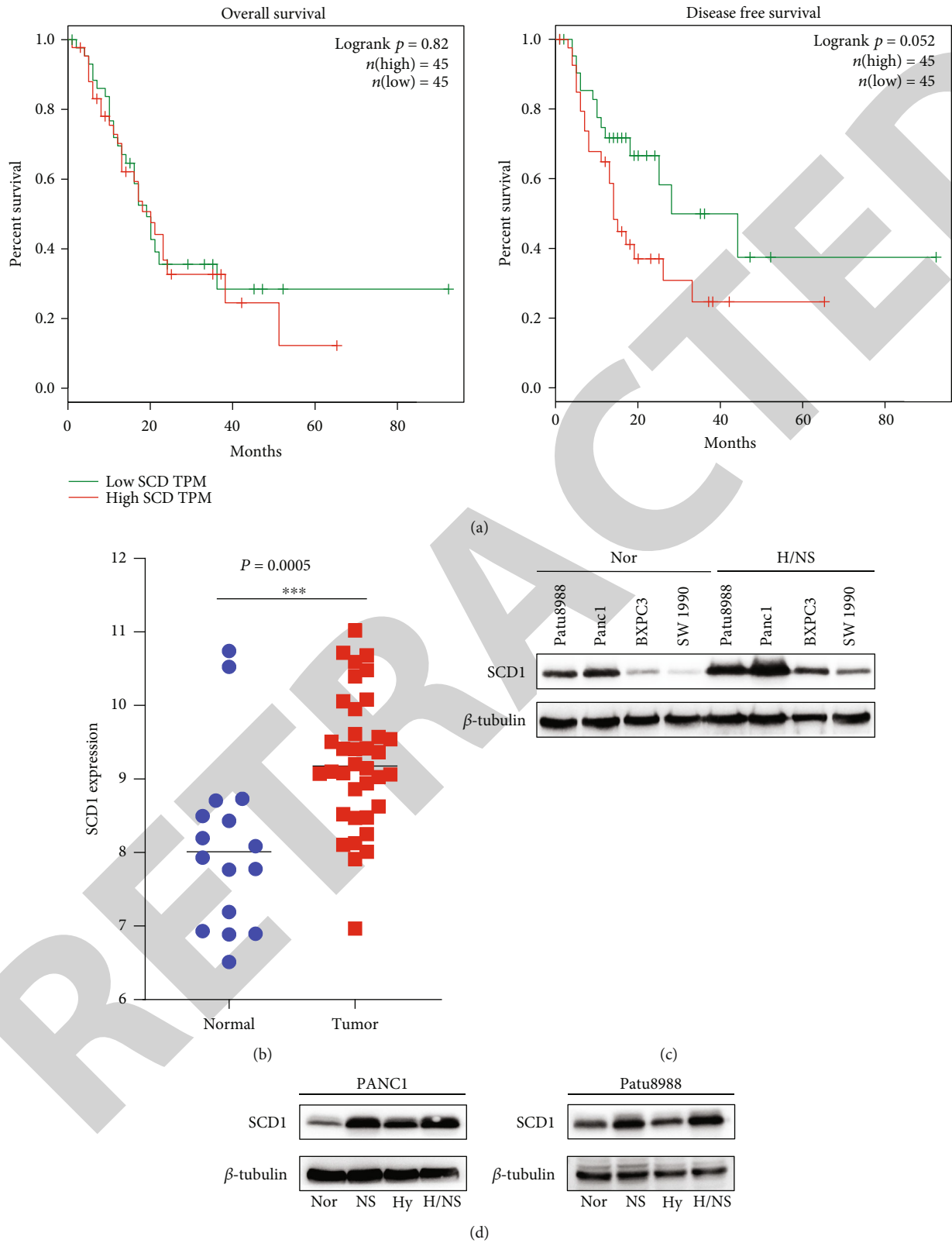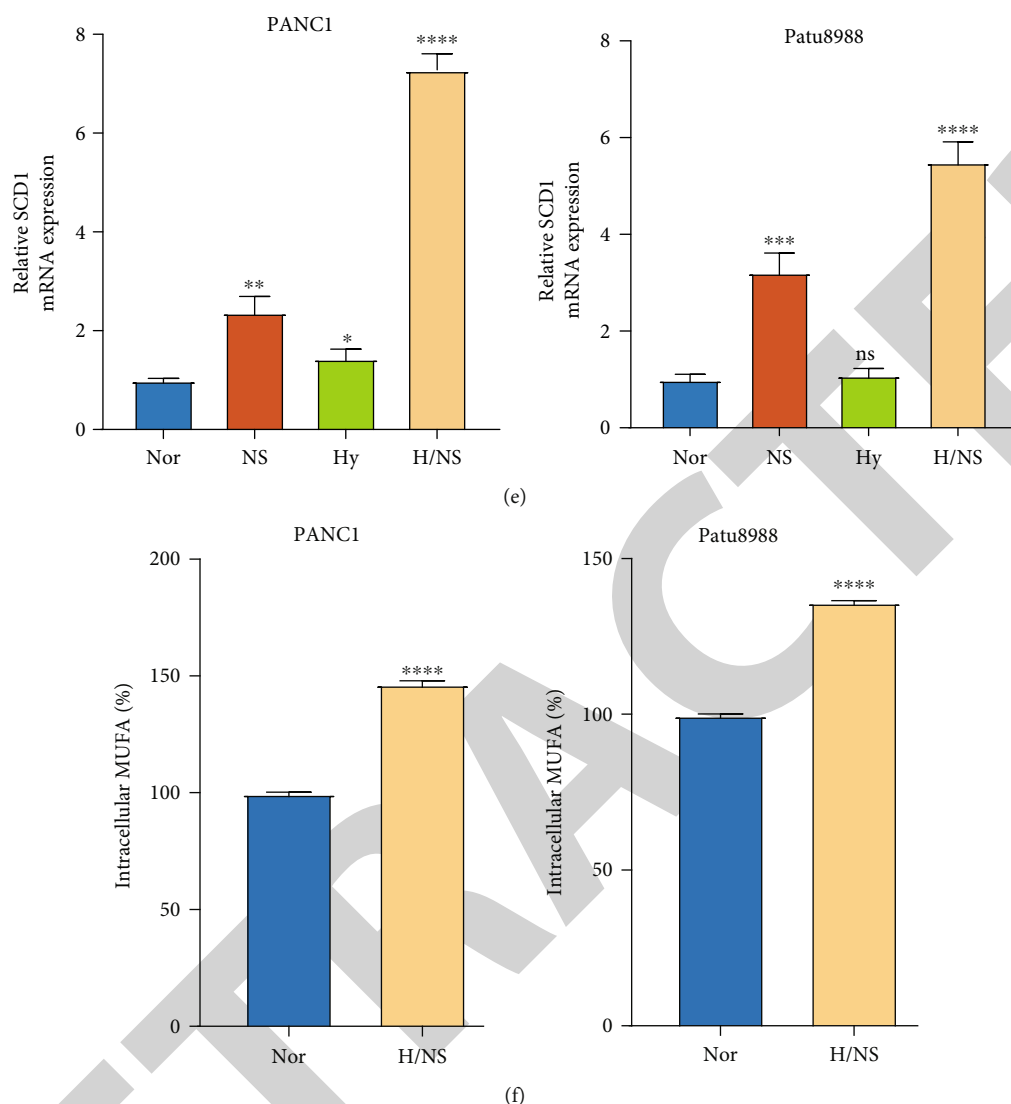
FIGURE 2: SCD1 expression is positively related to pancreatic cancer H/NS condition and progression. (a) TCGA database analysis of the association of SCD1 expression with overall survival rate and disease-free survival rate of patients. (b) Expression of SCD1 in GEO database (GSE16515). Pancreatic tumor tissues compared to pancreatic normal tissues. (c) Basal SCD1 protein expression levels in Patu8988, PANC1, BXPC3, and SW1990 cells cultured in normal or H/NS condition were detected by western blot. β-Tubulin expression was detected as a loading control. (d, e) Western blot and qRT-PCR analysis of protein and mRNA expression levels of SCD1 in PANC1 and Patu8988 cells cultured in normal, nutrient starvation, hypoxia, or H/NS condition. β-Tubulin expression was detected as a loading control for western blot. ACTB mRNA expression was detected as a loading control for qRT-PCR. (f) ELISA-based analysis of the MUFA concentration in PANC1 and Patu8988 cells under normal and H/NS conditions. Nor represents normal condition. NS represents for nutrient starvation condition. Hy represents for hypoxia condition. H/NS represents for hypoxia combination with nutrient starvation condition. Experiments were repeated three times and the data are expressed as the mean $\pm$ SEM. $^*P < 0.05$. $^{**}P < 0.01$. $^{***}P < 0.001$. $^{****}P < 0.0001$.

consistent with the fact that blockade of SCD1 causes multiple changes in cellular lipid content and induces apoptosis and ferroptosis in ovarian cancer cells [15].

Lipid peroxidation is the driver of ferroptotic cell death. Acyl-CoA Synthetase Long-Chain Family Member 4 (ACSL4) induces cancer cell ferroptosis through promoting arachidonic acid (AA) and adrenic acid (AdA) peroxidation [23]. MUFAs did not upregulate GPX4 expression, which reduces reactive phospholipids hydroperoxides to unreactive phospholipid alcohol. However, MUFAs hinder the accumulation of lipid ROS on the plasma membrane and decrease PUFA incorporation into phospholipids [10]. Our study found that PDAC cells increase the production of MUFAs with upregulated SCD1 expression under H/NS condition, which provokes a ferroptosis-resistant cell state. Moreover, a potential PDAC treatment strategy was highlighted by combing ferroptosis inducers with SCD1 inhibitors to eliminate the resistant effect originating from TME.

(a)

(b)

(c)
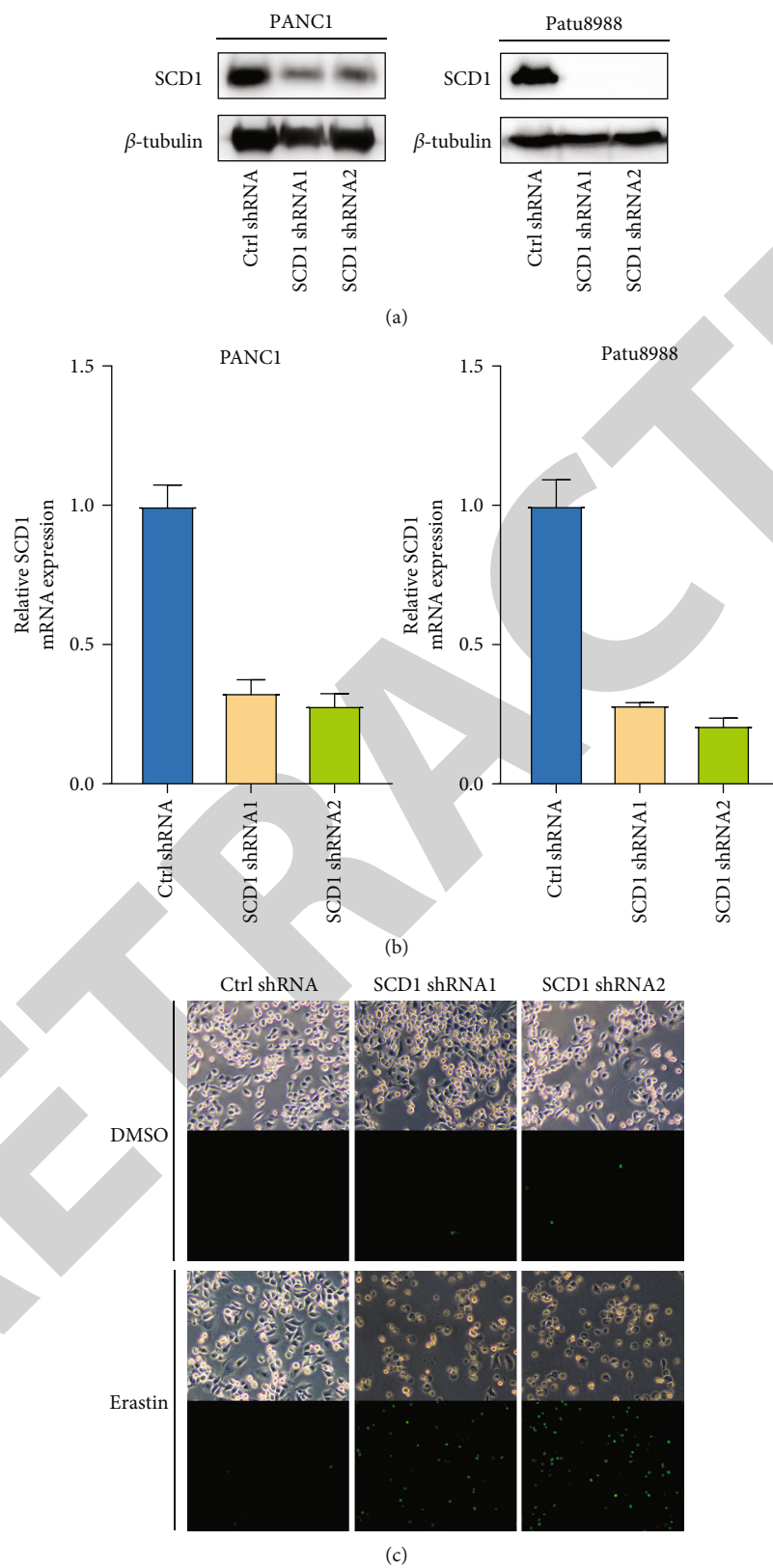
FIGURE 3: Continued.

(d)

(e)

(f)

Figure 3: Continued.

(g)
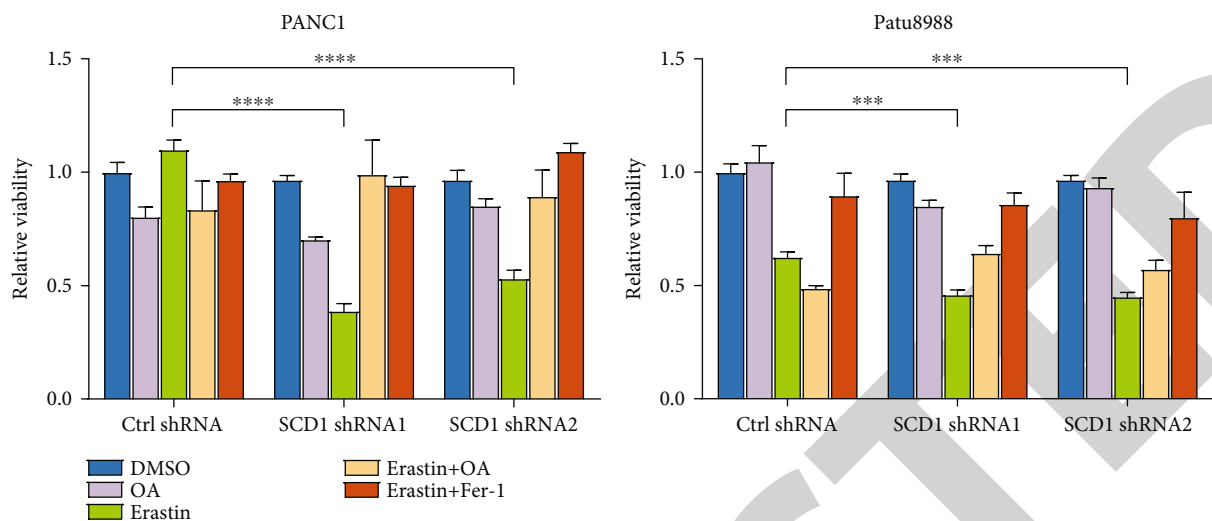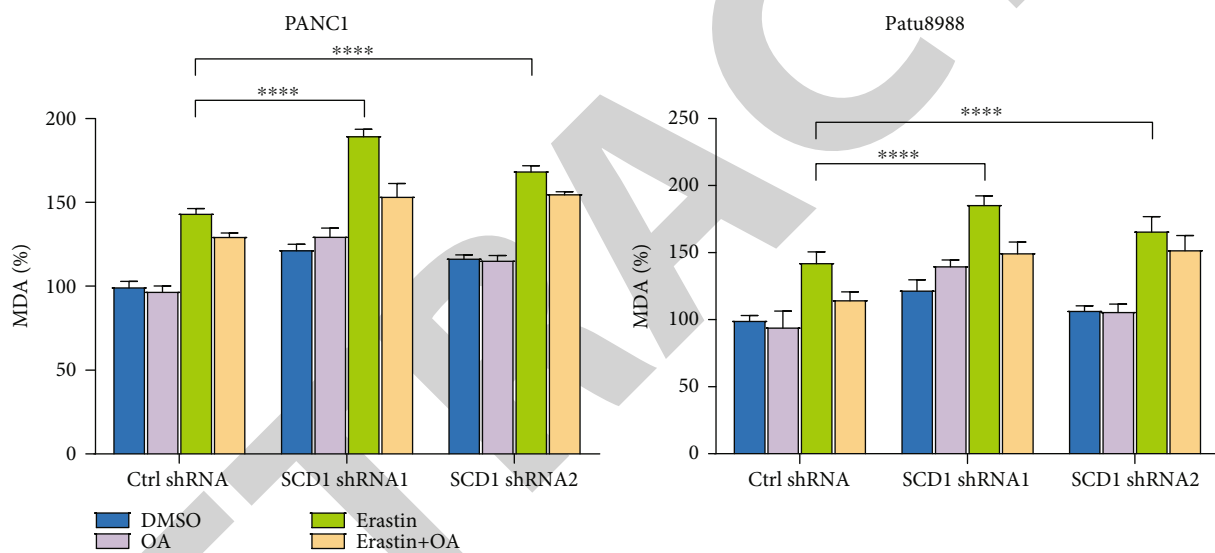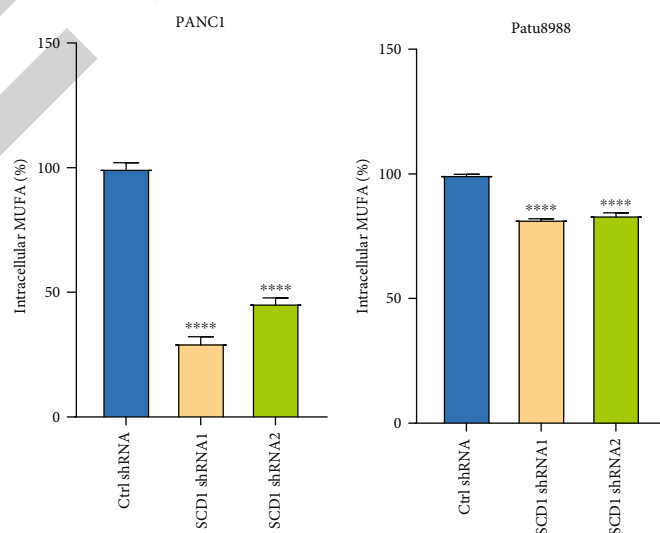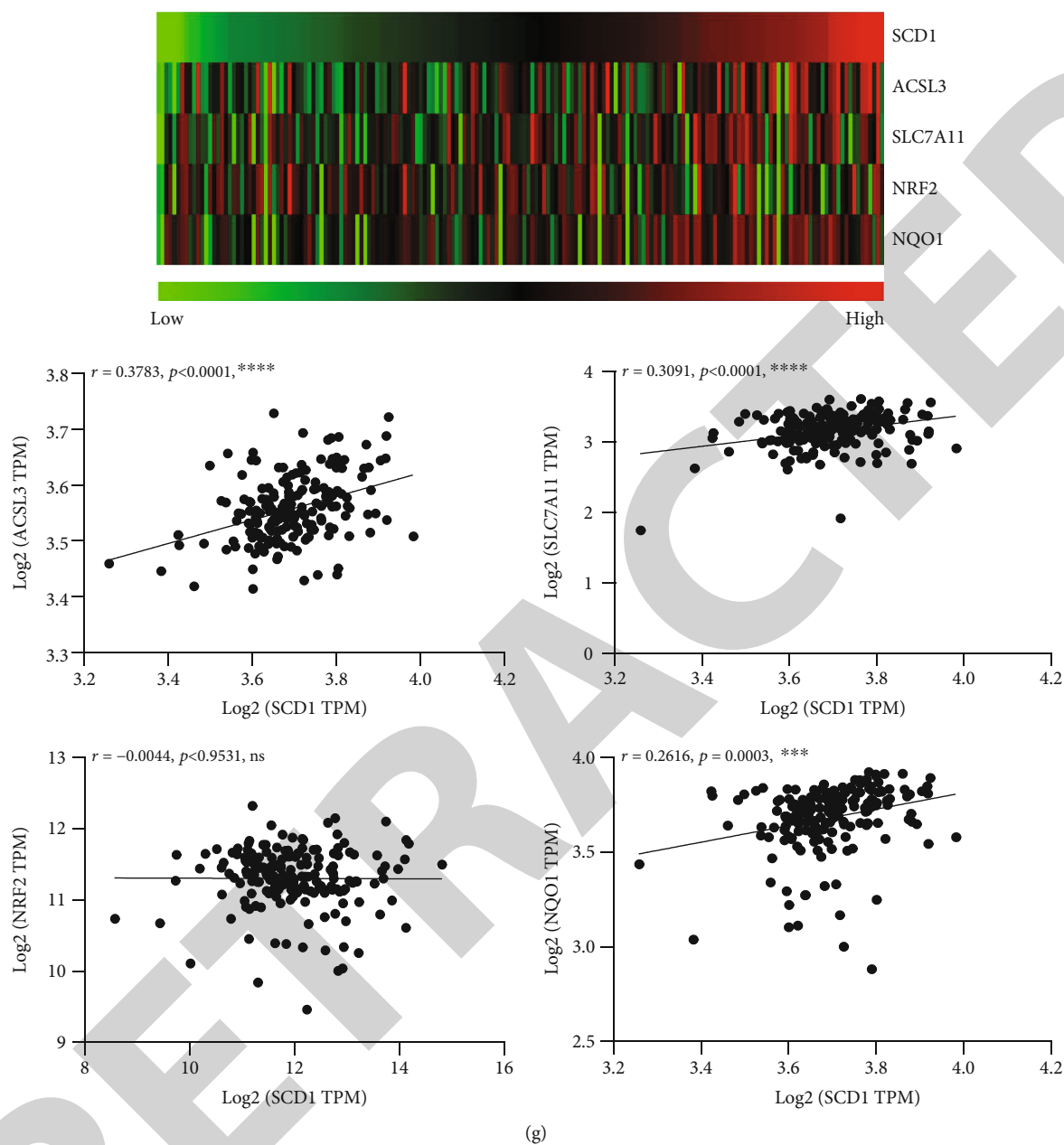
Figure 3: SCD1-mediated MUFA formation protects PDAC cells from ferroptosis under H/NS. (a, b) Western blot and qRT-PCR analysis of shRNA-mediated knockdown of SCD1 protein and mRNA expression levels in PANC1 and Patu8988 cells. β-Tubulin expression was detected as a loading control. ACTB mRNA expression was detected as a loading control for qRT-PCR. (c) Sytox green staining analysis of PANC1 (Ctrl shRNA), SCD1 knockdown PANC1 (SCD1 shRNA1 and SCD1 shRNA2) cancer cells treated with erastin (5μM) under H/NS condition. (d) PANC1 (Ctrl shRNA), SCD1 knockdown PANC1 (SCD1 shRNA1 and SCD1 shRNA2), Patu8988 (Ctrl shRNA), and SCD1 knockdown Patu8988 (SCD1 shRNA1 and SCD1 shRNA2) cancer cells were treated with erastin (5μM for PANC1 and 40μM for Patu8988) with or without OA (80μM) and Fer-1 (1μM for PANC1 and 5μM for Patu8988) under H/NS condition. Cell viability was accessed via CCK8 assay. (e) MDA assay analysis of PANC1 (Ctrl shRNA), SCD1 knockdown PANC1 (SCD1 shRNA1 and SCD1 shRNA2), Patu8988 (Ctrl shRNA), and SCD1 knockdown Patu8988 (SCD1 shRNA1 and SCD1 shRNA2) treated with erastin (5μM for PANC1 and 40μM for Patu8988) with or without OA (80μM) under H/NS condition. (f) Human MNSFA ELISA Kit was used to detect the content of monounsaturated fatty acids (MUFAs) in PANC1 (Ctrl shRNA), SCD1 knockdown PANC1 (SCD1 shRNA1 and SCD1 shRNA2), Patu8988 (Ctrl shRNA), and SCD1 knockdown Patu8988 (SCD1 shRNA1 and SCD1 shRNA2) cancer cells under normal or H/NS condition. (f) Analysis of the TCGA database for the correlation SCD1 mRNA expression level with the ferroptosis (ACSL3, SLC7A11, NRF2, and NQO1). The results are presented by heat map: $n = 183$. OA represents for oleic acid. Fer-1 represents for ferrostatin-1. Experiments were repeated three times and the data are expressed as the mean ± SEM. $^{*}P < 0.05$. $^{**}P < 0.01$. $^{***}P < 0.001$. $^{****}P < 0.0001$.

(a)

(b)

FIGURE 4: Continued.

BODIPY-C11 (510 nm, oxidized)
BODIPY-C11 (590 nm, reduced)
DAPI

(c)

(d)

(e)

(f)

Figure 4: Continued.

(g)
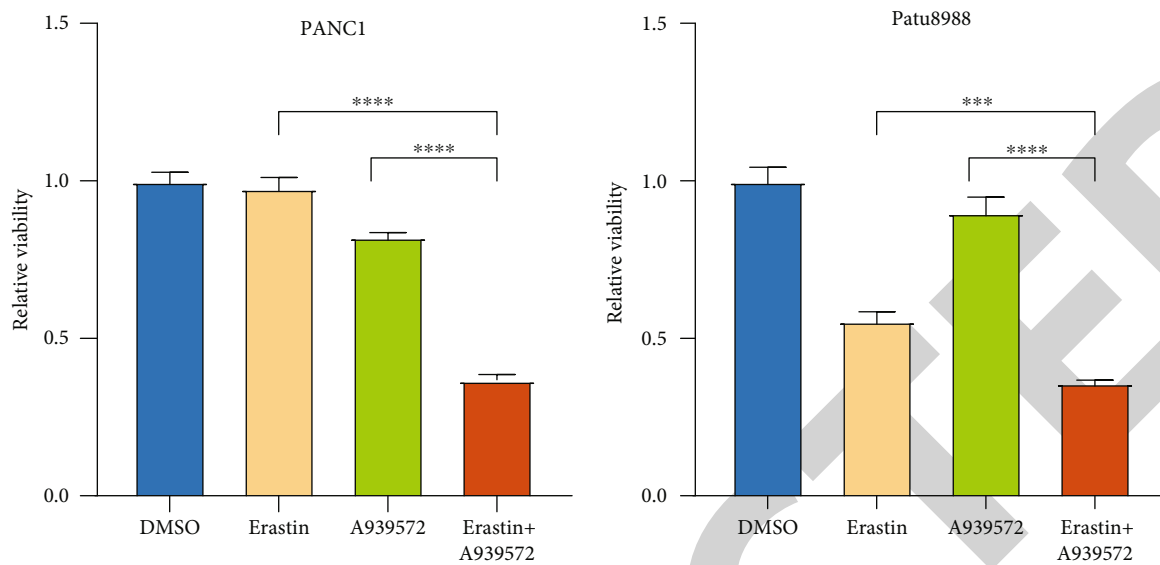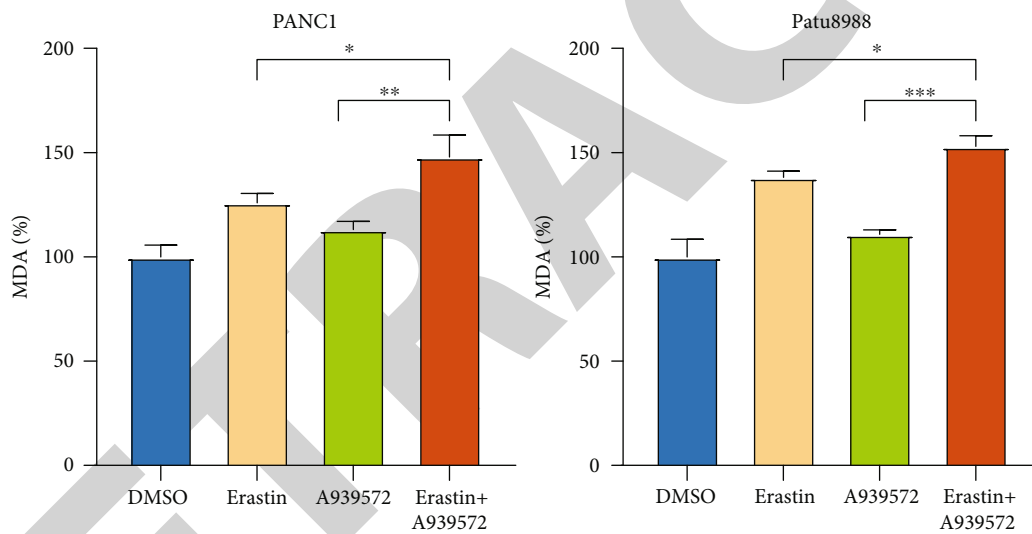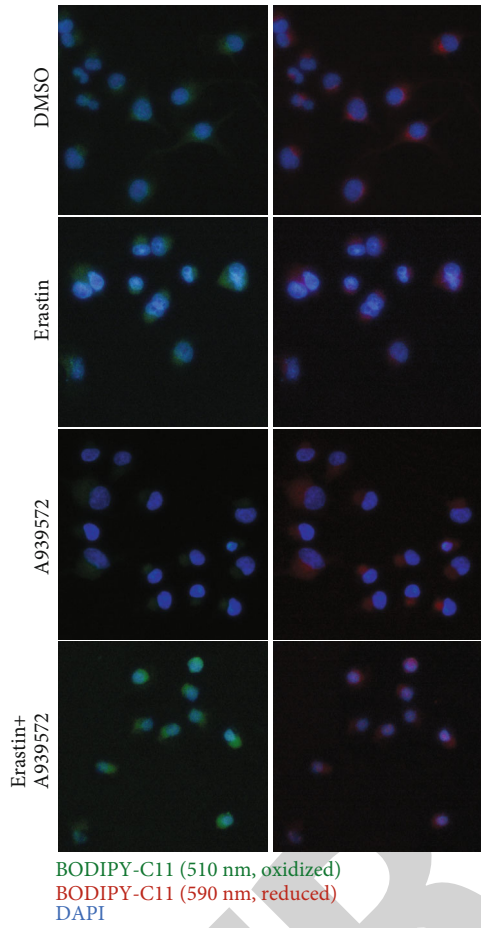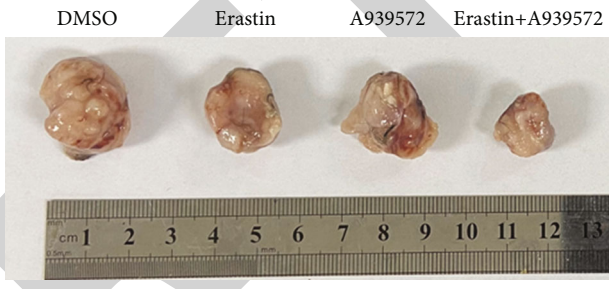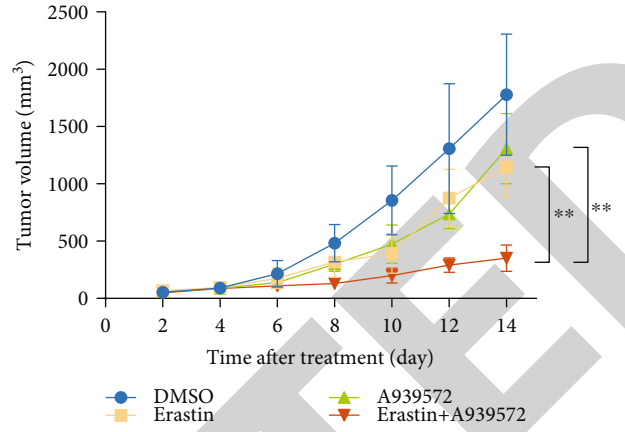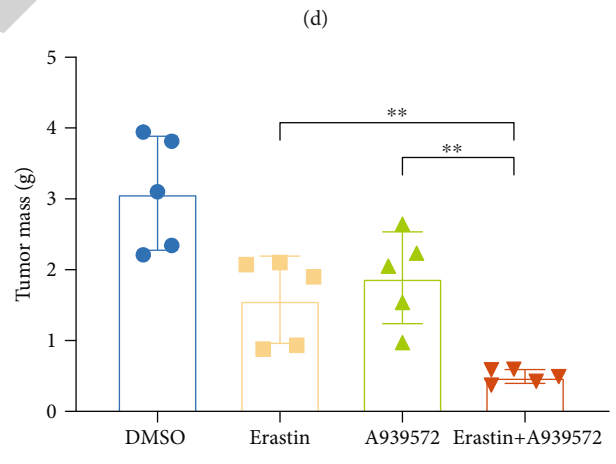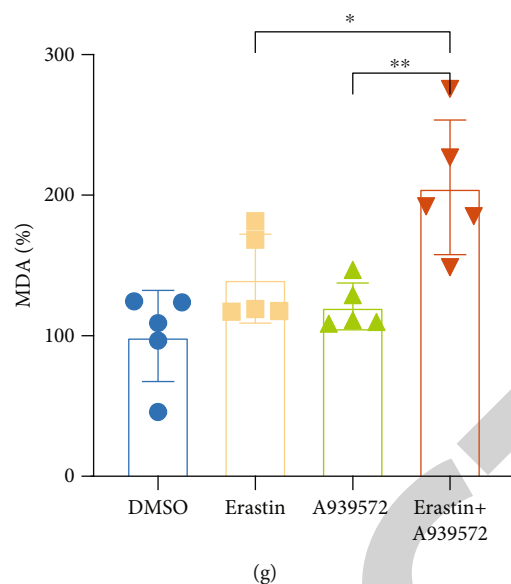
FIGURE 4: Inhibition of SCD1 activity sensitized pancreatic cancer ferroptosis in vitro and in vivo. (a, b) PANC1 and Patu8988 cancer cells were pretreated with DMSO or A939572 (5 μM) for 48 hours followed by the addition of erastin (5 μM for PANC1 and 40 μM for Patu8988) for an additional 24 hours. Cell viability was measured by a CCK8 kit (a). The relative levels of MDA were assayed (b). (c) Lipid ROS level was evaluated using fluorescent microscope images of BODIPY-C11 (oxidized, green; reduced, red). (d–f) C57BL/6 mice were injected subcutaneously with mice pancreatic cancer cells Panc02 (1×10^6 cells/mouse) and treated with DMSO, erastin (20 mg/kg/i.p., every two days), A939572 (1 mg/kg/i.p., every two days), or erastin (20 mg/kg/i.p., every two days) + A939572 (1 mg/kg/i.p., every two days). (c) Tumor volume was calculated every two days. Representative photographs (d) and tumor mass (e) of isolated tumor tissues in each treatment group at day 14. (g) MDA levels in isolated tumors were assayed at day 14 after treatment. Experiments were repeated three times and the data are expressed as the mean ± SEM. $^*P < 0.05$. $^{**}P < 0.01$. $^{***}P < 0.001$. $^{****}P < 0.0001$.
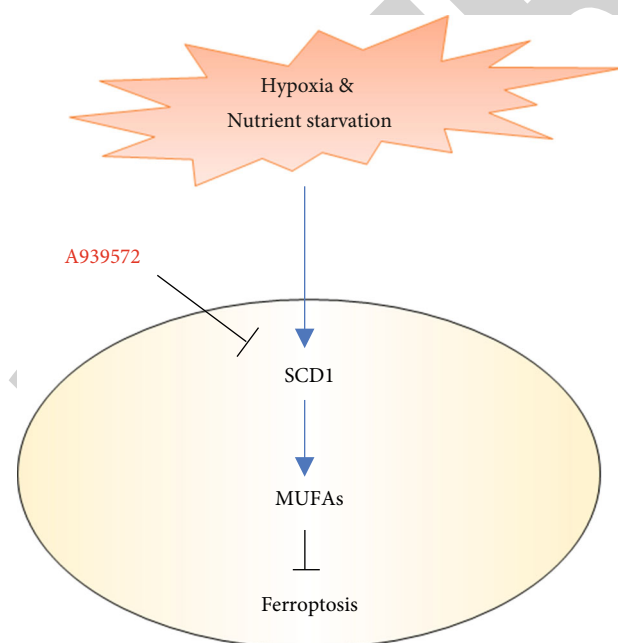
FIGURE 5: Schematic representation of the mechanisms of SCD1 potentiating hypoxic plus nutrient-deprived pancreatic cancer cell ferroptosis resistance.

Taken together, the current study reveals that the involvement of SCD1-mediated MUFA production results in a ferroptosis-resistant cell state under H/NS condition in PDAC cells (Figure 5). Further research is required to identify the novel PDAC therapy strategy in combination with SCD1 inhibitors and ferroptosis inducers.

Data Availability

To determine the expression of SCD1 in pancreatic cancer tissues and normal tissues, the datasets in GEO (GSE16515) concluding 52 samples were adopted. The Cancer Genome Atlas (TCGA) database(https://tcga.xenahubs.net/download/TCGA.PAAD .sampleMap/HiSeqV2.gz. sampleMap/HiSeqV2.gz) including those from 183 pancreatic carcinoma patient specimens were utilized to further analyze the association of SCD1 expression level with overall survival and disease-free survival rate. High and low groups were defined as above and below the quartile, respectively.

Conflicts of Interest

The authors declare no conflict of interests.

Authors' Contributions

Jie Gao, Zhengyang Zhang, and Yanfang Liu contributed equally to this work.

Research Article

Zoledronic Acid Enhanced the Antitumor Effect of Cisplatin on Orthotopic Osteosarcoma by ROS-PI3K/AKT Signaling and Attenuated Osteolysis

Liang Liu,[1] **Huan Geng,**[1] **Chengjie Mei,**[2] **and Liaobin Chen** ⓘ[1]

[1]*Department of Orthopedic Surgery, Zhongnan Hospital of Wuhan University, Wuhan 430071, China*
[2]*Department of Hepatobiliary and Pancreatic Surgery, Zhongnan Hospital of Wuhan University, Wuhan 430071, China*

Correspondence should be addressed to Liaobin Chen; lbchen@whu.edu.cn

Osteoclasts can interact with osteosarcoma to promote the growth of osteosarcoma. Cisplatin is common in adjuvant chemotherapy of osteosarcoma. However, due to chemoresistance, the efficacy is profoundly limited. Previous studies have found that zoledronic acid (ZA) has osteoclast activation inhibition and antitumor effect. However, the combined effect of ZA and cisplatin on osteosarcoma remains unclear. In vitro, the effects of ZA and cisplatin alone or in combination on 143B cell activity, proliferation, apoptosis, and ROS-PI3K/AKT signaling were detected. At the same time, the effect of ZA and cisplatin on osteoclast formation, survival, and activity was detected by TRAP staining and bone plate absorption test. These were further verified in mice. The results showed that in vitro, compared with the single treatment and control, the combination of ZA and cisplatin could significantly inhibit the activity and proliferation of 143B cells and induced their apoptosis and further promoted the generation of ROS and inhibited the phosphorylation of PI3K and AKT. ROS scavenger and the agonist of the PI3K/AKT pathway could reverse these results. In addition, cisplatin in synergy with ZA could significantly inhibit osteoclast formation and survival to reduce bone plate absorption. In vivo, compared with the single group, the tumor volume and cell proliferation were significantly reduced, apoptosis and necrosis of tumor cells increased, and TRAP⁺ osteoclasts and osteolysis destruction decreased in the combined group. In conclusion, ZA enhanced the antitumor effect of cisplatin on osteosarcoma by ROS-PI3K/AKT signaling, reducing the chemoresistance and osteoclast activation to enhance chemotherapy and inhibit osteolysis. And this present study raised the possibility that combining ZA and cisplatin may represent a novel strategy against osteosarcoma.

1. Introduction

Osteosarcoma, common in children and adolescents, is a primary malignant tumor, most of which occur in the metaphysis of long bones [1]. Clinically, surgical excision, adjuvant chemotherapy, and radiotherapy are the most important methods for the treatment of osteosarcoma [2]. With the development of surgical techniques and the use of adjuvant chemotherapy, the survival rate of patients with osteosarcoma has been greatly improved [3]. However, 5-year survival rates were reported to be still only 15 to 30% for patients with chemotherapy resistance or metastasis [3].

Cisplatin is a classical chemotherapy drug used to treat osteosarcoma [4]. In mechanism, on the one hand, cisplatin causes single or double strand damage to DNA by binding to bases on DNA molecules, which affects DNA replication to inhibit tumor cell proliferation. On the other hand, cisplatin plays an antitumor role through cell apoptosis mediated by organelles such as mitochondria and endoplasmic reticulum [5, 6]. But due to drug resistance and side effects, the efficacy of cisplatin in osteosarcoma has been deeply limited [5]. At present, the common multidrug combined chemotherapy can partially improve the effect on killing osteosarcoma cells, such as cisplatin, methotrexate (MTX), Adriamycin (ADM), and ifosfamide (IFO) [7]. However, there is no combined strategy for osteosarcoma that not only can significantly enhance the efficacy but also inhibit these side effects of the combined drugs. Therefore, a novel and

more effective treatment with lower side effects is needed to complement the current strategy to improve overall survival.

Osteosarcoma cells derive from osteoblasts. However, it has been found that osteoclasts also play an important role in the occurrence and development of osteosarcoma [8]. Osteoclasts and their progenitors express RANK receptors, while osteosarcoma cells can secrete a large number of RANK ligands (RANKLs) [8]. RANKLs promote the precursors to differentiate into osteoclasts and activate them, which then leads to osteolysis and releases a variety of growth factors, such as transforming growth factor beta (TGFβ), insulin-like growth factors (IGFs), and fibroblast growth factors (FGFs) [9–11]. In turn, these factors promote the growth of tumor cells to further promote the formation and activation of osteoclasts, thus forming a "vicious circle" [11]. Zoledronic acid (ZA), the third-generation clinical applied bisphosphonate with strong bone affinity, is widely used in the treatment of metabolic and metastatic bone diseases nowadays [12]. In mechanism, ZA can dwindle osteoclast function or enhance osteoclast apoptosis [13, 14]. Moreover, previous studies have found that ZA is the most potential bone resorption inhibitor for bone metastases [15]. Preclinical data also found that ZA can inhibit angiogenesis, tumor cell adhesion, and invasion of extracellular matrix to inhibit a variety of tumors, such as osteosarcoma, cervical cancer, and breast cancer [7, 16, 17]. However, as a classic antiosteoporosis drug, whether ZA combining cisplatin can enhance the inhibition of osteosarcoma growth remains unclear.

In this study, we examined the efficacy of combined therapy with cisplatin and ZA. We demonstrated that combination with cisplatin and ZA enhanced the chemotherapy effect of cisplatin on osteosarcoma. It could further induce the apoptosis and proliferation inhibition of osteosarcoma cells caused by cisplatin, and the mechanism of synergistic effect enhancement was mainly related to oxidative stress and PI3K/AKT inactivation, which play a crucial role in cell survival and proliferation. Furthermore, we confirmed the synergistic antitumor effect of combined treatment with ZA and cisplatin in mice, and it inhibited osteoclasts to break the "vicious circle" between osteoclasts and osteosarcoma cells and reduce osteolysis (an active resorption of bone matrix by osteoclasts).

2. Material and Methods

2.1. Reagents. Zoledronic acid (CAS No. 118072-93-8), cisplatin (CAS No. 15663-27-1), and 740 Y-P (CAS No. 1236188-16-1) were obtained from MedChemExpress (Wuhan, China). Isoflurane was obtained from Baxter Healthcare Co. (Deerfield, IL, USA). TRAP staining kit (HR0561) was purchased from Biolab Technology Co., Ltd. (Beijing, China). Reactive oxygen species (ROS) test kit (DHE) (HR8821) was obtained from Biolab (Beijing, China). Phospho-PI3 kinase (p-PI3K) (4228S) and AKT (4691S) antibodies were obtained from Cell Signaling Technology Co., Ltd. Phospho-AKT (AP0637), MRP-1 (A1703), MDR1 (A19093), and PI3K (A0265) antibodies were obtained from ABclonal Co., Ltd. (Wuhan, China). Goat polyclonal secondary antibody to rabbit IgG-H&L (Alexa Fluor® 488)

(ab150077) was obtained from Abcam. Annexin V-FITC/PI kit (BB-4101-50T) was purchased from BestBio (Shanghai, China); Ki-67 (GB13030-2), TMR (red) Tunel Cell Apoptosis Detection Kit (G1502), crystal violet (G1014), and CCK-8 kit (G4103) were purchased from Servicebio Co., Ltd. (Wuhan, China). TRIzol (CSA No. 5346994) was obtained from Invitrogen Co. (Carlsbad, CA, United States). Reverse transcription and real-time quantitative polymerase chain reaction (RT-qPCR) kits were obtained from TaKaRa Biotechnology (Dalian, China). The SYBR Green dye was purchased from Applied Biosystems by Thermo Fisher Scientific (ABI) (Foster City, CA, USA). The other chemicals and agents were analytical grade.

2.2. Cell Culture and Treatment. Human osteosarcoma 143B cell lines were purchased from Mingzhou Biological Technology Co., Ltd. (Zhejiang, China). Cells resistant to cisplatin were established by exposing the drug-sensitive 143B cells to stepwise increasing concentrations of cisplatin. All cells were cultured at 37°C in a constant temperature incubator with 5% CO_2 in DMEM medium (Gibco, USA), including 10% fetal bovine serum (HyClone, North America) and 100 μg/ml penicillin and streptomycin.

2.3. CCK-8 Assay and Synergy Effect Analysis. 143B cells were made into $1\text{-}5 \times 10^3$/l cell suspension and seeded in 96-well plates. Then, the cells were treated with ZA (0, 4, 8, 16, 32, 64, 128, and 256 μM) or cisplatin (0, 0.4, 1.0, 2.5, 5.0, 10, 20, and 40 μg/ml) alone or in combination. Finally, after CCK-8 reagents were added according to CCK-8 kits protocol and incubated for 0.5-4 hours in the cell culture incubator, the absorbance was measured at 450 nm in a microplate reader. After obtaining the data of cell activity, the synergy score was determined by the online application SynergyFinder 2.0 with four reference models with the "viability readout" [18]. And the inhibitory concentration 50 (IC_{50}) value of cisplatin was calculated by the survival curve.

2.4. Colony Formation Assay. The cells were seeded in six-well plates at the appropriate density (500 cells/well) and allowed to culture for 24 h. Once the cells completely adhered, the cells were divided into six groups: control, cisplatin, ZA, ZA+cisplatin, ZA+cisplatin+NAC, and ZA+cisplatin+740 Y-P, which were treated with 32 μM ZA, 5 μg/ml cisplatin, 5 mM NAC, or 50 μg/ml 740 Y-P for 48 h, respectively. Then, the cells were washed twice with PBS and cultured in a new medium. Eight days later, the cells were fixed with 4% paraformaldehyde and stained with crystal violet. The assay was repeated three times. The staining results were photographed, and the colonies with more than 50 cells were counted under an ordinary optical microscope.

2.5. Animals and Treatment. All experimental specific pathogen-free BALB/c nude mice (4-6 weeks old) (No. 2019-0012, license number: SCXK (Hubei), certification number: 42000800001149) were purchased from Hubei Provincial Center for Disease Control and Prevention (Hubei, China). All animal testing procedures comply with the Guidelines for the Care and Use of Laboratory Animals of the Chinese Animal Welfare Committee. The Animal

Experimental Ethics Committee of Wuhan University Medical College approved this study (license number: 18026). All animals were kept under sterile standard environmental conditions, allowing free access to food and water. After one week of adaptive feeding, we injected $40\,\mu l$ 143B cells into the right tibial plateau of the nude mice with an insulin needle. When the tumor was visible, the mice were randomly assigned to one of four groups: control, cisplatin (2 mg/kg), and combined group (ZA: 2 mg/kg+cisplatin: 2 mg/kg). The above reagents were injected intraperitoneally 3 times once every 5 days. The weight and tumor size of mice were measured every 3 days. The tumor size was then calculated based on the following equation: tumor volume = (length × width^2)/2. Finally, all nude mice were sacrificed with 2% isoflurane, the blood samples were collected, and the tumors and lower limbs were isolated for further analysis.

2.6. X-Ray and Micro-CT. Before the nude mice were sacrificed, the mice were anesthetized with 4% chloral hydrate and then examined tibia with X-rays under the mouse in vivo imager (including X-ray imaging module) (Bruker Xtreme BI, BRUKER, USA) and observed bone destruction. After the nude mice were sacrificed, the bones were soaked in ethanol. Then, we used a micro-CT scan (Quantum GX, PerkinElmer) to scan the tumor side tibia and femur and perform 3D reconstruction. Finally, we used the software (Analyze 12.0, PerkinElmer) to assess the trabecular bone microstructure with the parameters, including trabecular bone volume per tissue volume (BV/TV), trabecular number (Tb.N), trabecular thickness (Tb.Th), and trabecular separation (Tb.Sp) of the scanned femurs.

2.7. Immunofluorescence Staining and ROS Assay. After the cells were fixed with 4% formaldehyde for 15 min, the membranes were broken with 0.2% Triton X-100 for 5-10 min. Then, samples were incubated with 3% BSA at room temperature for 60 min. Soon afterward, they were incubated overnight at 4°C with primary antibodies in blocking buffer. After washing with TBST three times, the samples were incubated with 1 : 800 secondary antibody-labeled fluorescent for 60 min. The nucleus was then stained with DAPI for 5 min. After washing with PBS three times, fluorescence images were taken with confocal microscopy (Smartproof 5, Carl Zeiss, Oberkochen, Germany). 10 visual fields were collected for further analysis of each image. Differently, after the ROS reagent was directly added to the sample according to the protocol, it was immediately observed under a confocal microscope (Smartproof 5, Carl Zeiss, Oberkochen, Germany), and the ImageJ software (NIH, Bethesda, MD, USA) was used for quantitative analysis.

2.8. Formation of Osteoclast Cells and Bone Resorption Assay. Primary bone marrow cells were cultured in the complete medium supplemented with 50 ng/ml M-CSF for 3 days to obtain bone marrow-derived macrophages (BMMs). Then, we cultured the cells for 4 days with 50 ng/ml M-CSF and 50 ng/ml RANKL. To assess osteoclast survival, $32\,\mu M$ ZA and/or $5\,\mu g$/ml cisplatin were added for the first two days. The samples were fixed with 4% paraformaldehyde and

stained with the TRAP staining. As for bone resorption assay, after we cultured the BMMs in Osteo Assay Surface 24-well plates (Corning, Corning, NY, USA) for 24 h, a complete inducing medium replaced the previous medium. Similarly, $32\,\mu M$ ZA and/or $5\,\mu g$/ml cisplatin were added for the first two days. The cells were rinsed with 10% sodium hypochlorite and water three times after 6 days. Finally, we used an ordinary light microscope to take pictures, and the ImageJ software was used for quantitative analysis.

2.9. TRAP Staining. After the cells were treated, TRAP staining of osteoclasts was performed according to the TRAP staining kit protocol. Briefly, after removing the culture medium, the cells were immobilized by adding $50\,\mu l$ of 10% paraformaldehyde. After washing with ddH$_2$O, add tartrate-containing buffer and $50\,\mu l$ chromogenic substrate. After incubating at 37°C for 40 min, wash with ddH$_2$O. Finally, we used Nikon NIS Elements BR light microscope (Nikon, Tokyo, Japan) for photograph. The staining intensity was analyzed by measuring the mean optical density (MOD) in 10 fields.

2.10. H&E, Ki-67 Staining, and Tunel Assay. The specimens were sectioned at $5\,\mu m$ for further morphological staining analysis. According to the protocol, H&E staining was operated as follows: after dewaxing in xylene for 10 min, the slices were immersed in 100%, 95%, 85%, and 70% ethanol for 3 min. Next, after dyeing with hematoxylin for 10 min, the color was separated with 70% ethanol. After washing with running water for 15 min, dye with 0.2% eosin for 3 min and then dehydrate by 70%, 85%, 95%, and 100% ethanol successively. Finally, xylene was used for transparency. Ki-67 and Tunel staining was followed by an immunohistochemical staining protocol described in this article [19]. All images were pictured with Nikon NIS Elements BR light microscope (Nikon, Tokyo, Japan) for further analysis.

2.11. RT-qPCR. The total RNA of cells and bone tissue was extracted by the method of TRIzol according to the manufacturer's guidelines. As for the quantitative real-time PCR (RT-qPCR), the reactions were acted in a $10\,\mu l$ system (1 μl cDNA, reverse and forward primers, 3.6 μl ddH2O, and 5 μl SYBR Green Master Mix) with the Applied Biosystems PCR System (Thermo Fisher Scientific, USA): 95°C for 2 min, 40 cycles at 95°C for 15 s, and 60°C for 1 min. The cycle threshold (Ct) values were detected by the $2^{-\Delta\Delta Ct}$ method. And the relative mRNA expression was normalized with GAPDH. The primers of related genes are shown in Table S1.

2.12. Flow Cytometry. After different treatments, the experimental cells were centrifuged and collected after digestion with trypsin without EDTA. Then, we used an Annexin V-FITC Apoptosis Detection Kit (BB-4101-50T, Best Biotechnology, China) to detect apoptotic cells according to the protocol. In brief, after the cells were resuspended with $400\,\mu l$ 1x Annexin V binding buffer, $5\,\mu l$ Annexin V-FITC staining was added to the cell suspension, and the mixture was gently mixed and incubated at 2-8°C in the dark for 15 min. Then, PI dye solution was added and incubated at 2-8°C in the dark for 5 min. The prepared cells were

immediately detected by CytoFLEX (Beckman Coulter, United States) flow cytometry. And the results were analyzed with the CyteExpert software (Beckman Coulter, United States). According to the instructions, the sum of UR and LR quadrant cells is the total apoptosis rate. The experiment was repeated three times for statistical analysis.

2.13. Western Blotting. The prepared cells were rinsed with PBS twice, and then, RIPA Lysis Buffer was used to lyse the cells for 30 min on ice to extract total protein, and the protein sample was then obtained when the supernatant was collected and transferred to the 1.5 ml precooled centrifuge tube after being centrifuged for 10 min at 12000g and 4°C. An equal amount of protein (100 μl) was mixed with sodium dodecyl sulfate-polyacrylamide gel electrophoresis (SDS-PAGE) loading buffer (Beyotime, China) and heated at 95°C for 5 min. Finally, the protein sample obtained above was used for further protein quantification (p-PI3K, PI3K, p-AKT, AKT, MDR1, MRP1, and GAPDH). All results were repeated 3 times. The detailed steps of protein molecule separation and visualization were shown in our previous research [20]. The ImageJ software (NIH, Bethesda, MD, USA) was used to measure the gray values.

2.14. Statistical Analysis. SPSS 20 (SPSS Science Inc., Chicago, Illinois) and Prism 7 (GraphPad Software, La Jolla, CA, USA) were used for data statistics and graphing. Quantitative data were expressed as the mean ± SD. SNK-q was used for the comparison in two of multiple samples after one-way ANOVA that was used for the comparison of the control, single, and combined treatments. $P < 0.05$ was defined as statistically significant.

3. Results

3.1. Zoledronic Acid Enhanced Cisplatin-Induced Proliferation Inhibition and Apoptosis of Osteosarcoma Cells. Firstly, CCK-8 assay was used to detect the cell viability of 143B cells treated with ZA/cisplatin/combination in different concentrations and times. The results showed that the cell activity decreased in a concentration- or time-dependent manner whether in a separate group or the combined group, while the CCK-8 absorption curve in the combined group was significantly higher than alone or control (Figures 1(a) and 1(b); $P < 0.05$, $P < 0.01$). Cell clone and immunofluorescence were further used to measure the cell proliferation. The cell clone showed that clone formation was significantly lower in the combined group than either the cisplatin or ZA group, and all of that were lower than control (Figure 1(c); $P < 0.01$). The Ki-67 expression by RT-qPCR and immunofluorescence showed that Ki-67 mRNA and protein expressions in the cisplatin or ZA group were significantly lower than those in the control and higher than those in combination (Figures 1(d) and 1(e); $P < 0.01$). Furthermore, to investigate the apoptosis of 143B cells treated with ZA/cisplatin/combination, flow cytometry and RT-qPCR were used. The results showed that the expression of apoptosis-related genes (caspase 3/9 and Bax) and the apoptosis rate of 143B in the combined treatment group were

significantly higher than those in the control and single treatment groups (Figures 1(f) and 1(g), S2; $P < 0.05$, $P < 0.01$), while the antiapoptosis gene (Bcl-2) expression was the lowest in the combined treatment. Furthermore, the synergy score of cisplatin and ZA was determined by SynergyFinder 2.0 [18]. The results showed that all the averaged synergy scores using four reference models were more than ten, indicating there is a good synergistic antiosteosarcoma effect between cisplatin and ZA (Figure S1a–d). In short, cisplatin in synergy with ZA could significantly induce the proliferation inhibition and apoptosis of 143B cells.

3.2. Oxidative Stress and PI3K/AKT Signaling Inhibition Mediated Cisplatin in Synergy with Zoledronic Acid Induced Apoptosis and Proliferation Inhibition of Osteosarcoma Cells. To further explore the mechanism of ZA and cisplatin enhancing antitumor, immunofluorescence was used to detect ROS generation after single or combined action of ZA and cisplatin. The results showed that the ROS generation after ZA or cisplatin treatment was significantly increased compared with the control, but the ROS of the ZA group was lower than that of the cisplatin group, while the ROS production after combined treatment was higher (Figures 2(a) and 2(b); $P < 0.05$, $P < 0.01$). The PI3K/AKT signaling is a crucial pathway related to the proliferation and apoptosis of osteosarcoma [21]. We further detected the expression of the PI3K/AKT pathway by RT-qPCR and Western blotting. The results showed that the phosphorylation of PI3K and AKT was significantly decreased in ZA or cisplatin alone than the control while there was no significant change in the mRNA and protein expression of PI3K and AKT, and the combined treatment was more significant than the single treatment group (Figures 2(c)–2(e); $P < 0.05$, $P < 0.01$). Furthermore, when we treated 143B cells with ROS scavenger N-acetyl-L-Cysteine (NAC) and 740 Y-P (an agonist for PI3K/AKT signaling pathway [22]) in combination with ZA+cisplatin, the results of phosphorylation inactivation of PI3K and AKT, clone formation and proliferation inhibition, and increased apoptosis were reversed (Figures 1(c)–1(g) and 2(d) and 2(e); $P < 0.05$, $P < 0.01$). Therefore, these results suggested that ZA+cisplatin could inhibit PI3K/AKT signaling activation by promoting ROS generation to induce apoptosis and proliferation inhibition of osteosarcoma cells.

3.3. Cisplatin in Synergy with Zoledronic Acid Inhibited Osteoclast Differentiation and Promoted the Apoptosis. It has been reported that ZA can inhibit osteoclast differentiation and survival [23]. However, chemotherapy drugs such as cisplatin often caused complications such as bone loss [24]. Moreover, osteoclasts are the essential cells for osteosarcoma to invade and destroy the surrounding bone tissue [25]. Therefore, we examined whether ZA inhibited osteoclast differentiation and survival after cisplatin treatment. Physiologically, osteoclasts are derived from BMMs. Consequently, we treated the cells during the differentiation of BMMs into osteoclasts with cisplatin, ZA, or combination. The results showed that TRAP staining positive rate and the number of osteoclasts in the combined treatment group

(a)

(b)

(c)

(d)

(e)
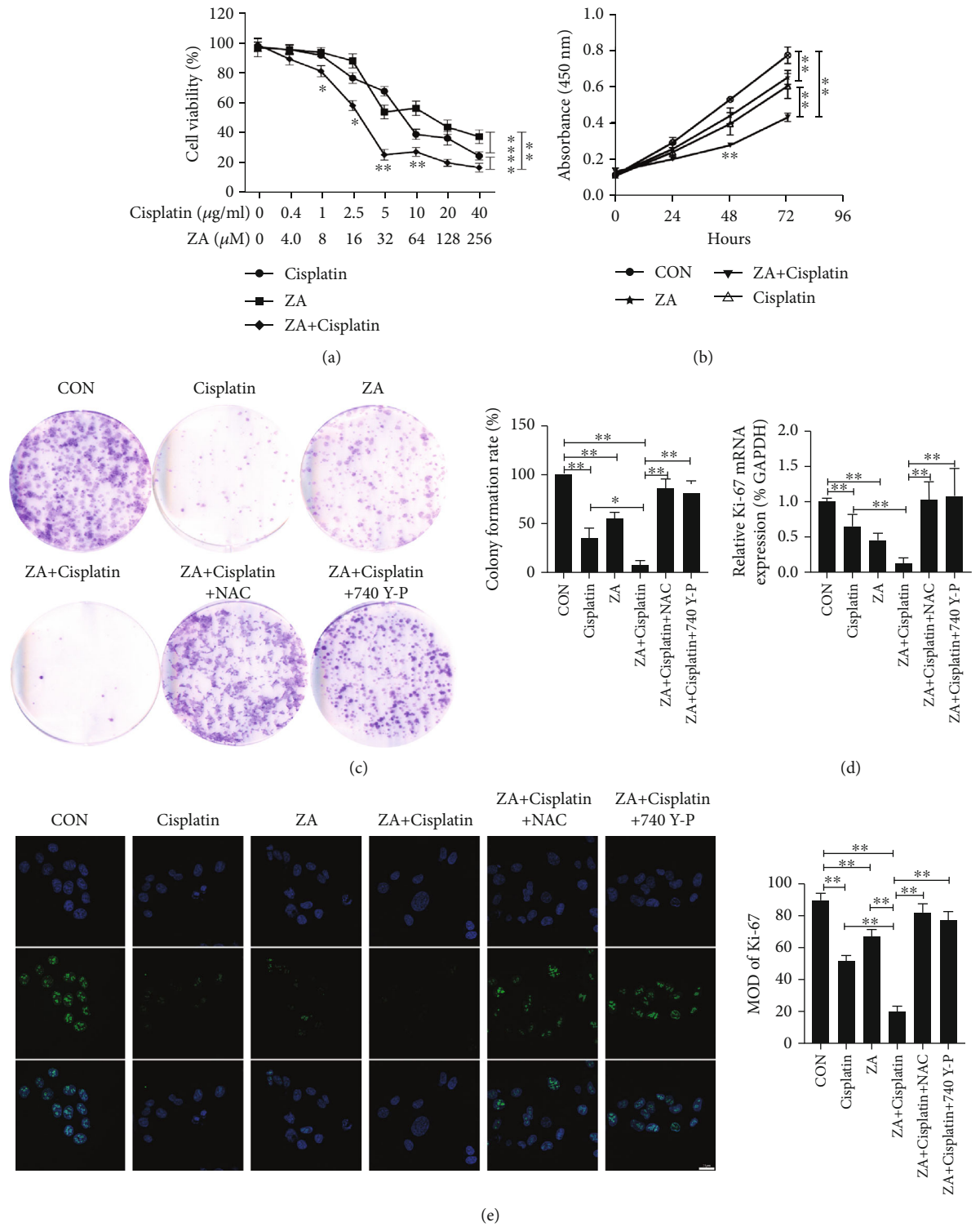
Figure 1: Continued.
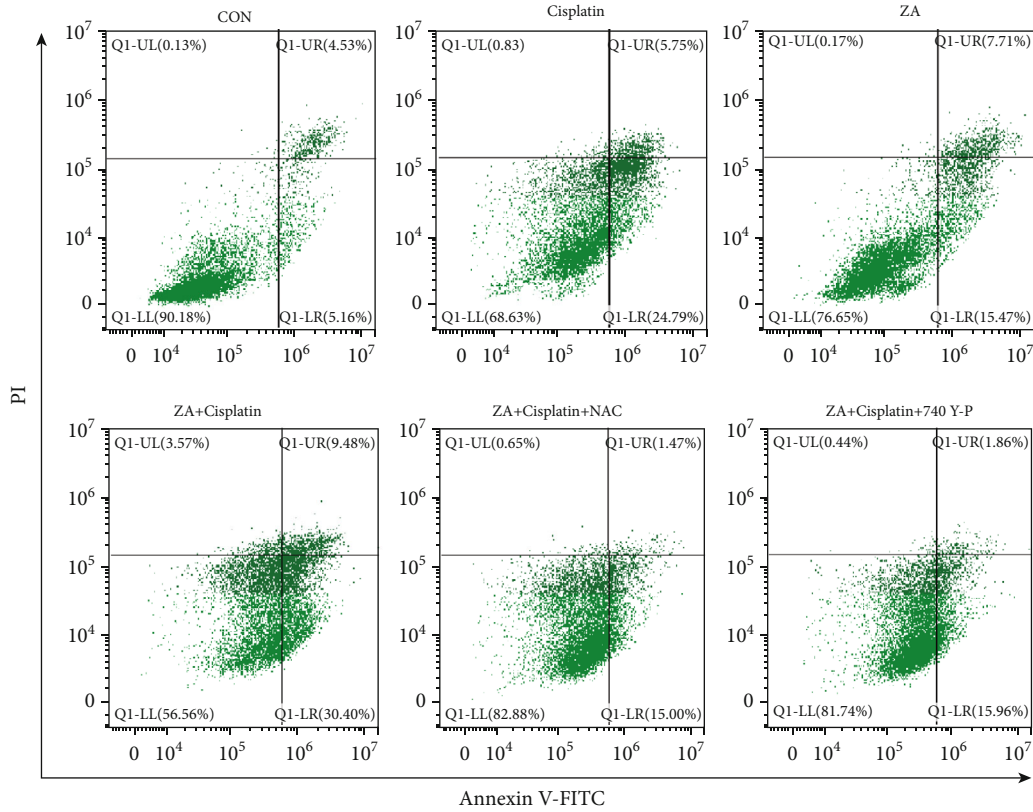
(f)
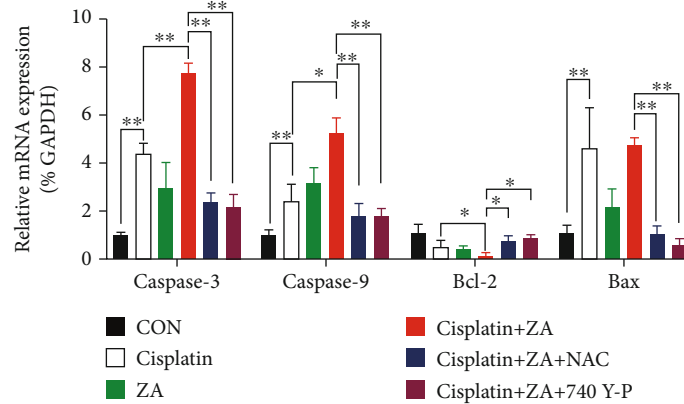
(g)

FIGURE 1: Zoledronic acid (ZA) increased cisplatin-induced apoptosis and proliferation inhibition in 143B cells. (a) Cell viability was measured by CCK-8 assay after 24 h in culture with the indicated concentrations of ZA/cisplatin/combination. (b) CCK-8 assay was performed to determine the cell viability of 143B cell after treatment with ZA/cisplatin/combination for 0, 24, 48, and 72 hours. (c) Cell clone formation of the 143B cells treated with cisplatin/ZA/ZA+cisplatin/ZA+cisplatin+NAC/ZA+cisplatin+740 Y-P. (d) The mRNA expression of Ki-67 was detected by RT-qPCR in 143B cells with the different treatment in the figures. (e) Immunofluorescence was used to detect Ki-67 protein expression in 143B cells treated by cisplatin/ZA/ZA+cisplatin/ZA+cisplatin+NAC/ZA+cisplatin+740 Y-P and quantification of the MOD value of the Ki-67 expression; scale bar = 25 μm. (f) Flow cytometry was used to detect apoptosis induced by cisplatin/ZA/ZA+cisplatin/ZA+cisplatin+NAC/ZA+cisplatin+740 Y-P. (g) RT-qPCR was used to detect the mRNA expression of caspase 3/9, Bcl-2, and Bax. CON: control; ZA: zoledronic acid; NAC: N-acetyl-L-Cysteine; MOD: mean optical density; Ki-67: marker of proliferation Ki-67; Bcl-2: protein phosphatase 1, regulatory subunit 50; Bax: BCL2-associated X protein omega. The values were the means ± SD, $n = 3$; $^{*}P < 0.05$, $^{**}P < 0.01$.

were significantly lower than those in the single treatment group, and both were lower than the control (Figures 3(a)–3(c); $P < 0.05$, $P < 0.01$). We further tested

the effects of ZA and cisplatin on the survival of osteoclasts. Consistent with differentiation, the osteoclast apoptosis in the ZA+cisplatin group was more than that in the control,

(a)

(b)

(c)

(d)

(e)
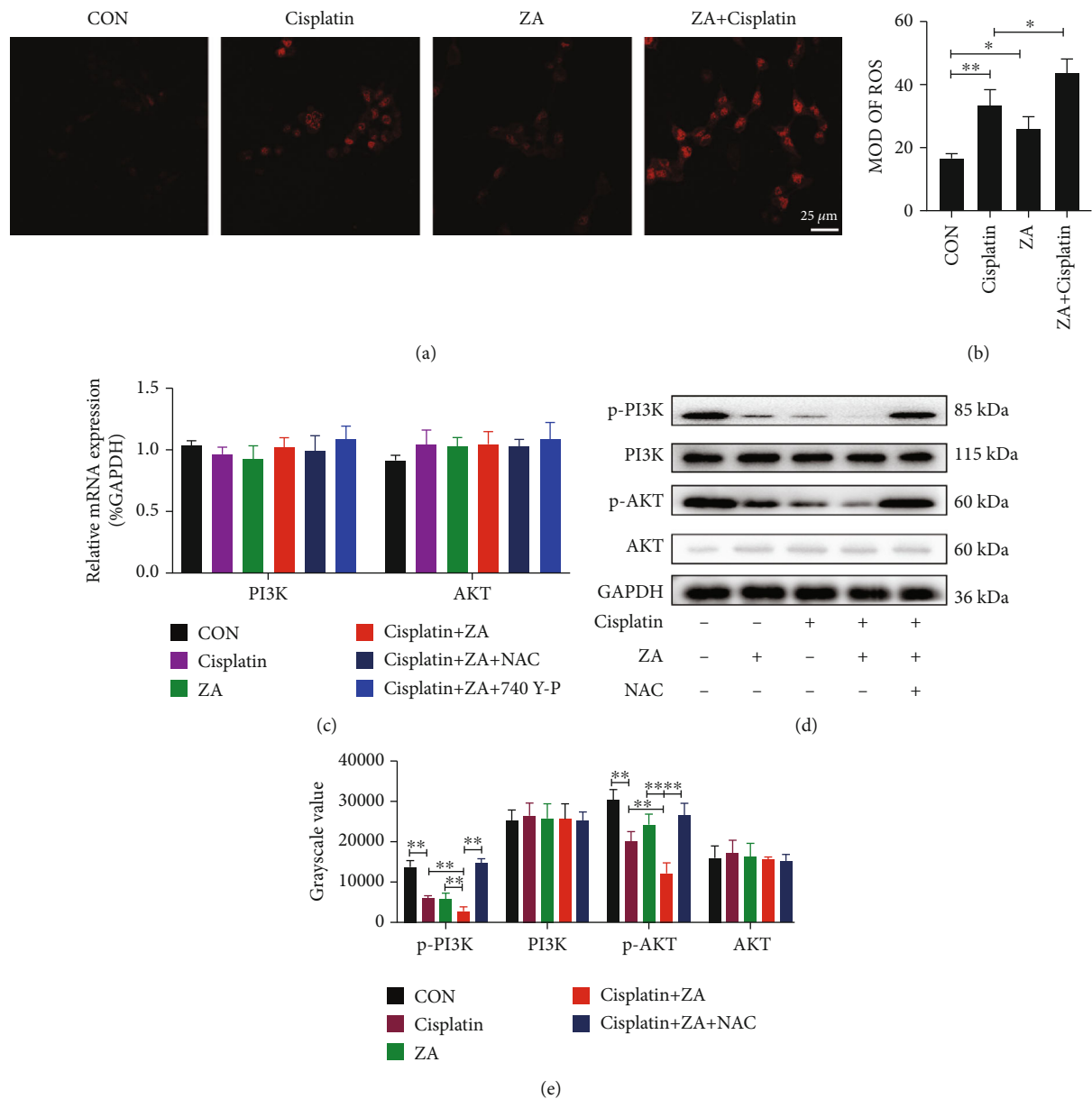
FIGURE 2: ROS-PI3K/AKT mediated the synergistic effect of ZA and cisplatin. (a) The ROS generated after ZA and cisplatin treated 143B cells alone or in combination, scale bar = 25 μm. (b) The quantitative analysis of ROS immunofluorescence. (c) The mRNA expression of PI3K and AKT was detected by RT-qPCR in 143B cells with different treatment. (d) Western blotting was used to detect the phosphorylated protein expression of 143B PI3K and AKT after different treatments. (e) Grayscale analysis of p-PI3K, PI3K, p-AKT, and AKT protein expression. CON: control; ZA: zoledronic acid; MOD: mean optical density; p-PI3K: phospho-PI3 kinase; p-AKT: phospho-AKT; ROS: reactive oxygen species; NAC: N-acetyl-L-Cysteine. The values were the means ± SD, $n = 3$; $^*P < 0.05$, $^{**}P < 0.01$.

but it was not significantly different from the single treatment group (Figures 3(d) and 3(e); $P < 0.05$, $P < 0.01$). Moreover, the bone resorption of the combined treatment group was significantly higher than that of the single treatment group, and both were stronger than the control (Figures 3(f) and 3(g); $P < 0.05$, $P < 0.01$). The above results indicated that either ZA or cisplatin could inhibit osteoclast formation, survival, and activation, but the combination was more effective.

3.4. Zoledronic Acid Enhanced Cisplatin-Induced Tumor Inhibition In Vivo. To further explore the effects in vivo, we

first established a nude mouse tibia orthotopic osteosarcoma model, and these model mice were then treated with cisplatin/ZA+cisplatin. The results showed that the tumors in the combined treatment group were significantly smaller visually than those in the single treatment and control (Figure 4(a)), and the weight of tumors was lower (Figure 4(b); $P < 0.01$). Furthermore, tumor volume and nude mouse body weight were measured, and tumor growth was significantly slower in the combined treatment group than in the other treatment and control (Figure 4(c); $P < 0.05$, $P < 0.01$), but there was no significant change in weight (Figure 4(d); $P > 0.05$). Further, we exfoliated the tumor and performed H&E, Ki-67, and
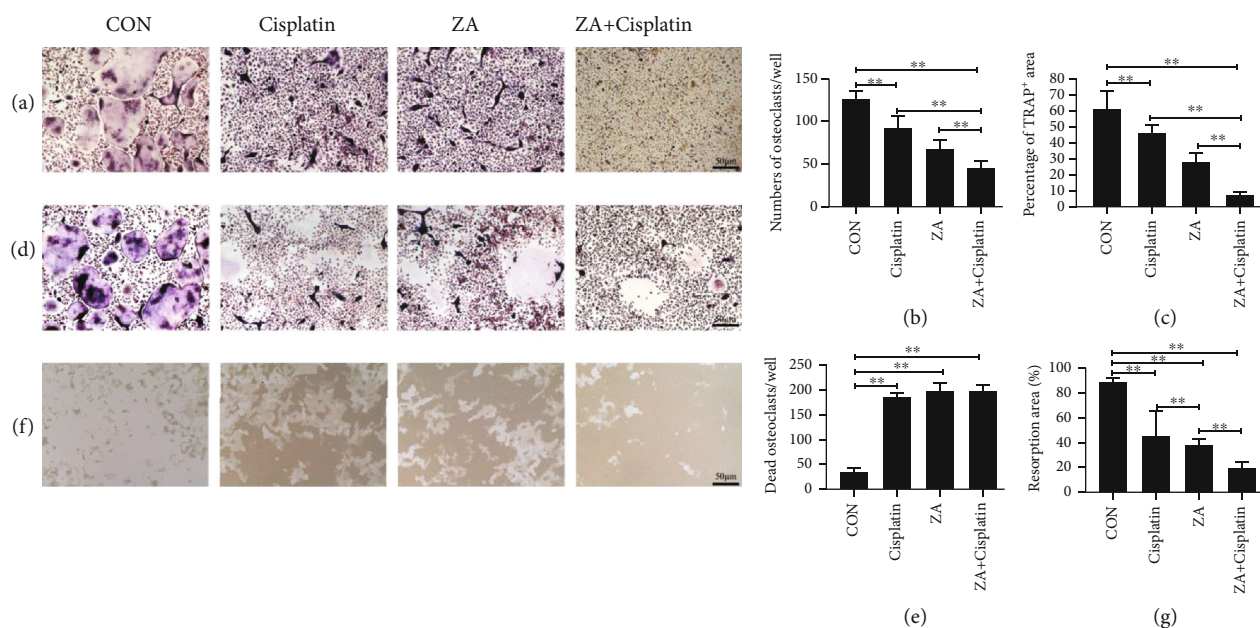
Figure 3: Cisplatin in synergy with zoledronic acid (ZA) inhibited osteoclast formation, survival, and activation. (a) The TRAP staining of BMMs treated with M-CSF and RANKL for 4 days in the presence of cisplatin/ZA+cisplatin. (b) The osteoclasts per well were counted. (c) The area of TRAP$^+$ multinucleated cells (nuclei > 3) was quantified. (d) The mature osteoclasts were treated by cisplatin/ZA+cisplatin. (e) The dead osteoclasts per well were counted. (f) The bone resorption on Corning Osteo Assay 24-well plates of osteoclasts treated by cisplatin/ZA+cisplatin. (g) The resorption area was quantitative. CON: control; ZA: zoledronic acid. The values were the means ± SD, $n =$ 3; scale bar = 50 μm; $^*P < 0.05$, $^{**}P < 0.01$.

Tunel staining. The results showed that the apoptosis and necrosis of tumor cells (Figures 4(e) and 4(g)) were significantly increased, while the proliferation (Figure 4(f)) was decreased. Finally, the function of the liver and kidney was tested because the hepatotoxicity and nephrotoxicity of chemotherapeutic drugs are the most common side effects [26, 27]. The results showed that the serum levels of ASL, ALT, CREA, and BUN in the combined group were not higher than those in the group treated by cisplatin, but they were all higher than those in the control (Figure S4a–d; $P < 0.05$, $P < 0.01$), indicating that the side effects of combined treatment were not higher than those of cisplatin alone.

3.5. Cisplatin in Synergy with Zoledronic Acid Attenuated Osteolytic Destruction. Biologically, osteoclasts and osteosarcoma cells interact to form a "vicious cycle" conducive to osteosarcoma growth and osteolysis [25]. Therefore, inhibition of osteolytic status is an important step in inhibiting the growth of osteosarcoma. In a nude mouse model of orthotopic osteosarcoma in the tibia, combined treatment with ZA and cisplatin resulted in significantly lower bone tissue destruction than that of the group treated with cisplatin alone or saline (Figure 5(a)). Three-dimensional reconstruction images of micro-CT further showed that there was less bone destruction in the combined treatment group (Figure 5(b)), and the decrease of femoral cancellous bone mass in the group treated with cisplatin could be reversed by the combined therapy, as manifested by a change in BV/TV, Tb.N, Tb.Th, and Tb.Sp (Figure 5(c); $^*P < 0.05$, ** $P < 0.01$). Finally, we detected the mRNA expression of marker genes of osteoclast differentiation (NFATc1) and

activity (TRAP and Ctsk) and performed TRAP staining on the tumor side tibia tissue. The results showed that the marker genes of osteoclast differentiation and activity were lower significantly in ZA+cisplatin than those in the group treated with saline or cisplatin (Figure 5(d); $^*P < 0.05$, $^{**}P < 0.01$). And TRAP staining-positive cells were also significantly reduced, indicating that osteoclasts in bone tissue were inhibited after ZA+cisplatin treatment (Figure 5(e)). In short, ZA could inhibit the formation of osteoclasts between osteosarcoma and normal bone, breaking the "vicious circle" between it and tumor cells to inhibit osteolytic destruction.

4. Discussion

Osteosarcoma, with extremely high nausea, is originated from osteoblast and often occurs in long tubular bone [28, 29]. Studies have shown that about 20% of bone tumors are osteosarcoma, which is common in adolescents [30]. With the development of surgery and adjuvant chemotherapy, the long-term survival rate of patients with osteosarcoma is increasing. However, the 5-year survival rate is still less than 70%, and osteosarcoma is still the main cause of cancer death in children and adolescents [4, 31]. Chemotherapy is one of the most important methods in the treatment of osteosarcoma [32]. The commonly used chemotherapy drugs include cisplatin, MTX, ADM, IFO, vincristine (VCR), epirubicin (EPI), cyclophosphamide (CTX), and etoposide (VP-16), among which cisplatin, MTX, ADM, and IFO are the most common [33]. However, the application of chemotherapy drugs such as cisplatin can easily lead to drug resistance and a variety of adverse reactions such as bone loss, which
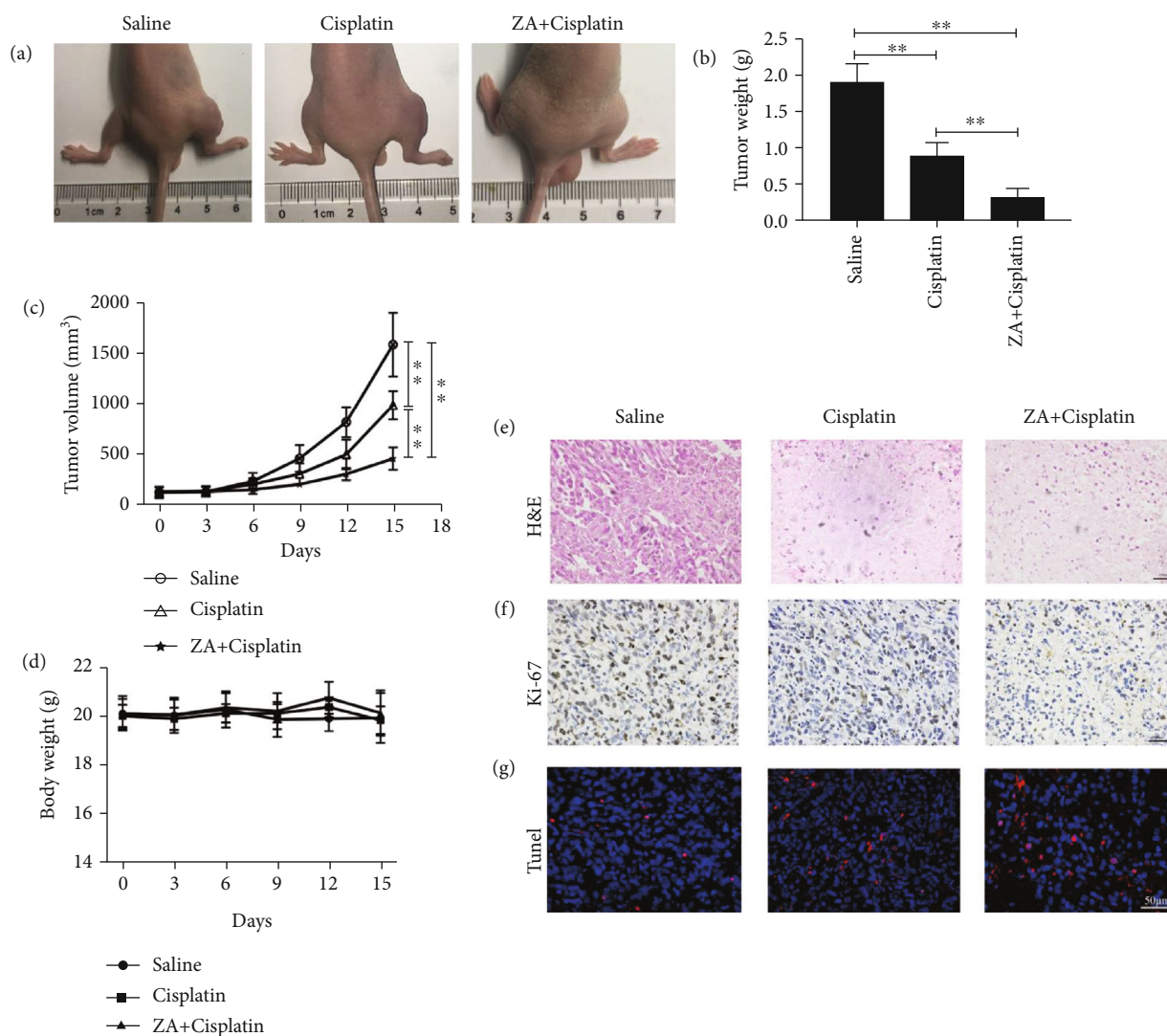
Figure 4: Cisplatin in synergy with zoledronic acid (ZA) inhibited osteosarcoma in vivo. (a) The tumor growth in nude mice. (b) Tumor weights were weighted after the mice were sacrificed. (c) Tumor volume was measured every 3 days. (d) Mouse body weights were measured per 3 days. (e) H&E staining of tumors, scale bar = 100 μm. (f) Immunohistochemical analysis of Ki-67 protein expression in tumor tissues, scale bar = 100 μm. (g) Tunel staining in tumor tissues indicated the apoptosis of tumor cells, scale bar = 50 μm. H&E: hematoxylin-eosin staining; CON: control; ZA: zoledronic acid. The values were the means ± SD, $n = 5$; $^{*}P < 0.05$, $^{**}P < 0.01$.

are pivotal reasons for the bottleneck in the treatment of osteosarcoma [34]. Therefore, it is urgent to explore new strategies to enhance the efficacy of chemotherapy drugs and reduce the side effects.

Bisphosphonates are the first-line drugs for the treatment of osteoporosis, whereas ZA is the third generation of nitrogen-containing bisphosphonates [35, 36]. However, increasing studies have shown that ZA has the effect of not only treating osteoporosis but also antitumor. Liu et al. showed that ZA can block the interaction between breast cancer cells and regulatory T cells, thereby reducing breast cancer invasion [16]. Wang et al. also showed that ZA can regulate cell cycle and apoptosis to inhibit the growth of cervical cancer cells [17]. However, the understanding of ZA in osteosarcoma is still lacking, and its combined effect and mechanism with commonly used chemotherapy drugs are still unclear. In this study, cisplatin alone or in combination

with ZA could reduce the activity of osteosarcoma cells, but the combined effect was more obvious. It took 48 hours for cisplatin alone to decrease the cell activity, but it decreased at 24 hours after the combination of cisplatin and ZA at the same dose. Moreover, after combined treatment whether in vitro or in vivo, the proliferation inhibition and apoptosis of osteosarcoma cells were more obvious, and the necrosis and growth inhibition of tumor were also obviously increased. The synergy score calculated by SynergyFinder was also more than ten. Therefore, these results showed that ZA could synergistically enhance the antitumor effect of cisplatin.

Cisplatin is one of the most commonly used and classic chemotherapy drugs in the treatment of osteosarcoma [37, 38]. However, its resistance limits its further application in clinic. Studies have shown that the mechanisms of cisplatin resistance include increased DNA repair, altered cellular aggregation, apoptosis resistance, and autophagy [39, 40].

(a)

(b)

(c)

(d)

(e)
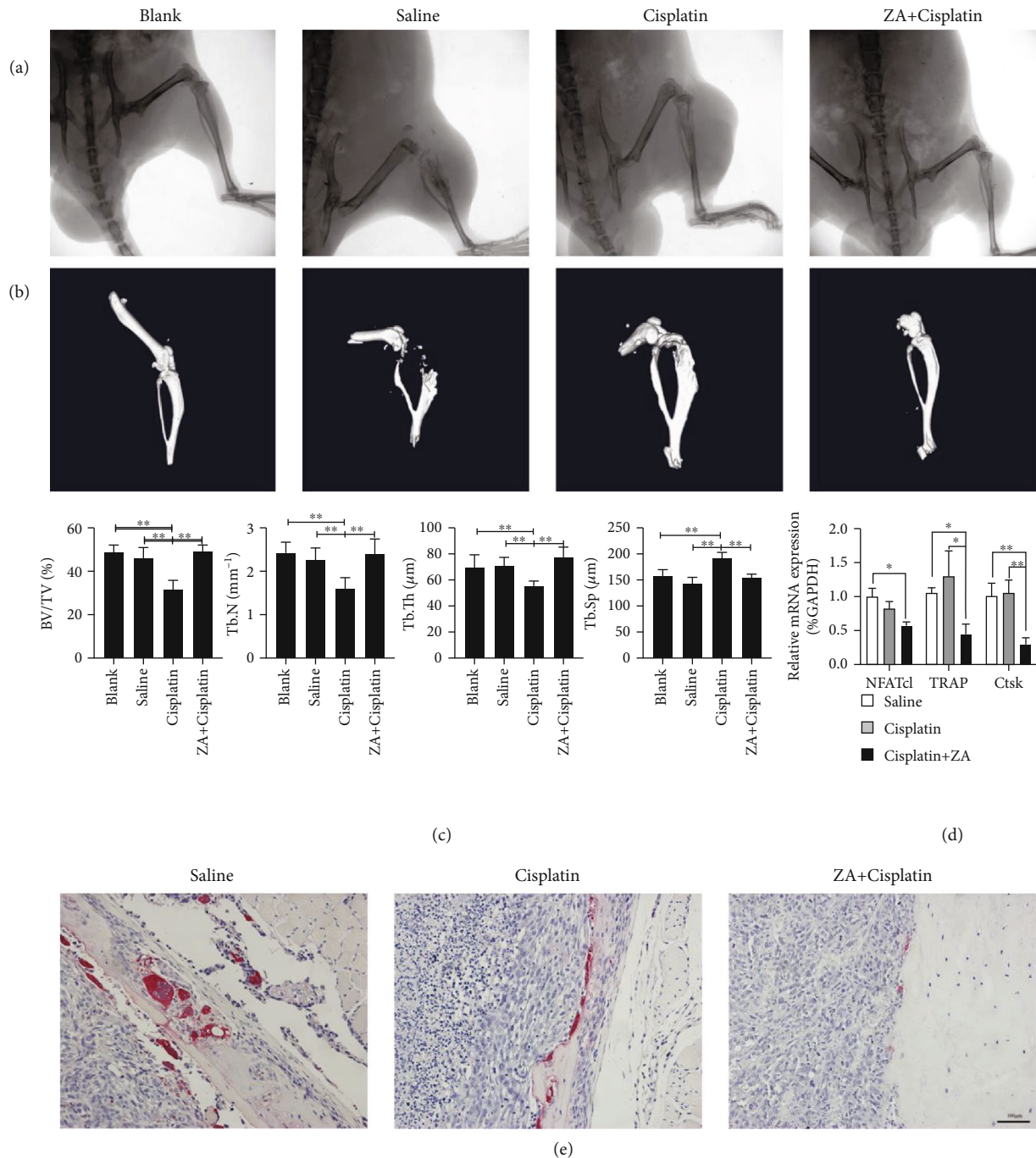
FIGURE 5: Cisplatin in synergy with zoledronic acid (ZA) attenuated osteolysis. (a) X-ray radiography of lower limb in the side of the tumor. (b) Three-dimensional reconstruction images of micro-CT. (c) Analysis of the femoral cancellous bone mass based on the data from micro-CT scan, including BV/TV, Tb.N, Tb.Th, and Tb.Sp. (d) The mRNA expression of NFATc1, TRAP, and Ctsk in the bone tissue at the site of tumor invasion. (e) The TRAP staining of the tibia containing the tumor, scale bar = 100 μm. ZA: zoledronic acid; BV/TV: bone volume/total volume; Tb.N: trabecular number; Tb.Th: trabecular thickness; Tb.Sp: trabecular separation; NFATc1: nuclear factor of activated T cells 1; TRAP: triiodothyronine receptor auxiliary protein; Ctsk: cathepsin K. The values were the means ± SD, $n = 3$; $^{*}P < 0.05$, $^{**}P < 0.01$.

Therefore, intervention in these mechanisms can inhibit the resistance of cisplatin. The PI3K/AKT signaling pathway is a classical tyrosine kinase cascade signal transduction pathway widely existing in organisms, which is involved in the occurrence and development of tumors, as well as the treatment and prognosis [41, 42]. PI3K is an intracellular phosphatidylinositol kinase with serine/threonine kinase

activity. After phosphorylation of PI3K, AKT is further phosphorylated, and the PI3K/AKT pathway is activated, thus promoting the proliferation of tumor cells and inhibiting their apoptosis [43]. In this present study, the combination of ZA and cisplatin further inhibited the activation of the PI3K/AKT singling pathway in osteosarcoma cells than cisplatin alone. Further study showed that ZA and cisplatin

combined treatment significantly increased the generation of ROS in osteosarcoma cells, while ROS scavengers could eliminate the inhibition of the PI3K/AKT pathway. What is more, in this study, ROS scavengers and the agonist of PI3K/AKT pathway (740 Y-P) could reverse the clone formation and proliferation inhibition and increased apoptosis of osteosarcoma induced by cisplatin+ZA. This was consistent with Deng's finding that dexamethasone can promote the generation of ROS in osteoblasts and thus inhibit the activation of PI3K/AKT [44]. However, how ROS induced the activation of the PI3K/AKT pathway remains to be further studied. Bugide et al. found that apoptosis resistance mediated by the PI3K/AKT pathway is closely related to cisplatin resistance [45]. Qiu et al. also proved that MNAT1 promotes cisplatin resistance of osteosarcoma cells via regulating the PI3K/AKT/mTOR pathway [46]. And another study by Zhao et al. further confirmed that activation of the PI3K/AKT signaling abolished poncirin-induced reduction of the mRNA and protein expression of multidrug resistance gene (MDR1, MPR1, and BCRP) in cisplatin-resistant osteosarcoma cells [47]. Therefore, we detected the effect of ZA+cisplatin on cisplatin resistance. The results showed that the IC_{50} values of cisplatin decreased significantly in the cisplatin-resistant osteosarcoma cells treated with $8\,\mu$M ZA (this concentration had no effect on the cell viability) (Figure S3a; $^{*}P < 0.05$, $^{**}P < 0.01$). And the apoptosis rate increased, and the mRNA and protein expression of the multidrug resistance gene (MDR1, MPR1) decreased in the cisplatin-resistant osteosarcoma cells treated with cisplatin +ZA (Figure S3b–e; $^{*}P < 0.05$, $^{**}P < 0.01$). In conclusion, the combination of ZA and cisplatin can inhibit ROS-PI3K/AKT signaling to enhance the antitumor efficacy and drug resistance of cisplatin.

Physiologically, osteoclasts remove old bone and osteoblasts form new bone, maintaining bone homeostasis. The formation and activation of osteoclasts require two factors: RANKL and macrophage colony-stimulating factor [48]. It has been found that osteosarcoma cells can produce RANKL, which can promote the production of osteoclasts and osteolysis [25], and activated osteoclasts can secrete a variety of cytokines, such as TGFβ, IGFs, and FGFs [9–11], to further promote the growth of tumor cells and form a "vicious circle." Therefore, inhibiting the formation and activation of osteoclasts is also the key to suppress the growth of osteosarcoma. In this study, we found that ZA and cisplatin could significantly inhibit osteoclast differentiation, promote osteoclast death, and inhibit bone resorption in vitro. In vivo, we also found that in the combined treatment group, the number of osteoclasts at the junction of tumor and bone decreased significantly, and the destruction of bone by tumor decreased significantly. Interestingly, our study and previous studies have shown that cisplatin can reduce bone mass [24], but we also found that cisplatin could inhibit osteoclast formation, survival, and activity. Osteoblasts are another important factor in maintaining bone mass [49]. Therefore, the decrease in bone mass induced by cisplatin might be related to the inhibition of osteoblasts. In addition, it has been found that there is an important relationship between the PI3K/AKT signal pathway and osteoclast differentiation,

survival, and the interaction of many kinds of cytokines [50, 51]. However, this study found that ZA and cisplatin could inhibit the activation of the PI3K/AKT signaling pathway in osteosarcoma cells, which might also be the reason for inhibiting the survival and formation of osteoclasts and reducing bone destruction, but it needs further confirmation.

5. Conclusion

In conclusion, this study confirmed that ZA can enhance the antiosteosarcoma effect of cisplatin and ameliorate chemoresistance in vivo and in vitro. The mechanism is related to the increased generation of ROS and inhibition of PI3K/AKT signal pathway activation. Moreover, the combination of ZA and cisplatin could inhibit osteoclast differentiation, survival, and activation, thus breaking the "vicious circle" to inhibit tumor growth and osteolysis destruction. Therefore, ZA may be used as an adjuvant chemotherapy drug beneficial to the treatment of osteosarcoma.

Data Availability

The data that support the findings of this study are available from the corresponding author upon reasonable request.

Conflicts of Interest

All authors declare no conflict of interest.

Authors' Contributions

Liang Liu and Huan Geng contributed equally to this work.

Acknowledgments

Supplementary Materials

Table S1: the primers used for a real-time quantitative polymerase chain reaction. $GAPDH_{(1)}$: glyceraldehyde 3-phosphate dehydrogenase from human; Ki-67: marker of proliferation Ki-67; caspase 3: apoptosis-related cysteine protease 3; caspase 9: apoptosis-related cysteine protease 9; Bcl-2: protein phosphatase 1, regulatory subunit 50; Bax: BCL2-associated X protein omega; PI3K: phosphatidylinositol-4,5-bisphosphate 3-kinase; AKT: AKT serine/threonine kinase 1; MDR1: ATP binding cassette subfamily B member 1; MRP1: ATP binding cassette subfamily C member 1; $GAPDH_{(2)}$: glyceraldehyde 3-phosphate dehydrogenase from mouse; NFATc1: nuclear factor of activated T cells 1; TRAP: triiodothyronine receptor auxiliary protein; Ctsk: cathepsin K. Figure S1: the combination of cisplatin and zoledronic acid

(ZA) showed a synergistic effect against the osteosarcoma cell. The synergistic effect was analyzed with SynergyFinder by four reference models. The synergy delta score was calculated by HAS (a), Loewe (b), Bliss (c), and ZIP (d) reference models, respectively. The values in the center of each panel showed the highest synergy score. HAS, Loewe, Bliss, and ZIP Synergy scores > 0 indicate synergism (red regions), while the scores < 0 suggest antagonism (green regions). Figure S2: detection of apoptosis rate of 143B cells by flow cytometry. 143B cell was treated with cisplatin (5 μg/ml) and/or ZA (32 μM) or cisplatin+ZA+NAC or cisplatin+ZA+740 Y-P. CON: control; ZA: zoledronic acid; NAC: N-acetyl-L-Cysteine. The values were the means ± SD, $n = 3$; $^*P < 0.05$, $^{**}P < 0.01$. Figure S3: ZA attenuated the resistance of osteosarcoma cells to cisplatin. (a) After 143B/CDDP was treated with 8 μM ZA for 12 h, the IC_{50} value of cisplatin was analyzed with a CCK-8 kit. (b, c) Flow cytometry was used to detect apoptosis of 143B/CDDP cells induced by cisplatin (5 μg/ml)/ZA (32 μM)/ZA+cisplatin. (d) RT-qPCR was used to detect the mRNA expression of MDR1 and MRP1 in 143B/CDDP cells treated with 8 μM ZA. (e) The protein expression of MDR1 and MRP1 was analyzed by Western blotting. CON: control; ZA: zoledronic acid; MDR1: ATP binding cassette subfamily B member 1; MRP1: ATP binding cassette subfamily C member 1. The values were the means ± SD, $n = 3$; $^*P < 0.05$, $^{**}P < 0.01$. Figure S4: the hepatotoxicity and nephrotoxicity in the nude mice bearing 143B osteosarcoma cell treated with cisplatin or/and zoledronic acid. The serum concentration of ASL (a), ALT (b), CREA (c), and BUN (d) detected by an automatic biochemical analyzer. ZA: zoledronic acid; AST: aspartate aminotransferase; ALT: alanine aminotransferase; BUN: blood urine nitrogen; CREA: creatinine. The values were the means ± SD, $n = 5$; $^*P < 0.05$, $^{**}P < 0.01$. *(Supplementary Materials)*

References

[1] C. Melim, I. Jarak, F. Veiga, and A. Figueiras, "The potential of micelleplexes as a therapeutic strategy for osteosarcoma disease," *3 Biotech*, vol. 10, no. 4, p. 147, 2020.

[2] J. Ritter and S. S. Bielack, "Osteosarcoma," *Annals of Oncology*, vol. 21, Supplement 7, pp. vii320–vii325, 2010.

[3] D. J. Harrison, D. S. Geller, J. D. Gill, V. O. Lewis, and R. Gorlick, "Current and future therapeutic approaches for osteosarcoma," *Expert Review of Anticancer Therapy*, vol. 18, no. 1, pp. 39–50, 2018.

[4] F. Sun, Y. Zhang, L. Xu et al., "Proteasome inhibitor MG132 enhances cisplatin-induced apoptosis in osteosarcoma cells and inhibits tumor growth," *Oncology Research*, vol. 26, no. 4, pp. 655–664, 2018.

[5] M. Kim, J. Y. Jung, S. Choi et al., "GFRA1 promotes cisplatin-induced chemoresistance in osteosarcoma by inducing autophagy," *Autophagy*, vol. 13, no. 1, pp. 149–168, 2017.

[6] A. Brozovic, A. Ambriović-Ristov, and M. Osmak, "The relationship between cisplatin-induced reactive oxygen species, glutathione, and BCL-2 and resistance to cisplatin," *Critical Reviews in Toxicology*, vol. 40, no. 4, pp. 347–359, 2010.

[7] S. Ferrari and E. Palmerini, "Adjuvant and neoadjuvant combination chemotherapy for osteogenic sarcoma," *Current Opinion in Oncology*, vol. 19, no. 4, pp. 341–346, 2007.

[8] F. C. Kelleher and H. O'Sullivan, "Monocytes, macrophages, and osteoclasts in osteosarcoma," *Journal of Adolescent and Young Adult Oncology*, vol. 6, no. 3, pp. 396–405, 2017.

[9] J. J. Yin, K. Selander, J. M. Chirgwin et al., "TGF-beta signaling blockade inhibits PTHrP secretion by breast cancer cells and bone metastases development," *The Journal of Clinical Investigation*, vol. 103, no. 2, pp. 197–206, 1999.

[10] Y. C. Kuo, C. H. Su, C. Y. Liu, T. H. Chen, C. P. Chen, and H. S. Wang, "Transforming growth factor-beta induces CD44 cleavage that promotes migration of MDA-MB-435s cells through the up-regulation of membrane type 1-matrix metalloproteinase," *International Journal of Cancer*, vol. 124, no. 11, pp. 2568–2576, 2009.

[11] L. Endo-Munoz, A. Evdokiou, and N. A. Saunders, "The role of osteoclasts and tumour-associated macrophages in osteosarcoma metastasis," *Biochimica et Biophysica Acta*, vol. 1826, no. 2, pp. 434–442, 2012.

[12] S. Zhang, G. Gangal, and H. Uludag, "'Magic bullets' for bone diseases: progress in rational design of bone-seeking medicinal agents," *Chemical Society Reviews*, vol. 36, no. 3, pp. 507–531, 2007.

[13] T. Ohba, J. M. M. Cates, H. A. Cole et al., "Pleiotropic effects of bisphosphonates on osteosarcoma," *Bone*, vol. 63, pp. 110–120, 2014.

[14] T. Bellido and L. I. Plotkin, "Novel actions of bisphosphonates in bone: preservation of osteoblast and osteocyte viability," *Bone*, vol. 49, no. 1, pp. 50–55, 2011.

[15] G. N. Hortobagyi, M. Zheng, and R. Mohanlal, "Indirect evaluation of bone saturation with zoledronic acid after long-term dosing," *The Oncologist*, vol. 24, no. 2, pp. 178–184, 2018.

[16] H. Liu, S. H. Wang, S. C. Chen, C. Y. Chen, and T. M. Lin, "Zoledronic acid blocks the interaction between breast cancer cells and regulatory T-cells," *BMC Cancer*, vol. 19, no. 1, p. 176, 2019.

[17] L. Wang, Y. Liu, Y. Zhou et al., "Zoledronic acid inhibits the growth of cancer stem cell derived from cervical cancer cell by attenuating their stemness phenotype and inducing apoptosis and cell cycle arrest through the Erk1/2 and Akt pathways," *Journal of Experimental & Clinical Cancer Research*, vol. 38, no. 1, p. 93, 2019.

[18] A. Ianevski, A. K. Giri, and T. Aittokallio, "SynergyFinder 2.0: visual analytics of multi-drug combination synergies," *Nucleic Acids Research*, vol. 48, no. W1, pp. W488–w493, 2020.

[19] G. Chene, A. Cayre, I. Raoelfils, N. Lagarde, J. Dauplat, and F. Penault-Llorca, "Morphological and immunohistochemical pattern of tubo-ovarian dysplasia and serous tubal intraepithelial carcinoma," *European Journal of Obstetrics, Gynecology, and Reproductive Biology*, vol. 183, pp. 89–95, 2014.

[20] B. Han, H. Geng, L. Liu, Z. Wu, and Y. Wang, "GSH attenuates RANKL-induced osteoclast formation in vitro and LPS-induced bone loss in vivo," *Biomedicine & Pharmacotherapy*, vol. 128, p. 110305, 2020.

[21] G. S. Zhao, Z. R. Gao, Q. Zhang et al., "TSSC3 promotes autophagy via inactivating the Src-mediated PI3K/Akt/mTOR pathway to suppress tumorigenesis and metastasis in osteosarcoma, and predicts a favorable prognosis," *Journal of Experimental & Clinical Cancer Research*, vol. 37, no. 1, p. 188, 2018.

[22] Z. Sun, L. Sun, and L. Tu, "GABAB receptor-mediated PI3K/Akt signaling pathway alleviates oxidative stress and neuronal cell injury in a rat model of Alzheimer's disease,"

Journal of Alzheimer's Disease, vol. 76, no. 4, pp. 1513–1526, 2020.

[23] V. Stresing, P. G. Fournier, A. Bellahcène et al., "Nitrogen-containing bisphosphonates can inhibit angiogenesis in vivo without the involvement of farnesyl pyrophosphate synthase," *Bone*, vol. 48, no. 2, pp. 259–266, 2011.

[24] A. L. Essex, F. Pin, J. R. Huot, L. F. Bonewald, L. I. Plotkin, and A. Bonetto, "Bisphosphonate treatment ameliorates chemotherapy-induced bone and muscle abnormalities in young mice," *Front Endocrinol (Lausanne)*, vol. 10, p. 809, 2019.

[25] K. Mori, B. le Goff, M. Berreur et al., "Human osteosarcoma cells express functional receptor activator of nuclear factor-kappa B," *The Journal of Pathology*, vol. 211, no. 5, pp. 555–562, 2007.

[26] T. Karasawa and P. S. Steyger, "An integrated view of cisplatin-induced nephrotoxicity and ototoxicity," *Toxicology Letters*, vol. 237, no. 3, pp. 219–227, 2015.

[27] T. Boroja, J. Katanić, G. Rosić et al., "Summer savory (*Satureja hortensis* L.) extract: phytochemical profile and modulation of cisplatin-induced liver, renal and testicular toxicity," *Food and Chemical Toxicology*, vol. 118, pp. 252–263, 2018.

[28] L. Pietrovito, A. Leo, V. Gori et al., "Bone marrow-derived mesenchymal stem cells promote invasiveness and transendothelial migration of osteosarcoma cells via a mesenchymal to amoeboid transition," *Molecular Oncology*, vol. 12, no. 5, pp. 659–676, 2018.

[29] A. Takeuchi, N. Yamamoto, K. Hayashi et al., "Joint-preservation surgery for pediatric osteosarcoma of the knee joint," *Cancer Metastasis Reviews*, vol. 38, no. 4, pp. 709–722, 2019.

[30] R. Kumar, M. Kumar, K. Malhotra, and S. Patel, "Primary osteosarcoma in the elderly revisited: current concepts in diagnosis and treatment," *Current Oncology Reports*, vol. 20, no. 2, p. 13, 2018.

[31] R. D. Roberts, M. M. Lizardo, D. R. Reed et al., "Provocative questions in osteosarcoma basic and translational biology: a report from the Children's Oncology Group," *Cancer*, vol. 125, no. 20, pp. 3514–3525, 2019.

[32] D. M. Gianferante, L. Mirabello, and S. A. Savage, "Germline and somatic genetics of osteosarcoma - connecting aetiology, biology and therapy," *Nature Reviews. Endocrinology*, vol. 13, no. 8, pp. 480–491, 2017.

[33] S. Ferrari, C. Meazza, E. Palmerini et al., "Nonmetastatic osteosarcoma of the extremity. Neoadjuvant chemotherapy with methotrexate, cisplatin, doxorubicin and ifosfamide. An Italian Sarcoma Group study (ISG/OS-Oss)," *Tumori Journal*, vol. 100, no. 6, pp. 612–619, 2018.

[34] X. Xiao, W. Wang, Y. Li et al., "HSP90AA1-mediated autophagy promotes drug resistance in osteosarcoma," *Journal of Experimental & Clinical Cancer Research*, vol. 37, no. 1, p. 201, 2018.

[35] J. Xie, S. Li, L. Xiao et al., "Zoledronic acid ameliorates the effects of secondary osteoporosis in rheumatoid arthritis patients," *Journal of Orthopaedic Surgery and Research*, vol. 14, no. 1, p. 421, 2019.

[36] N. K. Choi, D. H. Solomon, T. N. Tsacogianis, J. E. Landon, H. J. Song, and S. C. Kim, "Comparative safety and effectiveness of denosumab versus zoledronic acid in patients with osteoporosis: a cohort study," *Journal of Bone and Mineral Research*, vol. 32, no. 3, pp. 611–617, 2017.

[37] J. S. Whelan and L. E. Davis, "Osteosarcoma, chondrosarcoma, and chordoma," *Journal of Clinical Oncology*, vol. 36, no. 2, pp. 188–193, 2018.

[38] L. Wang, F. Jin, A. Qin et al., "Targeting Notch1 signaling pathway positively affects the sensitivity of osteosarcoma to cisplatin by regulating the expression and/or activity of caspase family," *Molecular Cancer*, vol. 13, no. 1, p. 139, 2014.

[39] L. Amable, "Cisplatin resistance and opportunities for precision medicine," *Pharmacological Research*, vol. 106, pp. 27–36, 2016.

[40] F. Liang, C. Ren, J. Wang et al., "The crosstalk between STAT3 and p53/RAS signaling controls cancer cell metastasis and cisplatin resistance via the Slug/MAPK/PI3K/AKT-mediated regulation of EMT and autophagy," *Oncogene*, vol. 8, no. 10, p. 59, 2019.

[41] J. S. O'Donnell, D. Massi, M. W. L. Teng, and M. Mandala, "PI3K-AKT-mTOR inhibition in cancer immunotherapy, redux," *Seminars in Cancer Biology*, vol. 48, pp. 91–103, 2018.

[42] Q. Yang, W. Jiang, and P. Hou, "Emerging role of PI3K/AKT in tumor-related epigenetic regulation," *Seminars in Cancer Biology*, vol. 59, pp. 112–124, 2019.

[43] Z. Xu, X. Han, D. Ou et al., "Targeting PI3K/AKT/mTOR-mediated autophagy for tumor therapy," *Applied Microbiology and Biotechnology*, vol. 104, no. 2, pp. 575–587, 2020.

[44] S. Deng, G. Dai, S. Chen et al., "Dexamethasone induces osteoblast apoptosis through ROS-PI3K/AKT/GSK3β signaling pathway," *Biomedicine & Pharmacotherapy*, vol. 110, pp. 602–608, 2019.

[45] S. Bugide, V. K. Gonugunta, V. Penugurti, V. L. Malisetty, R. K. Vadlamudi, and B. Manavathi, "HPIP promotes epithelial-mesenchymal transition and cisplatin resistance in ovarian cancer cells through PI3K/AKT pathway activation," *Cellular Oncology (Dordrecht)*, vol. 40, no. 2, pp. 133–144, 2017.

[46] C. Qiu, W. Su, N. Shen et al., "MNAT1 promotes proliferation and the chemo-resistance of osteosarcoma cell to cisplatin through regulating PI3K/Akt/mTOR pathway," *BMC Cancer*, vol. 20, no. 1, p. 1187, 2020.

[47] L. Zhao, W. Zhang, and F. Zhang, "Poncirin downregulates ATP-binding cassette transporters to enhance cisplatin sensitivity in cisplatin-resistant osteosarcoma cells," *Phytotherapy Research*, vol. 35, no. 1, pp. 278–288, 2021.

[48] R. J. Miron and D. D. Bosshardt, "OsteoMacs: key players around bone biomaterials," *Biomaterials*, vol. 82, pp. 1–19, 2016.

[49] I. Kanazawa, L. Canaff, J. Abi Rafeh et al., "Osteoblast menin regulates bone mass in vivo," *The Journal of Biological Chemistry*, vol. 290, no. 7, pp. 3910–3924, 2015.

[50] S. E. Lee, W. J. Chung, H. B. Kwak et al., "Tumor necrosis factor-α supports the survival of osteoclasts through the activation of Akt and ERK," *The Journal of Biological Chemistry*, vol. 276, no. 52, pp. 49343–49349, 2001.

[51] Z. H. Lee, S. E. Lee, C. W. Kim et al., "IL-1alpha stimulation of osteoclast survival through the PI 3-kinase/Akt and ERK pathways," *Journal of Biochemistry*, vol. 131, no. 1, pp. 161–166, 2002.

Research Article

Resveratrol Derivative, Trans-3, 5, 4′-Trimethoxystilbene Sensitizes Osteosarcoma Cells to Apoptosis via ROS-Induced Caspases Activation

Yu Feng,[1,2] **Jacob Clayton,**[3] **Wildman Yake,**[3] **Jinke Li,**[3] **Weijia Wang** (iD),[4] **Lauren Winne** (iD),[3] **and Ming Hong** (iD)[5,6]

[1]*Department of Traumatology, General Hospital of Ningxia Medical University, 804 Shengli South Road, Yinchuan, Ningxia Hui Autonomous Region 750004, China*

[2]*Department of Orthopaedics and Traumatology, The University of Hong Kong, 21 Sassoon Road, Hong Kong SAR 999077, China*

[3]*Department of Pharmacology & Toxicology, University of Kansas, 126 Strong Hall, Lawrence, KS 66045, USA*

[4]*Zhongshan People's Hospital, 2 Sun Wen East Road, Zhongshan, Guangdong 528400, China*

[5]*Institute of Advanced Diagnostic and Clinical Medicine, Zhongshan People's Hospital, Guangzhou University & Zhongshan People's Hospital Joint Biomedical Institute, 2 Sun Wen East Road, Zhongshan, Guangdong 528400, China*

[6]*Dongguan & Guangzhou University of Chinese Medicine Cooperative Academy of Mathematical Engineering for Chinese Medicine, Building 16, Songke Garden, Songshan Lake Science and Technology Industrial Park, Dongguan 523000, China*

Correspondence should be addressed to Weijia Wang; 530837226@qq.com, Lauren Winne; winnie_lsh@ku.edu, and Ming Hong; hongming530@126.com

Numerous studies have shown that resveratrol can induce apoptosis in cancer cells. Trans-3, 5, 4′-trimethoxystilbene (TMS), a novel derivative of resveratrol, is a more potent anticancer compound than resveratrol and can induce apoptosis in cancer cells. Herein, we examined the mechanisms involved in TMS-mediated sensitization of human osteosarcoma (143B) cells to TNF-related apoptosis-inducing ligand- (TRAIL-) induced apoptosis. Our results showed that cotreatment with TSM and TRAIL activated caspases and increased PARP-1 cleavage in 143B cells. Decreasing cellular ROS levels using NAC reversed TSM- and TRAIL-induced apoptosis in 143B cells. NAC abolished the upregulated expression of PUMA and p53 induced by treatment with TRAIL and TSM. Silencing the expression of p53 or PUMA using RNA interference attenuated TSM-mediated sensitization of 143B cells to TRAIL-induced apoptosis. Knockdown of Bax also reversed TSM-induced sensitization of 143B cell to TRAIL-mediated apoptotic cell death. These results indicate that cotreatment with TRAIL and TSM evaluated intracellular ROS level, promoted DNA damage, and activated the Bax/PUMA/p53 pathway, leading to activation of both mitochondrial and caspase-mediated apoptosis in 143B cells. Orthotopic implantation of 143B cells in mice also demonstrated that cotreatment with TRAIL and TSM reversed resistance to apoptosis in cells without obvious adverse effects in normal cells.

1. Introduction

Resveratrol, a natural polyphenolic compound that is abundant in blueberries, grapes, and peanuts, possesses numerous pharmacological activities. Previous studies have shown that resveratrol can induce apoptosis in various human tumor cells via ROS-dependent endoplasmic reticulum (ER) stress

[1, 2]. Although resveratrol has shown remarkable anticancer effects in numerous preclinical studies, its poor pharmacokinetic parameters have restricted its clinical application. Adding methoxy or hydroxyl groups to the stilbene backbone of resveratrol generates modified resveratrol derivatives that possess improved bioavailability and stability, resulting in increased transport of these agents into cells [3]. Unlike

resveratrol, TMS can bind membrane proteins with high binding affinity. Furthermore, upon uptake, TMS can enter cells unaltered, which increases its stability within cells [4–6].

In recent decades, several studies have shown that TMS can exert antitumor effects in several malignant human tumors, including lung malignancies, cholangiocarcinoma, prostate adenocarcinoma, and osteosarcoma [7–9]. Annick et al. have demonstrated that TMS exhibits stronger anticancer activity than that of resveratrol and can induce apoptosis in malignant MCF-7 cells [10, 11]. Additionally, TMS can decrease cellular viability and induce apoptosis in prostate adenocarcinoma cells. This TMS-mediated inhibition of cellular viability can be enhanced by combining TMS with TRAIL, thereby activating the reactive oxygen species- (ROS-) induced caspase cascade [12]. Indeed, $20 \mu M$ TSM increases intracellular ROS levels and induces apoptosis by phosphorylating JNK, p38, and MAPK [13, 14]. Another study has shown that $10 \mu m$ TSM sensitizes osteosarcoma cells to apoptosis by activating Bax, p53, and caspase-3 [15]. Additionally, $10 \mu m$ TMS suppresses the proliferation of human hepatocellular carcinoma MHCC-97H cells by inducing PUMA-dependent cellular apoptosis in vitro and in vivo, suggesting that TMS may sensitize cancer cells to apoptosis [16]. Although TMS possesses reduced cytotoxicity compared with that of resveratrol, $10 \mu m$ TMS may show some cytotoxicity in normal cells and tissues [17]. Therefore, in our current study, we treated osteosarcoma cells with TRAIL and low-dose TMS (2.5, $5 \mu m$) to evaluate whether TMS could sensitize these cells to TRAIL-mediated apoptotic cell death.

ROS induce apoptosis by destroying the basic structure of DNA, which increases the expressions of PUMA and Bax [11, 12]. As a proapoptotic protein, Bax can promote cytochrome C release from the mitochondria and induces subsequent caspase cascade. Excessive levels of intracellular ROS and DNA damage may activate the expression of p53 and upregulate that of PUMA, subsequently inducing cellular apoptosis [13]. Previous studies have shown that TMS $(10 \mu m)$ may inhibit cancer progression by promoting PUMA-dependent apoptosis [9]. Hence, we hypothesized that in osteosarcoma cells, treatment with TMS likely triggers Bax/PUMA/P53 signaling that contributes to intrinsic apoptosis, while cotreatment with TRAIL and TMS likely induces extrinsic apoptosis. To test this hypothesis, we treated osteosarcoma cells with TRAIL and low-dose TMS to evaluate whether TMS could sensitize these cells to TRAIL-mediated apoptosis.

2. Materials and Methods

2.1. Cell Lines and Chemicals.
Osteosarcoma cells 143B and Saos-2 were provided by Dr. Christopher Johnson (Medical center, University of Kansas); the MG-63 cells with specific genes knock-down were purchased form GeneTech corporation (San Francisco, CA, USA). Normal human osteoblast hFOB1.19 cells were provided by Dr. Ryan Taylor (Medical center, University of Kansas). hFOB1.19 cell was cultured in complete DMEM/F12, with 1% streptomycin-penicillin (Gibco), 0.5% Nonessential amino acids (HyClone), and 10% fetal bovine serum (FBS; HyClone). 143B and Saos-2 cells were cultured in DMEM with 1% penicillin-streptomycin, 10% FBS, and 1% L-glutathione (Gibco). All the cell lines were incubated under 5% CO2 atmosphere at 37°C, unless otherwise indicated. All the chemical agents were provided by Sino-pharm Chemical Reagent Company (Beijing, China), unless otherwise indicated. Recombinant human TRAIL was provided by Thermofisher Corp (Waltham, MA, USA) and reserved in PBS+0.01% BSA at -20°C.

2.2. Dosage Information.
The TMS concentration used in this study (2.5, 5, $10 \mu M$) for in vitro experiment was referred to previous studies. For control group, 1% DMSO were used as a vehicle [18, 19]. The TMS concentration used for in vivo experiment on mice was calculated according to the previous publications, which was 11 times as much as that for human beings [20]. This dosage is accomplishable for humans by available supplements via taking orally. Mice were pretreated with TMS (10 mg/kg) by intragastrical gavage every two days; 1% Dimethyl sulfoxide (DMSO) were used as a vehicle in control group. To evaluate the potential toxicity of TMS (10 mg/kg) in vivo, the results on kidney and liver function and the blood cell counts in mice were detected by commercial kits.

2.3. Cell Viability.
Cell viability was analyzed using trypan blue staining assay kit (Sigma, USA) and 3-(4,5-dimethyl-thiazol-2-yl)-2,5-diphenyltertrazolium bromide tetrazolium (MTT) assay (Sigma, USA). For trypan blue staining assay, 2×10^5 cells were cultured into 48-well plates after treatment for 24 hour. The cell viability was assessed after mixing $200 \mu L$ of cell suspension and $200 \mu L$ of 0.5% trypan blue solutions (Sigma, USA), and the cell counting was performed with a Neubauer chamber. The average of three readings for each group was counted, and the cell count was calculated based on the following equation: number of cells/mL = average cells count $\times 2 \times 10^5$. For MTT assay, $10 \mu L$ MTT solution was added into the medium (2×10^4 cells/well) and incubated at 37°C for 3.5 h. Then, the MTT mixture was discarded, and $100 \mu L$ DMSO was added. After agitating for 20 min, the absorbance of each sample at 570 nm was detected by a microplate reader (Bio-Rad, USA).

2.4. Western Blot Assay.
Cells were extracted with lysis buffer for obtaining total proteins. The proteins were transferred to PVDF membrane after separating on 4% SDS-PAGE. After blocking with 4% de-fat milk for 1.5 hour at 25°C, the membrane was washed with TBST for 2 times and following with the primary antibody incubation at 5°C for 12 hour. Then, the membrane was washed with TBST for 2 times and further incubated with secondary antibodies for 1.5 hour at 25°C. The protein blots were visualized by using an ECL system and quantified with ImageJ software (National Institutes of Health, USA). Actin was used as a loading control for normalizing the bands density. The information of primary antibodies used in this study are shown below. Caspase-8 (ab 20421), caspase-3 (ab13847) at dilutions 1 : 500, caspase-9 (ab2154) at dilutions 1 : 500, p53 (ab131162) at dilutions 1 : 1000, H2A.X (ab141768) at dilutions 1 : 200,

phospho-H2A.X (ab 51272) at dilutions 1 : 200, and PARP-1 (ab12633) at dilutions 1 : 1000 were purchased from Abcam (Cambridge, USA). The primary antibody for actin (CS4970) at dilutions 1 : 200 was purchased from Cell Signaling Technology (Trask Lane Danvers, USA); PUMA (sc-41606) and Bax (sc-43716) were provided by Santa Cruz Biotechnology (Santa Cruz, USA) that were used at dilutions 1 : 500 and 1 : 1000.

2.5. Apoptosis Assessment by DAPI Staining and TUNEL Assay. Osteosarcoma cells were cultured in a 40-dish at 5×10^4 cells/mL, stabilized for 12 hours, processed with TMS at different concentrations, then, cultured in an incubator for 12 hours. Nuclear fragmentation and condensation were examined by 4,6-diamidino-2-phenylindole (DAPI) staining. After incubation with TMS, the cells were harvested, washed, and resuspended in PBS, stained with 1 μg/mL DAPI and placed at 4°C with a cover slip, protected from light for 25 min. Then, the samples were washed three times with PBS and examined by fluorescence microscopy.(Thermo Scientific, USA). For TUNEL assay, paraffin-embedded cancer tissues were examined by TUNEL commercial kit (Invitrogen, USA). Briefly, cells were fixed with 4% paraformaldehyde for 10 min at 25°C and then washed with PBS twice. Paraffin tissue sections were processed with 20 μg/mL proteinase K for 5 min. Then, the samples were treated with the 3% H2O2 for 15 min and incubated with 10 μL TdT enzyme reaction buffer for 1 hr at 37°C. The digoxigenine-dUTP end-labeled DNA was examined by antidigoxigenin peroxidase antibodies (1 : 200; ROCHE, Swiss) following the manufactures instructions. *In vivo* fluorescence imaging quantification was analyzed on images captured using confocal microscopy (Olympus, Japan).

2.6. ROS Generation Assessment. Intracellular ROS in osteosarcoma cell was detected using CM-H2DCDFA, which is an uncharged and nonfluorescent ROS indicator. Briefly, 100 μg of CM-H2DCDFA (Life Technologies, USA) was added into each sample. The cells were harvested 25 minutes after CM-H2DCDFA incubation and kept in -80°C. Then, the cells were fixed with 5% PFA/PBS at 4°C for 10 min. After washed by PBS for twice, cells were detected under a fluorescent microscope (400x magnification). Both captured fluorescence and gray images were evaluated by DP controller 3.0 (Leica, Germany). Gray images for analyzing fluorescence intensity were processed by Image J 2.0.

2.7. DNA Comet Assay. To detect single- and double-stranded DNA breaks, DNA comet assay was performed in our study. The pretreated osteosarcoma cells were immersed in fresh lysing solutions in dark place at 4°C for 2 hours and then rinsed with neutralization buffer (200 mM Na2EDTA, 10 mM Tris-HCl, 3 M NaCl, 1% Triton X-100, and 9% DMSO) to eliminate salts and detergents. The samples were set in horizontal electrophoresis system at 5°C with alkaline buffer for 25 minutes (20 V, 250 mA), which promotes the damaged DNA to deviate from the nucleus. Then, the agarose gel was stained with ethidium bromide (20 μg/mL) (Vista Green, USA) for 15 minutes in dark. The slides were

TABLE 1: Sequences for siRNA transfection.

Gene bank ID	Gene name	siRNA sequences
AG072923	*PUMA*	F: 5′-CUCCAAACUGCGAUGACUU-3′ R: 5′-UAUCUCACAACGGCACGAC-3′
AK356651	*P53*	F: 5′-GUGCACCGGCUCUACAAUA-3′ R: 5′-ACUUACGGCAGCUCAGACC-3′

visualized using an epifluorescence microscope (ZEISS AXIOS A1, Germany) with a magnification of 400x, using a 580 nm filter. Tail moment was evaluated via calculation of percentage of tail length × tail DNA.

2.8. siRNA Transfection. siRNA targeting *p53* or *PUMA* were transfected into 143B cells based on the manufacturer's manual. Generally, siRNA (20 nM) against *p53* or *PUMA* (Table 1) was transfected with RNAiMAX transfection reagent (Invitrogen, USA) into 143B cells for 36 hours at 36°C. Cells were then washed with PBS, and the efficiency of transfection was validated by Western blotting.

2.9. Orthotopic Transplantation Tumor Model of Osteosarcoma. The female BALB/c-nu/nu nude mice (4-week-old) were purchased from the Experimental Animal Centre in University of Kansas (Kansas, USA), and the mice were treated according to the ethics committee's guidelines and regulations under the project license No. K8139B5G. The mouse was fed with standard diet. Before the surgical procedure, anesthesia was induced with 2.5% isoflurane and O2 at 2–4%. Osteosarcoma 143B cells were diluted in PBS (1×10^6 cells/mL) and 200 μL of cell suspension were injected to the tibial plateau of mouse. Then, nude mice were randomly divided into four groups ($n = 5$): TMS (1 μg/g), TRAIL (100 ng/g), TRAIL (100 ng/g) + TMS(1 μg/g), and control group (0.1% DMSO +PBS). Tumor volume and body weight were measured every 7 days. At the end of the experiment, the mice were sacrificed with carbon dioxide, and the tumors were dissected for further analysis. The blood was collected from the tail vein to assess kidney and hepatic function.

2.10. Immunohistochemistry. The mice' osteosarcoma tissue sections (5 μm thick) were dewaxed in xylene for 10 min; then, the samples were rehydrated with alcohol and wished by distilled water. 20 mM citrate buffer was used to process the tissue sections at 96°C for 15 min; fixative was applied to fix the samples. Next, the slides were blocked with 5% BSA for 45 min. Then, the slides were incubated with PUMA (1 : 2000, Abcam) and p53 (1 : 500, Abcam) antibodies at 4°C for 12 h, followed by incubation with secondary antibodies 24°C for 2 h. After washing by PBS, the samples were stained with hematoxylin and DAB. Finally, the slides were examined with a fluorescence microscope, and the brown color indicated the positive cells.

2.11. Statistics. One-sample *t*-test was applied for quantification of the band intensity of Western blotting, the two-

sample t-test was used for analyzing the means of two groups, and one-way ANOVA with Dunnett's multiple comparison was used to compare the means among more than two groups. Data are expressed as the mean ± standard deviation (SD). The data is considered as significant difference when $P < 0.05$.

3. Results

3.1. TRAIL Resistance in Osteosarcoma 143B Cells. To examine TRAIL resistance in osteosarcoma cell lines, 143B and Saos-2 cells were treated with 0-200 ng/mL TRAIL for 12 h. Our results indicate that 50-200 ng/mL TRAIL suppressed the viability of Saos-2 cells in a dose-dependent manner (Figures 1(a) and 1(b)). However, the viability of 143B cell was not significantly changed after TRAIL treatment; the survival of 143B cells was about 92% when pretreated with TRAIL (200 ng/mL). Cleaved poly (ADP-ribose) polymerase-1 (PARP-1), an indicator of apoptosis, was detected in Saos-2 cells only (Figures 1(a) and 1(b)). We then used DAPI staining and TUNEL labeling to determine whether apoptosis occurred after the cell was pretreated by 100 ng/mL TRAIL. DAPI staining results show chromosome condensation in Saos-2 cell after TRAIL treatment (100 ng/mL), while no significant subcellular morphological changes were detected in 143B cells pretreated with 100 ng/mL TRAIL (Figure 1(c)). The results of TUNEL assay were consistent with those obtained using DAPI staining. These results suggest that TRAIL-treated Saos-2 cells were sensitive, while TRAIL-treated 143B cells were resistant, to apoptosis.

3.2. The Effect of TMS on TRAIL-Resistant Osteosarcoma Cells. Next, we examined whether a noncytotoxic dose of TMS could induce apoptosis in 143B cells. For this, 143B cells were exposed to 0–10 μm TMS for 6 h, and then, cellular viability was examined using the Trypan blue dye exclusion method. Our results demonstrate that treatment with 2.5 μm TMS alone did not inhibit the survival of 143B cells (Figure 2(a)). However, cotreatment using TRAIL (50 ng/mL) and TMS (2.5 μm) for 6 hours did inhibit the survival of 143B cells (Figure 2(b)). Western blotting showed that the levels of PARP-1 cleavage were not increased in 143B cells after treating by 1–5 μm TMS or TRAIL (50 ng/mL). However, cotreatment with 2.5 μm TMS and 50 ng/mL TRAIL increased the expression of cleaved PARP-1 in 143B cells (Figure 2(c)). Interestingly, combination therapy by 2.5 μm TMS and 50 ng/mL TRAIL did not induce PARP-1 cleavage in normal human hFOB1.19 osteoblasts (Figure 2(d)). Furthermore, DAPI and TUNEL labeling confirmed that combined treatment using TRAIL and TMS did induce apoptosis in 143B cells (Figure 2(e)).

3.3. Cotreatment with TMS and TRAIL Activates Caspases Signaling. To explore the mechanisms underlying TMS- and TRAIL-induced apoptosis in 143B cells, we assessed the expression of cleaved PARP-1 and several caspases in 143B cells treated with TMS and/or TRAIL. No significant changes in the expressions of cleaved PARP-1 or caspases

were observed in 143B cells treated with TMS or TRAIL alone (Figure 3(a)). However, cotreatment using TMS (2.5 μm) and TRAIL (50 ng/mL) induced PARP-1 and caspase cleavage in a time-dependent manner (Figure 3(a)). Caspase cleavage was enhanced by TMS in a dose-dependent manner (Figure 3(b)). Next, we used different caspase inhibitors, including zlEHDfmk, zlETDfmk, and zDEVDfmk, to evaluate the possible roles of caspase cleavage in the survival of 143B cell cotreated with TMS and TRAIL. Our results show that PARP1 cleavage and apoptosis in 143B cells were inhibited by treatment with caspase inhibitors (Figure 3(c)). Together, these data suggest that cotreatment with TRAIL and TMS activated caspases and induced apoptosis in 143B cells.

3.4. TMS Increases Intracellular ROS Levels in 143B Cells. Reactive oxygen species (ROS) and mitochondria play important roles in the induction of apoptosis under conditions of physiologic and pathologic stress. Thus, we evaluated intracellular redox status in 143B cells after treatment with TMS and TRAIL. A CARBOYX-H$_2$DCFAD fluorescence probe was used to detect intracellular ROS levels in treated 143B cells. Our results show that 143B cells treated with positive control (H$_2$O$_2$) or 2.5 μm TMS emitted stronger fluorescent signal compared with that of the control group (Figure 4(a)). Results obtained using spectrofluorometry indicate that relative fluorescence intensity was increased in 143B cells after treatment with TMS, suggesting that TMS may have increased ROS levels in a dose-dependent manner (Figure 4(b)). Relative fluorescence intensity reached peak level 20 minutes after the cells received the recommended dose of TMS (2.5, 5 μm). Sixty minutes after reaching its peak level, relative fluorescence intensity rapidly decreased to its minimal value. Interestingly, 4 h after reaching its minimal value, relative fluorescence intensity increased again (Figure 4(c)). These results indicate that TMS may regulate intracellular ROS generation in 143B cells in biphasic pattern. For further exploring the possible roles of ROS in TRAIL- and TMS-mediated apoptosis of 143B cells, NAC (which is an ROS inhibitor) was used to treat 143B cells after treatment with TRAIL and/or TMS. Our results show that TRAIL (50 ng/mL) had no effect on intracellular ROS levels, while NAC (4 mM) reduced ROS level induced by TMS (Figure 4(d)). Additionally, NAC reversed the cellular apoptosis that had been induced by cotreatment with TMS and TRAIL in human 143B cells (Figure 4(e)). These results indicated that when ROS was inhibited by NAC, the proapoptotic effect of TMS and TRAIL could be attenuated. The P53 protein exerts dual effects under conditions of intracellular oxidative stress, providing cytoprotection at basal ROS levels and inducing senescence/apoptosis at high ROS levels [21]. Previous studies have shown that TMS-mediated cellular apoptosis is associated with increased expression of p53 and PUMA in osteosarcoma cells [22]. Thus, we used immunoblotting to detect the expression of cleaved PARP-1, p53, and PUMA in 143B cells cotreated with TMS and TRAIL. Our results show that combined treatment with TMS and TRAIL upregulated the expressions of cleaved PARP1, PUMA, and p53 in 143B cell. Interestingly, NAC (4 mM)

(a)

(b)

(c)

(d)
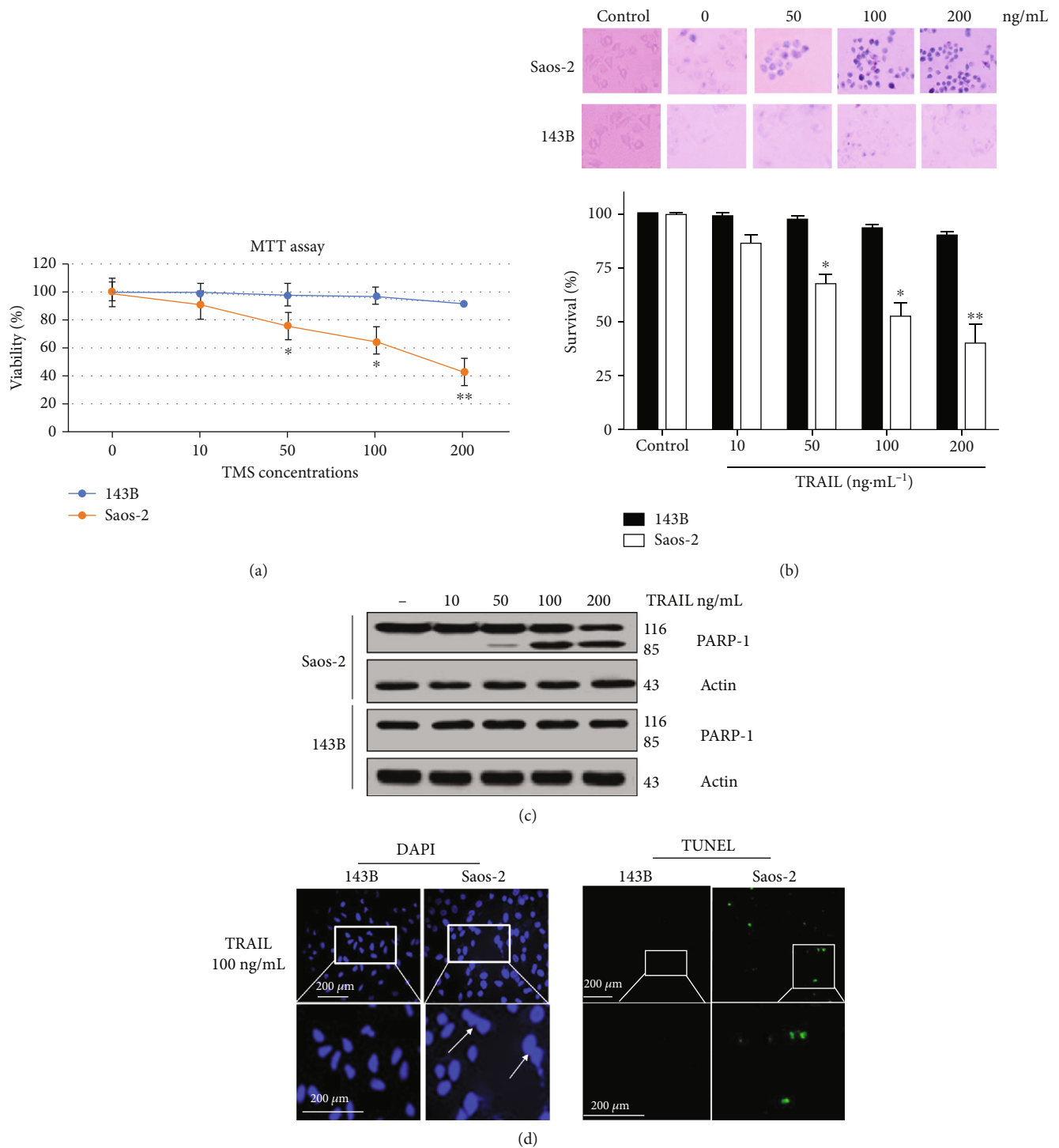
FIGURE 1: TRAIL suppresses viability and promotes apoptotic cell death in Saos-2 cells. MTT assay (a) and Trypan blue staining (20x objective lens) (b) were used to examine the survival of 143B and Saos-2 cells after treatment with 0–200 ng/mL TRAIL for 12 h. Equal volume of vehicle (0.01% BSA + PBS) was used to treat the control groups, $^*P < 0.05$; $^{**}P < 0.01$. (c) Western blotting was used to detect PRAP-1 cleavage in 143B and Saos-2 cells treated with 0–200 ng/mL TRAIL for 6 hour. (c) DAPI and TUNEL labeling were used to examine apoptosis in 143B and Saos-2 cells treated with 100 ng/mL TRAIL for 6 hours. White arrows indicate chromatin condensation in 143B and Saos-2 cells; spots of green fluorescence indicate morphological changes in 143B and Saos-2 cells (magnification ×200); additional higher-magnification images are also provided (magnification ×400).

reversed the effects of TMS and TRAIL on protein expression of cleaved PARP1, p53, and PUMA (Figure 4(f)). These findings indicate that combined treatment with TRAIL and TMS induced ROS generation in 143B cells and promoted intrinsic apoptotic signaling by upregulating the expression of p53 and PUMA.

(a)

(b)

(c)

(d)

(e)
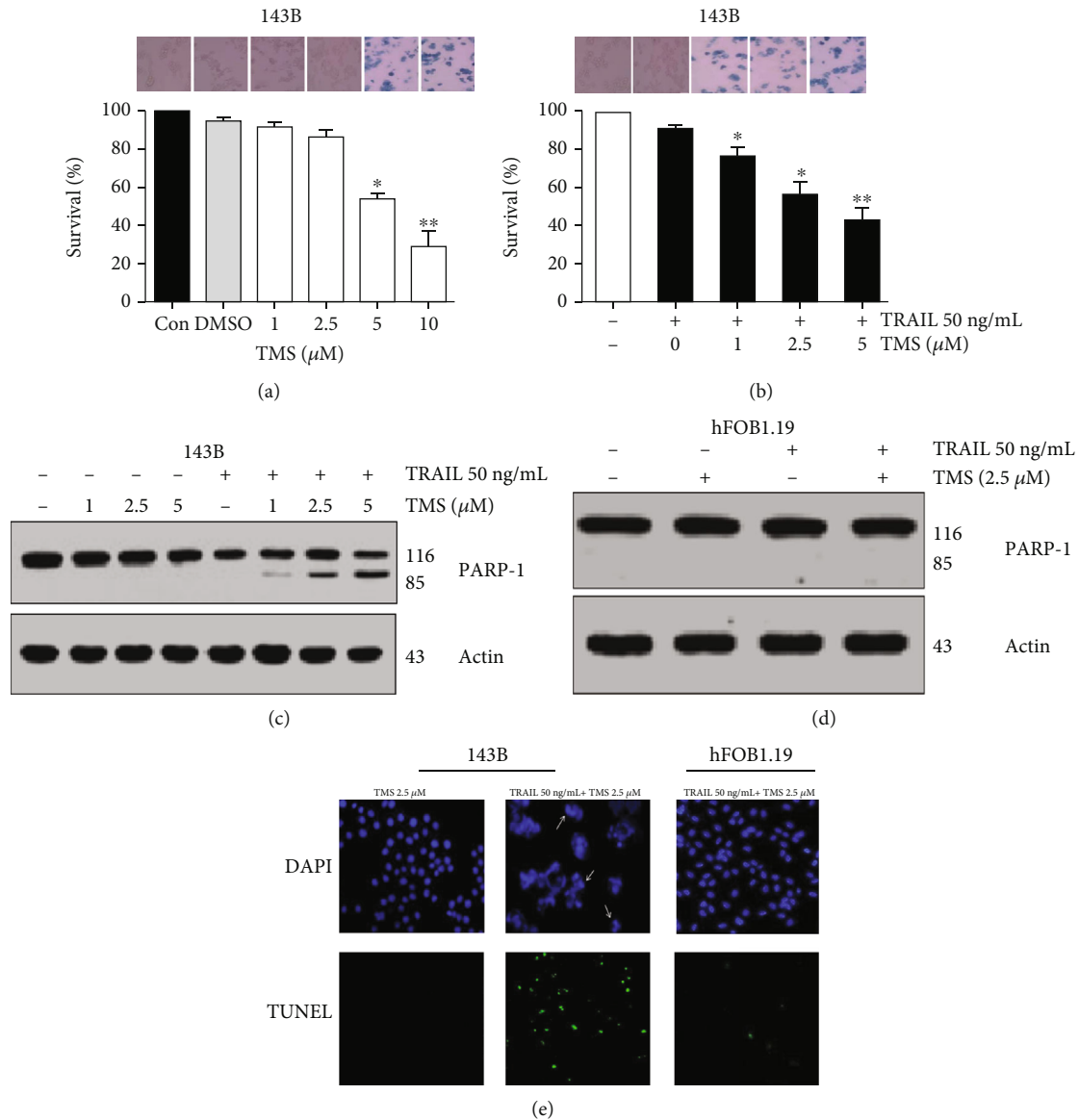
FIGURE 2: TMS reverses TRAIL-resistance in 143B cells. (a) After treatment with different doses of TMS for 6 h, the survival rate of 143B cells was examined using the Trypan blue dye exclusion method (20x objective lens). (b) Survival of 143B cells, treated with 0–10 μm TMS and/or 50 ng/mL TRAIL, was assessed using the Trypan blue dye exclusion method. (c) Human osteosarcoma 143B cells and (d) normal human hFOB1.19 osteoblasts were pretreated with 50 ng/mL TRAIL and 2.5 μm TMS for 10 hours. Western blotting was used to detect the levels of cleaved PARP1. (e) DAPI and TUNEL labeling were used to evaluate the apoptosis of 143B osteosarcoma cells and normal hFOB1.19 osteoblasts after treatment with TMS and/or TRAIL for 6 h (magnification ×400).

3.5. TMS Induces DNA Damage in 143B Cells.

ROS-induced oxidation of DNA is one of the major causes of gene mutation, resulting in various types of DNA damage such as double-strand breaks in the chromosome. DNA damage may result in apoptosis [23]. To examine the DNA damage potentially caused by exposure to TMS, we performed a comet assay to detect double-strand breaks in the chromosomes of TMS-treated 143B cells. Results of the comet assay indicate that the length of DNA migration (tail length), which reflects the extent of DNA damage, was increased in 143B cells treated with TMS (2.5 μM) (Figure 5(a)). These results show that TMS may have induced DNA damage and consequent apoptosis in 143B cells. H2AX is phosphor-

ylated on serine 139 and is then designated as γH2AX in a reaction involving DNA double-strand breaks [24, 25]. Therefore, the expression of H2AX and phosphorylation of H2AX-Ser139 were examined to confirm that treatment with TMS induced DNA damage in 143B cells. Our results indicate that TMS facilitated H2AX-Ser139 phosphorylation in 143B cells in a dose- and time-dependent manner (Figures 5(b) and 5(c)). Above data suggest that TMS may activate P53 and trigger apoptosis by increasing ROS levels and inducing DNA damage in 143B cells.

3.6. TMS Activates p53 and PUMA Expression in Osteosarcoma Cells.

Previous studies have confirmed that

(a)

(b)

(c)
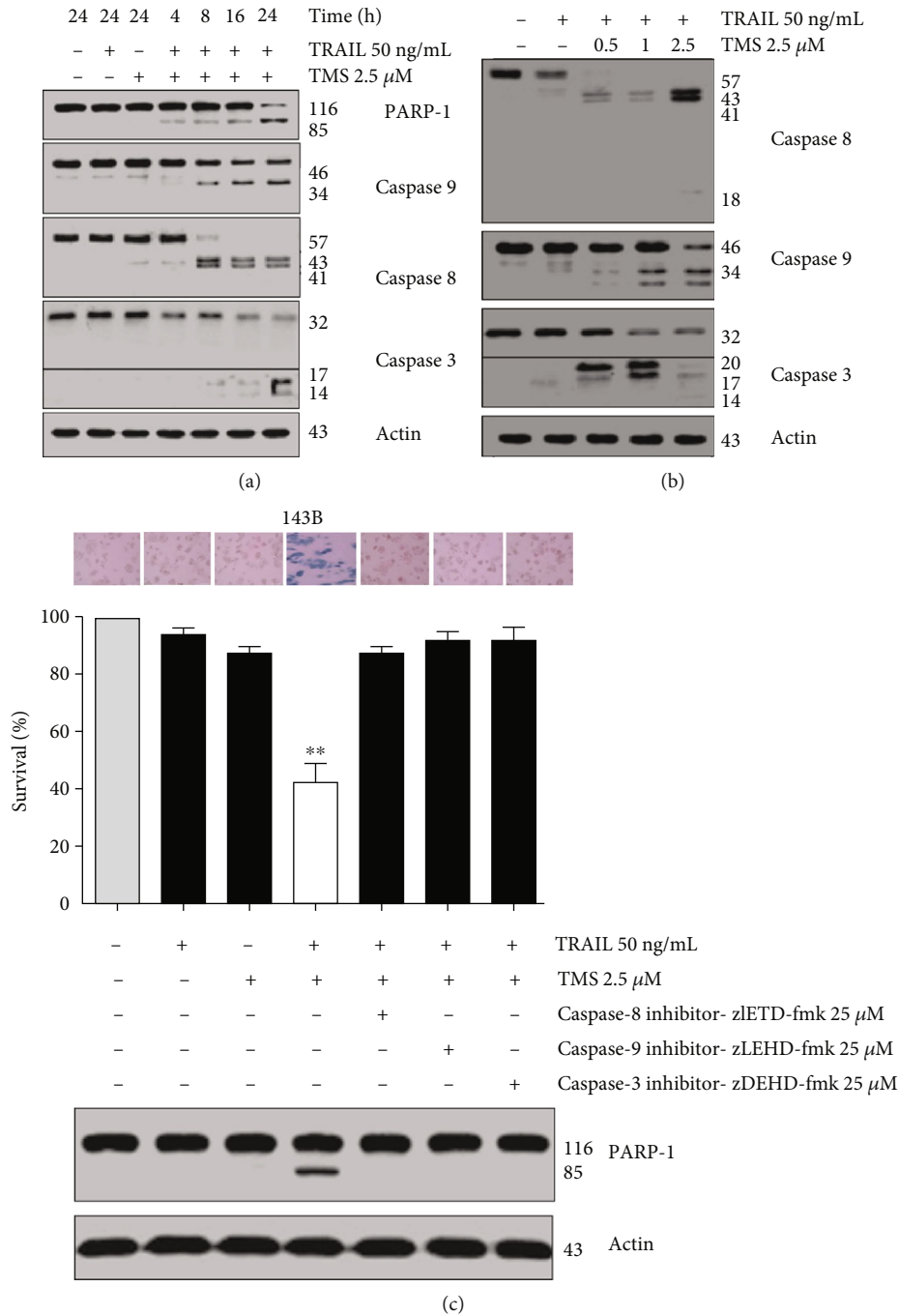
Figure 3: Cotreatment with TRAIL and TMS can activate caspases in 143B cells. (a) Western blotting was used to detect the expression of PARP-1 and caspase cleavage in 143B cells treated with TMS and/or TRAIL for different lengths of time. The control group was treated with an equal volume of 1% DMSO + PBS+0.01% BSA. (b) Caspase cleavage was examined by Western blotting in 143B cells after treatment with 50 ng/mL TRAIL and TMS (0.5–$2.5\,\mu$M) for 10 hours. (c) Caspase inhibitory agents, including zlEHDfmk, zlETDfmk, and zDEVDfmk, were used to block the caspase pathway in 143B cells. After the cells were pretreated with TMS and/or TRAIL for 10 hours, the Trypan blue dye exclusion method was used to evaluate cell survival (20x objective lens), and Western blotting was utilized to detect the expression of cleaved PARP1. $^{**}P < 0.05$.

p53 phosphorylation may affect its stabilization in cells [26]. In our study, we found that TMS could activate P53 by phosphorylation of P53 on Ser15, Ser46, and Ser392; this activity was crucial for p53 accumulation and stabilization in 143B cells (Figure 6(a)). As a downstream target gene of p53, *PUMA* is upregulated by p53 activation and can induce apo-

ptosis in cells exposed to TMS [22]. In this study, we further examined the roles of p53 and *PUMA* in the apoptosis of 143B cells after cotreatment with TMS and TRAIL. Figure 6(b) shows that TMS dose-dependently upregulated the expression p53 and PUMA. After cotreatment with TMS (1–$5\,\mu$M) and TRAIL (50 ng/mL), the expression of

(a)

(b)

(c)

(d)

(e)

FIGURE 4: Continued.

(f)
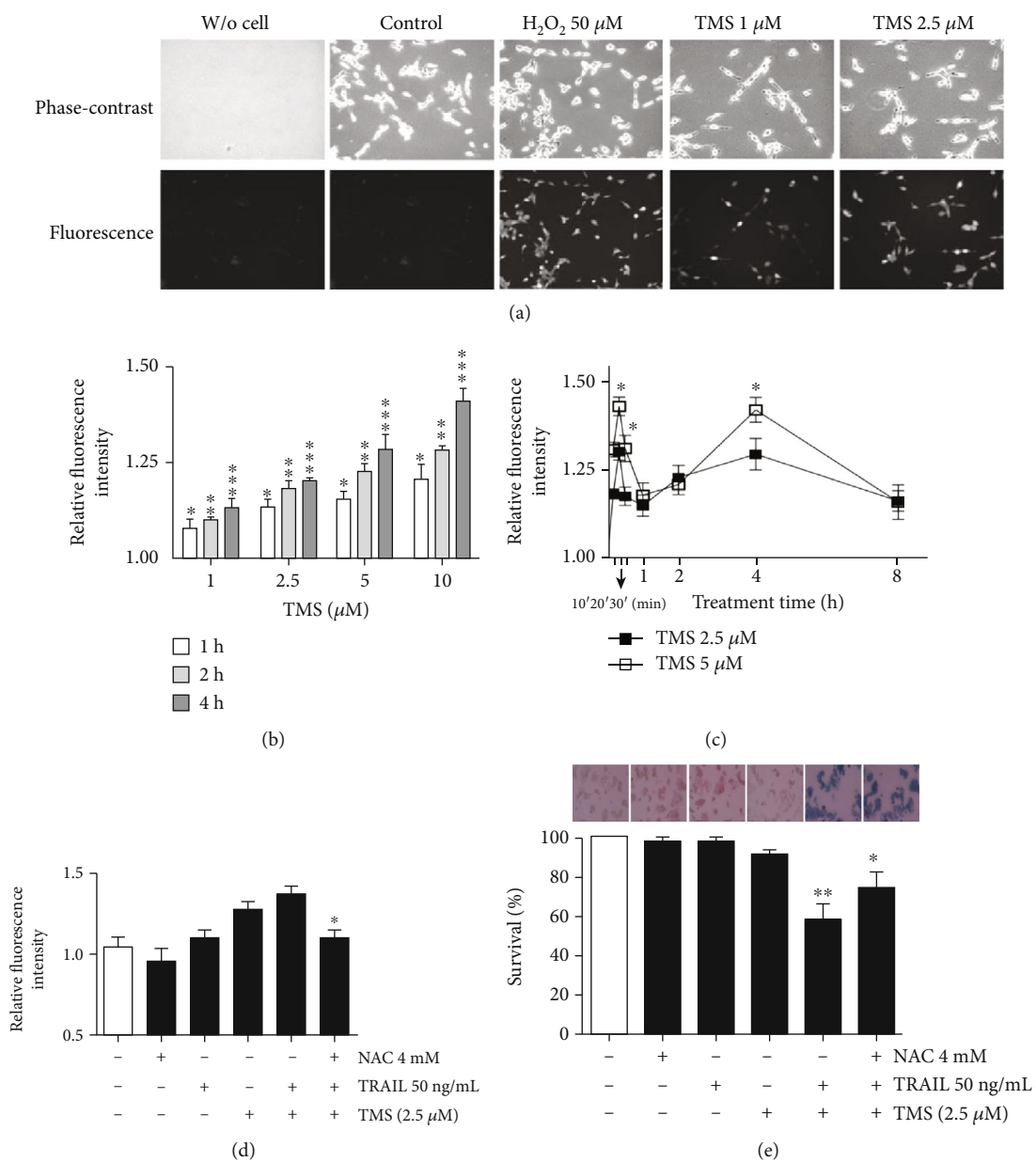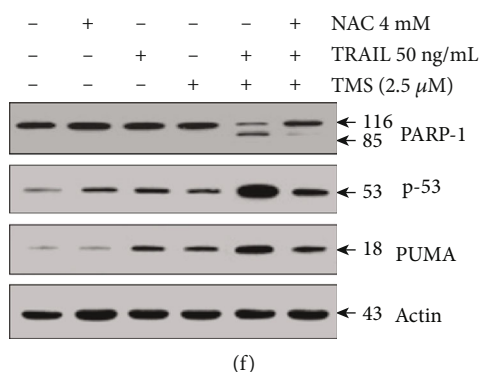
FIGURE 4: TMS increases ROS levels in 143B cells. (a) Intracellular ROS levels in 143B cells were detected using fluorescence microscopy. The cell was pretreated with positive control (H_2O_2) or TMS for 50 minutes and labeled with CMH2DFCDA for 15 minutes. Considerably higher fluorescence intensity was detected in cells treated with H_2O_2 or TMS compared with that of the 0.01% BSA+ PBS-treated control group. (b) 143B cell was pretreated with different doses of TMS for various periods of time. ROS generation was measured using relative fluorescence intensity in 143B cells. $**P < 0.05$. (c) After treatment with TMS (2.5, $5\,\mu m$) for various periods of time, 143B cell was labeled with CMH2DFCDA. ROS levels were analyzed at different time points according to the value of relative fluorescence intensity. (d) Pretreatment with NAC reduced ROS generation induced by TMS ($2.5\,\mu m$) and (e) attenuated TMS- and TRAIL-induced apoptosis in 143B cells. Trypan blue dye exclusion method was used to evaluate cell survival (20x objective lens). $*P < 0.05$; $**P < 0.01$. Cells in the control group were treated with an equal volume of PBS+0.1% DMSO. (f) Immunoblotting were used for examining the expression of cleaved PARP-1, p53, and PUMA in 143B cells after pretreatment with NAC and treatment with TRAIL and TMS.

(a)

(b)

(c)
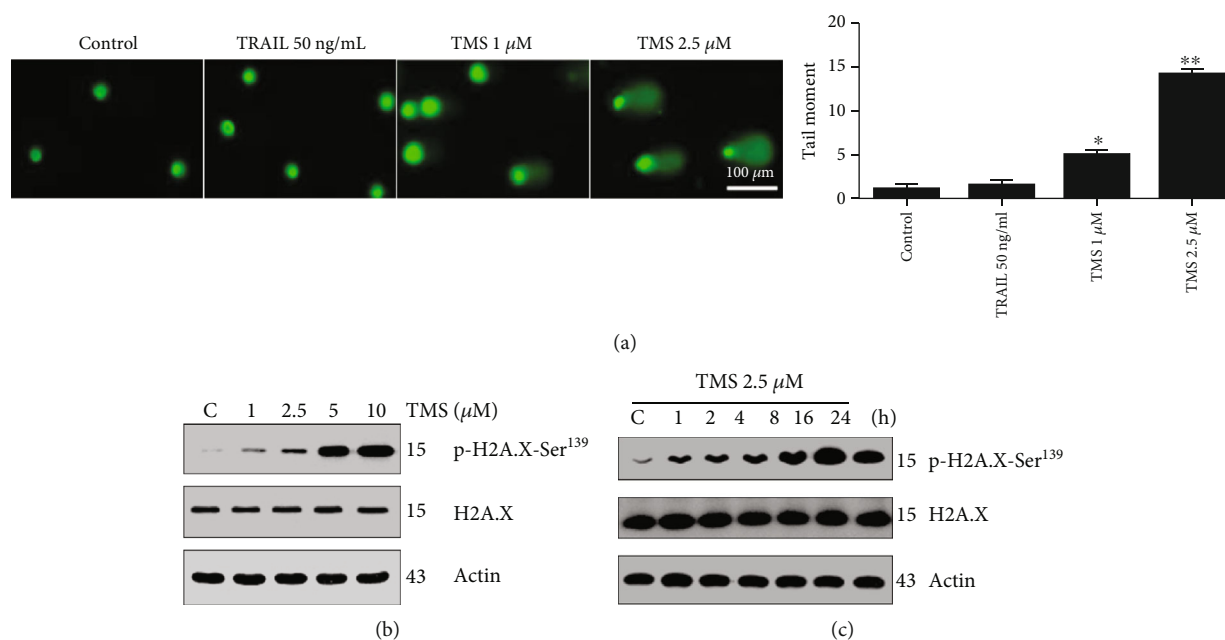
FIGURE 5: TMS induces DNA damage and facilitates phosphorylation of Ser-139 (H2AX) in 143B cells. (a) Comet assay was performed to examine DNA damage induced by treatment with TMS or TRAIL for 15 minutes. Tail moment were applied for quantifying double-strands break via calculating the tail length × percentage of tail DNA. $*P < 0.05$. (b) 143B cell was treated with 0–10 μM TMS for 24 hours, and Western blotting was used to examine the expression of H2AX and phospho-H2AX-Ser139 in 143B cells; 0.01% DMSO was used as vehicle control. (c) 143B cell was pretreated with TMS ($2.5\,\mu$M) for 0-24 hours, and immunoblotting was used to examine the expression of H2AX and phospho-H2AX-Ser139 expression in 143B cells; 0.01% DMSO was used as vehicle control.

PUMA and p53 was significantly increased in 143B cells (Figure 6(c)). RNA interference assay was used for downregulating the expressions of PUMA and P53 in order to confirm the critical roles of PUMA and p53 in TMS-mediated sensitization of 143B cells to TRAIL stimulus. Our results indicate that 48 h after transfection with PUMA or p53 siRNA, cleaved PARP-1 expression was significantly

decreased in 143B cells, which suggests that TMS-induced TRAIL sensitization was attenuated in p53- or PUMA-silenced cells (Figure 6(d)). DAPI staining confirmed that transfection with PUMA or p53 siRNA reversed apoptosis in 143B cells after cotreatment with TRAIL and TMS (Figure 6(e)). These findings suggest that activation of p53 and PUMA contributed to TMS-mediated TRAIL

(a)

(b)

(c)

(d)

(e)
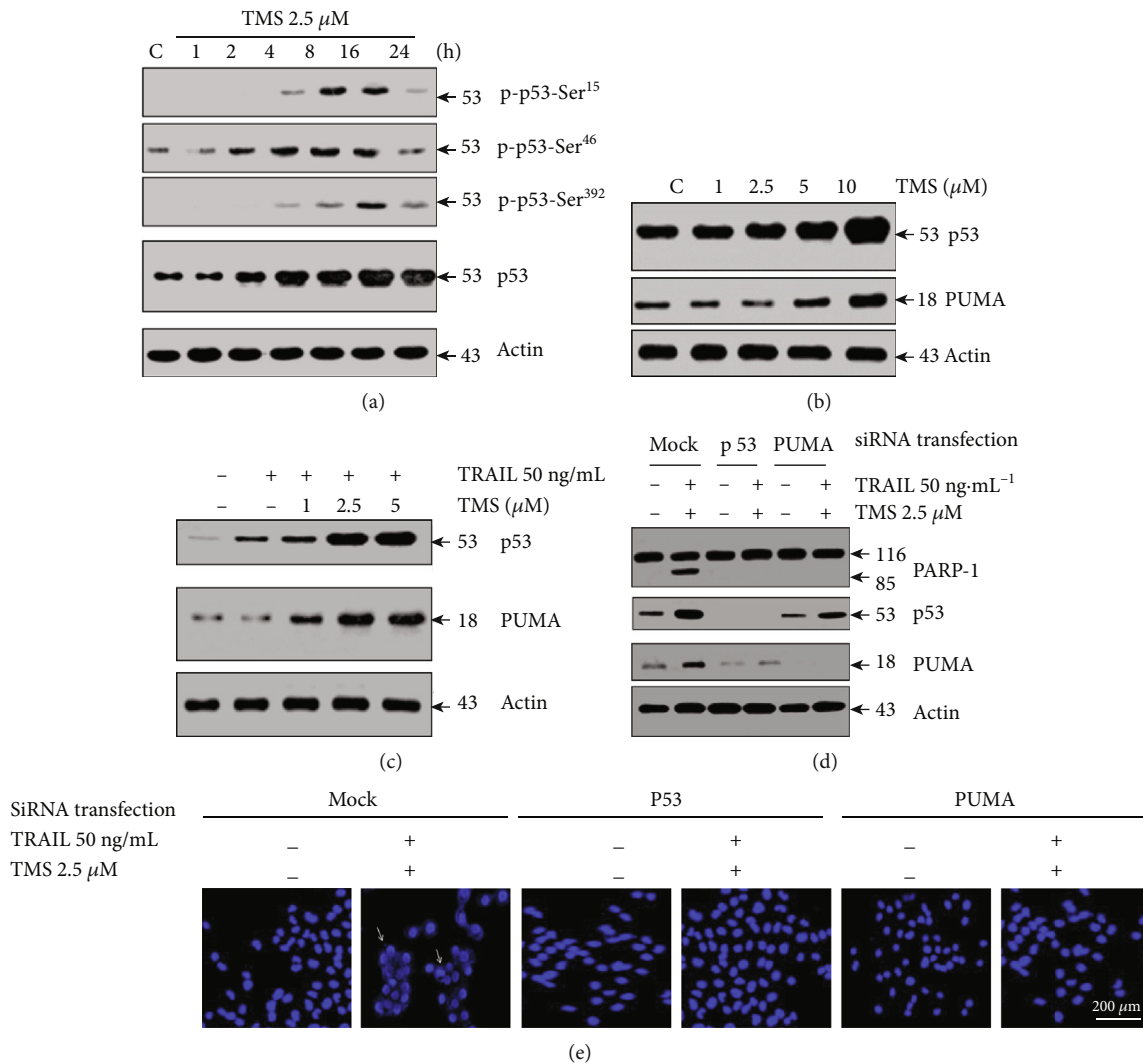
FIGURE 6: TMS activates PUMA and p53 expression in osteosarcoma cells. (a) TMS (2.5 μM) was used to treat 143B cells for 0–24 h, and protein expression of phosphorylated p53 (on Ser392, Ser46, or Ser15) was examined by Western blotting; 0.01% DMSO was used as vehicle control. (b) Different doses of TMS were used to treat 143B cells for 10 h, and Western blot assay was performed to detect the expressions of P53 and PUMA. (c) Different doses of TMS and TRAIL were used to treat 143B cells for 10 h, and Western blot assay was performed to detect the expressions of P53 and PUMA. (d) Gene expression of $p53$ and $PUMA$ was silenced by siRNA in 143B cells, and then, the cells were treated with TRAIL and TMS for 10 h. Western blotting was used to examine the expression of cleaved PARP1, P53, and PUMA. (e) Apoptotic cells were examined by DAPI staining after treating $p53$- or $PUMA$-silenced 143B cells with TMS and TRAIL. White arrows indicate condensed chromatin in 143B cells (magnification ×400).

sensitization and apoptosis in 143B cells. Next, we used MG-63 cells, another osteosarcoma cell line, for further verifying the effect of p53 in TMS- and TRAIL-induced apoptosis of osteosarcoma cells. Two strains of MG-63 cells, p53−/− and p53+/+, were treated using 2.5 μM TMS + TRAIL (50 ng/mL) for 0-24 h. Figures 7(a) and 7(b) show that TMS inhibited the viability of MG-63 p53+/+ cells and increased the expression of cleaved PARP-1. However, MG-63 p53−/− cells were not sensitive to treatment with TMS. Two other MG-63 cell lines (MG-63 PUMA+/+ and MG-63 PUMA−/−) were used to assess the role of PUMA in TRAIL- and TMS-induced apoptosis of osteosarcoma cells. Figures 7(c) and 7(d) show that TMS may have induced sensitization to TRAIL-induced apoptosis and increased the expression of cleaved PARP-1 in

MG-63 PUMA+/+ cells, while MG-63 PUMA−/− cells were not sensitive to the combined treatment. These results suggest that activation of PUMA or p53 was involved in TMS-mediated sensitization of osteosarcoma cells to TRAIL-induced apoptosis.

3.7. The Impact of BAX in TMS- and TRAIL-Mediated Apoptosis.
BAX is a key member of the antiapoptotic Bcl-2 family, which plays critical roles in the apoptosis of tumor cells. The coordinated activity of Bax and its upstream activators (PUMA and p53) can promote mitochondrial activation and apoptosis [27]. We next used 143B Bax+/− and 143B Bax −/− cells to confirm the role of Bax in TMS- and TRAIL-induced apoptosis. Our results show that TRAIL-mediated
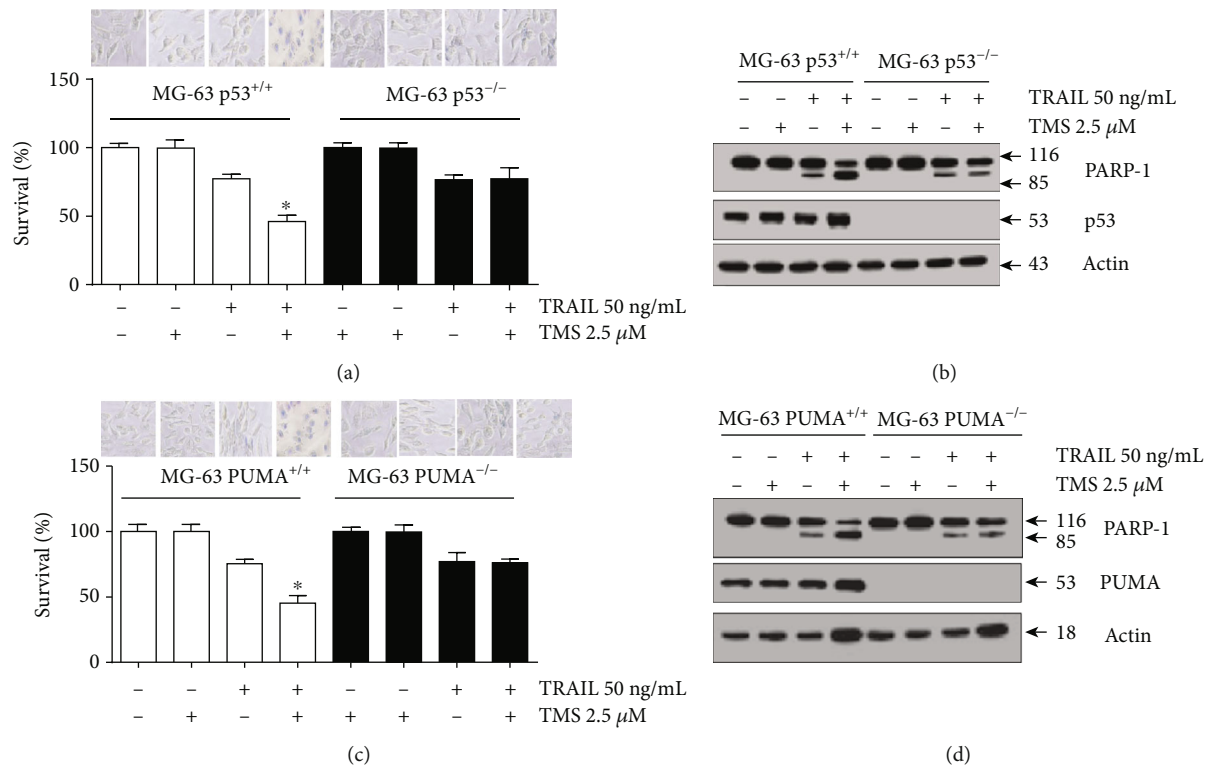
FIGURE 7: Treatment with TMS overcomes TRAIL resistance and promotes apoptotic cell death of MG-63 cell via activating p53 and PUMA. (a) Wild-type MG-63 cell, (b) p53−/− MG-63 cell or (c) wild-type MG-63 cell, and (d) PUMA −/− MG-63 cell were pretreated by TRAIL (50 ng/mL) and TMS (2.5 μm) for 10 h. Equal volume of PBS+0.1% DMSO 0.01% + BSA was used as vehicle control. Cell survival was examined as indicated in the experimental method section. Immunoblotting was used to detect the expression of cleaved PARP1, p53, or PUMA. *$P < 0.01$.

apoptosis and the expression of cleaved PARP1 were enhanced after 2.5 μm TMS treatment in 143B Bax+/− cells, instead of 143B Bax−/− cells (Figures 8(a) and 8(b)). Combined treatment with TRAIL and TMS significantly increased the expression of PUMA and p53 in both cell types (Figure 8(b)). Morphological assessment of apoptotic osteosarcoma cells by DAPI staining showed nuclear changes and apoptosis in 143B Bax+/− cells when treating by TMS and TRAIL (Figure 8(c)).

3.8. TMS and TRAIL Impair Osteosarcoma Growth In Vivo. A xenograft tumor model using 143B cell was set up in BALB/c mice for evaluating the effects of TMS and TRAIL on osteosarcoma progression. Our results show that tumor weight and volume were reduced in the group treated with TRAIL (100 ng/g) + TMS (1 μg/g) compared with those of the control group. Conversely, no differences in tumor volume or weight were observed between TRAIL (100 ng/g body weight)-treated mice and control mice (Figures 9(a) and 9(b)). The body weights of nude mice in TMS and/or TRAIL groups were similar to those of control-group mice during our in vivo studies (Figure 9(b)). Serum levels of alanine transaminase (ALT), aspartate aminotransferase (AST), and those of several renal function markers (creatinine (Cr) and blood urea nitrogen (BUN)) were analyzed in the cardiac blood of nude mice in order to evaluate the potential kidney and liver toxicity of cotreatment with TMS + TRAIL. Our

results show that hepatic and kidney function was normal in all the groups of mice used in our study (Table 2). Leukocyte, erythrocyte, and platelet count of the nude mice was also normal, suggesting that cotreatment with TMS + TRAIL exerted no significant hematological adverse effects within the present dosage (Table 3). These results indicate that cotreatment with TRAIL (100 ng/g) + TMS (1 μg/g) inhibited the development of osteosarcoma without significant toxicity in nude mice. Furthermore, the results of immunohistochemistry (IHC) show that the expressions of Bax, PUMA, and p53 were markedly increased in osteosarcoma tissues of TMS + TRAIL treated mice compared with those of the vehicle-treated mice ($P < 0.05$ Figure 9(c)). These results suggest that TMS likely triggers Bax/PUMA/P53 signaling that contributes to intrinsic apoptosis while cotreatment with TRAIL and TMS likely induces extrinsic apoptotic cell death in osteosarcoma.

4. Discussions

The intrinsic and extrinsic apoptosis pathways are naturally occurring or drug-induced processes by which cells are directed toward programmed cell death. Intracellular cues, such as cellular DNA damage, can induce apoptosis primarily via the intrinsic pathway. The intrinsic apoptosis pathway, which involves activation of conserved signaling proteins, such as that of p53, is physically associated with [28]. The

(a)

(b)

(c)
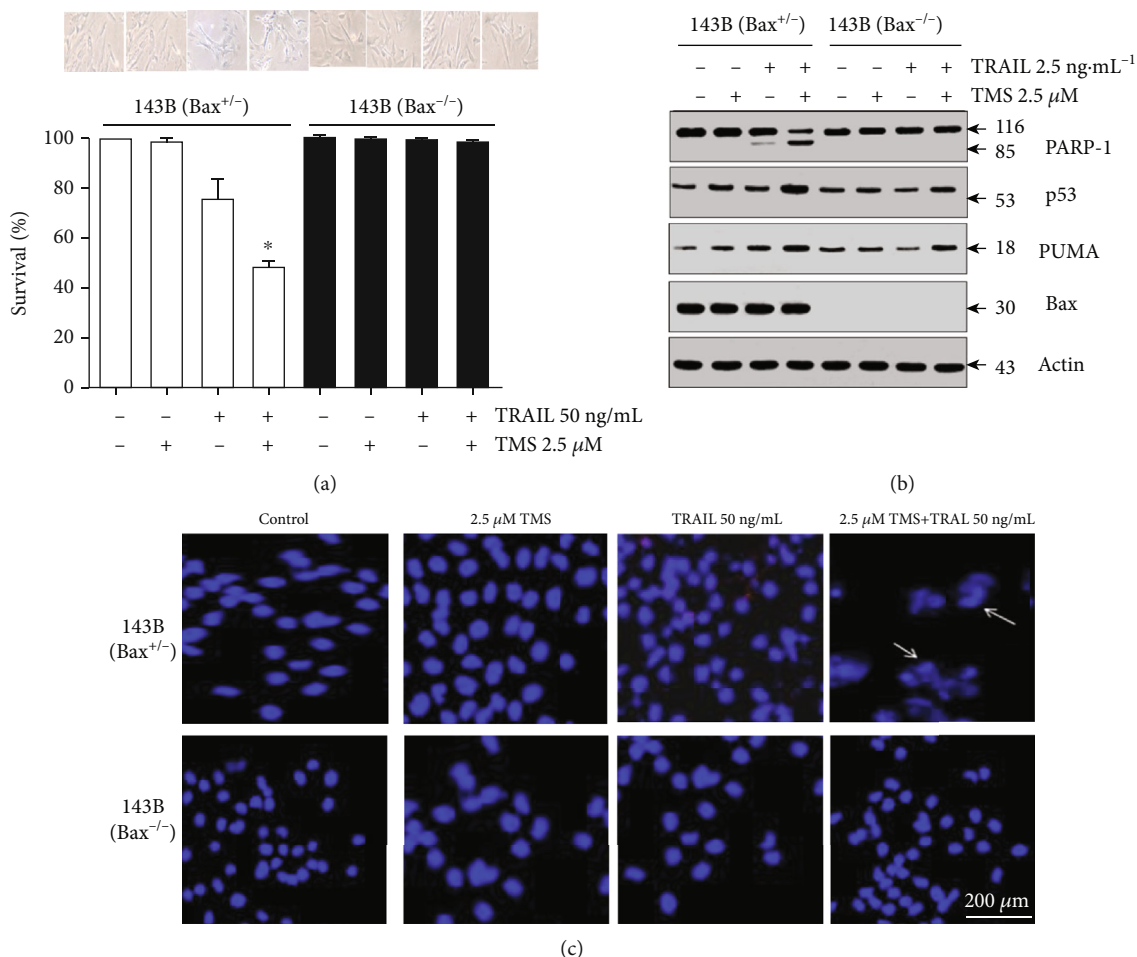
FIGURE 8: The role of BAX in TMS- and TRAIL-mediated apoptosis. (a, b) 143B Bax+/− and 143B Bax−/− cells were exposed to TMS and TRAIL for 10 h. Equal volume of 0.01% BSA + PBS+0.1% DMSO was used as vehicle control. Cell survival rate was analyzed as indicated in the experimental method section. Immunoblotting was used to examine the expression of cleaved PARP1, P53, Bax, and PUMA. $^*P < 0.05$. (c) DAPI was used as specific counterstain for apoptosis to evaluate the effects of cotreatment with TMS and TRAIL in 143B Bax+/− and 143B Bax−/− cells. White arrows indicate chromatin condensation in 143B cells evaluated by fluorescence microscopy (magnification ×400).

extrinsic apoptosis pathway is activated by extracellular ligands binding to cell-surface death receptors, which results in the formation of a death-inducing signaling complex (DISC). Caspases orchestrate both intrinsic and extrinsic apoptotic cell death by activating the cleavage of target proteins [29]. TRAIL, also called TNF superfamily 10, is a pleiotropic cytokine from the tumor necrosis factor superfamily. TRAIL has been shown to selectively induce apoptosis in various tumor cells by activating the extrinsic apoptosis pathway. Treating tumor cells with small molecular inhibitors may facilitate tumor-cell sensitivity to TRAIL-induced apoptosis while exempting normal cells from this fate [30]. Treatments combining TRAIL with small molecular inhibitors, such as the proteasome inhibitor [31], BCL-2 inhibitor [32], mammalian target of rapamycin (mTOR) inhibitor [33], and histone deacetylase (HDAC) inhibitor [34], are being assessed for inhibition of specific signaling proteins that can synergistically facilitate the TRAIL-mediated extrinsic apoptosis pathway. In the present study, our results demonstrate that TMS (used at a noncytotoxic dosage) sensitized

143B cells to TRAIL-mediated apoptosis by increasing the expression of PUMA, p53, and Bax via ROS-induced DNA damage. Mitochondria-mediated caspase-9 activation may have contributed to intrinsic apoptotic signaling induced by TMS by upregulating the levels of intracellular ROS, while death-receptor-mediated caspase 8 activation was likely involved in extrinsic apoptotic signaling triggered by treatment with TRAIL.

TRAIL can selectively induce apoptosis in various cancer cells, as shown in previous studies [12, 35–37]. However, various tumor cells are either intrinsically TRAIL-resistant or become resistant after exposure to TRAIL therapy [38]. Our present results indicate that treatment with TRAIL induced apoptosis in the osteosarcoma cell line Saos-2, while 143B cells showed considerable resistance to TRAIL. These results have consistently agreed with those of previous studies on TRAIL-resistant or TRAIL-sensitive osteosarcoma cell lines [32]. Our results also show that cotreatment using a noncytotoxic dose of TMS and TRAIL promoted apoptosis of 143B cells *in vitro*. These results demonstrate that TRAIL and
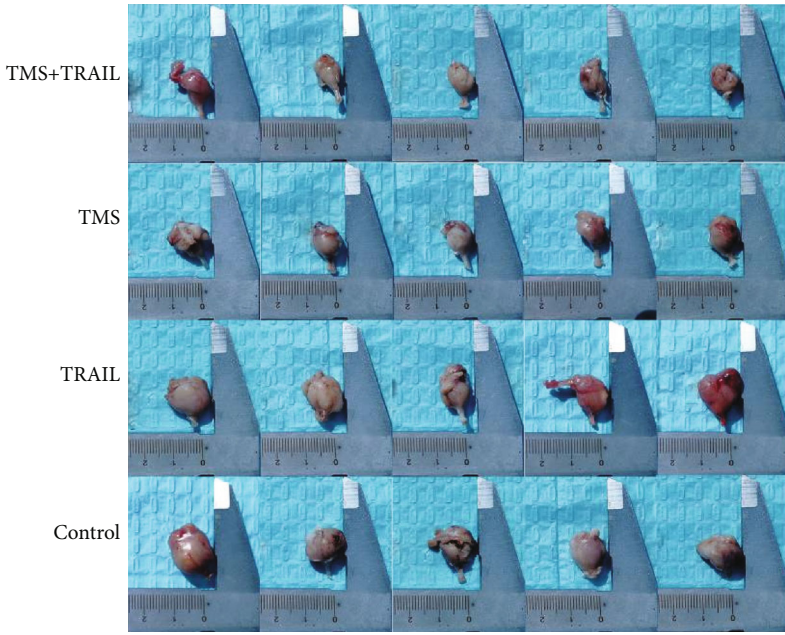
(a)
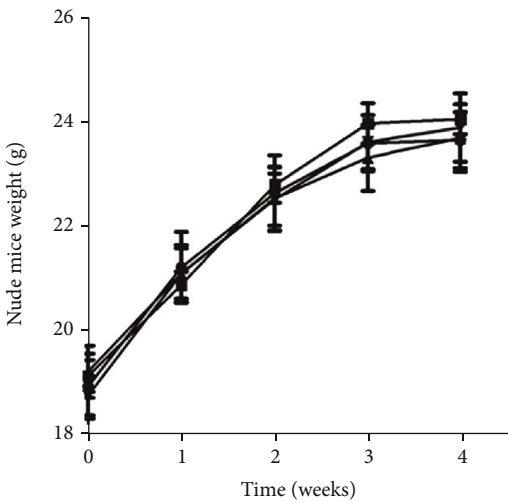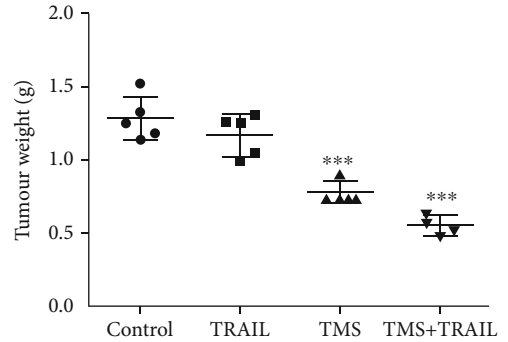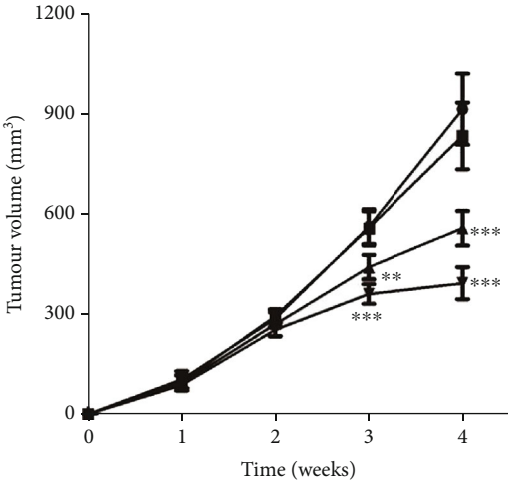
(b)

Figure 9: Continued.

(c)
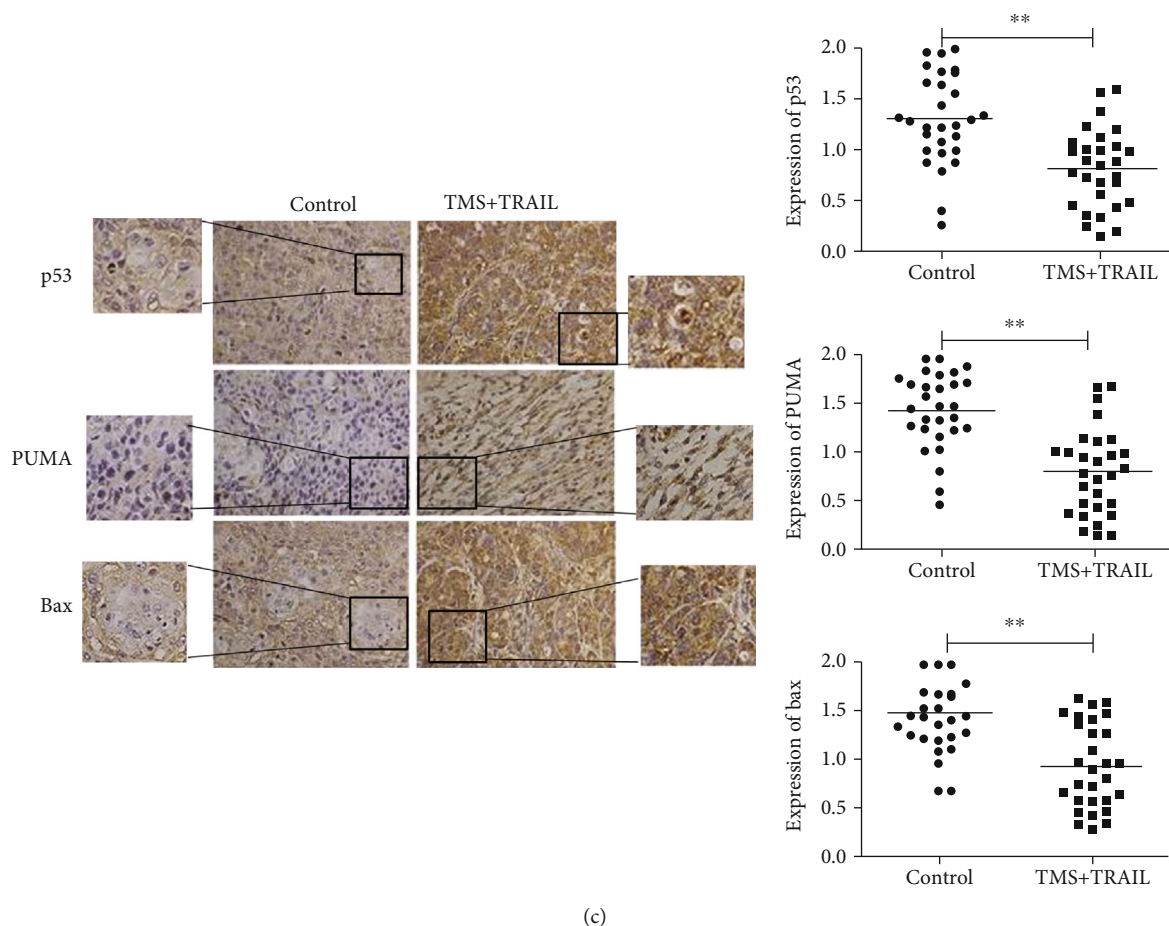
Figure 9: Cotreatment with TMS and TRAIL suppresses the proliferation of cancer cells in nude mice transplanted with osteosarcoma. (a) Sizes of osteosarcoma tumors in nude mice subjected to different treatment regimens. (b) Tumor volume and weight were significantly decreased in TRAIL (100 ng/g) + TMS (1 μg/g)-treated group compared with those of the other groups. No obvious changes in body weight were noted among mice subjected to different treatment regimens. $**P < 0.01$; $***P < 0.001$ versus control. (c) The expression of Bax, PUMA, and P53 was evaluated using immunohistochemistry (IHC). The scored IHC results were analyzed by multiplying the percentages of positive cells by the intensity score obtained using confocal microscopy. Signal intensity was analyzed and scored by two independent pathologists. The score of 0 indicates lack of staining, 1 indicates mild staining, and 2 indicates obvious staining. Osteosarcoma cells in five separate areas were chosen at random and analyzed according to the percentages of positively labeled cells ($**P < 0.01$).

Table 2: Effects of TMS + TRAIL on kidney and liver function *in vivo*.

Treatment	Number of mice	Cr (mmol/L)	ALT (μ/L)	AST (μ/L)	BUN (mmol/L)
Control	5	21.13 ± 2.10	31.14 ± 2.01	97.86 ± 9.20	6.19 ± 1.10
TMS	5	21.23 ± 3.30	29.14 ± 3.32	99.14 ± 16.35	5.97 ± 1.01
TRAIL	5	22.42 ± 3.16	28.95 ± 3.35	98.63 ± 12.32	5.76 ± 0.49
TMS + TRAIL	5	22.51 ± 3.67	31.13 ± 3.10	100.34 ± 21.60	5.98 ± 1.86

Cr: creatinine; ALT: alanine aminotransferase; AST: aspartate transaminase; BUN: blood urea nitrogen.

TMS may act synergistically to promote apoptotic cell death in osteosarcoma cell. The opening of the permeability transition pore complex in the membrane of mitochondria is pivotal to cytochrome-C release, apoptosome formation, and subsequent activation of the caspase cascade in intrinsic apoptosis signaling. Caspases, which are intracellular proteases, are responsible for the deliberate disassembly of cell into apoptotic body during apoptotic cell death. Activation of caspases during apoptotic cell death leads to cleavage of critical cellular substrates, such as lamins and poly(ADP-ribose) polymerase, thereby precipitating the dramatic morphological changes present in apoptotic cell death [39]. In our present study, we found that TMS and TRAIL synergistically increased the expression of caspases 9, 8, and 3, further

TABLE 3: Effects of TMS + TRAIL on blood cells count *in vivo*.

Treatment	Number of mice	Leukocyte ($\times 10^8$/L)	Erythrocyte ($\times 10^{10}$/L)	Platelet ($\times 10^8$/L)
Control	5	5.17 ± 0.54	7.78 ± 1.04	803.28 ± 84.72
TMS	5	5.02 ± 1.01	7.82 ± 1.03	741.52 ± 107.70
TRAIL	5	4.57 ± 0.63	7.66 ± 0.49	786.76 ± 71.71
TMS + TRAIL	5	4.65 ± 0.72	8.36 ± 0.64	795.46 ± 93.11

No significant changes were detected in the blood cells count among different group of mice ($P > 0.05$).
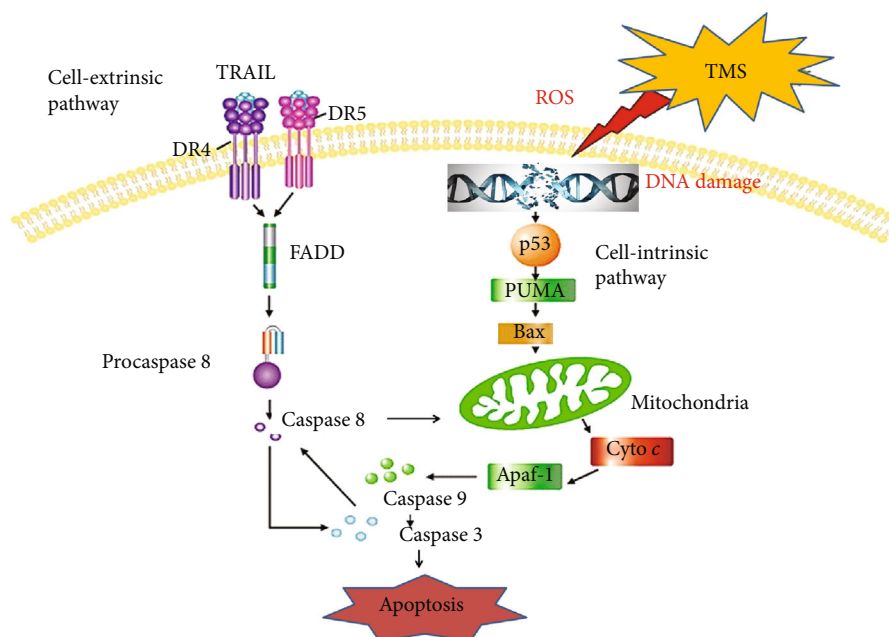
FIGURE 10: Schematic diagram of the mechanisms underlying TRAIL and TMS-mediated apoptosis in osteosarcoma.

highlighting the critical role played by caspases in the apoptosis of osteosarcoma cells. The opening of the mitochondrial permeability transition pore (MPTP), induced by the generation of reactive oxygen species (ROS), is related to the activation of Bax, a pore-destabilizing protein [11]. Our results indicate that increased ROS generation in osteosarcoma cells was detected after treatment with TMS. Furthermore, considerable levels of DNA double-strand breaks were detected in 143B cells after treatment with TMS. Cotreatment using noncytotoxic dosage of TMS and TRAIL led to caspase activation and PARP1 cleavage in 143B cell, which further enhanced ROS-mediated signaling involved in intrinsic apoptosis. However, pretreating cells with the antioxidant (NAC) significantly inhibited intracellular ROS generation and PARP-1 cleavage, thereby reversing apoptosis in osteosarcoma cells induced by cotreatment with TRAIL and TMS. The expression of PUMA and p53 was also decreased by treatment with NAC in 143B cells, which subsequently suppressed apoptosis in these osteosarcoma cells. As a Bcl-2-binding component, PUMA is a proapoptotic protein and can induce p53-dependent apoptosis by transducing a death signal into the mitochondria and activating Bax. Bax is a requisite gateway protein involved in mitochondrial dysfunction and caspase activation [29, 40]. Herein, we found

that combination therapy by TMS and TRAIL remarkably elevated the expression of PUMA and Bax in osteosarcoma cell lines 143B and Saos-2. However, siRNA-induced silencing of *TP53* and *PUMA* expression, or deficiency in the expression of *Bax*, attenuated TRAIL sensitization induced by TMS in osteosarcoma cells. These results indicate that treatment with TMS enhanced intracellular ROS generation, induced DNA damages, and activated the p53/PUMA/Bax signal pathway, resulting in the enhanced outer membrane of mitochondria permeabilization and caspase activation, as well as sensitizing osteosarcoma cell to TRAIL-mediated apoptotic cell death (Figure 10). Despite various novel small molecules and natural compounds have been identified and shown to cause apoptosis by facilitating ROS generation, the specific mechanisms involved in the production of ROS remain unknown [41, 42]. Therefore, in our future studies, we will focus on exploring the mechanisms underlying the biological activity of TMS in the promotion of ROS generation in osteosarcoma cells.

Finally, we explored the potential beneficial effect of cotreatment with TRAIL and TMS in nude mice subjected to orthotopic implantation. Our results demonstrate that cotreatment with TRAIL and TMS suppressed osteosarcoma development with no obvious toxicity in nude mice. The

results of IHC, conducted to assess the expression of PUMA, Bax, and p53 in osteosarcoma tissues collected from the implanted nude mice, further validated the data obtained using our previously described *in vitro* models. In conclusion, our results demonstrate that combined therapy using TRAIL and TMS facilitated intracellular ROS generation, DNA damage, and p53-induced expression of PUMA and Bax in osteosarcoma cells. Activation of p53-PUMA-Bax signaling activated the caspase cascade and induced apoptosis in 143B cells while sparing normal human osteoblasts hFOB1.19. Although our results indicate that TMS may be a safe and effective TRAIL sensitizer and can be used to induce apoptosis in osteosarcoma cells, certain factors require further study. For example, the mechanisms involved in TMS-mediated ROS generation and the efficacy and safety of TMS in patients with osteosarcoma need to be investigated and will be the subject of our future studies.

5. Conclusions

In conclusion, our results indicate that cotreatment with TRAIL and TMS evaluated intracellular ROS level, promoted DNA damage, and activated the Bax/PUMA/p53 pathway, leading to activation of both mitochondrial and caspase-mediated apoptosis in 143B cells.

Abbreviations

TRAIL: TNF-related apoptosis-inducing ligand
TMS: Trans-3, 5, 4′-trimethoxystilbene
ROS: Reactive oxygen species
ER: Endoplasmic reticulum
FBS: Fetal bovine serum
DAPI: 4,6-Diamidino-2-phenylindole
PARP-1: Cleaved poly (ADP-ribose) polymerase-1
MAPK: Mitogen-activated protein kinase
DMSO: Dimethyl sulfoxide
MTT: 3-(4,5-dimethylthiazol-2-yl)-2,5-diphenyltetrazolium bromide tetrazolium
PBS: Phosphate-buffered saline
mTOR: Mammalian target of rapamycin
MPTP: Mitochondrial permeability transition pore
DISC: Death-inducing signaling complex.

Data Availability

The primary data used to support the findings of this study are available from the corresponding author upon request.

Conflicts of Interest

The authors declare that there is no conflict of interests regarding the publication of this paper.

Authors' Contributions

M.H. and L.W. conceived the experiments; F.Y.,W.Y., J.L., and J.C. performed the experimental work and acquired and analyzed the data; M.H. wrote the manuscript. L.W. revised the manuscript. All authors reviewed and approved the manuscript.

References

[1] Q. Zhao, J. Zhong, Y. Bi et al., "Gambogenic acid induces Noxa-mediated apoptosis in colorectal cancer through ROS-dependent activation of IRE1α/JNK," *Phytomedicine*, vol. 78, article 153306, 2020.

[2] C. C. Yang, L. D. Hsiao, H. H. Lin et al., "Induction of HO-1 by 5, 8-Dihydroxy-4,7-Dimethoxyflavone via Activation of ROS/p38 MAPK/Nrf2 Attenuates Thrombin-Induced Connective Tissue Growth Factor Expression in Human Cardiac Fibroblasts," *Oxidative Medicine and Cellular Longevity*, vol. 2020, Article ID 1080168, 18 pages, 2020.

[3] M. Hong, J. Li, S. Li, and M. M. Almutairi, "Resveratrol Derivative,Trans-3, 5, 4'-Trimethoxystilbene, prevents the developing of atherosclerotic lesions and attenuates cholesterol accumulation in macrophage foam cells," *Molecular Nutrition & Food Research*, vol. 64, no. 6, article e1901115, 2020.

[4] H. Li, W. K. K. Wu, Z. Zheng et al., "2,3',4,4',5'-Pentamethoxy-trans-stilbene, a resveratrol derivative, is a potent inducer of apoptosis in colon cancer cells via targeting microtubules," *Biochemical Pharmacology*, vol. 78, no. 9, pp. 1224–1232, 2009.

[5] S. E. Aiyar, H. Park, P. B. Aldo et al., "TMS, a chemically modified herbal derivative of resveratrol, induces cell death by targeting Bax," *Breast Cancer Research and Treatment*, vol. 124, no. 1, pp. 265–277, 2010.

[6] F. S. Aldawsari and C. A. Velazquez-Martinez, "3,4',5-trans-Trimethoxystilbene; a natural analogue of resveratrol with enhanced anticancer potency," *Investigational New Drugs*, vol. 33, no. 3, pp. 775–786, 2015.

[7] S. H. Baek, J. H. Ko, H. Lee et al., "Resveratrol inhibits STAT3 signaling pathway through the induction of SOCS-1: role in apoptosis induction and radiosensitization in head and neck tumor cells," *Phytomedicine*, vol. 23, no. 5, pp. 566–577, 2016.

[8] I. Patties, R. D. Kortmann, and A. Glasow, "Inhibitory effects of epigenetic modulators and differentiation inducers on human medulloblastoma cell lines," *Journal of Experimental & Clinical Cancer Research*, vol. 32, no. 1, p. 27, 2013.

[9] M. P. Fuggetta, G. Lanzilli, M. Tricarico et al., "Effect of resveratrol on proliferation and telomerase activity of human colon cancer cells in vitro," *Journal of Experimental & Clinical Cancer Research*, vol. 25, no. 2, pp. 189–193, 2006.

[10] J. A. Giménez-Bastida, M. Á. Ávila-Gálvez, J. C. Espín, and A. González-Sarrías, "Conjugated physiological resveratrol metabolites induce senescence in breast cancer cells: role of p53/p21 and p16/Rb pathways, and ABC transporters," *Molecular Nutrition & Food Research*, vol. 63, no. 22, article e1900629, 2019.

[11] J. Iturri, A. Weber, A. Moreno-Cencerrado et al., "Resveratrol-induced temporal variation in the mechanical properties of MCF-7 breast cancer cells investigated by atomic force microscopy," *International Journal of Molecular Sciences*, vol. 20, no. 13, p. 3275, 2019.

[12] S. Fulda and K. M. Debatin, "Sensitization for tumor necrosis factor-related apoptosis-inducing ligand-induced apoptosis by the chemopreventive agent resveratrol," *Cancer Research*, vol. 64, no. 1, pp. 337–346, 2004.

[13] D. Delmas, C. Rébé, O. Micheau et al., "Redistribution of CD95, DR4 and DR5 in rafts accounts for the synergistic toxicity of resveratrol and death receptor ligands in colon carcinoma cells," *Oncogene*, vol. 23, no. 55, pp. 8979–8986, 2004.

[14] M. Á. Ávila-Gálvez, R. García-Villalba, F. Martínez-Díaz et al., "Metabolic profiling of dietary polyphenols and methylxanthines in normal and malignant mammary tissues from breast cancer patients," *Molecular Nutrition & Food Research*, vol. 63, no. 9, article e1801239, 2019.

[15] F. Möller, O. Zierau, A. Jandausch, R. Rettenberger, M. Kaszkin-Bettag, and G. Vollmer, "Subtype-specific activation of estrogen receptors by a special extract of Rheum rhaponticum (ERr 731), its aglycones and structurally related compounds in U2OS human osteosarcoma cells," *Phytomedicine*, vol. 14, no. 11, pp. 716–726, 2007.

[16] C. Braconi, F. Meng, E. Swenson, L. Khrapenko, N. Huang, and T. Patel, "Candidate therapeutic agents for hepatocellular cancer can be identified from phenotype-associated gene expression signatures," *Cancer*, vol. 115, no. 16, pp. 3738–3748, 2009.

[17] T. Einem Lindeman, M. C. Poirier, and R. L. Divi, "The resveratrol analogue, 2,3',4,5'-tetramethoxystilbene, does not inhibit CYP gene expression, enzyme activity and benzo[a]pyrene-DNA adduct formation in MCF-7 cells exposed to benzo[a]pyrene," *Mutagenesis*, vol. 26, no. 5, pp. 629–635, 2011.

[18] Y. H. Deng, D. Alex, H. Q. Huang et al., "Inhibition of TNF-α-mediated endothelial cell-monocyte cell adhesion and adhesion molecules expression by the resveratrol derivative, trans-3,5,4'-trimethoxystilbene," *Phytotherapy Research*, vol. 25, no. 3, pp. 451–457, 2011.

[19] D. Alex, E. C. Leong, Z. J. Zhang et al., "Resveratrol derivative, trans-3,5,4'-trimethoxystilbene, exerts antiangiogenic and vascular-disrupting effects in zebrafish through the downregulation of VEGFR2 and cell-cycle modulation," *Journal of Cellular Biochemistry*, vol. 109, no. 2, pp. 339–346, 2010.

[20] H. S. Lin and P. C. Ho, "Preclinical pharmacokinetic evaluation of resveratrol trimethyl ether in Sprague-Dawley rats: the impacts of aqueous solubility, dose escalation, food and repeated dosing on oral bioavailability," *Journal of Pharmaceutical Sciences*, vol. 100, no. 10, pp. 4491–4500, 2011.

[21] B. C. Su, C. Y. Pan, and J. Y. Chen, "Antimicrobial peptide TP4 induces ROS-mediated necrosis by triggering mitochondrial dysfunction in wild-type and mutant *p53* glioblastoma cells," *Cancers (Basel)*, vol. 11, no. 2, p. 171, 2019.

[22] S. H. Park, N. M. Phuc, J. Lee et al., "Identification of acetylshikonin as the novel CYP2J2 inhibitor with anti-cancer activity in HepG2 cells," *Phytomedicine*, vol. 24, pp. 134–140, 2017.

[23] M. J. Hsieh, C. W. Wang, J. T. Lin et al., "Celastrol, a plant-derived triterpene, induces cisplatin-resistance nasopharyngeal carcinoma cancer cell apoptosis though ERK1/2 and p38 MAPK signaling pathway," *Phytomedicine*, vol. 58, article 152805, 2019.

[24] U. Weyemi, B. D. Paul, D. Bhattacharya et al., "Histone H2AX promotes neuronal health by controlling mitochondrial homeostasis," *Proceedings of the National Academy of Sciences of the United States of America*, vol. 116, no. 15, pp. 7471–7476, 2019.

[25] E. Moeglin, D. Desplancq, S. Conic et al., "Uniform widespread nuclear phosphorylation of histone H2AX is an indicator of lethal DNA replication stress," *Cancers (Basel)*, vol. 11, no. 3, p. 355, 2019.

[26] E. Saint-Germain, L. Mignacca, G. Huot et al., "Phosphorylation of SOCS1 inhibits the SOCS1-p53 tumor suppressor axis," *Cancer Research*, vol. 79, no. 13, pp. 3306–3319, 2019.

[27] L. Sun, Y. Huang, Y. Liu et al., "Ipatasertib, a novel Akt inhibitor, induces transcription factor FoxO3a and NF-κB directly regulates PUMA-dependent apoptosis," *Cell Death & Disease*, vol. 9, no. 9, p. 911, 2018.

[28] Y. C. Hung, P. W. Wang, T. Y. Lin, P. M. Yang, J. S. You, and T. L. Pan, "Functional redox proteomics reveal that *Salvia miltiorrhiza* aqueous extract alleviates adriamycin-induced cardiomyopathy via inhibiting ROS-dependent apoptosis," *Oxidative Medicine and Cellular Longevity*, vol. 2020, Article ID 5136934, 15 pages, 2020.

[29] J. A. Pulikkan, M. Hegde, H. M. Ahmad et al., "CBFβ-SMMHC inhibition triggers apoptosis by disrupting MYC chromatin dynamics in acute myeloid leukemia," *Cell*, vol. 174, no. 5, p. 1325, 2018.

[30] X. Jiang, S. Fitch, C. Wang et al., "Nanoparticle engineered TRAIL-overexpressing adipose-derived stem cells target and eradicate glioblastoma via intracranial delivery," *Proceedings of the National Academy of Sciences of the United States of America*, vol. 113, no. 48, pp. 13857–13862, 2016.

[31] T. M. Ganten, R. Koschny, T. L. Haas et al., "Proteasome inhibition sensitizes hepatocellular carcinoma cells, but not human hepatocytes, to TRAIL," *Hepatology*, vol. 42, no. 3, pp. 588–597, 2005.

[32] G. Wang, Y. Zhan, H. Wang, and W. Li, "ABT-263 sensitizes TRAIL-resistant hepatocarcinoma cells by downregulating the Bcl-2 family of anti-apoptotic protein," *Cancer Chemotherapy and Pharmacology*, vol. 69, no. 3, pp. 799–805, 2012.

[33] A. Panner, A. T. Parsa, and R. O. Pieper, "Use of APO2L/TRAIL with mTOR inhibitors in the treatment of glioblastoma multiforme," *Expert Review of Anticancer Therapy*, vol. 6, no. 9, pp. 1313–1322, 2006.

[34] L. Kasman, P. Lu, and C. Voelkel-Johnson, "The histone deacetylase inhibitors depsipeptide and MS-275, enhance TRAIL gene therapy of LNCaP prostate cancer cells without adverse effects in normal prostate epithelial cells," *Cancer Gene Therapy*, vol. 14, no. 3, pp. 327–334, 2007.

[35] X. Dai, C. Yin, Y. Zhang et al., "Osthole inhibits triple negative breast cancer cells by suppressing STAT3," *Journal of Experimental & Clinical Cancer Research*, vol. 37, no. 1, p. 322, 2018.

[36] P. Mahalapbutr, P. Wonganan, W. Chavasiri, and T. Rungrotmongkol, "Butoxy Mansonone G inhibits STAT3 and Akt signaling pathways in non-small cell lung cancers: combined experimental and theoretical investigations," *Cancers (Basel)*, vol. 11, no. 4, p. 437, 2019.

[37] N. Chhiber, T. Kaur, and S. Singla, "Rottlerin, a polyphenolic compound from the fruits of Mallotus phillipensis (Lam.) Mull.Arg., impedes oxalate/calcium oxalate induced pathways of oxidative stress in male wistar rats," *Phytomedicine*, vol. 23, no. 10, pp. 989–997, 2016.

[38] D. I. Radke, Q. Ling, R. Häsler, G. Alp, H. Ungefroren, and A. Trauzold, "Downregulation of TRAIL-receptor 1 increases TGFβ type II receptor expression and TGFβ signalling via microRNA-370-3p in pancreatic cancer cells," *Cancers (Basel)*, vol. 10, no. 11, p. 399, 2018.

[39] D. P. Denning, V. Hatch, and H. R. Horvitz, "Programmed elimination of cells by caspase-independent cell extrusion in *C. elegans*," *Nature*, vol. 488, no. 7410, pp. 226–230, 2012.

[40] A. B. Hua, R. Justiniano, J. Perer et al., "Repurposing the electron transfer reactant phenazine methosulfate (PMS) for the apoptotic elimination of malignant melanoma cells through induction of lethal oxidative and mitochondriotoxic stress," *Cancers (Basel)*, vol. 11, no. 5, p. 590, 2019.

[41] X. Liu, P. Zhao, X. Wang et al., "Celastrol mediates autophagy and apoptosis via the ROS/JNK and Akt/mTOR signaling pathways in glioma cells," *Journal of Experimental & Clinical Cancer Research*, vol. 38, no. 1, p. 184, 2019.

[42] Y. Zhou, L. Wei, H. Zhang et al., "FV-429 induced apoptosis through ROS-mediated ERK2 nuclear translocation and p53 activation in gastric cancer cells," *Journal of Cellular Biochemistry*, vol. 116, no. 8, pp. 1624–1637, 2015.

Research Article

The Regulation of ROS- and BECN1-Mediated Autophagy by Human Telomerase Reverse Transcriptase in Glioblastoma

Xuelu Ding,[1,2,3] **Ziyang Nie,**[1,2] **Zhaoyuan She,**[1,2] **Xue Bai,**[1,2] **Qiuhui Yang,**[1,2] **Feng Wang,**[4] **Fei Wang** ⓘ**,**[5] **and Xin Geng** ⓘ[1,2]

[1]*Department of Biochemistry and Molecular Biology, School of Basic Medical Sciences, Tianjin Medical University, Tianjin 300070, China*
[2]*Key Laboratory of Immune Microenvironment and Disease (Ministry of Education), Tianjin Medical University, Tianjin 300070, China*
[3]*Department of Neurology, Tianjin Neurological Institute, Tianjin Medical University, General Hospital, Tianjin 300052, China*
[4]*Department of Genetics, School of Basic Medical Sciences, Tianjin Medical University, Tianjin 300070, China*
[5]*Department of Neurology, General Hospital, Tianjin Medical University, Tianjin 300052, China*

Correspondence should be addressed to Fei Wang; feiwang@tmu.edu.cn and Xin Geng; gengx@tmu.edu.cn

Xuelu Ding, Ziyang Nie, and Zhaoyuan She contributed equally to this work.

Glioblastoma (GBM) is the most common and aggressive malignant brain tumor with high morbidity and mortality. Human telomerase reverse transcriptase (hTERT), the catalytic subunit of human telomerase, is overexpressed in most cancers including GBM. It is well known that hTERT can compensate telomere shortening to immortalize cells. However, in addition to the canonical function, hTERT has the roles beyond canonical telomere maintenance. To further understand the effects of hTERT on glioblastoma progression, we investigated the role of hTERT in regulating autophagy—a conserved pathway, by which cells deliver cellular organic material and impaired organelles to the lysosomes for degradation and recycle these cargos to produce energy under a stressful condition. Our results showed that downregulation of hTERT impaired autophagy levels by suppressing BECN1/beclin-1 and induced an increase of reactive oxygen species (ROS), which resulted in cell death ultimately. On the contrary, overexpression of BECN1 or treating cells with the antioxidant N-acetylcysteine (NAC) could restore the survival of hTERT knockdown cells. Our study will provide an additional basis of telomerase-targeting therapy for future clinical anticancer treatment.

1. Introduction

Glioblastoma (GBM) is classified as grade IV glioma by the World Health Organization and accounts for about 20% of all brain tumors. From a global perspective, there are 0.59~3.69 cases out of 100,000 people [1]. Despite the improvement of medical technology and the rigorous treatment that patients received, it is still difficult to remove GBM tumors by surgical resection due to their invasion to the surrounding tissues. As a result, recurrence often occurs in GBM patients, and the median survival is less than two years after diagnosis [2–4]. According to the 2016 WHO classification, increasing evidence demonstrated the genetic heterogeneity of GBM [5]. To date, up to 45 genes were found to contain mutations, including *IDH1/IDH2*, *TP53*, *ATRX*, *TERT*, *NF1*, *PTEN*, and *EGFR* [6]. Thus, even within a single glioblastoma, a combination of treatments may be required for different cell subtypes, greatly exacerbating the difficulty of treating this type of tumor.

Telomerase is an RNA-dependent DNA polymerase, which can add TTAGGG repetitive sequences to telomeres via de novo DNA synthesis, thus enabling cell proliferation

and immortalization [7]. Telomerase is composed of two main subunits: telomerase reverse transcriptase (TERT) and an RNA component (TERC). TERT is the core catalytic subunit of telomerase holoenzyme, and the gene expression level is crucial to telomerase activity [8]. In normal somatic cells, telomerase activity is difficult to detect, while most cancer cells reactivate telomerase thus can proliferate unlimitedly [9]. In GBM, researchers found frequent mutations in TERT promoter, which are considered a mechanism of increasing TERT expression [10, 11]. Therefore, TERT may be involved in the progression and used for analyzing prognosis of glioblastoma. It is well studied that telomerase can lengthen telomeres to maintain the stability of chromatin structure. However, emerging evidence shows the extratelomeric roles of TERT, including mitochondria fitness regulation, antiapoptosis, and response to DNA break repair [12–14]. Furthermore, by interacting with transcription factors or chromatin modulating factor, such as MYC, NF-κB, and BRG1, the gene expression of TERT can be regulated independently of telomerase activity [15–17]. Hence, it is necessary to explore new features of TERT.

Autophagy is an evolutionally conserved process of degradation, by which double-membraned vesicles (autophagosomes) deliver intracellular components that need to be fused with lysosomes where the materials are resolved and recycled into the cytosol [18]. Basal autophagy maintains the stability of the intracellular environment via turnover of dysfunctional proteins and organelles [19]. However, when cells are under a stressful state (for example, nutrient deprivation), autophagy is strongly upregulated and provides a survival mechanism by promoting the circulation of nutrients, preventing the accumulation of misfolded proteins, decreasing reactive oxygen species (ROS), maintaining the function of organelles, and regulating intracellular signaling pathways [20]. In recent years, there has been increasing evidence in the role of oxygen free radicals in tumorigenesis and the dual function of antioxidants in the prevention and treatment of cancer [21, 22]. In comparison with healthy cells, cancer cells exhibit increased levels of ROS. This alteration of cellular redox homeostasis may have a series of effects on cancer cells, influencing cell proliferation, invasion, metastasis, and sensitivity to anticancer drugs. The altered oxidant/antioxidant balance, resulting from increased production of ROS, inactivation and decrease of the antioxidant enzymes, can induce oxidative damage and lipid peroxidation processes leading to cell death [22–24].

In the present study, we explore to demonstrate the regulation of ROS and autophagy by TERT and the subsequent effects on GBM survival, aiming to provide a more molecular basis for TERT-targeting therapies. We investigated the role of TERT in regulating ROS and autophagy, and the results showed that downregulation of hTERT can impair autophagy levels by suppressing BECN1 and lead to an increase of ROS, which resulted in cell death ultimately. On the contrary, overexpression of BECN1 or treating cells with the antioxidant N-acetylcysteine (NAC) could restore the survival of TERT knockdown cells. Our study will provide an additional basis of telomerase-targeting therapy for future clinical anticancer treatment.

2. Materials and Methods

2.1. Databases for Bioinformatics. The expression levels of hTERT in normal tissues and cancer tissues were searched in GEPIA database (http://gepia.cancer-pku.cn/) and CGGA database (http://www.cgga.org.cn/). The correlation of the expression levels of hTERT and patients' survival time in glioblastoma samples and normal samples were searched by TCGA database (http://portal.gdc.cancer.gov), and the statistical significance was analyzed by the SPSS software. The STRING database (http://string-db.org/) was used to query the interacting proteins of the TERT and BECN1 proteins. The STRING database can be used to annotate the structure, function, and evolutionary properties of proteins. It can also explore and predict protein interaction networks, provide new research directions for future experiments, and provide efficient mapping of cross-species predictions.

2.2. Cell Culture. The human glioblastoma cell line U87 was generously gifted by Professor Xudong Wu from Tianjin Medical University, originated from ATCC. Cells were cultured in Dulbecco's Modified Eagle's Medium (DMEM; Biological Industries), supplemented with 10% fetal bovine serum (FBS; Biological Industries) in a humidified chamber with 5% CO_2 at 37°C. To establish stable TERT knockdown cell line, lentiviruses carrying TERT-targeting shRNA (GenePharma) were transduced into U87 cells along with 5 μg/mL polybrene (GenePharma), and cells were sorted by 1 μg/mL puromycin (Thermo Fisher). Plasmid transfection was carried out using Lipofectamine 3000 (Invitrogen), as recommended by the manufacturer. We also used the ROS scavenger, N-acetylcysteine (NAC; Beyotime Biotechnology), at a concentration of 3 mM.

2.3. Plasmid. The *BECN1* gene was amplified by PCR from the cDNA of U87 cells. The PCR products were purified with a Gel Extraction Kit (TIANGEN). Then, restriction endonucleases were used to digest the purified products and pLVX-IRES-puro vectors. After purification, they were ligated by T4 DNA ligase (Takara). Finally, the plasmids were amplificated in DH5α *E. coli* cells and identified by sequencing.

2.4. Quantitative Real-Time PCR (qPCR). Total RNA was isolated using the Total RNA extraction kit (TIANGEN) according to the manufacturer's instructions. 1 μg RNA was used as a template to synthesize cDNA using the GoScript Reverse Transcription System (Promega). All qPCRs were carried out using the Roche LightCycler System with SYBR green incorporation (Roche). The primers used in this study are from primer bank (https://pga.mgh.harvard.edu/primerbank/index.html) and are as follows: GAPDH, 5$'$-GGAGCGAGATCCCTCCAAAAT-3$'$ and 5$'$-GGCTGTTGTCATACTTCTCATGG-3$'$; TERT, 5$'$-CCGATTGTGAACATGGACTACG-3$'$ and 5$'$-CACGCTGAACAGTGCCTTC-3$'$. Each sample was assayed in triplicate. The relative mRNA level was determined using the $2^{-\Delta\Delta Ct}$ method.

2.5. Western Blotting. Cells were lysed in RIPA lysis buffer supplemented with phosphatase inhibitor cocktail and

protease inhibitor cocktail (Roche). Protein content was measured with the BCA Protein Assay (Thermo Fisher Scientific). Equal amounts of protein extracts were separated on the SDS-PAGE gel, followed by electrotransfer onto a PVDF membrane (Millipore). The blots were subsequently incubated for 2 h in blocking buffer (5% nonfat milk in TBST). The membranes were incubated in 4°C overnight with monoclonal antibodies and followed by corresponding secondary anti-rabbit or anti-mouse antibodies for 2 h. The antibodies used for Western blot were as follows: Beta-actin (ProteinTech), TERT (ABclonal), mTOR (ABclonal), p-mTOR (Ser2448, Cell Signaling Technology), BENC1 (Santa Cruz Biotechnology), p62 (Cell Signaling Technology), LC3 (Abcam), and secondary anti-rabbit or anti-mouse antibodies (ProteinTech). The protein was detected with the ECL Blotting Detection Reagents (Thermo Fisher Scientific).

2.6. Telomere Repeat Amplification Protocol (TRAP) for Telomerase Activity. Telomerase activity of U87 cell was assayed with telomeric repeat amplification protocol (TRAP) performed as previously described. Briefly, after washing with PBS, 10^6 cells were resuspended in $500 \mu L$ $1 \times$ CHAPS lysis buffer, incubated on ice for 30 min, and then centrifuged at 13,000 g at 4°C for 30 min. Then, $1 \mu L$ was used for the PCR reaction. PCR products were separated on 12% nondenaturing polyacrylamide gels and then stained with SYBR Green I for 30 min, visualized by UVP imaging system. Fluorescence density was quantified by ImageJ.

2.7. Cell Proliferation Assay with CCK-8. Cells were counted and seeded in 96-well plates. The Cell Counting Kit-8 (CCK-8) (Beyotime Institute of Biotechnology) was used to determine the cell proliferation rate according to the manufacturer's instructions. Briefly, after the cells grew for 0, 24, 48, and 72 h, respectively, they were incubated in CCK-8 reagent at 37°C for 2 h. Then, absorbance at 450 nm was measured using a microplate reader.

2.8. Measurement of Cellular ROS. The intracellular ROS level was determined using DCFH-DA Reagent (Beyotime Institute of Biotechnology) following the manufacturer's instructions. Briefly, cells were incubated with DCFH-DA at 37°C for 20 min. Then, cells were washed with serum-free medium for 3 times. The fluorescence intensity of DCFH-DA was detected using a fluorescence microscope quantified by ImageJ or analyzed by flow cytometer.

2.9. Cell Viability Assessment. Cell viability measurements were conducted using CCK8 (Beyotime Institute of Biotechnology) a4ccording to the manufacturer's instructions. Briefly, the prepared cells grown in 96-well plates were treated with $10 \mu L$ of CCK-8 reagent after standard culture for 24 h. Next, cells were incubated at 37°C for 2 h. Finally, the absorbance at the wavelength of 450 nm was measured by a microplate reader.

2.10. Statistical Analysis. Data were analyzed by one-way ANOVA with Fisher's LSD test as indicated and shown as mean ± SEM from at least three independent experiments unless otherwise indicated. Data analysis was carried out using GraphPad Prism5.0 (GraphPad Software). *P* values of < 0.05 were considered statistically significant.

3. Results

3.1. TERT Is Overexpressed in GBM and Affects the Survival Rate of GBM Patients. By searching the GEPIA database, we found that hTERT mRNA levels were higher in low-grade gliomas (mainly including Grades II and III glioma) and glioblastoma (Grade IV glioma) than their corresponding normal tissues. And the difference between the tumor samples of GBM and the relative normal samples was statistically significant (Figure 1(a)). The expression levels of hTERT mRNA also increased from low malignancy to high malignancy in samples from Chinese GBM patients. Besides, the difference between samples of Grade II and Grade IV was statistically significant (Figure 1(b)). To further identify the importance of TERT in GBM, we also analyzed the relationship between TERT expression and survival time of GBM patients using datasets from TCGA. The results showed that GBM patients with lower expression levels lived longer than those with higher levels of TERT (Figure 1(c)). These results indicated that elevated expression of TERT may play a tumor promoting role during GBM progression.

3.2. Downregulation of TERT Impairs Cell Survival and Proliferation. To seek for the effects of TERT expression on cell proliferation of GBM, we transfected U87 cell lines with lentiviruses carrying TERT-targeting small hairpin RNA and constructed a stable cell line in which TERT expression was downregulated. After 48 h of transfection, we measured the silencing efficacy of TERT by qPCR and western blotting. The molecular weight of TERT protein detected was 127 kDa. The results showed that compared to control cells, the level of TERT expression was decreased by about 50% in TERT knockdown cells (Figure 1(d) and Figure 1(e)). The telomerase activity of TERT knockdown cells was significantly decreased assayed by TRAP (Figures 1(f) and Figure 1(g)). Besides, by cell clone formation experiment and cell proliferation detection, we found that TERT downregulation significantly suppressed cell survival rate (Figures 1(h) and 1(i)), indicating that TERT plays an important role in the growth and proliferation of GBM cells.

3.3. Autophagy and ROS Participate in the Regulation of GBM Growth and Proliferation by hTERT. Autophagy is an essential mechanism for cell homeostasis. When cells are subjected to various stress states, autophagy will be upregulated to promote cellular and mammalian survival. To explore the effects of TERT knockdown on autophagy in GBM, we detected the expression levels of some major molecular markers of autophagy, mTOR, p-mTOR, BECN1, p62, and LC3B by western blotting. As shown in Figure 2(a), TERT knockdown was found to decrease the expression of BECN1, the conversion of LC3B from LC3B-I to LC3B-II, and increase the expression of p62, indicating that TERT deficiency suppresses the process of autophagy in U87 cells. Interestingly, the expression level of p-mTOR did not significantly increase after TERT knockdown. Comparatively, the change of

(a)

(b)

Expression

—— TERT low $n = 45$

—— TERT high $n = 107$

(c)

(d)

(e)

(f)

FIGURE 1: Continued.

(g)   (h)   (i)
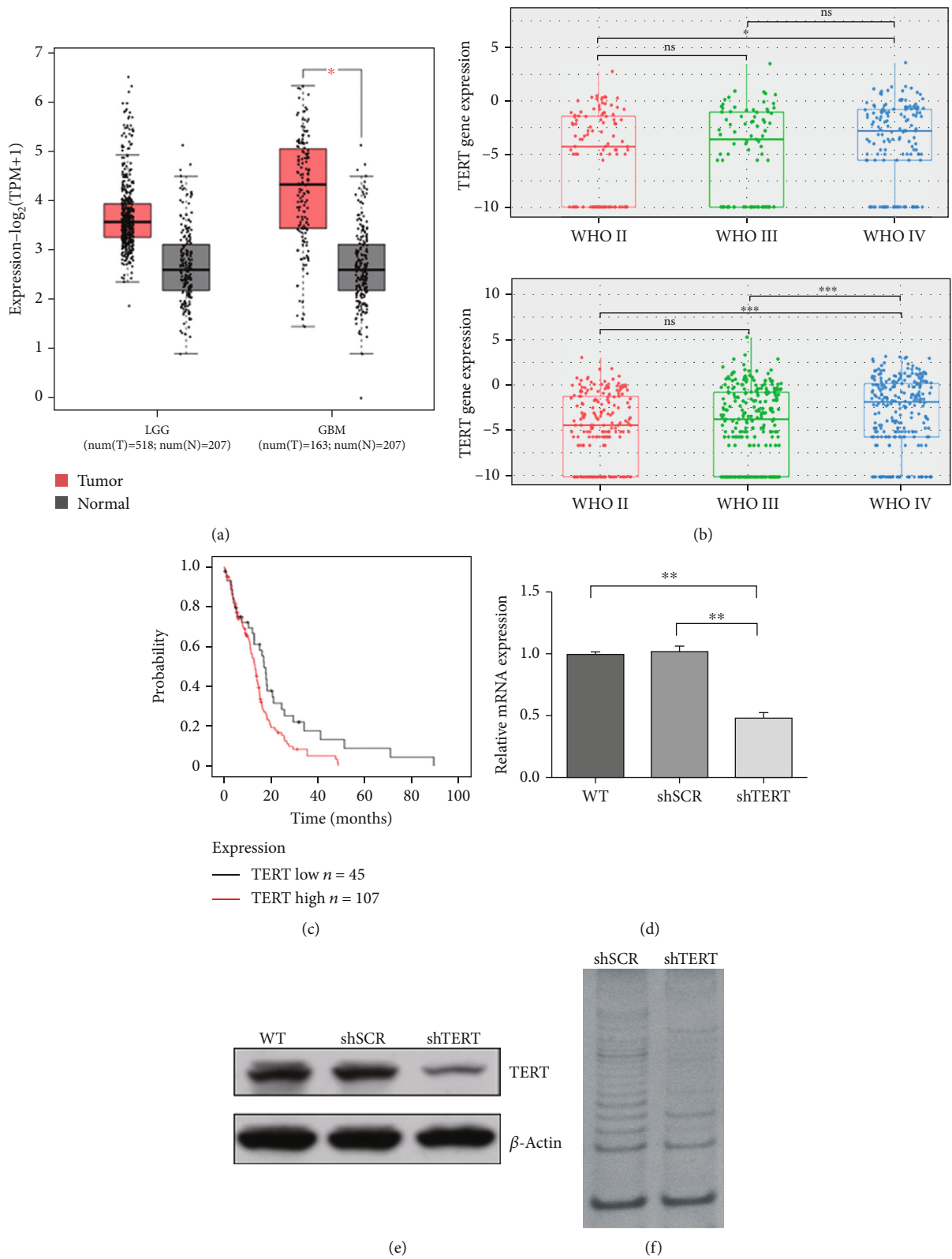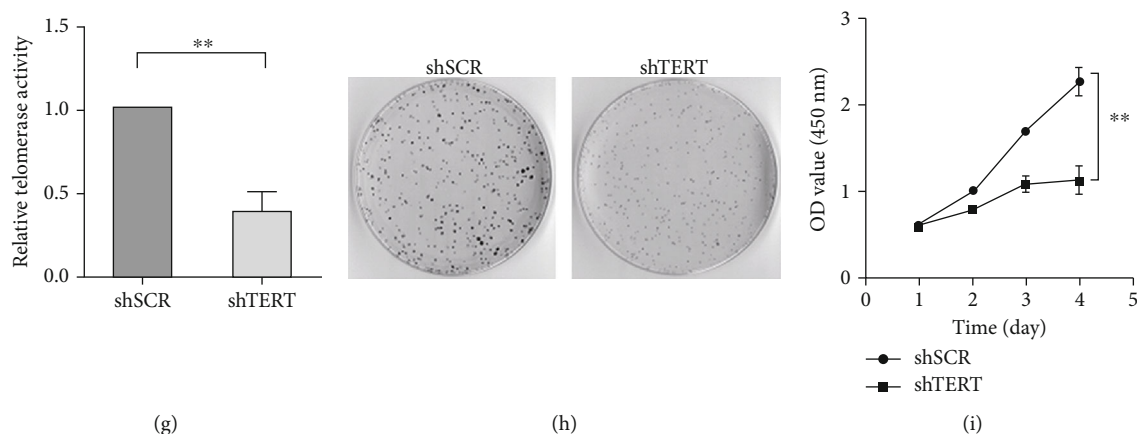
FIGURE 1: Bioinformatics analysis of hTERT in GBM and the influence of hTERT on telomerase activity, cell growth, and proliferation. (a) Box plot of LGG (low-grade glioma), GBM (glioblastoma) patients, and the corresponding normal controls from the GEPIA dataset. (b) Box plot of TERT gene expression in samples of Chinese glioma patients from CGGA dataset (above: CGGA mRNA-seq325: num (II) = 109, num (III) = 85, and num (IV) = 146; below: CGGA mRNA-seq693: num (II) = 194, num (III) = 261, and num (IV) = 256). (c) Survival analysis of GBM patients with high TERT levels and low TERT levels from TCGA dataset (TERT low: $n = 45$; TERT high: $n = 107$). (d) TERT mRNA levels and (e) protein levels in TERT knockdown cells and control cells. (f), (g) Telomerase activity assayed by TRAP. (h) Cell survival rate by clone formation experiment. (i) Growth curve of TERT knockdown cells and control cells by CCK-8. $**p < 0.01$ and $*p < 0.05$ were considered statistically significant.

BECN1 expression level was more significant than that of p-mTOR. Therefore, we speculated that BECN1 mediated the suppression of autophagy by TERT knockdown.

ROS are usually small and short-lived molecules, whose increase may lead to oxidative stress [22]. In comparison with healthy cells, cancer cells exhibit increased levels of ROS. This alteration of cellular redox homeostasis may have a series of effects on cancer cells, influencing cell proliferation, invasion, metastasis, and sensitivity to anticancer drugs. It is commonly accepted that increased level of ROS induces autophagy, which serves to decrease oxidative damage [25]. Here, we wonder that if intracellular ROS levels will accordingly rise after the inhibition of autophagy by TERT knockdown. Therefore, we detected cellular ROS levels using DCFH-DA probes and analyzed the results using fluorescence microscope followed by quantification with ImageJ (Figures 2(b) and 2(c)) or flow cytometer (Figure 2(d)). The results showed that the intracellular ROS level increased significantly after TERT knockdown. The results also suggested that increased level of ROS may be a factor mediating cell growth inhibition by TERT deficiency. To confirm this notion, we treated TERT-deficient cells with the antioxidant NAC and used PBS as a control, and then the viability of the cells was detected. As expected, the cell viability was significantly restored after ROS removal, indicating that ROS was involved in the regulation of hTERT on cell viability (Figure 2(e)).

3.4. BECN1 Mediates the Effects of TERT on Autophagy, ROS Level, and Cell Survival in GBM. BECN1 (Beclin-1) is a core mammalian autophagy protein necessary for the stage of vesicle nucleation. It binds to PI3K (phosphatidylinositol 3-kinase) to form a complex, which can recruit LC3 and initiate autophagy flux [26, 27]. To further investigate the mechanisms of TERT in regulating autophagy, we overexpressed

BECN1 in TERT-deficient cells. As shown in Figure 3(a), autophagy could be restored by BECN1 overexpression. Accordingly, ROS level was also reduced after the recovery of autophagy (Figure 3(b)). These results indicated that BECN1 mediated the suppression of autophagy by TERT deficiency. To verify the effect of autophagy on the growth and proliferation of TERT-deficient cells, the viability of cells was detected. The result showed that the cell viability significantly decreased after stable knockdown of TERT protein. On this basis, the overexpression of the autophagy-related gene *BECN1* restored cell viability, indicating that BECN1-dependent autophagy was involved in the regulation of hTERT on cell growth and survival (Figure 3(c)). In order to further study the interaction relationship between TERT and BECN1 proteins, the STRING database was used to analyze their interaction protein network. There were eleven important proteins, ATG14, BCL2L1, BID, CREBBP, CASP8, NCOA3, PI3KC3, PI3KR4, RELA, TP53, and UVRAG that may play roles and were involved in the protein network of TERT and BECN1 (Figure 3(d) and Table 1).

4. Discussion

GBM has been considered the most common brain tumor with high recurrence and lethality [28]. The current option of medical therapy is relied on surgical resection followed by temozolomide treatment and/or radiotherapy [29, 30]. GBM patients usually have a poor quality of life and terrible prognosis after diagnosis. Thus, it is urgently needed to develop effective therapies. TERT has long been regarded as an important marker of cancer and a target of cancer treatment, but it has not been applied to clinical treatment. Previous studies showed that the vast majority of glioblastomas contain mutations in TERT promoter [31, 32]. In addition, the mutations of TERT promoter enhance its activity and

(a)

(b)

(c)

(d)

(e)
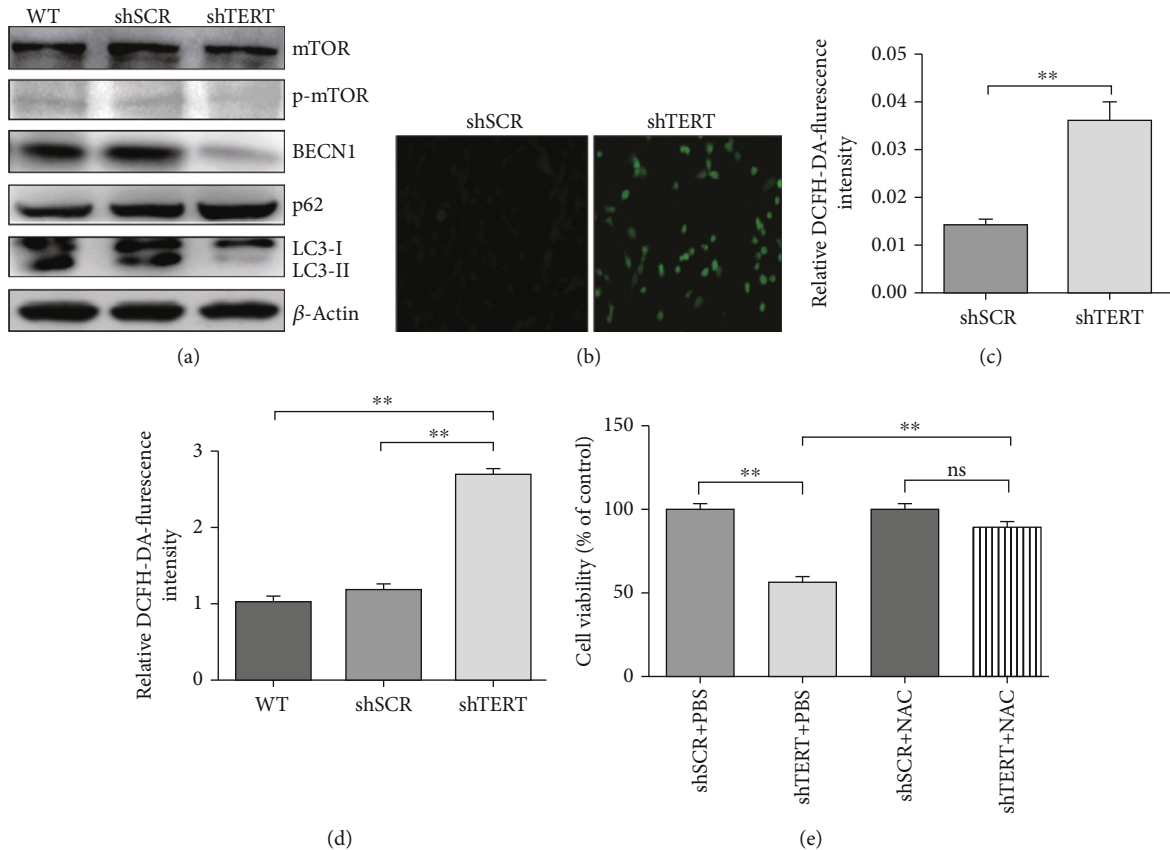
FIGURE 2: Autophagy and ROS participate in the regulation of GBM growth and proliferation by hTERT. (a) Western blotting images of autophagy-related proteins from TERT knockdown cells and control cells. (b, c) Graphical representation of ROS levels in TERT knockdown cells and control cells analyzed by fluorescence microscope. (d) Graphical representation of ROS levels in TERT knockdown cells and control cells analyzed by flow cytometer. (e) Cell viability of TERT knockdown cells treated with antioxidant NAC and PBS as a control. $**p < 0.01$ and $p < 0.05$ were considered statistically significant.

serve as a mechanism for its regulation [10]. In this regard, we explored the expression levels of TERT mRNA in GBM samples by bioinformatic methods. Consistent with previous studies TERT expression is upregulated in a variety of tumor cells and its reactivation is a key step in the development of cancer [33–35]. Our results showed that the expression levels of TERT mRNA were higher in glioblastoma samples than that in healthy controls. Besides, the results of survival analysis showed that patients with high TERT expression lived shorter than those with low TERT expression. Biological experiments manifested that downregulation of TERT suppressed the growth and proliferation of U87 cells. These results indicated that TERT may promote the progression of GBM. It is well known that TERT is able to stabilize chromatin ends by lengthening telomeres. Moreover, TERT has other roles in mitochondria fitness regulation, antiapoptosis, and response to DNA break repair. Here, we discussed the relationship between TERT and autophagy. Our results showed that TERT deficiency impaired the process of autophagy mediated by BECN1 and led to a subsequently increased level of ROS. In addition, Overexpression of BECN1 or treating cells with antioxidant NAC decreased the levels of ROS and rescued the worse survival rate caused by TERT deficiency.

Autophagy is a cellular degradation process that maintains the balance of the intracellular environment, regulates cellular signals, and promotes cell survival. Promoting the survival of tumor cells under stress is widely recognized as an essential role of autophagy and makes it an attractive therapeutic target for cancer [18, 36]. Our results showed that TERT deficiency significantly inhibited the occurrence of autophagy and was depended on BECN1. The initiation step of autophagy is regulated by Class I and Class III PI3K. Class I PI3K can inhibit autophagy indirectly via mTOR, whereas Class III PI3K directly enhances autophagy through interaction with BECN1. Accordingly, the two pathways of mTOR and BECN1 may work together in autophagy [37, 38]. Our present study showed that TERT knockdown significantly decreased the expression of BECN1, the conversion of LC3B from LC3B-I to LC3B-II, and increase the expression of p62, indicating that TERT deficiency suppresses the process of autophagy in U87 cells. Ali et al. reported that TERT inhibits the kinase activity of mTOR complex 1 (mTORC1) in multiple cell lines, resulting in the activation of autophagy under both basal and amino acid-deprived conditions [39], whereas, in our present study, the expression level of p-mTOR did not significantly increase after TERT knockdown in U87 glioma cells. The change of BECN1 expression level

(a)

(b)

(c)

(d)
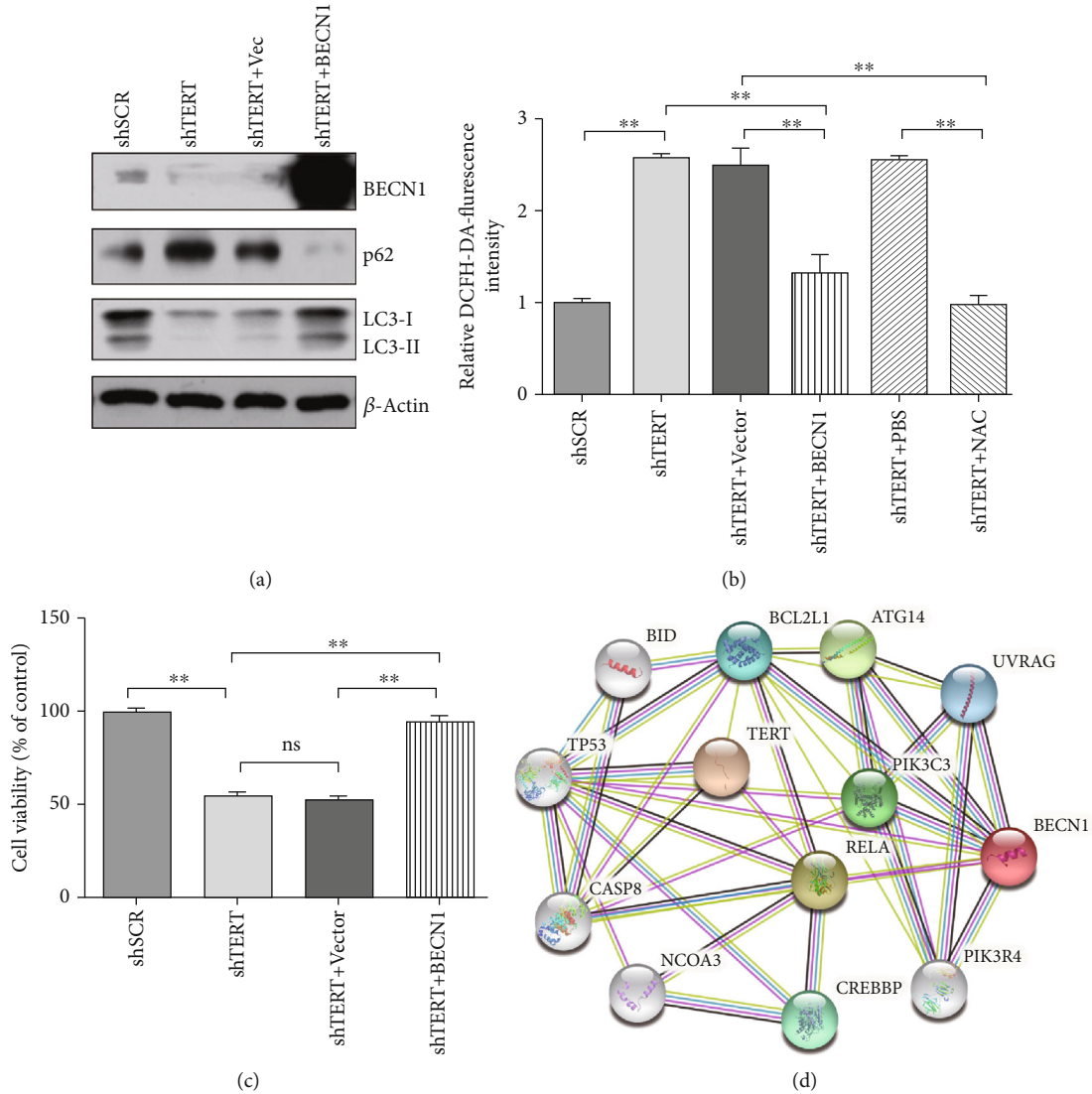
FIGURE 3: BECN1 mediates the effects of TERT on autophagy, ROS levels, and cell survival in GBM. (a) Western blotting images of autophagy-related proteins after overexpression of BECN1 in TERT knockdown cells. (b) Graphical representation of ROS levels in TERT knockdown cells overexpressed by BECN1 and treated with the antioxidant NAC. (c) Cell viability of TERT knockdown cells and control cells after overexpression of BECN1. $**p < 0.01$ and $p < 0.05$ were considered statistically significant. (d) Proteins in TERT-BECN1 interaction network searched by the STRING database.

TABLE 1: List of proteins in TERT-BECN1 interaction network.

Abbreviation of proteins	UniProtKB accession	Full names of proteins
ATG14	Q6ZNE5	Autophagy-related 14
BCL2L1	Q07817	Apoptosis regulator BCL-x
BID	P55957	BH3-interacting domain death agonist
CASP8	Q14790	Caspase 8, apoptosis-related cysteine peptidase
CREBBP	Q92793	CREB-binding protein
NCOA3	Q9Y6Q9	Nuclear receptor coactivator 3
PIK3C3	Q8NEB9	Phosphatidylinositol 3-kinase catalytic subunit type 3
PIK3R4	Q99570	Phosphoinositide-3-kinase regulatory subunit 4
RELA	Q04206	RELA protooncogene, NF-κB subunit
TP53	P04637	Tumor protein P53
UVRAG	Q9P2Y5	UV radiation resistance-associated gene protein

was more significant than that of p-mTOR. Therefore, we speculated that BECN1 mediated the suppression of autophagy by TERT knockdown in GBM.

However, the mechanism of TERT regulating the expression of BECN1 needs further studies. A strong hypothesis is that hTERT indirectly regulates gene expression by acting as a transcriptional cofactor or via a posttranscriptional mechanism [40]. One mechanism comes from the interaction between TERT and a subunit of nuclear factor kappa B (NF-κB), suggesting that TERT responds to the regulation of NF-κB target genes, such as cytokines involved in cancer progression [17]. Moreover, another study found conserved binding sites of NF-κB on the promoter of *BECN1* gene in mice and humans. The authors also showed that NF-κB family member p65/RELA could upregulate the expression of BECN1 and promote the initiation of autophagy [41]. Therefore, it is highly possible that TERT regulates the expression of BECN1 by interacting with NF-κB. Besides, a study showed that TERT contains a BH3-like motif, a short peptide sequence found in BCL-2 family proteins. TERT interacted with MCL-1 and BCL-xL, antiapoptotic BCL-2 family proteins, suggesting a functional link between TERT and apoptosis pathway [42]. There are other studies reported that the antiapoptotic proteins BCL-2 and BCL-xL inhibited autophagy through their binding to the BH3-only protein BECN1 [43, 44]. Thus, BCL-2 family proteins might link TERT to BECN1 and was involved in the autophagic processes. In order to further study the interaction relationship between TERT and BECN1 protein, the STRING database was used to analyze their interaction protein network. We found that eleven proteins, ATG14, BCL2L1, BID, CREBBP, CASP8, NCOA3, PI3KC3, PI3KR4, RELA, TP53, and UVRAG, were involved in the protein network of TERT and BECN. Our present results may provide a new idea for the mechanism of regulation of BECN1 by TERT.

Previous studies reported that TERT could function in response to oxidative stress and alleviate intracellular ROS levels [12, 45, 46], but the mechanisms are not well understood. It is suggested that an increase of cellular ROS can activate the process of autophagy, which will facilitate the removal of excessive ROS. On the contrary, when autophagy is impaired under certain conditions, ROS levels will be disturbed, which can affect the growth and proliferation of cells [47–49]. In the present study, we found that increased autophagy by BECN1 overexpression could lower the elevated ROS level in TERT knockdown cells. Based on these results, we speculated that BECN1-dependent autophagy may be a bridge builder mediating the regulation of ROS by TERT.

5. Conclusions

In summary, the present study provides insight into the roles of TERT on regulating ROS and autophagy during GBM progression. Our results demonstrate an interaction between TERT and autophagy mediated by BECN1. TERT deficiency impairs the process of BECN1-dependent autophagy, elevates the intracellular ROS level, and thus regulates cell survival and proliferation in GBM cells.

Data Availability

The data used to support the findings of this study are available from the corresponding authors upon request.

Conflicts of Interest

The authors declare that they have no conflicts of interest.

Authors' Contributions

Xuelu Ding, Ziyang Nie, and Zhaoyuan She contributed equally to this work and they are co-first authors.

References

[1] L. L. Morgan, "The epidemiology of glioma in adults: a "state of the science" review," *Neuro-Oncology*, vol. 17, no. 4, pp. 623-624, 2015.

[2] T. F. Cloughesy, W. K. Cavenee, and P. S. Mischel, "Glioblastoma: from molecular pathology to targeted treatment," *Annual Review of Pathology*, vol. 9, no. 1, pp. 1–25, 2014.

[3] R. Stupp, S. Taillibert, A. A. Kanner et al., "Maintenance therapy with tumor-treating fields plus temozolomide vs temozolomide alone for glioblastoma," *JAMA*, vol. 314, no. 23, pp. 2535–2543, 2015.

[4] M. C. de Gooijer, M. Guillén Navarro, R. Bernards, T. Wurdinger, and O. van Tellingen, "An Experimenter's Guide to Glioblastoma Invasion Pathways," *Trends in Molecular Medicine*, vol. 24, no. 9, pp. 763–780, 2018.

[5] D. N. Louis, A. Perry, G. Reifenberger et al., "The 2016 World Health Organization classification of tumors of the central nervous system: a summary," *Acta Neuropathologica*, vol. 131, no. 6, pp. 803–820, 2016.

[6] D. W. Parsons, S. Jones, X. Zhang et al., "An integrated genomic analysis of human glioblastoma multiforme," *Science*, vol. 321, no. 5897, pp. 1807–1812, 2008.

[7] C. W. Greider, "Telomere length regulation," *Annual Review of Biochemistry*, vol. 65, no. 1, pp. 337–365, 1996.

[8] S. Kyo, K. Masutomi, Y. Maida et al., "Significance of immunological detection of human telomerase reverse transcriptase: re-evaluation of expression and localization of human telomerase reverse transcriptase," *The American Journal of Pathology*, vol. 163, no. 3, pp. 859–867, 2003.

[9] N. W. Kim, M. A. Piatyszek, K. R. Prowse et al., "Specific association of human telomerase activity with immortal cells and cancer," *Science*, vol. 266, no. 5193, pp. 2011–2015, 1994.

[10] F. W. Huang, E. Hodis, M. J. Xu, G. V. Kryukov, L. Chin, and L. A. Garraway, "Highly recurrent TERT promoter mutations in human melanoma," *Science*, vol. 339, no. 6122, pp. 957–959, 2013.

[11] J. Vinagre, A. Almeida, H. Pópulo et al., "Frequency of _TERT_ promoter mutations in human cancers," *Nature Communications*, vol. 4, no. 1, p. ???, 2013.

[12] I. R. Indran, M. P. Hande, and S. Pervaiz, "hTERT overexpression alleviates intracellular ROS production, improves mitochondrial function, and inhibits ROS-mediated apoptosis in cancer cells," *Cancer Research*, vol. 71, no. 1, pp. 266–276, 2011.

[13] K. Masutomi, R. Possemato, J. M. Wong et al., "The telomerase reverse transcriptase regulates chromatin state and DNA damage responses," *Proceedings of the National Academy of Sciences of the United States of America*, vol. 102, no. 23, pp. 8222–8227, 2005.

[14] J. G. Ren, H. L. Xia, Y. M. Tian, T. Just, G. P. Cai, and Y. R. Dai, "Expression of telomerase inhibits hydroxyl radical-induced apoptosis in normal telomerase negative human lung fibroblasts," *FEBS Letters*, vol. 488, no. 3, pp. 133–138, 2001.

[15] C. M. Koh, E. Khattar, S. C. Leow et al., "Telomerase regulates MYC-driven oncogenesis independent of its reverse transcriptase activity," *The Journal of Clinical Investigation*, vol. 125, no. 5, pp. 2109–2122, 2015.

[16] J. I. Park, A. S. Venteicher, J. Y. Hong et al., "Telomerase modulates Wnt signalling by association with target gene chromatin," *Nature*, vol. 460, no. 7251, pp. 66–72, 2009.

[17] A. Ghosh, G. Saginc, S. C. Leow et al., "Telomerase directly regulates NF-κB-dependent transcription," *Nature Cell Biology*, vol. 14, no. 12, pp. 1270–1281, 2012.

[18] J. Kaur and J. Debnath, "Autophagy at the crossroads of catabolism and anabolism," *Nature Reviews. Molecular Cell Biology*, vol. 16, no. 8, pp. 461–472, 2015.

[19] L. Galluzzi, E. H. Baehrecke, A. Ballabio et al., "Molecular definitions of autophagy and related processes," *The EMBO Journal*, vol. 36, no. 13, pp. 1811–1836, 2017.

[20] N. Mizushima and D. J. Klionsky, "Protein turnover via autophagy: implications for metabolism," *Annual Review of Nutrition*, vol. 27, no. 1, pp. 19–40, 2007.

[21] S. K. Saha, S. B. Lee, J. Won et al., "Correlation between oxidative stress, nutrition, and cancer initiation," *International Journal of Molecular Sciences*, vol. 18, no. 7, p. 1544, 2017.

[22] I. S. Harris and G. M. Denicola, "The complex interplay between antioxidants and ROS in cancer," *Trends in Cell Biology*, vol. 30, no. 6, pp. 440–451, 2020.

[23] S. Toyokuni, K. Okamoto, J. Yodoi, and H. Hiai, "Persistent oxidative stress in cancer," *FEBS Letters*, vol. 358, no. 1, pp. 1–3, 1995.

[24] D. Trachootham, J. Alexandre, and P. Huang, "Targeting cancer cells by ROS-mediated mechanisms: a radical therapeutic approach?," *Nature Reviews. Drug Discovery*, vol. 8, no. 7, pp. 579–591, 2009.

[25] L. Li, J. Tan, Y. Miao, P. Lei, and Q. Zhang, "ROS and autophagy: interactions and molecular regulatory mechanisms," *Cellular and Molecular Neurobiology*, vol. 35, no. 5, pp. 615–621, 2015.

[26] X. H. Liang, S. Jackson, M. Seaman et al., "Induction of autophagy and inhibition of tumorigenesis by _beclin 1_," *Nature*, vol. 402, no. 6762, pp. 672–676, 1999.

[27] R. Kang, H. J. Zeh, M. T. Lotze, and D. Tang, "The Beclin 1 network regulates autophagy and apoptosis," *Cell Death and Differentiation*, vol. 18, no. 4, pp. 571–580, 2011.

[28] L. W. Xu, K. K. Chow, M. Lim, and G. Li, "Current vaccine trials in glioblastoma: a review," *Journal of Immunology Research*, vol. 2014, 10 pages, 2014.

[29] R. Stupp, M. E. Hegi, W. P. Mason et al., "Effects of radiotherapy with concomitant and adjuvant temozolomide versus radiotherapy alone on survival in glioblastoma in a randomised phase III study: 5-year analysis of the EORTC-NCIC trial," *The Lancet Oncology*, vol. 10, no. 5, pp. 459–466, 2009.

[30] M. Lim, Y. Xia, C. Bettegowda, and M. Weller, "Current state of immunotherapy for glioblastoma," *Nature Reviews. Clinical Oncology*, vol. 15, no. 7, pp. 422–442, 2018.

[31] F. K. Lorbeer and D. Hockemeyer, "_TERT_ promoter mutations and telomeres during tumorigenesis," *Current Opinion in Genetics & Development*, vol. 60, pp. 56–62, 2020.

[32] B. H. Diplas, X. He, J. A. Brosnan-Cashman et al., "The genomic landscape of _TERT_ promoter wildtype- _IDH_ wildtype glioblastoma," *Nature Communications*, vol. 9, no. 1, p. 2087, 2018.

[33] C. M. Counter, H. W. Hirte, S. Bacchetti, and C. B. Harley, "Telomerase activity in human ovarian carcinoma," *Proceedings of the National Academy of Sciences of the United States of America*, vol. 91, no. 8, pp. 2900–2904, 1994.

[34] J. W. Shay, Y. Zou, E. Hiyama, and W. E. Wright, "Telomerase and cancer," *Human Molecular Genetics*, vol. 10, no. 7, pp. 677–685, 2001.

[35] Y. S. Cong, W. E. Wright, and J. W. Shay, "Human telomerase and its regulation," *Microbiology and Molecular Biology Reviews*, vol. 66, no. 3, pp. 407–425, 2002.

[36] I. Ulasov, J. Fares, P. Timashev, and M. S. Lesniak, "Editing cytoprotective autophagy in glioma: an unfulfilled potential for therapy," *Trends in Molecular Medicine*, vol. 26, no. 3, pp. 252–262, 2020.

[37] X. Yu, Y. C. Long, and H. -M. Shen, "Differential regulatory functions of three classes of phosphatidylinositol and phosphoinositide 3-kinases in autophagy," *Autophagy*, vol. 11, no. 10, pp. 1711–1728, 2015.

[38] M. Jafari, E. Ghadami, T. Dadkhah, and H. Akhavan-Niaki, "PI3k/AKT signaling pathway: erythropoiesis and beyond," *Journal of Cellular Physiology*, vol. 234, no. 3, pp. 2373–2385, 2018.

[39] M. Ali, S. Devkota, J. I. Roh, J. Lee, and H. W. Lee, "Telomerase reverse transcriptase induces basal and amino acid starvation-induced autophagy through mTORC1," *Biochemical and Biophysical Research Communications*, vol. 478, no. 3, pp. 1198–1204, 2016.

[40] L. L. Smith, H. A. Coller, and J. M. Roberts, "Telomerase modulates expression of growth-controlling genes and enhances cell proliferation," *Nature Cell Biology*, vol. 5, no. 5, pp. 474–479, 2003.

[41] T. Copetti, C. Bertoli, E. Dalla, F. Demarchi, and C. Schneider, "p65/RelA modulates BECN1 transcription and autophagy," *Molecular and Cellular Biology*, vol. 29, no. 10, pp. 2594–2608, 2009.

[42] Y. Jin, L. You, H. J. Kim, and H. W. Lee, "Telomerase reverse transcriptase contains a BH3-like motif and interacts with BCL-2 family members," *Molecules and Cells*, vol. 41, no. 7, pp. 684–694, 2018.

[43] S. Pattingre, A. Tassa, X. Qu et al., "Bcl-2 antiapoptotic proteins inhibit Beclin 1-dependent autophagy," *Cell*, vol. 122, no. 6, pp. 927–939, 2005.

[44] M. C. Maiuri, G. le Toumelin, A. Criollo et al., "Functional and physical interaction between Bcl-X(L) and a BH3-like domain in Beclin-1," *The EMBO Journal*, vol. 26, no. 10, pp. 2527–2539, 2007.

[45] T. Kokubun, S. I. Saitoh, S. Miura, T. Ishida, and Y. Takeishi, "Telomerase plays a pivotal role in collateral growth under ischemia by suppressing age-induced oxidative stress, expression of p53, and pro-apoptotic proteins," *International Heart Journal*, vol. 60, no. 3, pp. 736–745, 2019.

[46] A. Spilsbury, S. Miwa, J. Attems, and G. Saretzki, "The role of telomerase protein TERT in Alzheimer's disease and in tau-related pathology in vitro," *The Journal of Neuroscience*, vol. 35, no. 4, pp. 1659–1674, 2015.

[47] X. Zhang, L. Yu, and H. Xu, "Lysosome calcium in ROS regulation of autophagy," *Autophagy*, vol. 12, no. 10, pp. 1954-1955, 2016.

[48] Q. Li, Y. Yin, Y. Zheng, F. Chen, and P. Jin, "Inhibition of autophagy promoted high glucose/ROS-mediated apoptosis in ADSCs," *Stem Cell Research & Therapy*, vol. 9, no. 1, p. 289, 2018.

[49] J. Pei, J. Deng, Z. Ye et al., "Absence of autophagy promotes apoptosis by modulating the ROS-dependent RLR signaling pathway in classical swine fever virus-infected cells," *Autophagy*, vol. 12, no. 10, pp. 1738–1758, 2016.

Research Article

VDAC1 Conversely Correlates with Cytc Expression and Predicts Poor Prognosis in Human Breast Cancer Patients

Fangfang Chen,[1] **Shuai Yin,**[2] **Bin Luo,**[1] **Xiaoyan Wu,**[1] **Honglin Yan,**[1] **Dandan Yan,**[1] **Chuang Chen,**[3] **Feng Guan,**[1] **and Jingping Yuan** [iD][1]

[1]*Department of Pathology, Renmin Hospital of Wuhan University, No. 99, Zhangzhidong Road, Wuchang District, Wuhan, 430060 Hubei, China*
[2]*Department of Gastroenterology, Jingzhou Central Hospital, The Second Clinical Medical College, Yangtze University, Jingzhou, Hubei, China*
[3]*Department of Breast and Thyroid Surgery, Renmin Hospital of Wuhan University, Wuhan, 430060 Hubei, China*

Correspondence should be addressed to Jingping Yuan; yuanjingping@whu.edu.cn

Aim. The main objective of this article was to evaluate the association of voltage-dependent anion channel 1 (VDAC1) with Cytochrome C (Cytc) expression, various clinicopathological features, and prognosis in breast cancer (BC) patients. Meanwhile, the correlation of Cytc expression with various clinical features and 5-year disease-free survival (5-DFS) of BC was also investigated. *Methods.* *In vivo*, expression of VDAC1 and Cytc was examined in 219 BC tissues and 100 benign breast lesions by immunohistochemical (IHC) analysis. *In vitro*, MTT and wound healing migration assay were performed to detect the effect of VDAC1 on BC cells. *Results.* Expression of VDAC1 is conversely associated with Cytc in BC ($P = 0.011$), especially in triple-negative breast cancer (TNBC) ($P = 0.004$). Knockdown of VDAC1 inhibited proliferation ($P < 0.001$) and migration ($P < 0.05$) of MCF-7 cells. High expression of VDAC1 and low expression of Cytc had a significant association with multiple clinicopathological parameters ($P < 0.05$) and poor 5-DFS ($P < 0.001$) in BC. *Conclusion.* VDAC1 was elevated in BC tissues and conversely associated with Cytc. Detection of VDAC1 may provide guidance for the poor prognosis of BC, especially TNBC.

1. Introduction

Breast cancer (BC) is by far the most common female malignant tumor in the world, with a high mortality rate, and is the leading cause of cancer-related death in women [1]. In China, 367900 new cases of BC were diagnosed in 2018, which accounts for 19.2% of all newly diagnosed female cancers [2]. In recent years, although breast conserving surgery, targeted therapy, endocrine therapy, and immunotherapy have made progress in breast cancer treatment, the incidence rate of the disease has increased [3]. And only limited success has been achieved in cases of advanced cancer [4]. The burden of this disease is heavy, and it remains a serious health threat for women relative to the large Chinese population [5]. Therefore, it is extremely important to find new prognostic markers and early diagnosis of BC, so that patients can receive better treatments.

Cancer cells have a series of common characteristics, including high proliferation and antiapoptosis [6, 7]. The formation of cancer is related to cell metabolic reprogramming, such as enhanced aerobic glycolysis (Warburg effect) [8, 9]. And the "Warburg effect" is postulated to be closely associated with the closure of voltage-dependent anion channel (VDAC) [10, 11]. VDAC has been identified as a 31 kDa pore-forming protein, which is present in the mitochondrial outermembrane (OMM) of all eukaryotes [12]. Three homologous genes encode three VDAC isoforms: VDAC1, VDAC2, and VDAC3 [13]. Among them, VDAC1 is the most abundantly expressed and best characterized one, which forms a channel for the entry and exit of

TABLE 1: Patient characteristics ($N = 219$).

Characteristic	N (%)
Age (years)	
≤50	135 (61.64%)
>50	84 (38.36%)
Menopause	
Before	125 (57.08%)
After	94 (42.92%)
TNM stage	
I/II	153 (69.86%)
III	66 (30.14%)
Histological grade	
G1/G2	165 (75.34%)
G3	54 (24.66%)
Lymph node metastasis	
No	95 (43.38%)
Yes	124 (56.62%)
ER status	
Negative	122 (55.71%)
Positive	97 (44.29%)
PR status	
Negative	124 (56.62%)
Positive	95 (43.38%)
HER2 gene	
Nonamplification	173 (79%)
Amplification	46 (21%)
Recurrence	
No	136 (62.1%)
Yes	83 (37.9%)

mitochondrial metabolites including ATP and NADH across the OMM, thereby regulating the activity of mitochondria [14]. VDAC1 plays a key role in the regulation of apoptosis by both interaction with proapoptotic (Bcl2 and Bcl-xL) proteins and antiapoptotic proteins (Bax, Bak, and Bim) [15, 16]. It has been proved that VDAC1 is involved in several diseases, such as neurodegenerative, cardiac injury, and neoplastic [17]. Several studies have demonstrated that VDAC1 is remarkable expressed in malignant tumors such as uterine cervical cancer [18], hepatocellular carcinoma [19], and cholangiocellular carcinoma [20], indicating that it plays a significant role in high energy-demanding cancer cells. Furthermore, VDAC1 has also been reported to promote tumor growth and play a controversial role in the prognosis of different cancers [21]. A number of anticancer agents have taken VDAC1 as a novel pharmacological target [12]. However, the correlation of VDAC1 expression with tumorigenesis and progression of solid tumor of BC and the role of VDAC1 acts in the prognosis of BC patients has not been well-documented.

Cytochrome C (Cytc) has been proposed to be a proapoptotic factor which is located in the inner membrane of mitochondria and plays an irreplaceable role in mitochon-

drial electron transport and intrinsic type II apoptosis [22, 23]. Cytc release forms an essential step in the apoptotic cascade, upon binding with apoptosis protease-activating factor 1 (Apaf-1), dATP, and procaspase-9 [24, 25]. A number of studies have shown that Cytc can induce apoptosis of cancer cells [26, 27]. Jamsheed et al. [28] demonstrated that in non-small-cell lung cancer patients, Cytc level was lower than healthy individuals, and the lower expression of Cytc were associated with advanced stages, high grade histological differentiation, and shorter overall survival. Rahul et al. [29] explored that in prostate cancer, the deficiency of Cytc contributed to tumor invasiveness and therapeutic resistance and led to faster recurrence. It has been widely reported that VDAC1 is involved in the release of Cytc, which is able to signal Cytc to initiate the mitochondrial-mediated cell death cascade [30]. In contrast, VDAC1 has also been reported to interact with antiapoptotic proteins such as Bcl-2 and hexokinase (HK) to control the release of Cytc [15]. In several melanoma and prostate cancer cell lines, the expression level of VDAC1 is related to the induction of Cytc release, which provides more possibilities for the pharmacological treatment of tumors [31]. However, the association of VDAC1 expression with Cytc in BC is still elusive and rarely addressed, thereby indicating further investigation is needed.

The main objectives of this article were as follows: (i) evaluate the association of VDAC1 expression with Cytc in BC; (ii) investigate the correlation of various clinical features and 5-year disease-free survival (5-DFS) of BC with VDAC1 and Cytc, respectively, and (iii) explore the effects of VDAC1 on cell proliferation and migration in BC cell line.

2. Material and Methods

2.1. Patient Tissue Samples. A total of 219 formalin-fixed, paraffin-embedded primary invasive breast cancer tissue samples were collected from the patients diagnosed with BC through histopathologic evaluation on surgical tissue specimens. 100 cases of benign breast lesions were collected as controls. All the patients underwent surgical treatment at Renmin Hospital of Wuhan University between August 2009 and December 2010. There were no any previous chemotherapies, radiotherapies, or other treatments before surgery in these patients. The patients' written informed consent was obtained before the operation, and the study was approved by the Ethics Committee of Renmin Hosptial of Wuhan University. Patients were all followed up for 5 years. The follow-up data was calculated as the period from the date of surgery to the end of follow-up or death. We followed up all the patients by telephone interviews or outpatient clinic visits.

2.2. Cell Culture. The breast cancer cell line MCF-7 was purchased from the Cell Bank of Chinese Academy of Sciences (Shanghai, China). These cells were incubated in Dulbecco's modified Eagle's medium (DMEM, Invitrogen, Carlsbad, CA, USA) supplemented with 10% fetal bovine serum (FBS, Invitrogen), routinely maintained at 37°C and in an atmosphere of 5% CO_2.

(a)

(b)

(c)

(d)
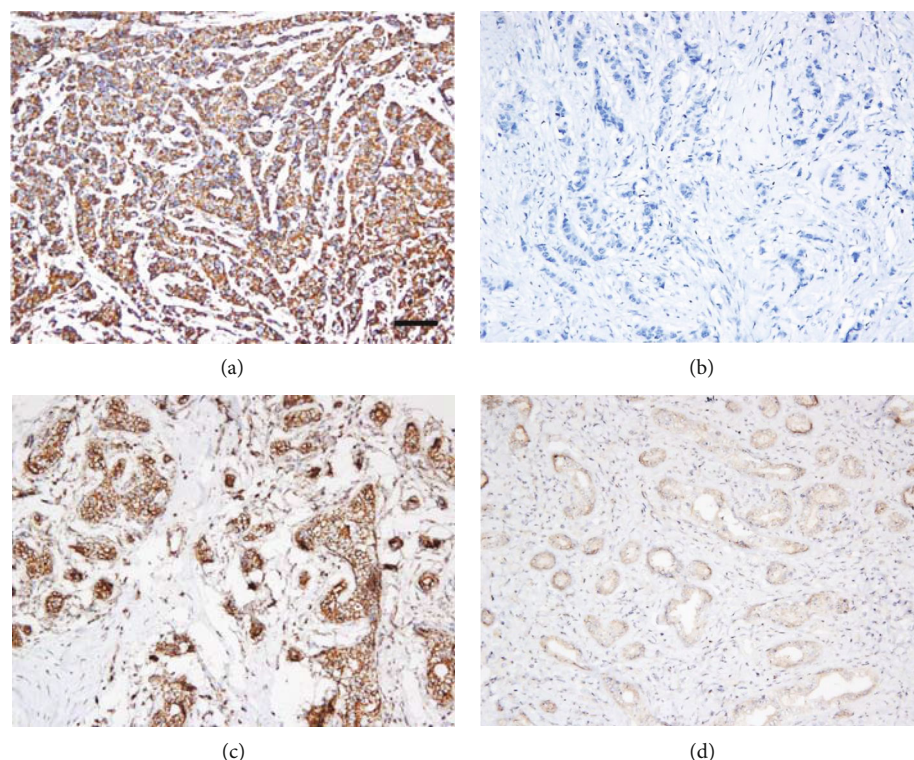
FIGURE 1: Immunohistochemical staining of VDAC1 in breast cancer (BC) lesions and benign breast lesions: (a) high expression of VDAC1 protein in BC; (b) low expression of VDAC1 protein in BC; (c) high expression of VDAC1 protein in benign breast lesions; (d) low expression of VDAC1 protein in benign breast lesions. Scale bar, 50?m.

TABLE 2: The expression of VDAC1 and Cytc protein in breast cancer and benign breast lesions.

| | VDAC1 | | P value | Cytc | | P value |
	High expression	Low expression		High expression	Low expression	
Breast cancer tissue ($n = 219$)	162 (73.97%)	57 (26.03%)	**0.001**	65 (29.68%)	154 (70.32%)	**0.004**
Benign breast lesions ($n = 100$)	55 (55%)	45 (45%)		47 (47%)	53 (53%)	

2.3. Immunohistochemistry (IHC). A tissue array was used which included two tumor samples from each patient. The paraffin-embedded tissues were cut into 4 μm thick sections, then deparaffinized and dehydrated following standard procedures. Subsequently, paraffin sections were rinsed with PBS (3 × 5 min) and then blocked with 3% hydrogen peroxide at 37°C for endogenous peroxidase ablation for 10 min. Antigen retrieval was conducted by microwave heating with citrate buffer (pH 6.0) for 20 min. Then, the samples were exposed to normal goat serum at 37°C for 20 min to decrease nonspecific antibody binding. The tissue sections were incubated overnight at 4°C with the primary antibody (anti-VDAC1, 1 : 1000, ab15895, Abcam, UK; anti-Cytc, 1 : 50, sc-13561, Santa Cruz Biotechnology, Inc., Santa Cruz, CA, USA). After rinsing in PBS, the tissue sections were incubated with horseradish peroxidase-labeled anti-rabbit antibodies at 37°C for 20 min. Then, the tissue sections were rinsed with PBS for 4 times and then dripped with freshly prepared 3,3-diaminobenzidine (DAB). Microscopically, the staining was terminated when the tissue sections were brown-yellow or brown. Subsequently, all the tissue sections were restained with hematoxylin for about 1 min. Finally, the

slices were dehydrated with ethanol and toluene and then sealed with neutral gum. PBS was used to replace the primary antibody as negative control.

2.4. Evaluation of Immunohistochemical Staining. The slides were viewed via Olympus BX53 (Tokyo, Japan) microscope. IHC staining was evaluated independently by two pathologists under the double-blind condition. VDAC1 was mainly expressed in membrane of tumor cells. VDAC1 immunohistochemical staining in tumor cells was evaluated semiquantitatively as follows: (1) staining intensity: 0 (no staining), 1 (weak staining), 2 (moderate staining), and 3 (strong staining); (2) the extent of staining: 0 (0%), 1 (1-20%), 2 (21-50%), and 3 (>50%). Five most representative fields of high magnification (400x) were selected to calculate the final score. The final immunohistochemical score was multiplied by staining intensity and extent, theoretically from 0 to 9. Scores less than or equal to 3 were defined as low expression, and scores greater than or equal to 4 were described as high expression. Cytc protein was predominantly located in membrane and cytoplasm of tumor cells. The staining intensity was classified as four grades as follows: 0 (no staining), 1
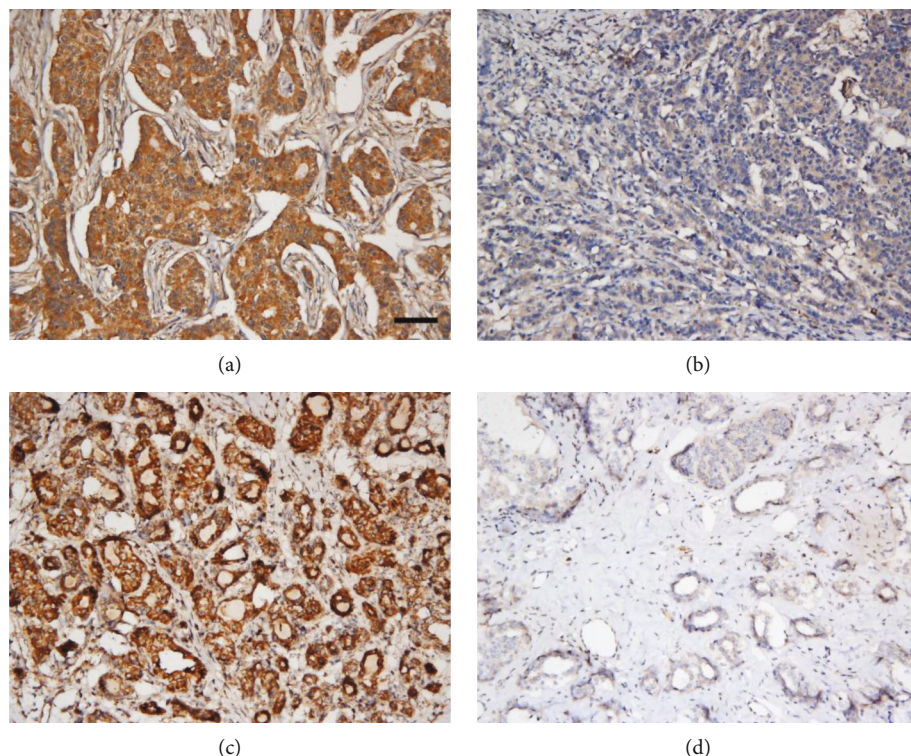
FIGURE 2: Immunohistochemical staining of Cytc in BC lesions and benign breast lesions: (a) high expression of Cytc protein in BC; (b) low expression of Cytc protein in BC; (c) high expression of Cytc protein in benign breast lesions; (d) low expression of Cytc protein in benign breast lesions. Scale bar, 50?m.

TABLE 3: Correlation analysis of the expression of VDAC1 with Cytc in benign breast lesions.

	High-VDAC1 expression ($n = 55$)	Low-VDAC1 expression ($n = 45$)	P value
Cytc expression			
High ($n = 47$)	28 (59.57%)	19 (40.43%)	0.425
Low ($n = 53$)	27 (50.94%)	26(49.06%)	

(light yellow), 2 (brown-yellow), and 3 (dark brown). The percentage of positive cells was classified as five grades as follows: 0 (0%), 1 (≤30%), 2 (31-50%), 3 (51-80%), and 4(≥80%). Five most representative fields of high magnification (400x) were selected to calculate the final score. The final immunohistochemical score was the product of staining intensity and extent, theoretically from 0 to 12. Scores less than 4 were defined as low expression, and scores greater than or equal to 4 were described as high expression.

2.5. Transfection. Small interfering RNA (siRNA) duplexes targeting human VDAC1 (si-VDAC1-1: GTCTAGGACTG-GAATTTCA, si-VDAC1-2: GGAGACCGCTGTCAATCTT, and si-VDAC1-3: GCTGCGACATGGATTTCGA) were designed and synthesized by Guangzhou Ruibo Biotechnology Co., Ltd (Guangzhou, China). SiRNA duplexes with nonspecific sequences were used as siRNA negative control. The transfections were carried out using Lipofectamine-RNAi MAX (Invitrogen) following the manufacturer's protocol. The siRNA-targeted human VDAC1 is designed from the messenger RNA (mRNA) sequences of human VDAC1 gene

(RefSeq: NM_003374). The effect of silencing was verified at the protein level.

2.6. Western Blot Analysis. Cultured cells were collected and lysed to harvest protein. Denatured protein samples were electrophoretically separated on 10% SDS-polyacrylamide gel (PAGE), and then, the proteins were transferred to polyvinylidenefluoride (PVDF) membranes. After transfer, the membranes were incubated with a blocking buffer consisting of 50 mm Tris-HCl (pH 7.5), 100 mm NaCl, 5% nonfat dry milk, and 0.05% Tween 20 for 2 h. Next, the membranes were incubated with primary antibodies against VDAC1 (Abcam Ab15895, 1 : 1000) and Cytc (Santa Cruz sc-13561, 1 : 100) at 4°C overnight. After being washed for three times, the membranes were further incubated with horseradish peroxidase-conjugated sheep antihuman (Amersham Biosciences, Piscataway, NJ) IgG antibodies at a dilution of 1 : 5000 for 2 h at room temperature. Protein was visualized using an enhanced chemiluminescence system (ECL) reagent (Key-GEN BioTECH, China). The volumes of target bands were normalized to GAPDH. Then, the membranes were detected

TABLE 4: Correlation analysis of the expression of VDAC1 with Cytc in breast cancer patients.

	High-VDAC1 expression ($n = 162$)	Low-VDAC1 expression ($n = 57$)	r value	P value
Cytc expression				
High ($n = 65$)	40 (61.54%)	25 (38.46%)		
Low ($n = 154$)	122 (79. 22%)	32 (20.78%)	-0.184	0.011
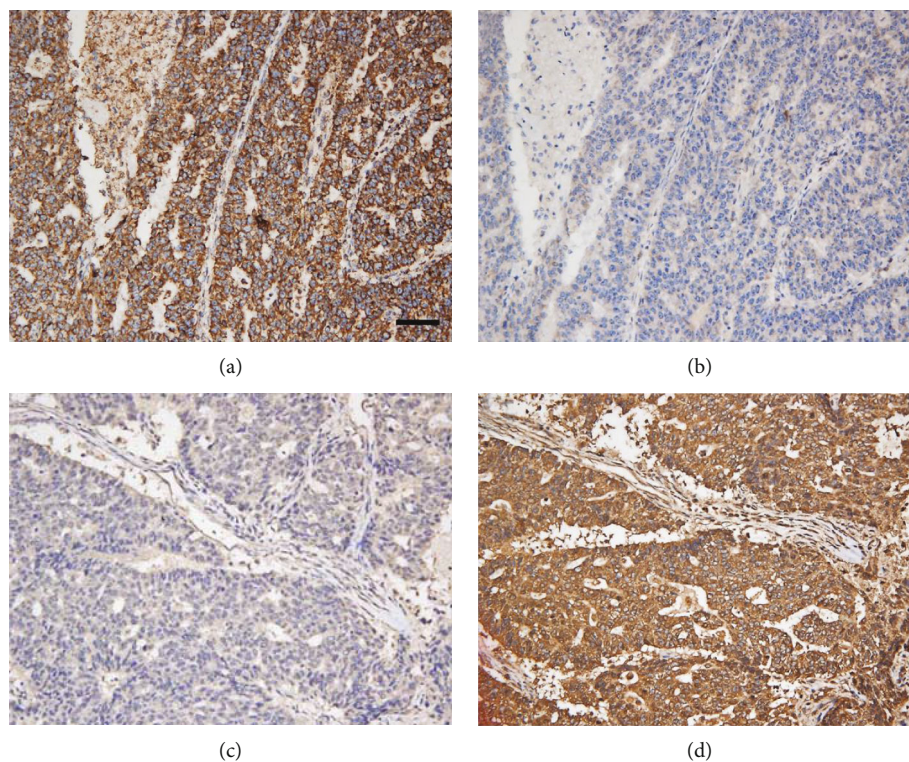
FIGURE 3: Immunohistochemical staining for VDAC1 and Cytc in breast cancer tissues: high expression of VDAC1 protein (a) with low Cytc expression (b); low expression of VDAC1 protein (c) with high Cytc expression (d). Scale bar, 50?m.

by automatic chemiluminescence analyzer, and the gray value of related bands was analyzed by Image J software (Broken Symmetry Software). Each experiment was repeated at least three times.

2.7. MTT Assay. Cell proliferation viability of MCF-7 cells was measured using the MTT assay. In brief, cells were seeded after transfection with siRNA for the indicated time in triplicate in 96-well plates at densities of 3×10^3 cells/well . The cells were incubated under standard conditions for 48 hours. Then, cells were treated by MTT dye (5 mg/ml 10 μl per well) for 4 h. The absorbance values were measured using a microplate reader at a wavelength of 490 nm. The growth assays were repeated three times and reported as percentage changes compared to the controls.

2.8. Wound Healing Migration Assay. A total of 1×106 cells were plated into a 6-well plate, and complete convergence was allowed. Wounds were created by scraping confluent cell monolayers with 200 μl pipette tips. The cells were washed with PBS twice, after which cells were cultured in 10% FBS DMEM. Three digital images were taken at 0 and 48 h after

wounding under a microscope (Olympus, Japan). The assays were accomplished in triplicate and repeated three times. The change of wound width was measured, and wound area filled was calculated by Image J software (Broken Symmetry Software).

2.9. Statistical Analysis. SPSS software version 17.0 was used to carry out all the statistical analyses. Chi-square test and Student's *t* test were used to analyze the association between categorical variables. Spearman's rank correlation analysis performed to evaluate correlations between variables. The survival curves were disposed by using the Kaplan-Meier method and log-rank test. We performed univariate and multivariate survival analysis through Cox proportional hazard regression model to assess the independent prognostic factors in BC patients. Hazard ratios (HRs) and their 95% confidence intervals (CIs) were calculated for both univariate and multivariate analyses. Two-tailed P values of <0.05 were considered statistically significant. Graph-Pad Prism 8.0.1 (GraphPad, San Diego, CA) software was used to present graphs.

TABLE 5: Correlation between the expression of VDAC1, Cytc, and clinicopathologic parameters.

	n	VDAC1		P value	Cytc		P value
		High ($n = 162$)	Low ($n = 57$)		High ($n = 65$)	Low ($n = 154$)	
Age				0.636			0.763
≤50	135	98 (72.59%)	37 (27.41%)		39 (28.89%)	96 (71.11%)	
>50	84	64 (76.19%)	20 (23.81%)		26 (30.95%)	58 (69.05%)	
Menopause				0.878			0.455
Before	125	93 (74.4%)	32 (25.6%)		40 (32%)	85 (68%)	
After	94	69 (73.4%)	25 (26.6%)		25 (26.6%)	69 (73.4%)	
Recurrence				**0.000**			**0.004**
No	136	85 (62.5%)	51 (37.5%)		50 (36.76%)	86 (63.24%)	
Yes	83	77 (92.77%)	6 (7.23%)		15 (18.07%)	68 (81.93%)	
TNM stage				**0.007**			0.895
I/II	153	105 (68.63%)	48 (31.37%)		45 (29.41%)	108 (70.59%)	
III	66	57 (86.36%)	9 (13.64%)		20 (30.3%)	46 (69.7%)	
Lymph node metastasis				**0.030**			0.953
No	95	63 (66.32%)	32 (33.68%)		28 (29.47%)	67 (70.53%)	
Yes	124	99 (79.84%)	25 (20.16%)		37 (29.84%)	87 (70.16%)	
Histological grade				**0.033**			**0.041**
G1/G2	165	116 (70.3%)	49 (29.7%)		55 (33.33%)	110 (66.67%)	
G3	54	46 (85.19%)	8 (14.81%)		10 (18.52%)	44 (81.48%)	
HER2 gene				**0.008**			0.591
Nonamplification	173	121 (69.94%)	52 (30.06%)		53 (30.64%)	120 (69.36%)	
Amplification	46	41 (89.13%)	5 (10.87%)		12 (26.09%)	34 (73.91%)	
ER status				0.440			**0.037**
Negative	122	93 (76.23%)	29 (23.77%)		29 (23.77%)	93 (76.23%)	
Positive	97	69 (71.13%)	28 (28.87%)		36 (37.11%)	61 (62.89%)	
PR status				0.535			**0.025**
Negative	124	94 (75.81%)	30 (24.19%)		29 (23.39%)	95 (76.61%)	
Positive	95	68 (71.58%)	27 (28.42%)		36 (37.89%)	59 (62.11%)	

3. Results

3.1. The Characteristics of Patients. The patients were composed of 219 females with a median age of 50 (age range, 29–78) years. Among the 219 cases, 165 (75.34%) were classified into G1 and G2 stages, 54 (24.66%) were defined with G3 on the basis of histological differentiation. 153 (69.86%) patients were classified as stages I and II, and 66 (30.14%) as III on the basis of tumor node metastasis (TNM) stage. Other basic clinicopathological characteristics, including age, menopausal status, lymph node metastasis (LNM), estrogen receptor (ER), progesterone receptor (PR), human epidermal growth factor receptor 2 (HER2), and recurrence, were presented in Table 1.

3.2. Expression of VDAC1 Is Significantly Higher in BC Tissues than in Benign Breast Lesions. To examine the expression level of VDAC1 protein, we performed IHC on 219 cases of BC tissues and 100 cases of the benign breast lesions. As shown in Figure 1, VDAC1 protein was mainly expressed in the membrane of breast cancer cells. Table 2 showed the result of IHC staining of VDAC1 protein. Of 219 BC samples, 162 (73.97%) showed high expression of VDAC1 protein,

and 57 (26.03%) showed low expression. In benign breast lesions, 55 (55%) showed high expression of VDAC1 protein, and 45 (45%) showed low expression. The expression of VDAC1 was significantly higher in BC tissues ($\chi^2 = 11.361$, $P = 0.001$) as determined by chi-square test.

3.3. Expression of Cytc Is Lower in BC Tissues than in Benign Breast Lesions. We examined the expression of Cytc by IHC in 219 cases of BC tissue and 100 cases of the benign breast lesions. As shown in Figure 2, Cytc protein was mainly expressed in the membrane and cytoplasm of BC tumor cells. The result of IHC staining of Cytc protein was summarized in Table 2, which showed that the rate of high Cytc expression was 29.68% (65/219) and the rate of low Cytc expression was 70.32% (154/219) in all BC samples. While in benign breast lesions, the rate of high Cytc expression was 47% (47/100), and the rate of low Cytc expression was 53% (53/100). Thus, the expression of Cytc was significantly lower in BC tissues than benign breast lesions ($\chi^2 = 9.039$, $P = 0.004$).

3.4. VDAC1 Protein Expression Correlates with Cytc Protein Expression and Clinicopathological Parameters in BC
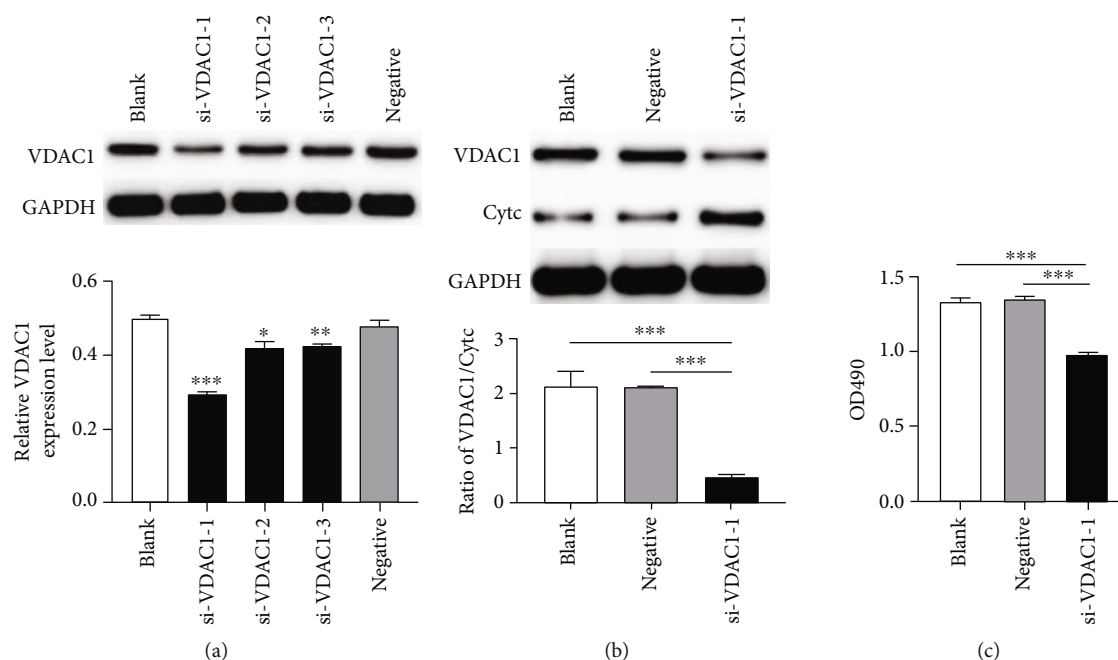
FIGURE 4: (a) VDAC1 expression was examined by Western blot in MCF-7 cells transfected with three different siRNAs targeting VDAC1 (si-VDAC1-1, siVDAC1-2, and si-VDAC1-3). (b) VDAC1 and Cytc expressions were examined by Western blot in MCF-7 cells transfected with si-VDAC1-1. After standardization with GADPH, the ratio of VDAC1/Cytc was calculated. (c) Proliferation of MCF-7 cells was demonstrated by MTT assay after knockdown of VDAC1. Each value represents the mean ± SD; $*P < 0.05$, $**P < 0.01$, $***P < 0.001$.
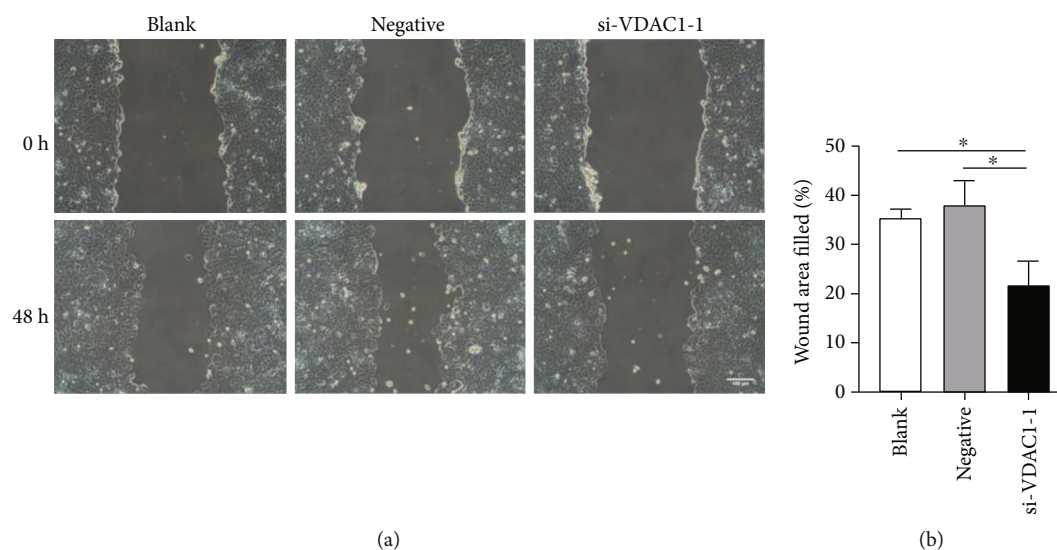
FIGURE 5: (a, b) Effects of VDAC1 knockdown on MCF-7 cells migration were assessed using a wound healing migration assay after 0 h and 48 h. Each value represents the mean ± SD; $*P < 0.05$, $**P < 0.01$, $***P < 0.001$.

Tissues, but Not in Benign Breast Lesions. In the benign breast lesions, there was no significant association between VDAC1 expression and Cytc protein expression ($\chi^2 = 0.75$, $P = 0.425$; Table 3). Conversely, as shown in Table 4, high expression of VDAC1 protein was inversely associated with Cytc protein expression in BC tissues ($\chi^2 = 7.423$, $r = -0.184$, $P = 0.011$), which was also shown in Figure 3. Furthermore, as shown in Table 5, high expression of VDAC1 protein was detected in 73.97% (162/219) of BC tissues, which was significantly

associated with advanced TNM stage ($\chi^2 = 7.534$, $P = 0.007$), higher histological grade ($\chi^2 = 4.68$, $P = 0.033$), recurrence ($\chi^2 = 24.532$, $P < 0.001$), HER2 gene amplification ($\chi^2 = 6.949$, $P = 0.008$), and lymph node metastasis ($\chi^2 = 5.109$, $P = 0.03$), but not with other examined clinico-pathological parameters, including age ($\chi^2 = 0.348$, $P = 0.636$), ER status ($\chi^2 = 0.729$, $P = 0.44$), PR status ($\chi^2 = 0.499$, $P = 0.535$), and menopause ($\chi^2 = 0.028$, $P = 0.878$).
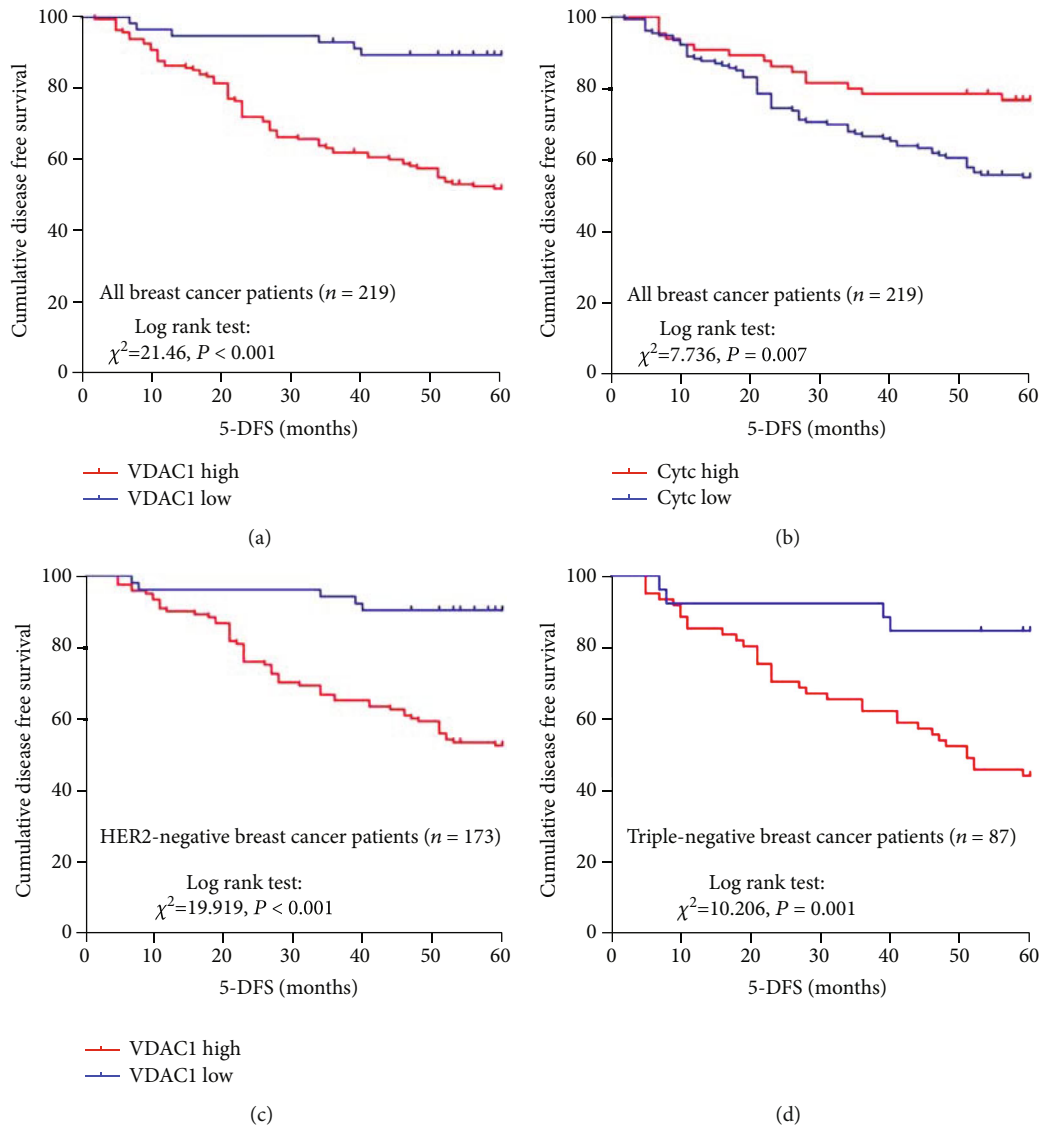
FIGURE 6: Kaplan-Meier survival analysis showing the correlation between VDAC1 expression (a), Cytc expression (b), and 5-DFS in breast cancer patients; the correlation between VDAC1 expression and 5-DFS in HER2-negative breast cancer (c) and triple-negative breast cancer (d) (log-rank test).

3.5. Cytc Expression Is Also Correlated with Various Clinical Features in BC Tissues. As is shown in Table 5, low expression of Cytc was associated with higher histological grade ($\chi^2 = 4.278$, $P = 0.041$), ER status ($\chi^2 = 4.609$, $P = 0.037$), PR status ($\chi^2 = 5.424$, $P = 0.025$), and recurrence ($\chi^2 = 8.629$, $P = 0.004$), but not age ($\chi^2 = 0.106$, $P = 0.763$), TNM stage ($\chi^2 = 0.018$, $P = 0.895$), lymph node metastasis ($\chi^2 = 0.003$, $P = 0.953$), HER2 gene amplification ($\chi^2 = 0.36$, $P = 0.591$), or menopause ($\chi^2 = 0.751$, $P = 0.455$) in tumor samples.

3.6. Expression Level of Cytc Protein Is Increased after VDAC1 Knockdown In Vitro. Firstly, we conducted transient silencing of VDAC1 in the MCF-7 cell line with three different siR-NAs and verified the knockdown efficiency with Western blot. Si-VDAC1-1 achieved more effective knockdown effi-

ciency, so it was used in all subsequent experiments ($P < 0.001$, Figure 4(a)).

As VDAC1 was conversely associated with Cytc expression in BC tissues, we also explored the expression level of Cytc *in vitro* after knockdown of VDAC1. Consistently, silencing of VDAC1 led to Cytc expression upregulation at the protein level in MCF-7 cells ($P < 0.001$, Figure 4(b)).

3.7. VDAC1 Promoted the Proliferation and Migration of BC Cells In Vitro. Additionally, we explored whether VDAC1 could affect the cell proliferation and migration. After transfection with si-VDAC1-1, a significant reduction in the proliferation rate of MCF-7 cells was observed with the MTT assay compared with the control ($P < 0.001$, Figure 4(c)). Afterwards, wound healing migration assay was performed. As a result, we validated that VDAC1 silencing obviously inhibited MCF-7 cell migration compared with the controls

TABLE 6: Univariate and multivariate analyses of predictive factors for disease free survival in BC patients.

	n	Univariate		Multivariate	
		P value	Hazard ratio, 95% CI	P value	Hazard ratio, 95% CI
VDAC1 expression		**0.000**	5.636 (2.454-12.942)	**0.001**	3.982 (1.723-9.207)
High	162				
Low	57				
Cytc expression		**0.007**	0.463 (0.265-0.811)	**0.035**	0.542 (0.307-0.959)
High	65				
Low	154				
Age		0.718	1.084 (0.699-1.683)		
≤50	135				
>50	84				
TNM stage		**0.000**	3.879 (2.512-5.989)	**0.028**	1.772 (1.063-2.956)
I/II	153				
III	66				
Lymph node metastasis		**0.000**	4.717 (2.692-8.265)	**0.003**	2.690 (1.401-5.164)
No	95				
Yes	124				
Histological grade		**0.000**	5.399 (3.489-8.356)	**0.000**	2.998 (1.899-4.731)
G1/G2	165				
G3	54				
HER2 gene		0.075	1.568 (0.956-2.574)		
Nonamplification	173				
Amplification	46				
ER status		**0.033**	0.613 (0.390-0.962)		
Negative	122				
Positive	97				
PR status		**0.001**	0.442 (0.275-0.711)	**0.016**	0.553 (0.341-0.896)
Negative	124				
Positive	95				
Menopause					
Before	125	0.184	1.339 (0.870-2.060)		
After	94				

($P < 0.05$, Figure 5). Therefore, knockdown of VDAC1 can suppress the proliferative and migrative ability of MCF-7 cells *in vitro*.

3.8. Correlation Analysis of the 5-DFS with the Expression of VDAC1, Cytc Protein, and Other Parameters in BC. Kaplan-Meier analysis showed that low VDAC1 protein expression in BC predicted a better survival and lower mortality rate (Figure 6(a), $P < 0.001$). Similarly, high expression of Cytc also predicted a better outcome of BC patients (Figure 6(b), $P = 0.007$). Univariate analysis of predictive factors for the 5-DFS in BC patients was performed by Cox proportional hazards regression model (Table 6). In univariate analysis, histological grade ($P < 0.001$), TNM stage ($P < 0.001$), ER status ($P = 0.033$), PR status ($P = 0.001$), and lymph node metastasis ($P < 0.001$) were also significantly correlated with the 5-DFS of BC patients. However, age, HER2 gene amplification, and menopause had no significant association with 5-DFS in BC patients ($P > 0.05$) (Table 6). In order to analyze

whether the above univariate was an independent prognostic factor, multivariate Cox proportional hazard model for 5-DFS was performed. The results indicated that both the expressions of VDAC1 and Cytc were independent prognostic parameters for 5-DFS of BC patients [HR: 3.982 (1.723-9.207), $P = 0.001$; HR: 0.542 (0.307-0.959), $P = 0.035$, respectively, Table 6]. Concurrently, TNM stage, PR status, lymph node metastasis, and histological grade were also independent predictors regarding the 5-DFS of breast cancer patients.

3.9. High Expression of VDAC1 Is Associated with the Poor Prognosis of HER2-Negative Breast Cancer. As is shown in Table 5, the expression of VDAC1 was significantly associated with HER2 gene, but not with ER and PR status. As targeted therapy can be implemented for HER2-positive breast cancer, we analyzed the correlation of VDAC1 protein expression with the prognosis of HER2-positive breast cancer patients and HER2-negative breast cancer patients,

TABLE 7: Univariate and multivariate analyses of predictive factors for disease free survival in TNBC.

	n	Univariate		Multivariate	
		P value	Hazard ratio, 95% CI	P value	Hazard ratio, 95% CI
VDAC1 expression		**0.001**	4.616 (1.635-13.029)	**0.009**	4.018 (1.415-11.407)
High	61				
Low	26				
Age		0.802	0.921 (0.484-1.753)		
≤50	49				
>50	38				
TNM stage		**0.000**	3.332 (1.757-6.317)	**0.003**	2.663 (1.381-5.135)
I/II	61				
III	26				
Lymph node metastasis		**0.002**	3.186 (1.504-6.747)		
No	38				
Yes	49				
Histological grade		**0.000**	3.149 (1.660-5.974)	**0.007**	2.469 (1.28-4.762)
G1/G2	59				
G3	28				
Menopause		0.590	0.839 (0.444-1.587)		
Before	43				
After	44				

respectively. Kaplan-Meier analysis showed that VDAC1 expression had no correlation with 5-DFS in HER2-positive breast cancer patients ($P = 0.159$). However, a significant relevance was found between high VDAC1 expression and shorter 5-DFS ($P < 0.001$) in HER2-negative breast cancer patients (Figure 6(c)). As triple-negative breast cancer (TNBC) is a special molecular subtype of HER2-negative breast cancer, which is defined by the absence of the ER, PR, and HER2 genes, with no standard treatment at present, we then explored the correlation of VDAC1 expression with the prognosis of TNBC. Interestingly, VDAC1 was also associated with reduced 5-DFS in TNBC ($P = 0.001$) (Figure 6(d)), predicting a poorer survival and higher mortality rate. To further validate the prognostic significance of VDAC1, Cox proportional hazards model analysis was also performed in TNBC. As presented in Table 7, VDAC1 was an independent predictor of poor 5-DFS [HR: 4.018 (1.415-11.407), $P = 0.009$]. Meanwhile, VDAC1 protein expression was inversely associated with Cytc in TNBC ($\chi^2 = 9.102$, $r = -0.323$, $P = 0.004$, Table 8, Figure 7). In summary, high expression of VDAC1 is associated with the prognosis of TNBC and inversely correlates with Cytc.

4. Discussion

In this study, we observed that VDAC1 was elevated while Cytc was decreased in breast carcinoma patients compared with benign breast lesions. VDAC1 protein expression was conversely associated with Cytc in BC, especially in TNBC. Meanwhile, knockdown of VDAC1 inhibits BC cell proliferation and migration *in vitro*. Furthermore, both high VDAC1 and low Cytc protein expression had significant positive cor-

relation with poor prognosis. VDAC1 expression can also be an independent prognostic factor of BC, especially TNBC.

VDAC1 participates in cancer metabolism via its modulatory roles in the transport of various metabolites [32]. In many types of cancer, the interaction of VDAC1 with HK, especially HK II, directly accesses to mitochondrial ATP for phosphorylation of glucose to glucose-6-phosphate and contributes to the cancer cells unrestricted growth and the inhibiting of apoptosis [21, 33]. VDAC1 has been found to be involved in tumor proliferation, migration, metastasis, and invasion [13]. It has been demonstrated that VDAC1 acts a controvertial role in the prognosis of different malignant tumors. For example, in uterine cervical cancer, high expression of VDAC1 was associated with exhibited deeper stromal invasion, larger tumor size, higher recurrence, and poorer overall survival [18]. Conversely, in cholangiocellular carcinoma, the low expression of VDAC1 correlated with higher cancer stage classification, lymph node involvement, and reduced survival [20]. These conflicting consequences demonstrate the differential effects of VDAC1 expression in different kinds of cancer and may need further exploration. In the present study, 219 cases of primary invasive breast cancer tissues were collected, and it was found that VDAC1 protein was primarily located in the membrane of breast cancer cells. The expression of VDAC1 protein in breast cancer solid tumors was significantly higher than that in benign breast lesions, and high expression of VDAC1 protein correlated with advanced TNM stage, higher histological grade, recurrence, lymph node metastasis, and HER2 gene amplification, thereby suggesting that high VDAC1 expression may play a role in promoting tumorigenesis and progression of BC. Interestingly, our present results in breast cancer were consistent with the reports in pancreatic cancer [34] and

TABLE 8: Correlation analysis of the expression of VDAC1 with Cytc in TNBC.

	High-VDAC1 expression (n = 61)	Low-VDAC1 expression (n = 26)	r value	P value
Cytc expression				
High (n =19)	8 (24.24%)	25 (75.76%)	-0.323	0.004
Low (n = 68)	53 (77.94%)	15 (22.06%)		

(a)

(b)

(c)

(d)
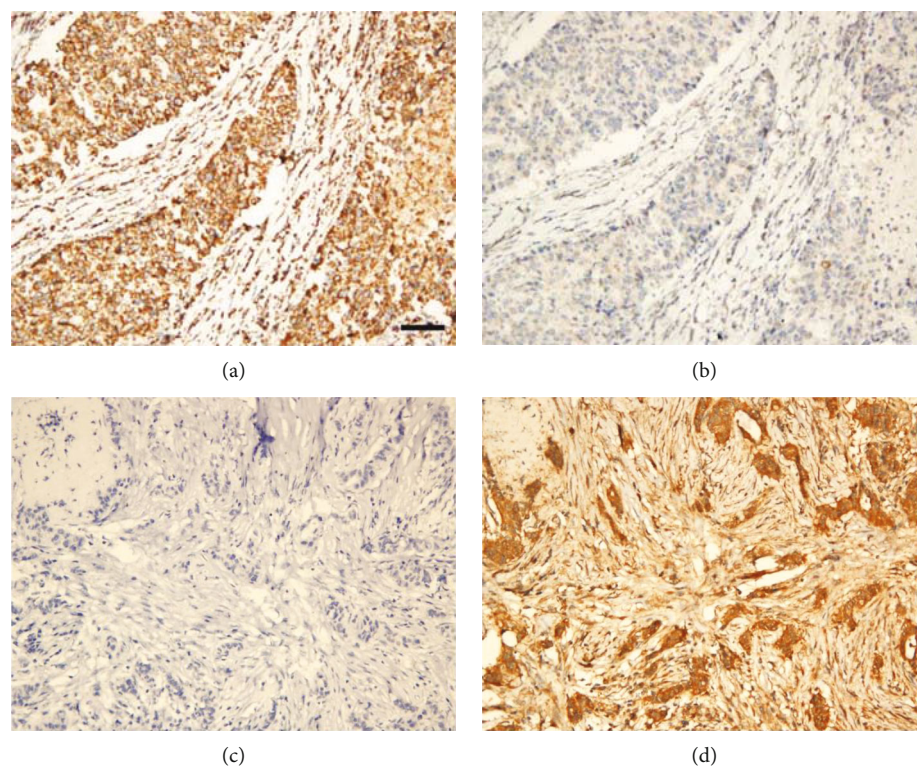
FIGURE 7: Immunohistochemical staining for VDAC1 and Cytc in triple-negative breast cancer lesions: high expression of VDAC1 protein (a) with low Cytc expression (b); low expression of VDAC1 protein (c) with high Cytc expression (d). Scale bar, 50?m.

colorectal cancer [35], which indicated VDAC1 expression was upregulated in tumor and promoted the growth and invasion of cancer cells. In addition, knockdown of VDAC1 in multiple types of cancer cell lines, including colon and lung cancer cells, has been demonstrated to block proliferation and migration of the cancer cells *in vitro* [36–38]. As is shown above, our studies achieved the similar results.

Furthermore, by the multivariate analysis, we found that overexpression of VDAC1 protein in BC tissues could be as an independent poor prognostic factor. Consistent with this result, Chih-Hsien and Eiran's studies also showed that high expression of VDAC1 was correlated with poorer prognosis in uterine cervical cancer and hepatocellular carcinoma [18, 19]. Therefore, these data suggest that VDAC1 has the potential to be a poor prognostic marker in BC. As TNBC showed more progressively malignant manifestation with worse clinical outcomes and is the most insensitive subtype of breast cancer to drug treatment, we next explored the correlation of VDAC1 expression with the prognosis of TNBC. Amazingly, our result demonstrated that high level of VDAC1 protein was also associated with reduced 5-DFS and acted as an independent predictor of poor prognosis in TNBC, suggest-

ing more potential use of VDAC1 should be exploited in prognostic marker and therapeutic target.

Cytc release from mitochondria is the driving force for apoptosome leading to apoptotic cell death in several malignant tumor [39], and VDAC1 has been widely reported to be interacted with pro- or antiapoptotic proteins such as Bcl-2 and HK, whereby mediating the release of Cytc [15, 40]. In many types of cancer cells, when HK2 binds to VDAC1, the interaction between VDAC1 and Bcl-2 protein family will be blocked, resulting in a decrease in Cytc release, thus protecting tumor cells from apoptosis [21]. In our present study, VDAC1 protein expression was inversely associated with Cytc in BC, especially in TNBC. Simultaneously, silencing of VDAC1 upregulated Cytc expression at the protein level in MCF-7 cells. Furthermore, Cytc was lower expressed in BC compared with benign breast lesions and low expression of Cytc was correlated with higher histological grade, ER status, PR status, and recurrence. A similar correlation was found in prostate cancer which Cytc deficiency contributed to tumor invasiveness and faster recurrence [29]. Importantly, we also found that decreased expression of Cytc was an independent prognostic factor and played a pivotal role

in the poorer 5-DFS of that cohort of BC patients. As a result, contrary to VDAC1, Cytc has the potential to be an improved prognostic marker in BC.

It should be acknowledged that there are also some limitations in this study. Firstly, due to the limited number of patients in this study, a larger cohort is required. Secondly, we took the benign breast tissues as control, which was not paired comparison, so associations should be interpreted with cognizance of these possible differences. Besides, more investigations need to be conducted to explore the mechanisms by which VDAC1 reduces Cytc expression in BC. Afterwards, the prognostic significance of VDAC1 in BC was discussed only at histological level. The exact role of VDAC1 in BC, especially in TNBC, still needs to be evaluated in follow-up mechanistic investigations. Finally, our study evaluated prognosis by 5-DFS rather than OS. Since DFS was not correlated with OS sometimes, the influence of VDAC1 expression on OS is still a topic for future research.

5. Conclusion

Our study showed for the first time that VDAC1 was elevated in BC tissues. Meanwhile, our findings firstly revealed that VDAC1 expression was conversely associated with Cytc, and knockdown of VDAC1 inhibited malignant behavior of BC. Besides, high VDAC1 level was associated with reduced 5-DFS of BC patients. By the multivariate analysis, we found that overexpression of VDAC1 could be employed as an independent poor prognostic factor in breast cancer, including TNBC, which was intractable in clinical. All in all, VDAC1 can be exploited as a potential prognostic marker and therapeutic target in BC, especially TNBC.

Data Availability

The datasets used and analyzed during the current study are available from the corresponding authors on reasonable request.

Ethical Approval

This study was approved by the Ethical Committee of Renmin Hospital of Wuhan University (WDRY2019-K010). The written informed consents were obtained from all the patients.

Conflicts of Interest

The authors declare that they have no competing interests.

Authors' Contributions

FC and JY made contributions to the conception and design of the study; CC and XW collected the samples and performed immunohistochemistry experiments; DY and HY made contributions to statistical analysis; BL and FG evaluated the immunohistochemical staining of all sections; SY made contributions to critical revision of the manuscript. All authors read and approved the final manuscript.

References

[1] Global Burden of Disease Cancer Collaboration, C. Fitzmaurice, D. Abate et al., "Global, regional, and national cancer incidence, mortality, years of life lost, years lived with disability, and disability-adjusted life-years for 29 cancer groups, 1990 to 2017: a systematic analysis for the global burden of disease study," *JAMA Oncology*, vol. 5, no. 12, pp. 1749–1768, 2019.

[2] F. Bray, J. Ferlay, I. Soerjomataram, R. L. Siegel, L. A. Torre, and A. Jemal, "Global cancer statistics 2018: GLOBOCAN estimates of incidence and mortality worldwide for 36 cancers in 185 countries," *CA: a Cancer Journal for Clinicians*, vol. 68, no. 6, pp. 394–424, 2018.

[3] C. E. DeSantis, J. Ma, M. M. Gaudet et al., "Breast cancer statistics, 2019," *CA: a Cancer Journal for Clinicians*, vol. 69, no. 6, pp. 438–451, 2019.

[4] A. Costa, Y. Kieffer, A. Scholer-Dahirel et al., "Fibroblast heterogeneity and immunosuppressive environment in human breast cancer," *Cancer Cell*, vol. 33, no. 3, pp. 463–479.e10, 2018, e10.

[5] P. Ji, Y. Gong, C. C. Jiang, X. Hu, G. H. di, and Z. M. Shao, "Association between socioeconomic factors at diagnosis and survival in breast cancer: a population-based study," *Cancer Medicine*, vol. 9, no. 5, pp. 1922–1936, 2020.

[6] D. Hanahan and R. A. Weinberg, "Hallmarks of cancer: the next generation," *Cell*, vol. 144, no. 5, pp. 646–674, 2011.

[7] K. Meehan and L. J. Vella, "The contribution of tumour-derived exosomes to the hallmarks of cancer," *Critical Reviews in Clinical Laboratory Sciences*, vol. 53, no. 2, pp. 121–131, 2015.

[8] W. H. Koppenol, P. L. Bounds, and C. V. Dang, "Otto Warburg's contributions to current concepts of cancer metabolism," *Nature Reviews. Cancer*, vol. 11, no. 5, pp. 325–337, 2011.

[9] J. Lu, M. Tan, and Q. Cai, "The Warburg effect in tumor progression: mitochondrial oxidative metabolism as an anti-metastasis mechanism," *Cancer Letters*, vol. 356, no. 2, pp. 156–164, 2015.

[10] V. V. Lemeshko, "VDAC electronics: 1. VDAC-hexo(gluco)kinase generator of the mitochondrial outer membrane potential," *Biochimica et Biophysica Acta*, vol. 1838, no. 5, pp. 1362–1371, 2014.

[11] V. V. Lemeshko, "VDAC electronics: 2. A new, anaerobic mechanism of generation of the membrane potentials in mitochondria," *Biochimica et Biophysica Acta*, vol. 1838, no. 7, pp. 1801–1808, 2014.

[12] V. Shoshan-Barmatz, Y. Krelin, A. Shteinfer-Kuzmine, and T. Arif, "Voltage-dependent anion channel 1 as an emerging drug target for novel anti-cancer therapeutics," *Frontiers in Oncology*, vol. 7, p. 154, 2017.

[13] V. Shoshan-Barmatz, D. Ben-Hail, L. Admoni, Y. Krelin, and S. S. Tripathi, "The mitochondrial voltage-dependent anion channel 1 in tumor cells," *Biochimica et Biophysica Acta (BBA) - Biomembranes*, vol. 1848, no. 10, pp. 2547–2575, 2015.

[14] V. Shoshan-Barmatz, S. Pittala, and D. Mizrachi, "VDAC1 and the TSPO: expression, interactions, and associated functions in health and disease states," *International Journal of Molecular Sciences*, vol. 20, no. 13, 13, p. 3348, 2019.

[15] A. K. S. Camara, Y. F. Zhou, P. C. Wen, E. Tajkhorshid, and W. M. Kwok, "Mitochondrial VDAC1: a key gatekeeper as potential therapeutic target," *Frontiers in Physiology*, vol. 8, p. 460, 2017.

[16] V. Shoshan-Barmatz, Y. Krelin, and A. Shteinfer-Kuzmine, "VDAC1 functions in Ca^{2+} homeostasis and cell life and death in health and disease," *Cell Calcium*, vol. 69, pp. 81–100, 2018.

[17] V. Shoshan-Barmatz, E. Nahon-Crystal, A. Shteinfer-Kuzmine, and R. Gupta, "VDAC1, mitochondrial dysfunction, and Alzheimer's disease," *Pharmacological Research*, vol. 131, pp. 87–101, 2018.

[18] C. H. Wu, Y. W. Lin, T. F. Wu, J. L. Ko, and P. H. Wang, "Clinical implication of voltage-dependent anion channel 1 in uterine cervical cancer and its action on cervical cancer cells," *Oncotarget*, vol. 7, no. 4, pp. 4210–4225, 2016.

[19] F. Wang, Y. Qiang, L. Zhu et al., "MicroRNA-7 downregulates the oncogene VDAC1 to influence hepatocellular carcinoma proliferation and metastasis," *Tumour Biology*, vol. 37, no. 8, pp. 10235–10246, 2016.

[20] R. G. Feichtinger, D. Neureiter, R. Kemmerling, J. A. Mayr, T. Kiesslich, and B. Kofler, "Low VDAC1 expression is associated with an aggressive phenotype and reduced overall patient survival in cholangiocellular carcinoma," *Cell*, vol. 8, no. 6, p. 539, 2019.

[21] A. Magri, S. Reina, and V. De Pinto, "VDAC1 as pharmacological target in cancer and neurodegeneration: focus on its role in apoptosis," *Frontiers in Chemistry*, vol. 6, p. 108, 2018.

[22] M. Zhang, J. Zheng, R. Nussinov, and B. Ma, "Release of cytochrome C from Bax pores at the mitochondrial membrane," *Scientific Reports*, vol. 7, no. 1, p. 2635, 2017.

[23] F. J. Bock and S. W. G. Tait, "Mitochondria as multifaceted regulators of cell death," *Nature Reviews. Molecular Cell Biology*, vol. 21, no. 2, pp. 85–100, 2020.

[24] R. Santucci, F. Sinibaldi, P. Cozza, F. Polticelli, and L. Fiorucci, "Cytochrome c: an extreme multifunctional protein with a key role in cell fate," *International Journal of Biological Macromolecules*, vol. 136, pp. 1237–1246, 2019.

[25] M. Zhou, Y. Li, Q. Hu et al., "Atomic structure of the apoptosome: mechanism of cytochrome c- and dATP-mediated activation of Apaf-1," *Genes & Development*, vol. 29, no. 22, pp. 2349–2361, 2015.

[26] N. Yadav, R. Gogada, J. O'Malley et al., "Molecular insights on cytochrome c and nucleotide regulation of apoptosome function and its implication in cancer," *Biochimica et Biophysica Acta (BBA) - Molecular Cell Research*, vol. 1867, no. 1, article 118573, 2020.

[27] C. M. Figueroa, B. N. Suarez, A. M. Molina, J. C. Fernandez, Z. Torres, and K. Griebenow, "Smart release nanoformulation of cytochrome C and hyaluronic acid induces apoptosis in cancer cells," *Journal of Nanomedicine & Nanotechnology*, vol. 8, no. 1, 2017.

[28] J. Javid, R. Mir, P. K. Julka, P. C. Ray, and A. Saxena, "Extracellular cytochrome c as a biomarker for monitoring therapeutic efficacy and prognosis of non-small cell lung cancer patients," *Tumour Biology*, vol. 36, no. 6, pp. 4253–4260, 2015.

[29] R. Kumar, T. A. Bhat, E. M. Walsh et al., "Cytochrome c deficiency confers apoptosome and mitochondrial dysfunction in African-American men with prostate cancer," *Cancer Research*, vol. 79, no. 7, pp. 1353–1368, 2019.

[30] V. Shoshan-Barmatz, S. De, and A. Meir, "The mitochondrial voltage-dependent anion channel 1, Ca^{2+} transport, apoptosis, and their regulation," *Frontiers in Oncology*, vol. 7, p. 60, 2017.

[31] J. C. Lai, W. Tan, L. Benimetskaya, P. Miller, M. Colombini, and C. A. Stein, "A pharmacologic target of G3139 in melanoma cells may be the mitochondrial VDAC," *Proceedings of the National Academy of Sciences of the United States of America*, vol. 103, no. 19, pp. 7494–7499, 2006.

[32] V. Shoshan-Barmatz, Y. Krelin, and Q. Chen, "VDAC1 as a player in mitochondria-mediated apoptosis and target for modulating apoptosis," *Current Medicinal Chemistry*, vol. 24, no. 40, pp. 4435–4446, 2017.

[33] V. Shoshan-Barmatz and M. Golan, "Mitochondrial VDAC1: function in cell life and death and a target for cancer therapy," *Current Medicinal Chemistry*, vol. 19, no. 5, pp. 714–735, 2012.

[34] W. Wang, T. Zhang, W. Zhao et al., "A single talent immunogenic membrane antigen and novel prognostic predictor: voltage-dependent anion channel 1 (VDAC1) in pancreatic cancer," *Scientific Reports*, vol. 6, no. 1, article 33648, 2016.

[35] X. Liu, B. He, T. Xu et al., "MiR-490-3p functions as a tumor suppressor by inhibiting oncogene VDAC1 expression in colorectal cancer," *Journal of Cancer*, vol. 9, no. 7, pp. 1218–1230, 2018.

[36] T. Arif, L. Vasilkovsky, Y. Refaely, A. Konson, and V. Shoshan-Barmatz, "Silencing VDAC1 expression by siRNA inhibits cancer cell proliferation and tumor growth in vivo," *Molecular therapy - Nucleic acids*, vol. 8, p. 493, 2017.

[37] S. Freitas, R. Martins, M. Costa et al., "Hierridin B isolated from a marine cyanobacterium alters VDAC1, mitochondrial activity, and cell cycle genes on HT-29 colon adenocarcinoma cells," *Marine Drugs*, vol. 14, no. 9, p. 158, 2016.

[38] A. Maimaiti, A. Aili, H. Kuerban, and X. Li, "VDAC1 mediated anticancer activity of gallic acid in human lung adenocarcinoma A549 cells," *Anti-Cancer Agents in Medicinal Chemistry*, vol. 18, no. 2, pp. 255–262, 2018.

[39] G. Ichim, J. Lopez, S. U. Ahmed et al., "Limited mitochondrial permeabilization causes DNA damage and genomic instability in the absence of cell death," *Molecular Cell*, vol. 57, no. 5, pp. 860–872, 2015.

[40] S. Xu and H. R. Herschman, "A tumor agnostic therapeutic strategy for hexokinase 1-null/hexokinase 2-positive cancers," *Cancer Research*, vol. 79, no. 23, pp. 5907–5914, 2019.

Review Article

Antioxidative Stress: Inhibiting Reactive Oxygen Species Production as a Cause of Radioresistance and Chemoresistance

Yanchi Chen ⓘ,[1,2] **Yiling Li** ⓘ,[1,2] **Linyang Huang** ⓘ,[1,2] **Yu Du** ⓘ,[1,2] **Feihong Gan** ⓘ,[1,2] **Yanxi Li** ⓘ,[1,2] **and Yang Yao** ⓘ[1,2]

[1]*State Key Laboratory of Oral Diseases, West China Hospital of Stomatology, Sichuan University, Chengdu, China*
[2]*West China School of Stomatology, Sichuan University, Chengdu, China*

Correspondence should be addressed to Yang Yao; yaoyang9999@126.com

Academic Editor: Qiang Tong

Radiotherapy and chemotherapy are the most effective nonsurgical treatments for cancer treatment. They usually induce regulated cell death by increasing the level of reactive oxygen species (ROS) in tumour cells. However, as intracellular ROS concentration increases, many antioxidant pathways are concurrently upregulated by cancer cells to inhibit ROS production, ultimately leading to drug resistance. Understanding the mechanism of antioxidant stress in tumour cells provides a new research direction for overcoming therapeutic resistance. In this review, we address (1) how radiotherapy and chemotherapy kill tumour cells by increasing the level of ROS, (2) the mechanism by which ROS activate antioxidant pathways and the subsequent cellular mitigation of ROS in radiotherapy and chemotherapy treatments, and (3) the potential research direction for targeted treatment to overcome therapeutic resistance.

1. Introduction

Reactive oxygen species (ROS) are derivatives of molecular oxygen formed by reduction–oxidation (redox) reactions or electronic excitation [1]. They are ubiquitous as by-products of chemical reactions in cell metabolism [2]. When the balance between ROS and antioxidants are disrupted, the body is under a state of oxidative stress [3]. This state may bring about inflammatory infiltration of neutrophils, increased secretion of proteases, and the production of large amount of oxidative intermediate products, all of which contribute to ageing and disease [4]. At excessive levels of intracellular ROS, cells take measures to clear ROS. These measures are called the antioxidant stress response [5]. ROS affect cell gene expression through various pathways. One classic pathway of cell resistance to ROS is the Keap1-Nrf2 system [6]. This system activates the transcription of a series of cytoprotective genes to increase the antioxidant level in the cell and reprogramme its metabolism to produce more gluta-thione and other substances. These effects can help the cell resist cell damage caused by ROS.

Radiotherapy and chemotherapy can kill tumour cells by several mechanisms, such as damaging DNA, increasing the ROS level, or damaging subcellular organelles [7, 8]. However, some tumour cells can survive these therapies and proliferate rapidly, limiting their therapeutic effect. This phenomenon is called therapeutic resistance. One way tumour cells develop this resistance is by increasing antioxidant levels and reprogramming metabolism to protect cells from the damage caused by ROS [4]. Some molecules receive signals of increased ROS in the cell, then enter the nucleus and react with some nucleic substances to regulate the transcription of some genes. The expression of these genes can increase the antioxidant level of the cell and reprogramme metabolism.

2. Killing Effect of Radiotherapy and Chemotherapy on Tumour Cells

2.1. Radiotherapy and Chemotherapy Increase Intracellular ROS Levels. In normal cells, ROS levels are kept low due to the antioxidant systems that maintain redox balance [9]. In

cancer cells, the level of ROS increases to meet the need of malignant proliferation and progression but stays below the threshold to avoid cytotoxicity [10]. Radiotherapy uses radiation to irradiate tumour tissues and kill tumour cells. On the one hand, radiation acts directly on cells and instantly produces a large number of free radicals. On the other hand, it indirectly produces lasting and severe therapeutic effects through the redox reaction of water [11]. Due to the high content of water in cells, when water absorbs the energy of low-LET rays, a redox reaction occurs and a large number of free radicals and free electrons are produced. The free radicals and electrons generated initiate cascade reactions that produce OH, H_2O_2, and $O_2 \cdot^-$, significantly increasing the level of ROS [12]. Notably, oxidative changes can persist for several months after initial radiotherapy. This feature is related to the continuous generation of ROS and its heritability in the offspring of irradiated cells and obviously enhances the curative effect [13].

The mainstream treatment for cancer, chemotherapy, also often works by changing the redox state of cancer cells. Quite a few chemotherapeutics induce oxidative stress and ROS-mediated cell damage in cancer cells by increasing ROS above the threshold to yield an anticancer effect [14]. Most of these drugs produce ROS directly in cancer cells to increase the level of ROS. The first drug developed to achieve therapeutic effects by producing ROS was procarbazine. Procarbazine can be oxidised in aqueous solution and produce H_2O_2 and ·OH. When coordinating with ionising radiation, procarbazine forms unstable peroxides to damage DNA in vitro [15]. It was approved for the treatment of primary brain tumours and other diseases 60 years ago [16]. Nowadays, drugs like anthracycline [17] are widely used in cancer treatment to promote ROS production.

Another characteristic of the redox system in tumour cells is that it can increase the activity of ROS scavenging enzymes to adapt to internal oxidative stress [18]. Therefore, recently more attention has been focused on the inhibition of key molecules in the antioxidant system. For instance, sulfasalazine (an inhibitor of significant antioxidant glutathione) [19], chaetocin (an inhibitor of thioredoxin system) [20], and some other novel chemotherapeutic drugs are all targeted to inhibit the antioxidant system and increase the level of ROS.

2.2. ROS Are Responsible for Triggering Cell Death. Radiotherapy can directly cause DNA double-strand breaks through the immediate power of ionising radiation, thus blocking the cell cycle, preventing the proliferation of tumour cells, and eventually leading to cell death [21]. In addition, radiotherapy can cause indirect cellular effects, including bystander responses [22] and low-dose hypersensitivity [23], leading to a more extensive and lasting cell killing effect. These indirect reactions are related to the mechanism of cell death initiated by ROS [24]. Some of these indirect effects such as bystander responses have also been observed with chemotherapy [25]. Here, we primarily focus on how the increased ROS levels caused by radiotherapy and chemotherapy trigger cell death.

In normal conditions, ROS are maintained at a low dynamic balance under the effects of oxidation and antioxidation in cells [26]. Low levels of ROS are implicated in many intracellular chemical reactions and adjust the structure and function of proteins and lipids, whereas high levels of ROS damage DNA, proteins, and other cell components nonspecifically to hurt cells [9]. ROS levels can be divided into three types according to the effect on cells: (I) low level, normal physiological stage; (II) moderate level, carcinogenic stage; and (III) high levels, cell damage stage [5]. These stages present a gradual transition, and the dividing line of each process is not obvious. When ROS rise to moderate levels, they cause random mutations in cells due to DNA damage [27] and promote cell proliferation and metastasis [28], which exceeds the threshold of cell control and repair. These factors lead to the transformation of cells into cancer cells. ROS levels that continue to rise to high levels will lead to cell death. At this level, ROS trigger different types of regulated cell death, including apoptosis, autophagy, and ferroptosis.

2.2.1. Apoptosis. Caspases, a family of proteases in cells, play an important role in apoptosis. They induce cell death by breaking down the key proteins in cells [29]. Caspases are activated by one of two pathways: death receptor-dependent pathway and mitochondrial-dependent pathway [30]. In the first pathway, the external apoptosis signal is triggered by death receptors on the cell surface and then activates caspase 8, producing a cascade reaction and finally leading to apoptosis [31]. ROS can induce apoptosis by regulating the expression of the death receptors and its ligand such as Fas-mediated apoptosis. Hydrogen peroxide (H_2O_2) promotes the expression of Fas by increasing its mRNA and protein levels [32]. In addition, it can upregulate the expression of death ligand Fas L and cause the activation of caspases 8 in Hela cells [33]. In the second pathway, mitochondria release caspase-activating proteins into the cytoplasm and cause apoptosis [34]. The permeability transition pore (PTP) on mitochondria plays a decisive role in this pathway [35]. Important regulators of the PTP opening are the Bcl-2 protein family, which can promote apoptosis [36]. ROS can oxidise and modify Bcl-2 proteins and then regulate apoptosis. B cell lymphoma-2 is an antiapoptotic member of the Bcl-2 protein family. Increased H_2O_2 induces the oxidative modification of B cell lymphoma-2 and downregulates its expression, promoting cell apoptosis [37].

2.2.2. Autophagy. Autophagy maintains cell homeostasis by decomposing damaged organelles and proteins through lysosomes [38]. At a low ROS levels, autophagy can be induced by ROS and inhibited by antioxidants, and the three are in dynamic balance to maintain cell homeostasis [39, 40]. In oxidative stress, ROS damage DNA, lipids, and proteins and initiate autophagy [41]. At the same time, ROS molecules themselves also induce autophagy. The core of autophagy regulation is the Atg4 family of cysteine proteases. The activation of Atg4 is regulated by signal molecules including ROS, and H_2O_2 directly targets the oxidation of Atg4 to promote the formation of autophagosomes [42]. Once

autophagy exceeds the limit of cell tolerance, it eventually causes autophagic death.

2.2.3. Ferroptosis.

Ferroptosis is a recently identified type of programmed cell death caused by lipid peroxidation [43]. Lipid peroxidation is a process in which ROS oxidise biofilms. ROS react with phospholipids, enzymes, and other macromolecules of biofilm to form lipid peroxidation products. It can directly change the fluidity and permeability of the cell membrane, destroy ion gradients, and affect the structure and function of cells [44]. In addition, the products of lipid peroxidation are highly bioactive, can disrupt the activity of DNA, proteins, and enzymes, and initiate cell death signalling pathways [45, 46]. Recent studies show that when radiotherapy induces increased intracellular ROS, the cells show the morphological characteristics of ferroptosis. Furthermore, the use of a ferroptosis inhibitor increases cell survival rates after radiation [47]. Therefore, high levels of intracellular ROS may directly promote ferroptosis by inducing lipid peroxidation.

The goal of radiotherapy and chemotherapy is to raise the level of ROS directly from type I/II to type III. And tumour resists the therapy by maintaining moderate ROS levels at type II. This is also the basic reason why radiotherapy and chemotherapy can achieve the purpose of tumour treatment and why tumours develop therapeutic resistance (Figure 1).

3. Antioxidative Stress-Related Pathways That Lead to Therapeutic Resistance

As prooxidant cancer therapy increases the effective ROS concentration in cancer cells, irreversible oxidative stress is generated that damages DNA, lipids, and proteins, causing the suppression of cancer cells [48, 49]. However, many cell signalling pathways that adapt to prooxidant therapy-induced oxidative stress are activated by this increased ROS. These pathways have various functions, such as increasing antioxidant levels and reprogramming metabolism [50], which can inhibit ROS production to adapt to oxidative stress and produce therapeutic resistance.

3.1. Keap1-Nrf2 Signalling Pathway

3.1.1. Activation of the Keap1-Nrf2 Signalling Pathway under Oxidative Stress.

The Keap1-Nrf2 signalling pathway performs a significant role in cell protection and adaptation against oxidative stress. This pathway comprises two main parts: Kelch-like ECH-associated protein 1 (Keap1) and nuclear factor erythroid 2-related factor 2 (Nrf2) [51]. Under normal physiological conditions, Keap1 interacts specifically with Cullin 3 (Cul3) and forms an E3 ligase complex to stimulate the ubiquitination of Nrf2, ultimately leading to the targeted degradation of Nrf2 by the 26S proteasome [52, 53] (Figure 2). In this case, the Nrf2 protein is inactivated and has a short half-life. Thus, the activation of the Keap-Nrf2 signalling pathway is prevented.

However, in case of radiotherapy or chemotherapy-meditated oxidative stress, Nrf2 can be activated by detaching from Keap1. With radiation and drugs increasing the level of ROS in cells, the cysteines which residues in Keap1 and function as redox sensors are oxidised causing the dissociation of Keap1 between Nrf2 and slowing down the speed of Nfr2 degradation. Three functionally important cysteines that regulate the activation of Keap1-Nrf2 have been found: Cys151, Cys273, and Cys288 [54]. Among them, Cys273 and Cys288, both of which reside in the region of the IVR domain, are critical for Keap1 to inhibit Nrf2 under normal conditions, whereas a subset of Nrf2 activators target Cys151 which locate in the BTB domain [55, 56]. Recent findings have shown that the modification of Cys151 residue in Keap1 is crucial in activating Nrf2 by artemisitene and curcumin [56, 57] (Figure 2). Apart from the canonical mechanism to activate Nrf2 by oxidising Keap1 cysteine, other noncanonical Nrf2 regulatory pathways have been found under stressful conditions. These include proteins containing an ETGE amino acid motif such as sequestosome 1/p62, dipeptidyl peptidase 3 [58]; kinases including protein kinase B (PKB/AKT, see Section 3.2.3), protein kinase C extracellular-regulated protein kinases [59], protein kinase-like endoplasmic reticulum kinase [51]; transcriptional factor EB [60]; and acetyltransferase p300 [61] (Figure 2). As Nrf2 and Keap1 detach, Nrf2 becomes dissociated and transferred to the nucleus to induce the adaptation to oxidative stress.

3.1.2. Activated Nrf2 Induces ROS Mitigation.

Activated NRF2 translocates into the nucleus and interacts with one of the small MAF (sMAF) proteins, forming the Nrf2-sMAF heterodimer [62, 63]. The heterodimer plays an important role in inducing the expression of cytoprotective genes, leading to radio- and chemoresistance in tumour cells. It binds to DNA sequences referred to as the antioxidant response element [64] or electrophile response element [65], now collectively defined as the CNC-sMAF binding element (CsMBE) [66]. Most of these sequences are cytoprotective genes. In addition, the way that these heterodimers bind to CsMBE is stress dependent [63] (Figure 2). The binding of the Nrf2-sMAF heterodimer and CsMBE primarily results in increased antioxidant levels and reprogrammed metabolism.

(1) Nrf2-sMAF and Increased Antioxidant Levels. The antioxidant function of Nrf2-sMAF is the most canonical way that Nrf2 promotes the adaptation of cancer cells to oxidative stress as it activates the transcription and translation of a number of antioxidant enzymes or proteins in a stress-dependent manner [67]. For the last two decades, using genome-wide chromatin immunoprecipitation analysis, scientists have targeted various Nrf2-dependent antioxidant genes including peroxiredoxin 1 (*PRDX1*), sulfiredoxin 1, thioredoxin, and thioredoxin reductase 1 [68–70]. Most of the related enzymes can be directly activated by Nrf2-sMAF; here, we primarily focus on PRDX1 as an example of the function of antioxidant enzymes. Peroxiredoxins (PRDXs) are a highly conserved family of peroxidases that reduce ROS [71]. PRDX1 is one of the 2-Cys PRDXs subfamily members that has been reported to have potential radio- and chemoprotective effects [72–74]. The established mechanism is that PRDX1 detoxifies H_2O_2 by reducing it with the thioredoxin (TRX) system and supplying reducing
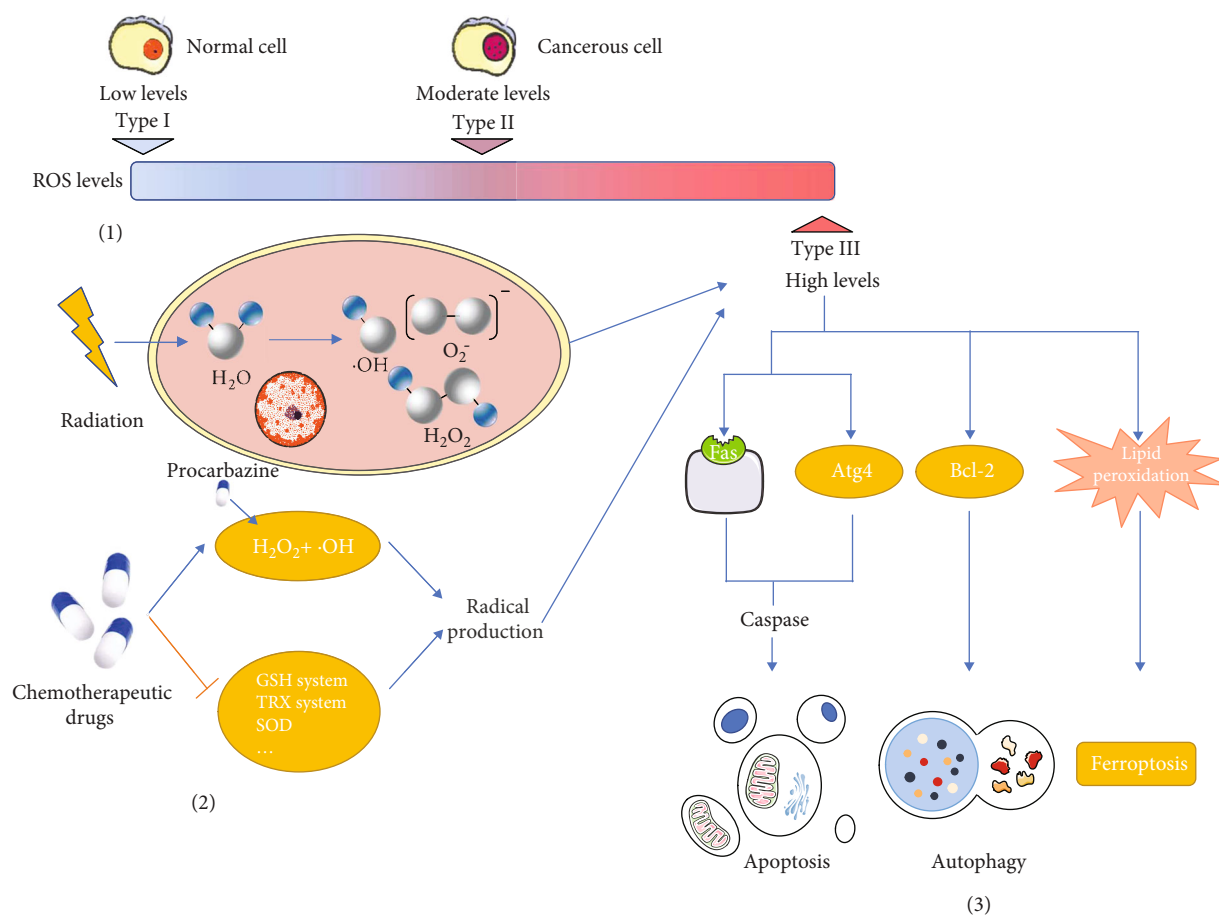
FIGURE 1: ROS are responsible for triggering cell death and the mechanisms of cancer treatment to trigger cell death. (1) ROS levels can be divided into three types according to their effects on cells. Type I is a low ROS level, wherein ROS only participate in normal cell physiological activities. Type II is a moderate ROS level, wherein ROS induce cell deformation within cancerous cells. Type III is a high ROS level, wherein ROS lead to cell death. (2) Radiotherapy and chemotherapy both increase the production of ROS. Radiotherapy causes the redox reaction of water and produces a large number of free radicals and free electrons. In chemotherapy, many drugs directly produce ROS in cancer cells to increase the level of ROS. (3) Radiotherapy and chemotherapy can cause indirect cellular effects by raising ROS levels to type III. High levels of ROS induce different types of regulated cell death. They regulate the expression of the death receptors such as Fas and Bcl-2 family proteins to induce apoptosis, target the oxidation of Atg4 to promote the formation of autophagosomes, which cause autophagic death, and directly promote ferroptosis by inducing lipid peroxidation.

equivalents [75]. However, PRDX1 may also play its antioxidant role by affecting ROS-dependent signalling pathways [72]. In one study, the downregulation of PRDX1 in lung cancer cells was found to reverse radioresistance and enhance radiosensitivity [76].

(2) Nrf2-sMAF and Reprogrammed Metabolism. Recent analyses show that Nrf2 contributes to stress adaptation by regulating intermediary metabolic pathways [77]. In addition, reprogrammed metabolism has been found to be closely related to the development of radio- and chemoresistance [78]. Some metabolic enzyme modulating sequences were identified as Nrf2-sMAF target genes including those involved in glutamine and glucose metabolism [77, 79, 80].

Glutathione (GSH) functions as antioxidant defence and plays an important role in maintaining the redox homeosta-

sis in cells. Nrf2 is thought to be a critical transcriptional controller of GSH metabolism by regulating a series of enzymes of GSH metabolism including the GSH de novo synthesis enzymes glutamate cysteine ligase (GCL) and glutathione synthase (GS), as well as the GSH regeneration enzyme glutathione reductase (GSR) [81, 82]. Specifically, Nrf2-sMAF controls the expression of catalytic and regulatory subunits of the rate-limiting enzyme complex, which are the major determinants of glutathione synthesis [83]. Besides the enzymes that control the glutamine metabolism directly, a cystine/glutamate exchange transporter called system X also plays a critical role in intracellular GSH biosynthesis [84]. The expression of the light chain of system X is promoted by Nrf2 under the stimulation of oxidative stress, which is closely related to radio- and chemoresistance in tumour cells [85, 86]. In Nrf2 knockdown cells, glutathione metabolism is affected [80], showing the pivotal role of Nrf2 in glutathione metabolism.
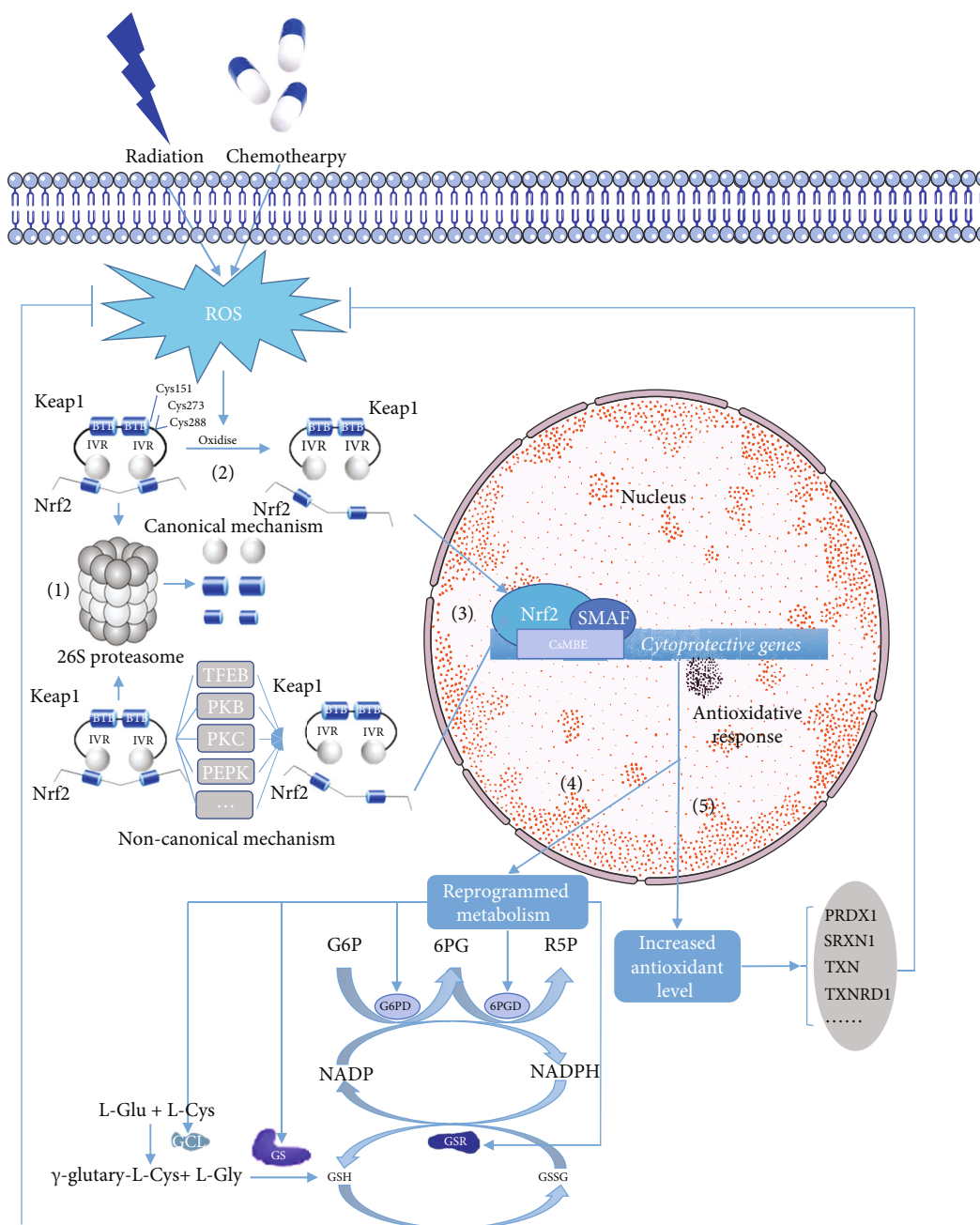
FIGURE 2: The role of the Keap1-Nrf2 signalling pathway in antioxidative stress-related radio- and chemoresistance. (1) Degradation of Nrf2. Under normal conditions, Keap1 combines with Nrf2 to promote the degradation of Nrf2 by the 26S proteasome. (2) Activation of Nrf2. Radiation and chemotherapies increase the effective ROS concentration in cancer cells via the redox reaction of water and direct production of ROS, respectively. Later, increased ROS oxidise three cysteines within Keap1 to activate Nrf2 by dissociating Nrf2 from Keap1 and slowing down the speed of Nfr2 degradation. (3) Translocation of Nrf2. Activated Nrf2 translocates into the nucleus, forming the Nrf2-sMAF heterodimer with one of the small MAF (sMAF) proteins. The Nrf2-sMAF heterodimer binds to the CNC-sMAF binding element (CsMBE), resulting in increased antioxidant levels and reprogrammed metabolism. (4) Increased antioxidant enzymes. Various antioxidant genes including peroxiredoxin 1 (*PRDX1*), sulfiredoxin 1 (*SRXN1*), thioredoxin (*TXN*), and thioredoxin reductase 1 (*TXNRD1*) can be activated by Nrf2. (5) Reprogrammed metabolism. G6PD and 6PGD are the two major enzymes in the pentose phosphate pathway (PPP), which generates NADPH. Glutamate cysteine ligase (GCL) and glutathione synthase (GS) are the two rate-limiting enzymes in glutathione (GSH) de novo synthesis. Nrf2 promotes the translation and expression of GCL, GS, GSR, G6PD, and 6PGD. Increased antioxidant enzymes and reprogrammed metabolism can protect cancer cells from ROS-triggered cell death, leading to radio- and chemoresistance.

The glucose metabolism phenomenon of cancer cells known as the Warburg effect indicates the paradoxical fact that most tumour cells rely on aerobic glycolysis even in an oxygen environment [87, 88]. Due to the Warburg effect, cancer cells have more glucose uptake than normal cells. When large amounts of glucose enrich cells, the pentose phosphate pathway (PPP), which generates NADPH, dominates [89]. NADPH is critical in cellular antioxidation systems and protects the cell from oxidative stress [89, 90]. Nrf2-sMAF mostly controls the production of NADPH via the PPP. The activation of Nrf2 signalling in cancer cells promotes the expression of PPP genes by weakening miR-1 and miR-206 expression, leading to the reprogramming of glucose metabolism [91].

The expression of some major enzymes of PPP is Nrf2 dependent. The increased expression and activity of glucose-6-phosphate dehydrogenase (G6PD), which is the first and rate-limiting enzyme in the PPP, is promoted by Nrf2 [92]. In addition, the overexpression of 6-phosphogluconate dehydrogenase (6PGD), the third oxidative decarboxylase of the PPP in cancer cells, is mediated by Nrf2 [78].

Another fact that should be seriously considered is the relationship between GSH, NADPH, and the antioxidant reaction. As the intracellular ROS level increases (e.g., H_2O_2), GSH can eliminate H_2O_2 and turn it into water under the catalysis of glutamate peroxidase. At the same time, GSH is converted to its oxidised form, GSSG. GSH is then reduced from GSSG by NADPH under the catalysis of GSR to detoxify ROS entirely. As mentioned above, the generation of GSH, the GSH regeneration enzyme, and the production of NADPH are all controlled by Nrf2, demonstrating the important role of activated Nrf2 in the cellular response to oxidative stress (Figure 2).

3.2. PI3K-AKT Signalling Pathway

3.2.1. Activation of the PI3K-AKT Signalling Pathway under Oxidative Stress.
The intricacies of the PI3K-AKT signalling pathway have already been reported by previous reviews in detail [93, 94]. Here, we primarily focus on the ROS-dependent activation of PI3K-AKT. When receptors are activated by their ligands such as G-protein-coupled receptors, it stimulates the recruitment of class 1 phosphoinositide-3-kinases (PI3Ks), which ultimately activate PI3K. Later, the activated PI3K phosphorylates phosphatidylinositol 4,5-bisphosphate (PIP2) to phosphatidylinositol 3,4,5-trisphosphate (PIP3) [95]. As PIP3 accumulates, it acts as a membranal signalling molecule and subsequently recruits and activates protein kinase B (PKB/AKT) [51, 96]. The serine–threonine kinase AKT is one of the most important downstream effectors of PI3K signalling, which controls a large number of pathways. When AKT binds to PIP3, it is activated with phosphoinositide-dependent protein kinase 1 and rapamycin complex 2, phosphorylating the T308 and S473, respectively [97]. Moreover, the primary functional antagonist of PI3K, phosphatase and tensin homolog (PTEN), inhibits the activation of AKT by dephosphorylating PIP3 to PIP2 [98].

As radiotherapy and chemotherapy change the redox state of cancer cells, the increased ROS has the ability to activate PI3K or AKT directly to amplify the downstream of PI3K-AKT signalling. Meanwhile, PTEN is inhibited, promoting the activation of PI3K-AKT [96]. Increased ROS not only oxidise the cysteine residue located in the active centre to modulate PTEN directly but also promote the phosphorylation of serine/threonine within the C-terminus of the protein by casein kinase II [98, 99]. The phosphorylation of PTEN prevents its recruitment to the membrane and promotes its ubiquitination, ultimately leading to the proteolytic degradation pathway [96, 98] (Figure 3).

3.2.2. Activated AKT Induces ROS Mitigation.
With further exploration of downstream effectors that mitigate ROS levels, the PI3K-AKT signalling pathway was recently found to induce the adaptation to oxidative stress separate from the Keap1-Nrf2 pathway [97]. The principal mechanism of PI3K-AKT to reduce ROS levels is to reprogramme metabolism, which promotes the production of NADPH. Activated AKT not only phosphorylates metabolic enzymes directly but also regulates several downstream effectors, among which mammalian target of rapamycin complex 1 (mTORC1), and Nrf2 (see Section 3.2.3) seems to play an important role [97].

The direct method by which AKT promotes NADPH production is closely related to NAD^+ kinase (NADK), a unique cytosolic enzyme that catalyses the phosphorylation of NAD^+ to $NADP^+$ using the magnesium ion as a cofactor and ATP as the phosphate donor [100, 101]. AKT directly stimulates the activation of NADK by phosphorylating three serine residues (Ser44, Ser46, and Ser48) within the N-terminal region [102]. Then, activated NADK promotes the production of $NADP^+$, which is subsequently reduced to NADPH. The synthesis of $NADP^+$ from NAD^+ via NADK enlarges the size of the $NADP^+$ and NADPH pool, which may resist the loss of oxidised NADPH and result in the adaptation to increased ROS level.

The mTORC1 has been reported to play an important role in producing NADPH and has received much attention as one of the downstream substrates of the PI3K-AKT signalling pathway. The tuberous sclerosis (TSC) 1 and TSC2 functional complex is the intermediate regulator of the PI3K-AKT-mTORC1 pathway. Under normal conditions, the complex inhibits mTOR, which meditates the inhibition of p70 ribosomal protein S6 kinase 1 (p70S6K, also S6K1) and the activation of eukaryotic initiation factor 4E binding protein 1 (4EBP1) [103]. As mentioned above, when intracellular ROS levels are increased by radiotherapy and chemotherapy, AKT becomes activated. Activated AKT directly phosphorylates TSC2, disrupting and inactivating the TSC1-TSC2 complex. The destabilisation of TC2 promotes Ras homolog enriched in brain activity, ultimately activating mTORC1 [104]. Thus, the two canonical key downstream proteins S6K1 and 4EBP1 are all phosphorylated by mTORC1, leading to activation and inactivation, respectively [105]. S6K1, the major substrate protein molecule of mTORC1, promotes the activation of sterol regulatory element-binding protein (SREBP) [106].
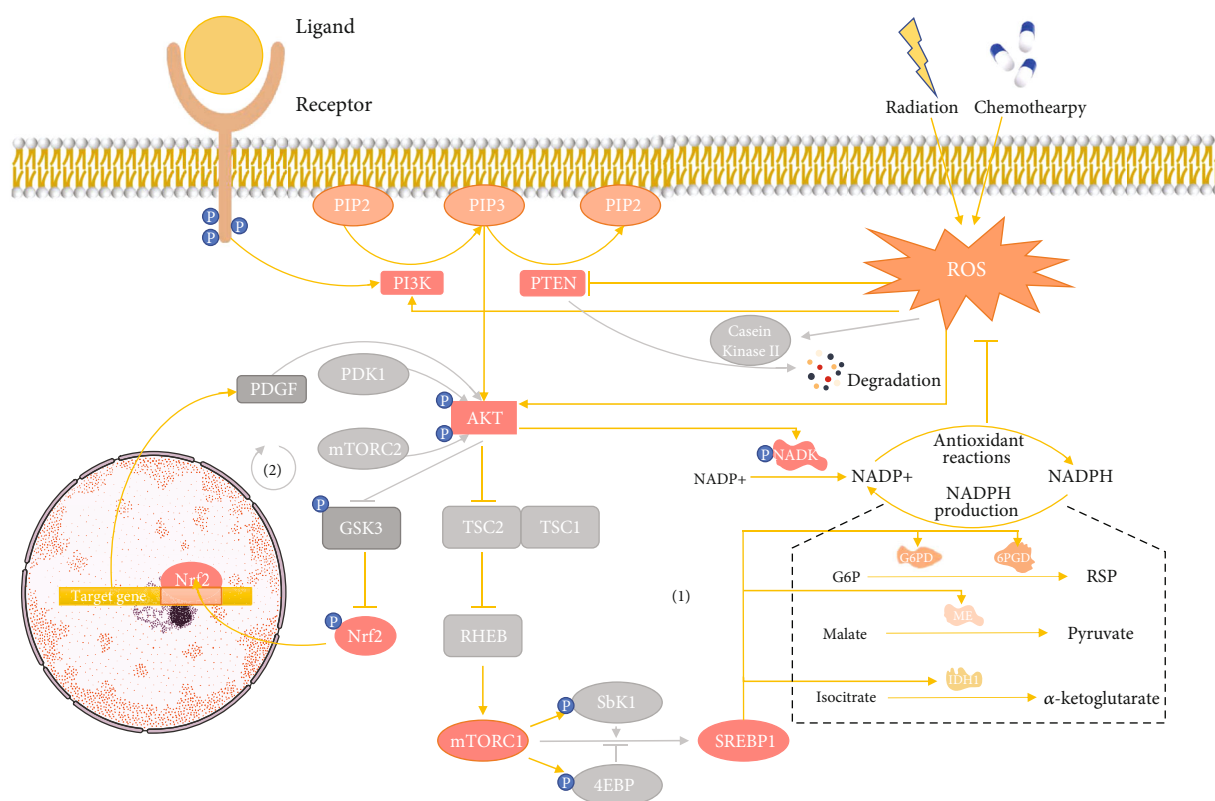
FIGURE 3: (1) The role of the PI3K-AKT signalling pathway in antioxidative stress related to radio- and chemoresistance. Phosphoinositide-3-kinases (PI3Ks) phosphorylate phosphatidylinositol 4,5-bisphosphate (PIP2) to phosphatidylinositol 3,4,5-trisphosphate (PIP3), which subsequently recruits and activates protein kinase B (PKB/AKT). However, these processes can be inhibited by phosphatase and tensin homolog (PTEN), which dephosphorylates PIP3 to PIP2. As radiation and chemotherapy continuously generate ROS via the redox reaction of water and direct production of ROS, respectively, increased intracellular ROS activate the PI3K-AKT pathway by directly promoting PI3K and AKT and inhibiting PTEN. PI3K-AKT signalling serves as defence against ROS by promoting NADPH production. Activated AKT regulates NADPH metabolism in direct and indirect ways via NAD^+ kinase (NADK) and rapamycin complex 1 (mTORC1), respectively. NADK is the unique cytosolic enzyme that catalyses the phosphorylation of NAD^+ to $NADP^+$, enlarging the size of the $NADP^+$ and NADPH pool. Downstream of mTORC1, sterol regulatory element-binding protein (SREBP) stimulates the expression of G6PD, 6PGD, IDH1, and ME, reducing $NADP^+$ to NADPH. (2) The loop formed between AKT and Nrf2. Glycogen synthase kinase 3 (GSK3) and platelet-derived growth factor (PDGF) act as a linker to connect AKT with Nrf2. PI3K-AKT signalling inhibits the Keap1-independent degradation of Nrf2 by phosphorylating GSK3. Activated Nrf2 translocates to the nucleus and upregulates the transcription of PDGF, binding with its cognate receptors to stimulate AKT.

In the cytoplasm, the most important pathway that reduces $NADP^+$ to NADPH is the oxidative PPP with G6PD and 6PGD catalysing the key steps. In addition, isocitrate dehydrogenase 1 (IDH1) and malic enzyme (ME) can regenerate NADPH from $NADP^+$. IDH1 and ME catalyse the oxidative decarboxylation of isocitrate to α-ketoglutarate and of malate to pyruvate, respectively, ultimately reducing $NADP^+$ to NADPH. SREBP can promote the production of NADPH by stimulating the expression of these four enzymes. The mRNAs for G6PD, 6PGD, and ME were found to be elevated in SREBP-overexpressed transgenic mice, indicating that these three enzymes are potentially activated by the ROS-mediated upregulation of SREBP [107]. Upregulated SREBPs bind with the IDH1-SRE sequence element GTGGGCTGAG within the promoter region to activate IDH1 [108]. Using 25-hydroxycholesterol or stains to inhibit or activate SREBP, respectively, Ricoult et al. demonstrated SREBP-mediated regulation on IDH1 expression [109]. The complicated mechanism of PI3K-AKT-mediated production of NADPH protects cancer cells against ROS, potentially revealing a new aspect of radio- and chemoresistance (Figure 3).

3.2.3. Crosstalk between PI3K-AKT and Keap1-Nrf2 Signalling Pathways.

Several studies have covered the interaction between PI3K-AKT and Keap-Nrf2 signalling pathways. For example, using the PI3K inhibitor LY294002 to repress the PI3K-AKT pathway inhibits the nuclear translocation of Nrf2 [110]. Nrf2 regulates metabolic reprogramming, and its function can be expanded by the continuous activation of the PI3K-AKT pathway [80]. He et al. found that in human hepatomegaly, all the factors including oxidative stress and liver cancer that stimulate Nrf2 result in the activation of AKT [111]. Interestingly, it seems that the PI3K-AKT and Keap-Nrf2 pathways form a loop so that both can act as the downstream effector of the other. Glycogen synthase kinase 3 (GSK3) is the intermediate factor of the PI3K-AKT-Nrf2 pathway and mediates the Keap1-independent

degradation of Nrf2 [112]. GSK3 phosphorylates NRF2 to stimulate the ubiquitination of Nrf2, which is subsequently marked for proteasomal degradation [113]. Given that the phosphorylation and inhibition of GSK3 are mediated by AKT activation [114], the activation of the PI3K-AKT pathway could promote the stabilisation of Nrf2 by inhibiting GSK3. By contrast, Nrf2 can stimulate the activation of AKT. When Nrf2 translocates to the nucleus, it recruits specificity protein 1 to the promoter of platelet-derived growth factor (PDGF) to upregulate its transcription [115]. In addition, the activation of AKT is closely related to the binding of PDGF and its cognate receptors [111]. To conclude, PI3K-AKT controls Nrf2 indirectly via the downstream kinase GSK3, whereas Nrf2 promotes the activation of AKT at transcriptional and translation levels through PDGF (Figure 3).

3.3. Prooxidant Therapy and Antioxidant Pathways.

3.3. Prooxidant Therapy and Antioxidant Pathways. It is generally acknowledged that ROS are one of the primary mediators of ionising radio- and chemotoxicity, which leads to the death of cancer cells. Radiation and some chemotherapy drugs trigger tumour cell death by upregulating ROS to the threshold needed to treat tumours. However, while prooxidant therapy increases intracellular ROS levels to treat the patient, many antioxidant pathways have also been activated to interfere with oxidative stress due to increased level of ROS, giving rise to radioresistance and chemoresistance. NADPH serves as the most significant reducing agent to antioxidant defence systems, which protect tumour cells from the cytotoxicity of ROS. ME- and IDH-dependent NADPH production and the oxidative PPP are the three primary pathways that enlarge the cytosolic NADPH pool. As mentioned above, the continuous generation of ROS from radio- and chemotherapy activates Keap1-Nrf2 and PI3K-AKT pathways, which regulate several antioxidative downstream effects. Both of these signalling pathways upregulate the expression of some major enzymes of the PPP including 6PGD and G6PD. Furthermore, the PI3K-AKT pathway stimulates the expression of ME and IDH, contributing to the regeneration of NADPH from $NADP^+$ via the middle effector SREBP. Apart from promoting the production of NADPH, the activated antioxidant pathways also increase antioxidant levels to mitigate ROS. Based on this mechanism, it is easy to conceive that as the Keap1-Nrf2 or PI3K-AKT signalling pathway is activated by increased ROS, cancer cells are facilitated with the ability to resist the prooxidant therapy-meditated generation of ROS, resulting in radio- and chemoresistance. In fact, several inhibitors of these two signalling pathways have been found, including halofuginone [116], trigonelline [117], delicaflavone [118], and perifosine [119], which are potential therapeutic strategies to weaken radioresistance and chemoresistance (Figure 4). Trigonelline, an effective inhibitor of Nrf2, was demonstrated to overcome oxaliplatin resistance in colon cancer cells [117]. Delicaflavone may potentially break down the therapy resistance in colorectal cancer by the significant inhibition of the phosphorylation levels of the PI3K-AKT signalling pathway and the subsequent generation of ROS [118] (see Section 4 for more details). Thus, the Keap1-Nrf2 and PI3K-AKT path-
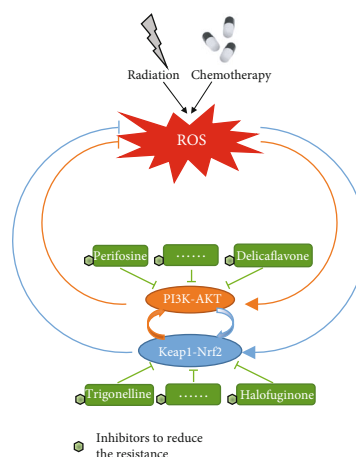
FIGURE 4: Effective treatment methods to overcome therapeutic resistance. PI3K-AKT and Keap1-Nrf2 signalling pathways are activated after radio- or chemotherapy for ROS production. The downstream antioxidant elements of these two pathways facilitate cancers with radio- and chemoresistance by resisting the cytotoxicity of high ROS. Halofuginone, trigonelline, delicaflavone, and perifosine are potential inhibitors of the PI3K-AKT or Keap1-Nrf2 pathway to reduce resistance and meet the need of radiosension and chemosension.

ways should be considered for radiosensitivity and chemosensitivity.

4. Role of ROS in Radiosension and Chemosension

While overproduced ROS adapt to the increased metabolism of tumour cells, high ROS levels caused by radiotherapy and chemotherapy also result in cytotoxicity, indicating a close connection between ROS levels and the sensitivity of cells to treatment [120–122]. To improve the sensitisation of tumours, much attention has been paid to targeted therapies that interfere with the changes in ROS levels, including generation, degradation, and regulation pathways [123]. Generally, current research has primarily focused on three aspects: (1) regulating the generation and elimination of ROS [124], (2) adjusting metabolism [125], and (3) ameliorating hypoxic environment [126]. Each aspect has its own unique treatment mechanism which is aimed at its target pathways. Therefore, to explore effective treatment methods to overcome therapeutic resistance, it is necessary to gain a full understanding of the key principles and their influences on redox homeostasis. Moreover, the treatment needs to be applied to the whole body to determine its effectiveness. This effectiveness should also consider the advantages and disadvantages between the damage of normal tissue and the killing of tumour tissue.

4.1. Regulating the Generation and Elimination of ROS.

4.1. Regulating the Generation and Elimination of ROS. Active metabolism in tumour cells leads to high production of ROS. To resist the cytotoxicity of high ROS, antioxidant systems are activated to maintain ROS at a relatively secure level [127]. To enhance their sensitivity, tumour cells increased ROS levels by promoting the production of ROS

or inhibiting the antioxidant system. As an important source of ROS, mitochondrial dysfunction is the primary reason for increased ROS production in cancer cells and provides a chief focus for targeted therapy [128]. Currently, targeted therapeutic drugs (e.g., elesclomol [129] and rotenone [130]) for ROS production mostly focus on the mitochondrial electron transport chain as a specific inhibitor to the complex. The increase of ROS production leads to apoptosis and ultimately is manifested as tumour sensitisation. In addition, some special ROS molecules produced through relatively independent pathways, such as nitric oxide (·NO), offer a completely different treatment idea. Although ·NO is inert in most cases, its reaction rate with $O_2^{·-}$ in cells is even faster than that of $O_2^{·-}$ disproportionation catalysed by SOD [131]. In this way, directly providing donors or regulating synthetases may be novel methods to increase the level of ROS [132, 133].

For the antioxidant system, due to the numerous pathways involved, more options are provided for the selection of inhibitors. The first choice at present is undoubtedly the direct inhibition of several important pathways, such as the pathways mentioned above (Figure 4). For the Keap1-Nrf2 pathway, halofuginone was reported to be able to deplete all Nrf2 in cells by inhibiting all protein synthesis, thus reducing the drug resistance of tumour cells in vivo and in vitro [116]. In addition, trigonelline is a potent inhibitor of Nrf2 and causes a higher repression on the expression of the downstream antioxidant response element [117]. Recent studies have indicated that trigonelline is a potential inhibitor to reduce resistance in the treatment of colon cancer and hepatocarcinoma [117, 134]. For the PI3K-AKT pathway, delicaflavone significant inhibited resistance and induced apoptosis effectively [118]. However, because the antioxidant system is complex, regulating its related factors can also indirectly inhibit the pathway. Cyclooxygenase-2 overexpression has been confirmed to mediate the activation of the PI3K-AKT pathway and is associated with drug resistance in non-small-cell carcinoma [135]. Moreover, cyclooxygenase-2 participates in the regulation of the NF-κB pathway, suggesting another method for regulating ROS elimination [136].

4.2. Adjusting Metabolism.

Tumour cells reprogramme metabolism to meet the need of malignant proliferation and metastasis [125]. The altered metabolism provides more sources for the increase in ROS, improving the resistance of the tumour. Pavlova et al. divided the known metabolic characteristic changes in tumours into six groups according to their effects on cell genes, differentiation, and the microenvironment [137]. While most cancers often display a few of these effects, the grouping provides a clearer direction for the research of treatments for a certain type of tumour. Among these groups, two are considered to be closely related to the change in ROS levels. One is the increase in glucose and glutamine catabolism. As two major nutrients for cell survival and biosynthesis, glucose and glutamine are consumed by tumour cells at a significantly increased rate [138, 139]. To adapt to these changes, tumour cells strictly control their own state by reprogramming the metabolic process [140]. Different metabolic modes also cause the increase in

ROS. This provides a direction for targeted therapy. As previously mentioned, Nrf2 affects cell metabolism. As a targeted inhibitor of Nrf2, $2',4'$-dihydroxy-$6'$-methoxy-$3',5'$-dimethylchalcone can significantly decrease GSH content and GST activity [141]. In addition, the inhibitor K-563 produced by Streptomyces sp. is able to reduce the production of GSH by inhibiting the Keap1-Nrf2 pathway [142]. Both inhibitors raise the sensitivity of tumour cells by adjusting glucose and glutamine catabolism.

The other related group is the change in the use of intermediate products in the tricarboxylic acid cycle. Tumour cells not only have increased demand for nutrients but also change the using ways of nutrients [88]. The variation in redox reactions of the tricarboxylic acid cycle supplies more opportunities for ROS induction. The key mechanism of NADPH oxidase 4 promoting cell growth is considered to be the PI3K/AKT pathway in the antioxidant system, indicating the connection between ROS levels and reprogramming metabolism [143]. Targeted therapy to inhibit the pathways related to these aspects is expected to be beneficial to the regulation of cellular ROS levels.

4.3. Ameliorating Hypoxic Environment.

As a marker of the tumour microenvironment, hypoxia greatly reduces the sensitivity of tumour cells to effective treatment. Various changes in cells caused by hypoxia promote the development of the tumour and the generation of therapeutic resistance [144]. In the process of the cell response, the HIF family plays a significant role as transcription factors [145]. Therefore, it is easy to think that the inhibition of HIF by targeted therapy would achieve a good prognosis. FTY720 (Fingolimod) [146], L-carnosine dipeptide [147], and LW6 [148] are inhibitors of HIF1 that are currently being studied. They primarily repress therapeutic resistance by inhibiting the accumulation of HIF factors, thus reducing the expression of target genes. However, although the inhibition therapy is the most direct and effective treatment in theory, the current treatment results are not ideal due adverse effects and low bioavailability [149]. At present, effective targeted therapy drugs are still under exploration.

Because tumour therapies are less effective due to hypoxia, another approach that has recently attracted attention is the combination of a nanosensitiser and traditional treatment, which is aimed at relieving the anoxic environment while delivering drugs. For instance, one study reported that a special nanoparticle consisting of doxorubicin (DOX) and a MnO shell can be delivered to tumour tissues and released by a near-infrared laser, then resolve HO to ameliorate the hypoxia environment [150]. Moreover, when the nanoparticles contain different materials, they play different auxiliary roles in diverse tumour treatment. For example, novel shell-stacked nanoparticle can wrap and deliver targeted medicine to tumour cells and neovascularization [151]. A prodrug system made up of hybrid nanoenzymes may improve hypoxic conditions in tumour cells and provide better basis for chemophotodynamic treatment [152]. Nanotechnology provides another possible method to stimulate the sensitivity of tumour cells and overcome therapeutic resistance.

4.4. Precise Regulation of ROS Levels under Systemic Condition. Although the inhibition of antioxidants can improve the therapeutic effects of adjuvant radiotherapy and chemotherapy, the role of the antioxidant system in normal tissue cannot be ignored. In most cases, the antioxidant system protects normal tissue by scavenging ROS [127]. Studies have shown that antioxidants play a significant role in protecting and preventing carcinogenesis [153]. As an antioxidant, isoflavone inhibits the activation of NF-κB in oxidative stress [154]. Due to its antioxidant ability, isoflavone can inhibit the production of H_2O_2 caused by tumour promoters *in vitro* and *in vivo*, indicating its potential ability to prevent carcinogenesis [155]. In addition, the antioxidant eugenol can effectively inhibit lipid peroxidation and reduce iron and copper ions, suggesting its strong antioxidant activity and free radical scavenging ability [156]. Eugenol has been shown to play a role in preventing skin cancer and reducing the incidence of gastric cancer, the actions of which are closely related to its antioxidant activity [157, 158]. However, some studies indicate that excessive antioxidation also has harmful effects on normal cells. In clinical trials, people taking antioxidant supplements have shown a higher risk of developing skin cancer [159, 160]. The antioxidant epigallocatechin gallate can induce DNA double-strand breaks in human lung and skin normal cells, resulting in DNA damage and cell death [161]. Moreover, high doses of synthetic antioxidants, which eliminate the interference of cytotoxicity, have been demonstrated to cause DNA damage in cultivated mesenchymal stem cells, finally inducing premature senescence [162]. Therefore, only antioxidants maintained within a certain concentration range can be beneficial to normal issue.

However, this does not mean that the idea of inhibiting antioxidants to enhance radiotherapy and chemotherapy is wrong. On the contrary, radiation protective agents such as the antioxidant 3,3'-diindolylmethane make use of the characteristic to reduce the damage to normal tissue caused by radiotherapy. 3,3'-Diindolylmethane can inhibit the accumulation of ROS and has strong free radical scavenging activity [163]. In addition, it prevents tumorigenesis by protecting DNA from damage in colon cancer [164]. Furthermore, it has been proposed as a radioprotective drug because it protects normal tissue from radiation damage [165]. Other representative drugs such as the cysteamine series also have strong protective effects [166]. Amifostine, which is widely used in clinical practice, significantly reduces the effect of radiotherapy on normal tissue by scavenging free radicals [167]. In fact, the ideal therapeutic method is to enhance the effect of antioxidants in normal tissue and suppress it in tumour tissue.

5. Conclusion

ROS are the redox products of cellular metabolism. Under normal conditions, the production and clearance of ROS are in balance to keep them at a stable low level. In tumour cells, the appropriate increase of ROS plays an important role in the malignant progression of cancer. However, high levels of ROS can also induce regulated cell death such as apoptosis, autophagy, and ferroptosis by affecting cell signalling pathways and promoting lipid peroxidation. As primary antitumour treatment methods, radiotherapy and chemotherapy primarily increase the level of ROS to achieve their therapeutic effect. However, in the process of treatment, tumour cells correspondingly enhance antioxidant stress to prevent ROS levels from being too high. Here, we review some important mechanisms of antioxidant stress in tumour resistance to radiotherapy and chemotherapy. Previous studies have shown that some important pathways, such as Keap1-Nrf2 and PI3K-AKT, are significantly upregulated to reduce ROS levels by increasing antioxidant levels, changing metabolism, or other mechanisms. These findings suggest that the inhibition of ROS production is an important reason for the therapeutic resistance of tumour cells. In this context, treatment targeting the antioxidative stress system is an important research direction to overcome radioresistance and chemoresistance. Prior research indicates that ROS levels can be increased by directly promoting ROS production, inhibiting antioxidant system, regulating metabolism, and ameliorating hypoxia environment. At present, the relevant research is still in the state of exploration but shows great potential for future study of the tumour cell antioxidant stress system.

Conflicts of Interest

The authors declare that they have no conflicts of interest.

Authors' Contributions

Yanchi Chen, Yiling Li, and Linyang Huang contributed equally to this work.

Acknowledgments

References

[1] H. Sies and D. P. Jones, "Reactive oxygen species (ROS) as pleiotropic physiological signalling agents," *Nature Reviews Molecular Cell Biology*, vol. 21, no. 7, pp. 363–383, 2020.

[2] E. I. Azzam, J. P. Jay-Gerin, and D. Pain, "Ionizing radiation-induced metabolic oxidative stress and prolonged cell injury," *Cancer Letters*, vol. 327, no. 1-2, pp. 48–60, 2012.

[3] H. Sies, "Oxidative stress: a concept in redox biology and medicine," *Redox Biology*, vol. 4, pp. 180–183, 2015.

[4] P. C. Fan, Y. Zhang, Y. Wang et al., "Quantitative proteomics reveals mitochondrial respiratory chain as a dominant target for carbon ion radiation: delayed reactive oxygen species generation caused DNA damage," *Free Radical Biology and Medicine*, vol. 130, pp. 436–445, 2019.

[5] C. Gorrini, I. Harris, and T. W. Mak, "Modulation of oxidative stress as an anticancer strategy," *Nature Reviews Drug Discovery*, vol. 12, no. 12, pp. 931–947, 2013.

[6] M. Yamamoto, T. Kensler, and H. Motohashi, "The KEAP1-NRF2 system: a thiol-based sensor-effector apparatus for maintaining redox homeostasis," *Physiological Reviews*, vol. 98, no. 3, pp. 1169–1203, 2018.

[7] B. Hybertson, B. Gao, S. Bose, and J. M. McCord, "Oxidative stress in health and disease: the therapeutic potential of Nrf2 activation," *Molecular Aspects of Medicine*, vol. 32, no. 4-6, pp. 234–246, 2011.

[8] H. Yang, R. M. Villani, H. Wang et al., "The role of cellular reactive oxygen species in cancer chemotherapy," *Journal of Experimental & Clinical Cancer Research*, vol. 37, no. 1, p. 266, 2018.

[9] P. T. Schumacker, "Reactive oxygen species in cancer: a dance with the devil," *Cancer Cell*, vol. 27, no. 2, pp. 156-157, 2015.

[10] B. Marengo, M. Nitti, A. L. Furfaro et al., "Redox homeostasis and cellular antioxidant systems: crucial players in cancer growth and therapy," *Oxidative Medicine and Cellular Longevity*, vol. 2016, Article ID 6235641, 16 pages, 2016.

[11] D. Spitz, E. Azzam, J. Jian Li, and D. Gius, "Metabolic oxidation/reduction reactions and cellular responses to ionizing radiation: a unifying concept in stress response biology," *Cancer and Metastasis Reviews*, vol. 23, no. 3/4, pp. 311–322, 2004.

[12] B. H. J. Bielski and D. E. Cabelli, "Highlights of current research involving superoxide and perhydroxyl radicals in aqueous solutions," *International Journal of Radiation Biology*, vol. 59, no. 2, pp. 291–319, 2009.

[13] J. Tamminga and O. Kovalchuk, "Role of DNA damage and epigenetic DNA methylation changes in radiation-induced genomic instability and bystander effects in germline in vivo," *Current Molecular Pharmacology*, vol. 4, no. 2, pp. 115–125, 2011.

[14] H. Pelicano, D. Carney, and P. Huang, "ROS stress in cancer cells and therapeutic implications," *Drug Resistance Updates*, vol. 7, no. 2, pp. 97–110, 2004.

[15] K. Berneis, W. Bollag, M. Kofler, and H. Lüthy, "The enhancement of the after effect of ionizing radiation by a cytotoxic methylhydrazine derivative," *European Journal of Cancer*, vol. 40, no. 13, pp. 1928–1933, 2004.

[16] S. W. Behrend, "Patients with primary brain tumors," *Oncology Nursing Forum*, vol. 41, no. 3, pp. 335-336, 2014.

[17] M. Songbo, H. Lang, C. Xinyong, X. Bin, Z. Ping, and S. Liang, "Oxidative stress injury in doxorubicin-induced cardiotoxicity," *Toxicology Letters*, vol. 307, pp. 41–48, 2019.

[18] S. Prasad, S. Gupta, and A. K. Tyagi, "Reactive oxygen species (ROS) and cancer: role of antioxidative nutraceuticals," *Cancer Letters*, vol. 387, pp. 95–105, 2017.

[19] Y. Song, J. Jang, T. H. Shin et al., "Sulfasalazine attenuates evading anticancer response of CD133-positive hepatocellular carcinoma cells," *Journal of Experimental & Clinical Cancer Research*, vol. 36, no. 1, p. 38, 2017.

[20] C. Wen, H. Wang, X. Wu et al., "ROS-mediated inactivation of the PI3K/AKT pathway is involved in the antigastric cancer effects of thioredoxin reductase-1 inhibitor chaetocin," *Cell Death & Disease*, vol. 10, no. 11, p. 809, 2019.

[21] K. E. Baidoo, K. Yong, and M. W. Brechbiel, "Molecular pathways: targeted α-particle radiation therapy," *Clinical Cancer Research*, vol. 19, no. 3, pp. 530–537, 2013.

[22] Y. Du, S. Du, L. Liu et al., "Radiation-induced bystander effect can be transmitted through exosomes using miRNAs as effector molecules," *Radiation Research*, vol. 194, no. 1, 2020.

[23] S. Wolff, "The adaptive response in radiobiology: evolving insights and implications," *Environmental Health Perspectives*, vol. 106, Supplement 1, pp. 277–283, 1998.

[24] K. M. Prise and J. M. O'Sullivan, "Radiation-induced bystander signalling in cancer therapy," *Nature Reviews Cancer*, vol. 9, no. 5, pp. 351–360, 2009.

[25] J. Alexandre, Y. Hu, W. Lu, H. Pelicano, and P. Huang, "Novel action of paclitaxel against cancer cells: bystander effect mediated by reactive oxygen species," *Cancer Research*, vol. 67, no. 8, pp. 3512–3517, 2007.

[26] J. D. Hayes, A. T. Dinkova-Kostova, and K. D. Tew, "Oxidative stress in cancer," *Cancer Cell*, vol. 38, no. 2, pp. 167–197, 2020.

[27] D. Ziech, R. Franco, A. Pappa, and M. I. Panayiotidis, "Reactive oxygen species (ROS)–induced genetic and epigenetic alterations in human carcinogenesis," *Mutation Research*, vol. 711, no. 1-2, pp. 167–173, 2011.

[28] U. Weyemi, O. Lagente-Chevallier, M. Boufraqech et al., "ROS-generating NADPH oxidase NOX4 is a critical mediator in oncogenic H-Ras- induced DNA damage and subsequent senescence," *Oncogene*, vol. 31, no. 9, pp. 1117–1129, 2012.

[29] D. Nicholson and N. A. Thornberry, "Caspases: killer proteases," *Trends in Biochemical Sciences*, vol. 22, no. 8, pp. 299–306, 1997.

[30] K. Vermeulen, D. R. Van Bockstaele, and Z. N. Berneman, "Apoptosis: mechanisms and relevance in cancer," *Annals of Hematology*, vol. 84, no. 10, pp. 627–639, 2005.

[31] A. Ashkenazi and V. M. Dixit, "Death receptors: signaling and modulation," *Science*, vol. 281, no. 5381, pp. 1305–1308, 1998.

[32] T. L. Denning, H. Takaishi, S. E. Crowe, I. Boldogh, A. Jevnikar, and P. B. Ernst, "Oxidative stress induces the expression of Fas and Fas ligand and apoptosis in murine intestinal epithelial cells," *Free Radical Biology and Medicine*, vol. 33, no. 12, pp. 1641–1650, 2002.

[33] P. Pallepati and D. A. Averill-Bates, "Mild thermotolerance induced at 40 °C protects HeLa cells against activation of death receptor-mediated apoptosis by hydrogen peroxide," *Free Radical Biology & Medicine*, vol. 50, no. 6, pp. 667–679, 2011.

[34] H. Zou, W. Henzel, X. Liu, A. Lutschg, and X. Wang, "Apaf-1, a human protein homologous to C. elegans CED-4, participates in cytochrome c-dependent activation of caspase-3," *Cell*, vol. 90, no. 3, pp. 405–413, 1997.

[35] C. P. Baines, R. A. Kaiser, N. H. Purcell et al., "Loss of cyclophilin D reveals a critical role for mitochondrial permeability transition in cell death," *Nature*, vol. 434, no. 7033, pp. 658–662, 2005.

[36] N. Festjens, M. van Gurp, G. van Loo, X. Saelens, and P. Vandenabeele, "Bcl-2 family members as sentinels of cellular integrity and role of mitochondrial intermembrane space proteins in apoptotic cell death," *Acta Haematologica*, vol. 111, no. 1-2, pp. 7–27, 2003.

[37] S. Luanpitpong, P. Chanvorachote, C. Stehlik et al., "Regulation of apoptosis by Bcl-2 cysteine oxidation in human lung epithelial cells," *Molecular Biology of the Cell*, vol. 24, no. 6, pp. 858–869, 2013.

[38] I. Dikic and Z. Elazar, "Mechanism and medical implications of mammalian autophagy," *Nature Reviews Molecular Cell Biology*, vol. 19, no. 6, pp. 349–364, 2018.

[39] D. M. Petibone, W. Majeed, and D. A. Casciano, "Autophagy function and its relationship to pathology, clinical applications, drug metabolism and toxicity," *Journal of Applied Toxicology*, vol. 37, no. 1, pp. 23–37, 2017.

[40] A. L. Levonen, B. G. Hill, E. Kansanen, J. Zhang, and V. M. Darley-Usmar, "Redox regulation of antioxidants, autophagy, and the response to stress: implications for electrophile therapeutics," *Free Radical Biology and Medicine*, vol. 71, pp. 196–207, 2014.

[41] R. Scherz-Shouval and Z. Elazar, "Regulation of autophagy by ROS: physiology and pathology," *Trends in Biochemical Sciences*, vol. 36, no. 1, pp. 30–38, 2011.

[42] R. Scherz-Shouval, E. Shvets, E. Fass, H. Shorer, L. Gil, and Z. Elazar, "Reactive oxygen species are essential for autophagy and specifically regulate the activity of Atg4," *The EMBO Journal*, vol. 26, no. 7, pp. 1749–1760, 2007.

[43] B. R. Stockwell, J. P. Friedmann Angeli, H. Bayir et al., "Ferroptosis: a regulated cell death nexus linking metabolism, redox biology, and disease," *Cell*, vol. 171, no. 2, pp. 273–285, 2017.

[44] M. Tafani, L. Sansone, F. Limana et al., "The interplay of reactive oxygen species, hypoxia, inflammation, and sirtuins in cancer initiation and progression," *Oxidative Medicine and Cellular Longevity*, vol. 2016, Article ID 3907147, 18 pages, 2016.

[45] K. Zarkovic, A. Jakovcevic, and N. Zarkovic, "Contribution of the HNE-immunohistochemistry to modern pathological concepts of major human diseases," *Free Radical Biology and Medicine*, vol. 111, pp. 110–126, 2017.

[46] W. Łuczaj, A. Gęgotek, and E. Skrzydlewska, "Antioxidants and HNE in redox homeostasis," *Free Radical Biology and Medicine*, vol. 111, pp. 87–101, 2017.

[47] G. Lei, Y. Zhang, P. Koppula et al., "The role of ferroptosis in ionizing radiation-induced cell death and tumor suppression," *Cell Research*, vol. 30, no. 2, pp. 146–162, 2020.

[48] J. Wang and J. Yi, "Cancer cell killing via ROS: to increase or decrease, that is the question," *Cancer Biology & Therapy*, vol. 7, no. 12, pp. 1875–1884, 2008.

[49] V. Sosa, T. Moliné, R. Somoza, R. Paciucci, H. Kondoh, and M. E. LLeonart, "Oxidative stress and cancer: an overview," *Ageing Research Reviews*, vol. 12, no. 1, pp. 376–390, 2013.

[50] W. Kim, Lee, Seo et al., "Cellular stress responses in radiotherapy," *Cells*, vol. 8, no. 9, p. 1105, 2019.

[51] J. Zhang, X. Wang, V. Vikash et al., "ROS and ROS-mediated cellular signaling," *Oxidative Medicine and Cellular Longevity*, vol. 2016, Article ID 4350965, 18 pages, 2016.

[52] A. Kobayashi, M. I. Kang, H. Okawa et al., "Oxidative stress sensor Keap1 functions as an adaptor for Cul3-based E3 ligase to regulate proteasomal degradation of Nrf2," *Molecular and Cellular Biology*, vol. 24, no. 16, pp. 7130–7139, 2004.

[53] N. Villeneuve, A. Lau, and D. D. Zhang, "Regulation of the Nrf2-Keap1 antioxidant response by the ubiquitin proteasome system: an insight into cullin-ring ubiquitin ligases," *Antioxidants & Redox Signaling*, vol. 13, no. 11, pp. 1699–1712, 2010.

[54] T. Yamamoto, T. Suzuki, A. Kobayashi et al., "Physiological significance of reactive cysteine residues of Keap1 in determining Nrf2 activity," *Molecular and Cellular Biology*, vol. 28, no. 8, pp. 2758–2770, 2008.

[55] H. M. Leinonen, E. Kansanen, P. Polonen, M. Heinaniemi, and A. L. Levonen, "Role of the Keap1-Nrf2 pathway in cancer," *Advances in Cancer Research*, vol. 122, pp. 281–320, 2014.

[56] J. W. Shin, K. S. Chun, D. H. Kim et al., "Curcumin induces stabilization of Nrf2 protein through Keap1 cysteine modification," *Biochemical Pharmacology*, vol. 173, article 113820, 2020.

[57] S. Liu, S. Xu, R. Wei et al., "Keap1 cystenine 151 as a potential target for artemisitene-induced Nrf2 activation," *BioMed Research International*, vol. 2019, Article ID 5198138, 8 pages, 2019.

[58] B. E. Hast, D. Goldfarb, K. M. Mulvaney et al., "Proteomic analysis of ubiquitin ligase KEAP1 reveals associated proteins that inhibit NRF2 ubiquitination," *Cancer Research*, vol. 73, no. 7, pp. 2199–2210, 2013.

[59] K. C. Kim, K. A. Kang, R. Zhang et al., "Up-regulation of Nrf2-mediated heme oxygenase-1 expression by eckol, a phlorotannin compound, through activation of Erk and PI3K/Akt," *The International Journal of Biochemistry & Cell Biology*, vol. 42, no. 2, pp. 297–305, 2010.

[60] J. Y. Park, S. Kim, H. Y. Sohn, Y. H. Koh, and C. Jo, "TFEB activates Nrf2 by repressing its E3 ubiquitin ligase DCAF11 and promoting phosphorylation of p62," *Scientific Reports*, vol. 9, no. 1, article 14354, 2019.

[61] A. Ganner, Z. C. Pfeiffer, L. Wingendorf et al., "The acetyltransferase p300 regulates NRF2 stability and localization," *Biochemical and Biophysical Research Communications*, vol. 524, no. 4, pp. 895–902, 2020.

[62] I. Bellezza, I. Giambanco, A. Minelli, and R. Donato, "Nrf2-Keap1 signaling in oxidative and reductive stress," *Biochimica et Biophysica Acta (BBA) - Molecular Cell Research*, vol. 1865, no. 5, pp. 721–733, 2018.

[63] K. Itoh, T. Chiba, S. Takahashi et al., "An Nrf2/Small Maf Heterodimer Mediates the Induction of Phase II Detoxifying Enzyme Genes through Antioxidant Response Elements," *Biochemical and Biophysical Research Communications*, vol. 236, no. 2, pp. 313–322, 1997.

[64] T. H. Rushmore and C. B. Pickett, "Transcriptional regulation of the rat glutathione S-transferase Ya subunit gene. Characterization of a xenobiotic-responsive element controlling inducible expression by phenolic antioxidants.," *Journal of Biological Chemistry*, vol. 265, no. 24, pp. 14648–14653, 1990.

[65] R. S. Friling, A. Bensimon, Y. Tichauer, and V. Daniel, "Xenobiotic-inducible expression of murine glutathione S-transferase Ya subunit gene is controlled by an electrophile-responsive element," *Proceedings of the National Academy of Sciences of the United States of America*, vol. 87, no. 16, pp. 6258–6262, 1990.

[66] A. Otsuki, M. Suzuki, F. Katsuoka et al., "Unique cistrome defined as CsMBE is strictly required for Nrf2-sMaf heterodimer function in cytoprotection," *Free Radical Biology & Medicine*, vol. 91, pp. 45–57, 2016.

[67] A. Otsuki and M. Yamamoto, "Cis-element architecture of Nrf2-sMaf heterodimer binding sites and its relation to diseases," *Archives of Pharmacal Research*, vol. 43, no. 3, pp. 275–285, 2020.

[68] T. Suzuki, H. Motohashi, and M. Yamamoto, "Toward clinical application of the Keap1–Nrf2 pathway," *Trends in Pharmacological Sciences*, vol. 34, no. 6, pp. 340–346, 2013.

[69] B. N. Chorley, M. R. Campbell, X. Wang et al., "Identification of novel NRF2-regulated genes by ChIP-Seq: influence on retinoid X receptor alpha," *Nucleic Acids Research*, vol. 40, no. 15, pp. 7416–7429, 2012.

[70] D. Malhotra, E. Portales-Casamar, A. Singh et al., "Global mapping of binding sites for Nrf2 identifies novel targets in cell survival response through ChIP-Seq profiling and network analysis," *Nucleic Acids Research*, vol. 38, no. 17, pp. 5718–5734, 2010.

[71] S. G. Rhee, "Overview on peroxiredoxin," *Molecules and Cells*, vol. 39, no. 1, pp. 1–5, 2016.

[72] C. Ding, X. Fan, and G. Wu, "Peroxiredoxin 1- an antioxidant enzyme in cancer," *Journal of Cellular and Molecular Medicine*, vol. 21, no. 1, pp. 193–202, 2017.

[73] W. C. Chen, W. H. McBride, K. S. Iwamoto et al., "Induction of radioprotective peroxiredoxin-I by ionizing irradiation," *Journal of Neuroscience Research*, vol. 70, no. 6, pp. 794–798, 2002.

[74] E. K. Kim, M. G. Jang, M. J. Song, D. Kim, Y. Kim, and H. H. Jang, "Redox-mediated mechanism of chemoresistance in cancer cells," *Antioxidants (Basel)*, vol. 8, no. 10, p. 471, 2019.

[75] B. Zhang, Y. Wang, and Y. Su, "Peroxiredoxins, a novel target in cancer radiotherapy," *Cancer Letters*, vol. 286, no. 2, pp. 154–160, 2009.

[76] G. Li, B. Xie, X. Li et al., "Downregulation of peroxiredoxin-1 by β-elemene enhances the radiosensitivity of lung adenocarcinoma xenografts," *Oncology Reports*, vol. 33, no. 3, pp. 1427–1433, 2015.

[77] J. D. Hayes and A. T. Dinkova-Kostova, "The Nrf2 regulatory network provides an interface between redox and intermediary metabolism," *Trends in Biochemical Sciences*, vol. 39, no. 4, pp. 199–218, 2014.

[78] I. Sarfraz, A. Rasul, G. Hussain et al., "6-Phosphogluconate dehydrogenase fuels multiple aspects of cancer cells: from cancer initiation to metastasis and chemoresistance," *BioFactors*, vol. 46, no. 4, pp. 550–562, 2020.

[79] Y. Hirotsu, F. Katsuoka, R. Funayama et al., "Nrf2-MafG heterodimers contribute globally to antioxidant and metabolic networks," *Nucleic Acids Research*, vol. 40, no. 20, pp. 10228–10239, 2012.

[80] Y. Mitsuishi, K. Taguchi, Y. Kawatani et al., "Nrf2 redirects glucose and glutamine into anabolic pathways in metabolic reprogramming," *Cancer Cell*, vol. 22, no. 1, pp. 66–79, 2012.

[81] R. K. Thimmulappa, K. H. Mai, S. Srisuma, T. W. Kensler, M. Yamamoto, and S. Biswal, "Identification of Nrf2-regulated genes induced by the chemopreventive agent sulforaphane by oligonucleotide microarray," *Cancer Research*, vol. 62, no. 18, pp. 5196–5203, 2002.

[82] J. Lewerenz, S. J. Hewett, Y. Huang et al., "The cystine/glutamate antiporter system x(c)(-) in health and disease: from molecular mechanisms to novel therapeutic opportunities," *Antioxidants & Redox Signaling*, vol. 18, no. 5, pp. 522–555, 2013.

[83] S. C. Lu, "Regulation of glutathione synthesis," *Molecular Aspects of Medicine*, vol. 30, no. 1-2, pp. 42–59, 2009.

[84] J. Liu, X. Xia, and P. Huang, "xCT: a critical molecule that links cancer metabolism to redox signaling," *Molecular Therapy*, vol. 28, no. 11, pp. 2358–2366, 2020.

[85] L. Liu, R. Liu, Y. Liu et al., "Cystine-glutamate antiporterxC-Tas a therapeutic target for cancer," *Cell Biochemistry and Function*, 2020.

[86] P. Koppula, Y. Zhang, L. Zhuang, and B. Gan, "Amino acid transporter SLC7A11/xCT at the crossroads of regulating redox homeostasis and nutrient dependency of cancer," *Cancer Communications*, vol. 38, no. 1, p. 12, 2018.

[87] A. J. Ong, S. Saeidi, N. H. K. Chi et al., "The positive feedback loop between Nrf2 and phosphogluconate dehydrogenase stimulates proliferation and clonogenicity of human hepatoma cells," *Free Radical Research*, pp. 1–12, 2020.

[88] M. G. Vander Heiden, L. C. Cantley, and C. B. Thompson, "Understanding the Warburg effect: the metabolic requirements of cell proliferation," *Science*, vol. 324, no. 5930, pp. 1029–1033, 2009.

[89] A. J. Levine and A. M. Puzio-Kuter, "The control of the metabolic switch in cancers by oncogenes and tumor suppressor genes," *Science*, vol. 330, no. 6009, pp. 1340–1344, 2010.

[90] W. Ying, "NAD+/NADH and NADP+/NADPH in cellular functions and cell death: regulation and biological consequences," *Antioxidants & Redox Signaling*, vol. 10, no. 2, pp. 179–206, 2008.

[91] A. Singh, C. Happel, S. K. Manna et al., "Transcription factor NRF2 regulates miR-1 and miR-206 to drive tumorigenesis," *Journal of Clinical Investigation*, vol. 123, no. 7, pp. 2921–2934, 2013.

[92] Y. Y. Wang, J. Chen, X. M. Liu, R. Zhao, and H. Zhe, "Nrf2-mediated metabolic reprogramming in cancer," *Oxidative Medicine and Cellular Longevity*, vol. 2018, Article ID 9304091, 7 pages, 2018.

[93] I. Vivanco and C. L. Sawyers, "The phosphatidylinositol 3-kinase–AKT pathway in human cancer," *Nature Reviews Cancer*, vol. 2, no. 7, pp. 489–501, 2002.

[94] D. A. Fruman, H. Chiu, B. D. Hopkins, S. Bagrodia, L. C. Cantley, and R. T. Abraham, "The PI3K pathway in human disease," *Cell*, vol. 170, no. 4, pp. 605–635, 2017.

[95] D. D. Sarbassov, D. A. Guertin, S. M. Ali, and D. M. Sabatini, "Phosphorylation and regulation of Akt/PKB by the rictor-mTOR complex," *Science*, vol. 307, no. 5712, pp. 1098–1101, 2005.

[96] N. Koundouros and G. Poulogiannis, "Phosphoinositide 3-kinase/Akt signaling and redox metabolism in cancer," *Frontiers in Oncology*, vol. 8, p. 160, 2018.

[97] G. Hoxhaj and B. D. Manning, "The PI3K-AKT network at the interface of oncogenic signalling and cancer metabolism," *Nature Reviews Cancer*, vol. 20, no. 2, pp. 74–88, 2020.

[98] N. R. Leslie and C. P. Downes, "PTEN: the down side of PI 3-kinase signalling," *Cellular Signalling*, vol. 14, no. 4, pp. 285–295, 2002.

[99] N. R. Leslie, I. H. Batty, H. Maccario, L. Davidson, and C. P. Downes, "Understanding PTEN regulation: PIP$_2$, polarity and protein stability," *Oncogene*, vol. 27, no. 41, pp. 5464–5476, 2008.

[100] P. M. Tedeschi, N. Bansal, J. E. Kerrigan, E. E. Abali, K. W. Scotto, and J. R. Bertino, "NAD+ kinase as a therapeutic target in cancer," *Clinical Cancer Research*, vol. 22, no. 21, pp. 5189–5195, 2016.

[101] F. Lerner, M. Niere, A. Ludwig, and M. Ziegler, "Structural and functional characterization of human NAD kinase," *Biochemical and Biophysical Research Communications*, vol. 288, no. 1, pp. 69–74, 2001.

[102] G. Hoxhaj, I. Ben-Sahra, S. E. Lockwood et al., "Direct stimulation of NADP synthesis through Akt-mediated

phosphorylation of NAD kinase," *Science*, vol. 363, no. 6431, pp. 1088–1092, 2019.

[103] K. Inoki, Y. Li, T. Zhu, J. Wu, and K. L. Guan, "TSC2 is phosphorylated and inhibited by Akt and suppresses mTOR signalling," *Nature Cell Biology*, vol. 4, no. 9, pp. 648–657, 2002.

[104] A. K. Murugan, "mTOR: role in cancer, metastasis and drug resistance," *Seminars in Cancer Biology*, vol. 59, pp. 92–111, 2019.

[105] P. E. Burnett, R. K. Barrow, N. A. Cohen, S. H. Snyder, and D. M. Sabatini, "RAFT1 phosphorylation of the translational regulators p70 S6 kinase and 4E-BP1," *Proceedings of the National Academy of Sciences of the United States of America*, vol. 95, no. 4, pp. 1432–1437, 1998.

[106] K. Düvel, J. L. Yecies, S. Menon et al., "Activation of a metabolic gene regulatory network downstream of mTOR complex 1," *Molecular Cell*, vol. 39, no. 2, pp. 171–183, 2010.

[107] I. Shimomura, H. Shimano, B. S. Korn, Y. Bashmakov, and J. D. Horton, "Nuclear sterol regulatory element-binding proteins activate genes responsible for the entire program of unsaturated fatty acid biosynthesis in transgenic mouse liver," *The Journal of Biological Chemistry*, vol. 273, no. 52, pp. 35299–35306, 1998.

[108] I. Shechter, P. Dai, L. Huo, and G. Guan, "IDH1 gene transcription is sterol regulated and activated by SREBP-1a and SREBP-2 in human hepatoma HepG2 cells: evidence that IDH1 may regulate lipogenesis in hepatic cells," *Journal of Lipid Research*, vol. 44, no. 11, pp. 2169–2180, 2003.

[109] S. J. H. Ricoult, C. C. Dibble, J. M. Asara, and B. D. Manning, "Sterol regulatory element binding protein regulates the expression and metabolic functions of wild-type and oncogenic IDH1," *Molecular and Cellular Biology*, vol. 36, no. 18, pp. 2384–2395, 2016.

[110] E. M. Harrison, S. J. McNally, L. Devey, O. J. Garden, J. A. Ross, and S. J. Wigmore, "Insulin induces heme oxygenase-1 through the phosphatidylinositol 3-kinase/Akt pathway and the Nrf2 transcription factor in renal cells," *The FEBS Journal*, vol. 273, no. 11, pp. 2345–2356, 2006.

[111] F. He, L. Antonucci, S. Yamachika et al., "NRF2 activates growth factor genes and downstream AKT signaling to induce mouse and human hepatomegaly," *Journal of Hepatology*, vol. 72, no. 6, pp. 1182–1195, 2020.

[112] M. Lu, P. Wang, Y. Qiao et al., "GSK3beta-mediated Keap1-independent regulation of Nrf2 antioxidant response: a molecular rheostat of acute kidney injury to chronic kidney disease transition," *Redox Biology*, vol. 26, article 101275, 2019.

[113] A. Cuadrado, "Structural and functional characterization of Nrf2 degradation by glycogen synthase kinase 3/β-TrCP," *Free Radical Biology & Medicine*, vol. 88, Part B, pp. 147–157, 2015.

[114] D. A. E. Cross, D. R. Alessi, P. Cohen, M. Andjelkovich, and B. A. Hemmings, "Inhibition of glycogen synthase kinase-3 by insulin mediated by protein kinase B," *Nature*, vol. 378, no. 6559, pp. 785–789, 1995.

[115] D. Liu, Y. Zhang, Y. Wei et al., "Activation of AKT pathway by Nrf2/PDGFA feedback loop contributes to HCC progression," *Oncotarget*, vol. 7, no. 40, pp. 65389–65402, 2016.

[116] K. Tsuchida, T. Tsujita, M. Hayashi et al., "Halofuginone enhances the chemo-sensitivity of cancer cells by suppressing NRF2 accumulation," *Free Radical Biology & Medicine*, vol. 103, pp. 236–247, 2017.

[117] A. Pirpour Tazehkand, R. Salehi, K. Velaei, and N. Samadi, "The potential impact of trigonelline loaded micelles on Nrf2 suppression to overcome oxaliplatin resistance in colon cancer cells," *Molecular Biology Reports*, vol. 47, no. 8, pp. 5817–5829, 2020.

[118] W. Yao, Z. Lin, P. Shi et al., "Delicaflavone induces ROS-mediated apoptosis and inhibits PI3K/AKT/mTOR and Ras/-MEK/Erk signaling pathways in colorectal cancer cells," *Biochemical Pharmacology*, vol. 171, article 113680, 2020.

[119] S. Ramezani, N. Vousooghi, F. Ramezani Kapourchali, and M. T. Joghataei, "Perifosine enhances bevacizumab-induced apoptosis and therapeutic efficacy by targeting PI3K/AKT pathway in a glioblastoma heterotopic model," *Apoptosis*, vol. 22, no. 8, pp. 1025–1034, 2017.

[120] P. C. Hart, M. Mao, A. L. P. de Abreu et al., "MnSOD upregulation sustains the Warburg effect via mitochondrial ROS and AMPK-dependent signalling in cancer," *Nature Communications*, vol. 6, no. 1, 2015.

[121] C. R. Reczek, K. Birsoy, H. Kong et al., "A CRISPR screen identifies a pathway required for paraquat-induced cell death," *Nature Chemical Biology*, vol. 13, no. 12, pp. 1274–1279, 2017.

[122] M. S. Weng, J. H. Chang, W. Y. Hung, Y. C. Yang, and M. H. Chien, "The interplay of reactive oxygen species and the epidermal growth factor receptor in tumor progression and drug resistance," *Journal of Experimental & Clinical Cancer Research*, vol. 37, no. 1, p. 61, 2018.

[123] Q. Cui, J. Q. Wang, Y. G. Assaraf et al., "Modulating ROS to overcome multidrug resistance in cancer," *Drug Resistance Updates*, vol. 41, pp. 1–25, 2018.

[124] E. Singer, J. Judkins, N. Salomonis et al., "Reactive oxygen species-mediated therapeutic response and resistance in glioblastoma," *Cell Death & Disease*, vol. 6, no. 1, article e1601, 2015.

[125] R. J. DeBerardinis and N. S. Chandel, "Fundamentals of cancer metabolism," *Science Advances*, vol. 2, no. 5, article e1600200, 2016.

[126] X. Jing, F. Yang, C. Shao et al., "Role of hypoxia in cancer therapy by regulating the tumor microenvironment," *Molecular Cancer*, vol. 18, no. 1, p. 157, 2019.

[127] K. Camphausen, D. Citrin, M. Krishna, and J. B. Mitchell, "Implications for tumor control during protection of normal tissues with antioxidants," *Journal of Clinical Oncology*, vol. 23, no. 24, pp. 5455–5457, 2005.

[128] P. E. Porporato, N. Filigheddu, J. M. B. S. Pedro, G. Kroemer, and L. Galluzzi, "Mitochondrial metabolism and cancer," *Cell Research*, vol. 28, no. 3, pp. 265–280, 2018.

[129] M. Nagai, N. H. Vo, L. Shin Ogawa et al., "The oncology drug elesclomol selectively transports copper to the mitochondria to induce oxidative stress in cancer cells," *Free Radical Biology and Medicine*, vol. 52, no. 10, pp. 2142–2150, 2012.

[130] L. K. Sharma, H. Fang, J. Liu, R. Vartak, J. Deng, and Y. Bai, "Mitochondrial respiratory complex I dysfunction promotes tumorigenesis through ROS alteration and AKT activation," *Human Molecular Genetics*, vol. 20, no. 23, pp. 4605–4616, 2011.

[131] J. Jay-Gerin and C. J. B. Ferradini, "Are there protective enzymatic pathways to regulate high local nitric oxide (.NO) concentrations in cells under stress conditions?," *Biochimie*, vol. 82, no. 2, pp. 161–166, 2000.

[132] B. Bonavida, "Regulation of cell death apoptotic pathways by nitric oxide in cancer: reversal of drug/immune resistance," *Redox Biology*, vol. 5, p. 415, 2015.

[133] H. Illum, D. H. Wang, J. E. Dowell et al., "Phase I dose escalation trial of nitroglycerin in addition to 5-fluorouracil and radiation therapy for neoadjuvant treatment of operable rectal cancer," *Surgery*, vol. 158, no. 2, pp. 460–465, 2015.

[134] J. C. Liao, K. T. Lee, B. J. You et al., "Raf/ERK/Nrf2 signaling pathway and MMP-7 expression involvement in the trigonelline-mediated inhibition of hepatocarcinoma cell migration," *Food & Nutrition Research*, vol. 59, no. 1, p. 29884, 2017.

[135] Q.-F. Deng, Q. Y. Fang, X. X. Ji, and S. W. Zhou, "Cyclooxygenase-2 mediates gefitinib resistance in non-small cell lung cancer through the EGFR/PI3K/AKT axis," *Journal of Cancer*, vol. 11, no. 12, pp. 3667–3674, 2020.

[136] X. Zhang, P. Qu, H. Zhao, T. Zhao, and N. Cao, "COX-2 promotes epithelial-mesenchymal transition and migration in osteosarcoma MG-63 cells via PI3K/AKT/NF-κB signaling," *Molecular Medicine Reports*, vol. 20, no. 4, pp. 3811–3819, 2019.

[137] N. Pavlova and C. B. Thompson, "The emerging hallmarks of cancer metabolism," *Cell Metabolism*, vol. 23, no. 1, pp. 27–47, 2016.

[138] P. Som, H. L. Atkins, D. Bandoypadhyay et al., "A fluorinated glucose analog, 2-fluoro-2-deoxy-D-glucose (F-18): nontoxic tracer for rapid tumor detection," *Journal of Nuclear Medicine*, vol. 21, no. 7, pp. 670–675, 1980.

[139] M. O. Yuneva, T. W. M. Fan, T. D. Allen et al., "The metabolic profile of tumors depends on both the responsible genetic lesion and tissue type," *Cell Metabolism*, vol. 15, no. 2, pp. 157–170, 2012.

[140] H. L. Wieman, J. A. Wofford, and J. C. Rathmell, "Cytokine stimulation promotes glucose uptake via phosphatidylinositol-3 kinase/Akt regulation of Glut1 activity and trafficking," *Molecular Biology of the Cell*, vol. 18, no. 4, pp. 1437–1446, 2007.

[141] X. Wei, X. Mo, F. An, X. Ji, and Y. Lu, "2$'$,4$'$-Dihydroxy-6$'$-methoxy-3$'$,5$'$-dimethylchalcone, a potent Nrf2/ARE pathway inhibitor, reverses drug resistance by decreasing glutathione synthesis and drug efflux in BEL-7402/5-FU cells," *Food and Chemical Toxicology*, vol. 119, pp. 252–259, 2018.

[142] R. Hori, K. Yamaguchi, H. Sato et al., "The discovery and characterization of K-563, a novel inhibitor of the Keap1/Nrf2 pathway produced by Streptomyces sp," *Cancer Medicine*, vol. 8, no. 3, pp. 1157–1168, 2019.

[143] T. Yu, L. Li, W. Liu, B. Ya, H. Cheng, and Q. Xin, "Silencing of NADPH oxidase 4 attenuates hypoxia resistance in neuroblastoma cells SH-SY5Y by inhibiting PI3K/Akt-dependent glycolysis," *Oncology Research Featuring Preclinical and Clinical Cancer Therapeutics*, vol. 27, no. 5, pp. 525–532, 2019.

[144] A. L. Harris, "Hypoxia – a key regulatory factor in tumour growth," *Nature Reviews Cancer*, vol. 2, no. 1, pp. 38–47, 2002.

[145] C. Wigerup, S. Påhlman, and D. Bexell, "Therapeutic targeting of hypoxia and hypoxia-inducible factors in cancer," *Pharmacology & Therapeutics*, vol. 164, pp. 152–169, 2016.

[146] C. Gstalder, I. Ader, and O. Cuvillier, "FTY720 (Fingolimod) inhibits HIF1 and HIF2 signaling, promotes vascular remodeling, and chemosensitizes in renal cell carcinoma animal model," *Molecular Cancer Therapeutics*, vol. 15, no. 10, pp. 2465–2474, 2016.

[147] B. Iovine, F. Guardia, C. Irace, and M. A. Bevilacqua, "l-carnosine dipeptide overcomes acquired resistance to 5-fluorouracil in HT29 human colon cancer cells via downregulation of HIF1-alpha and induction of apoptosis," *Biochimie*, vol. 127, pp. 196–204, 2016.

[148] M. Sato, K. Hirose, I. Kashiwakura et al., "LW6, a hypoxia-inducible factor 1 inhibitor, selectively induces apoptosis in hypoxic cells through depolarization of mitochondria in A549 human lung cancer cells," *Molecular Medicine Reports*, vol. 12, no. 3, pp. 3462–3468, 2015.

[149] S. Prasad, A. K. Tyagi, and B. B. Aggarwal, "Recent developments in delivery, bioavailability, absorption and metabolism of curcumin: the golden pigment from golden spice," *Cancer Research and Treatment*, vol. 46, no. 1, pp. 2–18, 2014.

[150] P. Sun, Q. Deng, L. Kang, Y. Sun, J. Ren, and X. Qu, "A smart nanoparticle-laden and remote-controlled self-destructive macrophage for enhanced chemo/chemodynamic synergistic therapy," *ACS Nano*, vol. 14, no. 10, pp. 13894–13904, 2020.

[151] J. Chen, Z. Jiang, W. Xu et al., "Spatiotemporally targeted nanomedicine overcomes hypoxia-induced drug resistance of tumor cells after disrupting neovasculature," *Nano Letters*, vol. 20, no. 8, pp. 6191–6198, 2020.

[152] X. Cheng, L. He, J. Xu et al., "Oxygen-producing catalase-based prodrug nanoparticles overcoming resistance in hypoxia-mediated chemo-photodynamic therapy," *Acta Biomaterialia*, vol. 112, pp. 234–249, 2020.

[153] N. Ahmad and H. Mukhtar, "Antioxidants meet molecular targets for cancer prevention and therapeutics," *Antioxidants & Redox Signaling*, vol. 19, no. 2, pp. 85–88, 2013.

[154] J. N. Davis, O. Kucuk, Z. Djuric, and F. H. Sarkar, "Soy isoflavone supplementation in healthy men prevents NF-κB activation by TNF-α in blood lymphocytes," *Free Radical Biology and Medicine*, vol. 30, no. 11, pp. 1293–1302, 2001.

[155] H. Wei, R. Bowen, Q. Cai, S. Barnes, and Y. Wang, "Antioxidant and antipromotional effects of the soybean isoflavone genistein," *Experimental Biology and Medicine*, vol. 208, no. 1, pp. 124–130, 1995.

[156] I. Gulcin, "Antioxidant activity of eugenol: a structure-activity relationship study," *Journal of Medicinal Food*, vol. 14, no. 9, pp. 975–985, 2011.

[157] G. Kaur, M. Athar, and M. S. Alam, "Eugenol precludes cutaneous chemical carcinogenesis in mouse by preventing oxidative stress and inflammation and by inducing apoptosis," *Molecular Carcinogenesis*, vol. 49, no. 3, pp. 290–301, 2010.

[158] P. Manikandan, G. Vinothini, R. Vidya Priyadarsini, D. Prathiba, and S. Nagini, "Eugenol inhibits cell proliferation via NF-kappaB suppression in a rat model of gastric carcinogenesis induced by MNNG," *Investigational New Drugs*, vol. 29, no. 1, pp. 110–117, 2011.

[159] S. Hercberg, K. Ezzedine, C. Guinot et al., "Antioxidant supplementation increases the risk of skin cancers in women but not in men," *The Journal of Nutrition*, vol. 137, no. 9, pp. 2098–2105, 2007.

[160] K. Ezzedine, J. Latreille, E. Kesse-Guyot et al., "Incidence of skin cancers during 5-year follow-up after stopping antioxidant vitamins and mineral supplementation," *European Journal of Cancer*, vol. 46, no. 18, pp. 3316–3322, 2010.

[161] L. Y. Lu, N. Ou, and Q. B. Lu, "Antioxidant induces DNA damage, cell death and mutagenicity in human lung and skin normal cells," *Scientific Reports*, vol. 3, no. 1, p. 3169, 2013.

[162] J. S. Kornienko, I. S. Smirnova, N. A. Pugovkina et al., "High doses of synthetic antioxidants induce premature senescence

in cultivated mesenchymal stem cells," *Scientific Reports*, vol. 9, no. 1, p. 1296, 2019.

[163] S. Benabadji, R. Wen, J. Zheng, X. Dong, and S. G. Yuan, "Anticarcinogenic and antioxidant activity of diindolyl-methane derivatives," *Pharmacologica Sinica*, vol. 25, no. 5, pp. 666–671, 2004.

[164] C. Bonnesen, I. M. Eggleston, and J. D. Hayes, "Dietary indoles and isothiocyanates that are generated from crucifer-ous vegetables can both stimulate apoptosis and confer pro-tection against DNA damage in human colon cell lines," *Cancer Research*, vol. 61, no. 16, pp. 6120–6130, 2001.

[165] S. Fan, Q. Meng, J. Xu et al., "DIM (3,3′-diindolylmethane) confers protection against ionizing radiation by a unique mechanism," *Proceedings of the National Academy of Sciences of the United States of America*, vol. 110, no. 46, pp. 18650–18655, 2013.

[166] J. C. Roberts, K. E. Koch, S. R. Detrick, R. L. Warters, and G. Lubec, "Thiazolidine prodrugs of cysteamine and cysteine as radioprotective agents," *Radiation Research*, vol. 143, no. 2, pp. 203–213, 1995.

[167] J. Gu, S. Zhu, X. Li, H. Wu, Y. Li, and F. Hua, "Effect of ami-fostine in head and neck cancer patients treated with radio-therapy: a systematic review and meta-analysis based on randomized controlled trials," *PLoS One*, vol. 9, no. 5, article e95968, 2014.

Research Article

Berbamine Suppresses the Progression of Bladder Cancer by Modulating the ROS/NF-κB Axis

Chenglin Han [ID],[1] **Zilong Wang** [ID],[1] **Shuxiao Chen**,[2] **Lin Li**,[3] **Yingkun Xu** [ID],[1] **Weiting Kang** [ID],[1] **Chunxiao Wei**,[4] **Hongbin Ma**,[5] **Muwen Wang** [ID],[1,4] and **Xunbo Jin** [ID][1,4]

[1]*Department of Urology, Shandong Provincial Hospital, Cheeloo College of Medicine, Shandong University, Jinan, Shandong 250021, China*

[2]*Department of Vascular Surgery, Shandong Provincial Hospital, Cheeloo College of Medicine, Shandong University, Jinan, Shandong 250021, China*

[3]*Department of Orthopedics, Shandong Provincial Hospital, Cheeloo College of Medicine, Shandong University, Jinan, Shandong 250021, China*

[4]*Department of Urology, Shandong Provincial Hospital Affiliated to Shandong First Medical University, Jinan, Shandong 250021, China*

[5]*Department of Hepatobiliary, The First Affiliated Hospital of Harbin Medical University, Harbin, Heilongjiang 150000, China*

Correspondence should be addressed to Muwen Wang; docwmw1@163.com and Xunbo Jin; jxb@sdu.edu.cn

Berbamine (BBM), one of the bioactive ingredients extracted from *Berberis* plants, has attracted intensive attention because of its significant antitumor activity against various malignancies. However, the exact role and potential molecular mechanism of berbamine in bladder cancer (BCa) remain unclear. In the present study, our results showed that berbamine inhibited cell viability, colony formation, and proliferation. Additionally, berbamine induced cell cycle arrest at S phase by a synergistic mechanism involving stimulation of P21 and P27 protein expression as well as downregulation of CyclinD, CyclinA2, and CDK2 protein expression. In addition to suppressing epithelial-mesenchymal transition (EMT), berbamine rearranged the cytoskeleton to inhibit cell metastasis. Mechanistically, the expression of P65, P-P65, and P-IκBα was decreased upon berbamine treatment, yet P65 overexpression abrogated the effects of berbamine on the proliferative and metastatic potential of BCa cells, which indicated that berbamine attenuated the malignant biological activities of BCa cells by inhibiting the NF-κB pathway. More importantly, berbamine increased the intracellular reactive oxygen species (ROS) level through the downregulation of antioxidative genes such as Nrf2, HO-1, SOD2, and GPX-1. Following ROS accumulation, the intrinsic apoptotic pathway was triggered by an increase in the ratio of Bax/Bcl-2. Furthermore, berbamine-mediated ROS accumulation negatively regulated the NF-κB pathway to a certain degree. Consistent with our in vitro results, berbamine successfully inhibited tumor growth and blocked the NF-κB pathway in our xenograft model. To summarize, our data demonstrated that berbamine exerts antitumor effects via the ROS/NF-κB signaling axis in bladder cancer, which provides a basis for further comprehensive study and presents a potential candidate for clinical treatment strategies against bladder cancer.

1. Introduction

Bladder cancer is the 7th most common malignancy in males and remains the leading cause of urinary disease-related death [1]. An estimated 549,000 new cases diagnosed as bladder cancer and 200,000 deaths occurred worldwide in 2018 [2]. In terms of clinical and pathological aspects, urothelial carcinoma, which accounts for 90% of primary bladder malignant tumors, is the major histological subtype. Among those bladder cancer patients, non-muscle-invasive bladder cancer (NMIBC) accounts for 70% of diagnoses. Moreover, as many as 40% of NMIBCs eventually develop into muscle-invasive bladder cancer (MIBC), which is extremely aggressive and has overall 5-year and 10-year survival rates

of 50% and 36%, respectively [3, 4]. To date, therapeutics such as surgical resection and chemotherapy, mainly based on the tumor's clinical stage, have made certain progress. However, some hurdles, including adverse side effects, drug resistance, and the high recurrence rate, restrict sustainable clinical benefits. Therefore, it is highly necessary to screen more effective alternatives with low toxicity and determine their underlying mechanisms for patients with BCa.

Chinese traditional herbs have a wide range of pharmacological effects for clinical applications, such as anti-inflammatory, lipid modulation, antivirus, and antitumor [5, 6]. Berbamine, initially identified as an effective antileukemic agent extracted from the herbal medicine *Berberis*, garnered much attention [7]. A large number of research achievements further corroborate the antitumor properties of berbamine and its derivatives in various carcinomas, such as colon cancer, ovarian cancer, prostate cancer, and liver cancer [8–11]. Nonetheless, there have been no reports so far involving the effects of berbamine on the biological activities of bladder cancer.

ROS are a class of highly reactive, oxygen-containing molecules, mainly including superoxide anion, hydrogen peroxide, hydroxyl radicals, and singlet oxygen [12, 13]. Regulation of the ROS signaling network is a complex process. Under physiological conditions, a moderate level of ROS guaranteed by redox balance is crucial to a series of biological processes. However, compared with normal cells, cancer cells inherently exhibit aberrantly higher ROS levels due to their high metabolic rate, which profoundly facilitates the onset and deterioration of various human cancers by mediating oxidative damage to DNA, proteins, and lipids. Due to their dualistic nature, ROS can exert opposite biological effects. Once the extremely high ROS level exceeds intracellular tolerance, it can induce mitochondrial dysfunction and destroy cellular homeostasis, ultimately eliciting apoptosis, which provides possible insights into cancer treatment [14].

The process of tumor progression is synergistic, involving various intracellular proteins and complex signal transduction. Emerging evidence has demonstrated that abnormal upregulation of the inducible transcription factor NF-κB is closely associated with unfavorable prognosis in patients with MIBC [15–17]. In general, inactive P65 and P50 heterodimers were bound to the inhibitor IκBα in the cytoplasm. For NF-κB to be activated, IκBα must undergo phosphorylation, ubiquitination, and degradation; then, free P65 is phosphorylated for nuclear translocation and binds to DNA sequences at the promoter region of downstream target genes to regulate cellular processes [18]. In cancer cells, NF-κB activation initiates the transcription of proliferative, metastatic, and angiogenic genes, all of which contribute to carcinogenesis [19]. Therefore, targeting the NF-κB pathway has emerged as an effective strategy for cancer therapeutics.

We aimed to investigate the broad-spectrum effects of berbamine on bladder cancer in vitro and in vivo and elucidate its underlying mechanism. Cell phenotype experiments have revealed that berbamine could inhibit bladder cancer cell survival, proliferation, and metastasis by suppressing the NF-κB pathway. Moreover, berbamine could induce cell cycle arrest at S phase accompanied by alteration of P21,

P27, CyclinD, CyclinA2, and CDK2 proteins. We further established that berbamine downregulated the expression of several key antioxidative genes and subsequently elicited mitochondrial ROS generation that ultimately mediated cell apoptosis and negatively regulated the NF-κB pathway to a certain degree. Collectively, these findings indicated that berbamine could attenuate the multiple biological properties of bladder cancer by modulating the ROS/NF-κB axis. This study improves our understanding of the antitumor mechanism of berbamine against bladder cancer, thereby providing a basis for further comprehensive studies.

2. Materials and Methods

2.1. Cell Lines and Culture Conditions. Bladder cancer cell lines (5637 and T24 cells) were purchased from the Chinese Academy of Sciences (Shanghai, China). The above cells were cultured at 37°C in a humidified incubator containing 5% CO_2 in RPMI-1640 medium (Gibco, China) supplemented with 10% fetal bovine serum (Gibco, USA) and 1% penicillin (Sigma-Aldrich, Italy) and streptomycin (Sigma-Aldrich, Italy).

2.2. Cell Counting Kit-8 Assay (CCK-8). The CCK-8 assay was applied to evaluate the viability of bladder cancer cell lines (Dojindo, Japan). Appropriate 5637 and T24 cells were cultured in 96-well plates overnight and treated at the indicated doses. Following a certain period, the supernatant solution was replaced by 110 μl fresh medium containing 10 μl CCK-8 solution; then, the cells were incubated for 2 h at 37°C. The absorbance of each well was measured with a microplate reader at a wavelength of 450 nm.

2.3. Colony Formation Assay. 5637 and T24 cells were uniformly dispersed in 6-well culture plates at an approximate density of 1000/well. Cells were cultured with the indicated berbamine for 48 h, and the medium was renewed every three days. After a two-week cultivation, the colonies were fixed in 4% paraformaldehyde, stained with hematoxylin (Solarbio), and counted using ImageJ.

2.4. Wound Healing Assay. Exponentially growing cells were seeded in 6-well culture plates and allowed to reach approximately 95% confluence in complete medium. A sterile pipette tip was applied to scratch the cell layer to create a wound. Subsequently, the cells were cultured in serum-free medium containing a specified berbamine concentration. The images of wound closure were captured using an inverted microscope, and the healing rate was assessed by Image J.

2.5. Transwell Assay. Appropriate 5637 and T24 cells resuspended in serum-free medium (200 μl) with a specific concentration of berbamine were placed in the Transwell chamber (24-well, 8 μm pore membrane, Corning Incorporated, NY, USA). For cell invasion, the upper chamber membrane was precoated with Matrigel (Corning Incorporated, NY), not for cell migration. Subsequently, 500 μl of medium containing 20% FBS was presented in the lower chamber. After incubation at 37°C for 48 h, the cells on the upper

surface of the membrane were wiped with a cotton swab, and then migrated or invaded cells were fixed in 4% paraformaldehyde and stained with hematoxylin (Solarbio, China). The images were taken in five randomly selected fields by a microscope (Leica Microsystems, GmbH).

2.6. Cell Cycle Analysis. 5637 and T24 cells were cultured for starvation overnight and then pretreated with berbamine for 48 h. Subsequently, the collected cells were resuspended and fixed with precooled 75% ethanol at 4°C overnight. Following incubation with 1 mg/ml RNase A at 37°C for 30 min, the cells were stained with the propidium iodide (PI) solution for 20 minutes in the dark. Ultimately, the distribution of the cell cycle phase was analyzed through flow cytometry using a BD FACSArray (BD Biosciences, USA).

2.7. Cell Apoptosis Analysis. The collected cells were resuspended in 100 μl 1x binding buffer supplemented with 5 μl Annexin V-FITC and 5 μl propionate (BD.559763), followed by incubation at room temperature in the dark for 15 minutes. After staining, the cell apoptosis rate was calculated using flow cytometry (BD Biosciences, USA) and FlowJo 7.6.2 software. At least 10000 cells were guaranteed before analysis.

2.8. 5-Ethynyl-2$'$-Deoxyuridine (EdU) Assay. 5637 and T24 cells were seeded in 24-well plates with berbamine treatment for 48 h and incubated with medium supplemented with 50 μM EdU. Two hours later, the cells were fixed with 4% paraformaldehyde at room temperature for 20 minutes, permeabilized in 0.5% Triton X-100 for 10 minutes, and stained with Apollo staining solution and Hoechst reagent. Finally, images were taken using fluorescence microscopy (Olympus, Tokyo, Japan).

2.9. Phalloidin Staining. After berbamine treatment for 48 h, 5637 and T24 cells were fixed with cooled carbinol and incubated with 50 μg/ml FITC-phalloidin (Sigma-Aldrich) at room temperature in the dark for 1 h. Next, the cells were counterstained with DAPI (Sigma-Aldrich, USA). Finally, cell morphology was observed under a fluorescence microscope (Olympus, Japan).

2.10. Cell Transfection. pcDNA3.1-P65 and the empty vector were obtained from Genomeditech (Shanghai, China). When the cell confluence was approximately 50% in 6-well plates, the OV-P65 plasmid and the empty vector were transfected into 5637 and T24 cells with Lipofectamine 3000 Reagent (Invitrogen, USA). After 48 h of transfection, the cells were collected for subsequent experiments.

2.11. Mitochondrial ROS Measurement. Briefly, berbamine-treated cells were incubated with 5 μM MitoSOX reagent working solution at room temperature in the dark for 10 minutes. Then, the cells were fixed in 4% paraformaldehyde and stained with DAPI. Finally, images were captured using a fluorescence microscope (Olympus, Japan).

2.12. Immunofluorescence. Cells were fixed with 4% paraformaldehyde for 20 minutes and permeabilized in 0.5% Triton X-100 for 10 minutes. Next, the cells were blocked with normal goat serum for 1 h and incubated overnight with the primary antibody at 4°C, followed by incubation with the Alexa Fluor 488-conjugated secondary antibody in the dark for 2 h. Finally, the cell nuclei were counterstained with DAPI, and images were captured using a fluorescence microscope (Olympus, Japan).

2.13. Quantitative Real-Time PCR (qRT-PCR). The total RNA was extracted from 5637 and T24 cells by using the TRIzol Reagent (Takara, China) and was subsequently reverse-transcribed into cDNA with the PrimeScript™ RT Reagent Kit (Takara) according to the manufacturer's instructions. qRT-PCR analysis was carried out using the TB Green™ Premix Ex Taq™ II (Takara). The primer sequences were as follows: GAPDH (forward: 5$'$-GCACCG TCAAGGCTGAGAAC-3$'$; reverse: 5$'$-TGGTGAAGACG CCAGTGGA-3$'$) and P65 (forward: 5$'$-GACGCATTGCT GTGCCTTC-3$'$; reverse: 5$'$-TTGATGGTGCTCAGGG ATGAC-3$'$). The GAPDH gene was regarded as an internal reference for P65 mRNA. The relative expression levels were calculated by the $2^{-\Delta\Delta Ct}$ method. All trials were conducted in triplicate (3 wells).

2.14. Western Blotting. Total protein was extracted from bladder cancer cells using RIPA lysis buffer (CST, USA) with 1% phosphatase inhibitors and 1% protease inhibitors on ice, and then quantified with the bicinchoninic acid (BCA) method (Solarbio). Each sample (25 μg) was separated by 10% SDS-PAGE, transferred to a polyvinylidene fluoride (PVDF) membrane, blocked with 5% skim milk powder, and incubated with the primary antibody overnight at 4°C. The next day, the membrane was incubated with the HRP-conjugated secondary antibody for 1 h and finally visualized using an enhanced chemiluminescence kit.

2.15. Xenografts. The animal protocol was approved by the Institutional Animal Care and Use Committee of Shandong University. A suspension containing 5×10^6 T24 cells was injected subcutaneously into the right axilla of nude mice (specific-pathogen-free (SPF) grade, 4 weeks old) that were randomly divided into the control group and BBM group ($n = 5$ for each group). When the tumor volume in each nude mouse was greater than 100 mm^3, the mice in the treatment group were intraperitoneally injected with berbamine at 35 mg/kg body weight every three days until the completion of the experiment. Simultaneously, the mice in the control group were exposed to the same concentration of DMSO. At the termination of the experiment, the mice were sacrificed by cervical dislocation, and solid tumors were removed for evaluation. In addition, a portion of tumor tissues were embedded in paraffin for immunohistochemistry (IHC).

2.16. IHC. Tumor tissues were fixed with 4% paraformaldehyde and embedded in paraffin for slicing. Subsequently, the samples were deparaffinized, rehydrated, and washed with PBS. These samples were immersed in the antigen retrieval solutions with 10 nM citrate buffer (pH 6.0) for 3 minutes and incubated with the Ki-67 antibody and P65 antibody at 4°C overnight. The next day, the sections were

incubated with the biotin-conjugated secondary antibody for 1 h. According to the manufacturer's procedures, protein staining was carried out with the DAB enzyme (Abcam, ab64238), and the nuclei were stained with hematoxylin (Abcam, ab143166). The stained slides were observed under a microscope.

2.17. Statistical Analysis. All values are expressed as the mean ± SD. Prism software (GraphPad, USA) was used to do statistical analysis. Statistical significance was determined using two-tailed Student's *t*-test or one-way ANOVA. Differences with *p* values less than 0.05 were considered statistically significant.

3. Results

3.1. Berbamine Suppressed the Growth of Bladder Cancer Cells In Vitro. The chemical structure of berbamine is displayed in Figure 1(a). The CCK-8 assay was first performed to delve into the cytotoxic effects of berbamine. Briefly, cells were treated with a range of concentrations of berbamine (8, 16, 24, 32, and 40 μM) for 24 h or 48 h, and cell survival was calculated in comparison with that of untreated cells. According to Figure 1(b), berbamine significantly suppressed the viability of both 5637 and T24 cells in a concentration- and time-dependent manner. The 50% inhibitory concentration (IC50) values of berbamine for 5637 and T24 cells at 48 h were 15.58 ± 2.489 and 19.09 ± 0.68 μmol/l, respectively. Therefore, we applied suitable concentrations (8 μM and 16 μM) of berbamine to subsequent experiments. As shown in Figures 1(c) and 1(d), berbamine treatment significantly decreased the number of colonies compared to that in the control group. Additionally, the EdU assay visually suggested an antiproliferative activity of berbamine, as it disturbed DNA replication. Following berbamine treatment, the percentages of EdU-positive 5637 and T24 cells were markedly reduced (Figure 1(e)). Consistent with the EdU assay, immunofluorescence assays indicated that the level of Ki-67, a vital marker of cell proliferation, was notably decreased in both cell lines in response to berbamine (Figure 1(f)). In conclusion, the above outcomes illustrated that berbamine strongly restrained bladder cancer cell growth in vitro.

3.2. Berbamine Induced Cell Cycle Arrest at S Phase in Bladder Cancer Cells. Cell cycle perturbation underlies aberrant cell proliferation, which characterizes a malignant phenotype [20]. Given that berbamine, a cycle-specific drug, could suppress tumor cell growth by disturbing cell cycle progression [8, 21], we measured the cycle ratio of 5637 and T24 cells with berbamine treatment by PI staining. As expected, berbamine increased the percentage of cells in S phase and exhibited a dose-dependent trend, but the proportion of cells in G0/G1 phase and G2/M phase did not change significantly (Figures 2(a) and 2(b)).

To clarify the molecular mechanism of how berbamine arrests the cell cycle, we assessed the levels of P21, P27, CyclinD, CyclinA2, and CDK2 proteins that are responsible for S-phase regulation [22]. As illustrated in Figures 2(c) and 2(d)), the expression of cyclin-dependent kinase inhibi-

tors p21 and p27 was clearly upregulated upon berbamine treatment. In contrast, berbamine dramatically downregulated the expression of CyclinD, CyclinA2, and CDK2. In summary, berbamine induced S-phase arrest by targeting and altering the expression of checkpoint regulators, thus suppressing the growth of bladder cancer cells.

3.3. Berbamine Suppressed the Migration and Invasion Activities of Bladder Cancer Cells. Considering that the metastasis of cancer cells is a vital factor in tumor progression, we performed a wound healing assay and a Transwell assay to assess the influences of berbamine on the metastatic potency of bladder cancer cells. As shown in Figure 3(a), berbamine retarded wound closure in a dose-dependent manner, indicating that berbamine apparently curbed the migratory capacity of bladder cancer cells. Consistently, a similar result was obtained in the Transwell assay (Figure 3(b)). After treatment for 48 h, berbamine induced significant decreases in the numbers of migrated cells. Besides, the Transwell invasion assay revealed that the number of cells that invaded the lower chamber through extracellular matrix (ECM) gels was remarkably reduced following berbamine treatment, which suggested that berbamine restricted the invasive capacity of bladder cancer cells.

The above experiments confirmed the antimetastatic effects of berbamine on BCa cells (Figure 3(c)). Given that the EMT process has been verified to engage in the migration and invasion of cancer cells, we investigated the levels of select markers involved in EMT following berbamine treatment. Data in Figures 3(d) and 3(e) show that berbamine augmented E-cadherin expression and concomitantly decreased the levels of N-cadherin, vimentin, and MMP-9 in both cell lines. Therefore, the outcomes validated that berbamine attenuated cell metastasis by repressing the EMT process.

The remodeling of the actin cytoskeleton also plays a vital role in metastasis [23]. Filopodia are actin-based protrusions that mainly arise on the ventral surface of the cell membrane to assimilated signals like chemokines, nutrients, and chemoattractants [24, 25]. We next stained the cytoskeleton and pseudopodia with fluorescein-conjugated phalloidin. An interesting observation showed that 5637 and T24 cells without berbamine treatment maintained the spindle- and fibroblast-like appearance with lamellipodia at the cell perimeter. However, the treated cells exhibited a cobblestone-like morphology (Figure 3(f)), which was a feature of epithelial cells. Furthermore, there were few cellular protrusions and contact surfaces between cancer cells. In summary, it seemed clear that the inhibitory effects of berbamine on metastasis were also associated with cytoskeletal rearrangement.

3.4. Berbamine Inhibited the Biological Activities of Bladder Cancer Cells by Suppressing the NF-κB Pathway. The exceptional NF-κB pathway is known as a crucial participant in cell proliferation and EMT in bladder cancer, and blockade of the NF-κB pathway could inhibit tumorigenesis and the progression of malignancies [26–28]. Previous studies have indeed identified berbamine as a novel inhibitor of the NF-κB

(a)

(b)

(c)

(d)

(e)

(f)
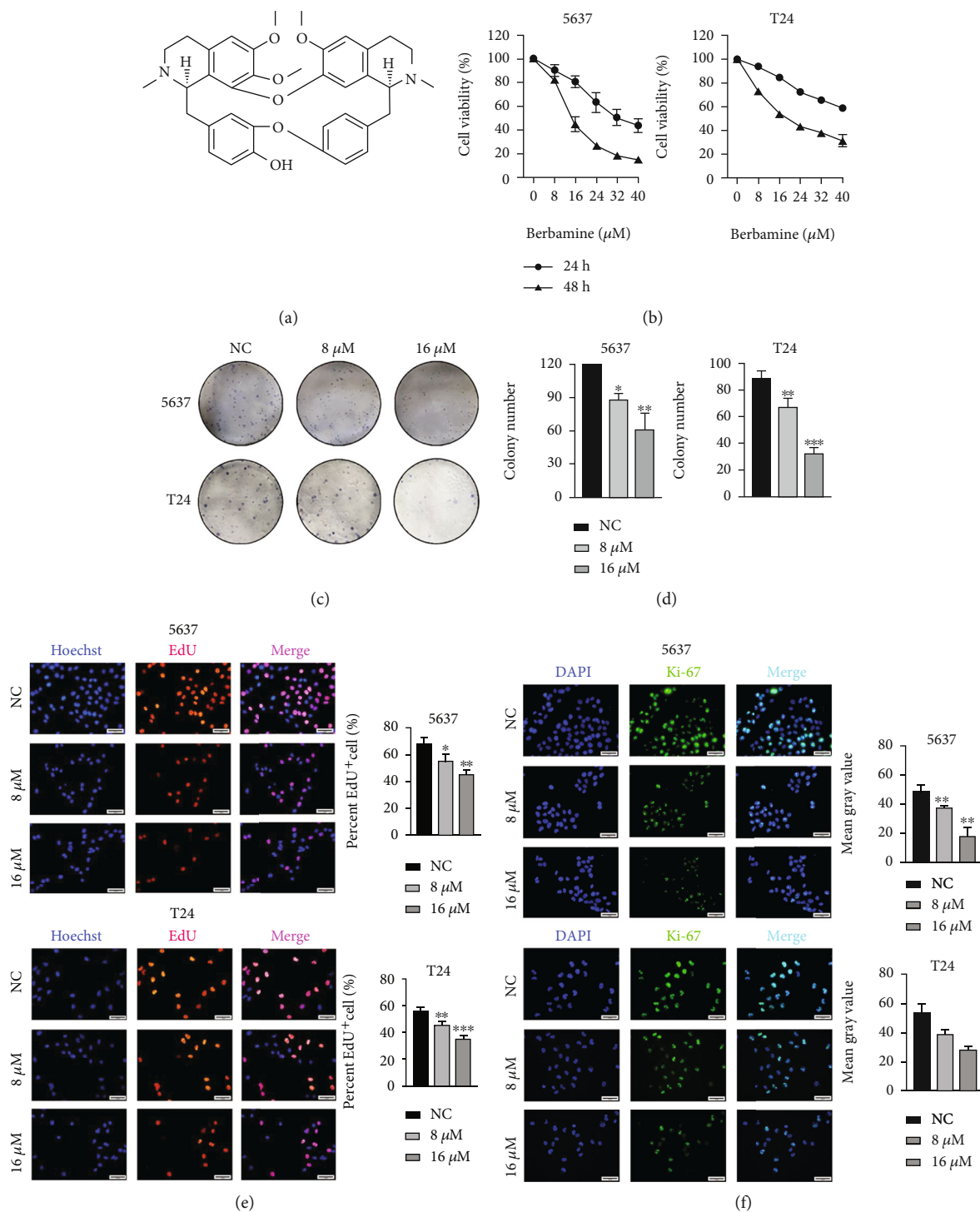
FIGURE 1: Inhibitory effects of berbamine on the proliferation of bladder cancer cells in vitro. (a) The chemical structure of berbamine was depicted. (b) A CCK-8 assay was conducted to evaluate the viability of 5637 and T24 cells treated with different concentrations of berbamine. (c, d) Representative images of colony formation assays and quantitative analysis of the numbers of colonies. (e) EdU assay: cell nuclear dye Hoechst (blue) and red fluorescence stands for DNA synthesis; percentage of EdU-positive cells of each group was calculated using a fluorescence microscope. (f) Representative images of the Ki-67 level in 5637 and T24 cells treated with berbamine. Green indicates Ki-67 intensity, and DAPI staining is for nuclei visualization. Values are represented (all dates are expressed) as the mean $\pm$ SD. The experiment was repeated at least three times. Statistical significance was determined using two-tailed Student's t-test or one-way ANOVA. $^*p < 0.5$; $^{**}p < 0.01$; $^{***}p < 0.001$.

(a)

(b)

(c)

(d)

Figure 2: Berbamine induced S-phase arrest in bladder cancer cells. (a, b) Representative images and quantitative cell cycle distribution was detected by flow cytometry. (c, d) The protein levels of a cell cycle regulator involving P21, P27, CyclinD, CyclinA2, and CDK2 were examined by western blotting, and ImageJ analyzed relative expression levels. Values are represented (all dates are expressed) as the mean ± SD. The experiment was repeated at least three times. Statistical significance was determined using two-tailed Student's t-test or one-way ANOVA. $^{*}p < 0.5$; $^{**}p < 0.01$; $^{***}p < 0.001$.

(a)

(b)

(c)

(d)

(e)

FIGURE 3: Continued.

(f)

FIGURE 3: Berbamine inhibited migration and invasion of bladder cancer cell lines. 5637 and T24 cells were treated with the indicated concentrations of berbamine for 48 h. (a) Wound-healing assays were performed to evaluate the migration capacity. (b) Transwell assays with or without Matrigel were performed to evaluate the migration and invasion capacity. (c) The results of wound-healing assays and Transwell assays were analyzed using ImageJ. (d, e) The expression of EMT-related biomarkers was examined by western blotting. (f) Phalloidin dyeing of the F-actin cytoskeleton was performed to display morphological changes. The images were captured under inverted fluorescent microscopy. Values are represented (all dates are expressed) as the mean ± SD. The experiment was repeated at least three times. Statistical significance was determined using two-tailed Student's t-test or one-way ANOVA. $^{*}p < 0.5$; $^{**}p < 0.01$; $^{***}p < 0.001$; $^{****}p < 0.0001$.

pathway with antitumor activity [29–31]. Thus, we hypothesized that the inhibition of NF-κB activation is a potential mechanism by which berbamine interferes with the biological activities of bladder cancer. We measured the expression of the critical genes involved in the NF-κB signaling pathway. As predicted, the levels of total P65, P-P65, and P-IκBα were significantly decreased in the presence of berbamine (Figures 4(a) and 4(b)). To determine whether inactivation of the NF-κB pathway caused by berbamine was responsible for the reduction in proliferation and metastasis, we initially chose the pathway-specific inhibitor BAY-11-7082 and then assessed cell viability by CCK-8 assay. Our results proved that BAY-11-7082 alone exhibited superior inhibitory activity and exacerbated cytotoxicity mediated by berbamine (Figure 4(c)). On the other hand, the pcDNA3.1-P65 plasmid was constructed and subsequently transfected into 5637 and T24 cells. As shown in Figures 4(d) and 4(g), the level of P65 dramatically increased, suggesting successful transfection. As expected, P65 overexpression partially abolished the inhibitory effect of berbamine on cell proliferation and metastasis in the rescue experiments (Figures 4(h) and 4(i)), which indicated that the antitumor action of berbamine against bladder cancer cells was mediated, at least in part, by inhibiting the activity of the NF-κB signaling pathway.

3.5. Berbamine Triggered ROS Generation and Cell Apoptosis in Bladder Cancer. Mitochondria are vital sources of intracellular ROS involved in the regulation of diverse pathophysio-
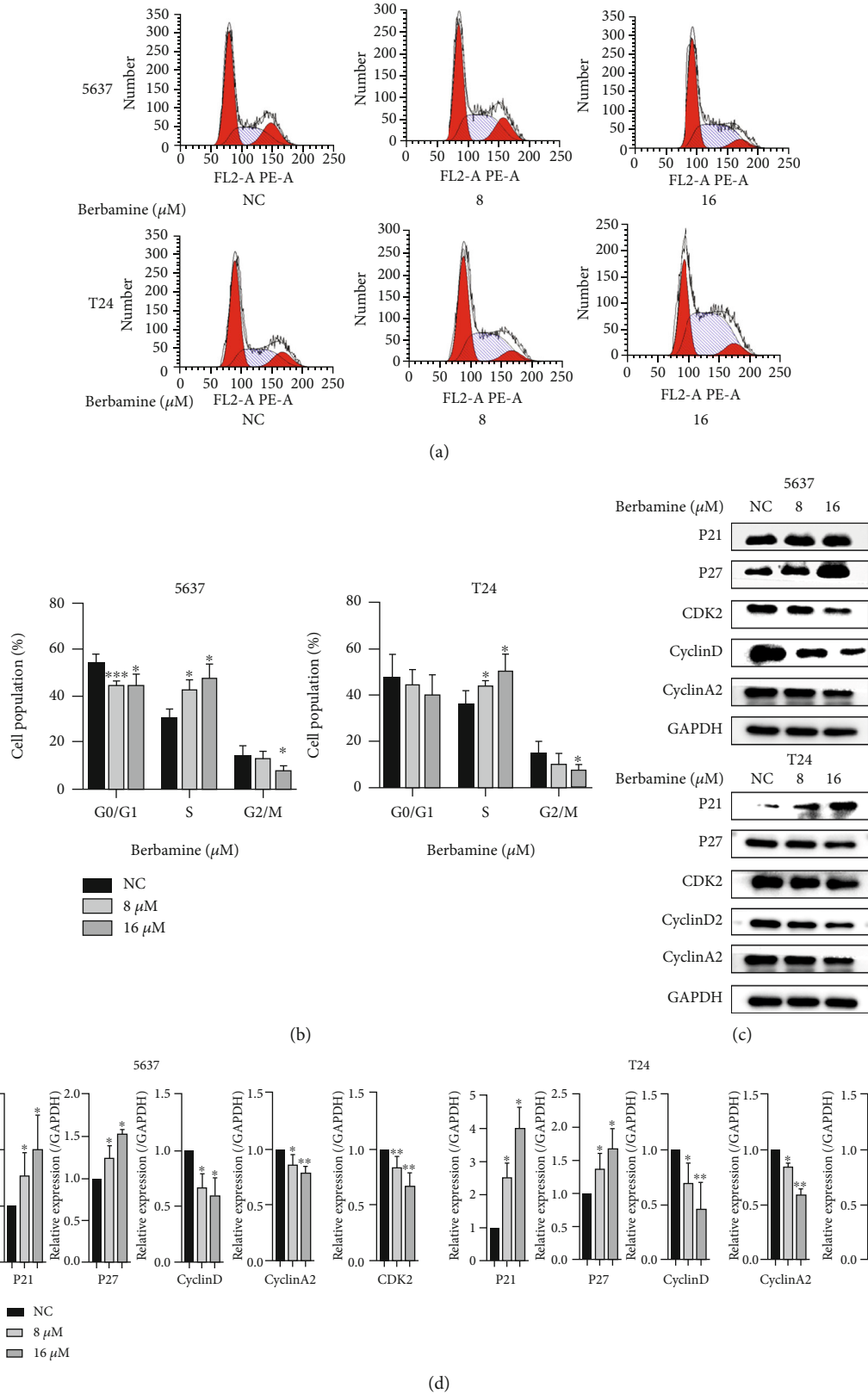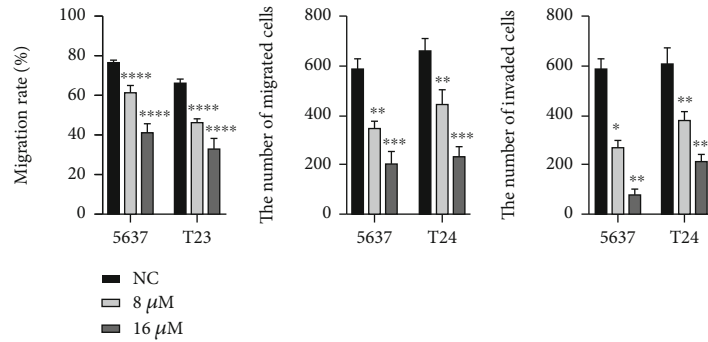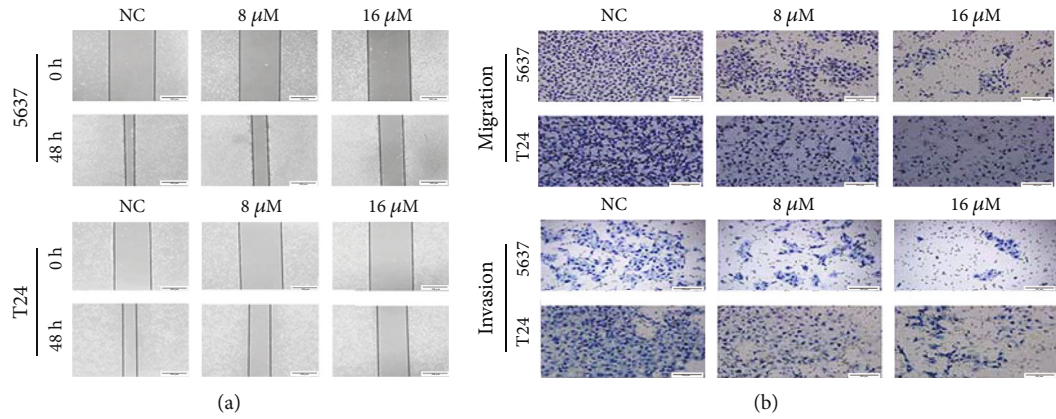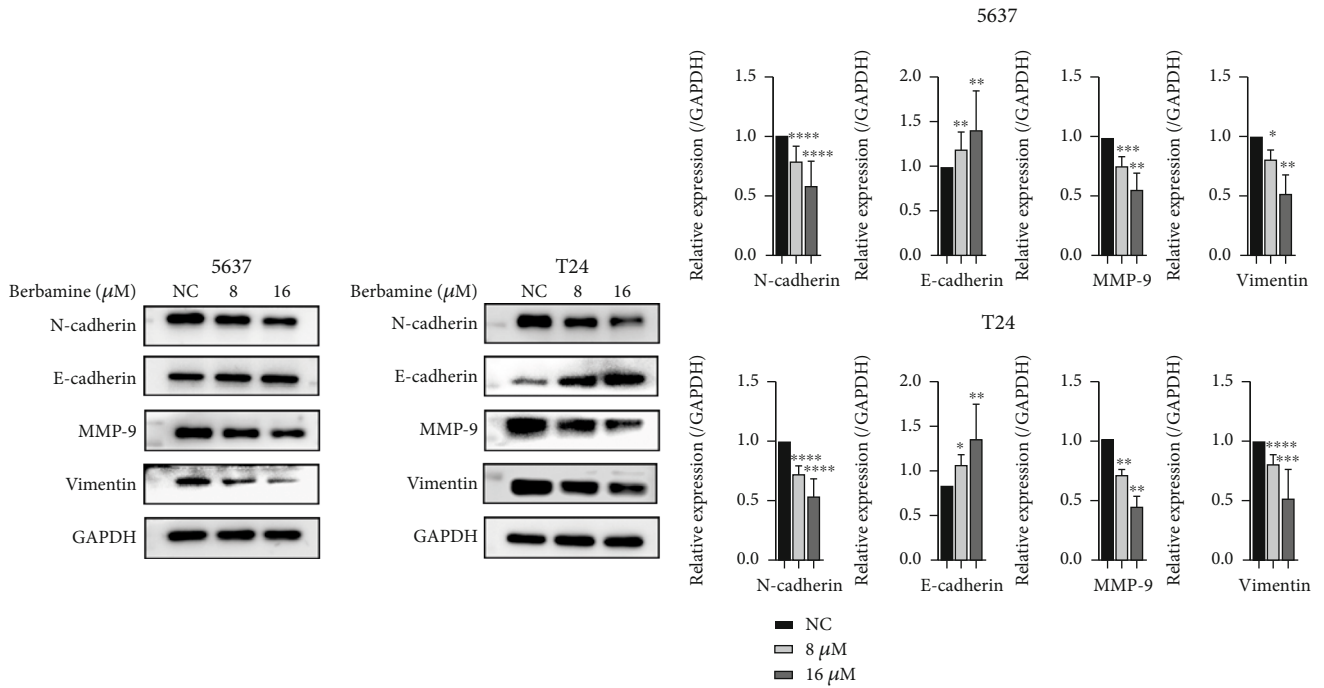
logic processes [32]. In addition, fluctuations in ROS levels could regulate the proliferation and apoptosis of cancer cells in response to multiple stimuli [33]. Due to their short half-lives, we evaluated the changes in ROS levels of 5637 and T24 cells incubated with 16 μM and 32 μM berbamine for 24 h. MitoSOX images (Figures 5(a) and 5(b)) showed that red fluorescence intensity was remarkably elevated, indicating that berbamine directly accelerated the generation of mitochondrial superoxide. In most cells, the level of ROS strictly depends on the dynamic equilibrium between ROS generation and antioxidant systems. Next, we detected the expression levels of a few antioxidative genes of bladder cancer cells following berbamine treatment. The Nrf2, HO-1, SOD2, and GPX-1 genes were substantially downregulated (Figures 5(c) and 5(d)), which explained that the ROS accumulation mediated by berbamine is associated with the deficiency of antioxidant defense.

We further used the Annexin V-FITC/PI double-staining method with flow cytometry to elucidate the cytotoxic effect of berbamine on BCa cells in more detail. As shown in Figures 5(e) and 5(f), an obvious increase in the apoptosis rate was found upon treatment with a higher concentration of berbamine. To understand the molecular evidence of berbamine-induced apoptosis, we analyzed the expression levels of Bcl-2 family proteins that are master regulators of mitochondrial apoptosis. Western blotting results showed that berbamine dose-dependently increased the expression of the proapoptotic Bax protein while significantly inhibiting

(a)

(b)

(c)

(d)

(e)

FIGURE 4: Continued.

(f)

(g)

(h)
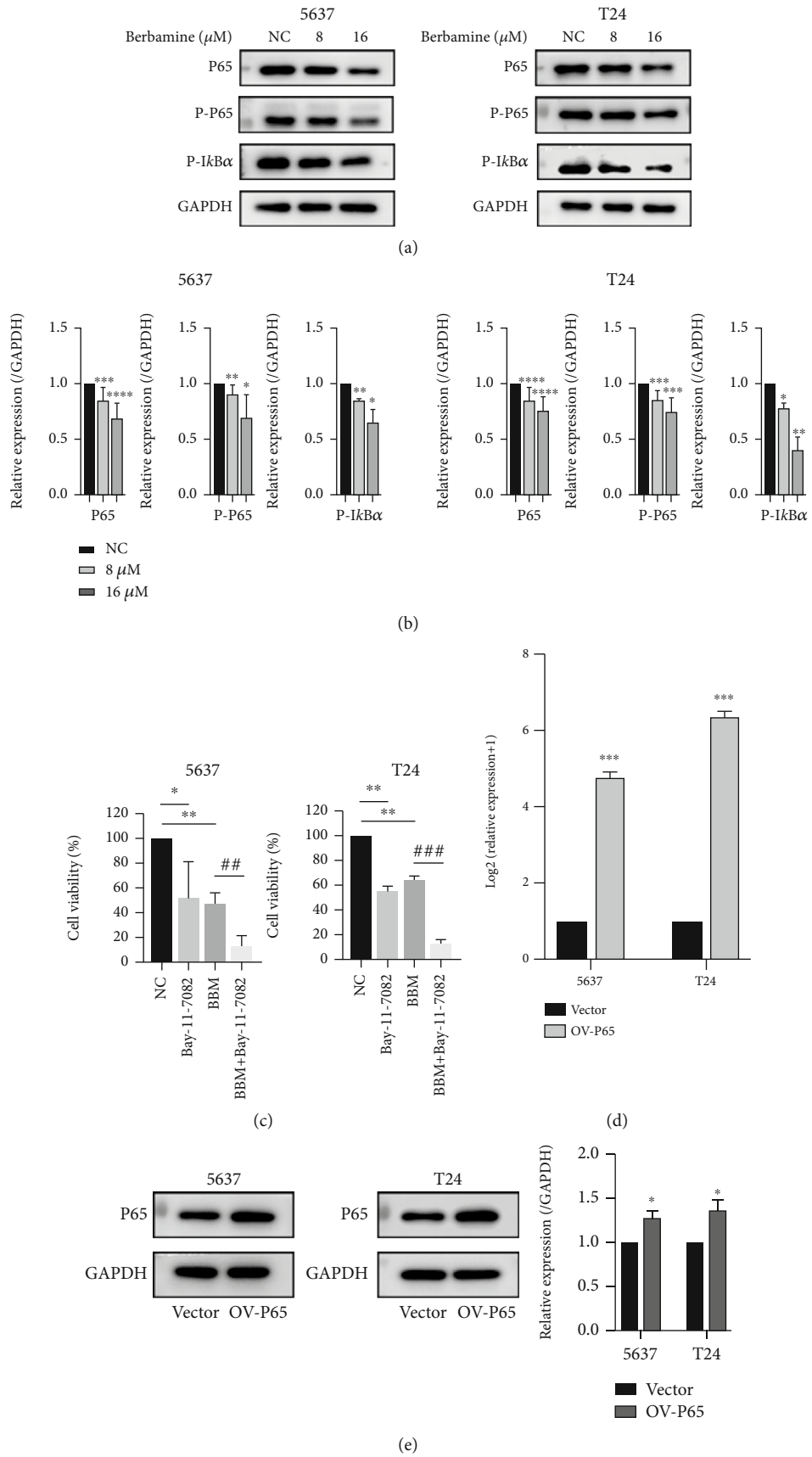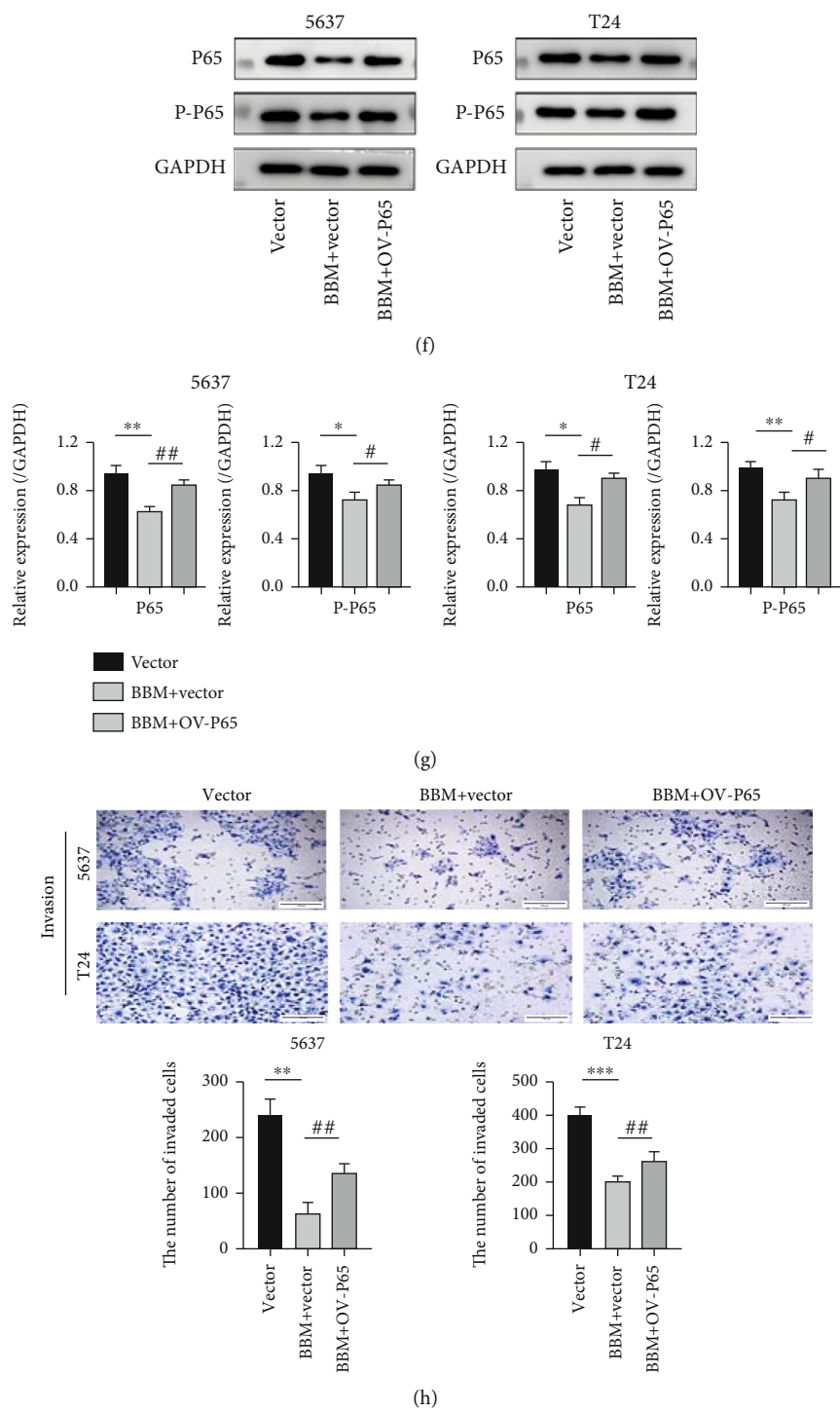
FIGURE 4: Continued.
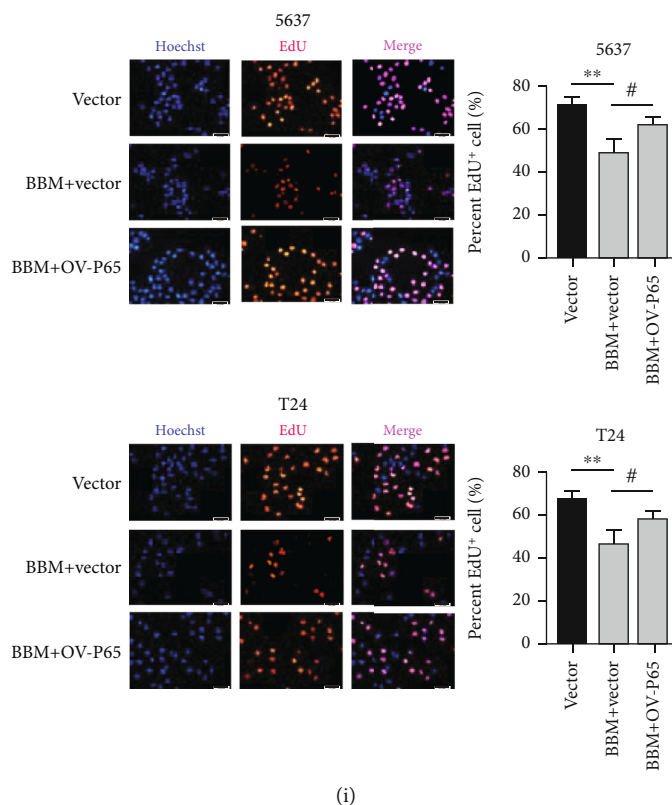
(i)

FIGURE 4: Berbamine inhibited the NF-κB pathway in bladder cancer cell lines. (a, b) Western blotting experiments were performed to detect the expression levels of NF-κB P65, P-P65, and P-IκBα in both 5637 and T24 cells following berbamine treatment for 48 h. (c) A CCK-8 assay evaluated cell viability via a comparison between group exposures to 16 μM berbamine and in the presence or absence of 10 μM BAY-11-7082. (d, e) To detect the effectiveness of transfection, qRT-PCR and western blotting were performed to measure the expression of P65 at 48 h posttransfection. (f, g) Western blotting was performed to detect the expression of P65 and P-P65 in 5637 and T24 cells after berbamine treatment with or without pcDNA3.1-P65. (h) In rescue experiments, the invasive potency of 5637 and T24 cells was evaluated by Transwell assays with Matrigel following berbamine treatment with or without pcDNA3.1-P65. (i) EdU assays were performed to detect the proliferative ability of 5637 and T24 cells following berbamine treatment with or without pcDNA3.1-P65. Values are represented (all dates are expressed) as the mean ± SD. The experiment was repeated at least three times. Statistical significance was determined using two-tailed Student's t-test or one-way ANOVA. $^*p < 0.5$; $^{**}p < 0.01$; $^{***}p < 0.001$; $^{****}p < 0.0001$; $^{\#}p < 0.5$; $^{\#\#}p < 0.01$.

the level of the antiapoptotic Bcl-2 protein in both cell lines (Figures 5(g) and 5(h)). Overall, berbamine increased the Bax/Bcl-2 ratio, which is critical for the initiation of the intrinsic apoptosis pathway.

3.6. Berbamine Exerted Antitumor Activity against Bladder Cancer Cells by Modulating the ROS/NF-κB Axis. It is well known that numerous anticancer drugs trigger cell apoptosis via a ROS-dependent pathway [34, 35]. Accordingly, we further explored whether cell apoptosis caused by berbamine is directly relevant to ROS accumulation. To confirm this hypothesis, we applied N-acetylcysteine (NAC), a ROS scavenger, to the berbamine-treated group in advance. As shown in Figures 6(a) and 6(b), pretreatment with NAC partially prevented berbamine-mediated mitochondrial ROS generation, followed by a decrease in bladder cancer cell apoptosis (Figures 6(c) and 6(d)). Consistent with the flow cytometry assay results, western blotting analysis showed that NAC partially reversed the effects of berbamine on the protein levels of Bcl-2 and Bax (Figures 6(e) and 6(f)). Numerous articles have demonstrated that ROS can modify cell-signaling pro-

teins to mediate multiple pathways. We further explored the correlation between ROS and NF-κB. We observed that the ROS inhibitor counteracted the NF-κB pathway suppression mediated by berbamine to a certain degree (Figures 6(g) and 6(h)). Taken together, these observations indicated that the ROS/NF-κB axis plays a vital role in the antitumor activity of berbamine against bladder cancer.

3.7. Antitumor Effect of Berbamine In Vivo. To further validate the antitumor effect of berbamine in vivo, we established a human-T24 subcutaneous xenograft in nude mice and recorded mouse weight and tumor weight throughout the experiment. As exhibited in Figures 7(a) and 7(b), berbamine exerted apparent cytotoxicity against cancer cells in vivo. The tumor volume and weight of the berbamine-treated group grew much more slowly than those of the control group (Figures 7(c) and 7(d)); however, there was no significant difference in the average weight of mice between the control group and the berbamine-treated group (Figure 7(e)), suggesting that berbamine possibly had no evident adverse effects in vivo.
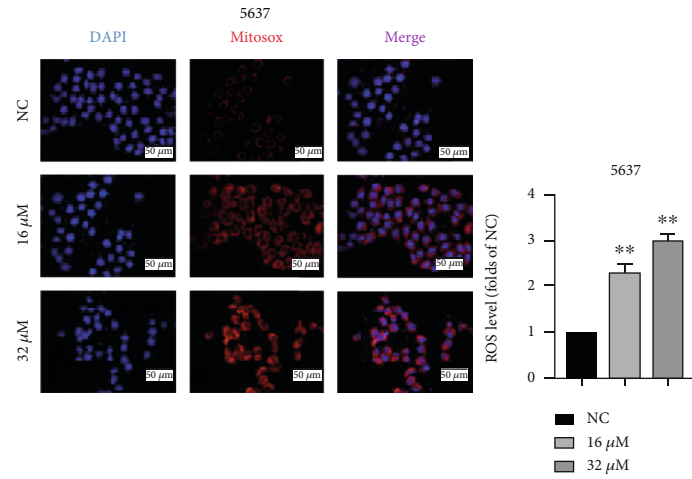
(a)
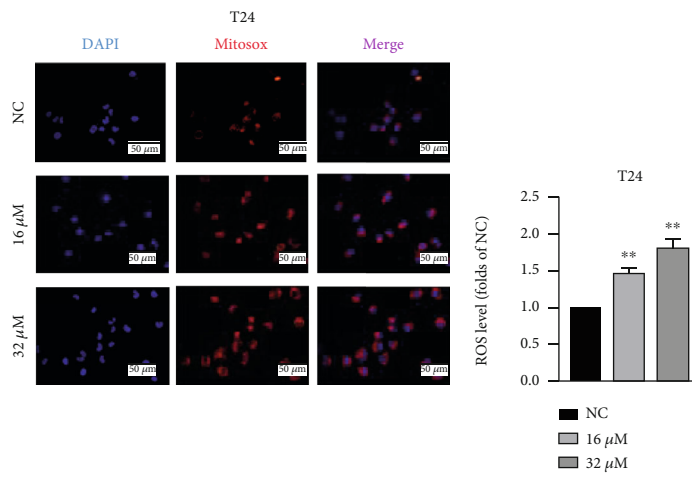
(b)
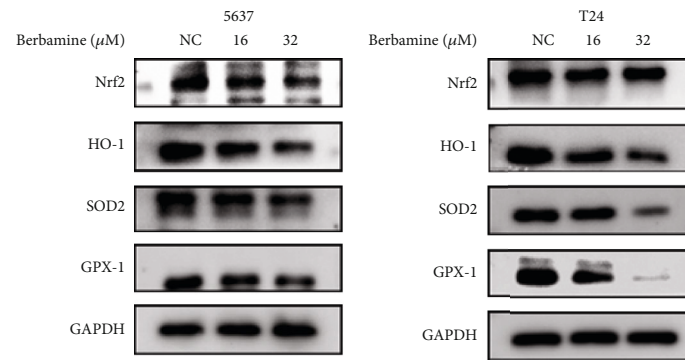
(c)

Figure 5: Continued.

(d)

(e)

(f)

(g)

Figure 5: Continued.

(h)
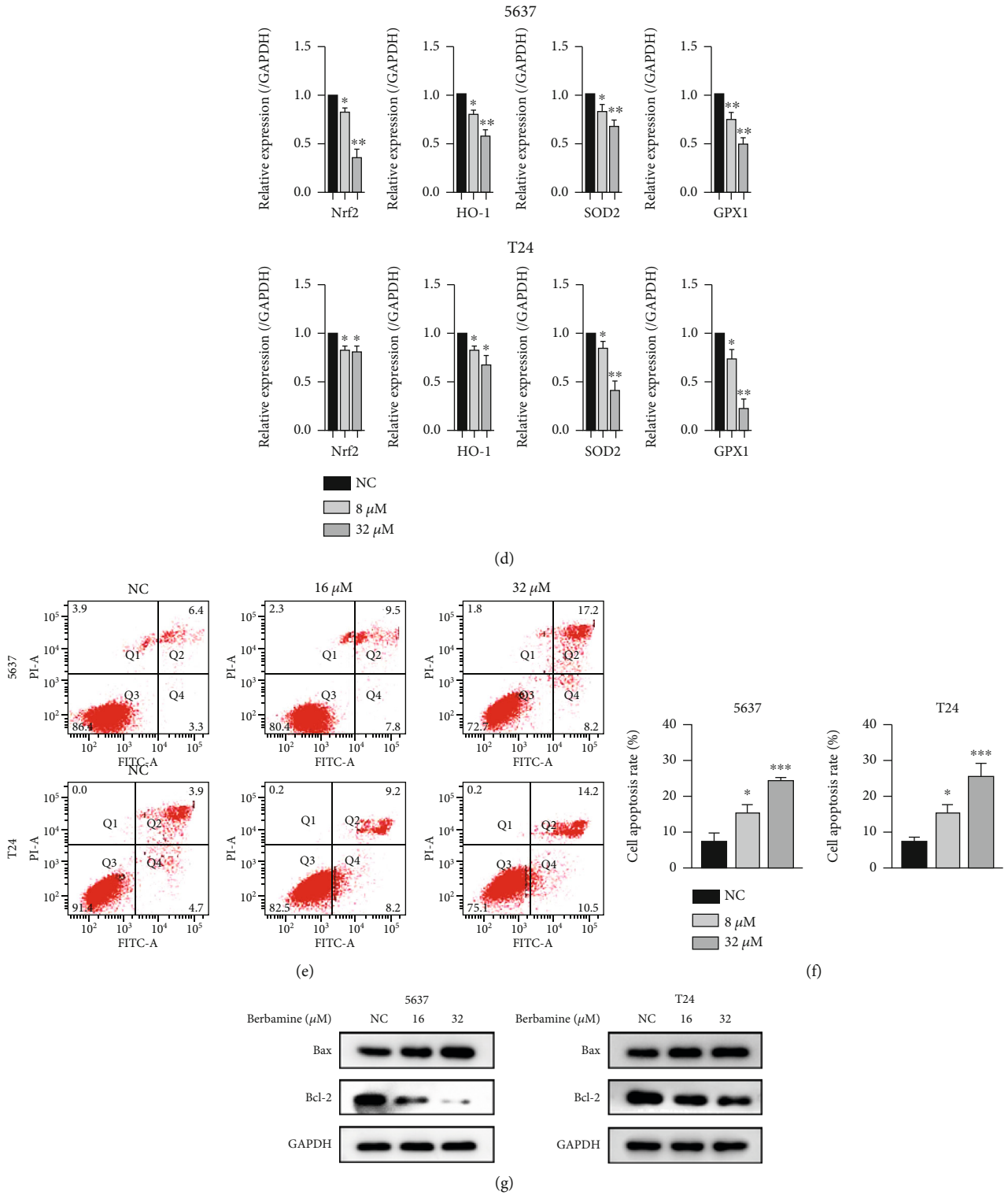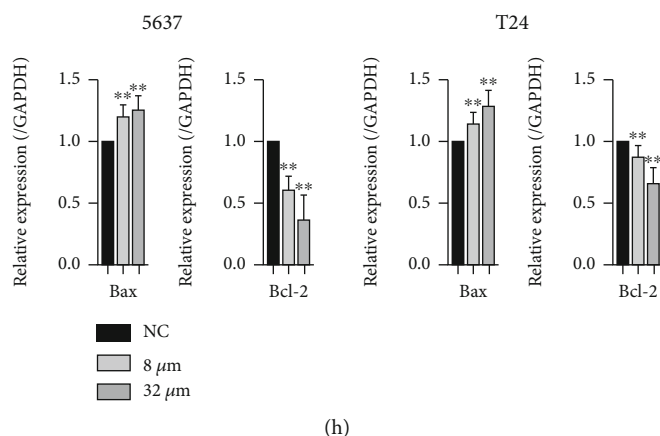
FIGURE 5: Berbamine-mediated ROS generation and apoptosis in bladder cancer cells. 5637 and T24 cells were incubated with $16\,\mu M$ and $32\,\mu M$ berbamine for 24 h. (a, b) MitoSOX fluorescence was performed to detect ROS generation. As a live-cell permeant fluorogenic dye, MitoSOX gets oxidized by mitochondrial superoxide to exhibit red fluorescence. Relative fluorescence intensity was analyzed by ImageJ. (c, d) The effects of berbamine on the levels of several antioxidant genes. (e, f) Flow cytometry was performed to determine the apoptotic percentage. (g, h) The effect of berbamine on the expression of Bcl-2 and Bax proteins. Values are represented (all dates are expressed) as the mean ± SD. The experiment was repeated at least three times. Statistical significance was determined using two-tailed Student's t-test or one-way ANOVA. $^{*}p < 0.5$; $^{**}p < 0.01$; $^{***}p < 0.001$.

4. Discussion

Bladder cancer is the most common malignant tumor of the urinary system, with high incidence and recurrence. Thus far, studies have extensively reported the pathogenesis and current therapeutic strategies of bladder cancer, consisting of surgical resection, immune checkpoint inhibition, and a combination of chemotherapy drugs. However, there are few studies on Chinese traditional medicine applications in clinical cancer therapy, which is possibly due to a lack of a comprehensive understanding of their mechanisms and safety. Berbamine is one of the active ingredients extracted from the herbal medicine *Berberis* and possesses multiple biological activities, including immunomodulatory, antihypertensive, and cardioprotective properties [36–38].

Natural compounds and their derivatives extracted from traditional Chinese herbs can be considered as ideal alternative anticancer agents owing to their lower cost, stronger effectiveness, and minimal side effects [11, 39]. Berbamine has exhibited favorable antitumor potential in previous studies, as it modulates various molecular targets and has low cytotoxicity in normal cells. For instance, berbamine suppressed cell growth and invasion ability while inducing G0/G1 cell cycle arrest and apoptosis by inhibiting Wnt/β-catenin signaling in ovarian cancer [9]. Additionally, berbamine exerted antitumor effects in vitro and in vivo through apoptosis induction partially relevant to the activation of the p53 gene in colorectal cancer [8]. Moreover, berbamine enhanced the efficacy of gefitinib in pancreatic cancer cells

IHC analysis showed that the positive rate of Ki-67 and P65 in the tumor tissue of the berbamine-treated group was significantly lower than that in the control group (Figures 7(f) and 7(g)), which is consistent with our in vitro results. Overall, our results suggested that berbamine reduces tumor growth and suppresses NF-κB signaling in vivo.

and radiosensitivity for head and neck squamous cell carcinoma by inhibiting the STAT3 pathway [40, 41]. Herein, we attempted to unambiguously investigate the effects and potential mechanisms of berbamine in bladder cancer in vitro and in vivo.

Cancer-cell-based experiments manifested that berbamine inhibited cell viability and impaired the colony formation ability of bladder cancer cells. Also, the EdU and Ki-67 immunofluorescence assay collectively revealed the antiproliferative effect of berbamine on bladder cancer.

Cell cycle deregulation leads to infinite cell proliferation, which is an elementary characteristic directly related to tumor progression. Thus, targeting the cell cycle pathway is emerging as a fundamental strategy to arrest neoplastic processes [33, 42]. The data of the present study demonstrated that berbamine induced significant S-phase arrest in bladder cancer cells. Regulations of the cell cycle are tightly dependent on the coordinated activity of protein kinase complexes that consist of cyclins, cyclin-dependent kinases (CDKs), and endogenous inhibitor proteins (CKIs). Progression through G1 phase is driven by activation of the CyclinA-CDK2 complex, and CyclinA is required for DNA replication throughout the S phase [43, 44]. To our knowledge, P21 and P27, inhibitors of CDKs, bind to these Cyclin-CDK complexes and induce their inactivation, thus halting cell cycle progression [45]. Concurrently, we observed that berbamine dramatically downregulated the expression of CyclinD, CyclinA2, and CDK2 and upregulated the levels of P21 and P27, which indicated that berbamine-induced S-phase arrest was mainly driven by enhanced initiation of S phase and concomitant suppression of S-phase progression.

Metastasis, the property that enables individual cancer cells to spread into local or distant tissues [46], remains a stumbling block limiting the effective therapy of bladder cancer and is also the leading cause of cancer mortality. EMT is a critical process responsible for the acquisition of malignant

(a)

(b)

(c)

(d)

(e)

(f)

(g)

Figure 6: Continued.

(h)

FIGURE 6: Berbamine exerted antitumor activity against bladder cancer cells by modulating the ROS/NF-κB axis. 5637 and T24 cells were treated with 32 μM berbamine in the presence or absence of 10 mM NAC. (a, b) Representative images of the ROS generation level were captured using a fluorescence microscope. (c, d) Flow cytometry was performed to measure cell apoptosis. (e, f) The levels of Bcl-2 and Bax proteins were measured by western blotting. (g, h) The levels of P65 and P-P65 proteins were measured by western blotting. Values are represented (all dates are expressed) as the mean ± SD. The experiment was repeated at least three times. Statistical significance was determined using two-tailed Student's t-test or one-way ANOVA. $^*p < 0.5$; $^{**}p < 0.01$; $^{***}p < 0.001$; $^{\#}p < 0.5$; $^{\#\#}p < 0.01$.

phenotypes in epithelial tumor cells [47]. In this process, cancer cells could lose cell adhesion attributes and acquire cytoskeletal activation [48]. Furthermore, EMT can endow tumor cells with stem cell characteristics, thus resulting in a poor prognosis for cancer patients [49]. Activation of NF-κB is correlated with the induction of a well-defined set of transcription factors involved in EMT, such as Snail, Slug, Twist, and ZEB1/ZEB2 [50]. It was reported that NF-κB P65, as a transcriptional activator, facilitated Snail transcription by directly binding to the promoter [51]. MMP-9 plays a crucial role in the invasive process of various solid tumors by degrading the extracellular matrix barrier [52]. The promoter of MMP-9 has been characterized as having a series of functional enhancer element-binding sites, such as NF-κB and activator proteins (AP-1) [50]. Therefore, the inactivation of NF-κB could decrease the basal transcriptional activity of the MMP-9 promoter, thus inhibiting the expression of the MMP-9 protein. Interestingly, we observed that berbamine could remarkably dampen the migration and invasion capacity of both cell lines. Western blotting revealed that berbamine increased E-cadherin expression while decreasing N-cadherin, vimentin, and MMP-9 expression. In our rescue experiment, P65 overexpression increased the number of invasive cells among those treated with berbamine. Thus, we postulated that berbamine might suppress the metastatic ability of bladder cancer cells through reversal of NF-κB-mediated EMT. Moreover, berbamine impaired the cytoskeletal organization of 5637 and T24 cells. The cytoskeleton changed into an epithelial morphology upon exposure to berbamine, which could facilitate tight adhesion to avoid cell metastasis.

Apoptosis, also known as type I genetically programmed cell death, is a normal physiological process that accompanies morphological and biochemical changes involving DNA fragmentation, chromatin condensation, and membrane blebbing. To the best of our knowledge, apoptosis can be activated by either the extrinsic pathway initiated by the death receptor or intrinsic pathway through the mitochondria to prevent tumor formation. In our results

presented here, berbamine elevates bladder cancer cell apoptosis in a dose-dependent manner. Previous studies confirmed that members of the Bcl-2 family, as key regulatory factors of the mitochondrial-mediated pathway, play an essential role in the antiapoptosis response [53–55]. Both Bax and Bcl-2 belong to the Bcl-2 family, and the ratio of Bax/Bcl-2 is relevant to the sensitivity or resistance of cancer cells to apoptotic stimuli and therapeutic drugs [56]. Western blotting revealed that berbamine reduced the level of the Bcl-2 protein but increased the level of the Bax protein. In a word, berbamine activates the mitochondrial-dependent apoptotic pathway by targeting the Bcl-2 family to exert a cytotoxic effect on bladder cancer cells.

Strict control of ROS levels is vital to regulate cell repair, survival, and differentiation [57]. Several lines of evidence highlight that once the redox status deviates to oxidation, the increased ROS function as redox messengers to accelerate the early events involving tumorigenesis and tumor progression. Mechanistically, as an upstream factor, ROS mediate DNA mutations and modulate various cellular signaling pathways, thus affecting several cancer hallmarks of metabolic reprogramming, angiogenesis, metastasis, and drug resistance development [58]. However, when the continued increase in ROS levels overwhelms intracellular antioxidant capacity, it can stimulate cell cycle arrest and cellular apoptosis [59]. Compared to normal cells, tumor cells are more sensitive to fluctuations in ROS levels, and excessive ROS induction is a common mechanism by which various antitumor agents scavenge cancer cells [60, 61]. ROS-mediated apoptosis is known to open the permeable transition pore of the mitochondrial membrane with the release of cytochrome c by regulating Bcl-2 family genes [62]. Representative MitoSOX images initially demonstrated that berbamine dose-dependently accumulated mitochondrial ROS in both cell lines. Not surprisingly, previous studies reported that berbamine, as a prooxidant, effectively induced intracellular ROS generation, thus enhancing the sensitivity of glioma cells to paclitaxel therapy [63]. It indicated that berbamine might modulate ROS levels to influence the biological
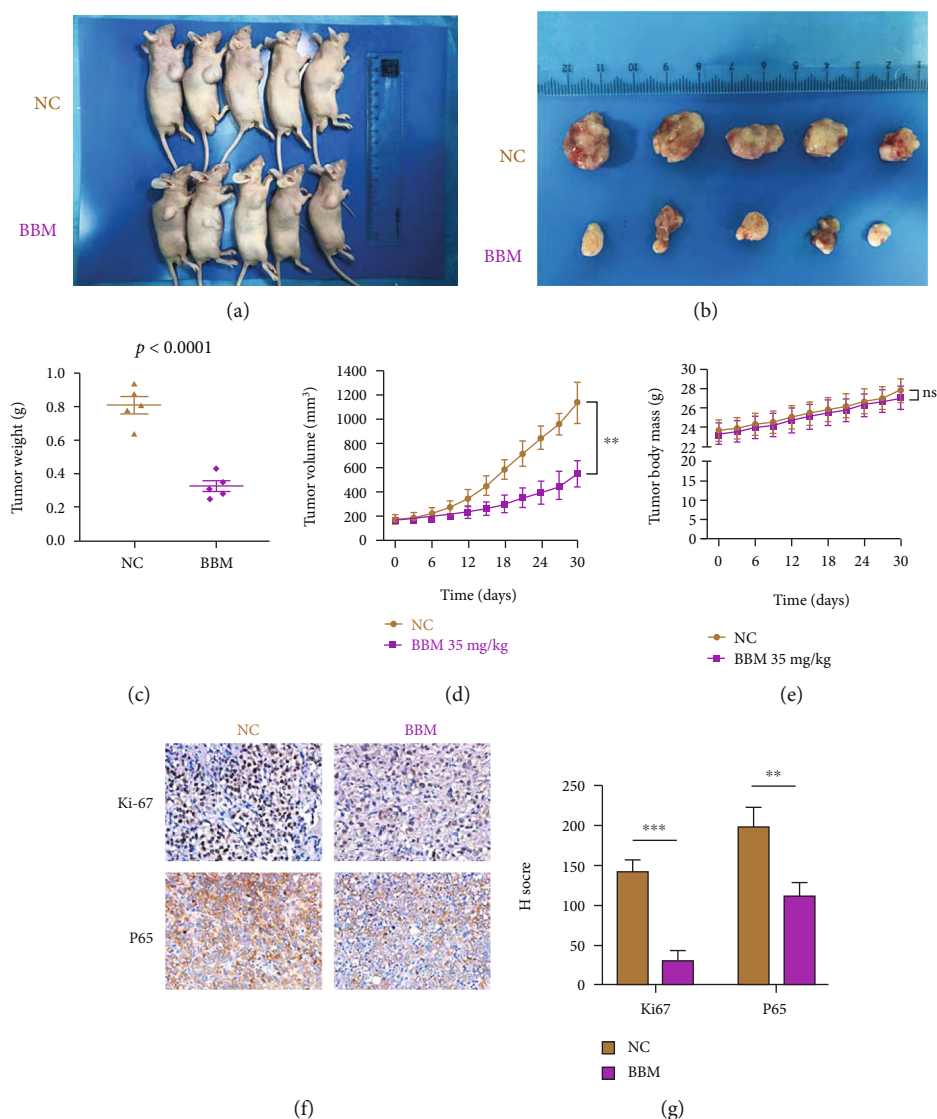
FIGURE 7: Berbamine inhibited the growth of the T24 xenograft tumor in vivo. Nude mice were treated with 35 mg/kg berbamine and the same DMSO via intraperitoneal injection every three days for 30 days. (a, b) Photographs of the tumors were taken at autopsy. (c) The weight of tumors in nude mice was measured. (d, e) The tumor volumes and body weight of nude mice were monitored every three days by the end of this experiment. (f) The levels of Ki-67 and P65 in tumor tissues were evaluated via IHC. (g) IHC staining score for Ki-67 and P65 protein. Values are represented (all dates are expressed) as the mean ± SD. The experiment was repeated at least three times. Statistical significance was determined using two-tailed Student's t-test or one-way ANOVA. $^{**}p < 0.01$; $^{***}p < 0.001$.

behaviors of cancer cells. To further explore the mechanism underlying ROS generation, we measured the expression of a few crucial antioxidative genes. Western blotting results suggested that the levels of the Nrf2, HO-1, SOD2, and GPX-1 genes were downregulated following berbamine treatment, which implies that berbamine impaired the functions of the antioxidant system, followed by ROS production. Intriguingly, the apoptosis caused by berbamine was mitigated following the use of the antioxidant NAC, along with the reversal of Bcl-2 and Bax expression. As stated previously, excessive ROS generation upon the tolerable threshold plays a crucial role in the proapoptotic effect of berbamine on bladder cancer.

In response to multiple stimuli, aberrant activation of the NF-κB signaling pathway participates in multiple malignant transformation processes by mediating the downstream oncogenic genes. However, earlier research confirmed that the NF-κB pathway is constitutively activated in bladder cancer and is associated with muscle-invasive clinical features [64]. Herein, western blot analysis showed that berbamine negatively regulated the expression of P65, P-P65, and P-IκBα, which indicated that berbamine blocked the NF-κB signaling pathway. However, it remains unclear whether inactivation of the NF-κB signaling pathway is sufficient to influence the progression of BCa cells. Suppression of NF-κB activity by the specific inhibitor BAY-11-7082 dramatically inhibited cell viability in both cell lines assessed. Meanwhile, our rescue experiment revealed that cell proliferation was reversed following P65 overexpression. In addition, the activity of NF-κB function can be regulated by ROS in
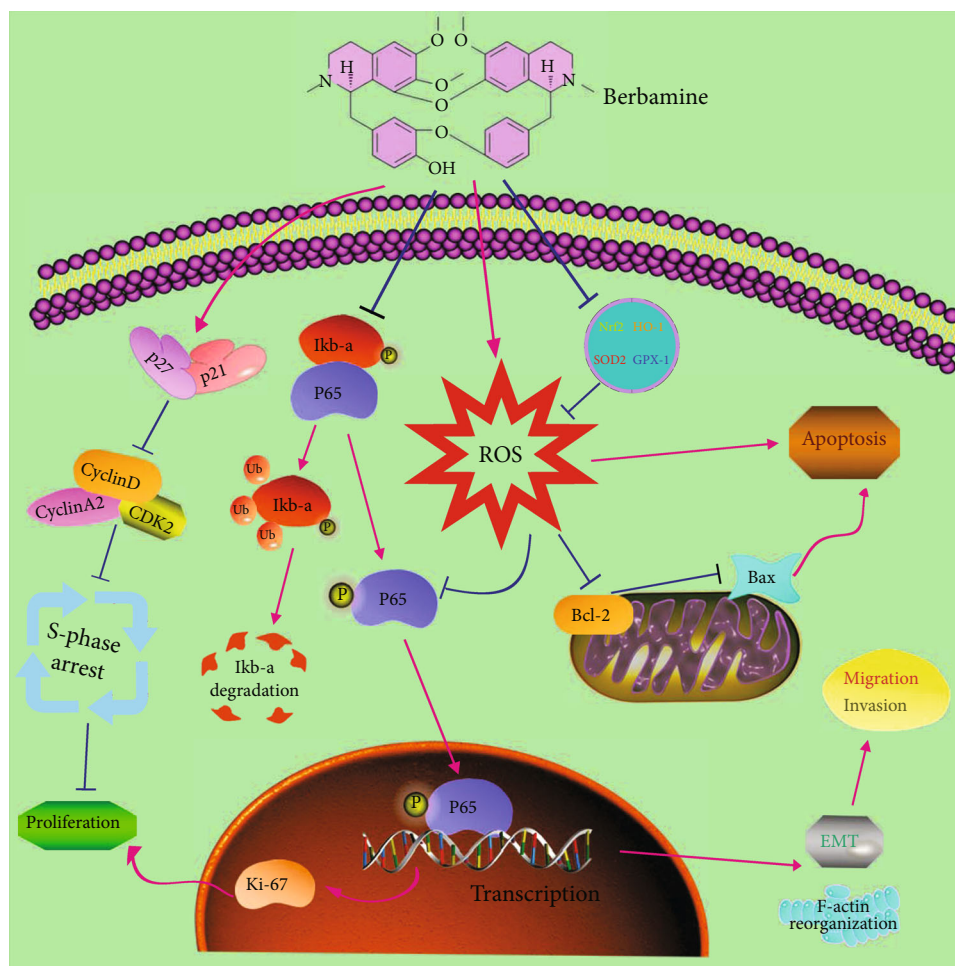
FIGURE 8: The potential mechanisms of berbamine occurring in bladder cancer cells.

different contexts [65]. NF-κB activation is associated with ROS-mediated oxidation and activation of inhibitors of NF-κB (IκB) kinases, which negatively control the stability of IκB. On the other hand, ROS inhibit NF-κB transcriptional activity by interfering with NF-κB DNA binding owing to the presence of oxidizable cysteines in the DNA-binding region [66]. In this paper, we identified a relationship in which ROS generated by berbamine acted as an upstream molecule to partially inhibit the NF-κB pathway, which implies the indispensable role of the ROS/NF-κB axis in berbamine-mediated antitumor activities against BCa cells.

Finally, a xenograft mouse model was established to further determine the inhibitory growth effects of berbamine in vivo. Consistent with the promising results in vitro, berbamine could reduce the tumor volume and weight. However, there was no significant difference in the average weight of mice between the control group and the berbamine-treated group, indicating that berbamine probably has no evident side effects in vivo. The results of human pharmacokinetic studies revealed that the half-life of berbamine was 39.25 h in the body, indicating that the compound's elimination was slow [67]. Thus, berbamine could be accumulated to an efficient concentration in vivo, although lower-dose drugs

are administered. Further clinical studies are needed to explore a better dosage regimen. As indicated by IHC, the positive staining rate of Ki-67 and P65 frequently declined in the tumor tissue after berbamine treatment, which suggests that berbamine suppresses tumor growth and NF-κB signaling in vivo.

5. Conclusion

We elucidated for the first time that berbamine could exert antitumor activities in bladder cancer by inhibiting cell proliferation and metastasis and inducing cell cycle arrest at S phase in vitro. Further analysis highlighted that berbamine suppresses the aberrantly active NF-κB signaling pathway to interfere with the progression of bladder cancer. In addition, ROS accumulation induced by berbamine contributes to the intrinsic apoptosis of bladder cancer cells and inhibits the NF-κB pathway to some extent (Figure 8). Finally, our in vivo experiments corroborate our in vitro findings. Based on the above results, it can be concluded that berbamine has potential clinical applications for patients with bladder cancer. Future studies are encouraged to ensure its drug safety and clarify its broader mechanisms.

Data Availability

The data used to support the findings of this study are available from the corresponding authors upon request.

Conflicts of Interest

All authors declare that they have no conflicts of interest related to this paper.

Authors' Contributions

Chenglin Han finished all of the experiments, analyzed data alone, and wrote the original draft. Chenglin Han, Zilong Wang, and Lin Li performed article revision. Weiting Kang and Chunxiao Wei performed supervision. Hongbin Ma provided suggestions in the experiment process. Muwen Wang and Xunbo Jin obtained funding and approved the final manuscript. Shuxiao Chen supplied additional experiment data.

Acknowledgments

References

[1] A. A. Proskokov, S. P. Darenkov, A. A. Agabekian, and A. D. Trofimchuk, "Current trends in the method used for urine derivation after radical cystectomy for muscle-invasive bladder cancer," *Urologiia*, no. 6, pp. 120–124, 2019.

[2] F. Bray, J. Ferlay, I. Soerjomataram, R. L. Siegel, L. A. Torre, and A. Jemal, "Global cancer statistics 2018: GLOBOCAN estimates of incidence and mortality worldwide for 36 cancers in 185 countries," *CA: a Cancer Journal for Clinicians*, vol. 68, no. 6, pp. 394–424, 2018.

[3] C. E. DeSantis, C. C. Lin, A. B. Mariotto et al., "Cancer treatment and survivorship statistics, 2014," *CA: a Cancer Journal for Clinicians*, vol. 64, no. 4, pp. 252–271, 2014.

[4] P. Vishnu, J. Mathew, and W. W. Tan, "Current therapeutic strategies for invasive and metastatic bladder cancer," *Oncotargets and Therapy*, vol. 4, pp. 97–113, 2011.

[5] M. Halasi, B. Hitchinson, B. N. Shah et al., "Honokiol is a FOXM1 antagonist," *Cell Death & Disease*, vol. 9, no. 2, p. 84, 2018.

[6] R. Z. Li, X. X. Fan, F. G. Duan et al., "Proscillaridin A induces apoptosis and suppresses non-small-cell lung cancer tumor growth via calcium-induced DR4 upregulation," *Cell Death & Disease*, vol. 9, no. 6, p. 696, 2018.

[7] W. Tan, J. Zhou, and G. Yuan, "Electrospray ionization mass spectrometry probing of binding affinity of berbamine, a flexible cyclic alkaloid from traditional Chinese medicine, with G-quadruplex DNA," *Rapid Communications in Mass Spectrometry*, vol. 28, no. 1, pp. 143–147, 2014.

[8] H. Zhang, Y. Jiao, C. Shi et al., "Berbamine suppresses cell viability and induces apoptosis in colorectal cancer via activating p53-dependent apoptotic signaling pathway," *Cytotechnology*, vol. 70, no. 1, pp. 321–329, 2018.

[9] H. Zhang, Y. Jiao, C. Shi et al., "Berbamine suppresses cell proliferation and promotes apoptosis in ovarian cancer partially via the inhibition of Wnt/β-catenin signaling," *Acta Biochim Biophys Sin (Shanghai)*, vol. 50, no. 6, pp. 532–539, 2018.

[10] Y. Zhao, J. J. Lv, J. Chen et al., "Berbamine inhibited the growth of prostate cancer cells in vivo and in vitro via triggering intrinsic pathway of apoptosis," *Prostate Cancer and Prostatic Diseases*, vol. 19, no. 4, pp. 358–366, 2016.

[11] Z. Meng, T. Li, X. Ma et al., "Berbamine inhibits the growth of liver cancer cells and cancer-initiating cells by targeting Ca^{2+}/-calmodulin-dependent protein kinase II," *Molecular Cancer Therapeutics*, vol. 12, no. 10, pp. 2067–2077, 2013.

[12] B. D'Autreaux and M. B. Toledano, "ROS as signalling molecules: mechanisms that generate specificity in ROS homeostasis," *Nature Reviews. Molecular Cell Biology*, vol. 8, no. 10, pp. 813–824, 2007.

[13] M. Hayyan, M. A. Hashim, and I. M. AlNashef, "Superoxide ion: generation and chemical implications," *Chemical Reviews*, vol. 116, no. 5, pp. 3029–3085, 2016.

[14] M. H. Raza, S. Siraj, A. Arshad et al., "ROS-modulated therapeutic approaches in cancer treatment," *Journal of Cancer Research and Clinical Oncology*, vol. 143, no. 9, pp. 1789–1809, 2017.

[15] S. L. Doyle and L. A. O'Neill, "Toll-like receptors: from the discovery of NFκB to new insights into transcriptional regulations in innate immunity," *Biochemical Pharmacology*, vol. 72, no. 9, pp. 1102–1113, 2006.

[16] N. D. Perkins and T. D. Gilmore, "Good cop, bad cop: the different faces of NF-κB," *Cell Death and Differentiation*, vol. 13, no. 5, pp. 759–772, 2006.

[17] C. H. Chiang, J. G. Chung, and F. T. Hsu, "Regorefenib induces extrinsic/intrinsic apoptosis and inhibits MAPK/NF-κB-modulated tumor progression in bladder cancer in vitro and in vivo," *Environmental Toxicology*, vol. 34, no. 6, pp. 679–688, 2019.

[18] R. Nehra, R. B. Riggins, A. N. Shajahan, A. Zwart, A. C. Crawford, and R. Clarke, "BCL2 and CASP8 regulation by NF-κB differentially affect mitochondrial function and cell fate in antiestrogen-sensitive and -resistant breast cancer cells," *The FASEB Journal*, vol. 24, no. 6, pp. 2040–2055, 2010.

[19] F. Li, J. Zhang, F. Arfuso et al., "NF-κB in cancer therapy," *Archives of Toxicology*, vol. 89, no. 5, pp. 711–731, 2015.

[20] G. H. Williams and K. Stoeber, "The cell cycle and cancer," *The Journal of Pathology*, vol. 226, no. 2, pp. 352–364, 2012.

[21] Y. Liang, X. Qiu, R. Z. Xu, and X. Y. Zhao, "Berbamine inhibits proliferation and induces apoptosis of KU812 cells by increasing Smad3 activity," *Journal of Zhejiang University. Science. B*, vol. 12, no. 7, pp. 568–574, 2011.

[22] M. Ingham and G. K. Schwartz, "Cell-cycle therapeutics come of age," *Journal of Clinical Oncology*, vol. 35, no. 25, pp. 2949–2959, 2017.

[23] V. Vasioukhin, C. Bauer, M. Yin, and E. Fuchs, "Directed actin polymerization is the driving force for epithelial cell-cell adhesion," *Cell*, vol. 100, no. 2, pp. 209–219, 2000.

[24] K. M. Alblazi and C. H. Siar, "Cellular protrusions—lamellipodia, filopodia, invadopodia and podosomes—and their roles in progression of orofacial tumours: current understanding," *Asian Pacific Journal of Cancer Prevention*, vol. 16, no. 6, pp. 2187–2191, 2015.

[25] M. Yilmaz and G. Christofori, "EMT, the cytoskeleton, and cancer cell invasion," *Cancer Metastasis Reviews*, vol. 28, no. 1-2, pp. 15–33, 2009.

[26] S. J. Stein and A. S. Baldwin, "NF-κB suppresses ROS levels in BCR-ABL$^+$ cells to prevent activation of JNK and cell death," *Oncogene*, vol. 30, no. 45, pp. 4557–4566, 2011.

[27] J. Y. Liu, Q. H. Zeng, P. G. Cao et al., "RIPK4 promotes bladder urothelial carcinoma cell aggressiveness by upregulating VEGF-A through the NF-κB pathway," *British Journal of Cancer*, vol. 118, no. 12, pp. 1617–1627, 2018.

[28] L. Zhang, W. Chen, and X. Li, "A novel anticancer effect of butein: inhibition of invasion through the ERK1/2 and NF-kappa B signaling pathways in bladder cancer cells," *FEBS Letters*, vol. 582, no. 13, pp. 1821–1828, 2008.

[29] Y. L. Wei, Y. Liang, L. Xu, and X. Y. Zhao, "The antiproliferation effect of berbamine on k562 resistant cells by inhibiting NF-κB pathway," *The Anatomical Record: Advances in Integrative Anatomy and Evolutionary Biology*, vol. 292, no. 7, pp. 945–950, 2009.

[30] Y. Liang, R. Z. Xu, L. Zhang, and X. Y. Zhao, "Berbamine, a novel nuclear factor κB inhibitor, inhibits growth and induces apoptosis in human myeloma cells," *Acta Pharmacologica Sinica*, vol. 30, no. 12, pp. 1659–1665, 2009.

[31] Y. Liang, X. He, X. Li et al., "4-Chlorbenzoyl berbamine, a novel derivative of the natural product berbamine, potently inhibits the growth of human myeloma cells by modulating the NF-κB and JNK signalling pathways," *Cancer Investigation*, vol. 34, no. 10, pp. 496–505, 2016.

[32] J. Jin, Z. Lu, X. Wang et al., "E3 ubiquitin ligase TRIM7 negatively regulates NF-kappa B signaling pathway by degrading p65 in lung cancer," *Cellular Signalling*, vol. 69, p. 109543, 2020.

[33] F. Yang, S. Nam, R. Zhao et al., "A novel synthetic derivative of the natural product berbamine inhibits cell viability and induces apoptosis of human osteosarcoma cells, associated with activation of JNK/AP-1 signaling," *Cancer Biology & Therapy*, vol. 14, no. 11, pp. 1024–1031, 2014.

[34] Y. C. Hseu, T. J. Tsai, M. Korivi et al., "Antitumor properties of Coenzyme Q$_0$ against human ovarian carcinoma cells _via_ induction of ROS-mediated apoptosis and cytoprotective autophagy," *Scientific Reports*, vol. 7, no. 1, p. 8062, 2017.

[35] B. Wang, T. Y. Zhou, C. H. Nie, D. L. Wan, and S. S. Zheng, "Bigelovin, a sesquiterpene lactone, suppresses tumor growth through inducing apoptosis and autophagy via the inhibition of mTOR pathway regulated by ROS generation in liver cancer," *Biochemical and Biophysical Research Communications*, vol. 499, no. 2, pp. 156–163, 2018.

[36] F. Yang, S. Nam, C. E. Brown et al., "A novel berbamine derivative inhibits cell viability and induces apoptosis in cancer stem-like cells of human glioblastoma, via up-regulation of miRNA-4284 and JNK/AP-1 signaling," *PLoS One*, vol. 9, no. 4, p. e94443, 2014.

[37] C. Q. Xu, D. L. Dong, Z. M. Du, Q. W. Chen, D. M. Gong, and B. F. Yang, "Comparison of the anti-arrhythmic effects of matrine and berbamine with amiodarone and RP58866," *Yao Xue Xue Bao*, vol. 39, no. 9, pp. 691–694, 2004.

[38] Y. Zheng, S. Gu, X. Li et al., "Berbamine postconditioning protects the heart from ischemia/reperfusion injury through modulation of autophagy," *Cell Death & Disease*, vol. 8, no. 2, p. e2577, 2017.

[39] X. Ding, F. S. Zhu, M. Li, and S. G. Gao, "Induction of apoptosis in human hepatoma SMMC-7721 cells by solamargine from *Solanum nigrum L.*," *Journal of Ethnopharmacology*, vol. 139, no. 2, pp. 599–604, 2012.

[40] B. Hu, H. Cai, S. Yang, J. Tu, X. Huang, and G. Chen, "Berbamine enhances the efficacy of gefitinib by suppressing STAT3 signaling in pancreatic cancer cells," *Oncotargets and Therapy*, vol. 12, pp. 11437–11451, 2019.

[41] H. Zhu, S. Ruan, F. Jia et al., "In vitro and in vivo superior radiosensitizing effect of berbamine for head and neck squamous cell carcinoma," *Oncotargets and Therapy*, vol. 11, pp. 8117–8125, 2018.

[42] S. Goel, M. J. DeCristo, S. S. McAllister, and J. J. Zhao, "CDK4/6 inhibition in cancer: beyond cell cycle arrest," *Trends in Cell Biology*, vol. 28, no. 11, pp. 911–925, 2018.

[43] V. Yadav, S. Sultana, J. Yadav, and N. Saini, "Gatifloxacin induces S and G2-phase cell cycle arrest in pancreatic cancer cells via p21/p27/p53," *PLoS One*, vol. 7, no. 10, p. e47796, 2012.

[44] J. L. Wang, Q. Quan, R. Ji et al., "Isorhamnetin suppresses PANC-1 pancreatic cancer cell proliferation through S phase arrest," *Biomedicine & Pharmacotherapy*, vol. 108, pp. 925–933, 2018.

[45] X. Zhou, Y. Yang, P. Ma et al., "TRIM44 is indispensable for glioma cell proliferation and cell cycle progression through AKT/p21/p27 signaling pathway," *Journal of Neuro-Oncology*, vol. 145, no. 2, pp. 211–222, 2019.

[46] M. Majumder, S. Debnath, R. L. Gajbhiye et al., "_Ricinus communis_ L. fruit extract inhibits migration/invasion, induces apoptosis in breast cancer cells and arrests tumor progression _in vivo_," *Scientific Reports*, vol. 9, no. 1, p. 14493, 2019.

[47] D. S. Micalizzi, S. M. Farabaugh, and H. L. Ford, "Epithelial-mesenchymal transition in cancer: parallels between normal development and tumor progression," *Journal of Mammary Gland Biology and Neoplasia*, vol. 15, no. 2, pp. 117–134, 2010.

[48] T. Chen, Y. You, H. Jiang, and Z. Z. Wang, "Epithelial-mesenchymal transition (EMT): a biological process in the development, stem cell differentiation, and tumorigenesis," *Journal of Cellular Physiology*, vol. 232, no. 12, pp. 3261–3272, 2017.

[49] S. A. Mani, W. Guo, M. J. Liao et al., "The epithelial-mesenchymal transition generates cells with properties of stem cells," *Cell*, vol. 133, no. 4, pp. 704–715, 2008.

[50] F. Wang, W. He, P. Fanghui, L. Wang, and Q. Fan, "NF-κBP65 promotes invasion and metastasis of oesophageal squamous cell cancer by regulating matrix metalloproteinase-9 and epithelial-to-mesenchymal transition," *Cell Biology International*, vol. 37, no. 8, pp. 780–788, 2013.

[51] S. Julien, I. Puig, E. Caretti et al., "Activation of NF-κB by Akt upregulates Snail expression and induces epithelium mesenchyme transition," *Oncogene*, vol. 26, no. 53, pp. 7445–7456, 2007.

[52] A. K. Chaudhary, S. Chaudhary, K. Ghosh, C. Shanmukaiah, and A. H. Nadkarni, "Secretion and expression of matrix metalloproteinase-2 and 9 from bone marrow mononuclear cells in myelodysplastic syndrome and acute myeloid leukemia," *Asian Pacific Journal of Cancer Prevention*, vol. 17, no. 3, pp. 1519–1529, 2016.

[53] Z. N. Oltvai, C. L. Milliman, and S. J. Korsmeyer, "Bcl-2 heterodimerizes in vivo with a conserved homolog, Bax, that accelerates programed cell death," *Cell*, vol. 74, no. 4, pp. 609–619, 1993.

[54] J. M. Hardwick and L. Soane, "Multiple functions of BCL-2 family proteins," *Cold Spring Harb Perspect Biol*, vol. 5, no. 2, 2013.

[55] C. Wang and R. J. Youle, "The role of mitochondria in apoptosis∗," *Annual Review of Genetics*, vol. 43, no. 1, pp. 95–118, 2009.

[56] X. Liu, H. Cai, H. Huang, Z. Long, Y. Shi, and Y. Wang, "The prognostic significance of apoptosis-related biological markers in Chinese gastric cancer patients," *PLoS One*, vol. 6, no. 12, p. e29670, 2011.

[57] L. Lu, H. Li, X. Wu et al., "HJC0152 suppresses human non-small-cell lung cancer by inhibiting STAT3 and modulating metabolism," *Cell Prolif*, vol. 53, no. 3, p. e12777, 2020.

[58] I. I. C. Chio and D. A. Tuveson, "ROS in cancer: the burning question," *Trends in Molecular Medicine*, vol. 23, no. 5, pp. 411–429, 2017.

[59] T. P. Szatrowski and C. F. Nathan, "Production of large amounts of hydrogen peroxide by human tumor cells," *Cancer Research*, vol. 51, no. 3, pp. 794–798, 1991.

[60] L. Lu, J. Dong, L. Wang et al., "Activation of STAT3 and Bcl-2 and reduction of reactive oxygen species (ROS) promote radioresistance in breast cancer and overcome of radioresistance with niclosamide," *Oncogene*, vol. 37, no. 39, pp. 5292–5304, 2018.

[61] D. R. Rhodes, S. Kalyana-Sundaram, V. Mahavisno et al., "Oncomine 3.0: genes, pathways, and networks in a collection of 18,000 cancer gene expression profiles," *Neoplasia*, vol. 9, no. 2, pp. 166–180, 2007.

[62] H. Sakurai, S. Suzuki, N. Kawasaki et al., "Tumor necrosis factor-α-induced IKK phosphorylation of NF-κB p65 on serine 536 is mediated through the TRAF2, TRAF5, and TAK1 signaling pathway," *The Journal of Biological Chemistry*, vol. 278, no. 38, pp. 36916–36923, 2003.

[63] F. Jia, S. Ruan, N. Liu, and L. Fu, "Synergistic antitumor effects of berbamine and paclitaxel through ROS/Akt pathway in glioma cells," *Evidence-based Complementary and Alternative Medicine*, vol. 2017, 2017.

[64] S. Inoue, H. Ide, T. Mizushima et al., "Nuclear factor-κB promotes urothelial tumorigenesis and cancer progression via cooperation with androgen receptor signaling," *Molecular Cancer Therapeutics*, vol. 17, no. 6, pp. 1303–1314, 2018.

[65] V. Oliveira-Marques, H. S. Marinho, L. Cyrne, and F. Antunes, "Role of hydrogen peroxide in NF-κB activation: from inducer to modulator," *Antioxidants & Redox Signaling*, vol. 11, no. 9, pp. 2223–2243, 2009.

[66] P. J. Halvey, J. M. Hansen, J. M. Johnson, Y. M. Go, A. Samali, and D. P. Jones, "Selective oxidative stress in cell nuclei by nuclear-targeted D-amino acid oxidase," *Antioxidants & Redox Signaling*, vol. 9, no. 7, pp. 807–816, 2007.

[67] G. Yang, C. Zhang, P. Hu, M. Zhu, M. Hu, and S. Gao, "An UPLC-MS/MS method for quantifying tetrandrine and its metabolite berbamine in human blood: application to a human pharmacokinetic study," *Journal of Chromatography. B, Analytical Technologies in the Biomedical and Life Sciences*, vol. 1070, pp. 92–96, 2017.

Research Article

An Oxidative Stress Index-Based Score for Prognostic Prediction in Colorectal Cancer Patients Undergoing Surgery

Yinghao Cao,[1] **Shenghe Deng,**[1] **Lizhao Yan,**[1] **Junnan Gu,**[1] **Fuwei Mao,**[1] **Yifan Xue,**[1] **Changmin Zheng,**[2] **Ming Yang,**[3] **Hongli Liu,**[4] **Li Liu,**[5] **Qian Liu** ⬤,[6] **and Kailin Cai** ⬤[1]

[1]*Department of Gastrointestinal Surgery, Union Hospital, Tongji Medical College, Huazhong University of Science and Technology, Wuhan, Hubei 430022, China*
[2]*School of Optical and Electronic Information, Huazhong University of Science and Technology, Wuhan 430074, China*
[3]*Department of Pathology, Union Hospital, Tongji Medical, Huazhong University of Science and Technology, Wuhan, Hubei 430022, China*
[4]*Cancer Center, Union Hospital, Tongji Medical College, Huazhong University of Science and Technology, Wuhan 430022, China*
[5]*Department of Epidemiology and Biostatistics, the Ministry of Education Key Lab of Environment and Health, School of Public Health, Tongji Medical College, Huazhong University of Science and Technology, Wuhan, Hubei 430022, China*
[6]*Department of Cardiology, Wuhan Women and Children Medical Care Center, Wuhan, Hubei 430022, China*

Correspondence should be addressed to Qian Liu; 2244307539@qq.com and Kailin Cai; caikailin@hust.edu.cn

Oxidative stress plays an important role in the development of colorectal cancer (CRC). This study is aimed at developing and validating a novel scoring system, based on oxidative stress indexes, for prognostic prediction in CRC patients. A retrospective analysis of 1422 CRC patients who underwent surgical resection between January 2013 and December 2017 was performed. These patients were randomly assigned to the training set ($n = 1022$) or the validation set ($n = 400$). Cox regression model was used to analyze the laboratory parameters. The CRC-Integrated Oxidative Stress Score (CIOSS) was developed from albumin (ALB), direct bilirubin (DBIL), and blood urea nitrogen (BUN), which were significantly associated with survival in CRC patients. Furthermore, a survival nomogram was generated by combining the CIOSS with other beneficial clinical characteristics. The CIOSS generated was as follows: $0.074 \times$ albumin (g/L), $-0.094 \times$ bilirubin (μmol/L), and $-0.099 \times$ blood urea nitrogen (mmol/L), based on the multivariable Cox regression analysis. Using 50% (0.1025) and 85% (0.481) of CIOSS as cutoff values, three prognostically distinct groups were formed. Patients with high CIOSS experienced worse overall survival (OS) (hazard ratio [HR] = 4.33; 95% confidence interval [CI], 2.80-6.68; $P < 0.001$) and worse disease-free survival (DFS) (HR = 3.02; 95% CI, 1.96-4.64; $P < 0.001$) compared to those with low CIOSS. This predictive nomogram had good calibration and discrimination. ROC analyses showed that the CIOSS possessed excellent performance (AUC = 0.818) in predicting DFS. The AUC of the OS nomogram based on CIOSS, TNM stage, T stage, and chemotherapy was 0.812, while that of the DFS nomogram based on CIOSS, T stage, and TNM stage was 0.855. Decision curve analysis showed that these two prediction models were clinically useful. CIOSS is a CRC-specific prognostic index based on the combination of available oxidative stress indexes. High CIOSS is a powerful indicator of poor prognosis. The CIOSS also showed better predictive performance compared to TNM stage in CRC patients.

1. Introduction

Colorectal cancer (CRC) is the third most common cancer, accounting for 9.7% of all cancers except melanoma skin cancer. It is the second and third most common cancer in women and men, respectively, accounting for 10% of all new cancer cases each year [1]. The "rise" of CRC in developed countries can be attributed to an ageing population, unfavorable modern dietary habits, and an increase in risk factors such as smoking, inadequate physical activity, and

obesity [2]. Despite significant advances in treatment strategies, the mortality rate from CRC remains high; from 1990 to 2013, the death rate from CRC increased by 57%. In 2013, there were 771,000 deaths from CRC, which now accounts for about 10% of the cancer-related deaths worldwide [3]. At present, the long-term prognosis of CRC patients is still not optimistic, warranting a reasonable and effective prediction model for the long-term prognostic assessment of CRC patients.

Integrating different types of information into an accurate, personalized CRC prognostic assessment tool is a challenge, but few assessments of the internal or external effectiveness of prognostic models are currently conducted [4]. At present, the common prognostic indicators of CRC patients include age, tumor location, tumor stage, tumor marker level, and presence of metastasis. Although CRC prognosis has been proved to be closely related to the aforementioned indicators, they have not been effectively verified externally and their prediction accuracy is also not high [5–7]. Considering that quite a few factors are closely related to the prognosis of CRC patients, a reasonable, simple, accurate, and low-cost prediction model should be designed to effectively predict the prognosis of patients.

In addition, oxidative stress, mainly associated with mutations in the colorectal genes, has an equally important predictive role in the occurrence, development, and prognosis of CRC [8]. Studies have also shown that some plant-based foods with the potential to inhibit inflammation and oxidative stress may be beneficial to CRC patients, especially those whose molecular markers point to severe inflammation and oxidative stress [9]. A multicenter randomized controlled study has found that a healthy diet has an important role in suppressing inflammation and oxidative stress in long-term disease outcome and survival in patients with CRC [10]. Given the critical role of oxidative stress in the progression of CRC, we attempted to investigate the prognostic significance of oxidative stress-related indexes in this study.

In the present study, we first created and validated a new CRC-Integrated Oxidative Stress Score (CIOSS) from a large sample of CRC patients undergoing surgical operation. Furthermore, we compared the predictive value of CIOSS and TNM staging system for the prediction of OS and DFS. Finally, we combined the new indicators with other common clinical variables to create and validate sequence diagrams for predicting OS and DFS in patients with CRC.

2. Materials and Methods

2.1. Patients and Study Design.
This clinical study was performed at the Wuhan Union Hospital with a total of 1422 CRC patients who underwent surgical resection between January 2013 and December 2017. The inclusion criteria were as follows: (1) confirmed CRC diagnosis by abdominal computed tomography (CT) or biopsy, (2) underwent surgical resection with no evidence of distant metastasis, and (3) availability of complete clinical and pathological data. Patients with the following conditions were excluded from the study: (1) history of tumor, coinfection, or blood disease;

(2) treatment with anti-inflammatory drugs prior to surgical resection; (3) presence of severe cardiovascular disease or metabolic diseases; (4) without clinical and follow-up information; (5) received chemotherapy or pharmacological treatment before surgery.

A total of 1422 surgically resected CRC patients with complete clinical and follow-up data were included in this study and randomly divided into the training ($n = 1022$) and validation ($n = 400$) groups. This study was approved by the ethics committee of Wuhan Union Medical College Hospital (No. 2018-S377) and was carried out in accordance with the Helsinki Declaration. All patients signed an informed consent regarding their understanding of the procedure and its potential complications, as well as their approval for participation in the research.

2.2. Data Collection.
Baseline clinicopathologic data obtained from hospital medical records included age, gender, smoking status, tumor history, intestinal obstruction, tumor differentiation, tumor size, tumor location, tumor T stage, tumor N stage, tumor TNM stage, perineural invasion, vascular invasion, and chemotherapy. Tumor stage was classified according to the 8th edition of the American Joint Committee on cancer staging system, and patients with high-risk stages II or above received adjuvant chemotherapy postoperation.

Follow-up data were obtained every three months, and whenever we suspected recurrence, gastroscopy and imaging were performed. The primary endpoint of this study was OS, and the secondary endpoint was DFS. OS was defined as the time interval from surgery to the last follow-up or death. DFS was defined from the date of definitive surgery to the date of first recurrence (local or distant) or the date of last follow-up.

2.3. Evaluation of the Oxidative Stress Indexes.
Routine blood and biochemistry tests were conducted from the first day of admission for each CRC patient. The oxidative stress indexes in our study comprised ALB, total bilirubin (TBIL), DBIL, BUN, and uric acid (UA). The cutoff values of these oxidative stress indexes were identified using the X-tile software [11].

2.4. Statistical Analysis.
Statistical analysis was performed using the SPSS 23.0 (SPSS Inc., Chicago, IL, USA) and R 4.0.0 software (Institute for Statistics and Mathematics, Vienna, Austria). Continuous data were expressed as mean ± standard deviation, unless otherwise specified. Patient characteristics were compared using t-tests for continuous variables and χ^2 or Fisher exact tests for categorical variables. X-tile 3.6.1 (Yale University, New Haven, CT, USA) was used to determine the optimal cutoff value for ALB, TBIL, DBIL, BUN, and UA levels. The training set was applied to develop the novel oxidative stress score based on the β coefficients from the multivariable Cox analysis [12]. CRC patients were divided into three risk groups (low risk, intermediate risk, and high risk) based on the 50th and 85th percentiles of CIOSS. Receiver operating characteristic (ROC) analyses were then performed to assess the predictive abilities of CIOSS and TNM stage for the prediction of survival outcomes. Moreover, univariate and multivariate Cox proportional hazards regression models were utilized to evaluate
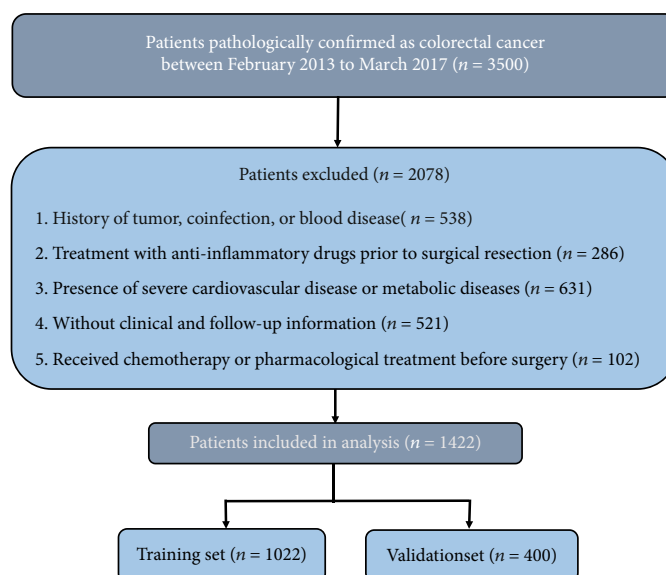
Figure 1: Strategies for selecting patients to be included in the study.

the prognostic factors for OS and DFS. A nomogram incorporating the important factors related to the OS or DFS was constructed with the R software. Td-ROC curves were drawn to assess the predictive performance of survival nomogram for 1-year, 3-year, and 5-year prediction. To further measure the calibration of the nomogram in predicting survival, a calibration curve was generated to compare the observed results with the predicted results. A value of $P < 0.05$ was considered significant.

3. Results and Discussion

3.1. Study Population.
A total of 1422 participants from Wuhan Union Hospital were included in this research; 825 were males, 597 were females, and mean age was 57.79 ± 11.26 years (range, 20-85). Of these, 70% ($n = 1022$) of the patients were randomly assigned to the training set while the remaining patients ($n = 400$) were included in the internal validation set. A detailed flow diagram of the patient selection process is shown in Figure 1. The clinical characteristics of CRC patients in the training and validation set are given in Table 1. The cutoff values for oxidative stress were determined using the X-tile software. Based on these cutoff values, all oxidative stress indicators included in our study were those that statistically correlated with OS (Fig. S1 A-E) and DFS (Fig. S1 F-J) in CRC patients.

3.2. Creation of the Novel Oxidative Stress Index.
As clearly shown in Table 1, we observed no significant differences in the clinical characteristics between the data sets. For the creation of CIOSS, we selected only informational oxidative stress indicators that significantly correlated with OS or DFS by performing Cox regression. As shown in Table 2, ALB, DBIL, and BUN were found to be independent risk factors for poor OS. Hence, based on the β coefficient, the prognostic model CRC-Integrated Oxidative Stress Score (CIOSS) was generated: $0.074 \times$ albumin (g/L), $-0.094 \times$ bilirubin

(μmol/L), and $-0.099 \times$ BUN (mmol/L). Using 50% (1.60) and 85% (2.10) of CIOSS as cutoff values, three prognostically distinct groups were obtained. Kaplan-Meier survival plots comparing OS and DFS stratified by CIOSS are shown in Figures 2(a)–2(d).

3.3. Univariate and Multivariate Analyses of Factors Associated with OS and DFS.
Univariate regression analysis was performed for all factors influencing the prognosis of patients. Then, multivariate Cox regression analysis was performed on the clinical features that were found to be significant in the univariate log-rank test. The results confirmed that TNM (hazard ratio [HR]: 3.44; confidence interval [CI]: 1.37-8.63; $P = 0.009$), T stage (HR: 2.79; CI: 1.10-7.09; $P = 0.031$), chemotherapy (HR: 0.72; CI: 0.52-0.98; $P = 0.045$), and CIOSS (Intermediate, HR: 2.93, CI: 1.99-4.32, and $P < 0.001$; High, HR: 4.33, CI: 2.80-6.68, and $P < 0.001$) were independent prognostic factors for OS (Table 3).

Furthermore, TNM (HR: 13.09; CI: 3.63-47.19; $P < 0.001$), T stage (HR: 6.8; CI: 1.60-28.87; $P = 0.009$), and CIOSS (Intermediate, HR: 1.88, CI: 1.29-2.76, and $P = 0.001$; High, HR: 3.02, CI: 1.96-4.64, and $P < 0.001$) were independent prognostic factors for DFS as well (Table 4).

3.4. Comparisons of the CIOSS and TNM Stage.
ROC analyses were further applied to assess the predictive significance of the CIOSS in predicting survival and comparing to TNM stage. The predictive ability of CIOSS as measured by AUC in predicting OS was 0.768 in the training set (Figure 3(a)) and 0.735 in the validation set (Figure 3(c)). Similarly, the CIOSS also showed remarkable performance in the prediction of DFS among CRC patients, as reflected by the AUC of 0.818 in the training set (Figure 3(b)) and 0.789 in the validation set (Figure 3(d)). The AUCs of TNM for OS were 0.706 in the training set and 0.715 in the validation set (Figure 3). The AUCs of TNM for DFS were 0.792 in the training set and 0.778 in the validation set. Thus, we

TABLE 1: Clinicopathological characteristics of all patients.

Characteristics	Test set (n=1022), %	Validation set (n=400), %	P
Age (years)			0.557
≥60	478 (46.8)	194 (48.5)	
<60	544 (53.2)	206 (51.5)	
Sex, male	590 (57.7)	235 (58.8)	0.726
Primary site			0.587
Left colon	310 (30.3)	124 (31.0)	
Right colon	197 (19.3)	83 (20.8)	
Rectum	515 (50.4)	193 (48.3)	
Family history of cancer	99 (9.7)	47 (11.8)	0.557
Histological grade			0.567
Well differentiated	153 (15.0)	60 (15.0)	
Moderately differentiated	800 (78.3)	319 (79.8)	
Poorly differentiated	69 (6.7)	21 (5.2)	
Tumor size			0.144
<2 cm	51 (5.0)	25 (6.2)	
2-5 cm	597 (58.4)	243 (60.8)	
≥5 cm	374 (36.6)	132 (33.0)	
Lymphovascular invasion			0.364
Yes	187 (18.3)	65 (16.3)	
No	835 (81.7)	335 (83.7)	
Circumferential resection margin			0.576
Yes	11 (1.1)	3 (0.8)	
No	1011 (98.9)	397 (99.2)	
T stage			0.505
T1	73 (7.1)	33 (8.3)	
T2	169 (16.5)	64 (16.0)	
T3	539 (52.7)	215 (53.7)	
T4	241 (23.7)	88 (22.0)	
N stage			0.065
N0	59 (5.8)	15 (3.8)	
N1	539 (52.7)	198 (49.5)	
N2	251 (24.6)	112 (28.0)	
N3	173 (16.9)	75 (18.7)	
TNM stage			0.563
Stage I	140 (13.7)	53 (13.2)	
Stage II	352 (34.4)	130 (32.5)	
Stage III	394 (38.6)	163 (40.8)	
Stage IV	136 (13.3)	54 (13.5)	
Adjuvant chemotherapy			0.529
Yes	492 (48.1)	200 (50.0)	
No	530 (51.9)	200 (50.0)	
Radiotherapy			0.499
Yes	55 (5.4)	18 (4.5)	
No	967 (94.6)	382 (95.5)	
Serum albumin			0.176
≥36.3 g/L	794 (77.7)	318 (79.5)	
<36.3 g/L	228 (22.3)	82 (20.5)	

TABLE 1: Continued.

Characteristics	Test set (n=1022), %	Validation set (n=400), %	P
Total bilirubin			0.431
≥12.2 μmol/L	389 (38.1)	159 (39.8)	
<12.2 μmol/L	633 (61.9)	241 (60.2)	
Direct bilirubin			0.732
≥5.2 μmol/L	227 (22.2)	105 (26.3)	
<5.2 μmol/L	795 (77.8)	295 (73.7)	
Urea nitrogen			0.144
≥4.6 mmol/L	616 (60.3)	233 (58.2)	
<4.6 mmol/L	406 (39.7)	167 (41.8)	
Uric acid			0.081
≥200.0 μmol/L	888 (86.9)	361 (90.3)	
<200.0 μmol/L	134 (13.1)	39 (9.8)	
Overall survival months	29.5 (21.8, 40.1)	29.6 (22.3, 40.7)	0.198
Disease-free survival months	20.0 (12.7, 30.2)	20.2 (13.1, 30.3)	0.732
Death, n (%)	174 (17.0)	59 (14.8)	0.298
Recurrence, n (%)	152 (14.9)	60 (15.0)	0.952

TABLE 2: Cox regression models of laboratory parameters in the test set.

	Univariate			Multivariate		
	β	HR	P	β	HR	P
ALB	-0.077	0.926	<0.001	-0.074	0.916	<0.001
TBIL	0.029	1.029	0.014	0.002	1.002	0.916
DBIL	0.110	1.116	<0.001	0.094	1.099	0.023
BUN	0.129	1.1138	0.001	0.099	1.104	0.011
UA	-0.001	0.999	0.488			

CRC-Integrated Oxidative Stress Score (CIOSS) = $0.054 \times$ ALB $-0.112 \times$ DBIL $- 0.147 \times$ BUN.

concluded that the performance of the CIOSS in predicting both OS and DFS was superior to TNM.

3.5. Construction and Validation of a Survival Nomogram.
Based on the multivariate Cox results for OS, four valuable factors, including TNM, T stage, chemotherapy, and CIOSS, were eventually selected to establish the predictive model (Figure 4(a)). Time-dependent- (TD-) receiver operating characteristic (ROC) analysis was used to estimate the efficiency of nomogram in predicting one-year, three-year, and five-year OS. When evaluating one-year, three-year, and five-year survival rates, the predictive power of survival nomograms measured by area under the ROC curve (AUC) in the training set was 0.868, 0.784, and 0.731, respectively (Figure 5(a)); in the validation set, it was 0.757, 0.780, and 0.792, respectively (Figure 5(b)).

For DFS, three valuable factors in the multivariate regression, including TNM, T stage, and CIOSS, were selected to establish the predictive model (Figure 4(b)). TD-ROC analysis was used to estimate the efficiency of nomogram in predicting one-year, three-year, and five-year DFS. When evaluating one-year, three-year, and five-year survival rates, the predictive power of survival nomograms measured by AUC in the training set was 0.889, 0.796, and 0.792, respec-

tively (Figure 5(c)); in the validation set, it was 0.855, 0.806, and 0.800, respectively (Figure 5(d)).

The calibration curves of the two nomograms for the probability of OS and DFS in the CRC showed good agreement between prediction and observation in the test and validation sets (Figures 6(a)–6(l)). Survival nomographs based on COISS and other important characteristics have better ability to distinguish between high-risk and low-risk CRC patients in terms of OS and DFS.

4. Discussion

In this study, we established the oxidative stress score for the first time to predict the prognosis of CRC patients. Oxidative stress is involved in the development of a variety of cancers, including CRC; whether it also plays a role in CRC prognosis is not clear. We assessed the relationship between biochemical indicators of oxidative stress and the prognosis of CRC. In establishing a predictive model of CRC comprehensive oxidative stress score (CIOSS), we found that patients with high CIOSS had worse OS (HR = 4.33; 95% CI, 2.80-6.68; $P <$ 0.001) and worse DFS (HR = 3.02; 95% CI, 1.96-4.64; $P <$ 0.001) compared with CRC patients with low CIOSS. We also observed that TNM and T stages are strongly related to

(a)   (b)

(c)   (d)
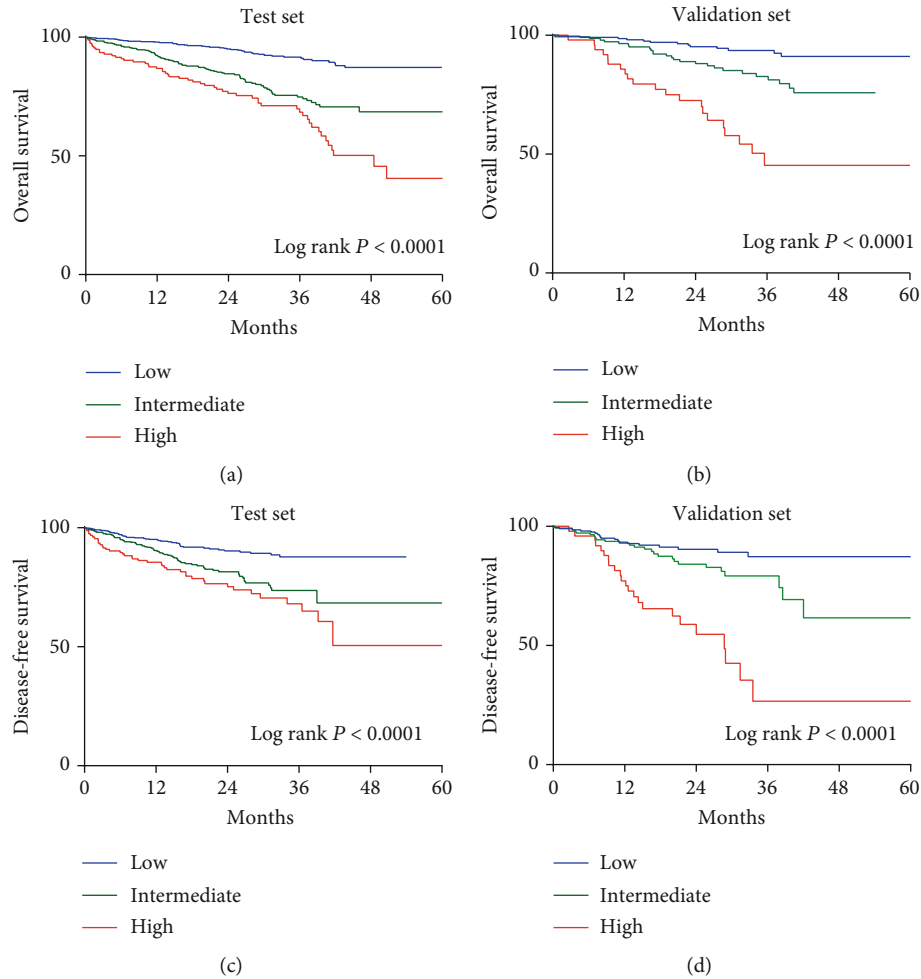
FIGURE 2: Kaplan-Meier survival plots comparing OS and DFS stratified by CRC-Integrated Oxidative Stress Score (CIOSS). OS: (a) training cohort (log rank $P < 0.001$) and (b) validation cohort (log rank $P < 0.001$); DFS: (c) training cohort (log rank $P < 0.001$) and (d) validation cohort (log rank $P < 0.001$).

the prognosis of CRC and that the inclusion of these indicators together can improve the prediction of CRC prognosis significantly. The predictive nomogram had good calibration and discrimination, with an AUC of 0.731 in the test set and 0.792 in the validation set on the five-year OS. In addition, the ROC curve prediction was 0.792 in the test set and 0.800 in the validation set for the five-year DFS. This suggests that oxidative stress has an important influence on premature death in CRC patients and shows the great potential of these biomarkers have in enhancing the prediction of CRC prognosis based on tumor stage.

It is believed that the development of cancer is the result of the damage of antioxidant system, high oxidative stress will increase the risk of colorectal cancer, and autophagy and reactive oxygen species in oxidative stress can cause genetic instability and posttranslational modification of cancer-related proteins, leading to the development of CRC [13, 14].

Autophagy is a core component of the comprehensive stress response and affects the development of colorectal cancer; it has been found that BRG1 isolates and alleviates colon inflammation and tumorigenesis through autophagy-dependent oxidative stress [15]. Port et al. found that oxidative stress was associated with the aggressiveness and poor prognosis of colorectal cancer. This study found that NUAK1 is a key component of the antioxidant stress response pathway, and the absence of NUAK1 can inhibit the formation of colorectal tumors. After oxidative stress, the expression of NUAK1 in colorectal cancer is increased, leading to a decrease in the invasive height and overall survival rate of colorectal cancer [12]. Studies have found that the clearance of oxidative stress compounds is crucial to protect the body from malignant tumors. In mouse cancer cell lines and E-coli-related cancer models, it was found that after oxidative stress-related pathways were abnormally regulated, GPRC5A deletion would reduce cell proliferation, increase cell apoptosis, and inhibit the occurrence of tumors in vivo. Studies have shown that GPRC5A is a potential biomarker for colon cancer and promotes the occurrence of tumors in colitis-associated cancers by stimulating vanin-1 expression and oxidative stress [16]. Inhibiting oxidative stress in a rat model of colon cancer helps to inhibit the risk of CRC and has the potential to further evaluate therapeutic objectives [17]. In a clinical study, antioxidant enzyme activity in CRC patients

TABLE 3: Univariate and multivariate analyses of factors associated with OS.

	Univariate analysis		Multivariate analysis	
	HR (95% CI)	P	HR (95% CI)	P
Age (years)				
≥60	1.14 (0.85-1.54)	0.378		
<60	Ref.	-		
Sex, male	1.18 (0.87-1.60)	0.296		
Primary site				
Left colon	1.56 (1.11-2.20)	0.011	1.29 (0.90-1.84)	0.169
Right colon	1.73 (1.18-2.54)	0.005	1.24 (0.83-1.86)	0.302
Rectum	Ref.	-	Ref.	-
Family history of cancer	1.03 (0.63-1.71)	0.901		
Histological grade				
Well differentiated	Ref.	-		
Moderately differentiated	1.23 (0.63-2.42)	0.547		
Poorly differentiated	1.44 (0.69-3.03)	0.336		
Tumor size				
<2 cm	0.60 (0.28-1.29)	0.190	0.82 (0.36-1.86)	0.628
2-5 cm	0.61 (0.45-0.83)	0.002	0.79 (0.58-1.09)	0.147
≥5 cm	Ref.	-	Ref.	-
Lymphovascular invasion				
Yes	1.01 (0.67-1.50)	0.983		
No	Ref.	-		
Circumferential resection margin				
Yes	0.62 (0.09-4.41)	0.630		
No	Ref.	-		
T stage				
T1	Ref.	-	Ref.	-
T2	0.83 (0.31-2.22)	0.714	0.84 (0.30-2.37)	0.748
T3	1.70 (0.74-3.91)	0.212	1.30 (0.51-3.29)	0.583
T4	5.38 (2.35-12.32)	<0.001	2.79 (1.10-7.09)	0.031
N stage				
N0	Ref.	-	Ref.	-
N1	0.56 (0.28-1.15)	0.114	0.65 (0.31-1.35)	0.245
N2	1.51 (0.74-3.05)	0.256	1.29 (0.59-2.83)	0.530
N3	2.86 (1.42-5.76)	0.003	1.82 (0.84-3.96)	0.132
TNM stage				
Stage I	Ref.	-	Ref.	-
Stage II	1.77 (0.78-4.02)	0.170	0.81 (0.32-2.08)	0.668
Stage III	4.07 (1.87-8.82)	<0.001	1.07 (0.42-2.71)	0.892
Stage IV	10.47 (4.78-22.93)	<0.001	3.44 (1.37-8.63)	0.009
Adjuvant chemotherapy				
Yes	0.66 (0.49-0.90)	0.008	0.72 (0.52-0.98)	0.045
No	Ref.	-	Ref.	-
Radiotherapy				
Yes	0.98 (0.48-1.98)	0.945		
No	Ref.	-		
CIOSS				
Low	Ref.	-	Ref.	-
Intermediate	3.08 (2.12-4.48)	<0.001	2.93 (1.99-4.32)	<0.001
High	5.09 (3.40-7.64)	<0.001	4.33 (2.80-6.68)	<0.001

TABLE 4: Univariate and multivariate analyses of factors associated with DFS.

|	Univariate analysis		Multivariate analysis	
	HR (95% CI)	P	HR (95% CI)	P
Age (years)				
≥60	1.13 (0.82-1.55)	0.457		
<60	Ref.	-		
Sex, male	1.02 (0.74-1.41)	0.886		
Primary site				
Left colon	1.40 (0.98-2.02)	0.068	1.15 (0.79-1.67)	0.481
Right colon	1.52 (1.01-2.29)	0.048	1.26 (0.82-1.93)	0.303
Rectum	Ref.	-		
Family history of cancer	1.26 (0.70-2.26)	0.450		
Histological grade				
Well differentiated	Ref.	-		
Moderately differentiated	1.31 (0.81-2.12)	0.279		
Poorly differentiated	1.50 (0.73-3.09)	0.272		
Tumor size				
<2 cm	0.71 (0.31-1.64)	0.421		
2-5 cm	0.88 (0.63-1.23)	0.453		
≥5 cm	Ref.	-		
Lymphovascular invasion				
Yes	0.96 (0.62-1.48)	0.845		
No	Ref.	-		
Circumferential resection margin				
Yes	1.49 (0.37-6.03)	0.573		
No	Ref.	-		
T stage				
T1	Ref.	-	Ref.	-
T2	2.21 (0.49-9.96)	0.303	2.93 (0.63-13.55)	0.170
T3	4.39 (1.07-17.92)	0.040	3.71 (0.88-15.73)	0.075
T4	13.23 (3.25-53.88)	<0.001	6.80 (1.60-28.87)	0.009
N stage				
N0	Ref.	-	Ref.	-
N1	0.83 (0.35-1.93)	0.659	1.02 (0.43-2.43)	0.958
N2	1.87 (0.80-4.38)	0.152	1.30 (0.53-3.19)	0.570
N3	4.00 (1.71-9.23)	0.001	1.88 (0.78-4.51)	0.160
TNM stage				
Stage I	Ref.	-	Ref.	-
Stage II	2.63 (0.78-8.81)	0.118	1.38 (0.37-5.16)	0.634
Stage III	5.64 (1.76-18.09)	0.004	2.24 (0.61-8.18)	0.223
Stage IV	33.45 (10.56-105.93)	<0.001	13.09 (3.63-47.19)	<0.001
Adjuvant chemotherapy				
Yes	0.82 (0.68-1.17)	0.328		
No	Ref.	-		
Radiotherapy				
Yes	0.51 (0.29-0.91)	0.022	0.92 (0.51-1.67)	0.794
No	Ref.	-	Ref.	-
CIOSS				
Low	Ref.	-	Ref.	-
Intermediate	2.17 (1.49-3.16)	<0.001	1.88 (1.29-2.76)	0.001
High	3.09 (2.02-4.71)	<0.001	3.02 (1.96-4.64)	<0.001
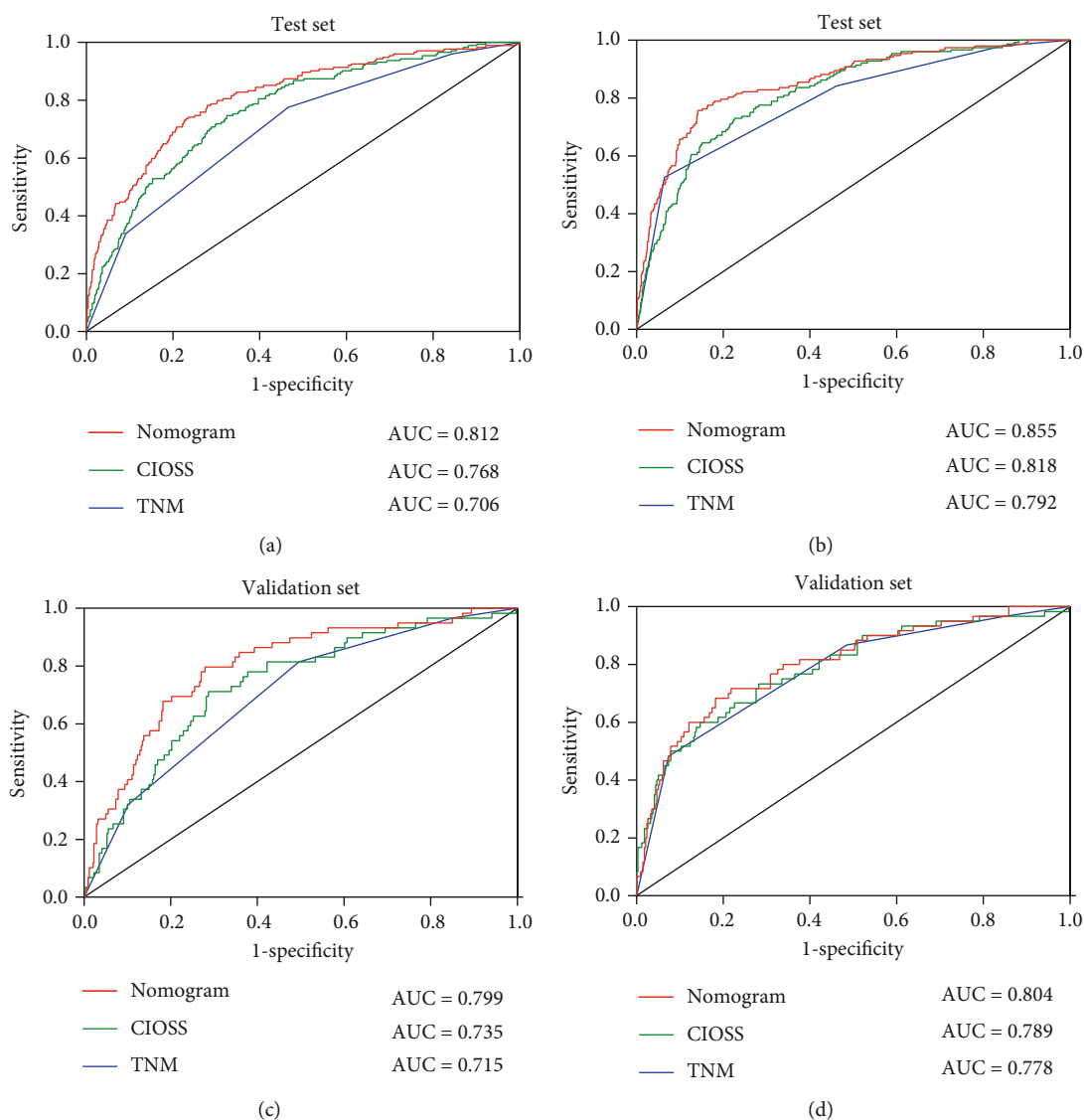
FIGURE 3: Receiver operating characteristic (ROC) curves of CIOSS, TNM stage, and the nomogram. The prognostic significance and predictive performance of the CIOSS, TNM stage, and nomogram in predicting OS and DFS in the (a, b) training sets and (c, d) validation sets, respectively.

was significantly lower than that in the normal population ($P < 0.01$). Assessment of oxidative stress and antioxidant administration are of great significance for the treatment and prevention of colorectal cancer [18]. Although current studies have found that oxidative stress is closely related to the occurrence and development of CRC, few studies have used the state of oxidative stress to establish CRC prediction model, and oxidative stress may be a potential indicator to improve the prediction accuracy of CRC prognosis.

In this study, we designed a new score, CIOSS, developed from a series of oxidative stress indicators significantly associated with survival in CRC patients and found that CIOSS was independent prognostic factors among patients with CRC. To build a highly accurate OS prediction model, important parameters from the univariate regression were further used for the multiple regression model. Four valuable factors, TNM, T staging, chemotherapy, and CIOSS, were

selected to establish the prediction model. In this study, ROC was compared with nomogram, CIOSS, and TNM. AUC in the OS test set was 0.813, 0.768, and 0.706, respectively, and 0.855, 0.818, and 0.792 in the validation set, respectively. The AUC in the DFS test set was 0.799, 0.735, and 0.715, respectively, and 0.804, 0.789, and 0.778 in the validation set. The nomogram and CIOSS showed good discrimination and calibration and had important clinical application.

At present, many studies also use relevant indicators to predict CRC prognosis and establish corresponding prediction models. Li et al. also established a nomogram model to predict CRC prognosis based on the NLR, PLR, lymphocytes and monocyte ratio (LMR), and albumin/globulin ratio (AGR) for five-year OS and DFS [19]. They found that NLR > 2.72, PLR > 219.00, 2.83, and AGR < 1.50 were associated with a significant reduction in DFS and OS

(a)

(b)
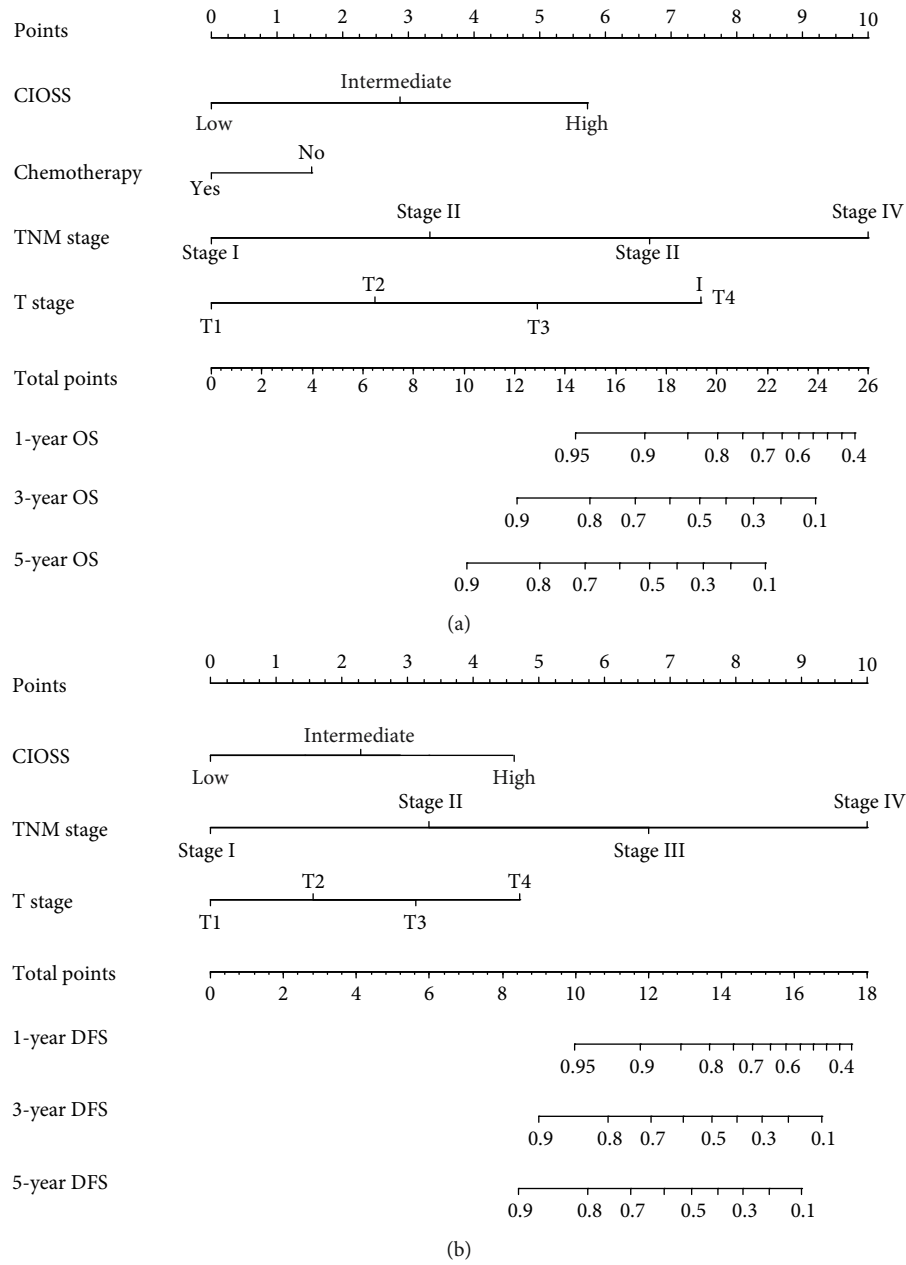
FIGURE 4: Evaluation of overall survival (OS) and disease-free survival- (DFS-) associated nomograms for resectable patients with colorectal cancer (CRC). (a) OS nomogram integrating the TNM stage, T stage, CIOSS, and chemotherapy for predicting 1-, 3-, and 5-year OS rates. (b) DFS nomogram integrating TNM stage, T stage, and CIOSS for predicting 1-, 3-, and 5-year DFS rates.

($P < 0.001$), and the Harrell's C-indexes for OS and DFS prediction were 0.765 and 0.735. In this study, an obvious limitation of this model is that it has not been effectively verified externally, so it needs further verification. There is another multicenter retrospective study using postoperative carcinoma embryonic antigen (CEA) level, depth of tumor invasion (T factor), lymph node metastasis (N factor), and number of metastatic organs as variables, and predicting OS with postoperative CEA level, T factor, and peritoneal metastasis using factor N as a useful tool for postoperative monitoring of stage IV CRC patients, the nomograms showed c-indices of 0.629 and 0.640 in the derivation set and 0.604 and 0.637 in the validation set for DFS and OS,

respectively [20]. This study is also an effective model based on common laboratory examination indicators, but its accuracy is slightly lower than that of our study. A few CRC prediction models with large sample data have also been established, and their validity has been verified both internally and externally. Boakye et al. used the Cox model and predefined variables (age, sex, stage, tumor location, and comorbidity score) to construct nomograms of relevant survival outcomes, which were found to significantly improve the prediction of CRC prognosis [21]. Li et al. established nomogram prediction for progression based on inflammatory biomarkers to predict the prognosis of CRC patients, and the results showed that the inflammatory factors

FIGURE 5: Nomograms of time-dependent receiver operating characteristic (ROC) curves associated with overall survival (OS) and disease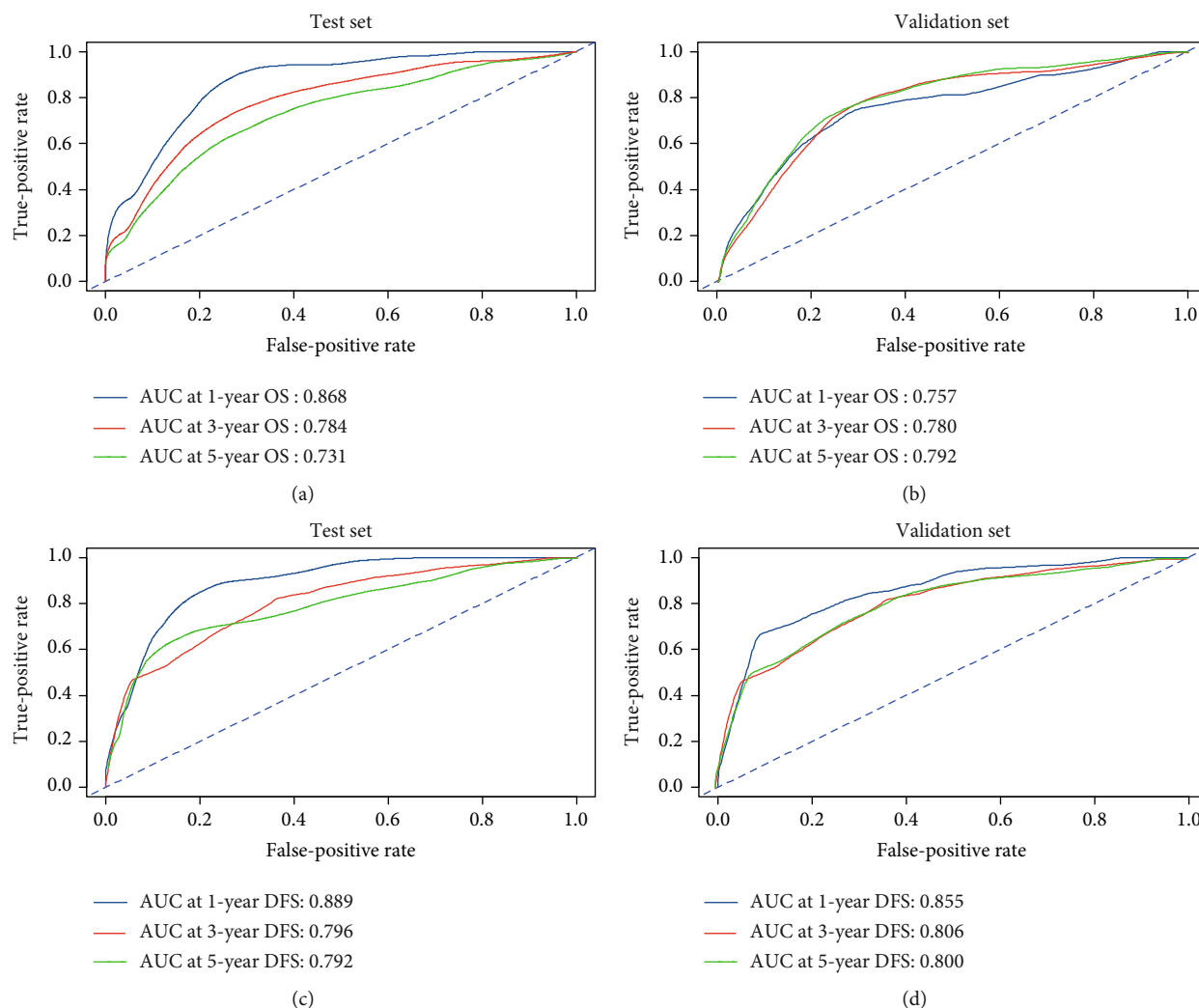-free survival (DFS). (a, c) Represent ROC curve of nomogram 1-, 3-, and 5-year OS rates for the training set and validation set; (b, d) represent ROC curve of nomogram 1-, 3-, and 5-year DFS rates for the training set and validation set.

included in these nomograms predicted accurate individual prognosis [22]. In addition to the combination of commonly used laboratory examination indicators into a prediction model, there have also been studies to predict the prognosis of CRC patients by combining laboratory examination and imaging examination into a prediction model. Huang et al. included a panel of radiology characteristics in their study where CT reports the status of lymph nodes and independent clinical risk factors, and through the group of radiology nomogram, model identification and calibration and applied in the validation queue nomogram still have good identification, the model showed good discrimination, with a C-index of 0.736 through internal validation, and in the validation cohort, it still gave good discrimination with C-index of 0.778 and good calibration [23]. The results of this study are of great significance, imaging examination and laboratory examination-related indicators are combined, and the prediction model is effectively validated both internally and externally. Although the accuracy of the prediction results is slightly lower than that of our study, it provides us with a

good reference and suggestion. It is worth further exploring whether the integration of our research indicators into imaging examination can significantly improve the prediction effect. At present, different indexes are included in the prognosis prediction model for CRC patients, and the prediction effect of each is different. However, a reasonable and effective prediction model still needs further study.

In our study, the independent predictors of OS and DFS in multivariate analysis of CRC patients were mainly related to T stage, TNM stage, adjuvant chemotherapy, and CIOSS. Tumor stage and chemotherapy have been previously validated as independent prognostic factors for CRC patients after surgery [24, 25]. CIOSS comprised the ALB, DBIL, and BUN, which are closely related to oxidative stress and play an important role in tissue damage and disease progression. An animal model experiment found that when the oxidative stress reaction was triggered in mice after receiving external stimulation, the oxidative stress factors increased and biochemical examination showed significantly high levels of TBIL, lactate dehydrogenase (LDH), CRE, and
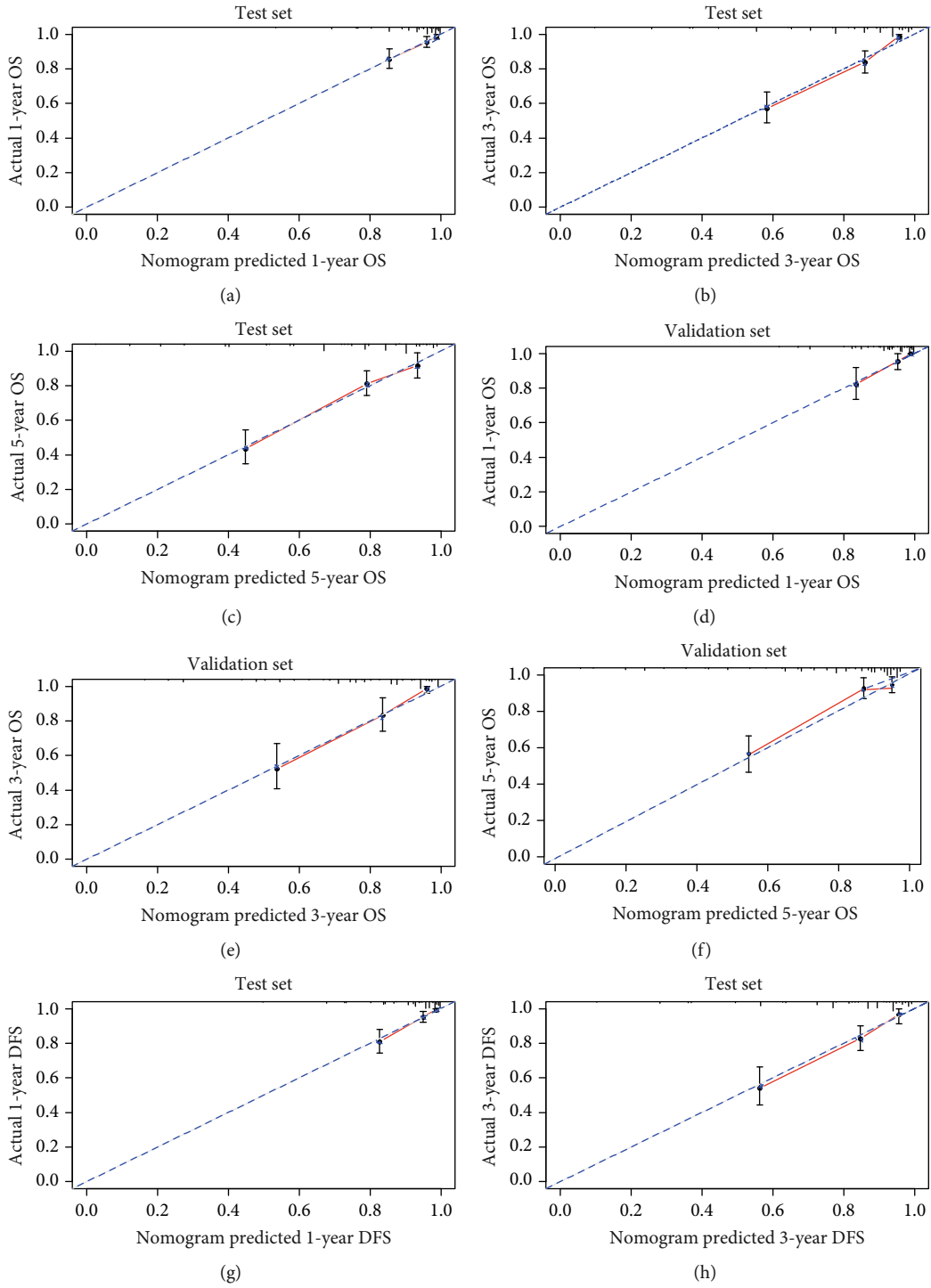
(a)

(b)

(c)

(d)

(e)
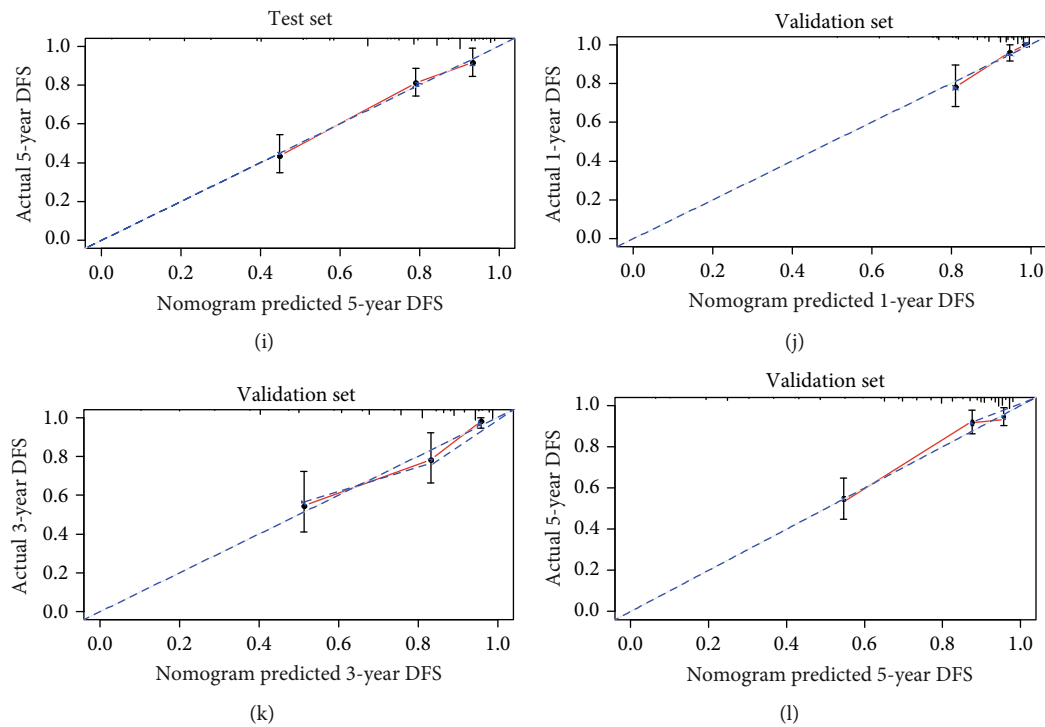
(f)

(g)

(h)

Figure 6: Continued.

FIGURE 6: Calibration curves for 1-, 3-, and 5-year nomogram predictions. The calibration curves for predicting overall survival (OS) in colorectal cancer (CRC) patients at (a) 1, (b) 3, and (c) 5 years in the training set and at (d) 1, (e) 3, and (f) 5 years in the validation set. The calibration curves for predicting disease-free survival (DFS) in CRC patients at (g) 1, (h) 3, and (i) 5 years in the training set and at (j) 1, (k) 3, and (l) 5 years in the validation set.

BUN [26]. In a prospective observational study, it was found that the levels of TBIL, ALB, LDH, and CRP were significantly increased in patients with oxidative stress. After antioxidant treatment, the respective scores were significantly lower in patients than those in the control group, and the incidence of mortality and sepsis was also lower [27]. A retrospective study showed that TBIL and DBIL were significantly associated with poor prognosis after surgical resection in stages II and III CRC patients, and high DBIL had higher percentage of lymph node metastasis and lymphovascular invasion as compared with low DBIL levels ($P < 0.05$) [28]. BUN and ALB have been confirmed to be closely related to the prognosis of CRC patients and are independent prognostic factors [29, 30]. In these studies, we find that the predictive value of a single indicator is limited, while the predictive value of a combination of indicators is higher. Therefore, CIOSS and nomograms were constructed to predict CRC prognosis by combining relevant biochemical examinations that can reflect oxidative stress status. This is a new prediction model, and it has been verified to be effective.

Although the sample size of our study is large, this clinical study has some limitations. First, this retrospective study was conducted at a single center and lacked external validation. Second, although we systematically collected the laboratory examination information of patients, the levels of relevant laboratory indicators changed over time and no continuous dynamic monitoring was carried out. Finally, due to the clinical limitations, the oxidative stress indicators were not fully included. Large-scale clinical studies with more

clinical and genetic characteristics conducted in multiple centers are needed to verify our results. Although there are some shortcomings, our research also has great application value. We used some common laboratory indicators to evaluate patients' oxidative stress status, which is more convenient to use and has high predictive effect and value. To our knowledge, few studies have established a CRC prognosis model from the direction of oxidative stress. This is the first time to predict the prognosis of CRC patients from the direction of oxidative stress, and our study can provide a new idea for the prediction of CRC prognosis.

5. Conclusions

CIOSS is a CRC-specific prognostic index based on a combination of available oxidative stress indexes. High CIOSS was found to be a powerful indicator of poor prognosis. The CIOSS also showed better predictive performance compared to TNM stage in CRC patients. The survival nomogram generated by combining the CIOSS with other beneficial clinical characteristics can potentially be a convenient and effective tool for predicting the prognosis of CRC patients.

Data Availability

The data used to support the findings of this study are available from the corresponding author upon request.

Disclosure

Conflicts of Interest

The authors declare that there is no conflict of interest regarding the publication of this paper.

Authors' Contributions

Yinghao Cao, Shenghe Deng, and Lizhao Yan contributed equally to this work.

Acknowledgments

Supplementary Materials

The supplementary pictures have been uploaded to the attachment. Fig S1: the oxidative stress indicators were statistically associated with OS and DFS in CRC patients. The curves of ALB, TBIL, DBIL, BUN, and UA for OS in CRC patients (A-E); the curves of ALB, TBIL, DBIL, BUN, and UA for DFS in CRC patients (F-J). (Supplementary Materials)

References

[1] GBD 2013 Mortality and Causes of Death Collaborators, M. Naghavi, H. Wang et al., "Global, regional and national levels of age-specific mortality and 240 causes of death, 1990–2013: a systematic analysis for the Global Burden of Disease Study 2013," *Lancet*, vol. 385, pp. 117–171, 2015.

[2] S. Ogino, A. T. Chan, C. S. Fuchs, and E. Giovannucci, "Molecular pathological epidemiology of colorectal neoplasia: an emerging transdisciplinary and interdisciplinary field," *Gut*, vol. 60, no. 3, 2011.

[3] E. J. Kuipers, W. M. Grady, D. Lieberman et al., "Colorectal cancer," *Nature Reviews. Disease Primers*, vol. 1, no. 1, pp. 1–51, 2015.

[4] A. L. Mahar, C. Compton, S. Halabi, K. R. Hess, M. R. Weiser, and P. A. Groome, "Personalizing prognosis in colorectal cancer: a systematic review of the quality and nature of clinical prognostic tools for survival outcomes," *Journal of Surgical Oncology*, vol. 116, no. 8, pp. 969–982, 2017.

[5] C. Carlomagno, A. De Stefano, M. Rosanova et al., "Multiple treatment lines and prognosis in metastatic colorectal cancer patients," *Cancer Metastasis Reviews*, vol. 38, no. 1-2, pp. 307–313, 2019.

[6] H. J. Lu, J. K. Lin, W. S. Chen et al., "The prognostic role of para-aortic lymph nodes in patients with colorectal cancer: is it regional or distant disease?," *PLoS One*, vol. 10, no. 6, article e0130345, 2015.

[7] J. Li, J. Gu, X. Ma et al., "Development and validation of a nomogram for predicting survival in Chinese han patients with resected colorectal cancer," *Journal of Surgical Oncology*, vol. 118, no. 6, pp. 1034–1041, 2018.

[8] B. Leggett and V. Whitehall, "Role of the serrated pathway in colorectal cancer pathogenesis," *Gastroenterology*, vol. 138, no. 6, pp. 2088–2100, 2010.

[9] R. Ostan, C. Lanzarini, E. Pini et al., "Inflammaging and cancer: a challenge for the Mediterranean diet," *Nutrients*, vol. 7, no. 4, pp. 2589–2621, 2015.

[10] H. B. Henriksen, H. Ræder, S. K. Bøhn et al., "The Norwegian dietary guidelines and colorectal cancer survival (CRC-NOR-DIET) study: a food-based multicentre randomized controlled trial," *BMC Cancer*, vol. 17, no. 1, p. 83, 2017.

[11] R. L. Camp, M. Dolled-Filhart, and D. L. Rimm, "X-tile: a new bio-informatics tool for biomarker assessment and outcome-based cut-point optimization," *Clinical Cancer Research*, vol. 10, no. 21, pp. 7252–7259, 2004.

[12] J. Port, N. Muthalagu, M. Raja et al., "Colorectal tumors require NUAK1 for protection from oxidative stress," *Cancer Discovery*, vol. 8, no. 5, pp. 632–647, 2018.

[13] S. P. Hussain, L. J. Hofseth, and C. C. Harris, "Radical causes of cancer," *Nature Reviews. Cancer*, vol. 3, no. 4, pp. 276–285, 2003.

[14] D. L. Oberreuther-Moschner, G. Rechkemmer, and B. L. Pool-Zobel, "Basal colon crypt cells are more sensitive than surface cells toward hydrogen peroxide, a factor of oxidative stress," *Toxicology Letters*, vol. 159, no. 3, pp. 212–218, 2005.

[15] M. Liu, T. Sun, N. Li et al., "BRG1 attenuates colonic inflammation and tumorigenesis through autophagy-dependent oxidative stress sequestration," *Nature Communications*, vol. 10, no. 1, p. 4614, 2019.

[16] L. Zhang, L. Li, G. Gao et al., "Elevation of GPRC5A expression in colorectal cancer promotes tumor progression through VNN-1 induced oxidative stress," *International Journal of Cancer*, vol. 140, no. 12, pp. 2734–2747, 2017.

[17] V. L. Kumar, S. Verma, and P. Das, "Artesunate suppresses inflammation and oxidative stress in a rat model of colorectal cancer," *Drug Development Research*, vol. 80, no. 8, pp. 1089–1097, 2019.

[18] D. Chang, F. Wang, Y. S. Zhao, and H. Z. Pan, "Evaluation of oxidative stress in colorectal cancer patients," *Biomedical and Environmental Sciences*, vol. 21, no. 4, pp. 286–289, 2008.

[19] Y. Li, H. Jia, W. Yu et al., "Nomograms for predicting prognostic value of inflammatory biomarkers in colorectal cancer patients after radical resection," *International Journal of Cancer*, vol. 139, no. 1, pp. 220–231, 2016.

[20] K. Kawai, S. Ishihara, H. Yamaguchi et al., "Nomograms for predicting the prognosis of stage IV colorectal cancer after curative resection: a multicenter retrospective study," *European Journal of Surgical Oncology*, vol. 41, no. 4, pp. 457–465, 2015.

[21] D. Boakye, L. Jansen, M. Schneider, J. Chang-Claude, M. Hoffmeister, and H. Brenner, "Personalizing the prediction of colorectal cancer prognosis by incorporating comorbidities and functional status into prognostic nomograms," *Cancers*, vol. 11, no. 10, p. 1435, 2019.

[22] X. Li, B. An, Q. Zhao et al., "Impact of tumor deposits on the prognosis and chemotherapy efficacy in stage III colorectal

cancer patients with different lymph node status: a retrospective cohort study in China," *International Journal of Surgery*, vol. 56, pp. 188–194, 2018.

[23] Y. Q. Huang, C. H. Liang, L. He et al., "Development and validation of a radiomics nomogram for preoperative prediction of lymph node metastasis in colorectal cancer," *Journal of Clinical Oncology*, vol. 34, no. 18, pp. 2157–2164, 2016.

[24] J. H. Kim, "Chemotherapy for colorectal cancer in the elderly," *World Journal of Gastroenterology*, vol. 21, no. 17, pp. 5158–5166, 2015.

[25] S. Periasamy, D. Z. Hsu, Y. H. Fu, and M. Y. Liu, "Sleep deprivation-induced multi-organ injury: role of oxidative stress and inflammation," *EXCLI Journal*, vol. 14, pp. 672–683, 2015.

[26] M. Sandesc, A. F. Rogobete, O. H. Bedreag et al., "Analysis of oxidative stress-related markers in critically ill polytrauma patients: an observational prospective single-center study," *Bosnian Journal of Basic Medical Sciences*, vol. 18, no. 2, pp. 191–197, 2018.

[27] W. G. Lima, M. E. S. Martins-Santos, and V. E. Chaves, "Uric acid as a modulator of glucose and lipid metabolism," *Biochimie*, vol. 116, pp. 17–23, 2015.

[28] Q. Zhang, X. Ma, Q. Xu et al., "Nomograms incorporated serum direct bilirubin level for predicting prognosis in stages II and III colorectal cancer after radical resection," *Oncotarget*, vol. 8, no. 41, pp. 71138–71146, 2017.

[29] Y. Wei, H. Xu, J. Dai et al., "Prognostic significance of serum lactic acid, lactate dehydrogenase, and albumin levels in patients with metastatic colorectal cancer," *BioMed Research International*, vol. 2018, Article ID 1804086, 2018.

[30] F. Zhang, Y. Zhang, W. Zhao et al., "Metabolomics for biomarker discovery in the diagnosis, prognosis, survival and recurrence of colorectal cancer: a systematic review," *Oncotarget*, vol. 8, no. 21, pp. 35460–35472, 2017.

Research Article

Development and Validation of a Nine-Redox-Related Long Noncoding RNA Signature in Renal Clear Cell Carcinoma

Xia Qi-Dong ![ORCID], **Xun Yang, Jun-Lin Lu, Chen-Qian Liu, Jian-Xuan Sun, Cong Li** ![ORCID], **and Shao-Gang Wang** ![ORCID]

Department and Institute of Urology, Tongji Hospital, Tongji Medical College, Huazhong University of Science and Technology, No. 1095 Jiefang Avenue, 430030 Wuhan, China

Correspondence should be addressed to Cong Li; licongtjm@163.com

Background. Redox plays an essential role in the pathogeneses and progression of tumors, which could be regulated by long noncoding RNA (lncRNA). We aimed to develop and verify a novel redox-related lncRNA-based prognostic signature for clear cell renal cell carcinoma (ccRCC). *Materials and Methods*. A total of 530 ccRCC patients from The Cancer Genome Atlas (TCGA) were included in this study. All the samples were randomly split into training and test group at a 1 : 1 ratio. Then, we screened differentially expressed redox-related lncRNAs and constructed a novel prognostic signature from the training group using the least absolute shrinkage and selection operation (LASSO) and COX regression. Next, to verify the accuracy of the signature, we conducted risk and survival analysis, as well as the construction of ROC curve, nomogram, and calibration curves in the training group, test group, and all samples. Finally, the redox gene-redox-related lncRNA interaction network was constructed, and gene set enrichment analysis (GSEA) was performed to investigate the status of redox-related functions between high/low-risk groups. *Results*. A nine-redox-related lncRNA signature consisted of *AC025580.3*, *COLCA1*, *AC027601.2*, *DLEU2*, *AC004918.3*, *AP006621.2*, *AL031670.1*, *SPINT1-AS1*, and *LAMA5-AS1* was significantly associated with overall survival in ccRCC patients. The signature proved efficient, and thus, a nomogram was successfully assembled. In addition, the GSEA results demonstrated that two major redox-related functions were enhanced in the high-risk group ccRCC patients. *Conclusions*. Our findings robustly demonstrate that the nine-redox-related lncRNA signature could serve as an efficient prognostic indicator for ccRCC.

1. Introduction

Renal cell carcinoma (RCC) is the most common malignant tumour in the kidney, accounting for nearly 90% of all kidney cancers [1]. Approximately 350,000 new cases of RCC were diagnosed worldwide per year, which caused more than 15,000 deaths per year in the USA and more than 140,000 deaths per year worldwide [2, 3]. RCC can have several histologic subtypes; clear cell renal cell carcinoma (ccRCC) is the most common RCC subtype in adults and accounts for approximately 70% of all RCC cases [4]. The prognosis of ccRCC varies widely. For patients with early and localized disease, the cure rate is high with a 5-year survival of more than 90%. However, 5-year survival was only 12% for patients with distant metastatic disease [5], which caused

most deaths in ccRCC patients. In addition to the most basic surgical resection, many emerging therapies for the treatment of metastatic ccRCC have been proposed with improved knowledge of disease biology. Cabozantinib, an antiangiogenic agent that targets the VEGF pathway, was approved as a first-line therapy for patients with advanced ccRCC [6]. Immunotherapy, such as programmed cell death 1 (PD-1) and cell death-ligand 1 (PD-L1) blockers, has also been developed in ccRCC [7, 8]. However, each of these treatments still has some limitations. Hence, it is urgent to improve the survival of patients with ccRCC. Whereas TNM (Tumor, Node, Metastasis) staging system has been the most commonly prognostic predictive system for ccRCC patients, it does not effectively predict the aggressiveness of the ccRCC [9]. Although there are several common

prognosis factors such as tumor stage, grade, and size, these factors also do not provide accurate predictions due to their molecular and genetic heterogeneity were ignored. Identifying potential valuable molecular biomarkers would enhance the prognostic value of the developed tools.

Redox homeostasis system regulates many biological processes, including cell signaling, proliferation, and differentiation by modulating intracellular antioxidant and redox signaling (ARS). Imbalances among oxidation and antioxidation can lead to oxidative stress and damage to cell functions, contributing to a variety of diseases [10, 11]. During the last decades, extensive research has revealed that disruption of the reduction–oxidation signaling can mediate cancer initiation and development by leading to molecular damage [12, 13]. Recent studies showed the imbalance of the redox homeostasis system is closely related to the RCC occurrence and progression [14, 15]. Hence, it is vital to discover potential valuable redox-related biomarkers to improve the prognostic prediction of patients with ccRCC.

In recent years, scientists have focused on molecular biomarkers in the development of a reliable prognostic biomarker in cancer [16]. The long noncoding RNA (lncRNA) is a type of noncoding RNA with transcripts of >200 nucleotides in length without any protein-coding capacity [17], but it plays important roles in the regulation of mRNA transcription and protein translation [18]. lncRNA modulated many important biological functions, such as cell growth and survival, genomic imprinting, chromatin modifications, and allosteric regulation of enzyme activities [19]. In tumor patients, abnormal expressions of lncRNA are frequent biological phenomena and closely associated with prognosis [20]. lncRNAs have been repeatedly suggested as well-accessible blood-based biomarkers in numerous urogenital malignancies, including RCC [21–23]. Therefore, the redox-related lncRNA may be used as a potential valuable biomarker or a potential therapeutic target.

In our study, we evaluated the interaction between redox and lncRNA. A nine-redox-related lncRNA signature with potential molecular prognostic value in ccRCC was identified by using both the LASSO and Cox regression analyses. We also constructed a nomogram based on this nine-redox-related lncRNA signature for improving the prognostic prediction of ccRCC patients, and it will serve as a reliable prognostic predictor tool for ccRCC patients in the future.

2. Materials and Methods

2.1. Data Sources. We searched TCGA-GDC (https://portal.gdc.cancer.gov/) for the transcriptome profiling and clinical data. We filtered the transcriptome profiling data using the following: the primary site is the kidney, the program name is TCGA, the project is TCGA-KIRC, the disease type is adenomas and adenocarcinomas, and the data category is transcriptome profiling while workflow type is HTSeq-FPKM. On the other hand, the filter criteria for clinical data included data category and format as clinical and bcr xml, respectively. We then downloaded the cart and metadata files for the transcriptome profiling data (611 samples) and the cart files for the clinical data (537

samples). The data files were decompressed and sorted into a matrix based on PERL programming. We searched the Ensembl database (http://asia.ensembl.org/index.html) for the human gene transfer format (gtf) file to transfer the gene id and annotate genes for mRNA or lncRNA. In addition, we searched GSEA-MSigDB (https://www.gsea-msigdb.org/gsea/msigdb) for the redox-related gene set by searching "redox" as keywords, and we download two redox-related gene sets as "GO_CELL_REDOX_HOMEOSTASIS" and "GO_RESPONSE_TO_REDOX_STATE."

2.2. Differentially Expressed Redox-Related lncRNAs (DERRlncRNAs). Having annotated the genes for mRNA or lncRNA, we extracted the expression of lncRNA and then used the "limma" package for the entire lncRNA data to identify the differentially expressed lncRNAs (DElncRNAs) with $|logFC| > 1$ and FDR < 0.05 between tumor and normal samples. Meanwhile, we extracted the expression of redox-related gene sets then identified redox-related lncRNAs by using the Pearson Correlation Test with $|Cor| > 0.5$ and p.adj < 0.001 between lncRNAs and expression of redox-related gene sets in tumor tissue. Finally, we took an intersection of DElncRNAs and redox-related lncRNAs to screen differentially expressed redox-related lncRNAs (DERRlncRNAs).

2.3. Random Grouping and Signature Construction. We merge the expression of DERRlncRNAs with their clinical survival data; then, all the samples were randomly split into the training and test groups at a 1 : 1 ratio. Following this, we performed univariate Cox regression of DERRlncRNAs in the training group to identify prognosis-related DERRlncRNAs with the filter criterion set at a significance of $p < 0.05$. Also, to avoid overfitting, we applied LASSO regression to screen appropriate variables from the prognosis-related DERRlncRNAs. Finally, a survival-predicting model was constructed by a multivariate Cox proportional hazard model. Importantly, a risk score formula was created based on the signature: Risk score $= \sum_{i=1}^{N} (\text{Exp}(i) \cdot \text{coe}(i))$. N is the number of redox-related lncRNA in the multivariate COX regression, Exp(i) is the expression value of lncRNA, and Coe(i) is the estimated regression coefficient of lncRNA in the multivariate Cox regression analysis. Then, the samples in both the training group and test group obtained a risk score calculated by the formula, and we set the medium value of the risk score in the training group as filter criteria that the higher risk score is high risk and the lower risk score is low risk.

2.4. Validation of the Survival-Predicting Model. According to the risk level judged by the risk score, we performed the Kaplan-Meier method survival analysis to test the survival-predicting availability of the signature and plot the survival curve for the samples in the training group, test group, and all group. Then, we merged the clinical data which contained age, gender, stage, and grade with the risk score of patients and rechecked to delete samples lacking accurate clinical data. Following this, we plotted the multivariate ROC curves to verify and compare the efficacy of the developed signature with the other clinical prognostic factors; the area under the curve (AUC) for multiple factors which contained age,

Table 1: Clinical characteristics of the KIRC patients.

	Overall	Test	Train	p
n	530	264	266	
Age (mean (SD))	60.56 (12.14)	60.48 (11.76)	60.65 (12.52)	0.875
Gender = female/male (%)	186/344 (35.1/64.9)	82/182 (31.1/68.9)	104/162 (39.1/60.9)	0.065
Grade (%)				0.432
G1	14 (2.6)	5 (1.9)	9 (3.4)	
G2	227 (42.8)	108 (40.9)	119 (44.7)	
G3	206 (38.9)	110 (41.7)	96 (36.1)	
G4	75 (14.2)	36 (13.6)	39 (14.7)	
GX	5 (0.9)	4 (1.5)	1 (0.4)	
Unknown	3 (0.6)	1 (0.4)	2 (0.8)	
Stage (%)				0.169
Stage I	265 (50.0)	125 (47.3)	140 (52.6)	
Stage II	57 (10.8)	26 (9.8)	31 (11.7)	
Stage III	123 (23.2)	68 (25.8)	55 (20.7)	
Stage IV	82 (15.5)	45 (17.0)	37 (13.9)	
Unknown	3 (0.6)	0 (0.0)	3 (1.1)	
T (%)				0.414
T1	21 (4.0)	10 (3.8)	11 (4.1)	
T1a	140 (26.4)	68 (25.8)	72 (27.1)	
T1b	110 (20.8)	49 (18.6)	61 (22.9)	
T2	55 (10.4)	27 (10.2)	28 (10.5)	
T2a	10 (1.9)	3 (1.1)	7 (2.6)	
T2b	4 (0.8)	1 (0.4)	3 (1.1)	
T3	5 (0.9)	2 (0.8)	3 (1.1)	
T3a	120 (22.6)	69 (26.1)	51 (19.2)	
T3b	52 (9.8)	30 (11.4)	22 (8.3)	
T3c	2 (0.4)	0 (0.0)	2 (0.8)	
T4	11 (2.1)	5 (1.9)	6 (2.3)	
M (%)				0.283
M0	420 (79.2)	209 (79.2)	211 (79.3)	
M1	78 (14.7)	43 (16.3)	35 (13.2)	
MX	30 (5.7)	12 (4.5)	18 (6.8)	
Unknown	2 (0.4)	0 (0.0)	2 (0.8)	
N (%)				0.68
N0	239 (45.1)	124 (47.0)	115 (43.2)	
N1	16 (3.0)	8 (3.0)	8 (3.0)	
NX	275 (51.9)	132 (50.0)	143 (53.8)	
Risk = high/low (%)	271/259 (51.1/48.9)	138/126 (52.3/47.7)	133/133 (50.0/50.0)	0.663

gender, stage, grade, and risk scores was calculated and compared with each other in the training group, test group, and all samples.

2.5. Construction and Validation of the Risk Score-Based Nomogram. To provide clinicians with a quantitative rather than qualitative approach for predicting survival, we assembled a nomogram according to the risk score and clinicopathologic characteristics from the samples in the training group, then performed internal cross-validation, and input test group and all samples as two external validation set to per-

form an external validation. All the calibration curve for 1 year, 3 years, and 5 years were plotted.

2.6. Gene Set Enrichment Analysis (GSEA) and Clinical Correlation. Though we had tested the survival-predicting availability of the signature, how the redox-related functions worked was still unknown; thus, we divided the transcriptome file for all samples into the high-risk group and low-risk group according to the medium value of risk score in the training group and then exported the data as "cls" and "gct" format files, which were then imported into GSEA
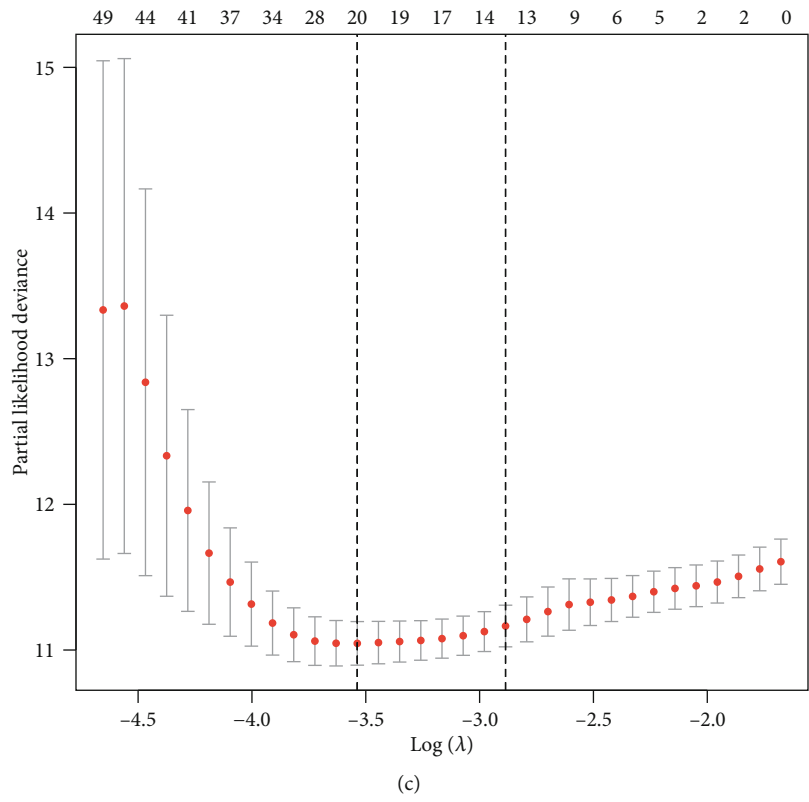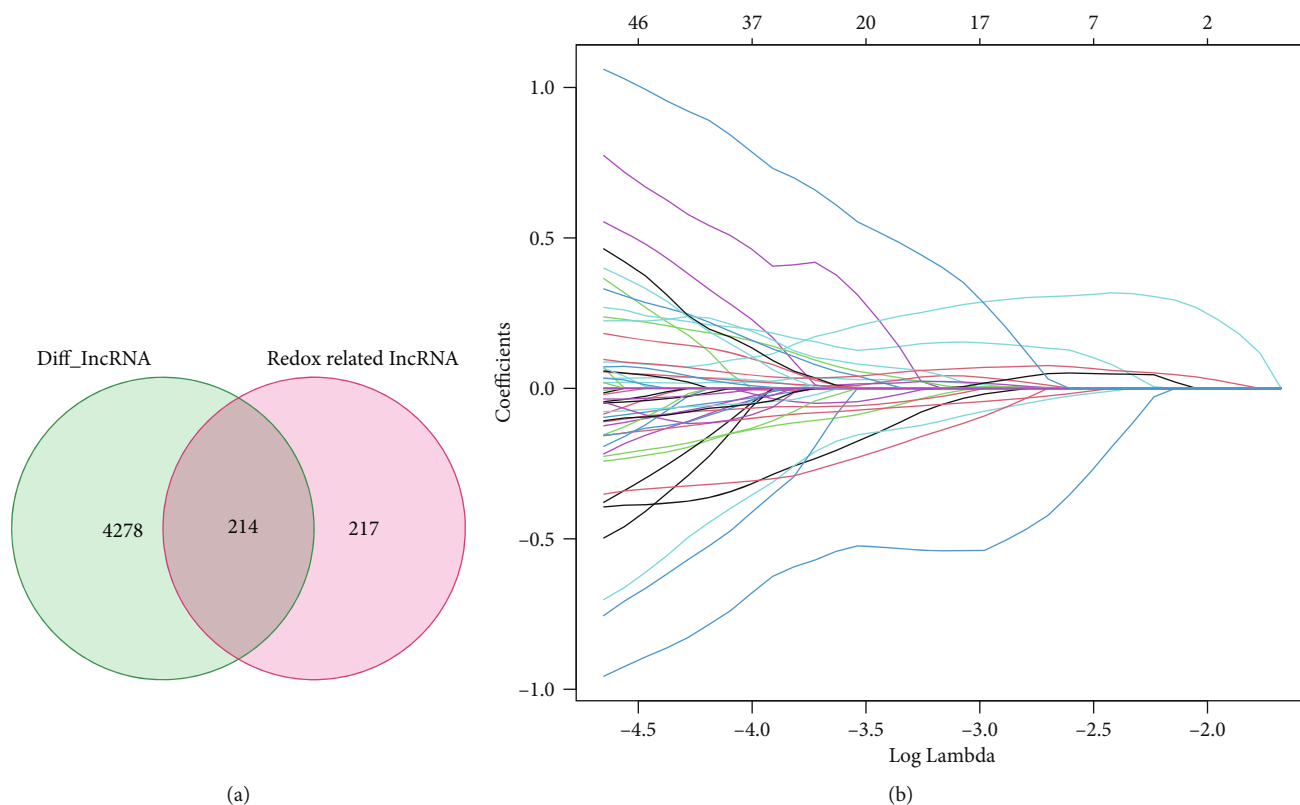
(a)

(b)

(c)

Figure 1: Continued.

Hazard ratio

AC025580.3	(N = 266)	0.57 (0.35 − 0.93)		0.024 *
COLCA1	(N = 266)	0.72 (0.48 − 1.08)		0.114
AC027601.2	(N = 266)	0.42 (0.22 − 0.80)		0.009 **
DLEU2	(N = 266)	3.41 (1.52 − 7.67)		0.003**
AC004918.3	(N = 266)	0.58 (0.43 − 0.79)		<0.001***
AP006621.2	(N = 266)	1.23 (1.07 − 1.42)		0.005**
AL031670.1	(N = 266)	2.43 (1.27 − 4.65)		0.007 **
SPINT1−AS1	(N = 266)	0.90 (0.79 − 1.02)		0.101
LAMA5−AS1	(N = 266)	1.30 (0.93 − 1.83)		0.125

#Events: 85; Global p−value (Log−Rank): 3.0805e−17
AIC: 762.49; Concordance Index: 0.79
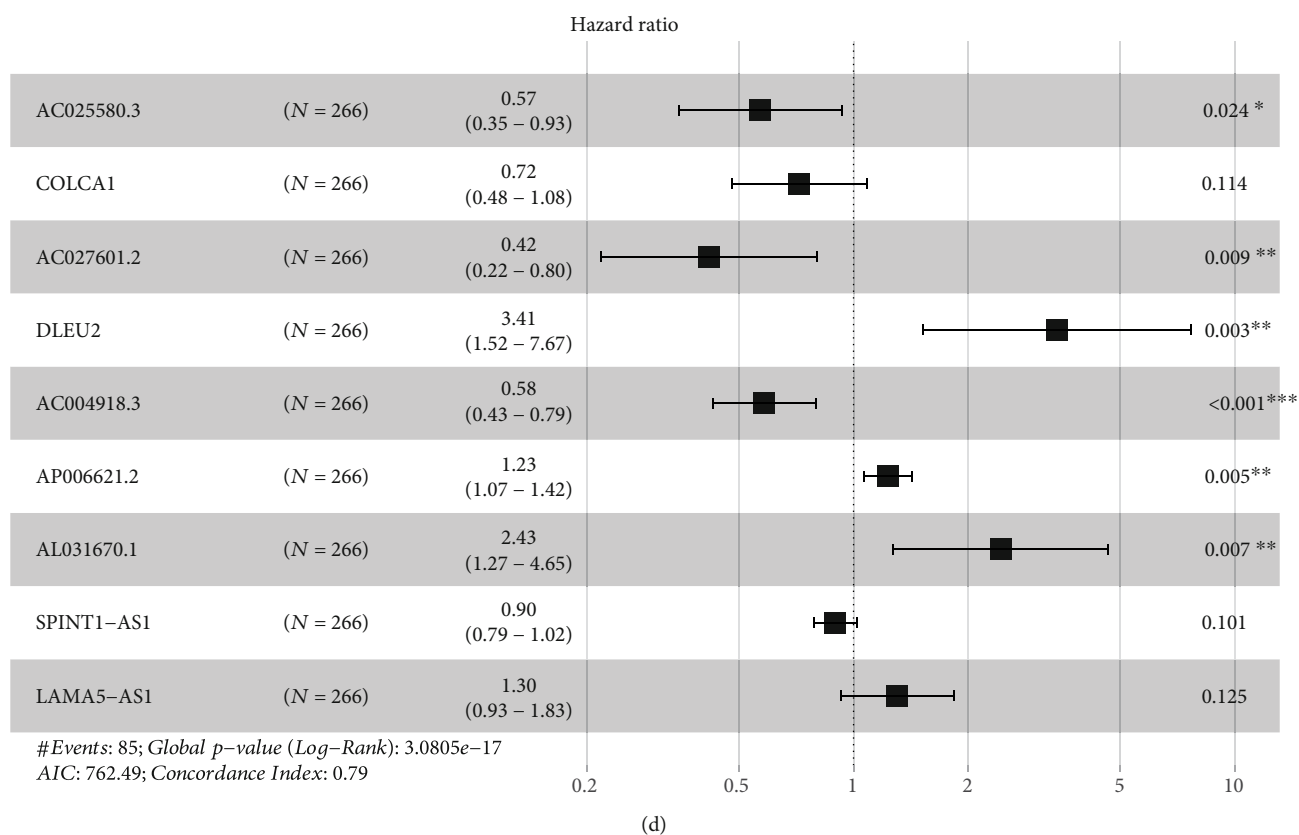
0.2 0.5 1 2 5 10

(d)

FIGURE 1: Development of the nine redox-related lncRNAs signature. (a) Screening of differentially expressed redox-related lncRNAs. (b) Variables going to zero as we increase the penalty (lambda) in the objective function of the LASSO. (c) 10-fold cross-validation for tuning parameter selection in the LASSO model, −4 < lambda.min < −3.5, and there were 20 variables (lncRNAs) left. (d) Results of the multivariate Cox proportional hazard model based on the 20 variables; nine lncRNA genes were screened to construct the signature.
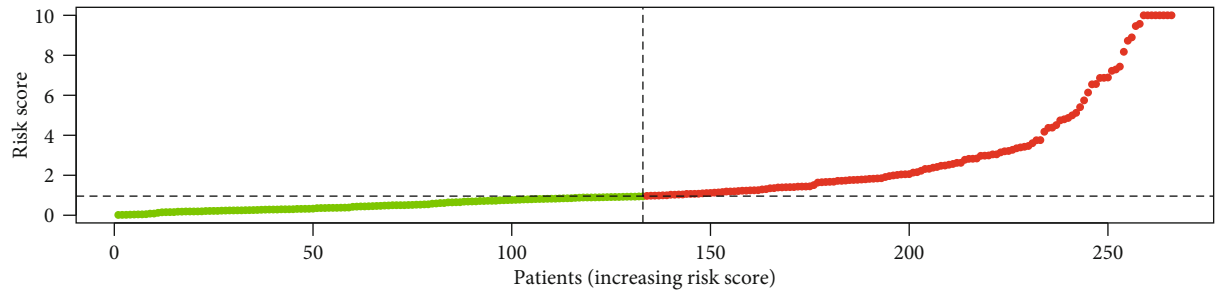
TABLE 2: The detailed information of the nine redox-related lncRNAs used to construct the prognostic signature.

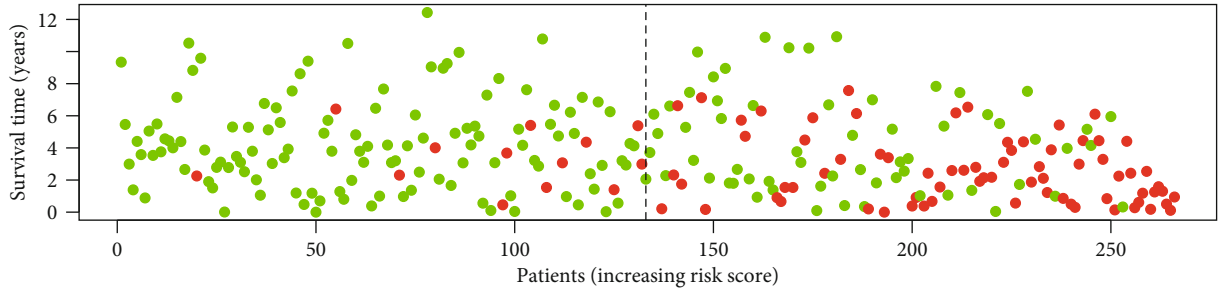| Gene symbol	Ensemble ID	Gene_biotype	Coef
AC025580.3	ENSG00000275672	Antisense (lncRNA)	-0.56136127
COLCA1	ENSG00000196167	Antisense (lncRNA)	-0.326969031
AC027601.2	ENSG00000262115	Antisense (lncRNA)	-0.873174537
DLEU2	ENSG00000231607	Antisense (lncRNA)	1.228067267
AC004918.3	ENSG00000270157	Sense intronic	-0.539291321
AP006621.2	ENSG00000255142	lincRNA	0.207380745
AL031670.1	ENSG00000275582	Antisense (lncRNA)	0.889174399
SPINT1-AS1	ENSG00000261183	Antisense (lncRNA)	-0.10982088
LAMA5-AS1	ENSG00000228812	Antisense (lncRNA)	0.264867342

Notes: Antisense: transcripts that overlap the genomic span (i.e., exon or introns) of a protein-coding locus on the opposite strand. Sense intronic: a long noncoding transcript in introns of a coding gene that does not overlap any exons. lincRNA (long intergenic ncRNA): transcripts that are long intergenic noncoding RNA locus with a length > 200 bp. Requires lack of coding potential and may not be conserved between species.

(version 4.0.3), and conducted the analysis to explore whether the redox-related functions were significantly differentially enriched between the two groups. In addition, the correlation between risk level and clinicopathologic characteristics were tested, and the differential expression of the nine redox-related lncRNAs between the high-risk and low-risk group was analyzed.

2.7. Coexpression Network, Correlation Plot, and Differential Expression Status. Having validated the efficacy of the nine redox-related lncRNA survival-predicting signature, we extracted the coexpression status of the redox genes and redox-related lncRNA from the primary PEARSON Correlation Test then used Cytoscape (version 3.8.0) to visualize the coexpression network. Also, the Sankey plot and correlation
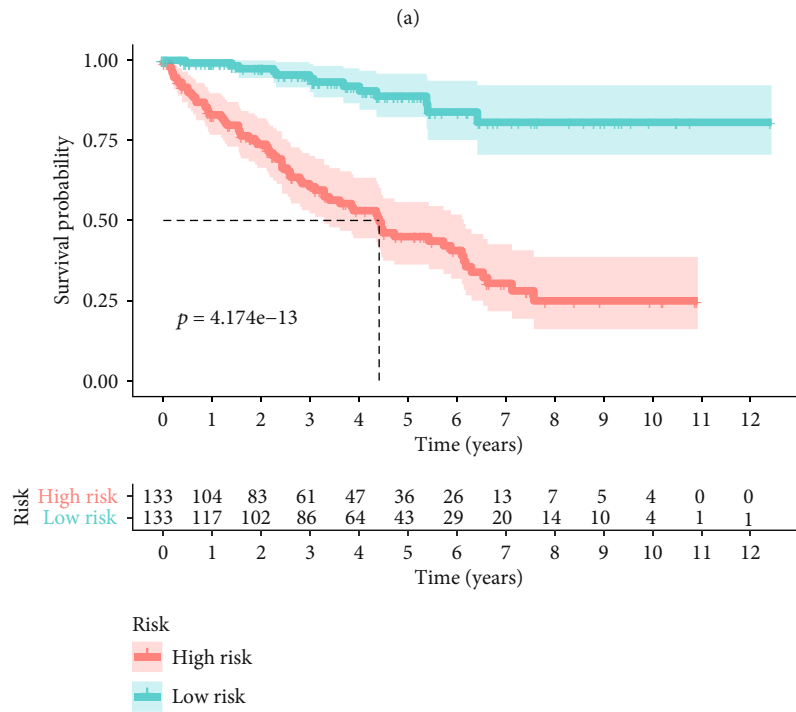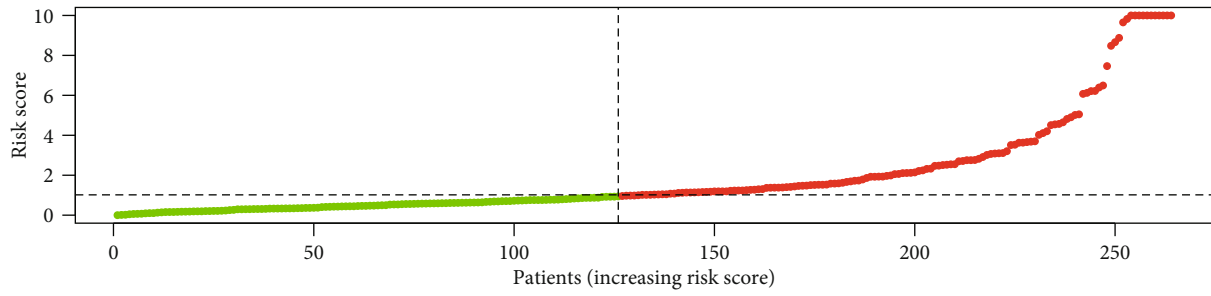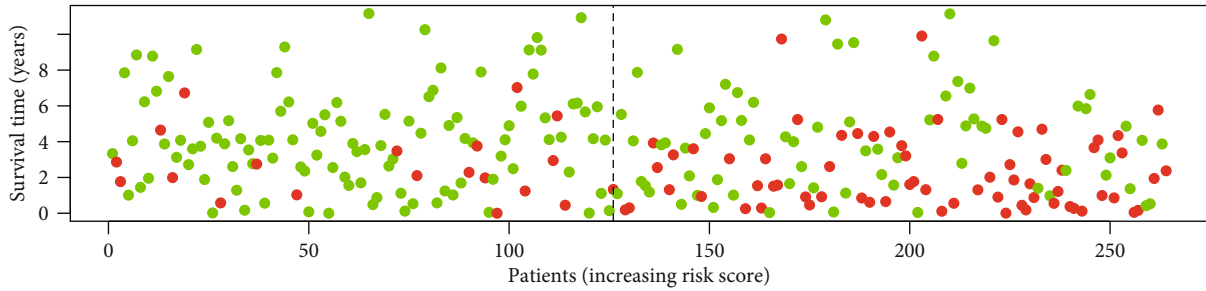
(a)

(b)

FIGURE 2: Continued.

(c)

(d)

FIGURE 2: Continued.

(e)

(f)
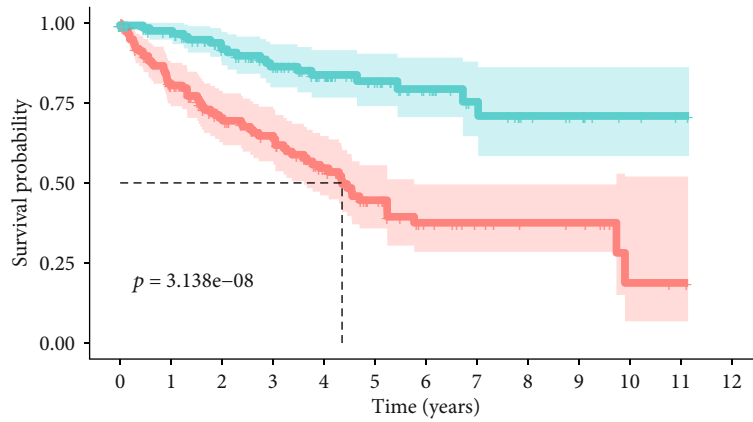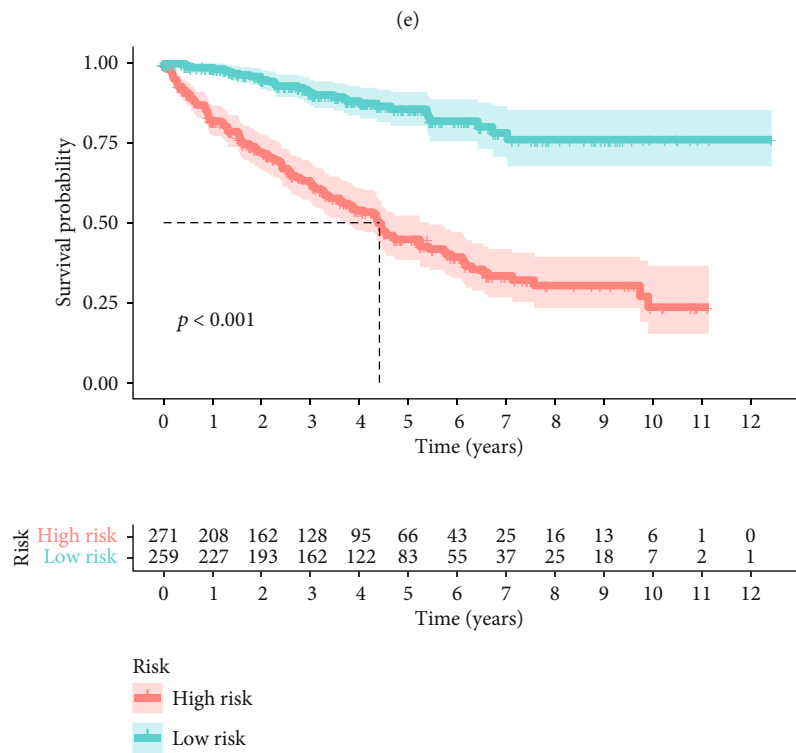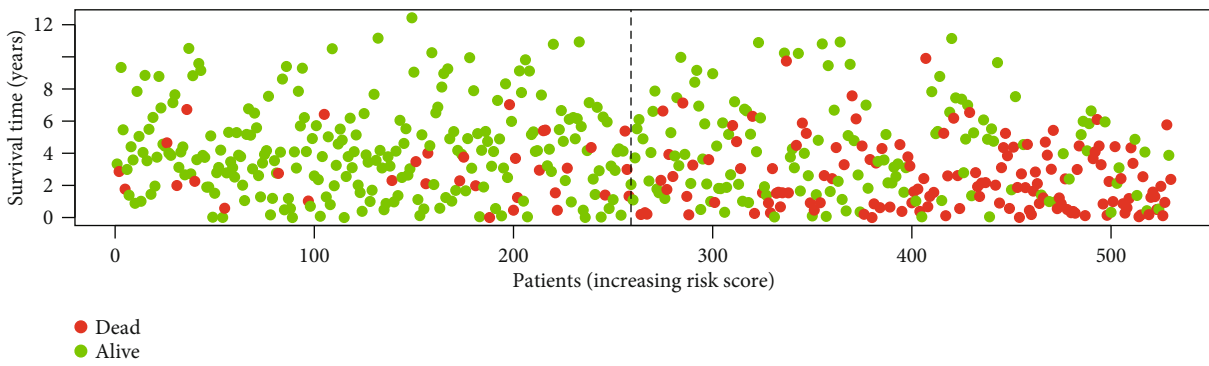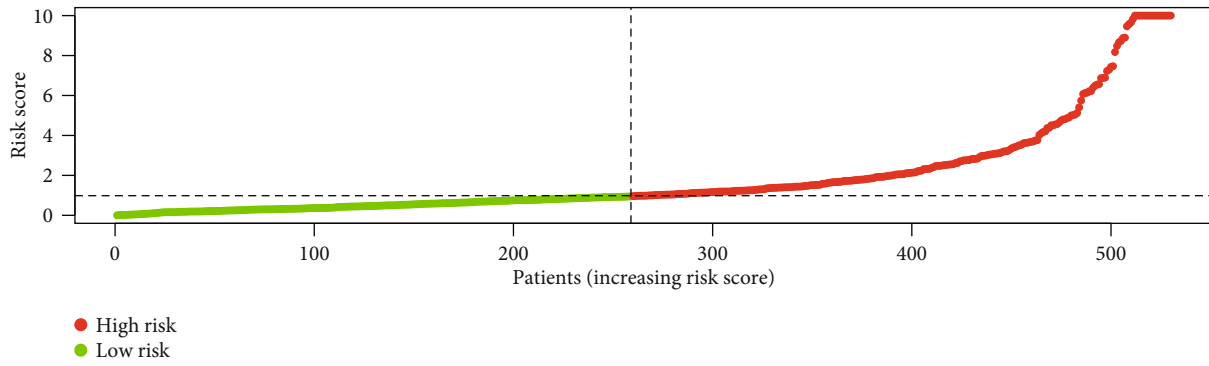
FIGURE 2: Risk plot and survival curves. (a) Risk plot of the training group. (b) Survival curve of the training group. (c) Risk plot of the test group. (d) Survival curve of the test group. (e) Risk plot of all samples. (f) Survival curve of all samples.
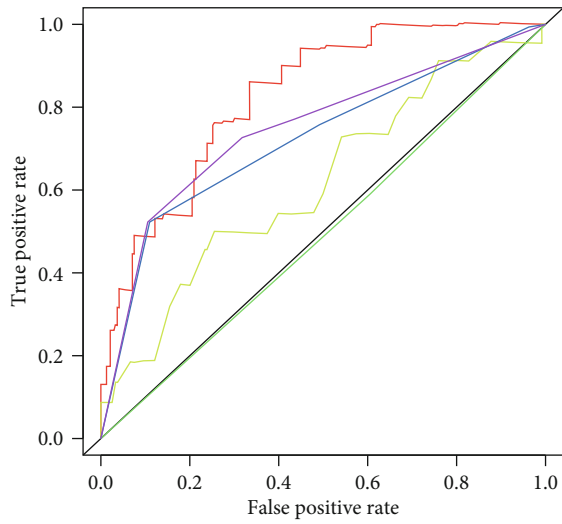
(a)

(b)

(c)

(d)
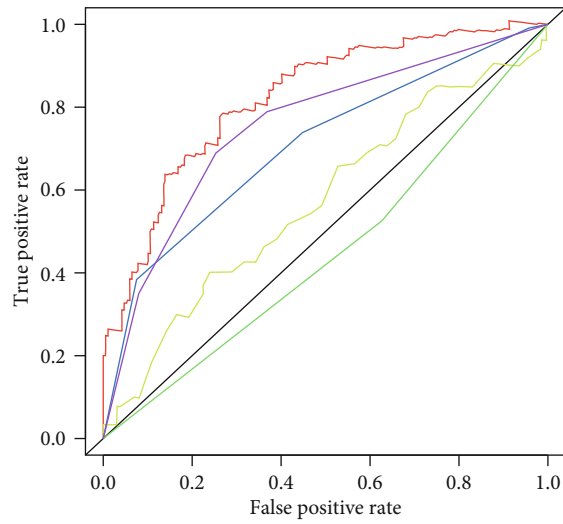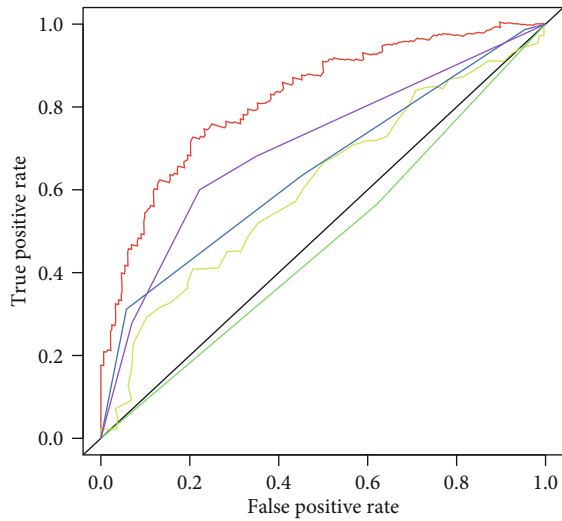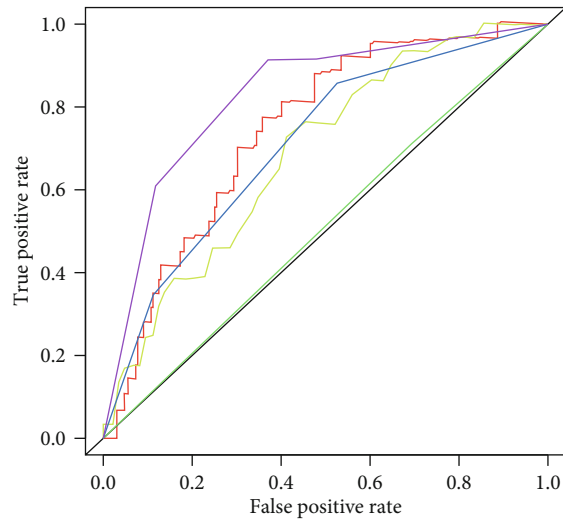
FIGURE 3: Continued.
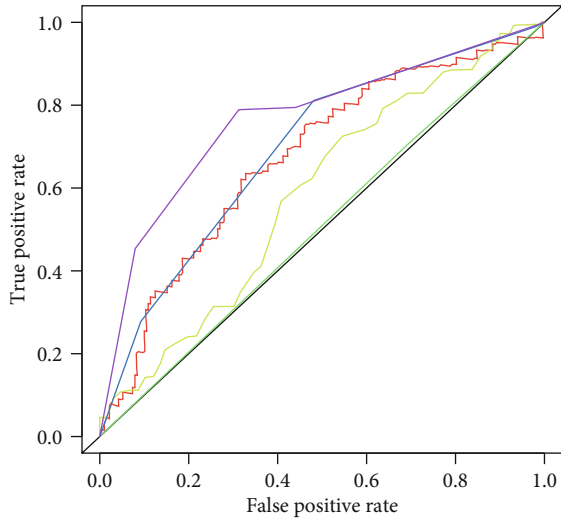
Risk score (AUC = 0.673)   Grade (AUC = 0.694)
Age (AUC = 0.586)   Stage (AUC = 0.766)
Gender (AUC = 0.506)

(e)
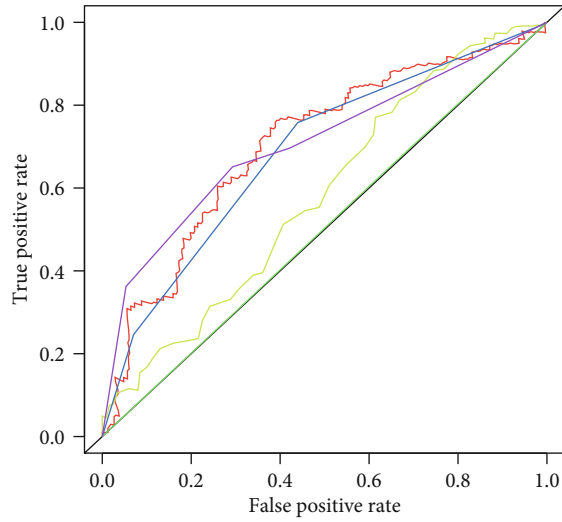
Risk score (AUC = 0.706)   Grade (AUC = 0.686)
Age (AUC = 0.582)   Stage (AUC = 0.708)
Gender (AUC = 0.502)

(f)
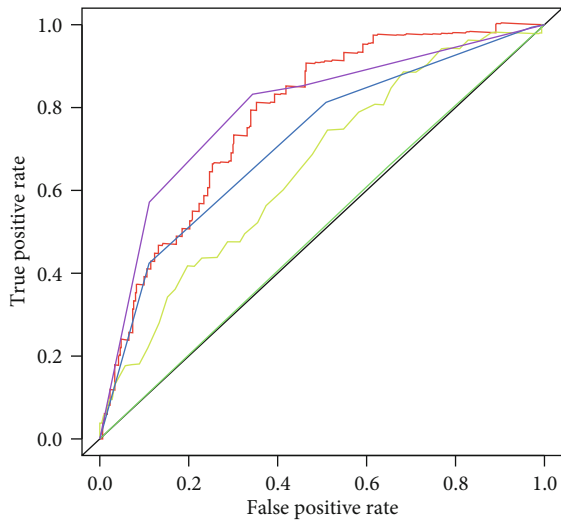
Risk score (AUC = 0.780)   Grade (AUC = 0.716)
Age (AUC = 0.654)   Stage (AUC = 0.793)
Gender (AUC = 0.505)

(g)
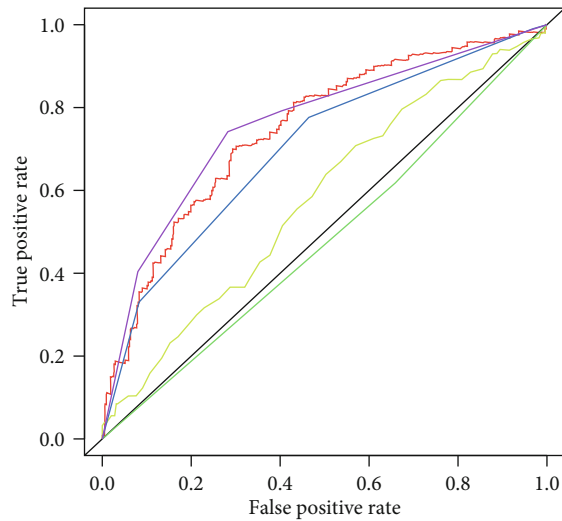
Risk score (AUC = 0.746)   Grade (AUC = 0.701)
Age (AUC = 0.578)   Stage (AUC = 0.759)
Gender (AUC = 0.480)

(h)

Figure 3: Continued.

(i)
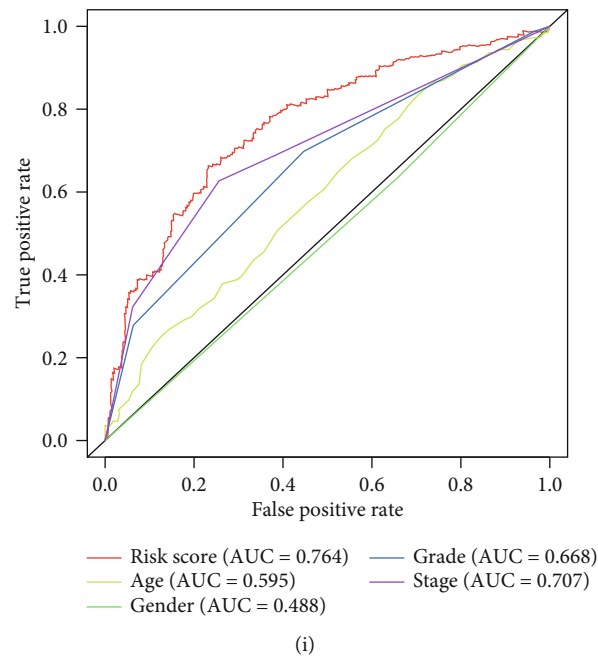
Figure 3: Time-dependent multivariate ROC curve. (a) One-year multivariate ROC curve in the training group. (b) Three-year multivariate ROC curve in the training group. (c) Five-year multivariate ROC curve in the training group. (d) One-year multivariate ROC curve in the test group. (e) Three-year multivariate ROC curve in the test group. (f) Five-year multivariate ROC curve in the test group. (g) One-year multivariate ROC curve in all samples. (h) Three-year multivariate ROC curve in all samples. (i) Five-year multivariate ROC curve in all samples.

circle plot were used to visualize the correlation between redox genes and nine redox-related lncRNAs. In addition, the differential expression of these nine redox-related lncRNAs between normal and tumor tissue, and between different clinicopathologic characteristics were analyzed and plotted.

2.8. Subgroup Analysis. To further explore the correlation between risk score and clinicopathological characteristics and verify the effectiveness of the prognostic signature in different clinicopathological subgroups, all samples were divided into subgroups according to age (>65 or ≤65), gender (male or female), stage (stage I-II or stage III-IV), and grade (G1-2 or G3-4). Then, we compared the mean risk score between the different groups and performed survival analysis to validate the effectiveness of our prognostic signature in different subgroups.

2.9. Statistical Analysis. The data was processed using the Strawberry PERL programming language (version 5.30.2.1). All statistical analyses were performed using the R software (version 4.0.2). $p < 0.05$ was regarded as statistically significant.

3. Results

3.1. Patients and Samples. There were 611 transcriptome profiles that contained 72 normal tissues and 539 tumor tissues from 530 KIRC patients, and we took the average of the tumor samples sequenced multiple times. Also, all samples were randomly split into the training and test group at a

1 : 1 ratio, and the characteristic of the samples in the training group, test group, and all samples are shown in Table 1. Fisher's exact test was performed to compare the differences between groups. It seemed that there was no significant difference between these groups.

3.2. Differentially Expressed Redox-Related lncRNAs (DERRlncRNAs). As shown in Figure 1(a), there are a total of 4492 differentially expressed lncRNAs with|logFC| > 1 andFDR < 0.05. And a total of 431 redox-related lncRNAs were screened with Pearson correlation coefficient |cor| > 0.5 and p.adjust < 0.001. Then, we took an intersection of them and acquired 214 differentially expressed redox-related lncRNAs (DERRlncRNAs).

3.3. Construction of the Redox-Related lncRNA Survival-Predicting Signature. In the training group, we performed univariate Cox regression and got 88 significant prognostic DERRlncRNAs. Then, the LASSO regression was used to avoid overfitting and screened 20 appropriate DERRlncRNAs as variates to do the following multivariate cox regression (Figures 1(b) and 1(c)). Finally, we performed multivariate Cox regression and developed a nine-redox-related lncRNA signature containing *AC025580.3*, *COLCA1*, *AC027601.2*, *DLEU2*, *AC004918.3*, *AP006621.2*, *AL031670.1*, *SPINT1-AS1*, and *LAMA5-AS1* to predict the survival of KIRC patients (Figure 1(d)), and their detailed information is shown in Table 2. The risk score for each sample was then calculated based on the expression levels of these nine redox-related lncRNAs. Risk score = 1.23•*DLEU*2 + 0.21•*AP*006621.2 + 0.89•*AL*031670.1 + 0.26•*LAMA*5 − *AS*1 − 0.56•*AC*025580.3

(a)

C-index = 0.782

(b)

Figure 4: Continued.

(c)

(d)

FIGURE 4: Continued.

(e)

(f)
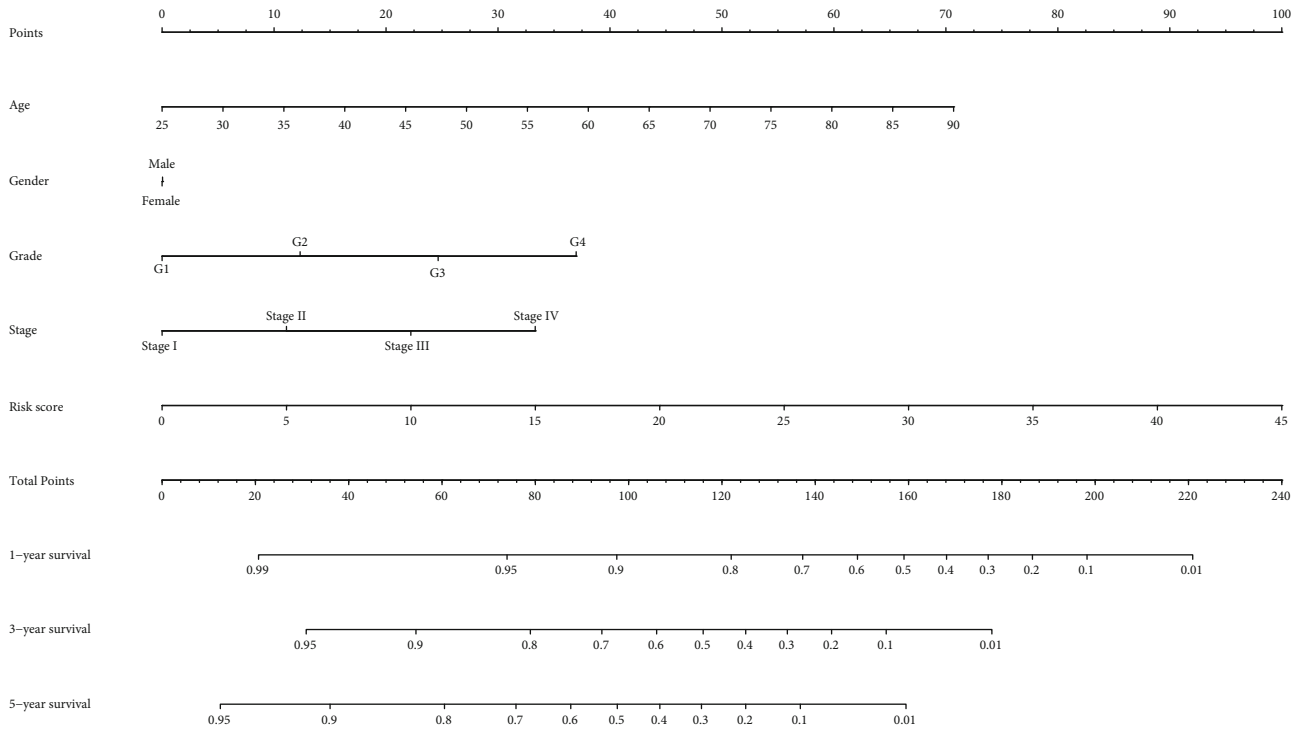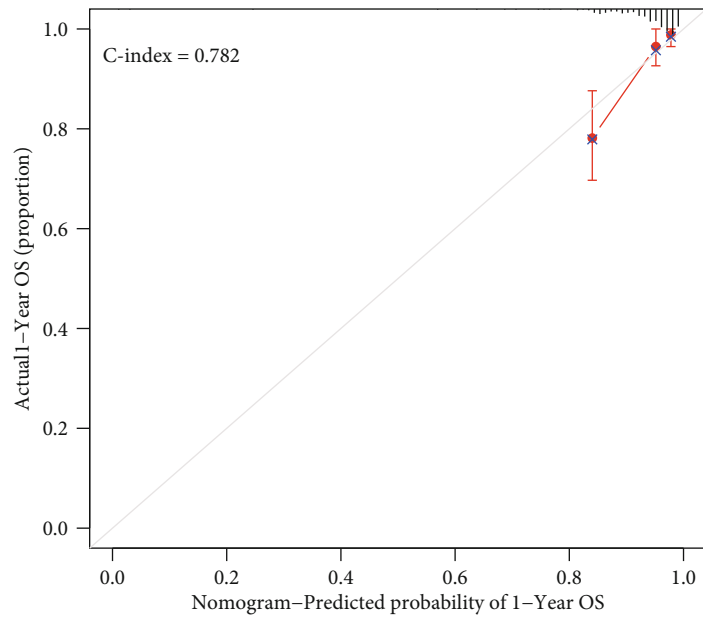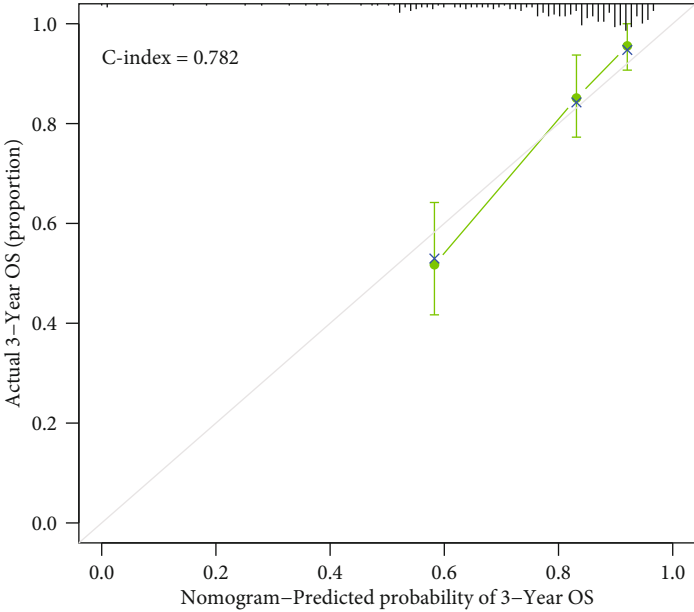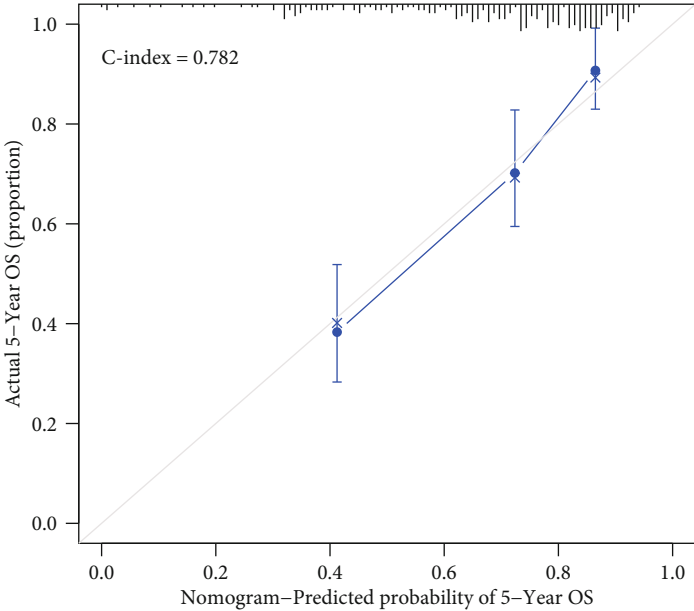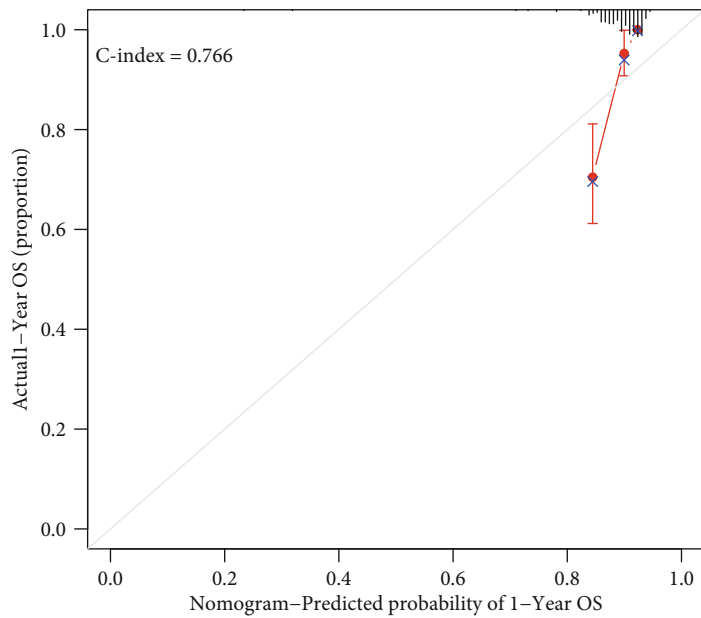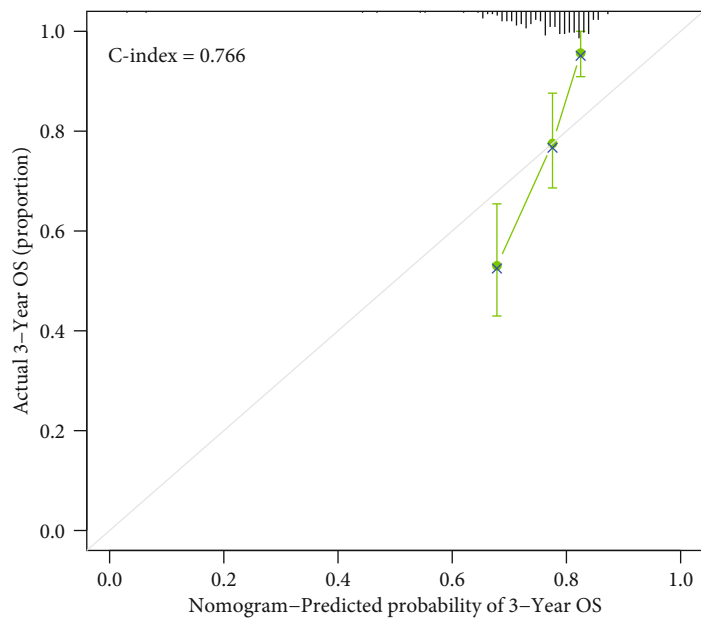
Figure 4: Continued.

(g)

(h)

FIGURE 4: Continued.

(i)

(j)
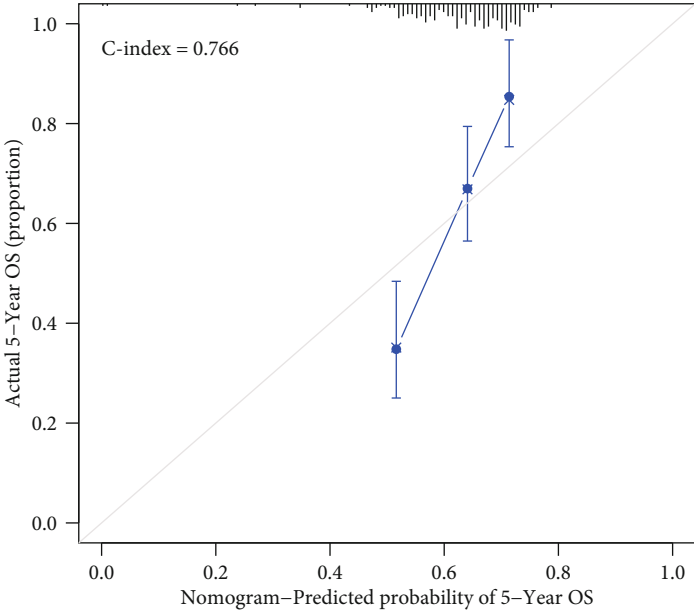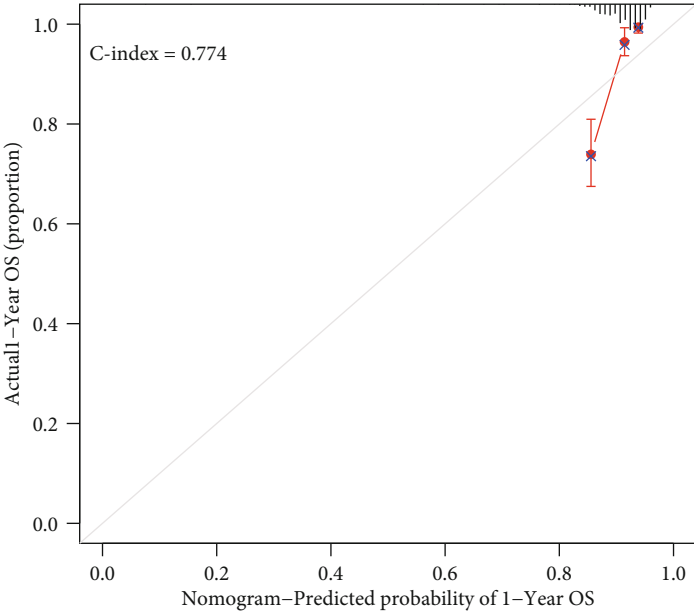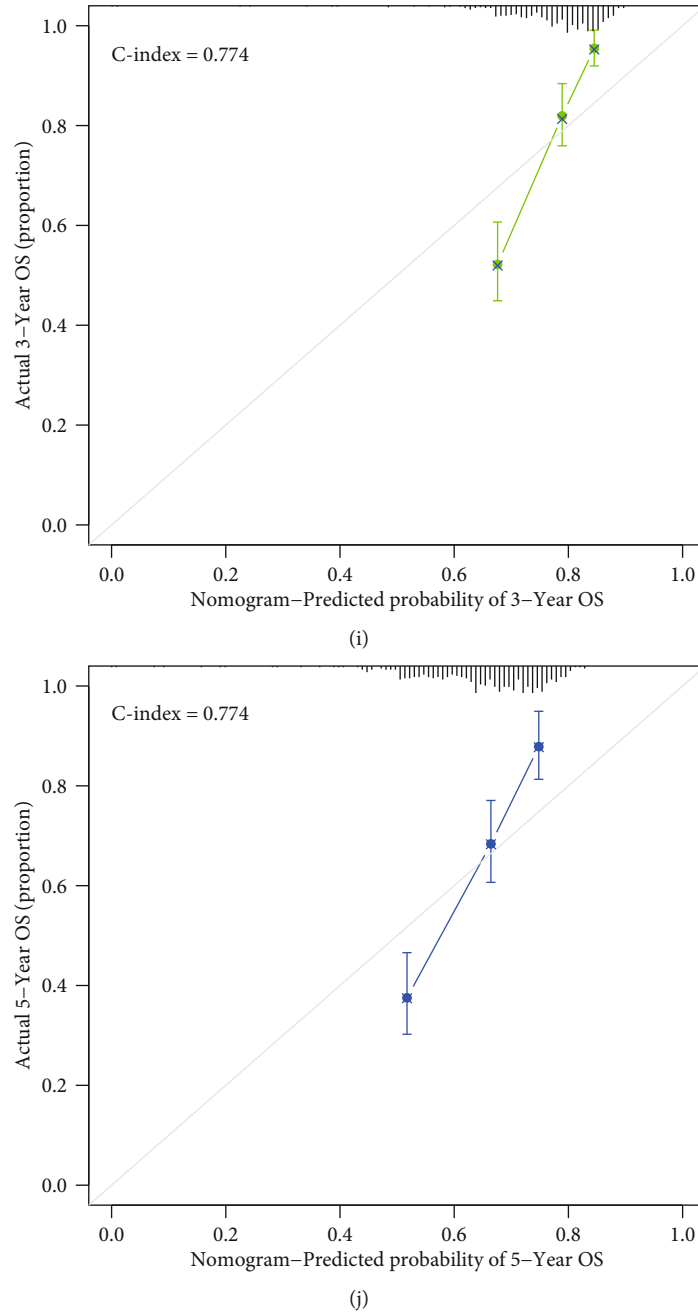
FIGURE 4: Nomogram and calibration curves. (a) Prognostic nomogram assembled from the training group to predict survival for ccRCC patients. (b, c, d) Calibration curves for the nomogram at 1-year, 3-year, and 5-year periods in the training group. (e, f, g) Calibration curves for the nomogram at 1-year, 3-year, and 5-year periods in the test group. (h, i, j) Calibration curves for the nomogram at 1-year, 3-year, and 5-year periods in all samples.

$-0.33 \bullet COLCA1 - 0.87 \bullet AC027601.2 - 0.54 \bullet AC004918.3 - 0.11 \bullet SPINT1 - AS1$.

3.4. *Validation of the Survival-Predicting Signature.* Having developed the nine redox-related lncRNA signature, all the samples both in the training group and test group acquired a risk score, and we set the medium value of the risk score in the training group as the cutoff to judge the risk level of patients as high risk or low risk (Figures 2(a),

2(c), 2(e)). Following this, survival analysis was performed to verify the survival-predicting availability of the signature (Figures 2(b), 2(d), 2(f)). Time-dependent ROC curve for 1 year, 3 years, and 5 years in the training group (Figures 3(a)–3(c)), test group (Figures 3(d)–3(f)), and all samples (Figures 3(g)–3(i)) were drawn, and the AUC for the risk score in these three groups showed that risk score could act as an efficient prognostic factor even compared with other commonly used clinical prognostic factor.
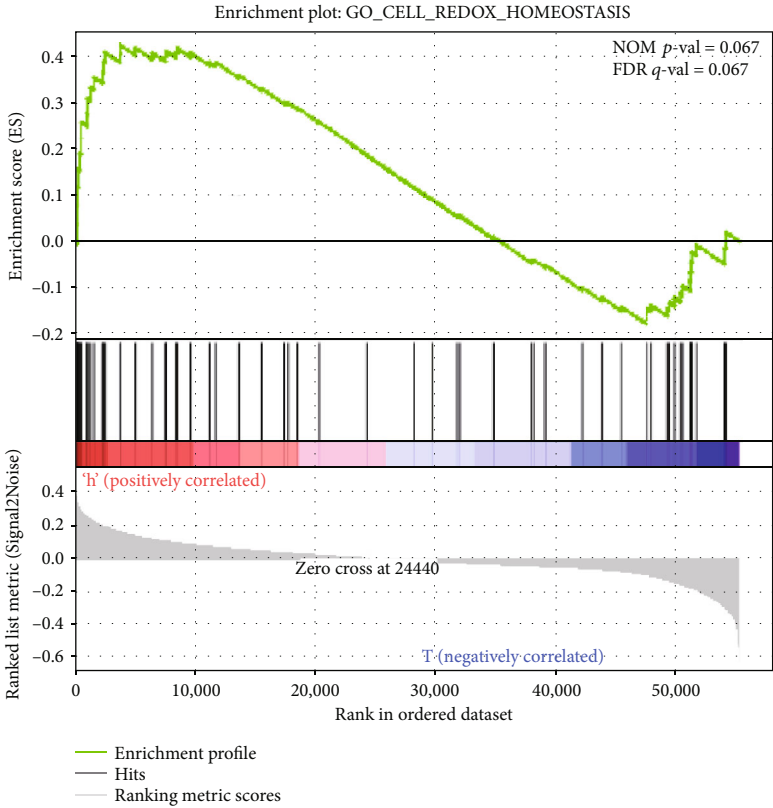
(a)

(b)

FIGURE 5: Continued.

(c)
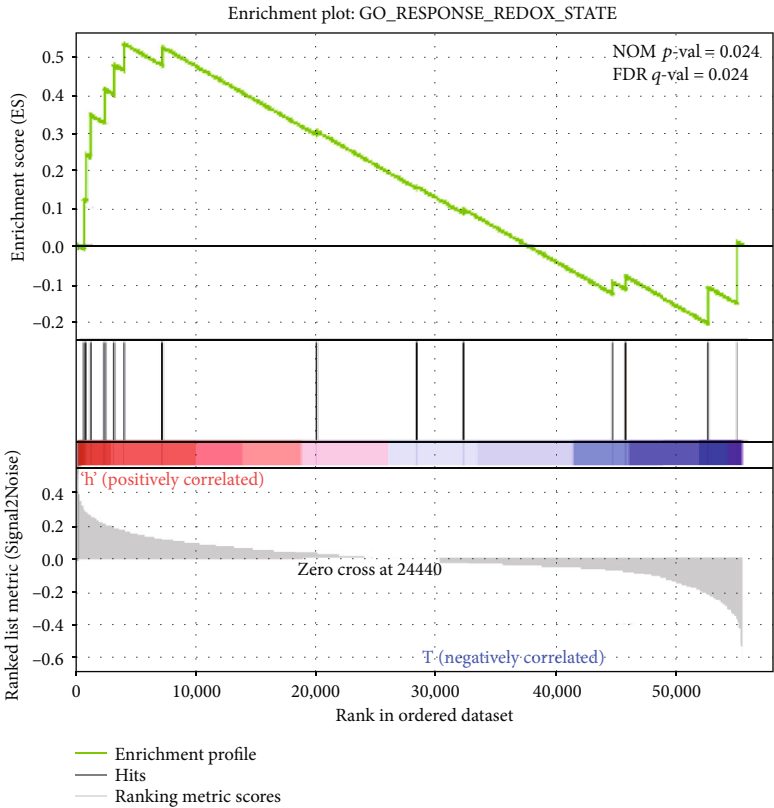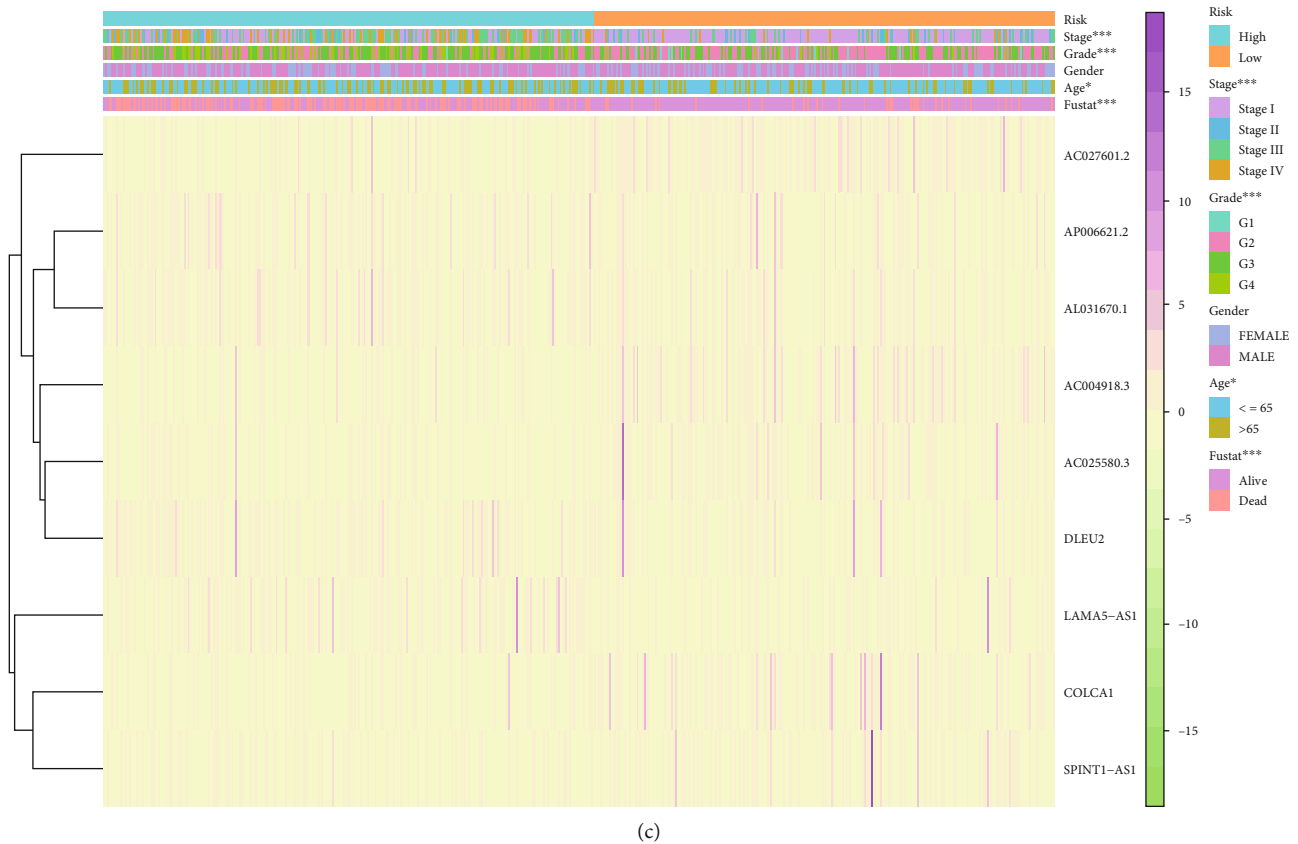
FIGURE 5: Gene set enrichment analysis (GSEA) of high-risk and low-risk ccRCC patients based on the redox-related lncRNA prognostic signature and expression heat map between high/low-risk patients. (a, b) The GSEA results show a significant enhancement of redox-related functions in the high-risk ccRCC patients. (c) Expression heat map for the nine redox-related lncRNAs in all samples.

3.5. Construction and Validation of the Risk Score-Based Nomogram. Having verified the efficacy of the signature, we would like to develop a more quantitative rather than qualitative approach for clinicians to predict the survival of the KIRC patients. Thus, we assembled a nomogram according to the risk score and clinicopathologic characteristics that contained age, gender, stage, and grade from the samples in the training group to predict the survival rate for 1 year, 3 years, and 5 years (Figure 4(a)). Also, the calibration curve for 1-year, 3-year, and 5-year survival rate in the training group (Figure 4(b)–4(d)), test group (Figure 4(e)–4(g)), and all KIRC samples (Figure 4(h)–4(j)) were plotted. Also, C-index was calculated to assess the performance of the nomogram assembled according to the training group, and that was 0.782, 0.766, and 0.774 in the training group, test group, and all samples, which showed the perfect performance of the nomogram.

3.6. GSEA and Clinical Correlation. To explore the different redox-related functions in the high/low-risk group, we performed the enrichment analysis by using GSEA version 4.0.3 as shown in Figures 5(a) and 5(b). It showed that both two redox-related functions were enhanced in the high-risk group, of which the GO term response to the redox state was significantly enhanced in the high-risk group (NOM p value = 0.024, FDR q-value = 0.024), while the other

GO term cell redox homeostasis was not significant (NOM p value = 0.065, FDR q value = 0.065). In addition, the correlation between risk level and clinical characteristics and the differential expression of the nine redox-related lncRNAs in high/low risk were analyzed as shown Figure 5(c). It seemed age, grade, and stage were all significantly related to the risk level, which was also consistent with the outcome that high risk resulted in high mortality.

3.7. Coexpression Network, Correlation Plot, and Differential Expression Status. Finally, we focused on these nine redox-related lncRNAs about their coexpression and differential expression. The redox gene-redox-related lncRNA coexpression network was constructed (Figure 6(a)), and the Sankey plot (Figure 6(b)) showed that 4 of them were protective and the other 5 were risky. In addition, the correlation between the redox gene and redox-related lncRNA was plotted as the correlation network (Figure 7(a)) and correlation circle plot (Figure 7(b)). The differential expression status of the nine redox-related lncRNAs between normal/tumor tissue as in Figure 7(c) showed that 7 of 9 redox-related lncRNAs were significantly high expression in the tumor tissue while the 2 left were significantly low expression in the tumor tissue. Besides, the correlation between the expression of these nine redox-related lncRNAs and the clinicopathological staging was explored and shown in Figure 7(d). As

(a)

(b)
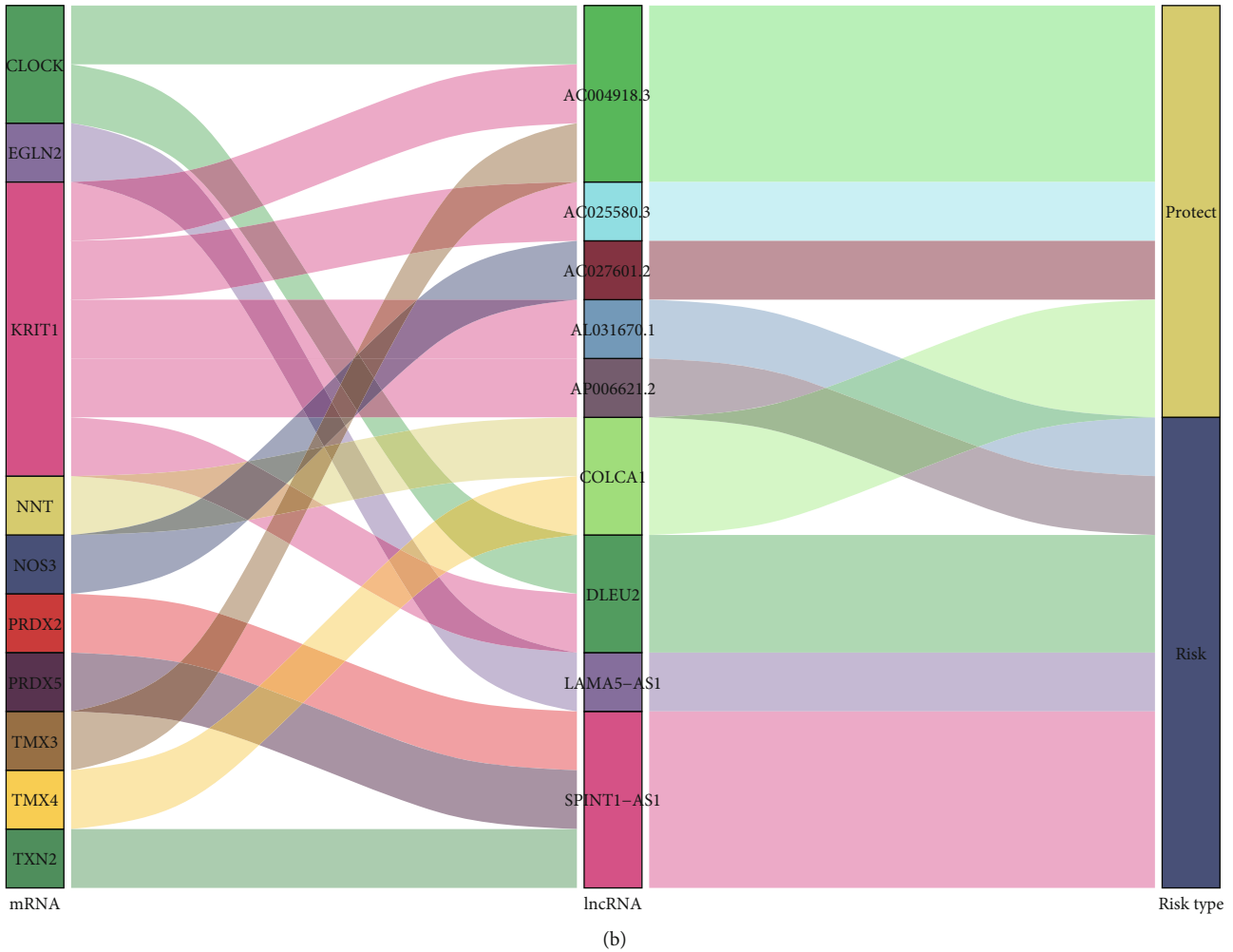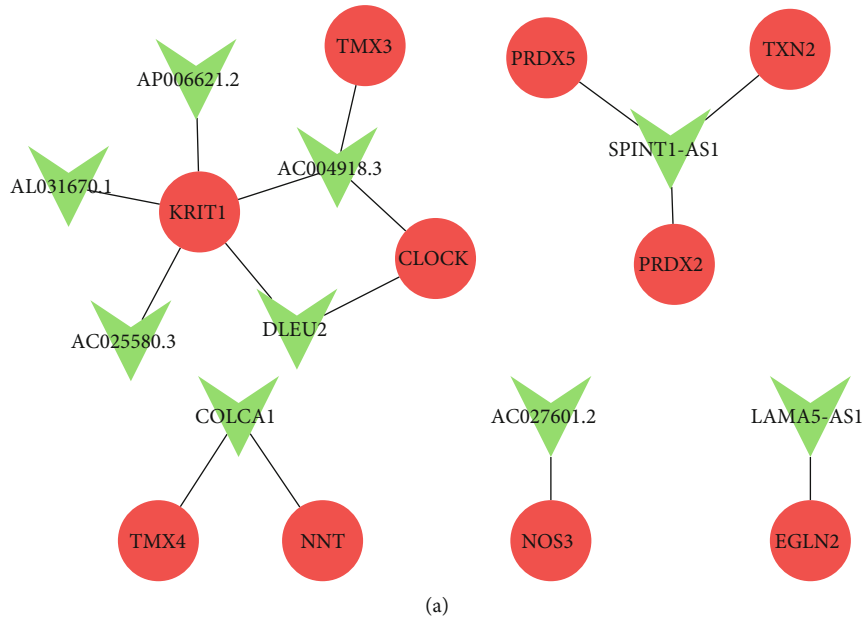
FIGURE 6: Redox gene-redox-related lncRNA interaction network and Sankey plot. (a) The interaction network between the redox-related lncRNA genes and redox-related protein-coding genes: red circle for redox-related mRNAs and green V-shape for redox-related lncRNAs. (b) In the Sankey plot for the interaction network, four of these redox-related lncRNAs were protective while the other five were indicative of risk.

(a)

(b)

FIGURE 7: Continued.

(c)
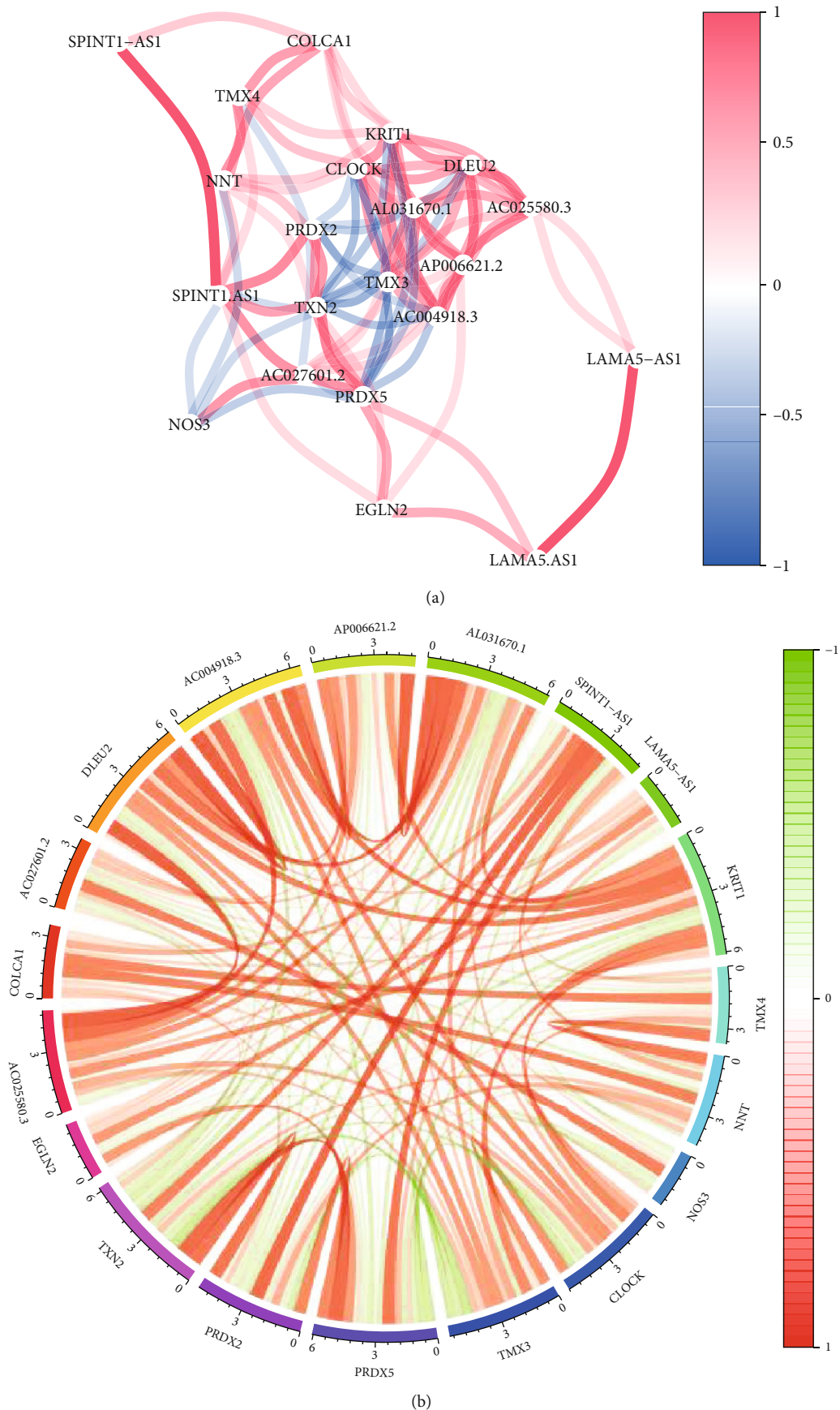
(d)
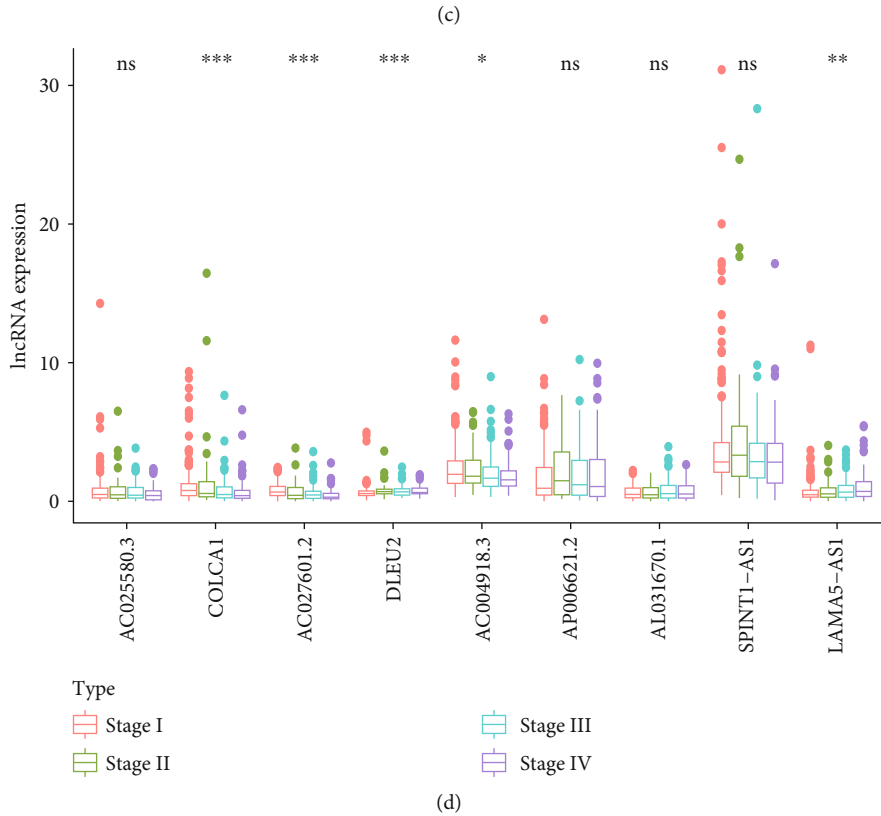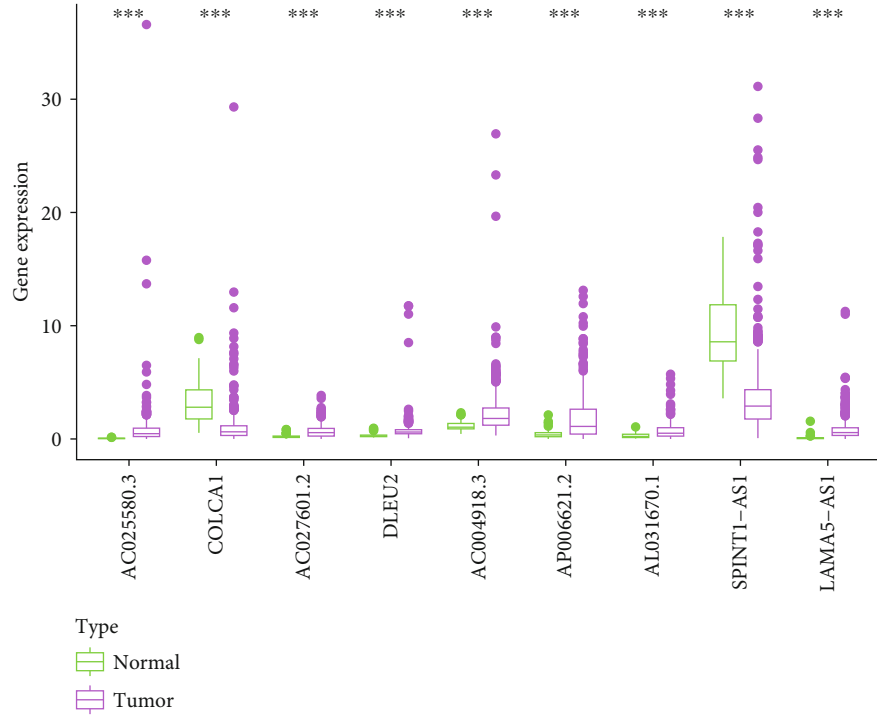
Figure 7: Correlation plot and the differential expression between normal/tumor tissue. (a) Correlation network for the redox gene and redox-related lncRNAs. (b) Circle plot for the correlation between redox gene and redox-related lncRNAs. (c) Differential expression for the nine redox-related lncRNAs between normal/tumor tissue. (d) Differential expression for the nine redox-related lncRNAs between stage I/II/III/IV patients.

(a)

(b)

Figure 8: Continued.

Patients with age>65

(c)



(d)

FIGURE 8: Continued.

Patients with FEMALE

(e)
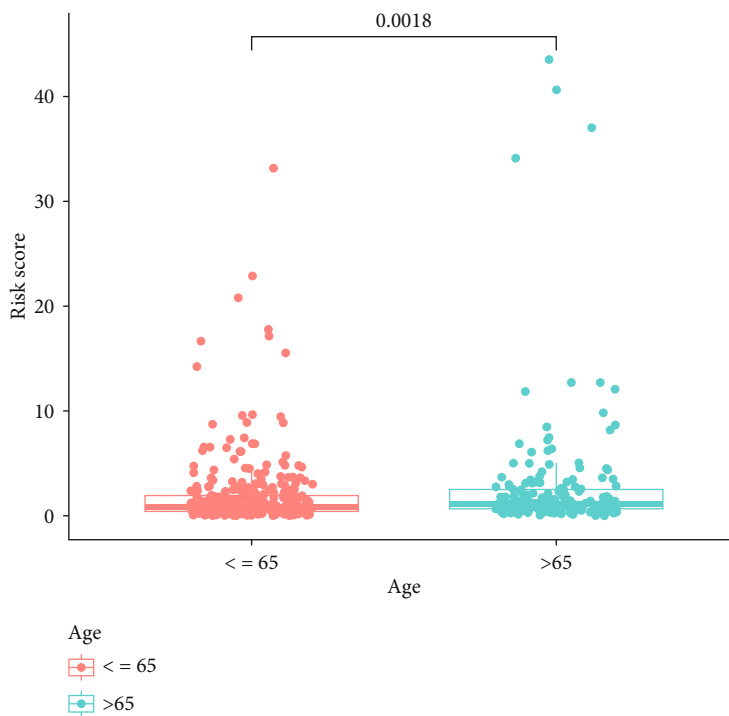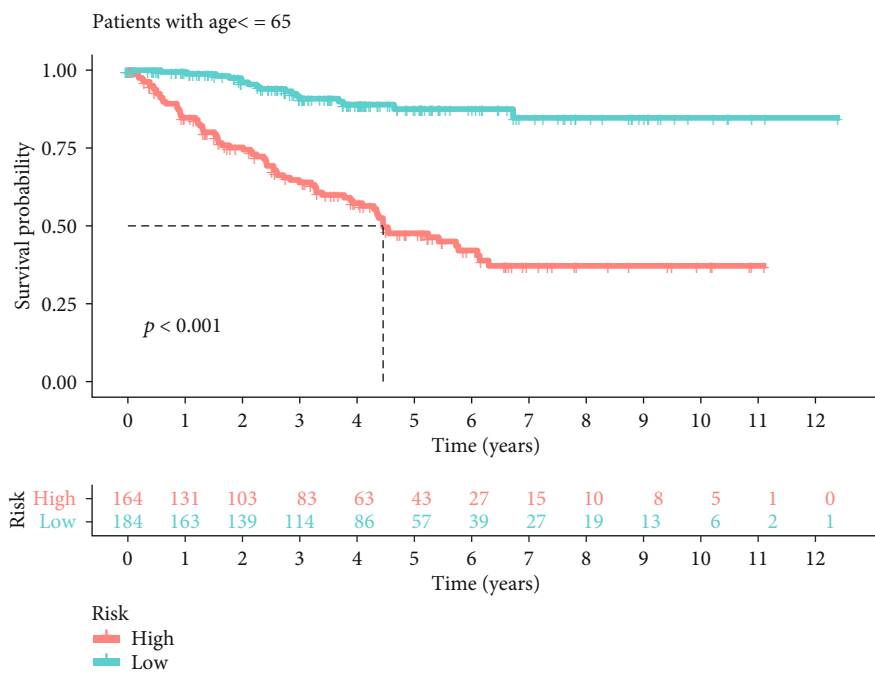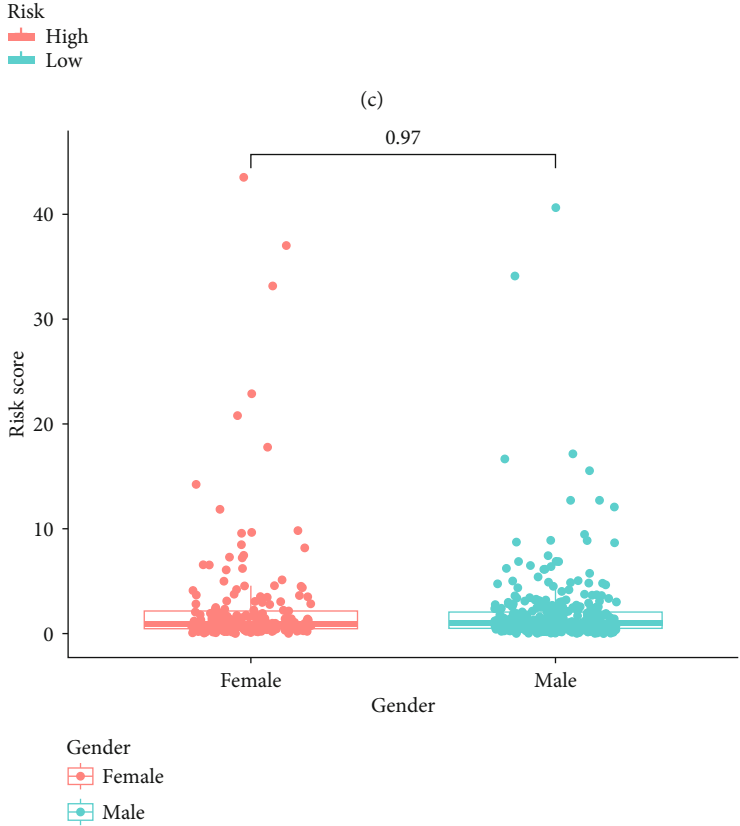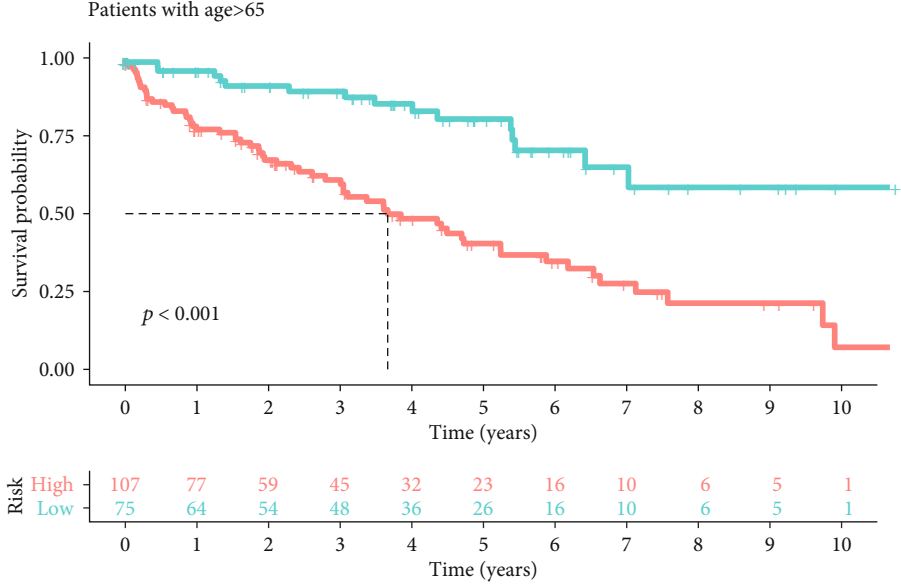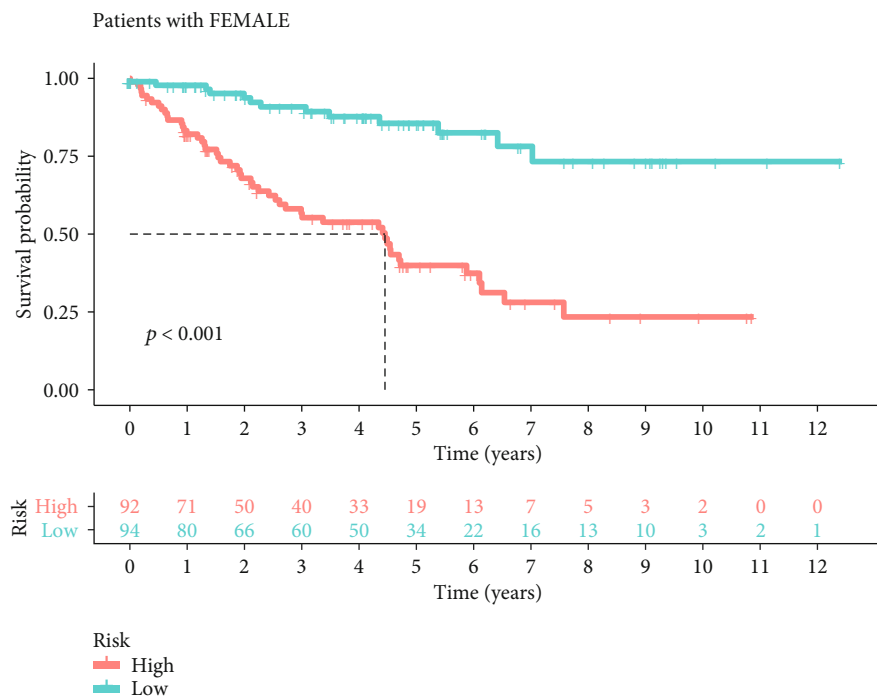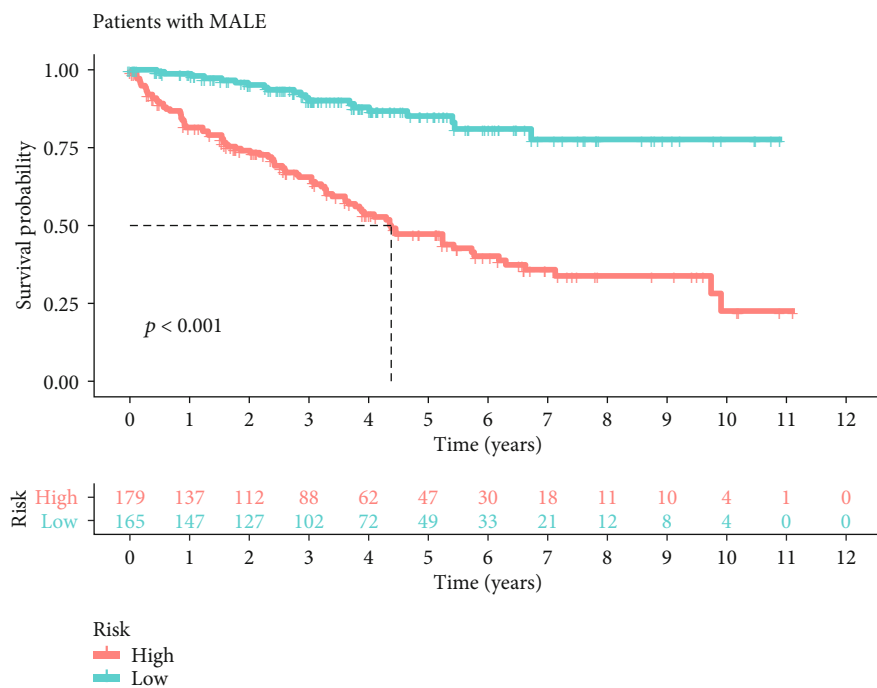
Patients with MALE

(f)

Figure 8: Continued.

(g)

(h)

Figure 8: Continued.

Patients with Stage III–IV

(i)

(j)

FIGURE 8: Continued.

(k)

(l)
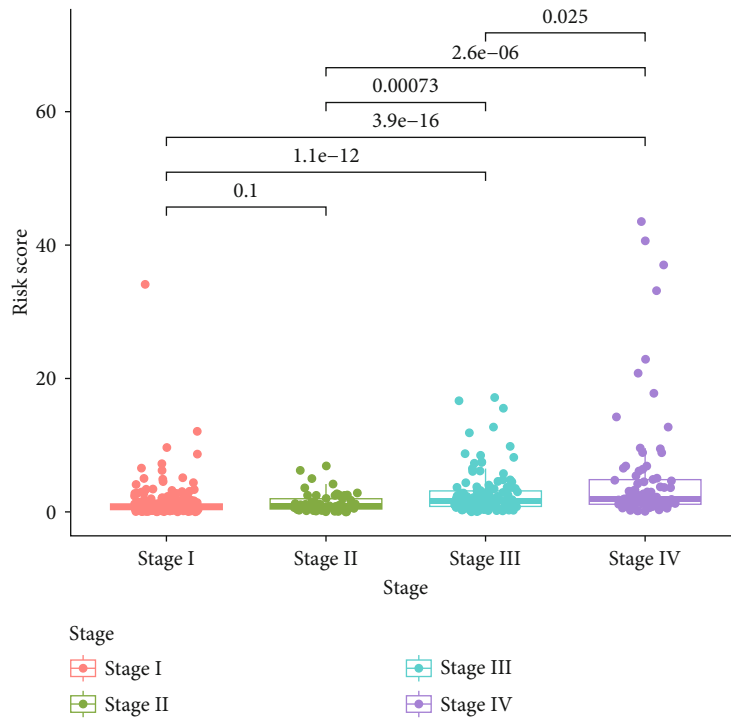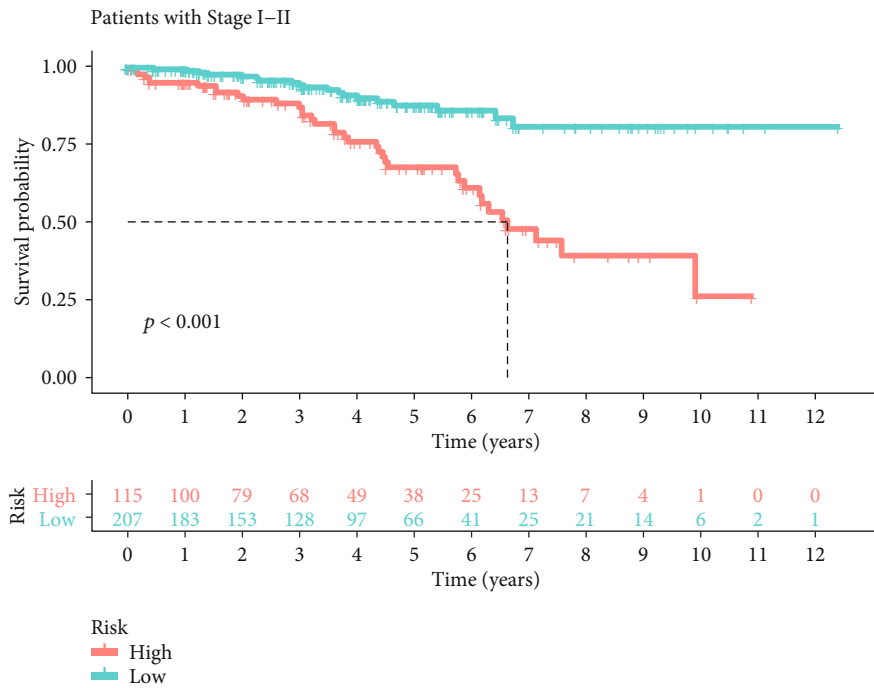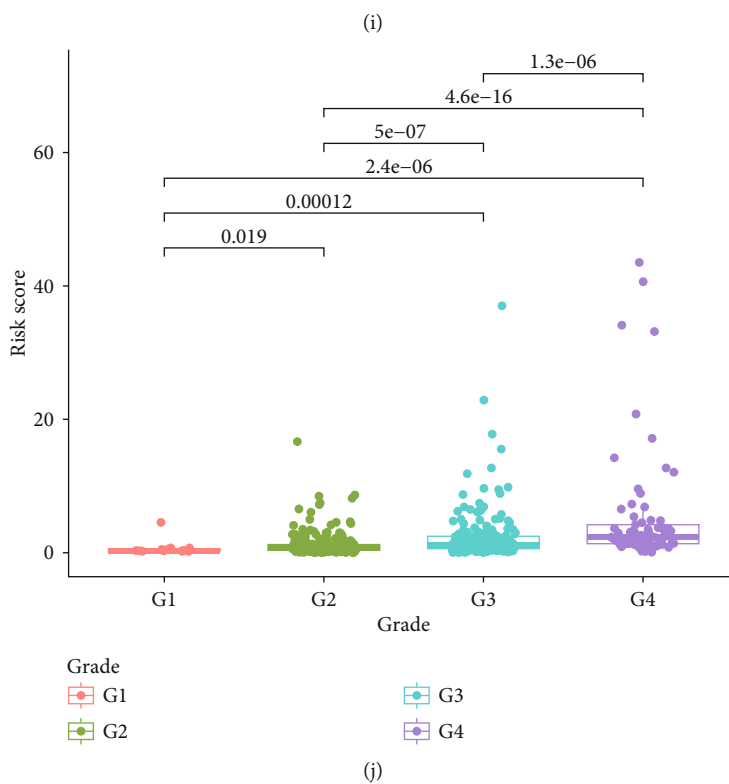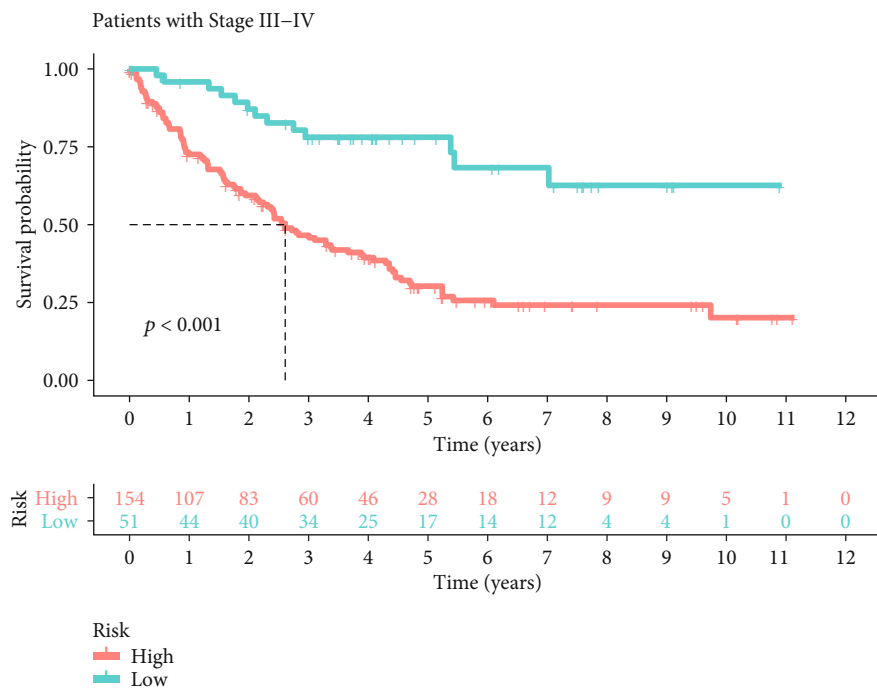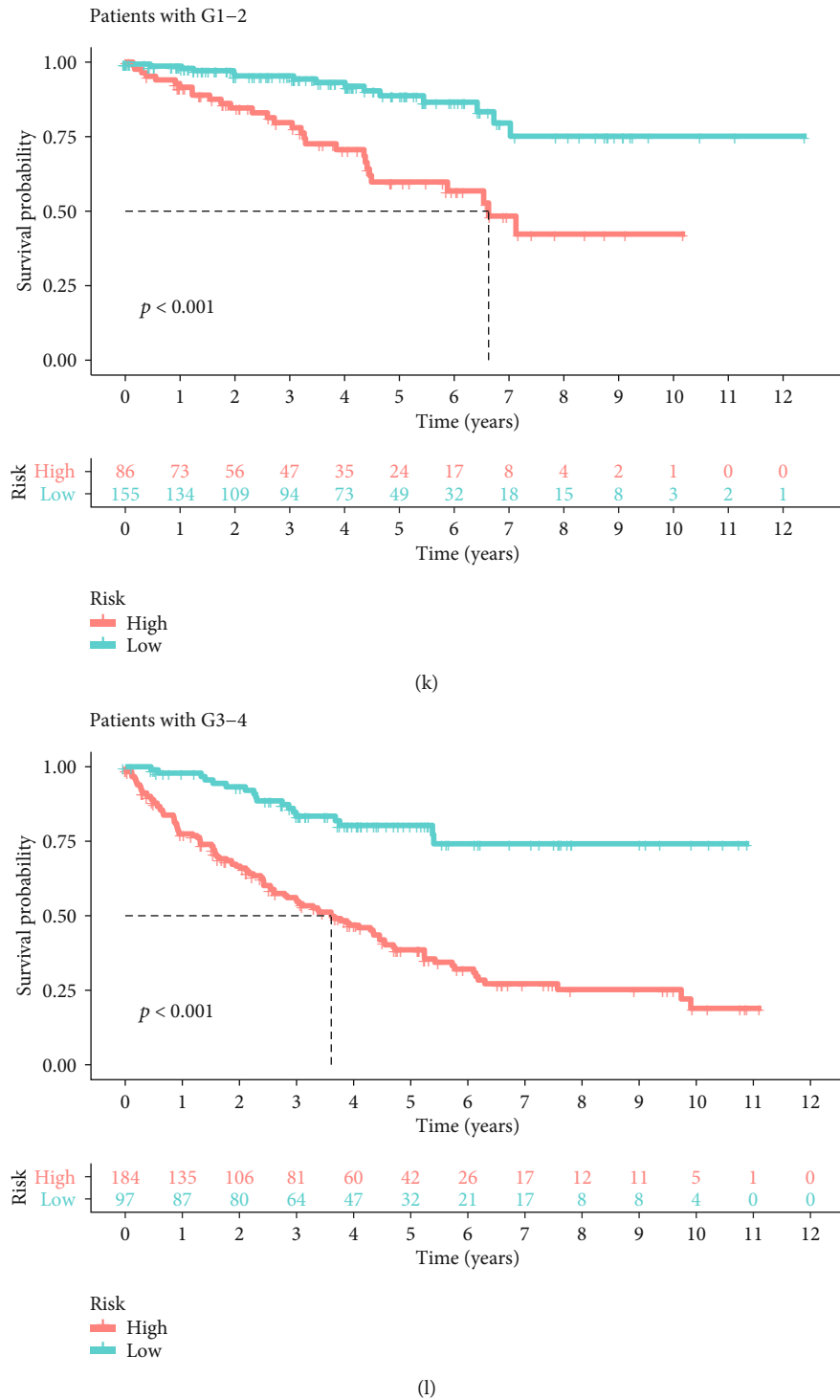
FIGURE 8: Difference in risk score between subgroups and further subgroup survival analysis. (a) Difference of risk score in patients with age ≤ 65 or >65. (b) Risk score-based survival analysis in patients with age ≤ 65. (c) Risk score-based survival analysis in patients with age > 65. (d) Difference of risk score in female or male patients. (e) Risk score-based survival analysis in female patients. (f) Risk score-based survival analysis in male patients. (g) Difference of risk score in patients with different stage. (h) Risk score-based survival analysis in patients with stage I-II. (i) Risk score-based survival analysis in patients with stage III-IV. (j) Difference of risk score in patients with different grade. (k) Risk score-based survival analysis in patients with G1-2. (l) Risk score-based survival analysis in patients with G3-4.

for the differential expression status of the nine redox-related lncRNAs in different age, gender, and grade, the boxplot is shown in the supplementary file (available here).

3.8. Subgroup Analysis. In age subgroups, risk score in patients with age > 65 was significantly higher than patients with age ≤ 65 (Figure 8(a)), and the prognostic signature

was verified effective in both age ≤ 5 (Figure 8(b)) and age > 65 (Figure 8(c)). In the gender subgroup, there was no significant difference in the risk score between female and male patients (Figure 8(d)). And the prognostic signature was also effective in both female (Figure 8(e)) and male (Figure 8(f)) subgroups. As for the stage subgroups (Figure 8(g)), the risk score in stage III was significantly higher than that in stage II, and stage IV was significantly higher than stage III. However, stage II was higher than stage I with no significant difference. And the prognostic signature was effective in both the stage I-II (Figure 8(h)) and stage III-IV (Figure 8(i)) subgroups. In the grade subgroups, the risk score was significantly increased between G1 and G2 and G3 and G4 (Figure 8(j)), and the prognostic signature was still effective in both the G1-2 (Figure 8(k)) and G3-4 (Figure 8(l)) subgroups.

4. Discussion

ccRCC is the most common type of RCC in humans. With the development of clinical management of ccRCC, several prognostic factors, such as tumor grade and stage, tumor size, and tumor number, are well characterized. However, ccRCC has complex genetic and molecular alterations [24], which could affect the biological processes, and some of the biological processes are closely associated with the prognosis of ccRCC patients, such as autophagy [25], ferroptosis [15], and redox [26]. Most of these commonly used prognostic factors do not consider either genetic and molecular alterations or dysregulated biological processes, and it made these commonly used prognostic factors not perfect for accurate prognostic prediction of ccRCC patients [27]. As an emerging genetic and molecular biomarker, lncRNA is a new class of noncoding RNA molecules that regulate cancer cell growth, progression, and survival [28]. Therefore, it is necessary to establish a lncRNA signature to predict the prognosis of ccRCC patients.

In this study, we focused on the redox process and constructed a nine redox-related lncRNA prognostic signature (Risk score = $1.23 \cdot DLEU2 + 0.21 \cdot AP006621.2 + 0.89 \cdot AL031670.1 + 0.26 \cdot LAMA5 - AS1 - 0.56 \cdot AC025580.3 - 0.33 \cdot COLCA1 - 0.87 \cdot AC027601.2 - 0.54 \cdot AC004918.3 - 0.11 \cdot SPINT1 - AS1$.) in the training group by the LASSO regression and COX regression, which considered both molecular alteration and dysregulated biological process. Meanwhile, χ^2-test or Fisher's exact test found the nine redox-related lncRNA signature was significantly related to tumor grade, stage, patients' age, and survival status of ccRCC patients. In addition, risk analysis, survival analysis, and 1-year, 3-year, 5-year multivariate ROC in both the training group and test group well verified the efficacy of the survival-predicting signature. Then, a concise nomogram consisted of the nine redox-related lncRNA signature, age, gender, grade, and stage was developed from the data in the training group for prognostic prediction of ccRCC patients; both internal cross-validation and external set validation showed great effectiveness, and the calibration curve showed great convergency to the standard curve. Further subgroup analysis verified the effectiveness of our prognostic signature and indicated the universality of this prognostic signature. Finally, having verified the effectiveness of our nine-redox-related lncRNA signature, we focused on the interaction between the redox genes and these nine redox-related lncRNAs, constructed a redox gene-lncRNA interaction network, and performed a GSEA analysis to explore the differences in redox functions between high/low risk. Interestingly, we found both GO CELL REDOX HOMEOSTASIS and GO RESPONSE TO REDOX STATE were enhanced in the high-risk group, which was consistent with the previous study that high redox level in cancer could influence the survival of tumor patients by initiating/stimulating tumorigenesis and supporting transformation/proliferation of cancer cells or causing cell death [29].

In this signature which consisted of nine prognostic lncRNAs related to redox genes, COLCA1 has been reported and identified as a key lncRNA in colorectal cancer [30–32], and DLEU2 has been reported related to the development of multiple cancers [33–36]. Chen et al. reported that lncRNA DLEU2 could regulate miR-30a-5p and related to the aggressiveness of ccRCC [37]. SPINT1-AS1 has been reported as a prognostic factor in esophageal squamous cell carcinoma and colorectal cancer [38, 39]. Xiang et al. also reported SPINT1-AS1 as a crucial factor for pan-cancer cell sensitivity to lapatinib [40]. LAMA5-AS1 has been reported as a significant factor in the pathogenesis of multiple myeloma [41]. As for the other 5 lncRNAs, there were few reports about them.

Redox plays an essential role in the pathogeneses and progression of tumors. Regulation of reactive oxygen species (ROS) production is crucial in highly proliferative cancer cells, owing to the presence of oncogenic mutations that promote aberrant metabolism and gene expression [42]. Cancer cells can produce ROS, which diffuses into the tumor microenvironment, then initiates stromal oxidative stress and autophagy, and leads to angiogenesis. Sosa et al. [43] revealed that cancer cells develop resistance to ROS by inducing a new redox balance, which further results in cellular adaptation and proliferation under increased oxidative pressure. Indeed, the imbalance of the redox homeostasis system is closely related to the RCC occurrence and progression. In RCC patients, cytosolic antioxidant enzyme activities are shown to be decreased [44]. In recent years, redox balance has been reported regulated by long noncoding RNAs [45]; more and more researchers developed to identify the significant lncRNA-redox regulation network. Chen et al. reported that lncRNA GAS5 regulated the redox balance and dysregulates the cell cycle and apoptosis in malignant melanoma cells [46]. He et al. reported lncRNA MACC1-AS1 promoted stemness and chemoresistance through fatty acid oxidation in gastric cancer [47]. Here, our works contributed to further the comprehension of these nine redox-related lncRNAs and their interaction with redox balance, which might provide potential targets for the treatment in the future.

However, our study still has some limitations. First, the training group and test group are both obtained from TCGA, and it would be better if there is an independent cohort as an external validation set. In addition, we did not define the mechanisms behind the lncRNA-based signature's mediation of redox in the initiation and progression of ccRCC. Despite these limitations, this is the first redox-related lncRNA-based

survival-predicting signature, and our nomogram provides a quantitative approach for clinicians to predict survival, which can easily separate patients with poor prognosis from all the ccRCC patients by performing PCR. Then, clinicians can perform more individualized treatment regimens for patients with different prognosis, which will contribute to individual treatment and save more public health resources. Meanwhile, this nomogram consisted of objective indicators, which can reduce the interobservers' differences and more accurately predict survival.

5. Conclusions

In summary, we successfully developed and verified a nine-redox-related lncRNA signature that could predict the overall survival of ccRCC patients. The prognostic signature proved superior compared to the other common prognostic factors. We further assembled a nomogram connecting this signature with clinicopathologic characteristics for 1-, 3-, and 5-year OS, which can provide clinicians with a quantitative rather than qualitative approach in predicting ccRCC survival. This will help clinicians make treatment decisions more easily and accurately in the future. It is, however, necessary to carry out a large-scale, multicenter prospective research to confirm our results.

Data Availability

The source data of this study were derived from the public repositories, as indicated in the section of "Materials and Methods" of the manuscript. And all data that support the findings of this study are available from the corresponding author upon reasonable request.

Conflicts of Interest

The authors declare that they have no conflicts of interest.

Authors' Contributions

XQD and XY contributed to the design, analysis, and interpretation of data; drafting of the manuscript; and critical revision of the manuscript. XQD and LJL contributed to the statistical analysis. XQD, XY, LJL, LCQ, SJX, LC, and WSG contributed to the methodology. LCQ, SJX, LC, and WSG contributed to the project administration. XQD and XY wrote the manuscript (original draft). XQD, LJL, LCQ, SJX, LC, and WSG wrote the manuscript (review and editing). Qi-Dong, Xia; Yang, Xun; Cong Li; and Shao-Gang Wang contributed equally to this work.

Acknowledgments

Supplementary Materials

Supplementary file. Differential expression of the nine redox-related lncRNAs in different groups. S1. Differential expression between age ≤ 65 and age > 65. S2. Differential expression between male and female. S3. Differential expression between different pathological grade. (Supplementary Materials)

References

[1] H. Moch, A. L. Cubilla, P. A. Humphrey, V. E. Reuter, and T. M. Ulbright, "The 2016 WHO classification of tumours of the urinary system and male genital organs—part a: renal, penile, and testicular tumours," *European Urology*, vol. 70, no. 1, pp. 93–105, 2016.

[2] R. L. Siegel, K. D. Miller, and A. Jemal, "Cancer statistics, 2020," *CA: a Cancer Journal for Clinicians*, vol. 70, no. 1, pp. 7–30, 2020.

[3] U. Capitanio and F. Montorsi, "Renal Cancer," *The Lancet*, vol. 387, no. 10021, pp. 894–906, 2016.

[4] E. Jonasch, J. Gao, and W. K. Rathmell, "Renal cell carcinoma," *BMJ*, vol. 349, 2014.

[5] M. B. Atkins and N. M. Tannir, "Current and emerging therapies for first-line treatment of metastatic clear cell renal cell carcinoma," *Cancer Treatment Reviews*, vol. 70, pp. 127–137, 2018.

[6] T. K. Choueiri, B. Escudier, T. Powles et al., "Cabozantinib versus everolimus in advanced renal cell carcinoma (METEOR): final results from a randomised, open-label, phase 3 trial," *The Lancet Oncology*, vol. 17, no. 7, pp. 917–927, 2016.

[7] R. J. Motzer, B. Escudier, D. F. McDermott et al., "Nivolumab versus everolimus in advanced renal-cell carcinoma," *The New England Journal of Medicine*, vol. 373, no. 19, pp. 1803–1813, 2015.

[8] R. J. Motzer, T. Powles, M. B. Atkins et al., "IMmotion151: a randomized phase III study of atezolizumab plus bevacizumab vs sunitinib in untreated metastatic renal cell carcinoma," in *Abstract (588) presented at the annual genitourinary cancers symposium of the American Society of Clinical Oncology*, San Francisco, CA, February 2018.

[9] V. Ficarra, A. Galfano, M. Mancini, G. Martignoni, and W. Artibani, "TNM staging system for renal-cell carcinoma: current status and future perspectives," *The Lancet Oncology*, vol. 8, no. 6, pp. 554–558, 2007.

[10] S. You, Y. Zhang, J. Xu et al., "The role of BRG1 in antioxidant and redox signaling," *Oxidative Medicine and Cellular Longevity*, vol. 2020, 12 pages, 2020.

[11] K. M. Holmström and T. Finkel, "Cellular mechanisms and physiological consequences of redox-dependent signalling," *Nature Reviews Molecular Cell Biology*, vol. 15, no. 6, pp. 411–421, 2014.

[12] S. Reuter, S. C. Gupta, M. M. Chaturvedi, and B. B. Aggarwal, "Oxidative stress, inflammation, and cancer: how are they linked?," *Free Radical Biology and Medicine*, vol. 49, no. 11, pp. 1603–1616, 2010.

[13] D. Zhou, L. Shao, and D. R. Spitz, "Reactive oxygen species in normal and tumor stem cells," in *Advances in Cancer Research*, pp. 1–67, Academic Press Inc., 2014.

[14] J. G. Costa, N. Saraiva, I. Batinic-Haberle, M. Castro, N. G. Oliveira, and A. S. Fernandes, "The SOD mimic MnTnHex-2-pyp5+ reduces the viability and migration of 786-O human renal cancer cells," *Antioxidants*, vol. 8, no. 10, p. 490, 2019.

[15] H. Miess, B. Dankworth, A. M. Gouw et al., "The glutathione redox system is essential to prevent ferroptosis caused by impaired lipid metabolism in clear cell renal cell carcinoma," *Oncogene*, vol. 37, no. 40, pp. 5435–5450, 2018.

[16] Y. Xiao, T. Xiao, W. Ou et al., "LncRNA SNHG16 as a potential biomarker and therapeutic target in human cancers," *Biomarker Research*, vol. 8, no. 1, 2020.

[17] M. Guttman and J. L. Rinn, "Modular regulatory principles of large non-coding RNAs," *Nature*, vol. 482, no. 7385, pp. 339–346, 2012.

[18] F. Kopp and J. T. Mendell, "Functional classification and experimental dissection of long noncoding RNAs," *Cell*, vol. 172, no. 3, pp. 393–407, 2018.

[19] J. J. Quinn and H. Y. Chang, "Unique features of long non-coding RNA biogenesis and function," *Nature Reviews Genetics*, vol. 17, no. 1, pp. 47–62, 2016.

[20] W. Jiang, Q. Guo, C. Wang, and Y. Zhu, "A nomogram based on 9-lncRNAs signature for improving prognostic prediction of clear cell renal cell carcinoma," *Cancer Cell International*, vol. 19, no. 1, 2019.

[21] Y. J. Su, J. Yu, Y. Q. Huang, and J. Yang, "Circulating long noncoding RNA as a potential target for prostate cancer," *International Journal of Molecular Sciences*, vol. 16, no. 12, pp. 13322–13338, 2015.

[22] L. Nandagopal and G. Sonpavde, "Circulating biomarkers in bladder cancer," *Bladder Cancer*, vol. 2, no. 4, pp. 369–379, 2016.

[23] X. Mao, X. Qin, L. Li et al., "A 15-long non-coding RNA signature to improve prognosis prediction of cervical squamous cell carcinoma," *Gynecologic Oncology*, vol. 149, no. 1, pp. 181–187, 2018.

[24] The Cancer Genome Atlas Research Network, "Comprehensive molecular characterization of clear cell renal cell carcinoma," *Nature*, vol. 499, no. 7456, pp. 43–49, 2013.

[25] T. M. Jones, J. S. Carew, and S. T. Nawrocki, "Therapeutic targeting of autophagy for renal cell carcinoma therapy," *Cancers (Basel)*, vol. 12, no. 5, article 1185, 2020.

[26] T. Radic, V. Coric, Z. Bukumiric et al., "GSTO1 ∗ CC genotype (Rs4925) predicts shorter survival in clear cell renal cell carcinoma male patients," *Cancers (Basel)*, vol. 11, no. 12, article 2038, 2019.

[27] H. Moch, W. Artibani, B. Delahunt et al., "Reassessing the current UICC/AJCC TNM staging for renal cell carcinoma," *European Urology*, vol. 56, no. 4, pp. 636–643, 2009.

[28] E. S. Martens-Uzunova, R. Böttcher, C. M. Croce, G. Jenster, T. Visakorpi, and G. A. Calin, "Long noncoding RNA in prostate, bladder, and kidney cancer," *European Urology*, vol. 65, no. 6, pp. 1140–1151, 2014.

[29] J. D. Hayes, A. T. Dinkova-Kostova, and K. D. Tew, "Oxidative stress in cancer," *Cancer Cell*, vol. 38, no. 2, pp. 167–197, 2020.

[30] N. Song, K. Kim, A. Shin et al., "Colorectal cancer susceptibility loci and influence on survival," *Genes, Chromosomes and Cancer*, vol. 57, no. 12, pp. 630–637, 2018.

[31] V. D. Peltekova, M. Lemire, A. M. Qazi et al., "Identification of genes expressed by immune cells of the colon that are regulated by colorectal cancer-associated variants," *International Journal of Cancer*, vol. 134, no. 10, pp. 2330–2341, 2014.

[32] A. Closa, D. Cordero, R. Sanz-Pamplona et al., "Identification of candidate susceptibility genes for colorectal cancer through eQTL analysis," *Carcinogenesis*, vol. 35, no. 9, pp. 2039–2046, 2014.

[33] V. K. Srinivasan, S. Naseem, N. Varma, D. P. Lad, and P. Malhotra, "Genomic alterations in chronic lymphocytic leukemia and their correlation with clinico-hematological parameters and disease progression," *Blood Research*, vol. 55, no. 3, pp. 131–138, 2020.

[34] W. Wu, Y. Zhao, E. Gao et al., "LncRNA DLEU2 accelerates the tumorigenesis and invasion of non–small cell lung cancer by sponging miR-30a-5p," *Journal of Cellular and Molecular Medicine*, vol. 24, no. 1, pp. 441–450, 2020.

[35] X. Li, F. Xu, Q. Meng et al., "Long noncoding RNA DLEU2 predicts a poor prognosis and enhances malignant properties in laryngeal squamous cell carcinoma through the miR-30c-5p/PIK3CD/Akt axis," *Cell Death & Disease*, vol. 11, no. 6, p. 472, 2020.

[36] T. Lu, R. Wang, H. Cai, and Y. Cui, "Long non-coding RNA DLEU2 promotes the progression of esophageal cancer through miR-30e-5p/E2F7 axis," *Biomedicine & Pharmacotherapy*, vol. 123, p. 109650, 2020.

[37] Z. Chen, J. Zhang, Z. Zhang et al., "The putative tumor suppressor microRNA-30a-5p modulates clear cell renal cell carcinoma aggressiveness through repression of ZEB2," *Cell Death & Disease*, vol. 8, no. 6, article e2859, 2017.

[38] F. F. Shen, Y. Pan, H. J. Yang et al., "Decreased expression of SPINT1-AS1 and SPINT1 mRNA might be independent unfavorable prognostic indicators in esophageal squamous cell carcinoma," *Oncotargets and Therapy*, vol. 12, pp. 4755–4763, 2019.

[39] C. Li, W. Li, Y. Zhang et al., "Increased expression of antisense lncRNA SPINT1-AS1 predicts a poor prognosis in colorectal cancer and is negatively correlated with its sense transcript," *Oncotargets and Therapy*, vol. 11, pp. 3969–3978, 2018.

[40] Z. Xiang, S. Song, Z. Zhu et al., "LncRNAs GIHCG and SPINT1-AS1 are crucial factors for pan-cancer cells sensitivity to lapatinib," *Frontiers in Genetics*, vol. 10, 2019.

[41] Y. Shen, Y. Feng, H. Chen et al., "Focusing on long non-coding RNA dysregulation in newly diagnosed multiple myeloma," *Life Sciences*, vol. 196, pp. 133–142, 2018.

[42] M. Pljesa-Ercegovac, A. Savic-Radojevic, V. Coric, T. Radic, and T. Simic, "Glutathione transferase genotypes may serve as determinants of risk and prognosis in renal cell carcinoma," *BioFactors*, vol. 46, no. 2, pp. 229–238, 2020.

[43] V. Sosa, T. Moliné, R. Somoza, R. Paciucci, H. Kondoh, and M. E. LLeonart, "Oxidative stress and cancer: an overview," *Ageing Research Reviews*, vol. 12, no. 1, pp. 376–390, 2013.

[44] M. Pljesa-Ercegovac, J. Mimic-Oka, D. Dragicevic et al., "Altered antioxidant capacity in human renal cell carcinoma: role of glutathione associated enzymes," *Urologic Oncology: Seminars and Original Investigations*, vol. 26, no. 2, pp. 175–181, 2008.

[45] M. S. Leisegang, K. Schröder, and R. P. Brandes, "Redox regulation and noncoding RNAs," *Antioxidants and Redox Signaling*, vol. 29, no. 9, pp. 793–812, 2018.

[46] L. Chen, H. Yang, Z. Yi et al., "LncRNA GAS5 regulates redox balance and dysregulates the cell cycle and apoptosis in malignant melanoma cells," *Journal of Cancer Research and Clinical Oncology*, vol. 145, no. 3, pp. 637–652, 2019.

[47] W. He, B. Liang, C. Wang et al., "MSC-regulated lncRNA MACC1-AS1 promotes stemness and chemoresistance through fatty acid oxidation in gastric cancer," *Oncogene*, vol. 38, no. 23, pp. 4637–4654, 2019.

Research Article

A Prognostic 14-Gene Expression Signature for Lung Adenocarcinoma: A Study Based on TCGA Data Mining

Jie Liu [1,2] **Shiqiang Hou** [3] **Jinyi Wang** [1] **Zhengjun Chai** [1] **Xuan Hong** [1] **Tian Zhao** [1] **Zhengliang Sun** [1] **Liandi Bai** [1] **Hongyan Gao** [1] **Jing Gao** [1] **and Guohan Chen** [1]

[1]Department of Thoracic Surgery, Shanghai East Hospital, Tongji University School of Medicine, Shanghai 200120, China
[2]Research Center for Translational Medicine, Shanghai East Hospital, Tongji University School of Medicine, Shanghai 200120, China
[3]Department of Cardiology, Zhongshan Hospital, Fudan University, Shanghai 200032, China

Correspondence should be addressed to Guohan Chen; chenguohan0160@126.com

Background. Lung adenocarcinoma (LUAD), a major and fatal subtype of lung cancer, caused lots of mortalities and showed different outcomes in prognosis. This study was to assess key genes and to develop a prognostic signature for the patient therapy with LUAD. *Method.* RNA expression profile and clinical data from 522 LUAD patients were accessed and downloaded from the Cancer Genome Atlas (TCGA) database. Differentially expressed genes (DEGs) were extracted and analyzed between normal tissues and LUAD samples. Then, a 14-DEG signature was developed and identified for the survival prediction in LUAD patients by means of univariate and multivariate Cox regression analyses. The gene ontology (GO) and Kyoto Encyclopedia of Genes and Genomes (KEGG) pathway enrichment analysis were performed to predict the potential biological functions and pathways of these DEGs. *Results.* Twenty-two out of 5924 DEGs in the TCGA dataset were screened and associated with the overall survival (OS) of LUAD patients. 14 DEGs were finally selected and included in our development and validation model by risk score analysis. The ROC analysis indicated that the specificity and sensitivity of this profile signature were high. Further functional enrichment analyses indicated that these DEGs might regulate genes that affect the function of release of sequestered calcium ion into cytosol and pathways that associated with vibrio cholerae infection. *Conclusion.* Our study developed a novel 14-DEG signature providing more efficient and persuasive prognostic information beyond conventional clinicopathological factors for survival prediction of LUAD patients.

1. Introduction

Lung cancer continues to be the leading cause of cancer-related mortality around the world [1], in which non-small-cell lung cancer (NSCLC) is the most often type, being mainly subdivided into adenocarcinoma (LUAD), squamous cell carcinomas (LUSC), and large cell carcinoma (LCC) [2, 3]. In the past decades, LUAD represents the major lung cancer population, increasingly accounting for approximately 40% of all lung cancers [4]. LUAD were characterized by distinct epidemiological, clinicopathological, and molecular properties [5]. Despite the improvements in diagnosis and therapy made during the past 30 years, the biomarkers for early detecting, prediction of high rate of relapse and mortality populations and the identification of target or immunological therapies for lung cancer patients are still unsatisfactory. Thus, identification of effective biomarkers for the prognosis of LUAD is critical for the diagnosis and treatment of LUAD patients.

Differentially expressed genes (DEGs) that regulated by gene transcription are implicated in diverse biological processes. Gene-expression profiling analysis made some progresses in predicting overall survival (OS) in NSCLC [1, 6, 7]. Mascaux et al. showed that immune activation and immune escape in tumor microenvironment (TME) occurred before lung cancer invasion [7]. With the importance of DEGs involved in cancer

research, the roles of DEGs as biomarkers and drivers of tumor oncogenesis and suppression have been identified. However, there are no definite and effective biomarkers in predicting the 5-year survival rate of LUAD patients, which bring great difficulty to clinical prognosis. Therefore, investigation in DEGs may be the solution to noninvasive biomarkers for LUAD.

Although several genes or long noncoding RNA expression signatures, including programmed death-ligand 1(PD-L1), have been recently proposed for predicting the OS in NSCLC [6, 8–10], the prognostic value of an effective and new biomarker of gene profile is still limited. DEG signatures identification related to patient OS in standard clinical samples may promote the development of molecular drug subtypes and potential therapy targets. LUAD and LUSC exhibit distinction in the epidemiology, molecular characteristics, and prognosis [5]. Although several prognostic DEG signatures have been discovered for NSCLC [11, 12], few of these research identify and pinpoint the prognostic value of DEGs biomarkers for LUAD patients in a large cohort. Therefore, we focused on the DEG signature of LUAD not previously published.

In this study, we identified a 14-DEG signature as a predictor of survival risk of LUAD patients using a cohort of 522 cases from The Cancer Genome Atlas (TCGA) database. We employed a survival-associated risk score formula to identify a novel 14-DEG prognostic signature from the TCGA dataset of 522 LUAD patient samples. To show the conscientiousness of this signature, the specificity and sensitivity of our model were examined by the area under ROC curve (AUROC) analysis. A 14-DEG signature which could distinguish patients between good and poor survival was developed by means of Cox regression analysis and risk score model method. A higher area under curve (AUC) of the receiver operating characteristic (ROC) curve confirmed good sensitivity and specificity of the prognostic model, while multivariate Cox regression analysis and stratified analysis indicated the independence of predictive capacity of the 14-DEG prognostic signature. Besides, the functional enrichment analysis demonstrated that the 14-DEG may be probably involved in the progression of LUAD through exerting their roles in LUAD-related function of release of sequestered calcium ion into cytosol and pathways that associated with vibrio cholerae infection. Therefore, our finding may provide insights into the predictive capacity of DEG signature elaborating LUAD.

2. Materials and Methods

2.1. The LUAD Patient Dataset. The RNA-Seq data set of patients with LUAD was downloaded from the TCGA database (https://cancergenome.nih.gov/), including clinical features. The patients with the following criteria were filtered: patients with complete information of RNA expression profiles and clinical factors (including age, gender, TNM stage, survival status, and survival time).

2.2. Differentially Expressed Gene Screening in LUAD. Raw gene-level counts were utilized in our analysis. All the data processing and normalization were performed and com-

pleted by using the Perl and R version 4.0.0. The gene expression profiling data of the 522 LUAD samples and 59 normal samples were downloaded from the TCGA database. The DEGs between normal and LUAD group were identified through the "edgeR" package from Bioconductor in R language [13]. |log 2FC| >2 and adjusted p value < 0.01 were set as the threshold for screening the expression difference of DEGs.

2.3. Cox Regression Analysis. The RNA-seq expression values were transformed in log2 format to normalize the data. Univariate Cox regression analysis using the "Survival" R package was performed to clarify the association between DEG expression and patient survival. The DEGs (p value < 1.0e-06) from the univariate analysis were considered as potential candidate DEGs associated with OS. To determine the independent predictive capacity of the 14-DEG signature for LUAD patients, a stepwise multivariate Cox regression analysis was executed to identify the predictive model with the best explanatory and informative efficacy.

2.4. Risk Score and ROC Curve. A mathematical formula (Riskscore $= \sum_{i=1}^{N}(\text{Exp}(i) \cdot \text{coe}(i))$) was developed to predict the risk score for each patient based on the multivariate Cox regression analysis. In accordance with our risk scoring system, patients were classified into high-risk and low-risk groups according to the median risk score. A Kaplan-Meier overall survival curve of the different stages was plotted, and the hazard ratio was calculated. Subsequently, the log-rank test was utilized to determine the survival differences between high-risk and low-risk groups. The sensitivity and specificity of the DEG prognostic model to predict clinical outcome were evaluated by calculating the area under curve (AUC) of the receiver operating characteristic (ROC) curve in the R package of "survival ROC" [14].

2.5. Differential Analysis of Scores and DEG Expression with Clinicopathological Stages. The clinicopathological characteristics data corresponding to the LUAD samples were downloaded from TCGA. The independence of the RiskScore from the clinical parameters, such as age, gender, and tumor stage, was determined, and the statistical analysis was performed by Kruskal–Wallis rank sum test or log-rank test as the significance test. In addition, the differential expression of the DEGs between distinct clinicopathologic stages was analyzed and plotted.

2.6. Function Enrichment Analysis. Gene ontology (GO) and Kyoto Encyclopedia of Genes and Genomes (KEGG) pathway enrichment analysis was carried out for DEGs with the aid of clusterProfiler R package. Only terms with p value < 0.05 were considered as significantly enriched in functions of prognostic DEGs and KEGG pathway analysis.

3. Results

3.1. Patient Characteristics. The whole construction process in our research was showed in Figure 1. On basis of the defined criteria, a total of 522 LUAD patients with both
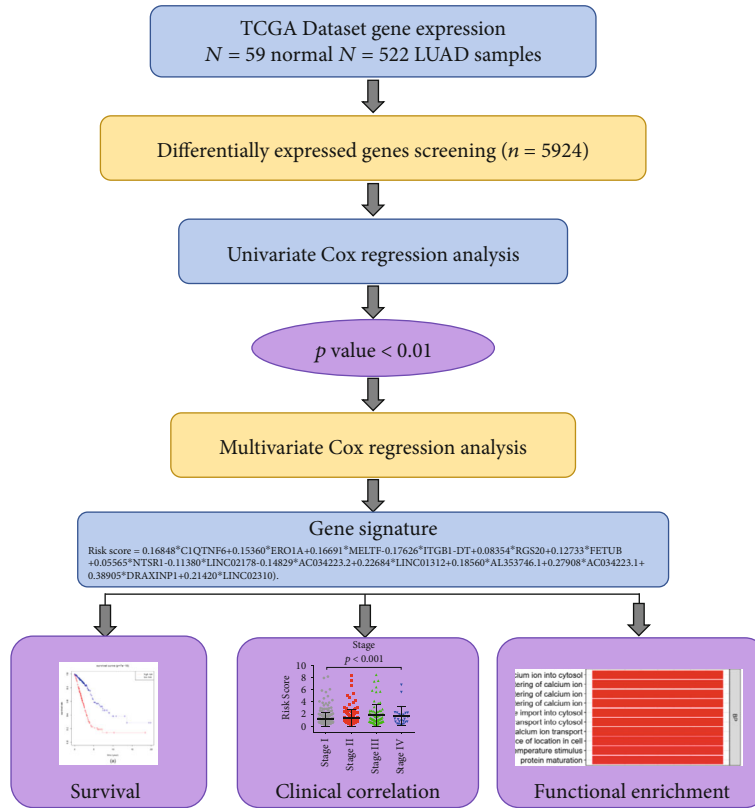
Figure 1: Workflow chart of the gene model construction.

RNA-seq expression profiles and clinical data were downloaded from the TCGA. The clinical covariates of the patients in normal or LUAD group were showed in Table 1. 47.89 percent of 522 LUAD patients was no more than and 52.11 percent was more than 65 years old. The female accounted for 53.64% and the male 46.36% in these patients. Of the 522 patients, 280 were classified as stage I, 130 as stage II, while 86 were labeled with stage III and 26 with stage IV disease. The survival time of 522 LUAD patients was 902.51 ± 892.15 days.

3.2. Differentially Expressed Genes in LUAD Patients.

According to the defined criteria, a total of 5924 DEGs (including 5147 upregulated and 777 downregulated) were extracted between LUAD and normal samples (Figure 2(a)). The results of unsupervised hierarchical cluster analysis in Figure 2(b) showed that the LUAD samples could be clearly distinguished from the normal controls with the expression of DEGs.

A total of 5924 DEGs were screened to be differentially expressed between LUAD and normal tissues and were used for survival analysis. To identify the DEGs which were related to patient survival in LUAD, univariate Cox regression analysis for all DEG expression data was assessed. With the significance level threshold of $1.0E\text{-}06$, a set of 22 DEGs was selected. These DEGs were utilized in stepwise multivariate Cox regression analysis, and finally, 14 DEGs (C1QTNF6, ERO1A, MELTF, ITGB1-DT, RGS20, FETUB, NTSR1, LINC02178, AC034223.2, LINC01312, AL353746.1, AC034223.1, DRAXINP1, and LINC02310) were

Table 1: Summary of LUAD patient clinical characteristics.

Covariates	Group	Patients ($N = 522$)	
		n	%
Survival time		902.51 ± 892.15	
Vital status	Alive	334	63.98
	Dead	188	36.02
Stage	I	280	53.64
	II	130	24.90
	III	86	16.48
	IV	26	4.98
T stage	T1	172	32.95
	T2	281	53.83
	T3	47	9.00
	T4	22	4.21
N stage	N0	342	65.52
	N1	99	18.97
	N2	75	14.37
	N3	6	1.15
M stage	M0	496	95.02
	M1	26	4.98
Age	≤65	250	47.89
	>65	272	52.11
Gender	Female	280	53.64
	Male	242	46.36

(a)

(b)

FIGURE 2: Continued.

(c)
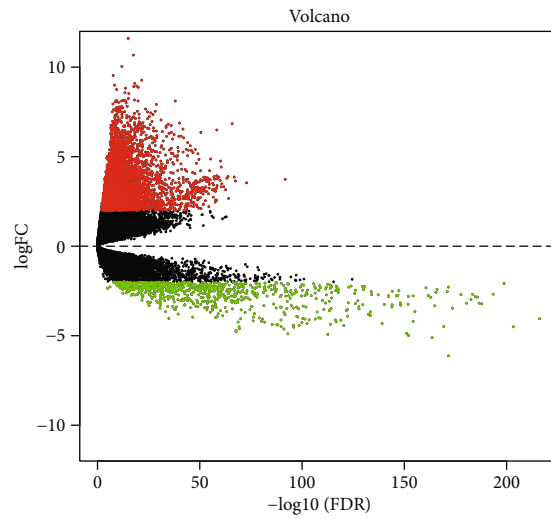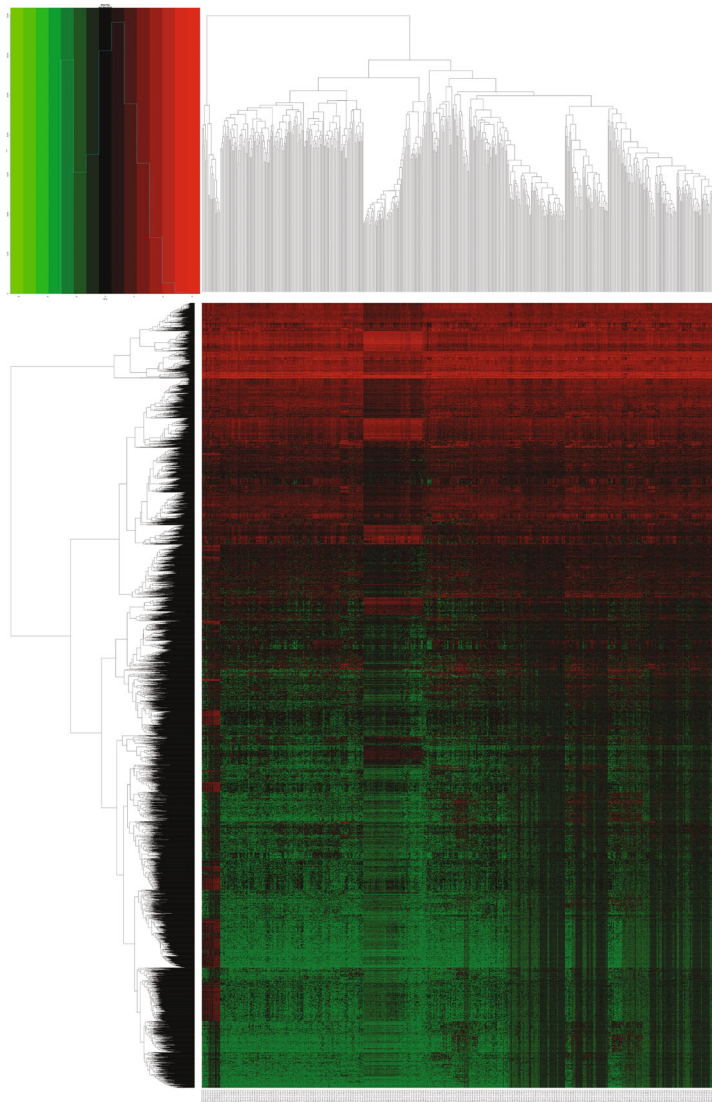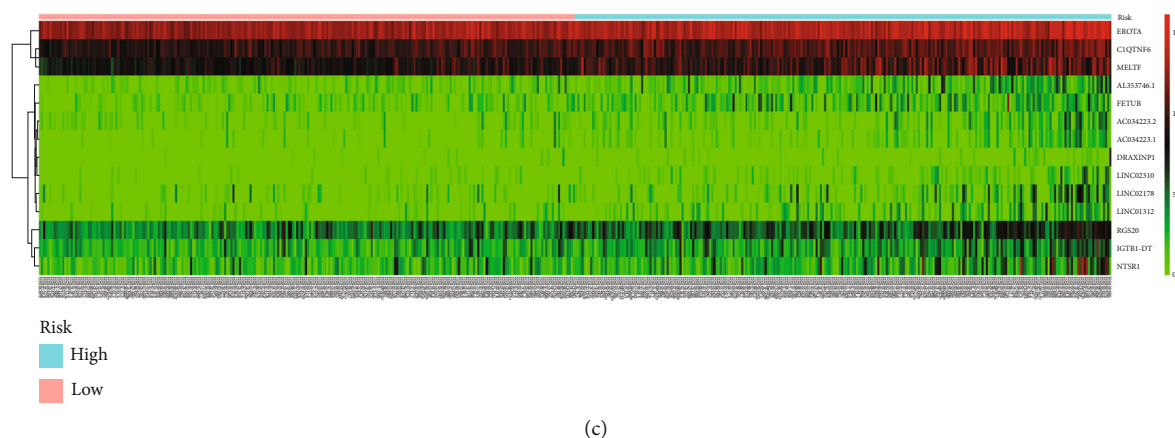
FIGURE 2: Prognostic evaluation of the 14-DEG signature in LUAD. (a) Volcano plots of DEGs in TCGA dataset. (b) Unsupervised hierarchical clustering analysis of the differentially expressed genes between LUAD and normal tissues. (c) The expression heat map of the 14 DEGs.

identified (Figure 2(c)). The risk score analysis of the 14 DEGs was conducted to calculate the risk score for each patient. The risk score formula for our model was presented in Table 2 (Risk score = 0.16848 ∗ C1QTNF6 + 0.15360 ∗ ERO1A + 0.16691 ∗ MELTF − 0.17626 ∗ ITGB1 − DT + 0.08354 ∗ RGS20 + 0.12733 ∗ FETUB + 0.05565 ∗ NTSR1 − 0.11380 ∗ LINC02178 − 0.14829 ∗ AC034223.2 + 0.22684 ∗ LINC01312 + 0.18560 ∗ AL353746.1 + 0.27908 ∗ AC034223.1 + 0.38905 ∗ DRAXINP1 + 0.21420 ∗ LINC 02310). Of these 14 genes, all were associated with high risk (Figure 2(c)).

3.3. The Development of the 14-Gene Prognostic Model.
We divided the patients into high-risk and low-risk groups according to the median risk score (value = 0.89) by calculating the expression levels of the 14 DEGs in each patient. The log-rank test was used to determine the survival differences. As depicted in Figure 3(a), Kaplan Meier curves showed that the high-risk group was correlated with poor prognosis ($p = 7e − 16$). ROC curves indicated that the AUC of the 14-gene signature was 0.769 (Figure 3(b)), which proved that the 14-gene signature had a high specificity and sensitivity in predicting the OS of LUAD patients.

3.4. The 14-DEG Signature Independence from Conventional Clinical Factors.
According to multivariate Cox regression analysis, we demonstrated that the 14-DEG signature risk score exhibited an independent predictive ability from other clinical factors ($p = 7e − 16$, shown in Figure 3(a)). Meanwhile, we found that TNM stage was an independent factor for predicting the OS of LUAD patients ($p < 0.001$) (Figure 4(a)). Therefore, stratification analysis was further performed to examine whether the 14-gene signature could provide predicted value for patients within the same TNM stage. Because the sample numbers in stage IV were too small to draw any reliable conclusions ($n = 26$), stratification analysis was carried out only in stage I, II, and III patients. Log-rank test for patients in stage I demonstrated that the 14-DEG signature could distinguish patients with significantly

different survival time ($p = 0.00018$, Figure 4(b)). Similar predictive outcome of the 14-DEG signature was achieved in stage II ($p = 1e − 05$) and III ($p = 9e − 05$) patients (Figures 4(c) and 4(d)). Besides, distinct expression of DEGs between different clinicopathological stage samples in Figure 4(e) showed that the DEG expression was positively related to clinicopathological stage. Altogether, these results manifested that the prognostic capability of the 14-DEG signature was independent from conventional clinical factors for predicting survival of LUAD patients.

3.5. Functional Enrichment Analysis of Biological Processes and Pathways Correlated with the Prognostic DEGs in LUAD.
The biological functions and pathway analyses were conducted using R package clusterProfiler. The results showed that DEGs were enriched in 181 GO biological process (BP), 10 cellular component (CC), and 14 molecular function (MF) terms. The GO categories of GO: 0051209~release of sequestered calcium ion into cytosol (BP), GO: 0005788~endoplasmic reticulum lumen (CC) and GO: 0008191~metalloendopeptidase inhibitor activity (MF) were mainly clustered, respectively (Figure 5(a)). The top 10 GO terms were shown in Table 3. The DEGs were enriched in three KEGG pathways which mainly focused on tumor metabolism, including hsa05110: vibrio cholerae infection, hsa04141: protein processing in endoplasmic reticulum, and hsa04020: calcium signaling pathway (Table 4, Figure 5(b)).

4. Discussion

NSCLC is a global health threat with high morbidity and mortality, up to 0.6 and 0.1 percent, respectively [11]. LUAD accounts for more than 40% of the lung cancer patients, showing its predominance among NSCLC. On account of the heterogeneity, conventional prognostic systems such as TNM stage sometimes exhibited predicting deficiency for risk stratification and clinical outcome estimations. Therefore, considerable outcomes are in urgent need in recent

TABLE 2: 14-DEG risk score model.

DEGs	Coef	Exp (coef)	Se (coef)	z	Univariate p value	Multivariate p value
C1QTNF6	0.168	1.18351	0.0848	1.987	3.230E-08	4.694E-02
ERO1A	0.154	1.16603	0.10023	1.532	2.970E-08	1.254E-01
MELTF	0.167	1.18164	0.05823	2.867	6.080E-07	4.150E-03
ITGB1-DT	-0.176	0.8384	0.06004	-2.936	2.230E-07	3.325E-03
RGS20	0.084	1.08713	0.0497	1.681	2.030E-07	9.280E-02
FETUB	0.127	1.13579	0.04674	2.724	5.180E-07	6.448E-03
NTSR1	0.056	1.05723	0.03601	1.545	9.590E-07	1.223E-01
LINC02178	-0.114	0.89244	0.06063	-1.877	3.630E-09	6.052E-02
AC034223.2	-0.148	0.86218	0.09964	-1.488	4.450E-07	1.367E-01
LINC01312	0.227	1.25463	0.06224	3.645	8.990E-09	2.680E-04
AL353746.1	0.186	1.20394	0.04763	3.896	1.750E-09	9.760E-05
AC034223.1	0.279	1.32191	0.11378	2.453	2.580E-09	1.417E-02
DRAXINP1	0.389	1.47558	0.09525	4.085	1.600E-08	4.410E-05
LINC02310	0.214	1.23888	0.08501	2.52	1.110E-09	1.174E-02

Coef: coefficient.

(a)

(b)
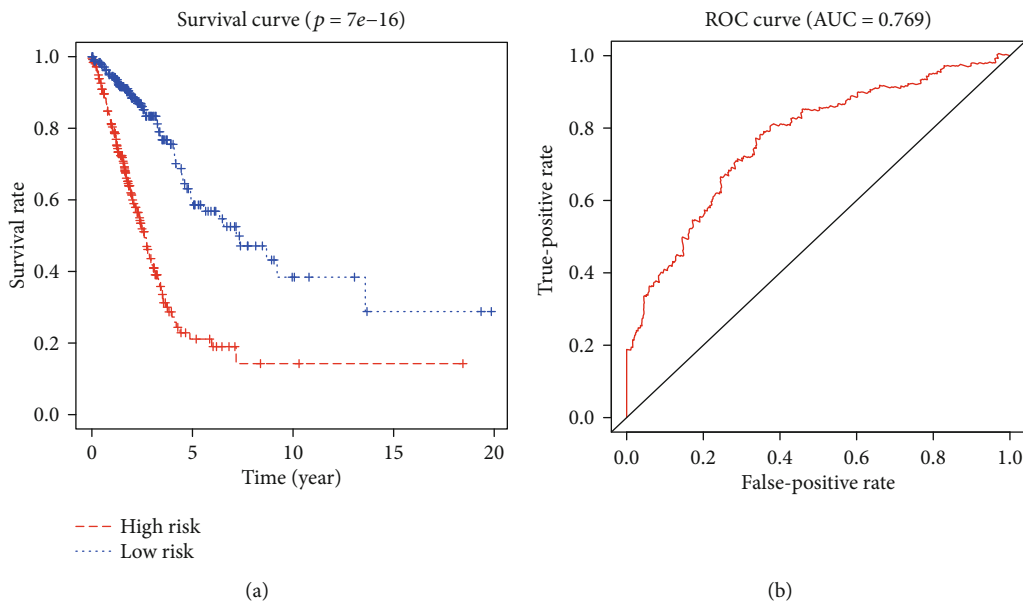
FIGURE 3: Kaplan-Meier and ROC curves for the 14-DEG signature. (a) Differences between the high-risk ($n = 252$) and low-risk ($n = 252$) groups were determined by the log-rank test ($p = 7e - 16$). Five-year overall survival was 21.1% (95% CI: 14.19%-31.4%) and 60.1% (95% CI:50.7%-71.2%) for the high-risk and low-risk groups, respectively. (b) ROC curves indicated that the area under receiver operating characteristic of 14-DEG model was 0.769.

decades to develop efficient prognostic signatures to promote the prediction of LUAD patient survival.

Increasing evidences suggest that DEGs play indispensable and important roles in the tumorigenesis, TNM staging, and progression of lung cancer. Although several researches have identified a number of DEGs with prognostic value in NSCLC, especially in LUSC [10, 11], few studies have concentrated on and analyzed the DEG expression specifically in LUAD. Moreover, because LUAD and LUSC are vastly distinct diseases at the molecular, pathological classification

and clinical level, such as distinct driver genetic changes, response to chemotherapy, or targeted therapy [4, 5], single-gene expression models are insufficient for accurate prediction of LUAD outcomes. Therefore, we focused on the molecular prognostic DEG signature patterns in LUAD.

In this study, 14-DEG signature related to overall survival of LUAD patients was identified. By means of univariate Cox regression analysis and stepwise multivariate Cox regression analysis, a novel 14-gene (C1QTNF6, ERO1A, MELTF, ITGB1-DT, RGS20, FETUB, NTSR1, LINC02178,
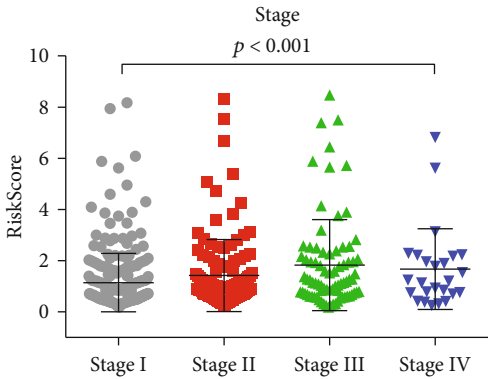
(a)
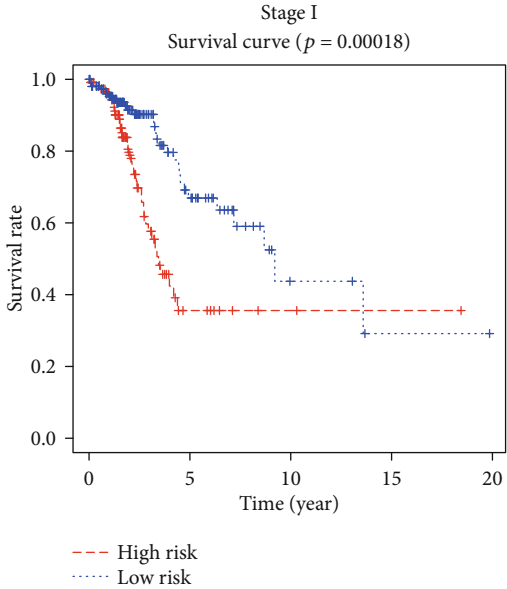
(b)

(c)

(d)
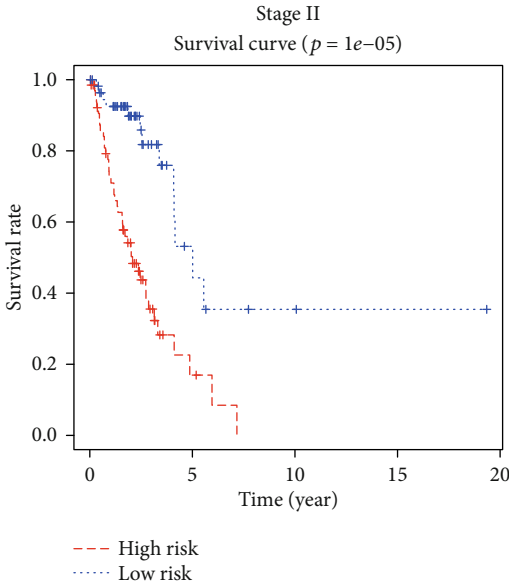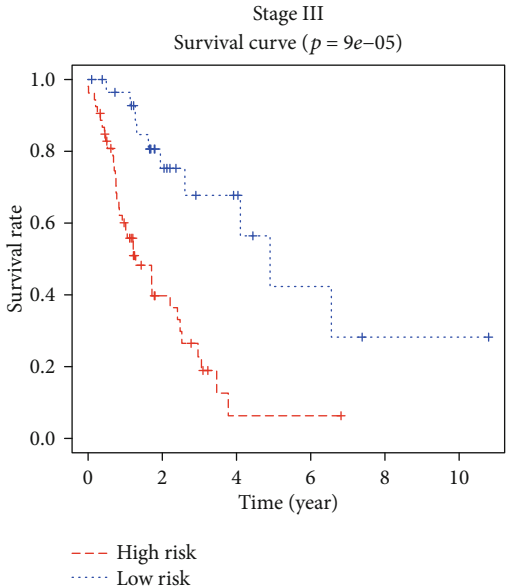
FIGURE 4: Continued.
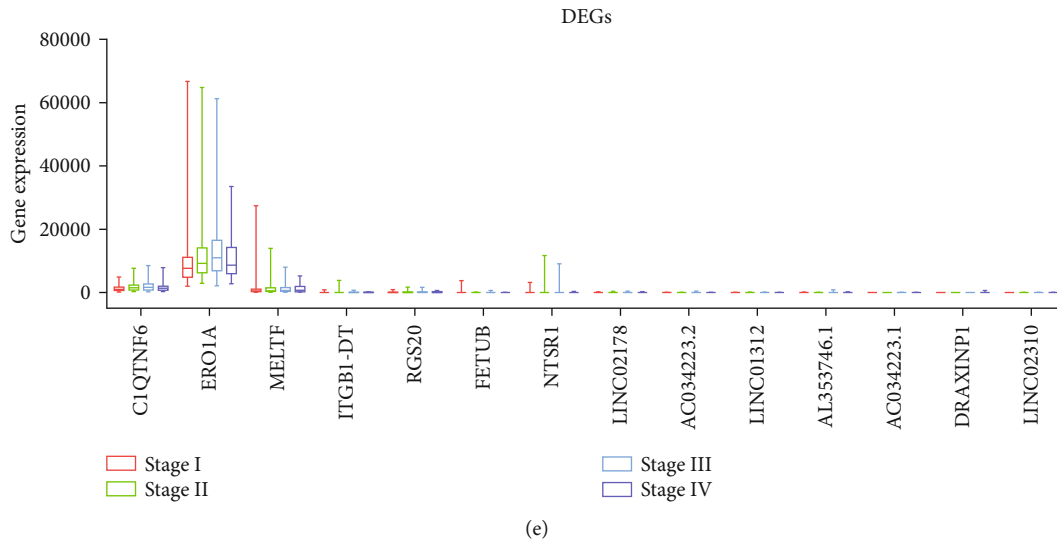
FIGURE 4: Correlation of RiskScore and survival rate (Kaplan-Meier curves) with clinicopathological staging characteristics. (a) Distribution of RiskScore in TNM stage. The $p < 0.001$ by Kruskal-Wallis rank sum test. (b) Differences between the high-risk ($n = 116$) and low-risk ($n = 155$) groups in stage I patients were determined by the log-rank test ($p = 2e - 4$). Five-year overall survival was 35.6% (95% CI: 23.5%-53.8%) and 66.9% (95% CI: 55.8%-80.3%) for the high-risk and low-risk groups, respectively. (c) Differences between the high-risk ($n = 67$) and low-risk ($n = 57$) groups in stage II patients were determined by the log-rank test ($p = 5e - 6$). Five-year overall survival was 16.95% (95% CI: 7.09%-40.6%) and 53.1% (95% CI: 33.5%-84.2%) for the high-risk and low-risk groups, respectively. (d) Differences between the high-risk ($n = 53$) and low-risk ($n = 30$) groups in stage III patients were determined by the log-rank test ($p = 9e - 5$). Five-year overall survival was 6.31% (95% CI: 1.09%-36.5%) and 42.3% (95% CI: 20.2%-88.6%) for the high-risk and low-risk groups, respectively. (e) Distinct expression of each DEG between different clinicopathological stage samples.

AC034223.2, LINC01312, AL353746.1, AC034223.1, DRAX-INP1, and LINC02310) prognostic signature was established and validated to demonstrate high specificity and sensitivity in predicting the overall survival time of LUAD patients. We calculated the RiskScore of each patient through the formula and the expression of selected DEGs. The patients were divided into high- and low-risk group by the median RiskScore (value = 0.89); then, we obtained the survival curve according to the survival rate of all LUAD patients. To our knowledge, C1QTNF6 has been recently identified as a novel biomarker exacerbating the outcome of lung adenocarcinoma patients [15]. Combined expression of protein disulfide isomerase and endoplasmic reticulum oxidoreductin 1-α (ERO1A) is a poor prognostic marker for non-small-cell lung cancer [16]. Level of melanotransferrin (MELTF) in tissue and sera serves as a prognostic marker of gastric cancer. Patients with high serum MELTF levels had poor prognosis [17]. It was demonstrated that ITGA5 and ITGB1 are prognostic in non-small-cell lung cancer by integrin and gene network analysis [18]. Regulator of G protein signaling 20 (RGS20) was identified as molecular marker for LUAD for its effect in enhancing cancer cell aggregation, migration, invasion, and adhesion [19, 20]. Fetuin-B (FETUB) was reported as a plasma biomarker candidate related to the severity of lung function in COPD [21]. Neurotensin (NTS) and its receptor (NTSR1) promote EGFR, HER2, and HER3 overexpression and their autocrine/paracrine activation in LUAD. Their expression is increased in 60% of lung cancer patients.

In a previous clinical study, NTSR1 overexpression was applied to predict a poor prognosis for 5-year OS in a stage I lung adenocarcinomas population treated by surgery alone [22]. Besides, LINC02178, LINC01312, AL353746.1, DRAXINP1, and LINC02310 were identified as the prognostic markers and prediction of the survival of LUAD by genome-scale analysis [23]. Among the identified 14 genes in this study, all were associated with high risk, indicating that the expression of these genes was positively related. Moreover, gene MELTF, AC034223.2, and AC034223.1 were firstly identified related to LUAD in our study.

The carcinogenesis of LUAD is a multistep process hallmarked by a series of genetic alterations. In order to gain a further insight into the functional roles of the 14 DEGs, the correlation between their expression levels and the coexpressed protein-coding genes were analyzed. In the present study, we performed GO and KEGG enrichment analysis to explore the functions of the predictive DEGs. The results indicated that the prognostic 14-DEGs were involved in significant functional process, such as release of sequestered calcium ion into cytosol (BP), endoplasmic reticulum lumen (CC), and metalloendopeptidase inhibitor activity (MF) and enriched in KEGG pathways including vibrio cholerae infection, protein processing in endoplasmic reticulum, and calcium signaling pathway. Therefore, it is convincing to infer that the fourteen prognostic DEGs participate in the progression of LUAD in these LUAD-related biological pathways. However, further
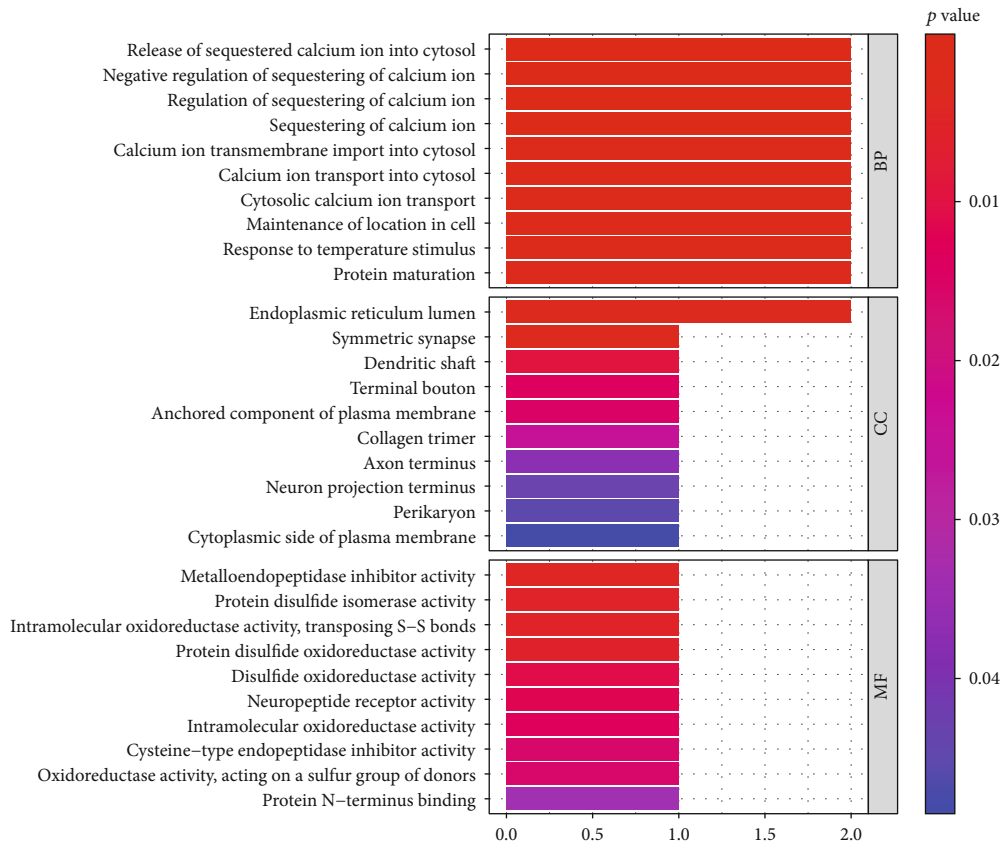
(a)
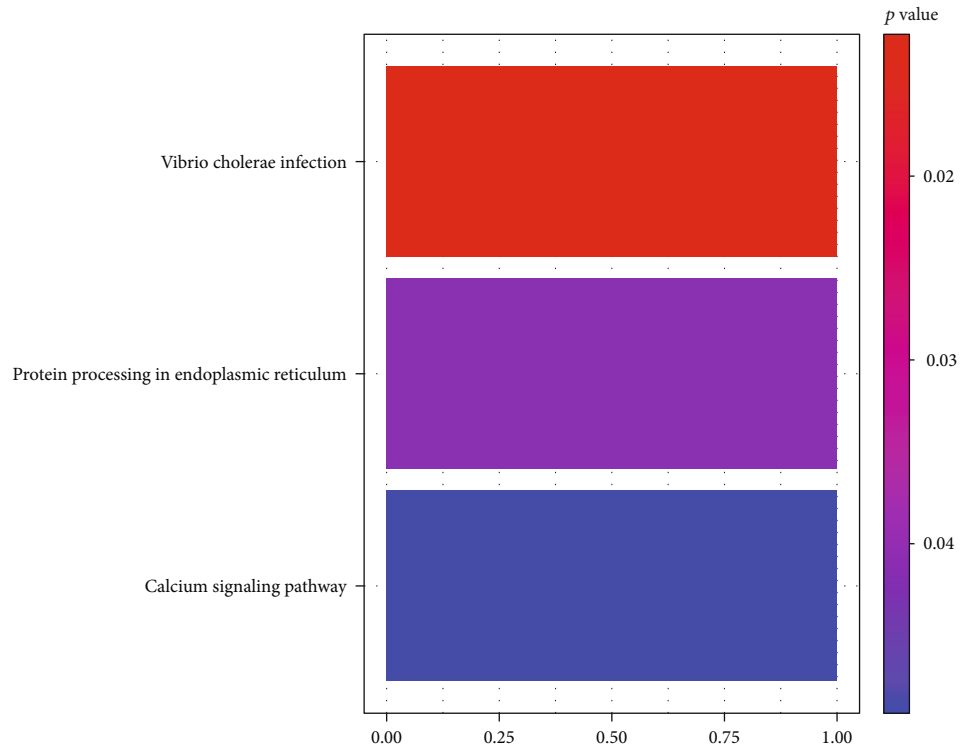
(b)

FIGURE 5: Identification of the DEGs related biological processes and pathways. (a) The functional enrichment analysis of Gene ontology (GO) terms. (b) KEGG pathways for DEGs.

TABLE 3: Enrichment analysis of top 10 GO BP, CC, and MF terms.

ONTOLOGY	ID	Description	p value	Count
BP	GO:0051209	Release of sequestered calcium ion into cytosol	0.000383	2
BP	GO:0051283	Negative regulation of sequestering of calcium ion	0.00039	2
BP	GO:0051282	Regulation of sequestering of calcium ion	0.000403	2
BP	GO:0051208	Sequestering of calcium ion	0.000423	2
BP	GO:0097553	Calcium ion transmembrane import into cytosol	0.000539	2
BP	GO:0060402	Calcium ion transport into cytosol	0.000686	2
BP	GO:0060401	Cytosolic calcium ion transport	0.000869	2
BP	GO:0051651	Maintenance of location in cell	0.001275	2
BP	GO:0009266	Response to temperature stimulus	0.001482	2
BP	GO:0051604	Protein maturation	0.002331	2
CC	GO:0005788	Endoplasmic reticulum lumen	0.003556	2
CC	GO:0032280	Symmetric synapse	0.003676	1
CC	GO:0043198	Dendritic shaft	0.011602	1
CC	GO:0043195	Terminal Bouton	0.017058	1
CC	GO:0046658	Anchored component of plasma membrane	0.018268	1
CC	GO:0005581	Collagen trimer	0.026397	1
CC	GO:0043679	Axon terminus	0.039227	1
CC	GO:0044306	Neuron projection terminus	0.044852	1
CC	GO:0043204	Perikaryon	0.046917	1
CC	GO:0009898	Cytoplasmic side of plasma membrane	0.049273	1
MF	GO:0008191	Metalloendopeptidase inhibitor activity	0.00522	1
MF	GO:0003756	Protein disulfide isomerase activity	0.006197	1
MF	GO:0016864	Intramolecular oxidoreductase activity, transposing S-S bonds	0.006197	1
MF	GO:0015035	Protein disulfide oxidoreductase activity	0.007172	1
MF	GO:0015036	Disulfide oxidoreductase activity	0.013332	1
MF	GO:0008188	Neuropeptide receptor activity	0.014624	1
MF	GO:0016860	Intramolecular oxidoreductase activity	0.016238	1
MF	GO:0004869	Cysteine-type endopeptidase inhibitor activity	0.019138	1
MF	GO:0016667	Oxidoreductase activity, acting on a sulfur group of donors	0.019138	1
MF	GO:0047485	Protein N-terminus binding	0.034481	1

TABLE 4: DEG-related KEGG pathways.

ID	Description	p value	Count
hsa05110	Vibrio cholerae infection	0.012345	1
hsa04141	Protein processing in endoplasmic reticulum	0.041902	1
hsa04020	Calcium signaling pathway	0.049161	1

experimental studies are needed to confirm the functions of these DEGs. Our findings provide insights into prognosis-related genes of LUAD and may have a positive clinical capacity for prognosis prediction and target therapy in LUAD management.

5. Conclusions

In summary, this study identified a novel 14-DEG prognostic signature which could predict the survival risk of LUAD patients. The signature exhibited independent prognostic capacity of clinicopathological factors and could predict survival outcomes of LUAD patients within the same TNM stage. This signature could be utilized to identify patients with high-risk scores who may be further desperate for more effective and individualized therapy. It could not only serve as a novel potential biomarker for the survival risk stratification of LUAD patient but also provide us a better understanding of molecular mechanisms involved in the development of LUAD. However, further molecular investigations, such as exploring the underlying mechanisms of these DEGs in LUAD development and performing

independent cohorts of large sample sizes from institutions across the country or world, are necessary to confirm accuracy and stability for the prediction signature.

Data Availability

The data used to support the findings of this study are included within the article.

Conflicts of Interest

The authors declare that there is no conflict of interest regarding the publication of this paper.

Authors' Contributions

Jie Liu, Shiqiang Hou, Jinyi Wang and Zhengjun Chai contributed equally to this work.

Acknowledgments

References

[1] K. W. Bi, X. G. Wei, X. X. Qin, and B. Li, "BTK has potential to be a prognostic factor for lung adenocarcinoma and an indicator for tumor microenvironment remodeling: a study based on TCGA data mining," *Frontiers in Oncology*, vol. 10, p. 424, 2020.

[2] M. J. Duffy and K. O'Byrne, "Tissue and blood biomarkers in lung cancer: a review," *Advances in Clinical Chemistry*, vol. 86, pp. 1–21, 2018.

[3] R. Yan, Y. Jiang, B. Lai, Y. Lin, and J. Wen, "The positive feedback loop FOXO3/CASC11/miR-498 promotes the tumorigenesis of non-small cell lung cancer," *Biochemical and Biophysical Research Communications*, vol. 519, no. 3, pp. 518–524, 2019.

[4] E. K. Kleczko, J. W. Kwak, E. L. Schenk, and R. A. Nemenoff, "Targeting the complement pathway as a therapeutic strategy in lung cancer," *Frontiers in Immunology*, vol. 10, p. 954, 2019.

[5] V. Relli, M. Trerotola, E. Guerra, and S. Alberti, "Abandoning the notion of non-small cell lung cancer," *Trends in Molecular Medicine*, vol. 25, no. 7, pp. 585–594, 2019.

[6] S. Zuo, M. Wei, H. Zhang et al., "A robust six-gene prognostic signature for prediction of both disease-free and overall survival in non-small cell lung cancer," *Journal of Translational Medicine*, vol. 17, no. 1, p. 152, 2019.

[7] C. Mascaux, M. Angelova, A. Vasaturo et al., "Immune evasion before tumour invasion in early lung squamous carcinogenesis," *Nature*, vol. 571, no. 7766, pp. 570–575, 2019.

[8] A. Prelaj, R. Tay, R. Ferrara, N. Chaput, B. Besse, and R. Califano, "Predictive biomarkers of response for immune checkpoint inhibitors in non-small-cell lung cancer," *European Journal of Cancer*, vol. 106, pp. 144–159, 2019.

[9] D. Luo, B. Deng, M. Weng, Z. Luo, and X. Nie, "A prognostic 4-lncRNA expression signature for lung squamous cell carcinoma," *Artif Cells Nanomed Biotechnol.*, vol. 46, no. 6, pp. 1207–1214, 2018.

[10] J. R. Kratz, M. J. Mann, and D. M. Jablons, "International trial of adjuvant therapy in high risk stage I non-squamous cell carcinoma identified by a 14-gene prognostic signature," *Transl Lung Cancer Res.*, vol. 2, no. 3, pp. 222–225, 2013.

[11] J. Li, J. Wang, Y. Chen, L. Yang, and S. Chen, "A prognostic 4-gene expression signature for squamous cell lung carcinoma," *Journal of Cellular Physiology*, vol. 232, no. 12, pp. 3702–3713, 2017.

[12] C.-Q. Zhu, D. Strumpf, C.-Y. Li et al., "Prognostic gene expression signature for squamous cell carcinoma of lung," *Clinical Cancer Research*, vol. 16, no. 20, pp. 5038–5047, 2010.

[13] M. D. Robinson, D. J. McCarthy, and G. K. Smyth, "edgeR: a bioconductor package for differential expression analysis of digital gene expression data," *Bioinformatics*, vol. 26, no. 1, pp. 139-140, 2010.

[14] P. J. Heagerty, T. Lumley, and M. S. Pepe, "Time-dependent ROC curves for censored survival data and a diagnostic marker," *Biometrics*, vol. 56, no. 2, pp. 337–344, 2000.

[15] M. Han, B. Wang, M. Zhu, and Y. Zhang, "C1QTNF6 as a novel biomarker regulates cellular behaviors in A549 cells and exacerbates the outcome of lung adenocarcinoma patients," *In Vitro Cellular & Developmental Biology. Animal*, vol. 55, no. 8, pp. 614–621, 2019.

[16] K. M. Kim, A. R. An, H. S. Park et al., "Combined expression of protein disulfide isomerase and endoplasmic reticulum oxidoreductin 1-α is a poor prognostic marker for non-small cell lung cancer," *Oncology Letters*, vol. 16, no. 5, pp. 5753–5760, 2018.

[17] K. Sawaki, M. Kanda, S. Umeda et al., "Level of melanotransferrin in tissue and sera serves as a prognostic marker of gastric cancer," *Anticancer Research*, vol. 39, no. 11, pp. 6125–6133, 2019.

[18] W. Zheng, C. Jiang, and R. Li, "Integrin and gene network analysis reveals that ITGA5 and ITGB1 are prognostic in non-small-cell lung cancer," *Oncotargets and Therapy*, vol. 9, pp. 2317–2327, 2016.

[19] J. Zhao, W. Cheng, X. He et al., "Construction of a specific SVM classifier and identification of molecular markers for lung adenocarcinoma based on lncRNA-miRNA-mRNA network," *Oncotargets and Therapy*, vol. Volume 11, pp. 3129–3140, 2018.

[20] L. Yang, M. M. Lee, M. M. Leung, and Y. H. Wong, "Regulator of G protein signaling 20 enhances cancer cell aggregation, migration, invasion and adhesion," *Cellular Signalling*, vol. 28, no. 11, pp. 1663–1672, 2016.

[21] W.-q. Diao, N. Shen, Y.-p. Du et al., "Fetuin-B (FETUB): a plasma biomarker candidate related to the severity of lung function in COPD," *Scientific Reports*, vol. 6, no. 1, article 30045, 2016.

[22] M. Younes, Z. Wu, S. Dupouy et al., "Neurotensin (NTS) and its receptor (NTSR1) causes EGFR, HER2 and HER3 overexpression and their autocrine/paracrine activation in lung tumors, confirming responsiveness to erlotinib," *Oncotarget*, vol. 5, no. 18, pp. 8252–8269, 2014.

[23] Y. Y. Li, C. Yang, P. Zhou, S. Zhang, Y. Yao, and D. Li, "Genome-scale analysis to identify prognostic markers and predict the survival of lung adenocarcinoma," *Journal of Cellular Biochemistry*, vol. 119, no. 11, pp. 8909–8921, 2018.

Review Article

The Protective Role of Probiotics against Colorectal Cancer

Sujuan Ding [ID], Chao Hu, Jun Fang [ID], and Gang Liu [ID]

College of Bioscience and Biotechnology, Hunan Agricultural University, Hunan Provincial Engineering Research Center of Applied Microbial Resources Development for Livestock and Poultry, Changsha, Hunan 410128, China

Correspondence should be addressed to Jun Fang; fangjun1973@hunau.edu.cn and Gang Liu; gangle.liu@gmail.com

Colorectal cancer (CRC) is the fourth leading cause of cancer-related deaths worldwide and a major global public health problem. With the rapid development of the economy, the incidence of CRC has increased linearly. Accumulating evidence indicates that changes in the gut microenvironment, such as undesirable changes in the microbiota composition, provide favorable conditions for intestinal inflammation and shaping the tumor growth environment, whereas administration of certain probiotics can reverse this situation to a certain extent. This review summarizes the roles of probiotics in the regulation of CRC, such as enhancing the immune barrier, regulating the intestinal immune state, inhibiting pathogenic enzyme activity, regulating CRC cell proliferation and apoptosis, regulating redox homeostasis, and reprograming intestinal microbial composition. Abundant studies have provided a theoretical foundation for the roles of probiotics in CRC prevention and treatment, but their mechanisms of action remain to be investigated, and further clinical trials are warranted for the application of probiotics in the target population.

1. Introduction

The global incidence of CRC is very high and continues to increase every year. Data show that CRC accounts for approximately 9% of all cancer-related deaths and is the third leading cause of death in women after breast cancer and the second leading cause of death in men after lung and prostate cancers [1, 2]. Despite advances in screening and early diagnosis of CRC, CRC remains the second leading cause of cancer-related deaths. Therefore, more research attention to CRC prevention, treatment, and prognosis is crucial.

Recent evidence has demonstrated that probiotics may contribute to the treatment of CRC [3]. According to the definition established in 2002 by the Food and Agriculture Organization of the United Nations (FAO) and the World Health Organization (WHO), probiotics are "live microorganisms which when administered in adequate amounts confer a health benefit on the host" [4]. Several studies have highlighted the critical role of probiotics in regulating intestinal disorders, such as diarrhea [5], inflammatory bowel disease [6], irritable bowel syndrome [7], *Helicobacter pylori* infection [8], and lactose intolerance [9]. Probiotics can also inhibit the development of CRC by modifying the intestinal microbial composition, intestinal epithelial system, and intestinal immune responses. *Akkermansia muciniphila* (AKK), an intestinal symbiotic bacterium living in the mucosal layer, has been shown to exhibit a high antitumor efficacy with favorable clinical outcomes [10, 11]. One study demonstrated that AKK initiates an antitumor immune response by activating the Toll-like receptor signaling pathway through its outer membrane protein Amuc. Meanwhile, it is found that the administration of AKK together with interleukin-(IL-) 2 protects the intestinal barrier function, suggesting a new therapeutic strategy for CRC [12].

2. Interaction between Probiotics and the Host

Probiotics used in foods are safe for human consumption, with most being certified as Generally Regarded as Safe (GRAS) by the U.S. FDA or as Qualified Presumption of Safety (QPS) by the E.U. EFSA [13]. Recent studies based on animal models and clinical interventions have demonstrated the critical role of probiotics in the prevention and treatment of several human diseases [14]. The interplay between probiotics and the human gastrointestinal tract (GIT), comprising the mucus layer, epithelial layer, and

gut-associated lymphoid tissue, influences the disease process in the human host [15]. The mucosal layer of the intestinal tract comprises a loose outer sublayer of gel-forming mucins and a dense inner sublayer of mucins. The outer sublayer is relatively abundant with bacteria, antimicrobial peptides, and immunoglobulin, whereas the inner sublayer has few or no microbes [16, 17]. The secondary interaction between probiotics and the intestinal tract occurs in the intestinal epithelial layer containing different cell subgroups and spanning across the entire intestinal cavity. The main functions of this layer are absorption of nutrients, secretion of mucin, and release of antimicrobial molecules such as defensin and lysozyme [18]. Bacteria affect the intestinal epithelial barrier function through pattern recognition receptors [19]. Probiotics interact with host intestinal epithelial cells (IECs) by adhering to the intestinal wall and stimulating the production of mucus, thereby enhancing the intestinal barrier [20]. Through such interaction, probiotics compete with pathogenic bacteria for niche occupancy [21], prevent pathogenic bacteria from growing and proliferating in the intestine by competing with them for nutrition and energy [22, 23], and reduce intestinal pH by fermenting dietary fiber to produce short-chain fatty acids (SCFAs) [24].

3. Colorectal Cancer

CRC causes nearly 700,000 deaths every year, making it the most fatal cancer in the world after lung cancer, liver cancer, and gastric cancer [25]. Unhealthy eating habits, especially frequent consumption of low-fiber and high-fat foods characteristic of the Western diet, are crucial factors in the development of intestinal disorders [26], which suggests that the prevalence of the Western diet and lifestyle also increases the incidence of CRC. CRC is a slow-developing disease, and survival rates have improved in recent decades owing to the improvements in preventive cancer screening, which allows early detection. Screening thus remains the mainstay for CRC prevention [27]. CRC is believed to be associated with aging, and the majority of people who undergo regular screening for CRC are older than 50 years; this underestimates the likelihood of CRC in younger patients, even when they present with abdominal pain and bloody stools [28].

Further advancements in the prevention and treatment of CRC warrant a complete understanding of the normal biology of the colon and the pathogenesis of CRC. The basic unit of the colon includes crypts and luminal surfaces. When the intestine is in a state of homeostasis, each colon crypt contains 14–16 pluripotent stem cells marked with the transmembrane protein leucine-rich repeat-containing G protein-coupled receptor 5 (LGR5). These stem cells can produce all differentiated cell types in the colon cavity [29, 30]. LGR5$^+$ stem cells can produce rapidly proliferating transit-amplifying (TA) cells, which account for approximately two-thirds of the crypts. TA cells mainly differentiate into four cell types, namely, absorbable IECs, goblet cells, cluster cells, and intestinal endocrine cells, which are renewed approximately once a week [31]. The main transcription target of the Wnt pathway in intestinal crypt stem cells is the serpentine transmembrane receptor LGR5, which inhibits

the expression of the oncogene *Myc* and of the basic helix-loop-helix (bHLH) transcription factor achaete-scute like 2 (ASCL2), which is associated with stem cell self-renewal [32]. Mutations in the adenomatous polyposis coli (*APC*) gene are the potential cause of familial adenomatous polyposis, known as hereditary colon cancer syndrome [33, 34]. APC loss is also the major driver of Wnt signaling in CRC [35]. Evidence indicates that different *APC* mutations result in different levels of Wnt signaling pathway activity, which is related to the typical tumor location in the large intestine [36, 37].

4. Gut Microbiota

The human gut microbiota is a rich, diverse, and complex microbial community composed of fungi, bacteria, archaea, viruses, bacteriophages, and protozoa living in a symbiotic relationship with the human host [38]. The composition and activity of the gut microbiota is a hot topic in the cross-research field of human microbiology and health, and it is directly related to the study of probiotics [15]. The commensal bacteria form a tight and complex interaction network with their hosts and are involved in protecting the gut from harmful substances [39]. Metagenomic evidence suggests that the gene set of different gut microbial species pools and the functional prediction of the community are the same and similar, respectively, among individuals. However, the composition and function of the gut microbiota vary with diet, location, sex, age, and race [40, 41]. Diet is the main regulator of the intestinal microbial function. In general, the ratio of the phyla Firmicutes/Bacteroidetes is higher in individuals following a Western-style diet, whereas the abundance of the genus *Prevotella*, belonging to the Bacteroidetes phylum, is higher in individuals following a subsistence diet [42–45]. In healthy individuals, more than 90% of the ingested diet is absorbed by the small intestine, whereas the complex carbohydrates that pass undigested from the small intestine, such as fiber, protein residues, and primary bile acids secreted by the body in response to fat intake, are digested in the colon [46]. These components of the diet influence the composition and function of the gut microbiota. Saccharolytic fermentation of complex carbohydrates by the colonic bacteria produces SCFAs, with acetic, propionic, and butyric acids (in a molar ratio of 3 : 1 : 1) accounting for approximately 90%–95% of colonic SCFAs [47, 48]. Butyrate regulates mucosal inflammation and antitumor activity by participating in intestinal microbial balance, proliferation inhibition, immune regulation, and epigenetic regulation [49].

The gut microbiota is composed of more than 1,000 bacterial species, including beneficial and pathogenic microbes, and is dominated by Firmicutes and Bacteroidetes. In healthy individuals, the beneficial microbes surpass the pathogenic microbes and inhibit their excessive growth [50]. The gut microbiota can thus be considered as an "organ" that performs significant roles, including the utilization of complex dietary constituents, anabolism of various important compounds, regulation of immune function, and maintenance of intestinal barrier integrity [51]. Hence, the role of the gut

microbiota in the pathogenesis of intestinal disorders cannot be underestimated, and its role in the pathogenesis of CRC has received much attention in recent years [52]. Whether microbiota dysbiosis is the cause or result of CRC is still unknown, which remains a foundational issue in understanding CRC [25]. The occurrence of CRC is usually closely related to the mucosal microbes near the site of tumorigenesis [53–55]. The main bacterial species that influence the development of CRC are not yet completely clear, but the available evidence suggests that the abundances of *Fusobacterium nucleatum* (Fn), *Escherichia coli*, *Helicobacter pylori*, and *Bacteroides fragilis* are closely associated with CRC [56]. It is also suggested that a decrease in bacterial diversity is related to the occurrence of tumors, but its role in tumorigenesis remains to be confirmed in further studies [57].

5. Mechanism Underlying the Role of Probiotics in the Regulation of CRC

Research on bioactive components and gut microbes has revealed that probiotics may play an important role in cancer prevention and treatment in addition to regulating the homeostasis and immune state of the intestinal epithelial system [58]. Multiple mechanisms have been hypothesized for the CRC-preventive and therapeutic effects of probiotics. For example, at the level of intestinal ecology, probiotics may reduce the number of pathogenic bacteria in the gut by competing with the pathogenic bacteria for intestinal niche occupancy or reduce the level of carcinogens [59]. In addition, SCFAs produced by microbial metabolism could stimulate the proliferation and differentiation of intestinal cells in the large and small intestines [60]. For instance, intestinal acetic acid produced by *Propionibacterium* can trigger the release of cathepsin D into the cytosol of cancer cells by increasing the permeability of their lysosomal membrane, thereby protecting the cells from apoptosis [61]. In this section, we focus on the various roles of probiotics, including enhancing the intestinal mucosal barrier, reducing intestinal inflammation, inhibiting the activity of pathogenic bacteria, regulating redox homeostasis, and reprogramming the composition of microorganisms, in the regulation of CRC (Figure 1).

5.1. Enhancing the Intestinal Mucosal Barrier.
The complete intestinal mucosal barrier includes physical, chemical, biological, and immune barriers. In a healthy state, the intestinal barrier can protect the gut from toxins and pathogens [62]. Probiotics stimulate mucus secretion by IECs, which functions as a barrier between the mucosa and microorganisms that prevents the translocation of bacteria and toxins and also inhibits the adhesion and invasion of pathogenic bacteria in IECs [63]. Probiotics enhance the intestinal barrier by regulating the expression of tight junction proteins, such as claudin-1 and occludin, and stimulating intestinal cells to suppress inflammation and accelerate epithelial cell remodeling by promoting mucin secretion [64–66]. Occludin is a transmembrane tight junction protein that forms the mechanical barrier of epithelial cells, and the level of occludin is a functional indicator of the intestinal mechanical barrier

[67]. *Bifidobacterium infantis* and *Lactobacillus acidophilus* were found to protect intestinal permeability by regulating the expression of occludin and claudin-1 proteins and protecting the activation of nuclear factor kappa-B (NF-κB) induced by IL-1β in Caco-2 cells [68]. *Lactobacillus plantarum* ZLP001 reversed the decrease in claudin-1 and occludin protein levels induced by enterotoxigenic *E. coli* and decreased the levels of the inflammatory cytokines IL-6, IL-8, and tumor necrosis factor alpha (TNF-α) [69]. Mucin-2 glycoprotein (MUC2) formed by goblet cells in the form of a disulfide cross-linked network is the main component of colonic mucus [70]. Muc2 gene inactivation in mice has been shown to increase close contact between bacteria and IECs, leading to inflammation and eventually colon cancer [71]. SCFAs produced by microbes through fermentation of complex carbohydrates can enhance barrier function by G protein-coupled receptor-mediated sensitization of the IEC inflammasome and reducing the oxygen concentration of IECs to induce hypoxia-inducible factors [56].

5.2. Reducing Intestinal Inflammation.
Immunotherapy involves the stimulation of innate immunity and the subsequent activation of antitumor immune responses [72]. Evidence suggests that the mechanism of inflammation is a driver of tumor maturation and that inflammation is closely associated with the risk of CRC [73]. The gut microbiota plays an important role in the formation of an inflammatory microenvironment, and the occurrence of inflammation in turn affects the composition of the gut microbiota. Intestinal tumorigenesis is driven by inflammation, microbes, and immunity [74]. Probiotics contribute to the normal functioning of the immune system and affect the host immune status by participating in the differentiation of immune cells and stimulating the production of anti-inflammatory substances, antioxidants, and antitumor components [66, 75, 76]. The colonic immune system contains many types of immune cells, with macrophage being one of the most abundant immune cell types [77–79]. A possible mechanism by which probiotics improve the stability of the colonic environment is by acting on the colonic macrophages [80]. Macrophages perform probiotic phagocytosis in a strain-dependent manner and prevent deep tissue destruction after infection by secreting anti-inflammatory mediators [60]. Evidence has revealed that the interaction between probiotics and Toll-like receptors expressed on IECs leads to the production of TNF in the cells, which inhibits NF-κB in macrophages and stimulates the production of IL-8 required for neutrophil production [81]. A study showed that heat-killed *Enterococcus faecalis* could reduce caspase-1 activity and IL-1β maturity, thereby achieving consistent activation of the NLRP3 inflammasome in macrophages [82]. Furthermore, SCFAs produced by dietary fiber fermentation are not only the main energy source for IECs but also the regulator of the intestinal immune response [83]. Mechanistically, the induction of a tumor phenotype may be due to the proliferation of colon epithelial cells induced by butyrate. However, butyric acid and its receptor GPR109A can also inhibit colitis and tumorigenesis, indicating that butyrate has anticancer potential [84].
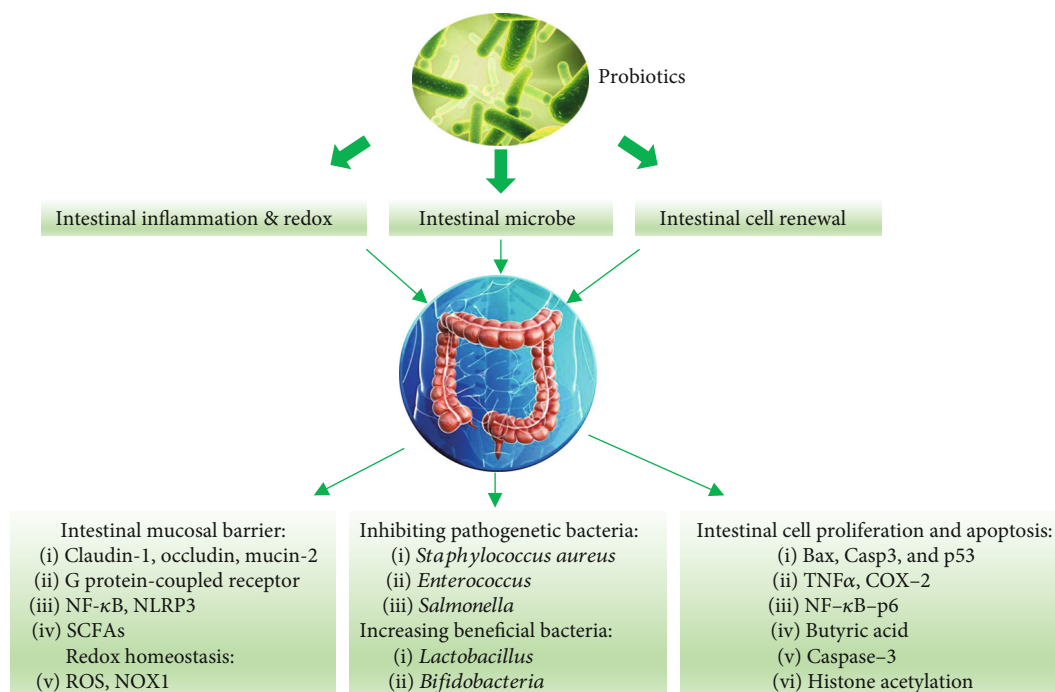
Figure 1: The various roles of probiotics in colorectal cancer prevention and treatment.

5.3. Regulating the Generation of Reactive Oxygen Species. Oxidative stress plays a vital role in the occurrence of CRC [85]. Reactive oxygen species (ROS) are by-products of normal cell metabolism in the GIT. The control of redox homeostasis by the intestinal epithelium, that is, the balance between antioxidation and oxidative stress, is a vital factor affecting intestinal functions such as digestion and absorption of nutrients, immune response, stem cell proliferation, and apoptosis of apical enterocyte [86–88]. ROS and its oxidation products may damage the antioxidant system of intestinal tissues and destroy the normal function of the intestine, potentially leading to intestinal mucosal hyperplasia [89–91]. DNA mutations caused by ROS are thought to be involved in the early inflammatory process of CRC development [92, 93]. Nicotinamide adenine dinucleotide phosphate oxidase (NOX), expressed on the surface of inflammatory phagocytes such as neutrophils and phagocytes, participates in ROS generation. It is also involved in the proliferation and invasion of epithelial tumor cells. ROS produced by NOX1 can in turn trigger angiogenesis in the epithelial tumor cells by inducing angiogenic factors, thus promoting their vascularization and proliferation [94, 95]. Gut microbial dysbiosis caused by the mucosa-associated immune system may promote leukocyte-induced inflammation and oxidative overreaction, consequently aggravating intestinal mucosal injury [96]. Of the colonic commensal bacteria considered to play a crucial role in CRC development, enterotoxigenic *Bacteroides fragilis* (ETBF) is suggested to cause inflammatory diarrhea by secreting toxins [97]. *B. fragilis* toxin promotes the production of ROS in IECs and dendritic cells [98, 99]. A study showed that commensal bacterial rapidly produced ROS on IECs both in vitro and in vivo and caused oxidative inactivation of the catalytic cysteine residue of Ubc12, resulting in the

suppression of the cullin-1 ubiquitination and the consequent inhibition of NF-κB and β-catenin signaling pathways [100].

Research on the role of the gut microbiota in regulating gastrointestinal redox homeostasis is still in its infancy. However, some preliminary data have uncovered the relationship between the microbiota and redox status, which plays an important role in the regulation of gastrointestinal health. Evidence suggests that the hosts' ROS is associated with the balance of the gut microbial composition; for instance, the oxidation state of the host is negatively correlated with the abundance of *Lactobacillus* and *Bifidobacterium* and positively correlated with that of *E. coli* [101]. Findings from mouse models have indicated that a high abundance of Bacteroidetes in the colon controls pathogen loads by inducing proinflammatory and prooxidative reactions, which play a key role in preventing intestinal infections [102]. The results of a study in a mouse model of CRC induced by azoxymethane showed that the structure of the intestinal microbiota was regulated by *Clostridium butyricum* administered by gavage, which involved a reduction of the ratio of Firmicutes/Bacteroidetes, an increase in the relative abundance of probiotics, an increase in tumor cell apoptosis, inhibition of the NF-κB pathway and IL-6 levels, and a reduction in CRC incidence [103]. In one study, the supernatants of *Musa paradisiaca* inflorescence fermented with *Lactobacillus casei* and *Bifidobacterium bifidum* were found to induce DNA damage, promote ROS generation, and initiate the apoptosis signaling pathway in HT-29 colon cancer cells [104]. Another study showed that *Lactobacillus paracasei* subsp. *paracasei* M5L suppressed HT-29 cell proliferation and could promote HT-29 cell apoptosis through ROS production and calreticulin translocation [105]. Moreover, *Lactobacillus* can

exert anticancer effects by producing antioxidants such as glutathione, superoxide dismutase, and catalase, suppressing inflammation and tumor size, and inhibiting the expression of tumor-specific proteins and polyamine components. However, the mechanism of the anticancer effect of *Lactobacillus* in relation to CRC needs to be investigated further [106–108].

5.4. Inhibiting the Enzyme Activity of Pathogenic Bacteria. Endogenous toxic compounds, such as N-nitroso, cresol, aglycones, and phenols, promote the development of CRC by participating in antiapoptotic pathways in the intestine. The carcinogenic effects of endogenous toxic and genotoxic compounds in the intestinal microenvironment may be further influenced by pathogenic bacterial enzymes such as 7-β-dehydroxylase, nitroreductase, β-glucuronidase, β-glucosidase, and azoreductase [109, 110]. For example, pathogenic bacteria such as *Staphylococcus aureus*, *Enterococcus*, and *Salmonella* synthesize azoreductase, which metabolizes dyes and drugs to generate toxic aromatic amines [111]. Polyketide synthase (pks) islands present in some strains of *E. coli* encode the genotoxin colicin, which can induce single-stranded DNA breaks [112]. Furthermore, the DNA damage response signaling pathway activated in infected cells tends to increase the mutation rate [113]. Enterotoxigenic *B. fragilis* has been reported to participate in CRC initiation by producing a toxin [114]. Nevertheless, studies have shown that probiotic supplementation may suppress the activity of bacterial enzymes [115, 116]. For example, *Lactobacillus* could suppress the dehydrogenation of *L. rhamnosus* GG (LGG) and reduce the level of primary bile acid by reducing the activity of β-glucuronidase [117]. Animal model studies have shown that yogurt starter bacteria could reduce the activity of bacterial enzymes, which may be the mechanism underlying the CRC-preventive effects of probiotics [118]. However, in healthy subjects, *L. acidophilus* A1, *L. plantarum* 299V, and *L. rhamnosus* DR20 could not decrease glucuronidase activity [119, 120].

5.5. Regulating the Proliferation and Apoptotic Responses of CRC Cells. Apoptosis plays a key role in regulating the number of cells by balancing cell renewal and eliminating mutant cells, which is one of the main mechanisms of tumor cell death in CRC. The decrease in apoptosis is an important disease event and is accompanied by disruption of cell proliferation regulation [121]. Therefore, apoptotic pathways are a promising target for disease prevention and treatment to manage cell survival and death through apoptosis regulation. Accumulating evidence has highlighted the critical role of probiotics in the regulation of cell proliferation and apoptosis, which may thus be a vital therapeutic and preventive measure against CRC [122]. In rat models, LGG decreased the incidence and size of dimethylhydrazine-induced tumors while inhibiting the expression of inflammatory proteins, namely, TNF-α, COX-2, and NF-κB–p6, reducing the expression of the antiapoptotic protein Bcl-2, and increasing the expression of the proapoptotic proteins Bax, Casp3, and p53, suggesting that LGG has the potential to prevent colon cancer [123]. In another study, *L. plantarum* DY-1 showed

a strong antiproliferative activity in an HT-29 cell model that involved retarding the development of the cell cycle from G0-G1 phase to G2-M phase and induction of cell apoptosis possibly via caspase-3, indicating that *L. plantarum* DY-1 has antitumor potential [124]. In addition, SCFAs reduce cancer risk by reducing tumor growth and activating apoptosis cascades via hyperacetylation of histones [125]. *Propionibacterium freudenreichii*, a probiotic in the human gut microbiota, has been found to suppress colorectal adenocarcinoma cells via SCFA-mediated apoptosis [126]. Butyric acid was found to prevent CRC by regulating the cell cycle, differentiation, and apoptosis of colon cancer cell lines [127–129].

5.6. Reprogramming the Composition of Gut Microbes. The ultimate goal of probiotic intervention is to exert regulatory effects, including immune regulation, immune barrier strengthening, and regulation of the gut microbial composition, against certain disorders [15]. Changes in the gut microbial composition are inextricably linked to the development of CRC. Substantial evidence from animal model studies suggests that probiotics, such as *Lactobacillus* and *Bifidobacterium*, have significant effects on intestinal microbial composition [130, 131]. The colon is teeming with microbes, and this large population is mostly benign, but some are pathogenic bacteria, and the increase in the abundance of these pathogens in the colon is associated with acute or chronic conditions, such as obesity, inflammatory bowel disease, and CRC [132]. *E. coli* is an intestinal symbiotic bacterium, and certain strains of it can promote intestinal inflammation leading to the production of colicin, a potential carcinogen [133]. Pathogenic *E. coli* exists in CRC tissues and is thus used as a marker in tumor staging and prognosis [134]. Furthermore, as noted earlier, *E. coli* containing pks islands, which encode colibactin, can induce single-stranded DNA breaks, and thus, changes in the *E. coli* gene set influence the phenotype of the disease [112, 135]. Compared with mice injected with *E. coli*, those injected with *Bacillus polyfermenticus* showed reduced tumor size, while HT-29 cells injected with *B. polyfermenticus* showed reduced expression of ErbB2 and ErbB3 at the protein and mRNA levels [136, 137]. Intestinal pathogenic microbes such as *Bacteroides* and *Clostridium* are associated with the pathogenesis of CRC [138]. A double-blind test of synbiotics (LGG, *Bifidobacterium lactis* Bb12, and oligofructose) in 37 patients with CRC and 43 colonic polypectomy patients demonstrated that the abundance of *Lactobacillus* and *Bifidobacterium* increased, whereas that of *Clostridium perfringens* decreased in CRC patients, and synbiotic intervention inhibited the colorectal cell proliferation ability and colon cell necrosis ability and improved epithelial cell barrier function in colonic polypectomy patients [139].

6. Perspectives

Although certain bacterial species are classified as probiotics due to their benefits to the host health, changes in host health status require the regulation of specific probiotic bacteria rather than the probiotic community in the gut. Substantial research has explored the role of probiotics in the prevention,

treatment, and prognosis of CRC. Such dedicated research has revealed a variety of regulatory roles of probiotics, such as enhancing the immune barrier, regulating the intestinal immune state, inhibiting pathogenic enzyme activity, regulating CRC cell proliferation and apoptosis, and regulating the intestinal microbial composition. Although the evidence from clinical or animal model experiments has provided a theoretical foundation for the application of probiotics, evidence from clinical trials on the benefits of probiotics in the prevention and treatment of CRC is lacking. Therefore, further clinical trials are warranted to explore the mechanisms of probiotics in the regulation of CRC. In addition, it remains unknown whether gut microbial dysbiosis is the cause or result of CRC. To address this knowledge gap, further studies on the interactions between probiotics and intestinal microorganisms in CRC development are warranted. Meanwhile, although the gut microbiota contains fungi and viruses in addition to bacteria, there is little evidence supporting the role of fungi and viruses in the gut microbial dysbiosis leading to CRC development.

Conflicts of Interest

The authors declare there is no conflict of interest to report.

Authors' Contributions

Writing (original draft preparation) was handled by S.D. and C.H.; writing (review and editing) was made by J.F. and G.L. All the authors contributed to manuscript revision and read and approved the submitted version.

Acknowledgments

References

[1] J. Ferlay, I. Soerjomataram, R. Dikshit et al., "Cancer incidence and mortality worldwide: sources, methods and major patterns in GLOBOCAN 2012," *International Journal of Cancer*, vol. 136, no. 5, pp. E359–E386, 2015.

[2] D. E. Beck, "The importance of colorectal cancer screening," *The Ochsner Journal*, vol. 15, no. 1, pp. 11-12, 2015.

[3] R. Fletcher, Y. J. Wang, R. E. Schoen, O. J. Finn, J. Yu, and L. Zhang, "Colorectal cancer prevention: immune modulation taking the stage," *Biochimica Et Biophysica Acta. Reviews on Cancer*, vol. 1869, no. 2, pp. 138–148, 2018.

[4] FAO, "Probiotics in food," *Food Nutrition Paper*, vol. 85, p. 71, 2001.

[5] C. Mantegazza, P. Molinari, E. D'Auria, M. Sonnino, L. Morelli, and G. V. Zuccotti, "Probiotics and antibiotic-associated diarrhea in children: a review and new evidence on Lactobacillus rhamnosus GG during and after antibiotic treatment," *Pharmacological Research*, vol. 128, pp. 63–72, 2018.

[6] M. Amer, M. Nadeem, S. U. R. Nazir et al., "Probiotics and their use in inflammatory bowel disease," *Alternative Therapies in Health and Medicine*, vol. 24, no. 3, pp. 16–23, 2018.

[7] H. F. Dale, S. H. Rasmussen, Ö. Asiller, and G. A. Lied, "Probiotics in irritable bowel syndrome: an up-to-date systematic review," *Nutrients*, vol. 11, no. 9, p. 2048, 2019.

[8] M. Homan and R. Orel, "Are probiotics useful in Helicobacter pylori eradication?," *World Journal of Gastroenterology*, vol. 21, no. 37, pp. 10644–10653, 2015.

[9] M. de Vrese, A. Stegelmann, B. Richter, S. Fenselau, C. Laue, and J. Schrezenmeir, "Probiotics–compensation for lactase insufficiency," *The American Journal of Clinical Nutrition*, vol. 73, no. 2, pp. 421s–429s, 2001.

[10] M. C. Collado, M. Derrien, E. Isolauri, W. M. de Vos, and S. Salminen, "Intestinal integrity and Akkermansia muciniphila, a mucin-degrading member of the intestinal microbiota present in infants, adults, and the elderly," *Applied and Environmental Microbiology*, vol. 73, no. 23, pp. 7767–7770, 2007.

[11] B. Routy, E. le Chatelier, L. Derosa et al., "Gut microbiome influences efficacy of PD-1-based immunotherapy against epithelial tumors," *Science*, vol. 359, no. 6371, pp. 91–97, 2018.

[12] L. Shi, J. Sheng, G. Chen et al., "Combining IL-2-based immunotherapy with commensal probiotics produces enhanced antitumor immune response and tumor clearance," *Journal for Immunotherapy of Cancer*, vol. 8, no. 2, article e000973, 2020.

[13] B. Sánchez, C. G. D. L. Reyes-Gavilán, A. Margolles, and M. Gueimonde, "Probiotic fermented milks: present and future," *International Journal of Dairy Technology*, vol. 62, no. 4, pp. 472–483, 2009.

[14] A. Q. Yu and L. Li, "The potential role of probiotics in cancer prevention and treatment," *Nutrition and Cancer*, vol. 68, no. 4, pp. 535–544, 2016.

[15] B. Sánchez, S. Delgado, A. Blanco-Míguez, A. Lourenço, M. Gueimonde, and A. Margolles, "Probiotics, gut microbiota, and their influence on host health and disease," *Molecular Nutrition & Food Research*, vol. 61, no. 1, 2017.

[16] C. L. Maynard, C. O. Elson, R. D. Hatton, and C. T. Weaver, "Reciprocal interactions of the intestinal microbiota and immune system," *Nature*, vol. 489, no. 7415, pp. 231–241, 2012.

[17] M. E. Johansson, J. M. Larsson, and G. C. Hansson, "The two mucus layers of colon are organized by the MUC2 mucin, whereas the outer layer is a legislator of host-microbial interactions," *Proceedings of the National Academy of Sciences*, vol. 108, Supplement_1, pp. 4659–4665, 2011.

[18] Y. Goto and I. I. Ivanov, "Intestinal epithelial cells as mediators of the commensal-host immune crosstalk," *Immunology and Cell Biology*, vol. 91, no. 3, pp. 204–214, 2013.

[19] S. Rakoff-Nahoum, J. Paglino, F. Eslami-Varzaneh, S. Edberg, and R. Medzhitov, "Recognition of commensal microflora by toll-like receptors is required for intestinal homeostasis," *Cell*, vol. 118, no. 2, pp. 229–241, 2004.

[20] S. Misra, D. Mohanty, and S. Mohapatra, "Applications of probiotics as a functional ingredient in food and gut health," *Journal of Food and Nutrition Research*, vol. 7, no. 3, pp. 213–223, 2019.

[21] C. M. Costello, R. M. Sorna, Y. L. Goh, I. Cengic, N. K. Jain, and J. C. March, "3-D intestinal scaffolds for evaluating the therapeutic potential of probiotics," *Molecular Pharmaceutics*, vol. 11, no. 7, pp. 2030–2039, 2014.

[22] Y. Lan, M. W. A. Verstegen, S. Tamminga, and B. A. Williams, "The role of the commensal gut microbial community in broiler chickens," *World's Poultry ence Journal*, vol. 61, no. 1, pp. 95–104, 2005.

[23] T. D. Lawley and A. W. Walker, "Intestinal colonization resistance," *Immunology*, vol. 138, no. 1, pp. 1–11, 2013.

[24] M. Wang, S. Wichienchot, X. He, X. Fu, Q. Huang, and B. Zhang, "In vitro colonic fermentation of dietary fibers: fermentation rate, short-chain fatty acid production and changes in microbiota," *Trends in Food Science & Technology*, vol. 88, pp. 1–9, 2019.

[25] H. Brody, "Colorectal cancer," *Nature*, vol. 521, no. 7551, p. S1, 2015.

[26] K. Vipperla and S. J. O'Keefe, "Diet, microbiota, and dysbiosis: a 'recipe' for colorectal cancer," *Food & Function*, vol. 7, no. 4, pp. 1731–1740, 2016.

[27] J. Björk, "Strategies for colon cancer prevention," *The EPMA Journal*, vol. 1, no. 3, pp. 513–521, 2010.

[28] O The Lancet, "Colorectal cancer: a disease of the young?," *The Lancet Oncology*, vol. 18, no. 4, p. 413, 2017.

[29] N. Barker, J. H. van Es, J. Kuipers et al., "Identification of stem cells in small intestine and colon by marker gene Lgr5," *Nature*, vol. 449, no. 7165, pp. 1003–1007, 2007.

[30] T. Sato, R. G. Vries, H. J. Snippert et al., "Single Lgr5 stem cells build crypt-villus structures in vitro without a mesenchymal niche," *Nature*, vol. 459, no. 7244, pp. 262–265, 2009.

[31] N. Barker, "Adult intestinal stem cells: critical drivers of epithelial homeostasis and regeneration," *Nature Reviews. Molecular Cell Biology*, vol. 15, no. 1, pp. 19–33, 2014.

[32] H. Clevers and E. Batlle, "SnapShot: the intestinal crypt," *Cell*, vol. 152, no. 5, pp. 1198–1198.e2, 2013.

[33] K. W. Kinzler, M. Nilbert, L. Su et al., "Identification of FAP locus genes from chromosome 5q21," *Science*, vol. 253, no. 5020, pp. 661–665, 1991.

[34] I. Nishisho, Y. Nakamura, Y. Miyoshi et al., "Mutations of chromosome 5q21 genes in FAP and colorectal cancer patients," *Science*, vol. 253, no. 5020, pp. 665–669, 1991.

[35] J. Drost, R. H. van Jaarsveld, B. Ponsioen et al., "Sequential cancer mutations in cultured human intestinal stem cells," *Nature*, vol. 521, no. 7550, pp. 43–47, 2015.

[36] M. Christie, R. N. Jorissen, D. Mouradov et al., "Different APC genotypes in proximal and distal sporadic colorectal cancers suggest distinct WNT/β-catenin signalling thresholds for tumourigenesis," *Oncogene*, vol. 32, no. 39, pp. 4675–4682, 2013.

[37] M. Buchert, D. Athineos, H. E. Abud et al., "Genetic dissection of differential signaling threshold requirements for the Wnt/beta-catenin pathway in vivo," *PLoS Genetics*, vol. 6, no. 1, article e1000816, 2010.

[38] B. A. Methé, K. E. Nelson, M. Pop et al., "A framework for human microbiome research," *Nature*, vol. 486, no. 7402, pp. 215–221, 2012.

[39] E. Rinaldi, A. Consonni, E. Guidesi, M. Elli, R. Mantegazza, and F. Baggi, "Gut microbiota and probiotics: novel immune system modulators in myasthenia gravis?," *Annals of the New York Academy of Sciences*, vol. 1413, no. 1, pp. 49–58, 2018.

[40] E. B. Hollister, C. Gao, and J. Versalovic, "Compositional and functional features of the gastrointestinal microbiome and their effects on human health," *Gastroenterology*, vol. 146, no. 6, pp. 1449–1458, 2014.

[41] C. Huttenhower, D. Gevers, R. Knight et al., "Structure, function and diversity of the healthy human microbiome," *Nature*, vol. 486, no. 7402, pp. 207–214, 2012.

[42] K. R. Amato, C. J. Yeoman, G. Cerda et al., "Variable responses of human and non-human primate gut microbiomes to a Western diet," *Microbiome*, vol. 3, no. 1, p. 53, 2015.

[43] C. Greenhill, "gut microbiota, host genetics and diet interact to affect the risk of developing obesity and the metabolic syndrome," *Nature Reviews. Endocrinology*, vol. 11, no. 11, p. 630, 2015.

[44] C. de Filippo, D. Cavalieri, M. di Paola et al., "Impact of diet in shaping gut microbiota revealed by a comparative study in children from Europe and rural Africa," *Proceedings of the National Academy of Sciences of the United States of America*, vol. 107, no. 33, pp. 14691–14696, 2010.

[45] Q. Guo, F. Li, Y. Duan et al., "Oxidative stress, nutritional antioxidants and beyond," *Science China. Life Sciences*, vol. 63, no. 6, pp. 866–874, 2020.

[46] J. Yang and J. Yu, "The association of diet, gut microbiota and colorectal cancer: what we eat may imply what we get," *Protein & Cell*, vol. 9, no. 5, pp. 474–487, 2018.

[47] S. J. O'Keefe, "Diet, microorganisms and their metabolites, and colon cancer," *Nature Reviews. Gastroenterology & Hepatology*, vol. 13, no. 12, pp. 691–706, 2016.

[48] D. J. Morrison and T. Preston, "Formation of short chain fatty acids by the gut microbiota and their impact on human metabolism," *Gut Microbes*, vol. 7, no. 3, pp. 189–200, 2016.

[49] X. Wu, Y. Wu, L. He, L. Wu, X. Wang, and Z. Liu, "Effects of the intestinal microbial metabolite butyrate on the development of colorectal cancer," *Journal of Cancer*, vol. 9, no. 14, pp. 2510–2517, 2018.

[50] V. Tremaroli and F. Bäckhed, "Functional interactions between the gut microbiota and host metabolism," *Nature*, vol. 489, no. 7415, pp. 242–249, 2012.

[51] M. Song, W. S. Garrett, and A. T. Chan, "Nutrients, foods, and colorectal cancer prevention," *Gastroenterology*, vol. 148, no. 6, pp. 1244–1260.e16, 2015.

[52] M. Candela, S. Turroni, E. Biagi et al., "Inflammation and colorectal cancer, when microbiota-host mutualism breaks," *World Journal of Gastroenterology*, vol. 20, no. 4, pp. 908–922, 2014.

[53] G. Nakatsu, X. Li, H. Zhou et al., "Gut mucosal microbiome across stages of colorectal carcinogenesis," *Nature Communications*, vol. 6, no. 1, p. 8727, 2015.

[54] C. Yazici, P. G. Wolf, H. Kim et al., "Race-dependent association of sulfidogenic bacteria with colorectal cancer," *Gut*, vol. 66, no. 11, pp. 1983–1994, 2017.

[55] D. Lv, X. Xiong, H. Yang et al., "Effect of dietary soy oil, glucose, and glutamine on growth performance, amino acid profile, blood profile, immunity, and antioxidant capacity in weaned piglets," *Science China. Life Sciences*, vol. 61, no. 10, pp. 1233–1242, 2018.

[56] H. Tilg, T. E. Adolph, R. R. Gerner, and A. R. Moschen, "The intestinal microbiota in colorectal cancer," *Cancer Cell*, vol. 33, no. 6, pp. 954–964, 2018.

[57] X. C. Morgan, N. Segata, and C. Huttenhower, "Biodiversity and functional genomics in the human microbiome," *Trends in Genetics*, vol. 29, no. 1, pp. 51–58, 2013.

[58] S. J. Bultman, "Interplay between diet, gut microbiota, epigenetic events, and colorectal cancer," *Molecular Nutrition & Food Research*, vol. 61, no. 1, 2017.

[59] J. Rafter, "The effects of probiotics on colon cancer development," *Nutrition Research Reviews*, vol. 17, no. 2, pp. 277–284, 2004.

[60] M. Eslami, B. Yousefi, P. Kokhaei et al., "Importance of probiotics in the prevention and treatment of colorectal cancer," *Journal of Cellular Physiology*, vol. 234, no. 10, pp. 17127–17143, 2019.

[61] P. Louis, G. L. Hold, and H. J. Flint, "The gut microbiota, bacterial metabolites and colorectal cancer," *Nature Reviews. Microbiology*, vol. 12, no. 10, pp. 661–672, 2014.

[62] A. Alhenaky, A. Abdelqader, M. Abuajamieh, and A. R. Al-Fataftah, "The effect of heat stress on intestinal integrity and Salmonella invasion in broiler birds," *Journal of Thermal Biology*, vol. 70, no. Part B, pp. 9–14, 2017.

[63] D. Liu, X. Y. Jiang, L. S. Zhou, J. H. Song, and X. Zhang, "Effects of probiotics on intestinal mucosa barrier in patients with colorectal cancer after operation: meta-analysis of randomized controlled trials," *Medicine (Baltimore)*, vol. 95, no. 15, article e3342, 2016.

[64] C.-S. Alvarez, J. Badia, M. Bosch, R. Giménez, and L. Baldomà, "Outer membrane vesicles and soluble factors released by probiotic Escherichia coli Nissle 1917 and commensal ECOR63 enhance barrier function by regulating expression of tight junction proteins in intestinal epithelial cells," *Frontiers in Microbiology*, vol. 7, p. 1981, 2016.

[65] R. Martín, C. Chamignon, N. Mhedbi-Hajri et al., "The potential probiotic Lactobacillus rhamnosus CNCM I-3690 strain protects the intestinal barrier by stimulating both mucus production and cytoprotective response," *Scientific Reports*, vol. 9, no. 1, p. 5398, 2019.

[66] Y. Xu, L. Lahaye, Z. He, J. Zhang, C. Yang, and X. Piao, "Micro-encapsulated essential oils and organic acids combination improves intestinal barrier function, inflammatory responses and microbiota of weaned piglets challenged with enterotoxigenic Escherichia coli F4 (K88(+))," *Animal Nutrition*, vol. 6, no. 3, pp. 269–277, 2020.

[67] Y. Li, A. S. Fanning, J. M. Anderson, and A. Lavie, "Structure of the conserved cytoplasmic C-terminal domain of occludin: identification of the ZO-1 binding surface," *Journal of Molecular Biology*, vol. 352, no. 1, pp. 151–164, 2005.

[68] S. Guo, T. Gillingham, Y. Guo et al., "Secretions of Bifidobacterium infantis and Lactobacillus acidophilus protect intestinal epithelial barrier function," *Journal of Pediatric Gastroenterology and Nutrition*, vol. 64, no. 3, pp. 404–412, 2017.

[69] J. Wang, H. Ji, S. Wang et al., "Probiotic Lactobacillus plantarum promotes intestinal barrier function by strengthening the epithelium and modulating gut microbiota," *Frontiers in Microbiology*, vol. 9, p. 1953, 2018.

[70] M. E. Johansson, M. Phillipson, J. Petersson, A. Velcich, L. Holm, and G. C. Hansson, "The inner of the two Muc2 mucin-dependent mucus layers in colon is devoid of bacteria," *Proceedings of the National Academy of Sciences of the United States of America*, vol. 105, no. 39, pp. 15064–15069, 2008.

[71] M. van der Sluis, B. A. E. de Koning, A. C. J. M. de Bruijn et al., "Muc2-deficient mice spontaneously develop colitis, indicating that MUC2 is critical for colonic protection," *Gastroenterology*, vol. 131, no. 1, pp. 117–129, 2006.

[72] W. Fong, Q. Li, and J. Yu, "Gut microbiota modulation: a novel strategy for prevention and treatment of colorectal cancer," *Oncogene*, vol. 39, no. 26, pp. 4925–4943, 2020.

[73] C. A. Brennan and W. S. Garrett, "Gut microbiota, inflammation, and colorectal cancer," *Annual Review of Microbiology*, vol. 70, no. 1, pp. 395–411, 2016.

[74] H. Tlaskalova-Hogenova, L. Vannucci, K. Klimesova, R. Stepankova, J. Krizan, and M. Kverka, "Microbiome and colorectal carcinoma: insights from germ-free and conventional animal models," *Cancer Journal*, vol. 20, no. 3, pp. 217–224, 2014.

[75] Y. H. Ding, L. Y. Qian, J. Pang et al., "The regulation of immune cells by lactobacilli: a potential therapeutic target for anti-atherosclerosis therapy," *Oncotarget*, vol. 8, no. 35, pp. 59915–59928, 2017.

[76] M. Molska and J. Reguła, "Potential mechanisms of probiotics action in the prevention and treatment of colorectal cancer," *Nutrients*, vol. 11, no. 10, p. 2453, 2019.

[77] S. H. Lee, P. M. Starkey, and S. Gordon, "Quantitative analysis of total macrophage content in adult mouse tissues. Immunochemical studies with monoclonal antibody F4/80," *The Journal of Experimental Medicine*, vol. 161, no. 3, pp. 475–489, 1985.

[78] A. M. Platt, C. C. Bain, Y. Bordon, D. P. Sester, and A. M. I. Mowat, "An independent subset of TLR expressing CCR2-dependent macrophages promotes colonic inflammation," *Journal of Immunology*, vol. 184, no. 12, pp. 6843–6854, 2010.

[79] E. Zigmond, C. Varol, J. Farache et al., "Ly6C hi monocytes in the inflamed colon give rise to proinflammatory effector cells and migratory antigen-presenting cells," *Immunity*, vol. 37, no. 6, pp. 1076–1090, 2012.

[80] R. A. Isidro and C. B. Appleyard, "Colonic macrophage polarization in homeostasis, inflammation, and cancer," *American Journal of Physiology. Gastrointestinal and Liver Physiology*, vol. 311, no. 1, pp. G59–G73, 2016.

[81] H. J. Wu and E. Wu, "The role of gut microbiota in immune homeostasis and autoimmunity," *Gut Microbes*, vol. 3, no. 1, pp. 4–14, 2014.

[82] I. C. Chung, C. N. OuYang, S. N. Yuan et al., "Pretreatment with a heat-killed probiotic modulates the NLRP3 inflammasome and attenuates colitis-associated colorectal cancer in mice," *Nutrients*, vol. 11, no. 3, p. 516, 2019.

[83] M. Kasubuchi, S. Hasegawa, T. Hiramatsu, A. Ichimura, and I. Kimura, "Dietary gut microbial metabolites, short-chain fatty acids, and host metabolic regulation," *Nutrients*, vol. 7, no. 4, pp. 2839–2849, 2015.

[84] N. Singh, A. Gurav, S. Sivaprakasam et al., "Activation of Gpr109a, receptor for niacin and the commensal metabolite butyrate, suppresses colonic inflammation and carcinogenesis," *Immunity*, vol. 40, no. 1, pp. 128–139, 2014.

[85] M. Perše, "Oxidative stress in the pathogenesis of colorectal cancer: cause or consequence?," *BioMed Research International*, vol. 2013, Article ID 725710, 9 pages, 2013.

[86] M. L. Circu and T. Y. Aw, "Intestinal redox biology and oxidative stress," *Seminars in Cell & Developmental Biology*, vol. 23, no. 7, pp. 729–737, 2012.

[87] N. Mach and D. Fuster-Botella, "Endurance exercise and gut microbiota: a review," *Journal of Sport and Health Science*, vol. 6, no. 2, pp. 179–197, 2017.

[88] G. Guan, S. Ding, Y. Yin, V. Duraipandiyan, N. A. al-Dhabi, and G. Liu, "Macleaya cordata extract alleviated oxidative stress and altered innate immune response in mice challenged with enterotoxigenic Escherichia coli," *Science China. Life Sciences*, vol. 62, no. 8, pp. 1019–1027, 2019.

[89] K. Richter and T. Kietzmann, "Reactive oxygen species and fibrosis: further evidence of a significant liaison," *Cell and Tissue Research*, vol. 365, no. 3, pp. 591–605, 2016.

[90] I. Amrouche-Mekkioui and B. Djerdjouri, "N-acetylcysteine improves redox status, mitochondrial dysfunction, mucin-depleted crypts and epithelial hyperplasia in dextran sulfate sodium-induced oxidative colitis in mice," *European Journal of Pharmacology*, vol. 691, no. 1-3, pp. 209–217, 2012.

[91] W. Tang, J. Wu, S. Jin et al., "Glutamate and aspartate alleviate testicular/epididymal oxidative stress by supporting antioxidant enzymes and immune defense systems in boars," *Science China. Life Sciences*, vol. 63, no. 1, pp. 116–124, 2020.

[92] X. Hua, A. I. Phipps, A. N. Burnett-Hartman et al., "Timing of aspirin and other nonsteroidal anti-inflammatory drug use among patients with colorectal cancer in relation to tumor markers and survival," *Journal of Clinical Oncology*, vol. 35, no. 24, pp. 2806–2813, 2017.

[93] G. J. Tsioulias, M. F. Go, and B. Rigas, "NSAIDs and colorectal cancer control: promise and challenges," *Current Pharmacology Reports*, vol. 1, no. 5, pp. 295–301, 2015.

[94] J. L. Arbiser, J. Petros, R. Klafter et al., "Reactive oxygen generated by Nox1 triggers the angiogenic switch," *Proceedings of the National Academy of Sciences of the United States of America*, vol. 99, no. 2, pp. 715–720, 2002.

[95] K. Rokutan, T. Kawahara, Y. Kuwano, K. Tominaga, A. Sekiyama, and S. Teshima-Kondo, "NADPH oxidases in the gastrointestinal tract: a potential role of Nox1 in innate immune response and carcinogenesis," *Antioxidants & Redox Signaling*, vol. 8, no. 9-10, pp. 1573–1582, 2006.

[96] A. Mangerich, P. C. Dedon, J. G. Fox, S. R. Tannenbaum, and G. N. Wogan, "Chemistry meets biology in colitis-associated carcinogenesis," *Free Radical Research*, vol. 47, no. 11, pp. 958–986, 2013.

[97] M. E. Hope, G. L. Hold, R. Kain, and E. M. El-Omar, "Sporadic colorectal cancer–role of the commensal microbiota," *FEMS Microbiology Letters*, vol. 244, no. 1, pp. 1–7, 2005.

[98] A. C. Goodwin, C. E. D. Shields, S. Wu et al., "Polyamine catabolism contributes to enterotoxigenic Bacteroides fragilis-induced colon tumorigenesis," *Proceedings of the National Academy of Sciences of the United States of America*, vol. 108, no. 37, pp. 15354–15359, 2011.

[99] S. H. Ko, J. I. Jeon, H. A. Woo, and J. M. Kim, "Bacteroides fragilisenterotoxin upregulates heme oxygenase-1 in dendritic cellsviareactive oxygen species-, mitogen-activated protein kinase-, and Nrf2-dependent pathway," *World Journal of Gastroenterology*, vol. 26, no. 3, pp. 291–306, 2020.

[100] A. Kumar, H. Wu, L. S. Collier-Hyams et al., "Commensal bacteria modulate cullin-dependent signaling via generation of reactive oxygen species," *The EMBO Journal*, vol. 26, no. 21, pp. 4457–4466, 2007.

[101] J. Xu, C. Xu, X. Chen et al., "Regulation of an antioxidant blend on intestinal redox status and major microbiota in early weaned piglets," *Nutrition*, vol. 30, no. 5, pp. 584–589, 2014.

[102] S. Ghosh, C. Dai, K. Brown et al., "Colonic microbiota alters host susceptibility to infectious colitis by modulating inflammation, redox status, and ion transporter gene expression," *American Journal of Physiology. Gastrointestinal and Liver Physiology*, vol. 301, no. 1, pp. G39–G49, 2011.

[103] M. Liu, W. Xie, X. Wan, and T. Deng, "Clostridium butyricum modulates gut microbiota and reduces colitis associated colon cancer in mice," *International Immunopharmacology*, vol. 88, p. 106862, 2020.

[104] K. B. Arun, A. Madhavan, T. R. Reshmitha, S. Thomas, and P. Nisha, "Short chain fatty acids enriched fermentation metabolites of soluble dietary fibre from Musa paradisiaca drives HT29 colon cancer cells to apoptosis," *PLoS ONE*, vol. 14, no. 5, article e0216604, 2019.

[105] P. Hu, W. Song, Y. Shan et al., "Lactobacillus paracasei subsp. paracasei M5L induces cell cycle arrest and calreticulin translocation via the generation of reactive oxygen species in HT-29 cell apoptosis," *Food & Function*, vol. 6, no. 7, pp. 2257–2265, 2015.

[106] Y. Zhang and Y. Li, "Engineering the antioxidative properties of lactic acid bacteria for improving its robustness," *Current Opinion in Biotechnology*, vol. 24, no. 2, pp. 142–147, 2013.

[107] M. Linsalata, A. Cavallini, C. Messa, A. Orlando, M. Refolo, and F. Russo, "Lactobacillus rhamnosus GG influences polyamine metabolism in HGC-27 gastric cancer cell line: a strategy toward nutritional approach to chemoprevention of gastric cancer," *Current Pharmaceutical Design*, vol. 16, no. 7, pp. 847–853, 2010.

[108] K. Dev, N. A. Mir, A. Biswas et al., "Dietary synbiotic supplementation improves the growth performance, body antioxidant pool, serum biochemistry, meat quality, and lipid oxidative stability in broiler chickens," *Animal Nutrition*, vol. 6, no. 3, pp. 325–332, 2020.

[109] I. Wollowski, G. Rechkemmer, and B. L. Pool-Zobel, "Protective role of probiotics and prebiotics in colon cancer," *The American Journal of Clinical Nutrition*, vol. 73, no. 2, pp. 451s–455s, 2001.

[110] H. Tjalsma, A. Boleij, J. R. Marchesi, and B. E. Dutilh, "A bacterial driver-passenger model for colorectal cancer: beyond the usual suspects," *Nature Reviews. Microbiology*, vol. 10, no. 8, pp. 575–582, 2012.

[111] K. M. Tuohy, G. C. Rouzaud, W. M. Brück, and G. R. Gibson, "Modulation of the human gut microflora towards improved health using prebiotics–assessment of efficacy," *Current Pharmaceutical Design*, vol. 11, no. 1, pp. 75–90, 2005.

[112] J. P. Nougayrède, S. Homburg, F. Taieb et al., "Escherichia coli induces DNA double-strand breaks in eukaryotic cells," *Science*, vol. 313, no. 5788, pp. 848–851, 2006.

[113] G. Cuevas-Ramos, C. R. Petit, I. Marcq, M. Boury, E. Oswald, and J. P. Nougayrede, "Escherichia coli induces DNA damage in vivo and triggers genomic instability in mammalian cells," *Proceedings of the National Academy of Sciences of the United States of America*, vol. 107, no. 25, pp. 11537–11542, 2010.

[114] N. Ulger Toprak, A. Yagci, B. M. Gulluoglu et al., "A possible role of Bacteroides fragilis enterotoxin in the aetiology of colorectal cancer," *Clinical Microbiology and Infection*, vol. 12, no. 8, pp. 782–786, 2006.

[115] A. Verma and G. Shukla, "Probiotics Lactobacillus rhamnosus GG, Lactobacillus acidophilus suppresses DMH-induced procarcinogenic fecal enzymes and preneoplastic aberrant crypt foci in early colon carcinogenesis in Sprague Dawley rats," *Nutrition and Cancer*, vol. 65, no. 1, pp. 84–91, 2013.

[116] A. Nowak, K. Śliżewska, J. Błasiak, and Z. Libudzisz, "The influence of Lactobacillus casei DN 114 001 on the activity of faecal enzymes and genotoxicity of faecal water in the presence of heterocyclic aromatic amines," *Anaerobe*, vol. 30, pp. 129–136, 2014.

[117] C. L. Vernazza, B. A. Rabiu, and G. R. Gibson, "Human Colonic Microbiology and the Role of Dietary Intervention: Introduction to Prebiotic," in *Prebiotics: Development & Application*, John Wiley & Sons, Ltd, 2012.

[118] A. de Moreno de LeBlanc and G. Perdigón, "Reduction of β-Glucuronidase and nitroreductase activity by yoghurt in a murine colon cancer model," *Biocell*, vol. 29, no. 1, pp. 15–24, 2005.

[119] P. Marteau, P. Pochart, B. Flourié et al., "Effect of chronic ingestion of a fermented dairy product containing Lactobacillus acidophilus and Bifidobacterium bifidum on metabolic activities of the colonic flora in humans," *The American Journal of Clinical Nutrition*, vol. 52, no. 4, pp. 685–688, 1990.

[120] D. Goossens, D. Jonkers, M. Russel, E. Stobberingh, A. van den Bogaard, and R. StockbrÜgger, "The effect of Lactobacillus plantarum 299v on the bacterial composition and metabolic activity in faeces of healthy volunteers: a placebo-controlled study on the onset and duration of effects," *Alimentary Pharmacology & Therapeutics*, vol. 18, no. 5, pp. 495–505, 2003.

[121] S. Elmore, "Apoptosis: a review of programmed cell death10.1080/01926230701320337," *Toxicologic Pathology*, vol. 35, no. 4, pp. 495–516, 2007.

[122] S. W. Fesik, "Promoting apoptosis as a strategy for cancer drug discovery," *Nature Reviews. Cancer*, vol. 5, no. 11, pp. 876–885, 2005.

[123] Y. Gamallat, A. Meyiah, E. D. Kuugbee et al., "Lactobacillus rhamnosus induced epithelial cell apoptosis, ameliorates inflammation and prevents colon cancer development in an animal model," *Biomedicine & Pharmacotherapy*, vol. 83, pp. 536–541, 2016.

[124] J. Y. Zhang, X. Xiao, Y. Dong, J. Wu, F. Yao, and X. H. Zhou, "Effect of fermented wheat germ extract with Lactobacillus plantarum dy-1 on HT-29 cell proliferation and apoptosis," *Journal of Agricultural and Food Chemistry*, vol. 63, no. 9, pp. 2449–2457, 2015.

[125] C. Avivi-Green, S. Polak-Charcon, Z. Madar, and B. Schwartz, "Apoptosis cascade proteins are regulated in vivo by high intracolonic butyrate concentration: correlation with colon cancer inhibition," *Oncology Research*, vol. 12, no. 2, pp. 83–95, 2000.

[126] A. Lan, D. Lagadic-Gossmann, C. Lemaire, C. Brenner, and G. Jan, "Acidic extracellular pH shifts colorectal cancer cell death from apoptosis to necrosis upon exposure to propionate and acetate, major end-products of the human probiotic propionibacteria," *Apoptosis*, vol. 12, no. 3, pp. 573–591, 2007.

[127] L. Pattayil and H. T. Balakrishnan-Saraswathi, "In vitroevaluation of apoptotic induction of butyric acid derivatives in colorectal carcinoma cells," *Anticancer Research*, vol. 39, no. 7, pp. 3795–3801, 2019.

[128] M. Comalada, E. Bailón, O. de Haro et al., "The effects of short-chain fatty acids on colon epithelial proliferation and survival depend on the cellular phenotype," *Journal of Cancer Research and Clinical Oncology*, vol. 132, no. 8, pp. 487–497, 2006.

[129] N. Mustapha, A. Pinon, Y. Limami et al., "Crataegus azarolus leaves induce antiproliferative activity, cell cycle arrest, and apoptosis in human HT-29 and HCT-116 colorectal cancer cells," *Journal of Cellular Biochemistry*, vol. 117, no. 5, pp. 1262–1272, 2016.

[130] A. Bharwani, M. F. Mian, M. G. Surette, J. Bienenstock, and P. Forsythe, "Oral treatment with Lactobacillus rhamnosus attenuates behavioural deficits and immune changes in chronic social stress," *BMC Medicine*, vol. 15, no. 1, p. 7, 2017.

[131] A. Quagliariello, I. Aloisio, N. Bozzi Cionci et al., "Effect of *Bifidobacterium breve* on the intestinal microbiota of coeliac children on a gluten free diet: a pilot study," *Nutrients*, vol. 8, no. 10, p. 660, 2016.

[132] T. S. Manning and G. R. Gibson, "Microbial-gut interactions in health and disease. Prebiotics," *Best Practice & Research. Clinical Gastroenterology*, vol. 18, no. 2, pp. 287–298, 2004.

[133] J. Denizot, A. Desrichard, A. Agus et al., "Diet-induced hypoxia responsive element demethylation increases CEACAM6 expression, favouring Crohn's disease-associated Escherichia coli colonisation," *Gut*, vol. 64, no. 3, pp. 428–437, 2015.

[134] M. Bonnet, E. Buc, P. Sauvanet et al., "Colonization of the human gut by E. coli and colorectal cancer risk," *Clinical Cancer Research*, vol. 20, no. 4, pp. 859–867, 2014.

[135] J. C. Arthur, R. Z. Gharaibeh, M. Mühlbauer et al., "Microbial genomic analysis reveals the essential role of inflammation in bacteria-induced colorectal cancer," *Nature Communications*, vol. 5, no. 1, p. 4724, 2014.

[136] E. L. Ma, Y. J. Choi, J. Choi, C. Pothoulakis, S. H. Rhee, and E. Im, "The anticancer effect of probioticBacillus polyfermenticuson human colon cancer cells is mediated through ErbB2 and ErbB3 inhibition," *International Journal of Cancer*, vol. 127, no. 4, article NA-790, 2010.

[137] C. G. Olnood, S. S. M. Beski, P. A. Iji, and M. Choct, "Delivery routes for probiotics: effects on broiler performance, intestinal morphology and gut microflora," *Animal Nutrition*, vol. 1, no. 3, pp. 192–202, 2015.

[138] K. Saito, S. Koido, T. Odamaki et al., "Metagenomic analyses of the gut microbiota associated with colorectal adenoma," *PLoS ONE*, vol. 14, no. 2, article e0212406, 2019.

[139] J. Rafter, M. Bennett, G. Caderni et al., "Dietary synbiotics reduce cancer risk factors in polypectomized and colon cancer patients," *The American Journal of Clinical Nutrition*, vol. 85, no. 2, pp. 488–496, 2007.

Research Article

The Nrf2/PGC1α Pathway Regulates Antioxidant and Proteasomal Activity to Alter Cisplatin Sensitivity in Ovarian Cancer

Xinyue Deng (ID)**, Nan Lin, Jiaying Fu, Long Xu, Haoge Luo, Yao Jin, Yanan Liu, Liankun Sun** (ID)**, and Jing Su** (ID)

Key Laboratory of Pathobiology, Ministry of Education, Department of Pathophysiology, College of Basic Medical Sciences, Jilin University, Changchun, China

Correspondence should be addressed to Liankun Sun; sunlk@jlu.edu.cn and Jing Su; sujing@jlu.edu.cn

Drug resistance remains a barrier in the clinical treatment of ovarian cancer. Proteasomal and antioxidant activities play important roles in tumor drug resistance, and increasing evidence suggests the existence of an interaction between antioxidant and proteasomal activities. However, the mechanism of the synergistic effects of proteasomal activity and antioxidation on tumor drug resistance is not completely clear. In this study, we compared two ovarian cancer cells, A2780 and SKOV3 cells. Among them, SKOV3 cell is a human clear cell carcinoma cell line that is resistant to platinum. We found that compared with the findings in A2780 cells, SKOV3 cells were less sensitive to both proteasomal inhibitor and cisplatin. Proteasomal inhibition enhanced the sensitivity of A2780 cells, but not SKOV3 cells, to cisplatin. Notably, the Nrf2-mediated antioxidant pathway was identified as a resistance mechanism in proteasome inhibitor-resistant cells, but this was not the only factor identified in our research. In SKOV3 cells, PGC1α regulated the antioxidant activity of Nrf2 by increasing the phosphorylation of GSK3β, and in turn, Nrf2 regulated the transcriptional activity of PGC1α. Thus, Nrf2 and PGC1α synergistically participate in the regulation of proteasomal activity. Furthermore, the Nrf2/PGC1α pathway participated in the regulation of mitochondrial function and homeostasis, further regulating proteasomal activity in SKOV3 cells. Therefore, exploring the roles of PGC1α and Nrf2 in the regulation of proteasomal activity by antioxidant and mitochondrial functions may provide new avenues for reversing drug resistance in ovarian cancer.

1. Introduction

Ovarian cancer is the most deadly gynecological malignancy, and drug resistance has become a major challenge in its treatment in recent years. Resistance to chemotherapy in tumor cells is related to multiple factors, including the repair of DNA damage, blockade of drug-induced apoptosis, reactive oxygen species- (ROS-) mediated redox state, and protein degradation [1–3]. Current research suggests that exploring the mechanisms of the interaction between different signals can shed light on the mechanisms of tumor drug resistance. Proteasomal activity plays important roles in tumorigenesis and chemotherapy resistance, and abnormally elevated proteasome levels are found in a variety of cancers [4–6]. The proteasome can eliminate oxidative and damaged proteins to reduce oxidative stress damage, and enhanced antioxidant

capacity can promote the expression of 20S and 19S proteasome subunits [7, 8]. These findings suggest the existence of an interaction between proteasomal activity and redox function, and exploring this relationship will be more helpful in solving the problem of chemotherapy resistance in ovarian cancer.

The ubiquitin-proteasome system (UPS) maintains cell homeostasis by regulating proteins involved in signal transduction and cell cycle pathways [9]. Inhibition of the proteasome can cause the accumulation of proapoptotic proteins and induce tumor cell apoptosis. However, recent clinical studies found that some tumors are not sensitive to proteasome inhibitors. Proteasome inhibitor-resistant tumors generally have higher expression levels of antioxidant genes [10]. The nuclear factor E2-related factor 2 (Nrf2, gene name NFE2l2)-mediated antioxidant stress pathway was identified

as a resistance mechanism in the proteasome inhibitor-resistant phenotype. Nrf2 can regulate the transcriptional activity of proteasome mature protein, which can promote resistance to proteasome inhibitors [11]. This suggests that Nrf2-mediated antioxidant activity may be related to proteasome-mediated tumor resistance.

Nrf2 is an important element of the antioxidant response element (ARE) transcription complex, and it can regulate the expression of various protective genes. Nrf2- and antioxidant-related gene expression is elevated in drug-resistant tumor cells, and its activity is regulated by a variety of factors, including transcription and posttranscription modification. The dissociation of Nrf2 and Kelch-like ECH-associated protein 1 (Keap1) enables Nrf2 to enter the nuclear and regulate the transcription of the oxidase gene [12, 13]. What's more, glycogen synthase kinase 3β (GSK3β) can inhibit Nrf2 by preventing nuclear accumulation of the CNC-bZIP factor, and evidence has provided that GSK3β interferes with Nrf2 transactivating activity and nuclear exclusion of the Nrf2 [14, 15]. Peroxisome proliferator-activated receptor-γ coactivator 1α (PGC1α, gene name PPARGC1A) can also coordinate the expression of multiple antioxidant genes to protect cells against oxidative stress damage. PGC1α is involved in the regulation of Nrf2 expression and activity, and studies have confirmed the protein-protein interaction between them [16, 17], but the specific mechanism is not completely clear. Therefore, the mechanism by which PGC1α and Nrf2 interact may play a synergistic role in antioxidation, but it is unclear whether their interaction is related to drug resistance.

In addition, the maintenance of mitochondrial redox homeostasis plays an important role in proteasome activity. Mitochondria are the main sources of ROS, and excessive ROS production can increase the burden on the UPS and decrease the proteasomal activity induced by increased oxidation and damaged proteasome subunits [18]. Nrf2 can inhibit mitochondrial ROS production by upregulating heme oxidase (HO-1) and the primary mitochondrial antioxidant enzyme superoxide dismutase 2 (SOD2), thereby inhibiting mitochondrial oxidative stress damage [19, 20]. Mitochondrial protein stability and structural integrity are regulated through interactions with a variety of mitochondrial proteins, including PGC1α and PGC1β [21–23]. These results suggest that the antioxidation mediated by Nrf2 and PGC1α also regulates the homeostasis of mitochondrial function and thus maintains proteasome activity.

In this study, the "UPS-Antioxidation Axis" was taken as the entry point to explore the roles of PGC1α and Nrf2 in the regulation of antioxidant and mitochondrial functions in maintaining proteasome activity. The findings provide new ideas for reversing drug resistance in ovarian cancer.

2. Methods and Materials

2.1. Reagents and Antibodies.
The human ovarian cancer cell lines A2780 and SKOV3 were obtained from the Shanghai Cell Bank of Chinese Academy of Sciences (Shanghai, China). Both cell lines were cultured in RPMI-1640 medium (Gibco, Carlsbad, CA, USA). Cisplatin (CDDP) and 3-(4, 5-dimethylthiazol-2-yl)-2,5-diphenyltetrazolium bromide (MTT) were purchased from Sigma-Aldrich (St. Louis, MO, USA). Epoxomicin (Epox), GSK3β inhibitor (CHIR99021), and the PGC1α activator ZLN005 were purchased from MedChemExpress (Monmouth Junction, NJ, USA). Transfections were performed using Lipofectamine 2000 (Invitrogen, Carlsbad, CA, USA). Anti-Keap1 and anti-lamin B antibodies were obtained from Santa Cruz Biotechnology (Santa Cruz, CA, USA). Anti-p38, anti-GSK3β, anti-phospho-p38, anti-phospho-GSK3β, and anti-AKT antibodies were acquired from Cell Signaling Technology (Danvers, MA, USA). Anti-Nrf2, anti-Bcl-2, anti-Bax, anti-cleaved caspase 3, and anti-β-actin antibodies were procured from Proteintech (Chicago, IL, USA). Total OXPHOS Human WB Antibody Cocktail and anti-PGC1α antibodies were purchased from Abcam (Cambridge, MA, USA).

2.2. Cell Viability Assay.
Cells (10,000 cells/well) were seeded in 96-well plates, incubated overnight, and treated with various reagents for the indicated times. Cells were then incubated with MTT reagent for 4–6 h. Absorbance values were recorded at 570 nm using an enzyme-linked immunosorbent assay reader.

2.3. Plasmids and Cell Transfections.
The pcDNA3.1 vector (NC) and a full-length human Nrf2 expression vector (pcDNA3.1-Nrf2) were purchased from Genepharma (Shanghai, China). PGC1α shRNA and a nontarget sequence (Scr shRNA) were constructed by Genechem (Shanghai, China). The shRNA sequences were as follows: PGC1α-shRNA 1, 5′-GTT-ATA-CCT-GTG-ATG-CTT-T-3′; PGC1α-shRNA 2, 5′-CAG-CGA-AGA-TGA-AAG-TGA-T-3′; and Scr-shRNA, 5′-TTC-TCC-GAA-CGT-GTC-ACG-T-3′. Cells were transfected using Lipofectamine 2000 according to the manufacturer's instructions.

2.4. Luciferase Assay.
The PPARGC1A promoter region spanning from −2000 to +1 bp was cloned into a pGL4 basic vector. The reporter gene construct and Renilla luciferase reporter (pRL-TK) plasmid were transfected into SKOV3 cells alone or together with pcDNA3.1-Nrf2 (Nrf2) or pcDNA3.1 vector (NC) using Lipofectamine 2000. Luciferase activity was determined using a dual-luciferase reporter assay kit (Promega, Madison, WI, USA).

2.5. Flow Cytometry.
Apoptotic cells were counted using Annexin V-FITC and propidium iodide (PI) (Annexin V Apoptosis Detection Kit, BD Pharmingen, San Jose, CA, USA) according to the manufacturer's protocol. Mitochondrial membrane potential (MMP) and ROS production were determined using JC-1 or DCFH-DA staining (Beyotime Biotechnology, Shanghai, China). Mitotracker™ Red (Sigma-Aldrich) staining was used to evaluate the alteration of mitochondrial mass. The analysis was performed using a BD Accuri C6 flow cytometer (BD Biosciences, New Jersey, USA).

2.6. Western Blotting.
Whole cells were lysed in RIPA lysis buffer containing protease inhibitors. Lysates diluted with 5x SDS-PAGE loading buffer were boiled at 95°C for

10 min, separated by SDS-PAGE, and then transferred to PVDF membranes. The membranes were blocked with 5% milk followed by incubation with primary antibodies overnight at 4°C. The next day, the membranes were incubated with HRP-conjugated secondary antibodies. The bands were incubated in ECL reagent (Thermo Fisher Scientific, Waltham, MA, USA) for chemiluminescence and visualized using Syngene Bio Imaging (Synoptics, Cambridge, UK).

2.7. Immunoprecipitation. Cell lysates were solubilized in NP40 buffer containing a protease inhibitor mixture for 1–2 h at 4°C. After adding monoclonal antibodies, supernatants were rotated at 4°C overnight. The next day, the protein lysates were incubated with 30 μl of protein A/G Plus-agarose beads (Santa Cruz Biotechnology, Inc., Santa Cruz, CA, USA) overnight at 4°C. The agarose beads were washed three times, SDS-PAGE loading buffer was added, and then, samples were analyzed via Western blotting.

2.8. Nuclear and Mitochondrial Isolation. Cells were harvested after treatment with various reagents. Nuclear and mitochondrial fractions were extracted using a nuclear fractionation kit and mitochondrial fractionation kit, respectively (Invent Biotechnologies, MN, USA).

2.9. ATP Production. Cells were treated with 100 nM Epox for 12 h or transfected with Nrf2 or pcDNA3.1 (vector plasmid was used in the NC group). ATP production was determined using an ATP Bioluminescence Assay Kit (Beyotime Technology). An Omega luminometer was used to measure the values (BMG Labtech, Ortenberg, Germany).

2.10. Oxygen Consumption Rates (OCRs). Cells were seeded in 96-well plates overnight. The next day, cells were incubated with a mixture of reagents and the oxygen-sensitive probe Mito-Xpress (Luxcel Bioscience, Cork, Ireland) and examined using an Omega luminometer for 6 h.

2.11. Real-Time Quantitative PCR (RT-qPCR). Total RNA was extracted using TRIzol reagent (Sigma-Aldrich). The reverse transcription reaction was performed using a SuperScript RT-PCR kit (Promega), and RT-qPCR was performed using the MX3000P instrument (Agilent, USA). mRNA levels were normalized to those of β-actin. The primer sequences are *ACTB*: 5′-ATATCGCGTCGCTGGTCGTC-3′ (forward) and 5′-AGGATGGCGTGAGGGAGAGC-3′ (reverse); *PPARGC1A*: 5′-CAGAGAGTATGAGAAGCGA GAG-3′ (forward) and 5′-AGCATCACAGGTATAACGG TAG-3′ (reverse); *NFE2l2*: 5′-ATCAGCAACAGCATGC CCTC-3′ (forward) and 5′-ATGCCACACTGGGACT TGTG-3′ (reverse); *NQO-1*: 5′-AGTATCCTGCCGAGTC TGTTCTGG-3′ (forward) and 5′-AATATCACAAGGTC TGCGGCTTCC-3′ (reverse); *GCLC*: 5′-TGTCCGAGTTC AATACAGTTGA-3′ (forward) and 5′-ACAGCCTAATC TGGGAAATGAA-3′ (reverse); *G6PDH*: 5′-TCACCAAGA ACATTCACGAGTC-3′ (forward) and 5′-GAAGATCCT GTTGGCAAATCTC-3′ (reverse); *HMOX-1*: 5′-CCTCCC TGTACCACATCTATGT-3′ (forward) and 5′-GCTCTT

CTGGGAAGTAGACAG-3′ (reverse); and *SOD2*: 5′-AACCTCACATCAACGCGCAGATC-3′ (forward) and 5′-CTCCTGGTACTTCTCCTCGGTGAC-3′ (reverse).

2.12. Determination of the Relative mtDNA Copy Number. Total DNA was extracted using a TIANamp Genomic DNA kit (Tiangen Biotech Co., Ltd., Beijing, China). qPCR was used to measure the mitochondrial-encoded nicotinamide adenine dinucleotide dehydrogenase 1 (ND1) level relative to that of nuclear-encoded gene 18S rRNA (18S), as described previously [24]. Each sample was analyzed in triplicate using the MX3000P instrument. The relative mtDNA copy number was calculated as the ratio of ND1 to 18S and was normalized to the respective control group. The primer sequences are *18s rRNA*: 5′-TAGAGGGACAAGTGGC GTTC-3′ (forward) and 5′-CGCTGAGCCAGTCAGTGT-3′ (reverse) and *ND1*: 5′-CACCCAAGAACAGGGTTTGT-3′ (forward) and 5′-TGGCCATGGATTGTTGTTAA-3′ (reverse).

2.13. Immunofluorescence Staining and Microscopy. Cells were washed with PBS, fixed with 4% paraformaldehyde for 20 min, and permeabilized with 0.1% Triton X-100 for 8 min. After blocking with 5% bovine serum albumin for 30 min, cells were incubated with primary antibody overnight at 4°C. After PBS washing, the cells were incubated at room temperature for 1 h in the dark with FITC/Texas Red-conjugated secondary antibodies (Proteintech). The images were observed on an Echo-lab Revolve microscope (CA, USA).

2.14. Statistical Analysis. Data are expressed as the mean ± SD. $^{*}P < 0.05$ was considered statistically significant. Statistical analysis was performed with GraphPad Prism 5 (La Jolla, CA, USA). All experiments were repeated at least three times.

3. Results

3.1. Proteasome Inhibition Can Enhance the Sensitivity of A2780 Cells to Cisplatin, but Not SKOV3 Cells. Drug resistance remains an important obstacle that limits the efficacy of platinum-based treatment in ovarian cancer [25], and targeting the ubiquitin-proteasome pathway can overcome cancer chemoresistance [26]. The MTT assay illustrated that compared with the findings in SKOV3 cells, the proteasome inhibitor Epox (a new-generation proteasome inhibitor that can noncovalently bind to the subunits of the proteasome in an irreversible manner [27]) decreased the viability of A2780 cells in a concentration-dependent manner (Figure 1(a)). As shown in Figure 1(b), the IC$_{50}$ values of cisplatin in A2780 and SKOV3 cells were 5.5 ± 0.18 and 17.89 ± 4.02 μg/ml, respectively. This demonstrated that SKOV3 cells were less sensitive to both cisplatin and proteasome inhibition. To further determine the effect of proteasomes on the sensitivity of ovarian cancer cells to cisplatin, we treated A2780 and SKOV3 cells with 100 nM Epox and different concentrations of cisplatin for 24 h and detected survival using MTT assays. The results demonstrated that Epox increased the sensitivity of A2780 cells, but not SKOV3

(a)

■ Cisplatin
■ Cisplatin+Epox

(b)
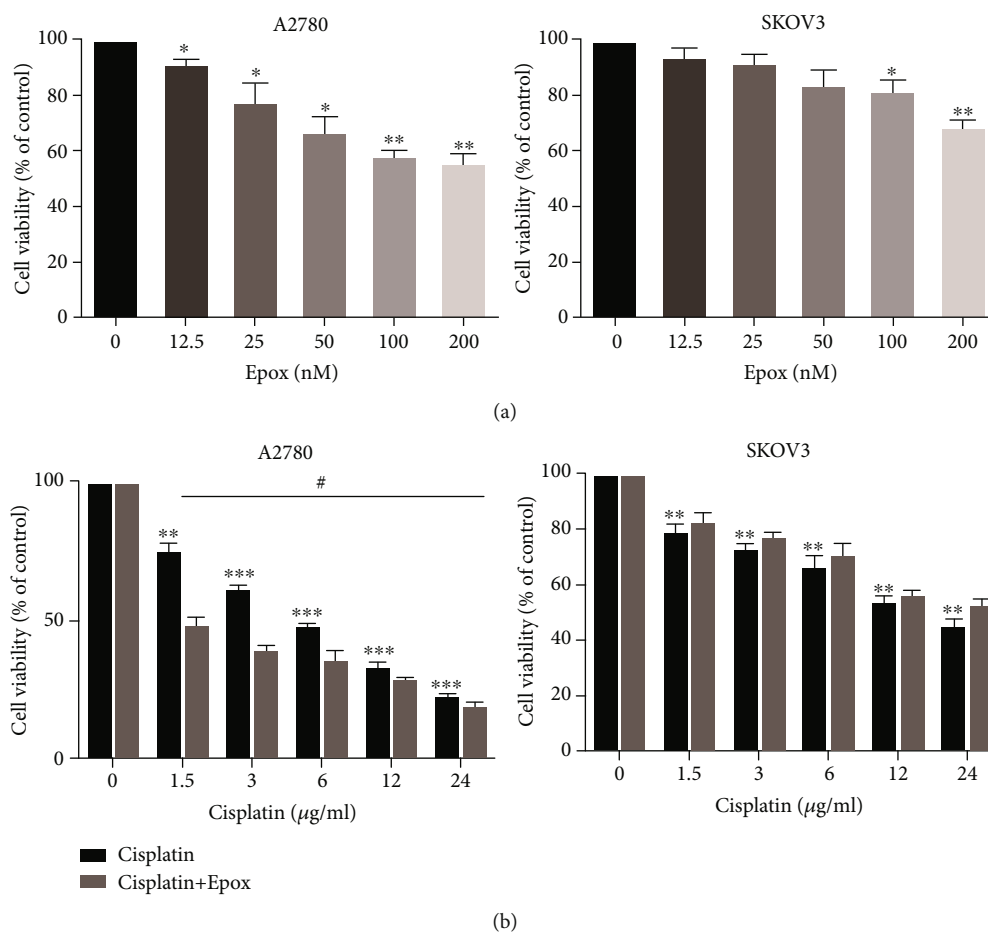
Figure 1: Proteasome inhibition can enhance the sensitivity of A2780 cells to cisplatin compared with SKOV3 cells. (a) A2780 and SKOV3 cells were treated with different concentrations of Epox for 24 h, and cell viability was determined using the MTT assay. Data are presented as the mean ± SD, $n = 3$, $^*P < 0.05$, $^{**}P < 0.01$ compared with the respective controls. (b) A2780 and SKOV3 cells were treated with 100 nM Epox and different concentrations of cisplatin for 24 h, and cell viability was determined using the MTT assay. Data are presented as the mean ± SD ($n = 3$), $^{**}P < 0.01$, $^{***}P < 0.001$ compared with the respective control, $^{#}P < 0.05$ compared with the cisplatin-treated groups.

cells, to cisplatin. These results suggested that the proteasome plays an important role in cisplatin resistance in SKOV3 cells.

3.2. Proteasome Inhibition Promotes Nrf2 Localization to the Nucleus through the Keap1/Nrf2 Pathway. Although inhibition of the proteasome pathway has emerged as an important strategy for anticancer therapy [28], not all cancer cells are sensitive to proteasome inhibitors. Studies have identified the Nrf2 pathway as one of the mechanisms of resistance to proteasome inhibitors [29]. To investigate whether Nrf2 is involved in resistance to proteasome inhibitors, the expression of Nrf2 in the nucleus was examined. After treatment with Epox for 12 h, an increased expression of Nrf2 in the nucleus was observed in both A2780 and SKOV3 cells (Figures 2(a) and 2(b)). The immunofluorescence assay also revealed that the localization of Nrf2 in the nucleus was enhanced by Epox treatment (Figure 2(c)). As the Keap1/Nrf2 pathway plays an important role in the stabilization of Nrf2, we further detected the colocalization of Keap1 and Nrf2. The immunoprecipitation and immunofluorescence results revealed that Keap1 and Nrf2 colocalization

was decreased by Epox treatment (Figures 2(d) and 2(e)). These results suggested that proteasome inhibition promotes Nrf2 localization to the nucleus through the Keap1/Nrf2 pathway.

3.3. Proteasome Inhibition Enhances Antioxidant and Antiapoptosis Activity in SKOV3 Cells Compared with A2780 Cells. Nrf2 translocates to the nucleus to activate the transcription of ARE-containing genes [30], and thus, we determined the expression of genes in the Nrf2 pathway. To our surprise, the expression of NQO-1, GCLC, HO-1, SOD2, and G6PDH genes was all reduced after treatment with Epox for 12 h in A2780 cells, whereas the opposite results were obtained in SKOV3 cells (Figure 3(a)). To further determine the effect of proteasome inhibition on redox levels, we detected ROS levels via flow cytometry. The results revealed that Epox increased ROS levels in A2780 cells, whereas no significant changes were noted in SKOV3 cells (Figure 3(b)). In addition, Annexin V/PI staining revealed that the rate of apoptosis after exposure to Epox for 24 h was higher in A2780 cells than in SKOV3 cells (Figure 3(c)). This suggested that the increased expression

(a)

(b)

(c)

(d)

(e)
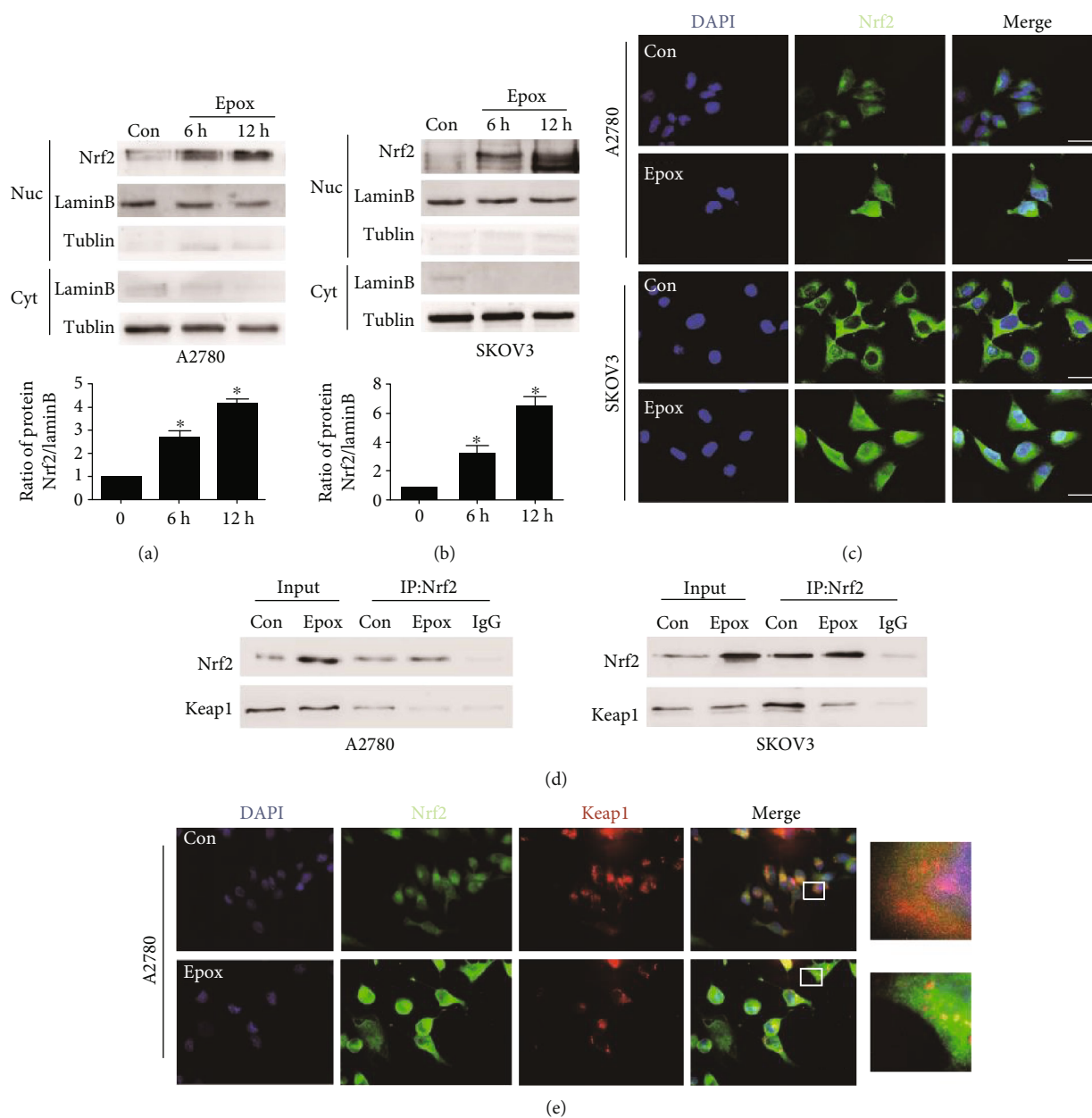
FIGURE 2: Proteasome inhibition promotes nuclear factor E2-related factor 2 (Nrf2) localization to the nucleus through the Kelch-like ECH-associated protein 1 (Keap1)/Nrf2 pathway. (a, b) The nuclear proteins of A2780 and SKOV3 cells were collected after treatment with 100 nM Epox for 6 or 12 h, and Nrf2 levels were measured via Western blotting. Data are presented as the mean ± SD, $n = 3$, $^*P < 0.05$ compared with the respective controls. A2780 and SKOV3 cells were treated with 100 nM Epox for 12 h. (c) Immunofluorescence staining was used to determine the location of Nrf2 in the nucleus (magnification, ×400). (d) Immunoprecipitation was performed using anti-Nrf2 antibody followed by Western blotting using anti-Nrf2 and anti-Keap1 antibodies. (e) Immunofluorescence staining was used to assess the colocalization of Nrf2 with Keap1 (magnification, ×400).

of Nrf2 in the nucleus did not necessarily exert antioxidant activity after proteasome inhibition; there may be regulatory factors regulating its transcriptional activity. It has been reported that PGC1α is also associated with the expression of mitochondrial ROS-detoxifying enzymes [31], and the activity of Nrf2 dose depends on PGC1α upon redox imbalance [17]. Therefore, we examined the gene expression of PGC1α and found that Epox can reduce its level in A2780 cells but increase its level in SKOV3 cells (Figure 3(d)). Notably, the expression of PGC1α was higher in SKOV3 cells than

in A2780 cells (Figure 3(e)). These results indicated that compared with A2780 cells, proteasome inhibition enhances antioxidant and antiapoptosis activity in SKOV3 cells, and this may have resulted from the synergistic roles of Nrf2 and PGC1α.

3.4. PGC1α Regulates the Antioxidant Activity of Nrf2 through GSK3β after Proteasome Inhibition in SKOV3 Cells. There is protein-protein interaction between PGC1α and Nrf2. In our experiment, proteasome inhibition increased

(a)

(b)

(c)

(d)

(e)
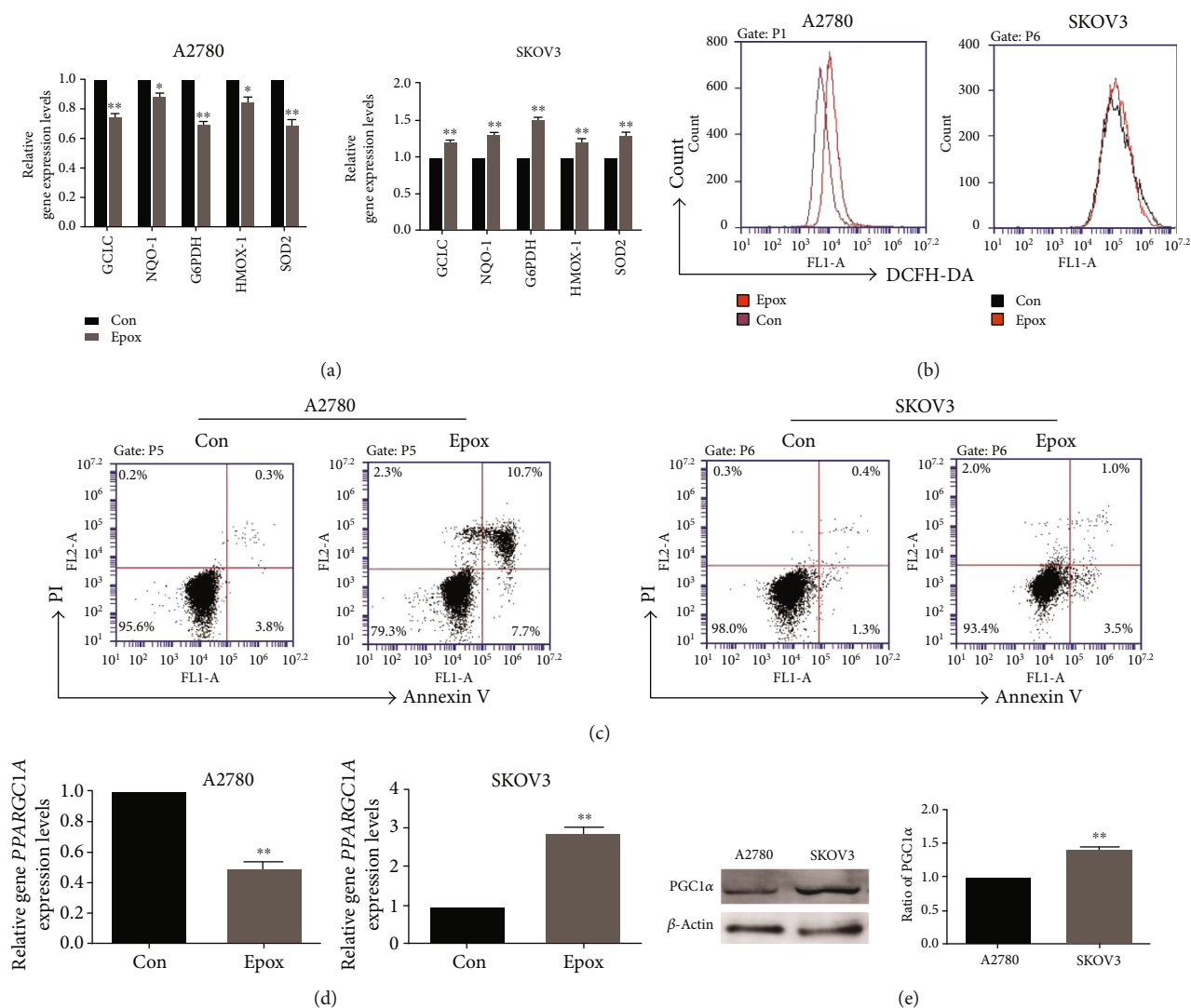
Figure 3: Proteasome inhibition enhances the antioxidant and antiapoptosis activity in SKOV3 cells but not A2780 cells. A2780 and SKOV3 cells were both treated with 100 nM Epox for 12 h. (a) RT-qPCR was used to detect the mRNA expression of *GCLC*, *NQO-1*, *SOD2*, *HMOX-1*, and *G6PDH*. Data are presented as the mean ± SD, $n = 3$, $^*P < 0.05$, $^{**}P < 0.01$ compared with the respective controls. (b) DCFH-DA staining was used to evaluate reactive oxygen species (ROS) levels. (c) Annexin V/PI staining was used to evaluate apoptosis levels after exposure to Epox for 24 h. (d) Relative *PPARGC1A* mRNA expression was measured by RT-qPCR after exposure to Epox for 12 h. Data are presented as the mean ± SD, $n = 3$, $^{**}P < 0.01$ compared with the respective controls. (e) Western blot analysis of peroxisome proliferator-activated receptor-γ coactivator 1α (PGC1α) expression in A2780 and SKOV3 cells. Data are presented as the mean ± SD, $n = 3$, $^{**}P < 0.01$ compared with A2780 cells.

the colocalization of Nrf2 and PGC1α in the nucleus (Figure 4(a)). PGC1α could coactivate Nrf2 and assist the induction of antioxidant genes. So, we investigated whether PGC1α was involved in the regulation of Nrf2 antioxidant activity after proteasome inhibition in SKOV3 cells. RT-qPCR analyzed the expression of genes in the Nrf2 pathway, and the result illustrated that the increased levels of Nrf2 and antioxidant genes after Epox treatment were reversed by PGC1α silencing (Figures 4(b) and 4(c)). GSK3β interferes with Nrf2 transactivating activity, so we further investigated whether PGC1α regulated Nrf2 activity through GSK3β. Results from our Western blot analysis demonstrated that PGC1α silencing reduced the level of Ser9 phosphorylated GSK3β, whereas ZLN005 (a PGC1α transcription activator)

enhanced its level (Figures 4(d) and 4(e)). When combined with GSK3β inhibitor (CHIR99021) in the presence of PGC1α silencing, the decreased levels of Nrf2 and antioxidant genes were reversed (Figure 4(f)). These results indicated that in SKOV3 cells, PGC1α regulates Nrf2 activity via GSK3β inactivation after proteasome inhibition. But whether GSK3β regulates Nrf2 directly or indirectly after Epox treatment and the specific mechanism of regulation needs to be further explored in future research.

3.5. Nrf2 Regulates PGC1α at the Transcriptional Level in SKOV3 Cells. The PGC1α promoter contains a conserved ARE sequence that can be bound by Nrf2, so we also determined whether Nrf2 directly binds to the PGC1α promoter
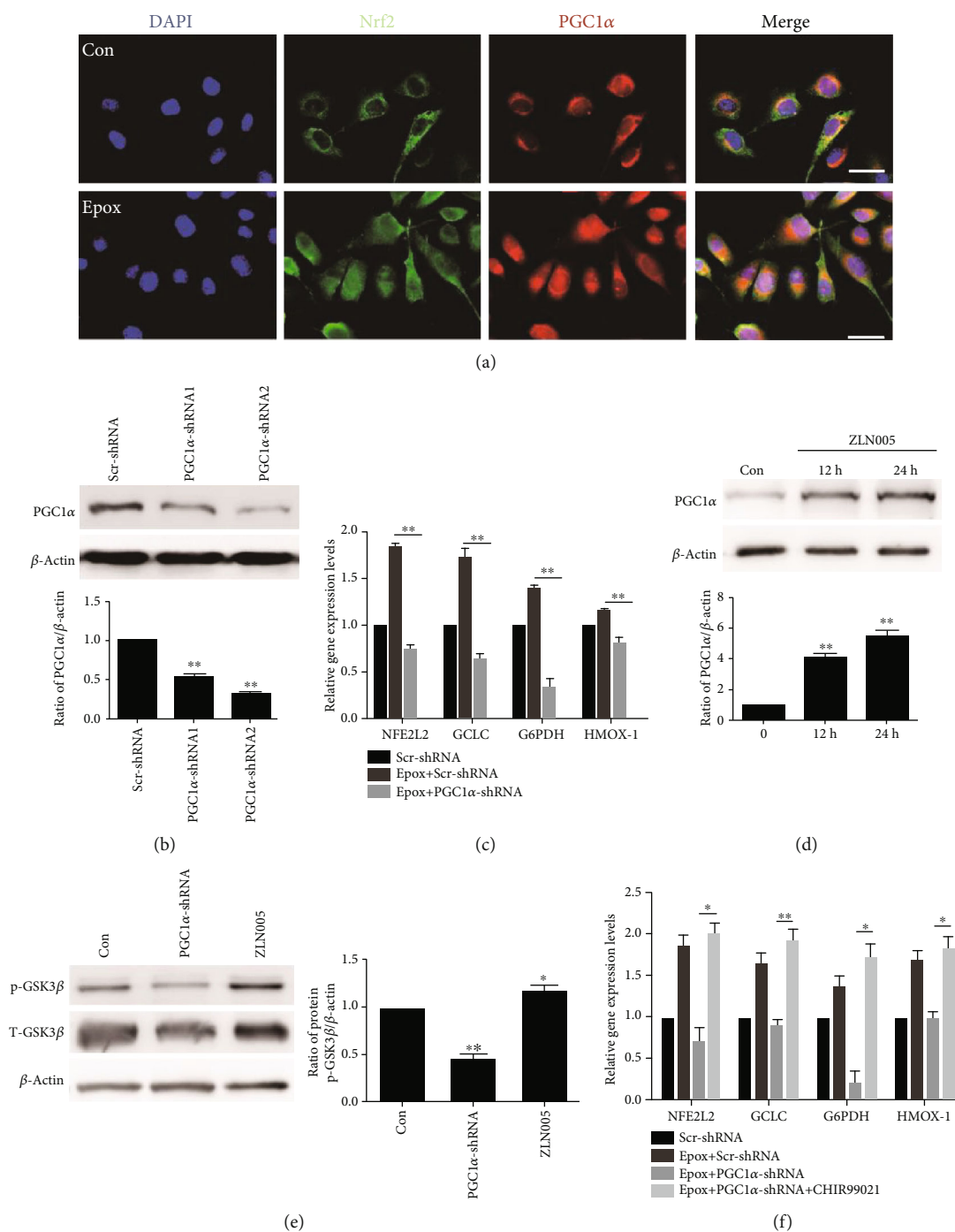
FIGURE 4: Proliferator-activated receptor-γ coactivator 1α (PGC1α) regulates the antioxidant activity of Nrf2 through glycogen synthase kinase 3β (GSK3β) after proteasome inhibition in SKOV3 cells. (a) SKOV3 cells were treated with Epox for 12 h. The colocalization of Nrf2 and PGC1α in the nucleus was determined via staining and observed via fluorescence microscopy (magnification, ×400). Western blotting was used to measure the expression of PGC1α after transfection with Scr-shRNA or PGC1α-shRNA plasmids (b) or treatment with 20 μM ZLN005 for 12 or 24 h (d). Data are presented as the mean ± SD, $n = 3$, **$P < 0.01$ compared with the respective controls. (c) After transfection with Scr-shRNA or PGC1α-shRNA plasmids, SKOV3 cells were treated with 100 nM Epox for 12 h. RT-qPCR was used to detect the expression of *NFE2l2*, *GCLC*, *HMOX-1*, and *G6PDH* mRNA. Data are presented as the mean ± SD, $n = 3$, **$P < 0.01$. (e) SKOV3 cells were treated with 20 μM ZLN005 for 24 h or transfected with PGC1α shRNA plasmids. Western blot analysis of the expression of p-GSK3β and GSK3β. Data are presented as the mean ± SD, $n = 3$, *$P < 0.05$, **$P < 0.01$ compared with the control. (f) After transfection with Scr-shRNA or PGC1α-shRNA plasmids, cells were treated with Epox (100 nM, 12 h) with or without CHIR99021 (5 μM, 36 h). Relative *NFE2l2*, *GCLC*, *HMOX-1*, and *G6PDH* mRNA expression was measured by RT-qPCR. Data are presented as the mean ± SD, $n = 3$, *$P < 0.05$, **$P < 0.01$.

(a)

(b)

(c)
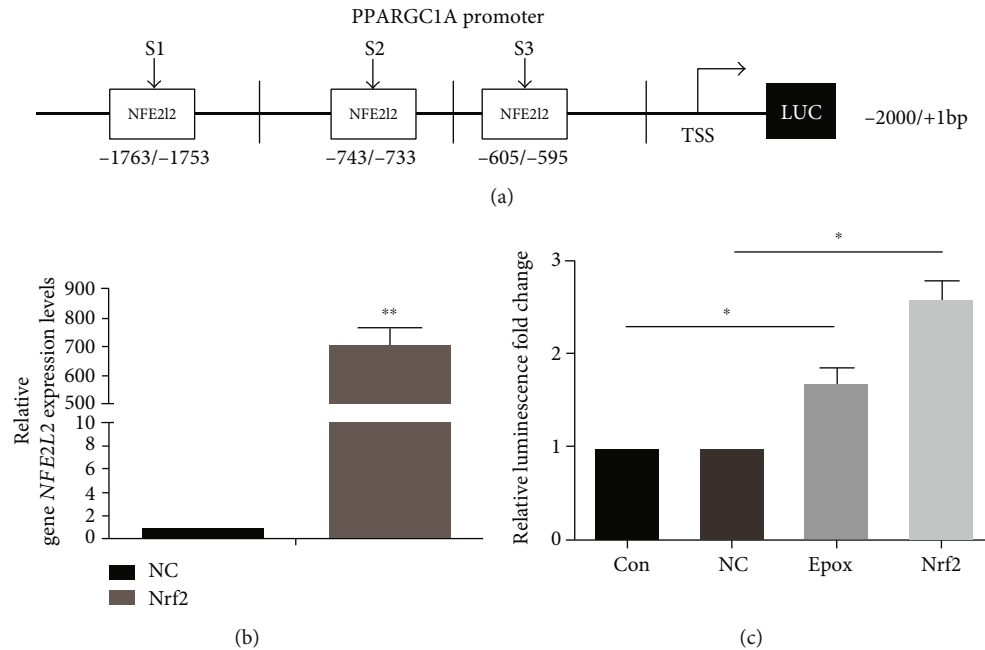
Figure 5: Nuclear factor E2-related factor 2 (Nrf2) regulates peroxisome proliferator-activated receptor-γ coactivator 1α (PGC1α) at the transcriptional level in SKOV3 cells. (a) Schematic diagram of the sequence spanning from -2000 to $+1$ relative to the translational start site (TSS) of the PGC1α promoter containing the Nrf2 motif. (b) SKOV3 cells were transfected with Nrf2 or pcDNA3.1 plasmids (vector plasmid as the NC group). Relative *NFE2l2* mRNA expression was measured by RT-qPCR. Data are presented as the mean $\pm$ SD, $n = 3$, ** $P < 0.01$ compared with NC group. (c) The luciferase activities of Epox-treated or Nrf2 overexpression SKOV3 cells transfected with pGL4-PGC1α and *Renilla* luciferase reporter (pRL-TK) plasmids were determined using dual-luciferase reporter assays. Data are presented as the mean $\pm$ SD, $n = 3$, *$P < 0.05$.

after proteasome inhibition in SKOV3 cells. We analyzed the PGC1α promoter sequence using the JASPAR database (http://jaspardev.genereg.net/) and predicted three potential Nrf2-binding fragments (Figure 5(a)). To further confirm that Nrf2 regulates PGC1α promoter activity, we performed a dual-luciferase reporter assay. The PGC1α promoter fragment $-2000/+1$ bp was cloned in to the pGL4-basic vector and then cotransfected with a *Renilla* luciferase reporter plasmid into SKOV3 cells. We observed that both overexpression of Nrf2 or treatment with Epox markedly upregulated the transcriptional activity of PGC1α (Figures 5(b) and 5(c)). These data provide evidence that Nrf2 regulates PGC1α expression at the transcriptional level in SKOV3 cells.

3.6. Nrf2 Activation Enhances Mitochondrial Function in SKOV3 Cells. In addition to antioxidant properties, Nrf2 has an emerging role in mitochondrial function, and this may be through activating the transcription of PGC1α. To confirm this, we treated SKOV3 cells with Epox for 12 h or overexpressed Nrf2. JC-1 fluorescent staining was used to measure mitochondrial membrane potential (MMP, $\Delta\Psi$m) (Figure 6(a)), and MitoTracker Red staining was used to measure mitochondrial mass (Figure 6(b)). The results indicated that Epox treatment or Nrf2 overexpression increased MMP and mitochondrial mass. ATP levels and mitochondrial DNA (mtDNA) copy numbers were both enhanced after treatment with Epox or Nrf2 overexpression (Figures 6(c) and 6(d)). Furthermore, we analyzed the effect of Nrf2 on the oxygen consumption rates (OCR) and found

that exposure to Epox or overexpression of Nrf2 increased the OCR in SKOV3 cells (Figure 6(e)). To detect the effect of Nrf2 activation on the mitochondrial chain, we extracted mitochondria and used Western blotting to measure protein expression. As shown in Figure 6(f), Epox treatment or Nrf2 overexpression significantly increased the expression of complex I (NDUFB8), complex II (SDHB), complex III (UQCRC2), complex IV (COXII), and complex V (ATP5A). However, mitochondrial-related functions were downregulated in A2780 cells (Supplementary Figure 1), further indicating that the increased nucleus expression of Nrf2 after treatment with Epox did not have activity in A2780 cells. In summary, we conclude that the activation of Nrf2 through Epox treatment or Nrf2 overexpression enhanced mitochondrial function in SKOV3 cells.

3.7. PGC1α Silencing Combined with Epox Treatment Promotes Apoptosis by Reducing Mitochondrial Function. To further verify whether Nrf2/PGC1α signaling-mediated antioxidation and mitochondrial function play important roles in Epox resistance in SKOV3 cells, PGC1α was silenced via transient shRNA transfection. Decreased MMP is an early event of apoptosis. Flow cytometry was used to determine the effect of PGC1α silencing on MMP. The results demonstrated that PGC1α silencing reduced MMP, and the effect was further exacerbated by combined treatment with Epox (Figure 7(a)). Furthermore, Annexin V/PI staining revealed that PGC1α silencing increased the rate of apoptosis, which was further increased in cells treated with PGC1α shRNA

(a)

(b)

(c)

(d)

(e)

FIGURE 6: Continued.

(f)
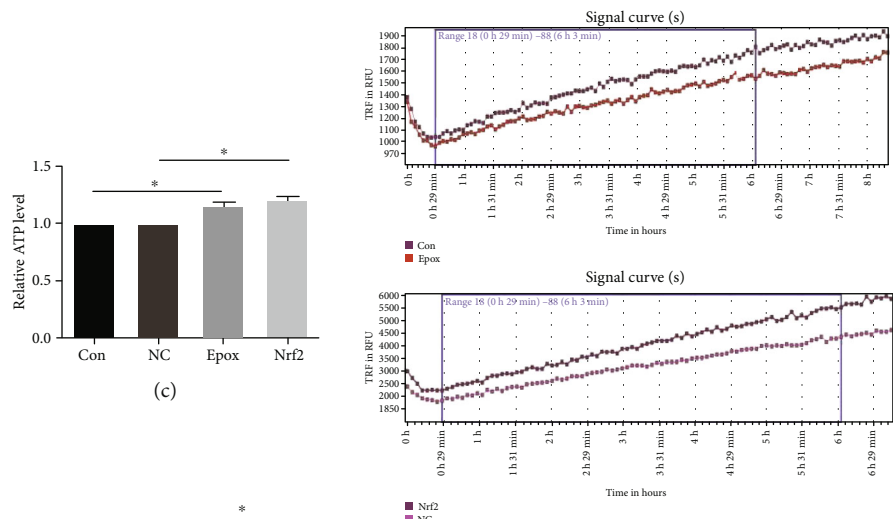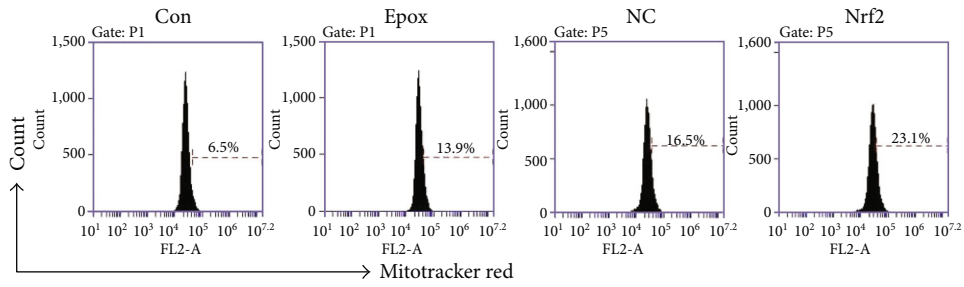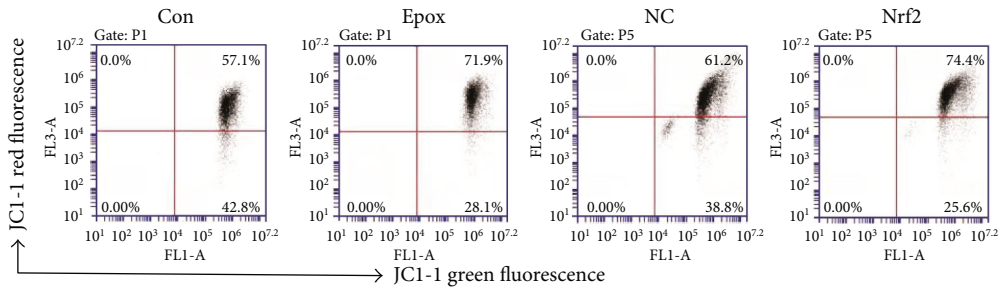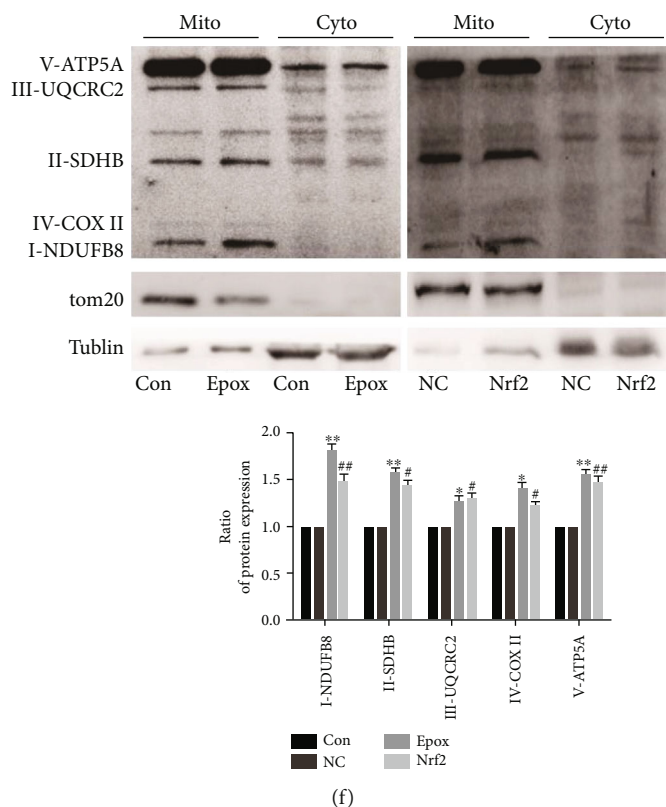
FIGURE 6: Nuclear factor E2-related factor 2 (Nrf2) activation enhances mitochondrial function in SKOV3 cells. SKOV3 cells were treated with 100 nM Epox for 12 h or transfected with Nrf2 or pcDNA3.1 plasmids (vector plasmid as the NC group). (a) JC-1 staining was used to evaluate MMP, and (b) MitoTracker™ Red staining was used to evaluate the alteration of mitochondrial mass via flow cytometry. (c) ATP production was determined using an ATP Bioluminescence Assay Kit, and (d) relative mtDNA copy numbers were determined by RT-qPCR. Data are presented as the mean $\pm$ SD, $n = 3$, $^*P < 0.05$. (e) The oxygen consumption rate was detected using fluorescent oxygen-sensitive probes. Data are presented as the mean $\pm$ SD, $n = 3$, $^*P < 0.05$. (f) Mitochondrial proteins were collected, and the expression of mitochondrial respiratory chain proteins was analyzed via Western blotting. Data are presented as the mean $\pm$ SD, $n = 3$, $^*P < 0.05$, $^{**}P < 0.01$ compared with the control, $^\#P < 0.05$, $^{\#\#}P < 0.01$ compared with NC.

and Epox (Figure 7(b)). In addition, we examined the expression of Bcl2 family members in SKOV3 cells after treatment with Epox and transfection with PGC1α shRNA. The Bcl2/Bax ratio was reduced by PGC1α silencing, and further decreases were observed in cells treated with both Epox and PGC1α shRNA. The expression of cleaved caspase 3 was also intensified in the combination treatment group (Figure 7(c)). What is more, the MTT assay demonstrated that PGC1α silencing increased the sensitivity of SKOV3 cells to Epox compared with the Scr-shRNA group (Figure 7(d)). These results suggested that PGC1α silencing combined with Epox treatment promotes apoptosis by reducing mitochondrial function.

4. Discussion

Chemotherapy resistance remains a barrier in the clinical treatment of ovarian cancer. When considering chemotherapy resistance, different aspects of drug resistance must be considered comprehensively [32]. Protein degradation and antioxidation are considered two factors of resistance to chemotherapy. Abnormally increased proteasomal activity has been observed in a variety of cancers, including breast cancer,

colon cancer, and leukemia [6, 7, 33]. Kwak et al. demonstrated that antioxidants can induce the expression of multiple proteasome subunits in mouse fibroblasts [8]. Therefore, antioxidants are involved in the regulation of proteasomal activity, and they play important roles in tumorigenesis and development. In this study, we compared two ovarian cancer cells, A2780 and SKOV3. SKOV3 cell was chosen because it is platinum-resistant and possesses several key oncogenic characteristics, like epidermal growth factor receptor (EGFR) overexpression and p53 mutation [34, 35]. In our study, compared with the findings in A2780 cells, SKOV3 cells were less sensitive to both proteasome inhibitors and cisplatin. When the proteasome was inhibited, the antioxidant capacity was decreased, and the sensitivity of A2780 cells to cisplatin was increased. The opposite results were observed in SKOV3 cells. This suggests that proteasomes and antioxidants may be involved in the differing sensitivity of A2780 and SKOV3 cells to cisplatin.

Proteasomes are closely involved in the regulation of multiple pathways within cells, and increased proteasomal activity is essential for tumor cell survival based on their ability to regulate tumor cell drug resistance through multiple pathways [7, 36, 37]. Inhibition of the proteasome can further

(a)

(b)

(c)

(d)

FIGURE 7: Continued.

(e)
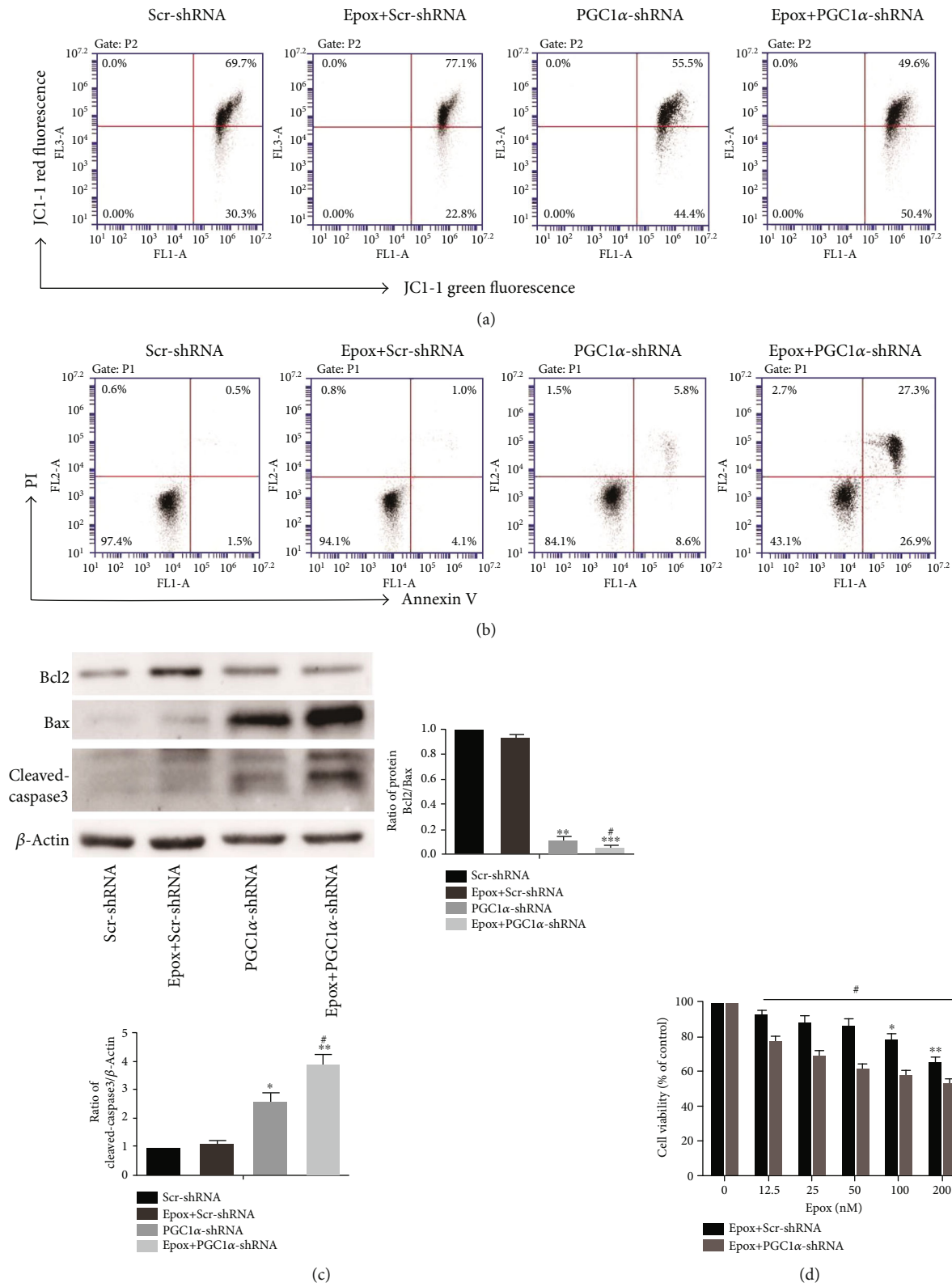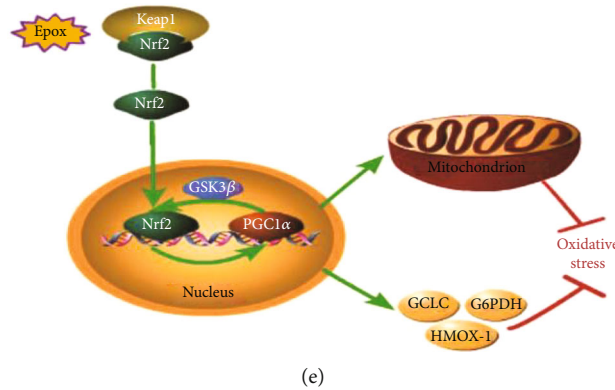
FIGURE 7: Proliferator-activated receptor-γ coactivator 1α (PGC1α) silencing combined with Epox treatment promotes apoptosis by reducing mitochondrial function. (a) SKOV3 cells were transfected with Scr-shRNA or PGC1α-shRNA plasmids for 24 h and/or treated with 100 nM Epox for 12 h. JC-1 staining was used to evaluate MMP. SKOV3 cells were transfected with Scr-shRNA or PGC1α-shRNA plasmids for 24 h and/or treated with 100 nM Epox for 24 h. (b) Annexin V/PI staining was used to evaluate the apoptotic fraction, and (c) apoptosis protein expression was analyzed via Western blotting. Data are presented as the mean ± SD, $n = 3$, *$P < 0.05$, **$P < 0.01$, ***$P < 0.001$ compared with the control, #$P < 0.05$ compared with treatment with Epox+Scr-shRNA and PGC1α-shRNA. (d) SKOV3 cells were transfected with Scr-shRNA or PGC1α-shRNA plasmids and/or treated with 100 nM Epox for 24 h, and cell viability was determined using the MTT assay. Data are presented as the mean ± SD, $n = 3$, *$P < 0.05$, **$P < 0.01$ compared with the control, #$P < 0.05$ compared with Epox+Scr-shRNA. (e) Proposed model of the antioxidant activity regulated by Nrf2 and PGC1α after Epox treatment.

increase oxidative stress in tumor cells, thereby promoting tumor cell apoptosis. However, recent studies have found that not all tumor cells are sensitive to proteasome inhibitors. A study in multiple myeloma demonstrated that the Nrf2 signaling pathway may be involved in proteasome-mediated tumor resistance [38]. Nrf2 has seven Neh domains, and of these, Neh1 can combine with Maf protein to form a heterodimer and bind to AREs and regulate the expression of antioxidant genes such as HO-1 and NQO-1 after Nrf2 translocates to the nucleus [39, 40]. In our study, although proteasome inhibition increased the nuclear expression of Nrf2 in both A2780 and SKOV3 cells, inhibiting the proteasome significantly reduced antioxidant levels and enhanced ROS production in A2780 cells. Conversely, the opposite results were obtained in SKOV3 cells. This suggested that the increased nuclear expression of Nrf2 did not necessarily exert antioxidant activity after proteasome inhibition; there may be regulatory factors regulating its transcriptional activity. Notably, PGC1α can regulate the expression of various antioxidant genes and play an important regulatory role in redox homeostasis [41]. Bruns et al. reported that PGC1α plays an important role in the clearance of ROS by regulating SOD1 and SOD2 in GBM glioblastoma cells [42]. In addition, a study using an aging disease model found that PGC1α can regulate Nrf2 expression and play a synergistic role in antioxidation [17]. Our study compared the expression of PGC1α in two cell lines and found that PGC1α expression was significantly higher in SKOV3 cells than in A2780 cells. After inhibiting proteasomes, PPARGC1A gene expression was increased in SKOV3 cells but decreased in A2780 cells, suggesting that PGC1α is also involved in proteasome inhibition-mediated antioxidant regulation. Thus, PGC1α and Nrf2 may jointly mediate the antioxidant regulation of proteasome inhibitor resistance in SKOV3 cells.

Recent studies revealed that PGC1α coactivate Nrf2, and there is a protein-protein interaction between PGC1α and

Nrf2. Here, we deeply investigated the mutual regulation between PGC1α and Nrf2 in SKOV3 cells. First, we found that proteasome inhibition in SKOV3 cells can increase the colocalization of Nrf2 and PGC1α in the nucleus. Cherry et al. demonstrated that PGC1α was important for the activation of gene downstream of Nrf2 during sepsis [43]. In our study, the increased Nrf2 and antioxidant gene mRNA levels after Epox treatment were reversed by PGC1α silencing, which suggested that PGC1α was involved in the antioxidant regulation by Nrf2 during proteasome inhibition. Furthermore, Nrf2 activity is mediated by GSK3β-TrCP-dependent Cul1-based ubiquitin ligase. Choi et al. demonstrated that PGC1α can upregulate Nrf2 through the p38/GSK3β pathway to protect HK-2 cells against hydrogen peroxide-induced oxidative stress injury [44]. This is consistent with our findings that PGC1α can mediate Nrf2 activity through the inactivation of GSK3β in SKOV3 cells. Therefore, PGC1α can regulate the antioxidant activity of Nrf2 via GSK3β after proteasome inhibition. But whether GSK3β regulates Nrf2 directly or indirectly after Epox treatment and the specific mechanism of regulation needs to be further explored in future research.

Although Clark and Simon previously proposed that the PGC1α promoter region contains a conserved ARE sequence that can be bound by Nrf2, it is unclear whether a transcription factor and PGC1α can form a complex to regulate Nrf2 expression or whether Nrf2 can directly bind to the PGC1α promoter region [41, 45]. After analyzing the PGC1α promoter sequence, three potential Nrf2-binding fragments were found. The dual-luciferase reporter assay found that Nrf2 upregulated the transcriptional activity of PGC1α after proteasome inhibition. The aforementioned data provided evidence that Nrf2 regulates PGC1α expression at the transcriptional level in SKOV3 cells. However, the specific molecular mechanism and promoter elements responsible for Nrf2 regulation need to be further explored. So far, we have

revealed a feedback loop between PGC1α and Nrf2, which enables them to play synergistic roles in the antioxidant function that maintains proteasomal activity.

Ross proposed that efficient UPS activity is essential for maintaining mitochondrial health, which is also necessary for maintaining UPS efficiency [18]. Inhibition of OXPHOS in mouse cortical neurons can inhibit proteasomal activity and protein ubiquitin [46]. Inhibition of ATP production via complex I inhibition can also inhibit proteasomal activity in primary mesencephalic cells [47]. Interestingly, Nrf2 also plays an inestimable role in regulating mitochondrial function. Nrf2 can regulate mitochondrial function through interactions with various mitochondrial proteins such as PGC1α. In SKOV3 cells, proteasome inhibition can enhance MMP, mitochondrial number, and mitochondrial complex protein expression, which in turn increase ATP and oxygen consumption. Overexpression of Nrf2 produced the same results, further proving that inhibiting proteasomes can enhance mitochondrial function through Nrf2. This is consistent with the findings of Shen et al., who reported that Nrf2 agonists can induce related mitochondrial functions such as mitochondrial proliferation in mouse 3T3-L1 adipocytes [48]. In addition, mitochondrial redox homeostasis is also important for maintaining proteasome activity. Gao et al. revealed that Nrf2 can upregulate mitochondrial antioxidant enzymes such as Sirt3 and SOD2 to maintain mitochondrial ROS homeostasis to protect neurons from oxidative stress [20]. In SKOV3 cells, we also observed that increased nuclear Nrf2 expression can upregulate the gene expression of SOD2. This indicated that the Nrf2/PGC1α pathway also participated in the regulation of proteasomal activity through the regulation of mitochondrial function and homeostasis in SKOV3 cells.

Finally, to further verify that the Nrf2/PGC1α pathway plays a role in resistance to proteasome inhibitors, we transfected shRNA-PGC1α plasmids into SKOV3 cells. The results illustrated that silencing of PGC1α could significantly promote apoptosis and decrease mitochondrial membrane potential of SKOV3 cells. When combined with Epox, apoptosis activity was further increased, and mitochondrial membrane potential was further decreased. This demonstrated that the Nrf2/PGC1α pathway is involved in the resistance of SKOV3 cells to proteasome inhibitors.

In summary, Nrf2 cooperates with PGC1α to mediate antioxidant function and mitochondrial function, thereby regulating the maintenance of proteasome activity and influencing differences in cisplatin sensitivity in ovarian cancer cells (Figure 7(e)).

Abbreviations

PGC1α: Peroxisome proliferator-activated receptor coactivator
MTT: 3-(4,5-Dimethylthiazol-2-yl)-2,5-diphenyltetrazolium bromide
GSK3β: Glycogen synthase kinase
Nrf2:   Nuclear factor (nuclear factor E2-related factor 2)
ND1:   Nicotinamide adenine dinucleotide dehydrogenase 1
UPS: Ubiquitin-proteasome system.

Data Availability

The datasets in the current study are available from the corresponding authors on reasonable request.

Conflicts of Interest

The authors declare that they have no competing interests.

Authors' Contributions

XYD performed cell research; NL and LX performed data curation; HGL, JYF, and YJ performed cell research. LKS and JS designed the research and supervised this study; XYD wrote the manuscript; JS and YNL reviewed and edited the draft. All authors have read and approved the final manuscript.

Acknowledgments

Supplementary Materials

EPOX decreases mitochobdrial function in A2780 cells. *(Supplementary Materials)*

References

[1] S. Kachalaki, M. Ebrahimi, L. Mohamed Khosroshahi, S. Mohammadinejad, and B. Baradaran, "Cancer chemoresistance; biochemical and molecular aspects: a brief overview," *European Journal of Pharmaceutical Sciences Official Journal of the European Federation for Pharmaceutical Sciences*, vol. 89, pp. 20–30, 2016.

[2] A. C. Lai and C. M. Crews, "Induced protein degradation: an emerging drug discovery paradigm," *Nature Reviews Drug Discovery*, vol. 16, no. 2, pp. 101–114, 2017.

[3] Q. Cui, J.-Q. Wang, Y. G. Assaraf et al., "Modulating ROS to overcome multidrug resistance in cancer," *Drug Resistance Updates*, vol. 41, pp. 1–25, 2018.

[4] L. N. Micel, J. J. Tentler, P. G. Smith, and G. S. Eckhardt, "Role of ubiquitin ligases and the proteasome in oncogenesis: novel targets for anticancer therapies," *Journal of Clinical Oncology*, vol. 31, no. 9, pp. 1231–1238, 2013.

[5] B. Wu, X. Chu, C. Feng et al., "Heat shock protein gp96 decreases p53 stability by regulating Mdm2 E3 ligase activity in liver cancer," *Cancer Letters*, vol. 359, no. 2, pp. 325–334, 2015.

[6] A. Kumatori, K. Tanaka, N. Inamura et al., "Abnormally high expression of proteasomes in human leukemic cells," *Proceedings of the National Academy of Sciences of the United States of America*, vol. 87, no. 18, pp. 7071–7075, 1990.

[7] A. Arlt, I. Bauer, C. Schafmayer et al., "Increased proteasome subunit protein expression and proteasome activity in colon cancer relate to an enhanced activation of nuclear factor E2-related factor 2 (Nrf2)," *Oncogene*, vol. 28, no. 45, pp. 3983–3996, 2009.

[8] M. K. Kwak, N. Wakabayashi, J. L. Greenlaw, M. Yamamoto, and T. W. Kensler, "Antioxidants enhance mammalian proteasome expression through the Keap1-Nrf2 signaling pathway," *Molecular & Cellular Biology*, vol. 23, no. 23, pp. 8786–8794, 2013.

[9] J. Adams, V. J. Palombella, and P. J. Elliott, "Proteasome inhibition: a new strategy in cancer treatment," *Investigational New Drugs*, vol. 18, no. 2, pp. 109–121, 2000.

[10] M. A. Weniger, E. G. Rizzatti, P. Perez-Galan et al., "Treatment-induced oxidative stress and cellular antioxidant capacity determine response to bortezomib in mantle cell lymphoma," *Clinical Cancer Research An Official Journal of the American Association for Cancer Research*, vol. 17, no. 15, pp. 5101–5112, 2011.

[11] H. A. Stessman, L. B. Baughn, A. Sarver et al., "Profiling bortezomib resistance identifies secondary therapies in a mouse myeloma model," *Molecular Cancer Therapeutics*, vol. 12, no. 6, pp. 1140–1150, 2013.

[12] X. Hou, X. Bai, X. Gou et al., "3′,4′,5′,5,7-Pentamethoxyflavone sensitizes cisplatin-resistant A549 cells to cisplatin by inhibition of Nrf2 pathway," *Molecules and Cells*, vol. 38, no. 5, pp. 396–401, 2015.

[13] H. M. Leinonen, E. Kansanen, P. Pölönen, M. Heinäniemi, and A. L. Levonen, "Role of the Keap1-Nrf2 pathway in cancer," *Advances in Cancer Research*, vol. 122, no. 4, pp. 281–320, 2014.

[14] M. Salazar, A. I. Rojo, D. Velasco, R. M. de Sagarra, and A. Cuadrado, "Glycogen synthase kinase-3β inhibits the xenobiotic and antioxidant cell response by direct phosphorylation and nuclear exclusion of the transcription factor Nrf2," *The Journal of Biological Chemistry*, vol. 281, no. 21, pp. 14841–14851, 2006.

[15] S. Chowdhry, Y. Zhang, M. McMahon, C. Sutherland, A. Cuadrado, and J. D. Hayes, "Nrf2 is controlled by two distinct β-TrCP recognition motifs in its Neh6 domain, one of which can be modulated by GSK-3 activity," *Oncogene*, vol. 32, no. 32, pp. 3765–3781, 2013.

[16] S. Baldelli, K. Aquilano, and M. R. Ciriolo, "Punctum on two different transcription factors regulated by PGC-1α: nuclear factor erythroid-derived 2-like 2 and nuclear respiratory factor 2," *Biochimica et biophysica acta*, vol. 1830, no. 8, pp. 4137–4146, 2013.

[17] K. Aquilano, S. Baldelli, B. Pagliei, S. M. Cannata, G. Rotilio, and M. R. Ciriolo, "p53 orchestrates the PGC-1α-mediated antioxidant response upon mild redox and metabolic imbalance," *Antioxidants & Redox Signaling*, vol. 18, no. 4, pp. 386–399, 2013.

[18] J. Ross, L. Olson, and G. Coppotelli, "Mitochondrial and ubiquitin proteasome system dysfunction in ageing and disease: two sides of the same coin?," *International Journal of Molecular Sciences*, vol. 16, no. 8, pp. 19458–19476, 2015.

[19] I. Smyrnias, X. Zhang, M. Zhang et al., "Nicotinamide adenine dinucleotide phosphate oxidase-4-dependent upregulation of nuclear factor erythroid-derived 2-like 2 protects the heart during chronic pressure Overload," *Hypertension*, vol. 65, no. 3, pp. 547–553, 2015.

[20] J. Gao, S. Liu, F. Xu et al., "Trilobatin protects against oxidative injury in neuronal PC12 cells through regulating mitochondrial ROS homeostasis mediated by AMPK/Nrf2/Sirt3 signaling pathway," *Frontiers in Molecular Neuroscience*, vol. 11, 2018.

[21] A. T. Dinkova-Kostova and A. Y. Abramov, "The emerging role of Nrf2 in mitochondrial function," *Free Radical Biology & Medicine*, vol. 88, no. Part B, pp. 179–188, 2015.

[22] A. S. Agyeman, R. Chaerkady, P. G. Shaw et al., "Transcriptomic and proteomic profiling of KEAP1 disrupted and sulforaphane-treated human breast epithelial cells reveals common expression profiles," *Breast Cancer Research and Treatment*, vol. 132, no. 1, pp. 175–187, 2012.

[23] R. D. Brose, G. Shin, M. C. McGuinness et al., "Activation of the stress proteome as a mechanism for small molecule therapeutics," *Human Molecular Genetics*, vol. 21, no. 19, pp. 4237–4252, 2012.

[24] M. A. Lebedeva, J. S. Eaton, and G. S. Shadel, "Loss of p53 causes mitochondrial DNA depletion and altered mitochondrial reactive oxygen species homeostasis," *Biochimica et biophysica acta*, vol. 1787, no. 5, pp. 328–334, 2009.

[25] N. G. Alkema, G. B. A. Wisman, A. G. J. van der Zee, M. A. T. M. van Vugt, and S. de Jong, "Studying platinum sensitivity and resistance in high-grade serous ovarian cancer: different models for different questions," *Drug Resistance Updates*, vol. 24, pp. 55–69, 2016.

[26] S. Narayanan, C.-Y. Cai, Y. G. Assaraf et al., "Targeting the ubiquitin-proteasome pathway to overcome anti-cancer drug resistance," *Drug Resistance Updates*, vol. 48, p. 100663, 2020.

[27] L. Meng, R. Mohan, B. H. B. Kwok, M. Elofsson, N. Sin, and C. M. Crews, "Epoxomicin, a potent and selective proteasome inhibitor, exhibits in vivo antiinflammatory activity," *Proceedings of the National Academy of Sciences of the United States of America*, vol. 96, no. 18, pp. 10403–10408, 1999.

[28] L. J. Crawford, B. Walker, and A. E. Irvine, "Proteasome inhibitors in cancer therapy," *Journal of Cell Communication and Signaling*, vol. 5, no. 2, pp. 101–110, 2011.

[29] E. E. Manasanch and R. Z. Orlowski, "Proteasome inhibitors in cancer therapy," *Nature Reviews. Clinical Oncology*, vol. 14, no. 7, pp. 417–433, 2017.

[30] M. Kobayashi and M. Yamamoto, "Nrf2-Keap1 regulation of cellular defense mechanisms against electrophiles and reactive oxygen species," *Advances in Enzyme Regulation*, vol. 46, no. 1, pp. 113–140, 2006.

[31] S. Kroeller-Schoen, T. Jansen, M. Hausding et al., "Deletion of peroxisome proliferator coactivator-1alpha accelerates angiotensin II induced endothelial dyfunction by increasing mitochondrial oxidative stress," *European Heart Journal*, vol. 34, (supplement 1, pp. P594–P594, 2013.

[32] D. J. Konieczkowski, C. M. Johannessen, and L. A. Garraway, "A convergence-based framework for cancer drug resistance," *Cancer Cell*, vol. 33, no. 5, pp. 801–815, 2018.

[33] L. Chen and K. Madura, "Increased proteasome activity, Ubiquitin-conjugating enzymes, and eEF1A translation factor detected in breast cancer tissue," *Cancer Research*, vol. 65, no. 13, pp. 5599–5606, 2005.

[34] Xin Tan, N. Sidell, A. Mancini et al., "Multiple anticancer activities of EF24, a novel curcumin analog, on human ovarian carcinoma cells," *Reproductive Sciences*, vol. 17, no. 10, pp. 931–940, 2010.

[35] N. Aide, K. Kinross, C. Cullinane et al., "18F-FLT PET as a surrogate marker of drug efficacy during mTOR inhibition

by everolimus in a preclinical cisplatin-resistant ovarian tumor model," *Journal of Nuclear Medicine*, vol. 51, no. 10, pp. 1559–1564, 2010.

[36] G. Sari, Z. Okat, A. Sahin, and B. Karademir, "Proteasome inhibitors in cancer therapy and their relation to redox regulation," *Current Pharmaceutical Design*, vol. 24, no. 44, pp. 5252–5267, 2019.

[37] C. T. Aiken, R. M. Kaake, X. Wang, and L. Huang, "Oxidative stress-mediated regulation of proteasome complexes," *Molecular & Cellular Proteomics*, vol. 10, no. 5, p. R110.006924, 2011.

[38] B. Li, J. Fu, P. Chen et al., "The nuclear factor (erythroid-derived 2)-like 2 and proteasome maturation protein axis Mediate bortezomib resistance in multiple myeloma," *Journal of Biological Chemistry*, vol. 290, no. 50, pp. 29854–29868, 2015.

[39] V. Krajka-Kuźniak, J. Paluszczak, and W. Baer-Dubowska, "The Nrf2-ARE signaling pathway: an update on its regulation and possible role in cancer prevention and treatment," *Pharmacological Reports*, vol. 69, no. 3, pp. 393–402, 2017.

[40] S. M. Poulose, D. F. Bielinski, A. Carey, A. G. Schauss, and B. Shukitt-Hale, "Modulation of oxidative stress, inflammation, autophagy and expression of Nrf2 in hippocampus and frontal cortex of rats fed with açaí-enriched diets," *Nutritional Neuroscience*, vol. 20, no. 5, pp. 305–315, 2016.

[41] J. St-Pierre, S. Drori, M. Uldry et al., "Suppression of reactive oxygen species and neurodegeneration by the PGC-1 transcriptional coactivators," *Cell*, vol. 127, no. 2, pp. 397–408, 2006.

[42] I. Bruns, B. Sauer, M. C. Burger et al., "Disruption of peroxisome proliferator-activated receptor gamma coactivator (PGC)-1α reverts key features of the neoplastic phenotype of glioma cells," *The Journal of Biological Chemistry*, vol. 294, no. 9, pp. 3037–3050, 2019.

[43] A. D. Cherry, H. B. Suliman, R. R. Bartz, and C. A. Piantadosi, "Peroxisome proliferator-activated receptor γ co-activator 1-α as a critical co-activator of the murine hepatic oxidative stress response and mitochondrial biogenesis in Staphylococcus aureus sepsis," *Journal of Biological Chemistry*, vol. 289, no. 1, pp. 41–52, 2014.

[44] H.-I. Choi, H.-J. Kim, J.-S. Park et al., "PGC-1α attenuates hydrogen peroxide-induced apoptotic cell death by upregulating Nrf-2 via GSK3β inactivation mediated by activated p38 in HK-2 Cells," *Scientific Reports*, vol. 7, no. 1, p. 4319, 2017.

[45] J. Clark and D. K. Simon, "Transcribe to survive: transcriptional control of antioxidant defense programs for neuroprotection in Parkinson's disease," *Antioxidants & Redox Signaling*, vol. 11, no. 3, pp. 509–528, 2009.

[46] Q. Huang, H. Wang, S. W. Perry, and M. E. Figueiredo-Pereira, "Negative regulation of 26S proteasome stability via calpain-mediated cleavage of Rpn10 subunit upon mitochondrial dysfunction in neurons," *Journal of Biological Chemistry*, vol. 288, no. 17, pp. 12161–12174, 2013.

[47] G. U. Höglinger, G. Carrard, P. P. Michel et al., "Dysfunction of mitochondrial complex I and the proteasome: interactions between two biochemical deficits in a cellular model of Parkinson's disease," *Journal of Neurochemistry*, vol. 86, no. 5, pp. 1297–1307, 2003.

[48] W. Shen, K. Liu, C. Tian et al., "R-α-Lipoic acid and acetyl-l-carnitine complementarily promote mitochondrial biogenesis in murine 3T3-L1 adipocytes," *Diabetologia*, vol. 51, no. 1, pp. 165–174, 2007.

Research Article

Mild Oxidative Stress Reduces NRF2 SUMOylation to Promote *Kras/Lkb1/Keap1* Mutant Lung Adenocarcinoma Cell Migration and Invasion

Jiaqian Xu,[1] **Haoyan Guo,**[1,2] **Zhengcao Xing,**[1,3] **Wenlong Zhang,**[1] **Jianli He,**[1] **Jinke Cheng,**[1] **and Rong Cai** [1]

[1]*Department of Biochemistry & Molecular Cell Biology, Shanghai Jiao Tong University School of Medicine, Shanghai 200025, China*
[2]*Department of Pathology, Beijing Obstetrics and Gynecology Hospital, Capital Medical University, Beijing 100026, China*
[3]*Department of Cell Biology, Shaanxi Normal University, Xi'an 710062, China*

Correspondence should be addressed to Rong Cai; rongcai@shsmu.edu.cn

Nuclear factor erythroid 2-related factor 2 (NRF2) is a crucial transcription factor for cell adaptation and defense against oxidative stress. NRF2 activation confers *Kras/Lkb1/Keap1* (KLK) mutant tumor cells with greater resistance to oxidative insults. We previously reported that SUMOylation at lysine residue 110 is important for the ability of NRF2 to promote reactive oxygen species (ROS) clearance in hepatocellular carcinoma. In this study, we investigated whether SUMOylation is necessary for the ability of NRF2 to inhibit KLK lung adenocarcinoma (LUAD) cell migration and invasion. Our experiments showed that mild oxidative stress reduced NRF2 SUMOylation, which promoted KLK LUAD cell migration and invasion. Mechanistically, NRF2 SUMOylation increased the antioxidant ability of NRF2 and reduced cellular ROS levels, mainly by transcriptionally activating *Cat* in KLK LUAD cells. With reduced NRF2 SUMOylation, increased ROS acted as signaling molecules to activate the JNK/c-Jun axis, which enhanced cell mobility and cell adhesion, to promote LUAD cell migration and invasion. Taken together, the results of this study reveal a novel signaling process in which reduced NRF2 SUMOylation permits increased KLK LUAD cell migration and invasion under mild oxidative stress.

1. Introduction

The role of reactive oxygen species (ROS) in cancer has remained controversial for decades, in part, because different levels of ROS confer different outcomes in cancer cells. High ROS levels are harmful to cell, but mild oxidative stress at sublethal levels activates signaling pathways to promote tumor growth and progression [1, 2]. Cancer cell migration and invasion are the initial steps of tumor metastasis. During cell migration and invasion, members of the mitogen-activated protein kinase (MAPK) family of proteins are activated by ROS [3–5]. In lung adenocarcinoma cells (LUAD), H_2O_2 activates epidermal growth factor (EGF) receptors [6]; hence, oxidization of receptor tyrosine kinases (RTKs) facilitates MAPK signaling activation and promotes migration and invasion [7].

In *Kras*-mutant LUAD, *Lkb1* is frequently inactivated [8–11]. LKB1 loss leads to increased oxidative stress in tumors [12, 13], which is tolerated at least partially through concurrent mutation of KEAP1 [11, 14]. KEAP1 mutation stabilizes nuclear factor erythroid 2-related factor 2 (NRF2) and increases its activity in LUAD [15, 16]. NRF2 is an important transcription factor in the defense of cancer cells against oxidative insults, through upregulation of antioxidant enzymes and detoxification proteins [17]. Thus, NRF2 activity is critical for reducing cellular ROS levels and maintaining redox homeostasis.

Previous research showed that drugs used in type 2 diabetes mellitus activate nuclear factor erythroid 2-related factor 2 (NRF2) and accelerate metastasis [18]. Recently, concurrent studies by two research groups demonstrated that activation of NRF2 caused by KEAP1 inactivation promotes

LUAD cell migration and metastasis by stabilizing the transcription factor BACH1, in $Kras^{LSL/+}$; $Trp53^{flox/flox}$ (KP) mice [19, 20]. However, the role of NRF2 activation in $Kras/Lkb1/-Keap1$ (KLK) mutant LUAD cell migration and metastasis remains unknown.

Multiple studies have reported that NRF2 is a SUMOylated protein [21–23]. Our previous research revealed that SUMOylation of lysine residue 110 (K110) of NRF2 reduces ROS levels, promotes de novo serine synthesis, and maintains hepatocellular carcinoma tumorigenesis [23]. In the present study, we investigated the effects of NRF2 on KLK LUAD cell migration and invasion, and whether SUMOylation is critical for these effects. We studied the effect of mild oxidative stress on NRF2 SUMOylation and then investigated the underlying mechanism by which NFR2 influences KLK LUAD cell migration and invasion.

2. Materials and Methods

2.1. Antibodies, Plasmids, and Reagents.
The sources for antibodies were as follows: NRF2 (Abcam; ab62352), BACH1 (R&D Systems; AF5776-SP), Catalase (Abcam; ab76024), GPX2 (GeneTex; GTX100292), SAPK/JNK (Cell Signaling Technology; 9252), phospho-SAPK/JNK (Thr183/Tyr185) (Cell Signaling Technology; 4668), ERK1+ERK2 (Abcam; ab36991), ERK1 (pT202/pY204)+ERK2 (pT185/pY187) (Abcam; ab50011), c-Jun (Cell Signaling Technology; 9165), Phospho-c-Jun (Ser73) (Cell Signaling Technology; 3270), p38 MAPK (Cell Signaling Technology; 9212), phospho-p38 MAPK (Thr180/Tyr182) (Cell Signaling Technology; 4511), His (Qiagen; 1007598), and β-actin (Abcam; ab8226). Plasmids PCDH-Vector, PCDH-NRF2, and PCDH-NRF2 K110R were constructed as previously reported [23]; PCDH-His-SUMO1 was cloned into PCDH-vector using standard PCR-based cloning strategies and the primers listed in Table S1. The shNRF2 lentivirus was designed and packaged by Genomeditech as previously reported [23]. The SimpleChIP® Plus Sonication Chromatin IP Kit was purchased from Cell Signaling Technology; the Amplite™ Colorimetric Hydrogen Peroxide Assay Kit was purchased from AAT Bioquest; the eBioscience™ Annexin V Apoptosis Detection Kit was purchased from Invitrogen; the GSH and GSSG Assay Kit was purchased from Beyotime Biotechnology; and the CellROX® Deep Red Flow Cytometry Assay Kit was purchased from Invitrogen.

2.2. Cell Culture and Construction of Stable Cell Lines.
The human LUAD cell line A549 was cultured in F12K medium (Gibco), while H2122 and H23 cells were cultured in RPMI medium (HyClone). Each medium contained 10% fetal bovine serum (Gibco) and 1% penicillin/streptomycin. These cells were cultured in a humidified 37°C incubator with 5% CO_2. Cells were infected by shNRF2 and/or PCDH-NRF2/NRF2 K110R lentivirus and then selected by Blasticidin S or Puromycin for 1 week.

2.3. Western Blotting.
Cells were washed with phosphate-buffered saline (PBS), lysed in radio immunoprecipitation assay (RIPA) buffer (150 mM NaCl, 50 mM Tris base, 0.1% SDS, 1% Triton-X-100, pH 7.4) on ice for 20 min, and then ultrasonicated until the solution became clear. Protease and phosphatase inhibitors were added to the RIPA buffer in advance. The cell lysates were centrifuged at 12,000 rpm for 15 min at 4°C, and the supernatant was collected for Western blotting. Total protein was resolved in 10% SDS/PAGE gels, followed by electrophoretic transfer to PVDF membranes in a Tris-glycine buffer. The membranes were blocked at room temperature for 1 h in 5% nonfat milk with TBS-Tween (TBS-T) on a shaker and then incubated with the primary antibodies overnight at 4°C. The membranes were washed in TBST at least 5 times (5 min each) and then incubated with HRP conjugated anti-rabbit or anti-mouse IgG at room temperature for 1 h with gentle shaking. The ECL substrate was added, and the results were visualized using Image-Quant LAS 4000 (GE). β-Actin was used as loading control.

2.4. Quantitative Real-Time PCR.
Total RNA was isolated using TRIzol universal reagent (TianGen). Then, 1 μg RNA was reverse transcribed into complementary DNA (cDNA) using the Fast King gDNA Dispelling RT SuperMix kit (Tian-Gen). Quantitative real-time PCR was performed on Light-Cycler 480 (Roche) using TB Green Premix (Takara). 18S rRNA was used as a control for normalization. The primers used in this study are listed in Supplementary Table S1.

2.5. Migration and Invasion Assay.
For the migration assay, cells were resuspended in serum-free medium and plated in the upper chamber of Transwells (Corning) in a 24-well plate. The cell numbers were 1×10^4 to 1×10^5 per well. For the invasion assay, Transwells were coated with Matrigel matrix (Corning). Medium with 10% fetal bovine serum (FBS) was added in the bottom chamber of the Transwells. The cells on the upper surface of the chamber were removed using a cotton swab, and the cells on the bottom of the chamber were fixed with 4% paraformaldehyde and stained with crystal violet 12-16 h later. For H_2O_2 treatment, 0.5, 50, or 500 μM H_2O_2 was added into the upper chamber. The migrating and invading cells were counted in micrographs taken of 5 random fields using Photoshop, and the data were analyzed using Graphpad Prism.

2.6. NRF2 SUMOylation by Ni^{2+}-NTA Pull-down Assay.
Cells were infected with PCDH-His-SUMO1 lentivirus and selected by puromycin for 1 week. Once the cells reached 70% confluency, they were treated with H_2O_2 (0.5, 50, or 500 μM) for 12 h. For NAC (N-acety-L-cysteine) treatment, cells were pretreated with 1 mM NAC for 1 h, and then, H_2O_2 was added for further incubation for 12 h. Ni^{2+}-NTA pull-down assay was performed as previously reported [23].

2.7. Measurement of Intracellular ROS.
Cells were digested by trypsin and incubated with CellROX (final concentration of 100 nM; Invitrogen) in complete medium for 20 min at 37°C. Cells were then washed and resuspended in fluorescence-activated cell sorting (FACS) buffer. Intracellular ROS levels were measured by flow cytometry (Becton Dickinson).

2.8. Measurement of H_2O_2.
Cells were resuspended in a 96-well plate, and the H_2O_2 concentration in each well was

(a)

(b)

Figure 1: Continued.

(c)
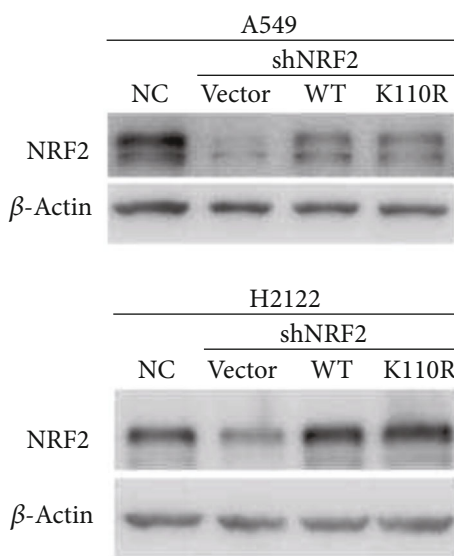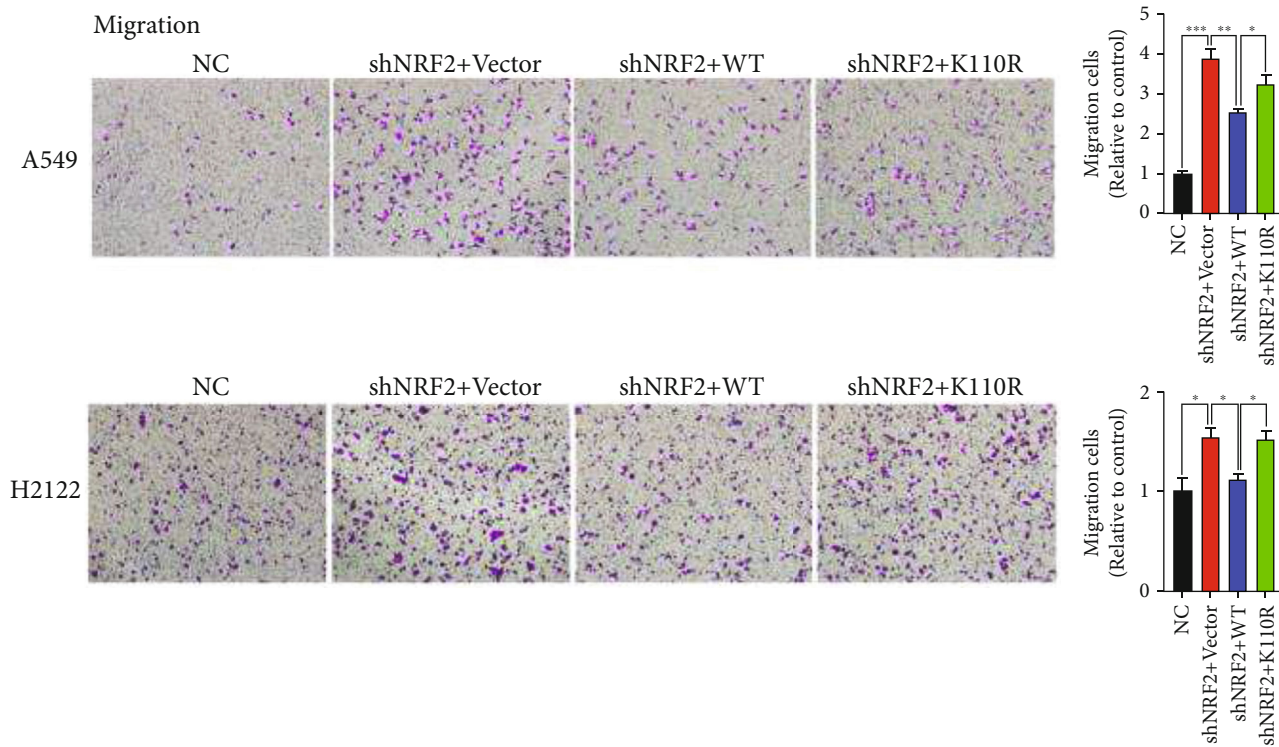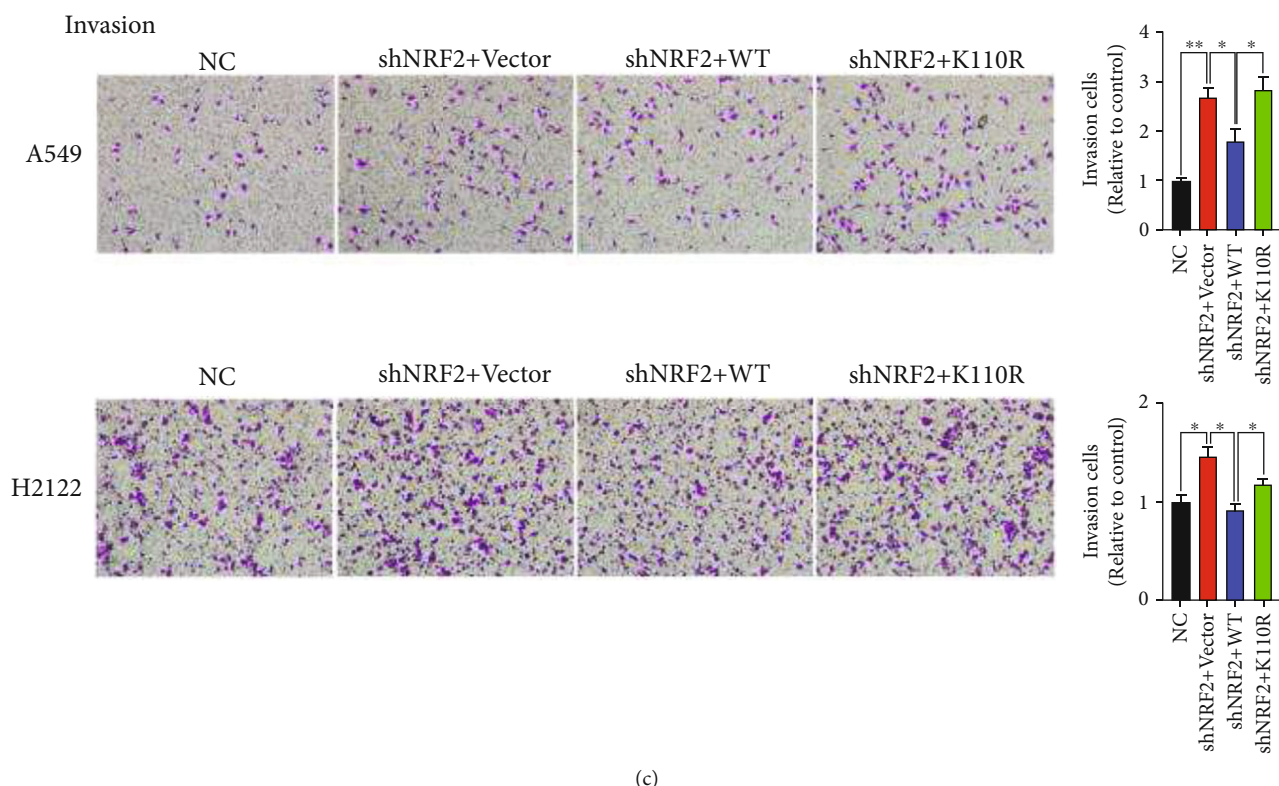
FIGURE 1: SUMOylation of NRF2 is critical for its inhibition of KLK LUAD cell migration and invasion. (a) Establishment of KLK LUAD A549 and H2122 cells, which have endogenous NRF2 knockdown, stably expressing NRF2 wild-type, and NRF2 K110R. (b) The migration of four stable cell lines derived from A549 and H2122 cells, as detected by Transwell assays (3 replicates per group). (c) The invasion of four stable cell lines derived from A549 and H2122 cell as detected by Transwell assay (3 replicates per group). KLK: *Kras*-activated mutation, *Lkb1*-inactivated mutation, and *Keap1*-inactivated mutation; LUAD: lung adenocarcinoma. $*P < 0.05$, $**P < 0.01$, and $***P < 0.001$.

measured using the Amplite Colorimetric Hydrogen Peroxide Assay Kit (AAT Bioquest) the next day. Briefly, $50\,\mu l$ of H_2O_2 cell working solution was added to each well of cells and H_2O_2 standards to make the total H_2O_2 assay volume of $100\,\mu l$/well. The reaction was incubated at room temperature for 10-60 min and protected from light. Then, the absorbance at 650 nm was measured by an absorbance plate reader.

2.9. RNA-Seq. RNA-Seq was performed by KangChen Biotech, Shanghai, China. Briefly, the RNA-seq library was prepared using Illumina kits. The sequencing was performed using Illumina Hiseq 4000. Sequencing was carried out by running 150 cycles. Principal component analysis (PCA), hierarchical clustering, correlation analysis, pathway analysis, and gene ontology (GO) were performed, and volcano plots and scatter plots were generated to identify the differentially expressed genes using R or Python environment for statistical computing and graphics.

2.10. Measurement of GSH and GSSG. Total glutathione (GSH+GSSG) and oxidized glutathione disulfide (GSSG) were measured using a GSH and GSSG Assay Kit (Beyotime) according to the manufacturer's instructions. The GSH/GSSG ratio was then calculated.

2.11. Chromatin Immunoprecipitation Assay. The chromatin immunoprecipitation (ChIP) assay was performed using the Simple ChIP Plus Sonication Chromatin IP Kit (Cell Signaling Technology) according to the manufacturer's protocol. Briefly, cells were fixed with formaldehyde, and the chromatin was sheared with sonication into 200–1000 bp DNA-protein fragments. Then, the NRF2 antibody (or IgG antibody as a control) was added. The complex was coprecipitated and captured by Protein G beads. The protein-DNA cross-links were reversed, and the DNA was purified. Then, the enrichment of the *Cat* promoter was detected by RT-PCR. The primers used in this assay are listed in Supplementary Table S2.

2.12. Statistical Analysis. All results were obtained from at least three independent experimental replicates and are presented as mean ± standard error of the mean (S.E.M.). Significance was determined by Student's t test. $P < 0.05$ was considered significant.

3. Results

3.1. SUMOylation of NRF2 Is Critical for Its Inhibition of KLK LUAD Cell Migration and Invasion. As expected, NRF2 expression was significantly lower in *Kras/Lkb1* (KL) mutant

(a)

(b)

(c)

(d)
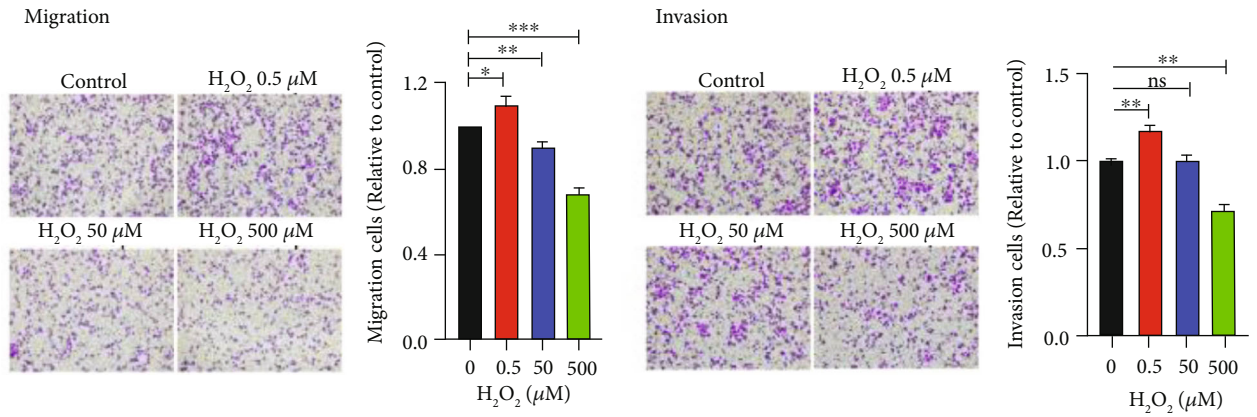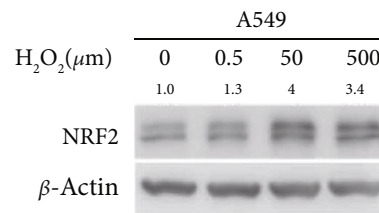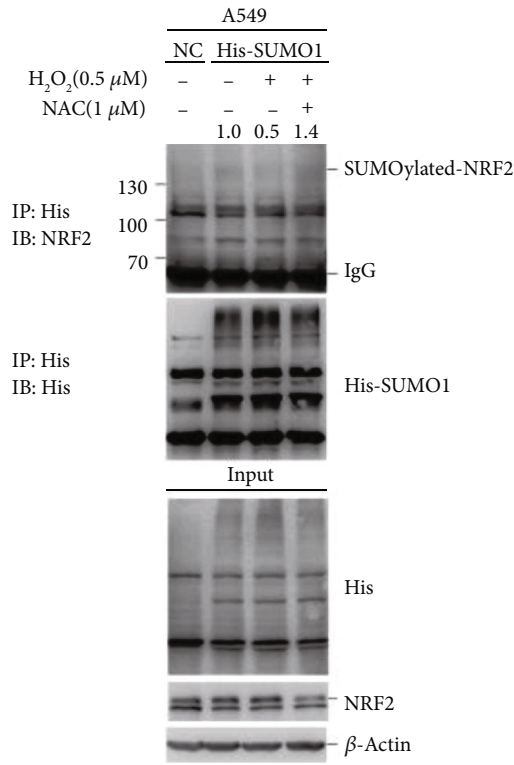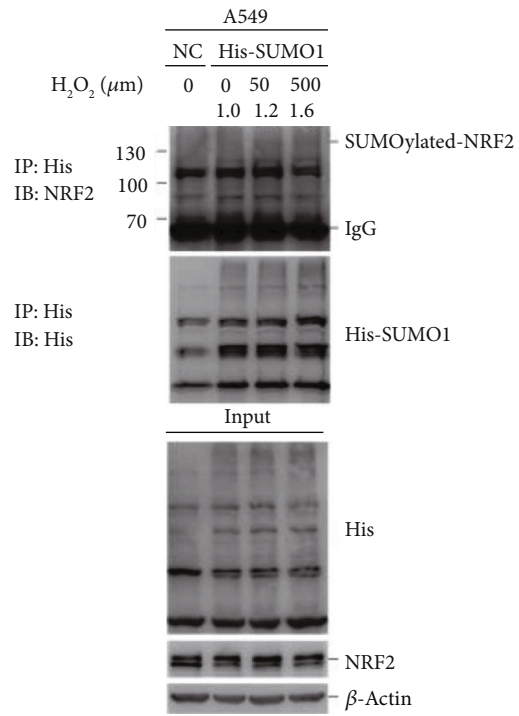
FIGURE 2: Continued.
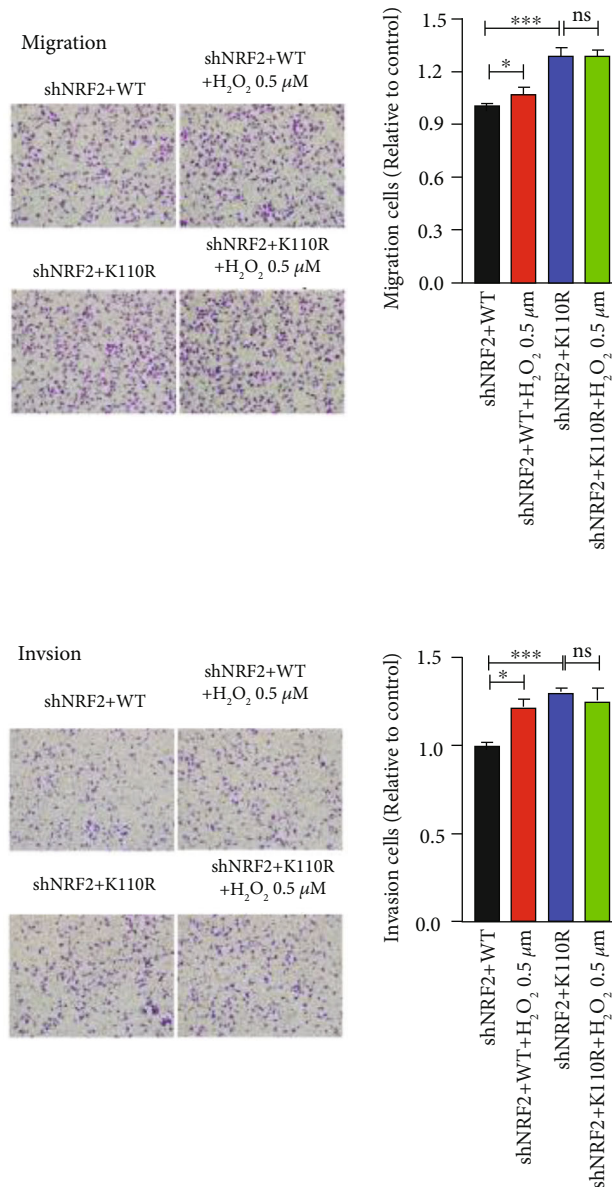
(e)

FIGURE 2: Mild oxidative stress reduces NRF2 SUMOylation to induce KLK LUAD cell migration and invasion. (a) The migration and invasion of A549 cells treated with 0.5, 50, or 500 μM H_2O_2 individually for 12 h (3 replicates per group). (b) NRF2 expression in A549 cells treated with 0.5, 50, or 500 μM H_2O_2 for 12 h. Blots were quantified and normalized to β-actin expression. (c) NRF2 SUMOylation in A549-His-SUMO1 cells treated with 0.5 μM H_2O_2 for 12 h. SUMOylated proteins with His tag were purified from cell lysates using Ni^{2+}-NTA agarose bead pull-down, and SUMOylated NRF2 was detected by immunoblotting with anti-NRF2 antibody. Blots were quantified and normalized to β-actin expression. (d) NRF2 SUMOylation in A549-His-SUMO1 cells treated with 50 or 500 μM H_2O_2 for 12 h. (e) The migration and invasion of A549-shNRF2+WT and A549-shNRF2+K110R cells treated with 0.5 μM H_2O_2 for 12 h (3 replicates per group). H_2O_2: hydrogen peroxide. $*P < 0.05$, $**P < 0.01$, and $***P < 0.001$.

LUAD H23 cells than in KLK LUAD A549 and H2122 cells (Figure S1A). Correspondingly, H23 cells showed a higher intracellular ROS level than A549 and H2122 cells did (Figure S1B). Upon knockdown of NRF2, the ROS levels in A549 and H2122 cells were elevated, whereas the ROS level in H23 cells was not altered (Figure S1C and S1D). Additionally, KLK LUAD cell migration and invasion were increased with NRF2 knockdown (Figure S1E), revealing that NRF2 inhibits KLK LUAD cell migration and invasion. In contrast, NRF2 knockdown in H23 cells delayed cell migration and invasion (Figure S1E), which is consistent with previous studies showing that downregulation of BACH1 inhibits lung cancer metastasis [19, 20]. However, in the KLK LUAD cell lines, BACH1 expression was not affected (Figure S1F), indicating that NRF2 regulates KLK LUAD migration and invasion independent of BACH1.

(a)

(b)

(c)

Figure 3: Continued.

(d)

(e)

(f)
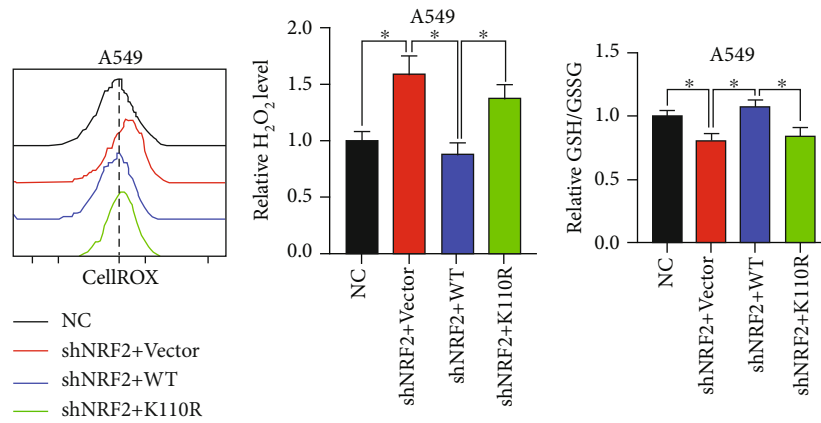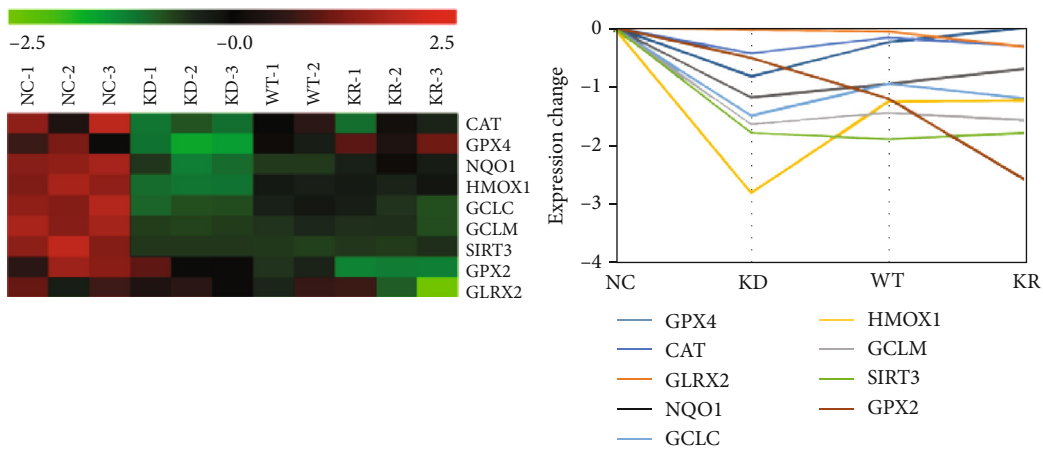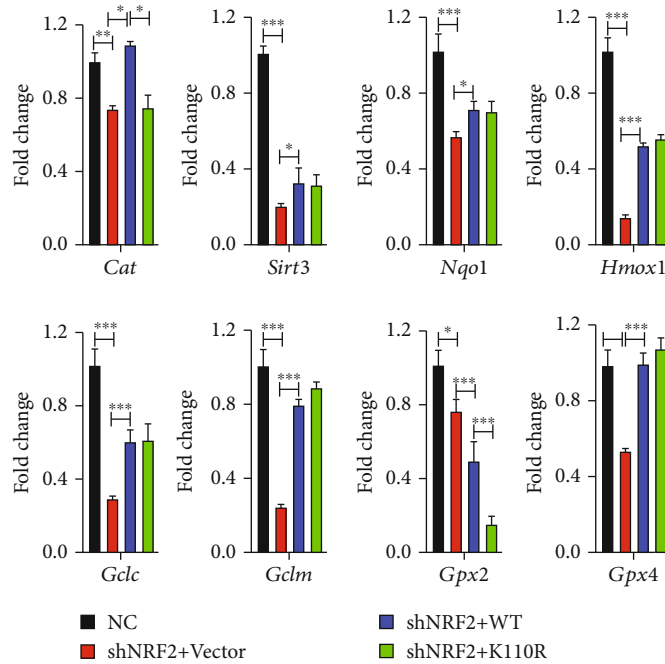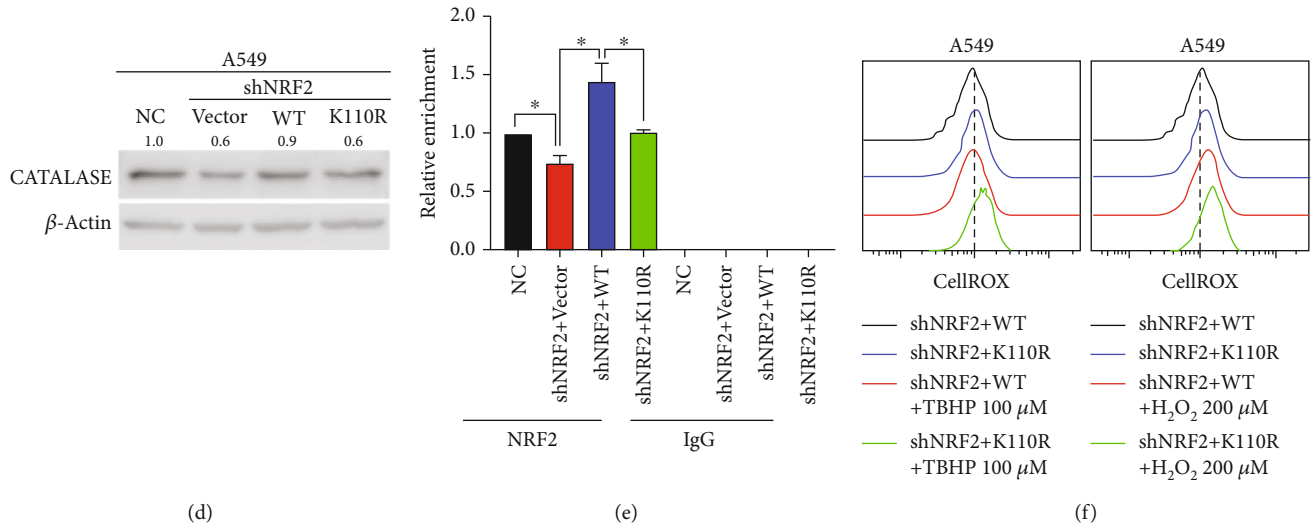
FIGURE 3: SUMOylation of NRF2 is critical for its antioxidant ability in KLK LUAD *via* transcriptional activation of *Cat*. (a) The intracellular ROS and H_2O_2 levels and GSH/GSSG ratio in four stable cell lines constructed from A549 cells (3 replicates per group). (b) Heat map and trend graph comparing the patterns of antioxidant gene expression in four stable cell lines constructed from A549 cells. (c) Validation of gene expression involved in antioxidant pathways by quantitative real-time PCR in four stable cell lines constructed from A549 cells (3 replicates per group). *Cat*: catalase; *Sirt3*: Sirtuin 3; *Nqo1*: NAD(P)H quinone dehydrogenase 1; *Hmox1*: heme oxygenase 1; *Gclc*: glutamate-cysteine ligase catalytic subunit; *Gclm*: glutamate-cysteine ligase modifier subunit; *Gpx2*: glutathione peroxidase 2; *Gpx4*: glutathione peroxidase 4. (d) Catalase protein expression analyzed by Western blotting in four stable cell lines constructed from A549 cells. Blots were quantified and normalized to β-actin expression. (e) ChIP assay of NRF2 occupancy in the locus of *Cat* promoter in A549-shNRF2+WT and A549-shNRF2+K110R cells. (f) A549-shNRF2+WT and A549-shNRF2+K110R cells were treated with $100\,\mu M$ TBHP or $200\,\mu M$ H_2O_2 for 12 h. The intracellular ROS level was then measured by flow cytometry. TBHP: tert-butyl hydroperoxide; H_2O_2: hydrogen peroxide. $*P < 0.05$, $**P < 0.01$, and $***P < 0.001$.

To investigate the role of NRF2 and its SUMOylation in KLK cell migration and invasion, we restored NRF2 wild-type and NRF2 with SUMOylation site mutation (K110R) expression individually in A549 and H2122 cells (Figure 1(a)). Expression of NRF2 wild-type inhibited cell migration and invasion, which had been enhanced by NRF2 knockdown, but NRF2 K110R did not exhibit this inhibitory capability (Figures 1(b) and 1(c)). Although NRF2 SUMOylation promoted KLK LUAD tumorigenesis and did not affect KLK LUAD cell apoptosis (Figure S2), as reported in HCC previously [23], the results in Figure 1 suggest that SUMOylation is critical for the inhibitory effect of NRF2 on KLK cell migration and invasion.

3.2. Mild Oxidative Stress Reduces NRF2 SUMOylation to Induce KLK LUAD Cell Migration and Invasion. Hydrogen peroxide acts as a signaling molecule to induce cancer cell migration and invasion. In A549 cells, we found that mild oxidative stress generated by treatment with $0.5\,\mu M$ H_2O_2 induced cell migration and invasion, whereas moderate/severe oxidative stress ($50\,\mu M/500\,\mu M$ H_2O_2) did not induce and even reduced cell migration and invasion (Figure 2(a)). Consistent with previous reports, moderate/severe oxidative stress induced NRF2 expression as a cellular defense response, whereas mild oxidative stress had no impact on NRF2 expression (Figure 2(b)). Because endogenous NRF2 SUMOylation is difficult to detect experimentally, we constructed a His-SUMO1 overexpressing stable cell line named A549-His-SUMO1 and pulled down SUMO1-

modified proteins with Ni^{2+}-NTA. Surprisingly, we detected that mild oxidative stress ($0.5\,\mu M$ H_2O_2) reduced NRF2 SUMOylation in A549-His-SUMO1 cells (Figure 2(c)), whereas SUMOylation of NRF2 was increased after treatment with $50\,\mu M$ or $500\,\mu M$ H_2O_2 given that NRF2 expression was increased (Figure 2(d)). More importantly, the decrease in NRF2 SUMOylation caused by mild H_2O_2 ($0.5\,\mu M$) was reversed when antioxidant NAC (N-acety-L-cysteine) was added (Figure 2(c)). With a deficiency in NRF2 SUMOylation, as shown in shNRF2+K110R A549 cells, mild oxidative stress no longer induced cell migration and invasion (Figure 2(e)), indicating that mild oxidative stress in KLK LUAD cells induces cell migration and invasion by reducing NRF2 SUMOylation.

3.3. SUMOylation Is Critical for the Antioxidant Ability of NRF2 via Transcriptional Activation of Cat in KLK LUAD Cells. We previously reported that NRF2 SUMOylation reduces the intracellular ROS level in HCC cells [23]. In A549 cells, NRF2 SUMOylation reduced both the total ROS and H_2O_2 levels (Figure 3(a)). In addition, the reduced glutathione (GSH) to oxidized glutathione disulfide (GSSG) (GSH/GSSG) ratio was relatively higher in A549 cells in which NRF2 wild-type expression was rescued (Figure 3(a)). To explore the underlying mechanism, we performed RNA sequencing (RNA-Seq) analysis to compare the gene expression levels in A549 cells before (normal control, NC group) and after NRF2 knockdown (KD group), as well as in A549 cells expressing NRF2 wild-type (WT group) and NRF2
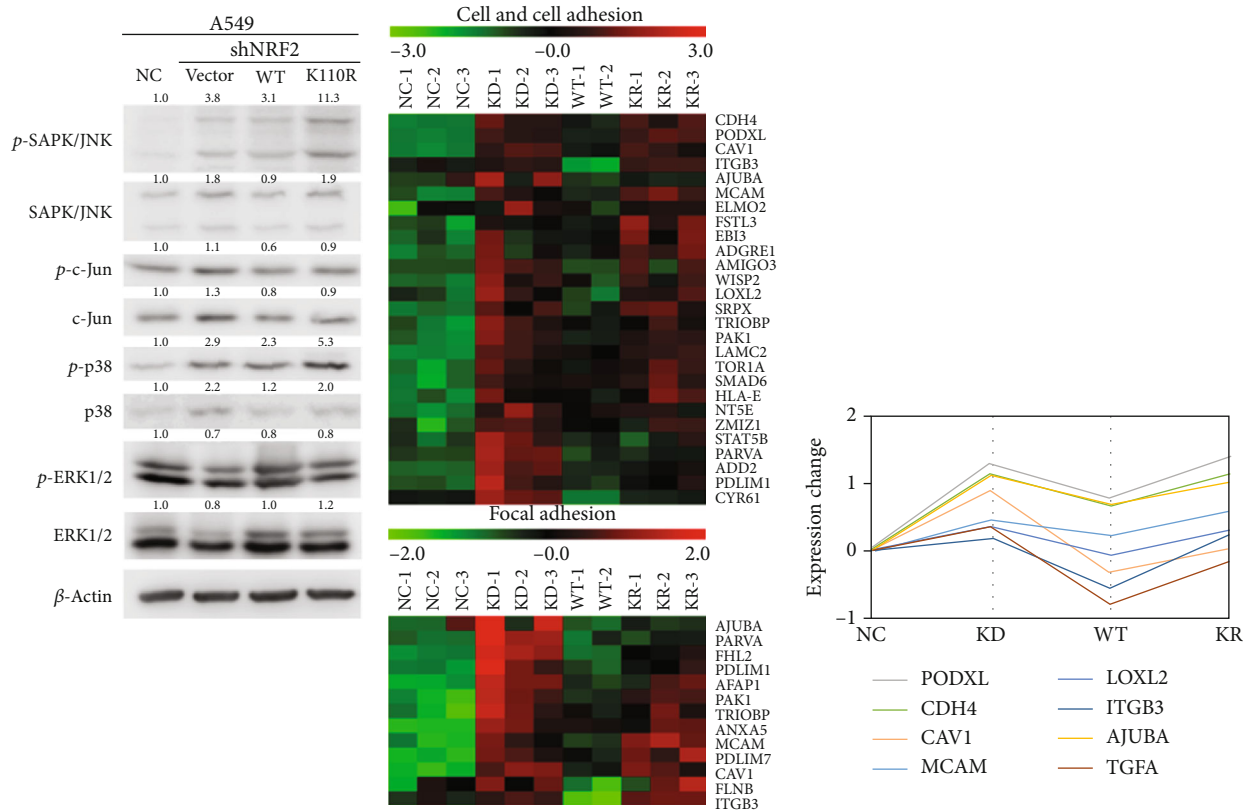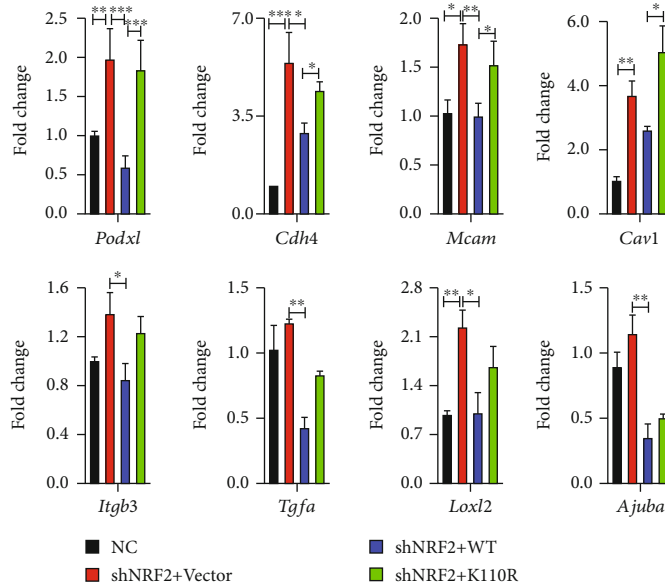
FIGURE 4: Mild ROS act as signaling molecules to activate the JNK/c-Jun axis and promote KLK LUAD cell migration and invasion. (a) The altered activation of MAPK signaling pathways (ERK, JNK, and p38 signaling pathways) in four stable cell lines constructed from A549 cells. MAPK: mitogen-activated protein kinase; ERK: extracellular signal-regulated kinase; JNK: c-Jun NH-2 terminal kinase. Blots were quantified and normalized to β-actin expression. (b) Heat map comparing patterns of gene expression related to cell and cell adhesion as well as focal adhesion in four stable cell lines constructed from A549 cells. (c) Trend graph comparing patterns of gene expression related to cell and cell adhesion as well as focal adhesion in four stable cell lines constructed from A549 cells. (d) Validation of expression of genes involved in cell and cell adhesion as well as focal adhesion by quantitative real-time PCR in four stable cell lines constructed from A549 cells (3 replicates per group). *Podxl*: podocalyxin like; *Cdh4*: cadherin 4; *Mcam*: melanoma cell adhesion molecule; *Cav1*: caveolin 1; *Itgb3*: integrin subunit beta 3; *Tgfa*: transforming growth factor alpha; *Loxl2*: lysyl oxidase like 2; *Ajuba*: Ajuba LIM protein. $*P < 0.05$, $**P < 0.01$, and $***P < 0.001$.
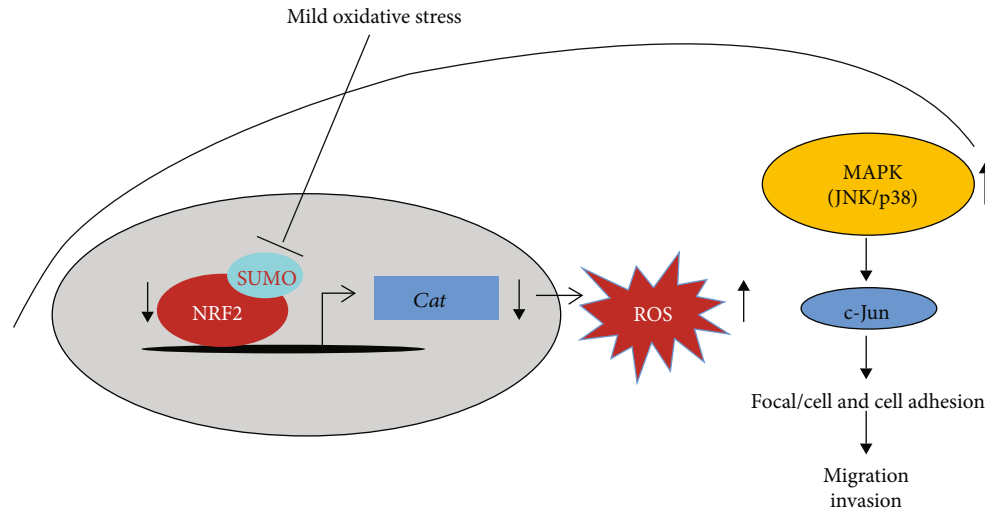
FIGURE 5: Model depicting how mild oxidative stress reduces NRF2 SUMOylation to promote KLK LUAD migration and invasion.

K110R (KR group). Volcano plots showed that 1299 genes were significantly upregulated, and 687 genes were downregulated in the KD group versus NC group (Figure S3A), and 99 genes were significantly upregulated, and 255 genes were downregulated in the KR group versus WT group (Figure S3C). Gene ontology (GO) analyses showed that upon NRF2 knockdown, pathways involved in the response to oxidative stress and the response to hydrogen peroxide were downregulated (Figure S3B). The heat map and trend graph revealed that in A549 cells, NRF2 SUMOylation promotes H_2O_2 removal mainly by activating *Cat* transcription, which was validated by our quantitative real-time polymerase chain reaction (PCR) and Western blot results (Figures 3(b)–3(d)). Different from our previous report [23], NRF2 SUMOylation did not alter the protein expression of GPX2 in KLK cells (Figure S3E). ChIP assay showed that NRF2 K110R had a significantly decreased ability to bind with the *Cat* gene promoter (Figure 3(e)). Moreover, upon challenge of A549 cells with oxidants (tert-butyl hydroperoxide [TBHP] and H_2O_2), the antioxidant ability of NRF2 was reduced when its SUMOylation site was mutated (Figure 3(f)). These results collectively reveal that SUMOylation is critical for the antioxidant ability of NRF2, mainly *via* the transcriptional activation of *Cat* in KLK LUAD cells.

3.4. Increased ROS Level due to NRF2 SUMOylation Deficiency Promotes KLK LUAD Cell Migration and Invasion via JNK/c-Jun Axis. Based on our finding that ROS and H_2O_2 levels were increased with deficient NRF2 SUMOylation (Figure 3(a)), we then asked whether increased intracellular ROS act as signaling molecules to activate pathways that promote KLK LUAD cell migration and invasion. As shown in Figure 4(a), when NRF2 expression was inhibited and the intracellular ROS level was increased, the JNK/c-Jun axis was activated in KLK LUAD cells. Expression of NRF2 wild-type inhibited the activation of the JNK/c-Jun axis, whereas expression of NRF2 K110R did not (Figure 4(a)). Furthermore, the results of RNA-Seq and quantitative real-time PCR analyses revealed that through

increasing the gene expression related with cell motility and cell adhesion, JNK/c-Jun axis activation promoted the migration and invasion in KLK LUAD cells (Figure S3D and Figures 4(b)–4(d)). In addition, we demonstrated NRF2 SUMOylation inhibited cell migration and invasion by activating *Cat* transcription and inactivating the JNK/c-Jun axis by reducing the cellular ROS level, in KLK LUAD H2122 cells (Figure S4).

4. Discussion

In KLK LUAD, KEAP1 mutation leads to NRF2 activation, which influences many of the hallmarks of cancer and confers "NRF2 addition" [24]. High NRF2 activity renders KLK LUAD more resistant to ROS accumulation compared with KL LUAD [14]. In contrast, to promote tumorigenesis, NRF2 SUMOylation inhibits the migration and invasion of KLK LUAD cells (Figure 1), further complicating the anti- versus protumorigenic roles of ROS in cancer cells. The extent of ROS increase often determines the adaptive consequences of the cellular response to the oxidative insult. We revealed in the present study that, in comparison to severe oxidative stress, which inhibited cell migration and invasion, mild oxidative stress promoted the migration and invasion of KLK LUAD cells (Figure 2(a)). SUMOylation of vimentin (VIM), a type III intermediate filament protein involved in cytoskeleton organization and cell motility, favors cell motility and migration [25]. However, whether protein SUMOylation is involved in ROS-triggered cancer cell migration and invasion has remained largely unknown. The results of the present study demonstrate that the SUMOylation of NRF2, an essential antioxidant factor, plays a role in the inhibition of KLK LUAD migration and invasion.

NRF2 is stabilized upon hyperoxidation of cysteines on KEAP1 which disrupts the binding of the two proteins [15, 17]. Here, we revealed that mild oxidative stress reduced NRF2 SUMOylation (Figure 2(c)), rather than increasing NRF2 expression as seen with moderate/severe oxidative stress (Figure 2(b)), suggesting a mechanism by which

NRF2 activity is regulated independently of KEAP1. It has been reported that SUMO-specific protease 3 (SENP3) is a redox sensor that is stabilized under mild oxidative stress and consequently de-SUMOyltates p300 and hypoxia inducible factor (HIF)-1α [26, 27]. Recently, Zhou et al. reported that NRF2 activity is regulated by SENP3 in laryngeal carcinoma after cisplatin-induced ROS stress [28]. Because SENP1 is also reported de-SUMOylate NRF2 [22], whether mild oxidative stress decreases NRF2 SUMOylation by increasing SENP3 expression or by increasing the expression and/or activities of other SENPs, in KLK LUAD cells, needs to be explored in future experiments.

In the present study, we showed that NRF2 SUMOylation reduced the intracellular ROS level mainly *via* the transcriptional activation of *Cat* to promote H_2O_2 removal (Figure 3). We also found that NRF2 SUMOylation reduced the intracellular ROS level by enhancing GPX2 protein expression in KLK LUAD cells (Figure S3C). We found that the increase in the H_2O_2 level caused by NRF2 SUMOylation deficiency in A549 cells was in the nanomolar range. Hence, at mildly increased level, H_2O_2 acts as a signaling molecule to activate the JNK/c-Jun pathway, which enhances cell-cell adhesion as well as focal adhesion, to promote cell migration and invasion (Figure 4). However, how the level of increased ROS brought about by NRF2 SUMOylation deficiency specifically regulates JNK/c-Jun axis activation in KLK LUAD cells remains to be determined in future research.

A recent report showed that ROS restriction by TIGAR supports premalignant tumor initiation while restricting metastasis in pancreatic ductal adenocarcinoma, indicating that the complexity of ROS regulation underpins full malignant progression [29]. The present study demonstrated that by reducing the ROS level, NRF2 SUMOylation can regulate KLK LUAD progression in a stage-specific manner. Thus, we conclude that NRF2 SUMOylation promotes KLK LUAD tumorigenesis. However, during the initiation stage of tumor metastasis, mildly increased oxidative stress resulting from detachment may reduce NRF2 SUMOylation to induce cell migration and invasion, a potential mechanism that should be investigated *in vivo* in future studies. Our findings herein are helpful in understanding the *Kras*-dependent pathways that promote LUAD progression and provide insights for the identification of potential therapeutic targets and the development of new treatments for KRAS mutant LUAD.

5. Conclusions

On the basis of our current findings, we depict a model that mild oxidative stress reduces NRF2 SUMOylation to promote KLK LUAD migration and invasion (Figure 5). Mild oxidative stress reduces NRF2 SUMOylation, which promotes KLK LUAD cell migration and invasion. Mechanistically, NRF2 SUMOylation increases the antioxidant ability of NRF2 and reduces cellular ROS levels, mainly by transcriptionally activating *Cat* in KLK LUAD cells. With reduced NRF2 SUMOylation, increased ROS act as signaling molecules to activate the JNK/c-Jun axis, which enhances cell mobility and cell adhesion, to promote LUAD cell migration and invasion.

Data Availability

The data used to support the findings of this study are available from the corresponding author upon request.

Conflicts of Interest

The authors declare no competing interest.

Authors' Contributions

JQX, HYG, ZCX, and WLZ carried out experiments and analyzed data. JLH and JKC provided technical, administrative, and material support. RC designed the study, conceived the experiments, and wrote the paper.

Acknowledgments

Supplementary Materials

Supplemental Experimental Procedures. Supplementary Table S1: primers used for PCDH-His-SUMO1 construction. Supplementary Table S2: primers for ChIP assay. Figure S1: NRF2 inhibits KLK LUAD cell migration and invasion independent of BACH1. Figure S2: NRF2 SUMOylation maintains KLK LUAD tumorigenesis and has no effect on KLK LUAD cell apoptosis. Figure S3: volcano plots of RNA-Seq results and GPX2 protein expression in four stable cell lines derived from A549 cells. Figure S4: NRF2 SUMOylation reduces ROS level in H2122 cells *via* transcriptional activation of *Cat* and inhibits migration and invasion through JNK/c-Jun axis. *(Supplementary Materials)*

References

[1] M. Schieber and N. S. Chandel, "ROS function in redox signaling and oxidative stress," *Current biology*, vol. 24, no. 10, pp. R453–R462, 2014.

[2] C. Hegedűs, K. Kovács, Z. Polgár et al., "Redox control of cancer cell destruction," *Redox Biology*, vol. 16, pp. 59–74, 2018.

[3] L. Tochhawng, S. Deng, S. Pervaiz, and C. T. Yap, "Redox regulation of cancer cell migration and invasion," *Mitochondrion*, vol. 13, no. 3, pp. 246–253, 2013.

[4] A. M. Day and E. A. Veal, "Hydrogen peroxide-sensitive cysteines in the Sty1 MAPK regulate the transcriptional response to oxidative stress," *The Journal of Biological Chemistry*, vol. 285, no. 10, pp. 7505–7516, 2010.

[5] A. L. Schroyer, N. W. Stimes, W. F. Abi Saab, and D. N. Chadee, "MLK3 phosphorylation by ERK1/2 is required for oxidative stress-induced invasion of colorectal cancer cells," *Oncogene*, vol. 37, no. 8, pp. 1031–1040, 2018.

[6] T. Goldkorn, N. Balaban, K. Matsukuma et al., "EGF-receptor phosphorylation and signaling are targeted by H2O2 redox stress," *American Journal of Respiratory Cell and Molecular Biology*, vol. 19, no. 5, pp. 786–798, 1998.

[7] A. Salmeen and D. Barford, "Functions and mechanisms of redox regulation of cysteine-based phosphatases," *Antioxidants & Redox Signaling*, vol. 7, no. 5-6, pp. 560–577, 2005.

[8] B. A. Weir, M. S. Woo, G. Getz et al., "Characterizing the cancer genome in lung adenocarcinoma," *Nature*, vol. 450, no. 7171, pp. 893–898, 2007.

[9] F. Skoulidis, L. A. Byers, L. Diao et al., "Co-occurring genomic alterations define major subsets of KRAS-mutant lung adenocarcinoma with distinct biology, immune profiles, and therapeutic vulnerabilities," *Cancer Discovery*, vol. 5, no. 8, pp. 860–877, 2015.

[10] H. Ji, M. R. Ramsey, D. N. Hayes et al., "LKB1 modulates lung cancer differentiation and metastasis," *Nature*, vol. 448, no. 7155, pp. 807–810, 2007.

[11] A. Calles, L. M. Sholl, S. J. Rodig et al., "Immunohistochemical loss of LKB1 is a biomarker for more aggressive biology in KRAS-mutant lung adenocarcinoma," *Clinical cancer research : an official journal of the American Association for Cancer Research*, vol. 21, no. 12, pp. 2851–2860, 2015.

[12] F. Li, X. Han, F. Li et al., "LKB1 inactivation elicits a redox imbalance to modulate non-small cell lung cancer plasticity and therapeutic response," *Cancer Cell*, vol. 27, no. 5, pp. 698–711, 2015.

[13] J. Kim, Z. Hu, L. Cai et al., "CPS1 maintains pyrimidine pools and DNA synthesis in KRAS/LKB1-mutant lung cancer cells," *Nature*, vol. 546, no. 7656, pp. 168–172, 2017.

[14] A. Galan-Cobo, P. Sitthideatphaiboon, X. Qu et al., "LKB1 and KEAP1/NRF2 pathways cooperatively promote metabolic reprogramming with enhanced glutamine dependence inKRAS-mutant lung adenocarcinoma," *Cancer Research*, vol. 79, no. 13, pp. 3251–3267, 2019.

[15] T. Ohta, K. Iijima, M. Miyamoto et al., "Loss of Keap1 function activates Nrf2 and provides advantages for lung cancer cell growth," *Cancer Research*, vol. 68, no. 5, pp. 1303–1309, 2008.

[16] L. M. Solis, C. Behrens, W. Dong et al., "Nrf2 and Keap1 abnormalities in non-small cell lung carcinoma and association with clinicopathologic features," *Clinical cancer research : an official journal of the American Association for Cancer Research*, vol. 16, no. 14, pp. 3743–3753, 2010.

[17] M. C. Jaramillo and D. D. Zhang, "The emerging role of the Nrf2-Keap1 signaling pathway in cancer," *Genes & Development*, vol. 27, no. 20, pp. 2179–2191, 2013.

[18] H. Wang, X. Liu, M. Long et al., "NRF2 activation by antioxidant antidiabetic agents accelerates tumor metastasis," *Science translational medicine*, vol. 8, 2016.

[19] L. Lignitto, S. E. LeBoeuf, H. Homer et al., "Nrf2 activation promotes lung cancer metastasis by inhibiting the degradation of Bach1," *Cell*, vol. 178, no. 2, pp. 316–329.e18, 2019, e318.

[20] C. Wiel, K. Le Gal, M. X. Ibrahim et al., "BACH1 stabilization by antioxidants stimulates lung cancer metastasis," *Cell*, vol. 178, no. 2, pp. 330–345.e22, 2019, e322.

[21] K. Ramani, M. L. Tomasi, H. Yang, K. Ko, and S. C. Lu, "Mechanism and significance of changes in glutamate-cysteine ligase expression during hepatic fibrogenesis," *The Journal of Biological Chemistry*, vol. 287, no. 43, pp. 36341–36355, 2012.

[22] M. T. Malloy, D. J. McIntosh, T. S. Walters, A. Flores, J. S. Goodwin, and I. J. Arinze, "Trafficking of the transcription factor Nrf2 to promyelocytic leukemia-nuclear bodies: implications for degradation of NRF2 in the nucleus," *The Journal of Biological Chemistry*, vol. 288, no. 20, pp. 14569–14583, 2013.

[23] H. Guo, J. Xu, Q. Zheng et al., "NRF2 SUMOylation promotes de novo serine synthesis and maintains HCC tumorigenesis," *Cancer Letters*, vol. 466, pp. 39–48, 2019.

[24] A. Hammad, A. Namani, M. Elshaer, X. J. Wang, and X. Tang, ""NRF2 addiction" in lung cancer cells and its impact on cancer therapy," *Cancer Letters*, vol. 467, pp. 40–49, 2019.

[25] C. Li, F. P. McManus, C. Plutoni et al., "Quantitative SUMO proteomics identifies PIAS1 substrates involved in cell migration and motility," *Nature Communications*, vol. 11, no. 1, p. 834, 2020.

[26] Y. Han, C. Huang, X. Sun et al., "SENP3-mediated deconjugation of SUMO2/3 from promyelocytic leukemia is correlated with accelerated cell proliferation under mild oxidative stress," *The Journal of Biological Chemistry*, vol. 285, no. 17, pp. 12906–12915, 2010.

[27] C. Huang, Y. Han, Y. Wang et al., "SENP3 is responsible for HIF-1 transactivation under mild oxidative stress via p300 de-SUMOylation," *The EMBO Journal*, vol. 28, no. 18, pp. 2748–2762, 2009.

[28] Z. Zhou, J. Xu, X. Bao et al., "Nuclear Nrf2 activity in laryngeal carcinoma is regulated by SENP3 after cisplatin-induced reactive oxygen species stress," *Journal of Cancer*, vol. 10, no. 15, pp. 3427–3434, 2019.

[29] E. C. Cheung, G. M. DeNicola, C. Nixon et al., "Dynamic ROS control by TIGAR regulates the initiation and progression of pancreatic cancer," *Cancer Cell*, vol. 37, no. 2, pp. 168–182.e4, 2020, e164.

Research Article

Effects of ATP9A on Extracellular Vesicle Release and Exosomal Lipid Composition

Xiao Xu [1,2] **Limei Xu,**[1,2] **Peng Zhang,**[2] **Kan Ouyang,**[1] **Yin Xiao,**[3] **Jianyi Xiong,**[1] **Daping Wang,**[1] **Yujie Liang** [4] **and Li Duan** [1]

[1]*Department of Orthopedics, Shenzhen Intelligent Orthopaedics and Biomedical Innovation Platform, Guangdong Artificial Intelligence Biomedical Innovation Platform, Shenzhen Second People's Hospital, The First Affiliated Hospital of Shenzhen University Health Science Center, Shenzhen, Guangdong 518035, China*
[2]*Shenzhen Institute of Advanced Technology, Chinese Academy of Sciences, Shenzhen, Guangdong 518055, China*
[3]*Institute of Health and Biomedical Innovation, Faculty of Science and Engineering, Queensland University of Technology, Kelvin Grove Campus, Brisbane, QLD 4059, Australia*
[4]*Shenzhen Kangning Hospital, Shenzhen Mental Health Center, Shenzhen, Guangdong 518020, China*

Correspondence should be addressed to Yujie Liang; liangyjie@gmail.com and Li Duan; duanl@szu.edu.cn

Numerous biological processes are regulated by the intercellular communications arising from extracellular vesicles (EVs) released from cells. However, the mechanisms that regulate the quantity of EV discharged have yet to be understood. While it is known that ATP9A, a P4-ATPase, is involved in endosomal recycling, it is not clear whether it also contributes to the release of EVs and the makeup of exosomal lipids. This study is aimed at exploring the role of human ATP9A in the process of EV release and, further, to analyze the profiles of EV lipids regulated by ATP9A. Our results demonstrate that ATP9A is located in both the intracellular compartments and the plasma membrane. The percentage of ceramides and sphingosine was found to be significantly greater in the control cells than in the ATP9A overexpression and ATP9A knockout groups. However, EV release was greater in ATP9A knockout cells, indicating that ATP9A inhibits the release of EVs. This study revealed the effects of ATP9A on the release of EVs and the lipid composition of exosomes.

1. Introduction

As extracellular vesicles (EVs) released from cells are mediators of intercellular communications, they can transmit information between cells and are involved in tissue development and disease progression [1, 2]. EVs are categorized according to diameter, which ranges from 50 to 1000 nm. Based on the formation of EVs, they are categorized as either ectosomes or exosomes [3]. Ectosomes are created directly by the plasma membrane forming outward buds. Exosomes, however, are combination products of multivesicular endosomes (MVEs) fusing with the plasma membrane which are then discharged into extracellular space [4, 5].

One distinctive characteristic of eukaryotic cells is the composition of phospholipids in the plasma membrane, which are not distributed symmetrically. This has long been recognized as a potential influence on the release of vesicles. The distribution of phospholipid species differs in the two leaflets of biological membranes. The leaflet exposed to cytosol consists of phosphatidylserine (PS) and phosphatidylethanolamine (PE), whereas the exoplasmic leaflet contains mostly phosphatidylcholine (PC) and sphingomyelin [6]. This asymmetric phospholipid distribution is an important aspect in numerous diseases, such as cancer, cardiovascular disease, hepatic steatosis, and metabolic disorders. The asymmetric distribution is also involved in many physiological

processes, including apoptosis, blood coagulation, apoptosis, cell signaling, cell and organelle morphology, host-virus interactions, intracellular vesicle trafficking, membrane permeability and stability, and regulation of membrane proteins [7, 8].

Usually, ATP-dependent lipid transporters are responsible for maintaining homeostasis of the phospholipid distribution; however, PS can be redistributed to the exoplasmic leaflet in response to pathophysiological conditions. This has been observed in platelet activation, in exosome release from tumor tissues, and in the majority of immune cell types, such as activated B cells, bone marrow-derived monocytes, dendritic cells, and macrophages [9].

The asymmetry of lipids is maintained actively by a variety of transporter families [10, 11]. One particular family is the P-type ATPase family, and the members of its largest subfamily, P4-ATPase, are known as flippases [7, 12]. These ATP-dependent enzymes relocate certain phospholipids away from the membrane's outer leaflet and toward the inner leaflet. This maintains the membrane's lipid asymmetry, which has been highlighted previously to be critical to several cellular processes. Mounting evidence indicates that in eukaryotic cells, P4-ATPases play a key role in the biogenesis of the transport vesicles involved in the biosynthetic and endocytic pathways [11].

Models characterizing the role of P4-ATPases in lipid translocation pathways have been informed by site-directed mutagenesis and structural modeling studies [13, 14]; however, the fundamental features of the transport pathway, the electrogenic properties of the flippases, and the mechanisms by which flipping occurs remain unclear. Using TAT-5, the P4-ATPase of *Caenorhabditis elegans*, Wehman et al. showed that the enzyme was involved in the release of EVs and maintenance of PE asymmetry [15]. Whereas, human ATP9A and ATP9B, which are orthologous to TAT-5, are primarily found inside intracellular compartments [16]. ATP9A is recognized as a regulator for endosomal recycling [17]; whether it contributes to EV release and the lipid profiles of exosomes has not yet been determined. It is well-known that during cell division, fusion, and death, cells regulate PE asymmetry and EV release [18]. Therefore, we hypothesized that ATP9 is involved in plasma membrane biosynthesis, cell outward budding, and EV release. This study examines the effects of ATP9A on the composition of exosomal lipids and the release of EVs in a human embryonic kidney 293 (HEK293) cell line.

2. Materials and Methods

2.1. Cell Culture. DMEM medium (DMEM; Life Technologies) plus 10% fetal bovine serum (FBS, Gibco) supplement was used to sustain the HEK293 cell line at 37°C and 5% CO_2. Synovial fluid-derived human mesenchymal stem cells (SF-MSCs) were cultured in MesenGro Chemically Defined Medium.

2.2. Overexpression of ATP9A. Control for this study was provided by the lentivirus empty vector, pLenti-C-RFP, which does not contain any human genes. The 293T cells

were variously transfected with pLenti-C-RFP, pMD2.G, and psPAX2. After 48 h, lentivirus was harvested and used to infect MSCs, followed by puromycin selection (used as plv-NC group). The whole length of the ATP9A gene was subcloned into the destination pLenti-C-RFP plasmids. pLenti ATP9A-RFP plasmids were then cotransfected into HEK293T cells along with psPAX2 and pMD2.G packaging vectors. Lentivirus particles released from HEK293T cells were harvested and filtered and then used to infect MSCs. Puromycin was used to select cells expressing ATP9A-OV.

2.3. ATP9A Knockout. The lentiCRISPRv2 plasmid was used, as this vector expresses Cas9 nuclease and inserts ATP9A-specific single-guide RNA (sgRNA) simultaneously [19]. The online tool CRISPR DESIGN (https://CRISPR.mit.edu) was used to design sgRNA. The oligo sequence 5′-AGGA GATCCGATGCTACGTG-3′ was created and then annealed before subcloning into lentiCRISPRv2. To produce the lentivirus, cloned lenti-CRISPRv2 sgATP9A plasmids were transferred into HEK293T cells with packaging plasmids pMD2.G and psPAX2 using Lipofectamine 3000 (Invitrogen, Carlsbad, CA, USA). MSCs were infected with purified lentivirus, and a monoclonal cell line was selected using puromycin.

2.4. Confocal Microscopy. Cells were stably infected with lentivirus ATP9A-RFP on a 35 mm confocal dish at 37°C. After 48 h, cells were washed twice with PBS. To fix the cells, 4% paraformaldehyde was used. DAPI-containing mounting medium was used to mount the cells. Using a 60x oil objective, an LSM 800 confocal laser scanning microscope (Carl Zeiss) was used to collect images. The device was equipped with DAPI (405 nm) and red (568 nm) lasers.

2.5. Quantification of EVs in Culture Medium. To detect and analyze the concentrations and sizes of exosomes, NanoSight N3000 (Malvern, Ltd., Malvern, UK) nanoparticle tracking analysis (NTA) was used. The measuring duration was 60 s, and parameters were applied according to the manufacturer's instructions. The EVs were diluted to 1 ml with PBS; the NTA 3.2 software (version 3.2.16) calculated exosome distribution and size [20].

2.6. Purification of Exosomes. To remove apoptotic cell bodies and cellular debris, the medium (20 ml) was centrifuged at 200 G for 10 min, and then again at 2,000 G for 20 min. To remove macrovesicles, the supernatant was ultracentrifuged at 10,000 G for 25 min. Ultracentrifugation was used at 100,000 G for 60 min to retrieve exosomes. Exosome pellets were washed once with PBS, then centrifuged again at 100,000 G for 60 min. The resultant pellets were resuspended in 500 μl PBS. A Bradford assay was conducted to determine the concentration of protein. Western blotting was performed to detect exosome marker CD9, tumor susceptibility gene 101 (TSG101), Alix, and endoplasmic reticulum (ER) marker calnexin.

2.7. Metabolite Extraction and Lipidomics. A solution of exosome pellets in chloroform/methanol/water (2/1/1, *v/v/v*) was vortexed for 1 min then centrifuged for 10 min at 3000 G. The organic phage was harvested and transferred to a fresh tube,

(a)

(b)
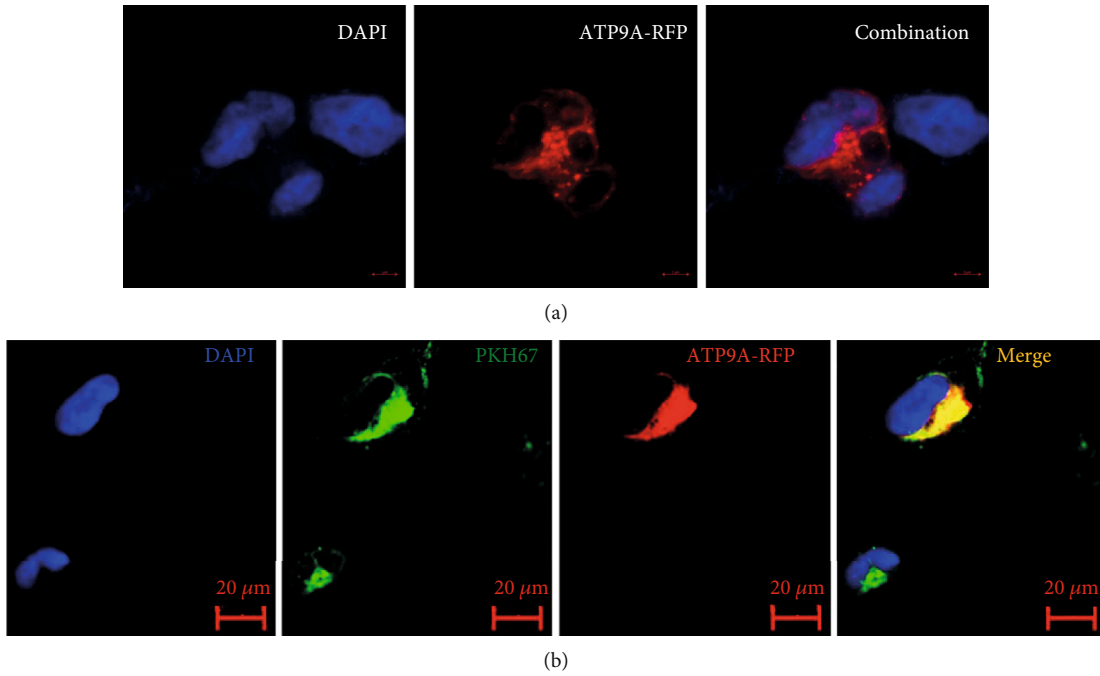
Figure 1: ATP9A localizes to intracellular vesicles and the plasma membrane. (a) To investigate ATP9A localization, HEK293 cells overexpressing ATP9A-RFP were detected using confocal microscopy. (b) HEK293 cells overexpressing ATP9A-RFP were labeled with general cell membrane dye PKH67-green.

(a)

(b)
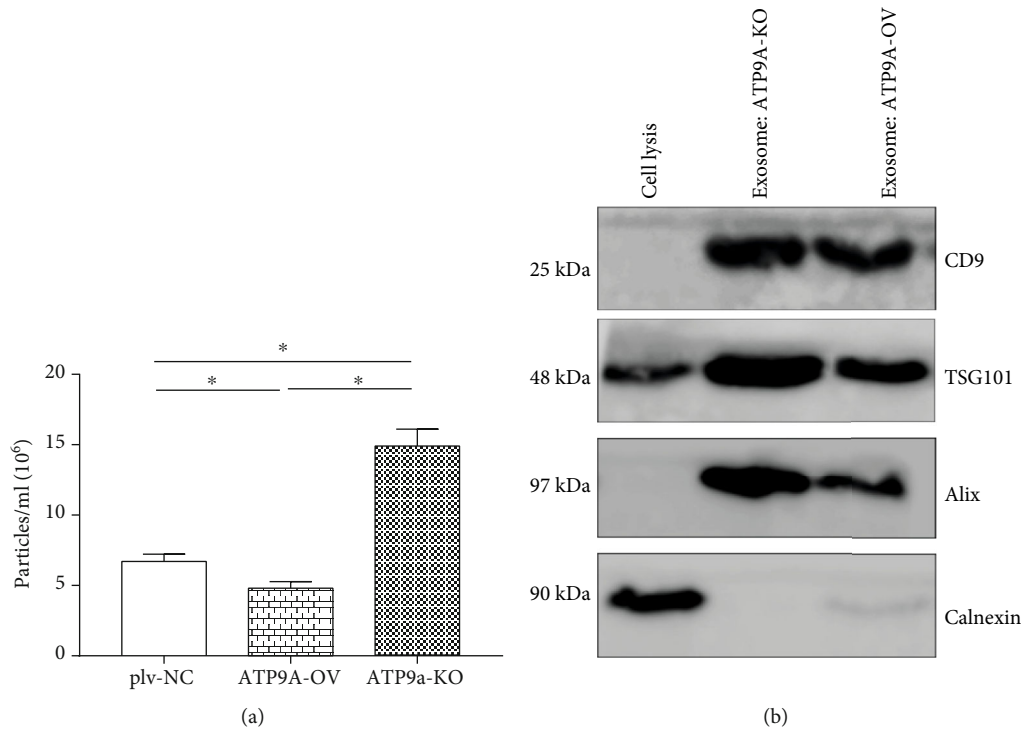
Figure 2: The total number of EVs is significantly greater in ATP9A knockdown cells. (a) EV secretion was evaluated in ATP9A knockdown (ATP9A-KO), ATP9A overexpression (ATP9A-OV), and plv-NC cells. (b) Exosome preparation was positive for exosome markers CD9, TSG101, and Alix and negative for ER marker calnexin. Tests were repeated in triplicate. $^*P < 0.05$.

$R^2X(1) = 0.432$ $R^2X(2) = 0.277$ Ellipse: Hotelling's T^2 (95%)

● plv-NC
■ ATP9a-KO

(a)

$R^2X(1) = 0.5$ $R^2X(2) = 0.29$ Ellipse: Hotelling's T^2 (95%)

● plv-NC
▲ ATP9a-OV

(b)

$R^2X(1) = 0.393$ $R^2X(2) = 0.294$ Ellipse: Hotelling's T^2 (95%)

■ ATP-9a-KO
▲ ATP9a-OV

(c)
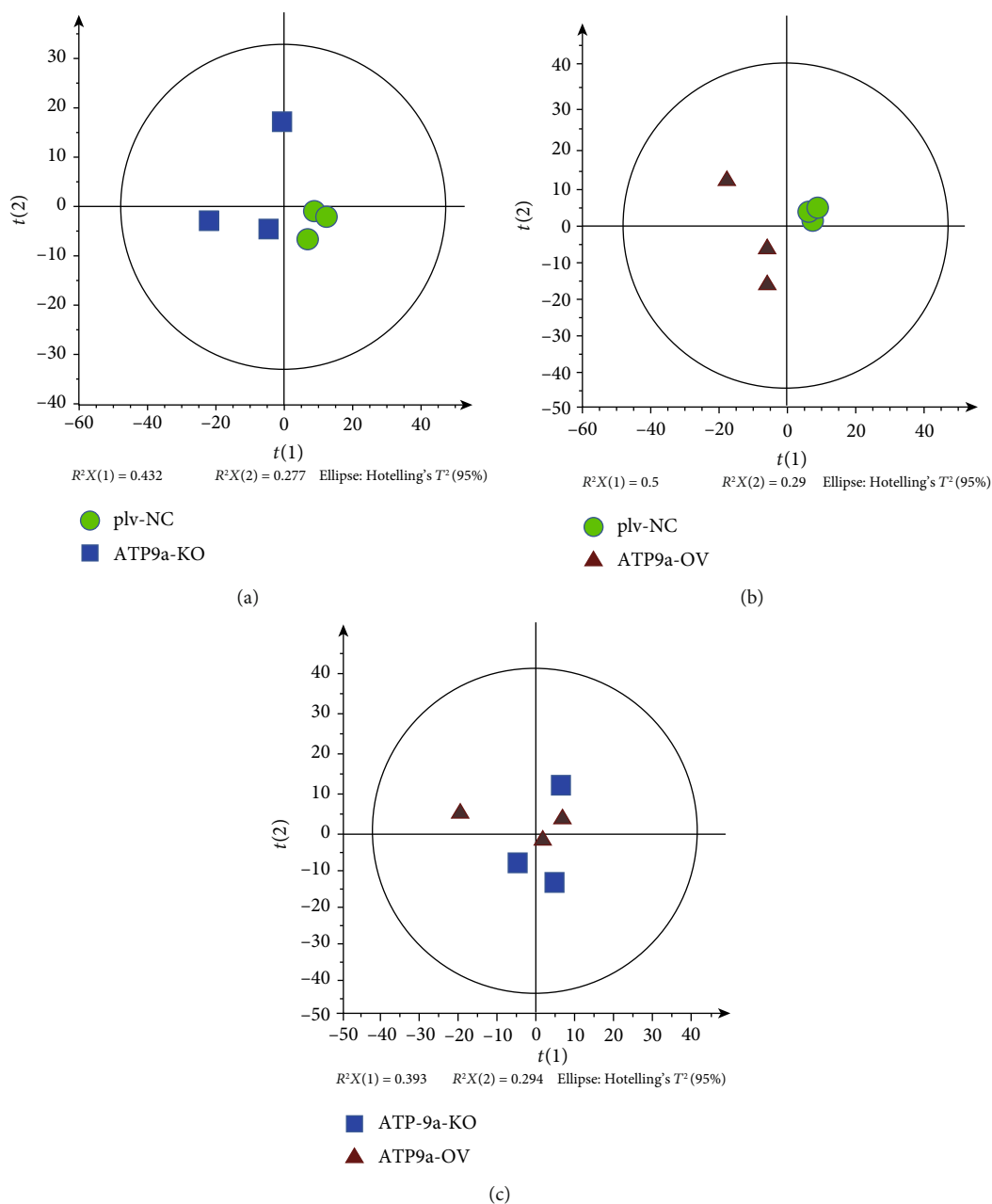
FIGURE 3: The PCA analysis of lipids in the plv-NC, ATP9A-OV, and ATP9A-KO groups. The PCA score plots obtained by comparing the three groups showed that three clusters were separated in the positive mode by the first two components. (a) PCA score between the plv-NC and ATP9A-KO groups. (b) PCA score between the plv-NC and ATP9A-OV groups. (c) PCA score between the ATP9A-KO and ATP9A-OV groups.

and nitrogen was used to lyophilize the phage. Isopropanol/-methanol (1/1, v/v) solution (400 μl) was used to reconstitute dried metabolites. These were then vortexed and centrifuged at 10,000 G for 5 min at 4°C. LC-MS and a Kinetex C18 column (100 × 2.1 mm, 1.9 μm) were used to analyze supernatant. The flow rate was set at 0.4 ml/min. Lipidomic assays in positive mode and negative mode were conducted following the protocol described in a previous report [21].

Lipid Search v 4.0.20 software (Thermo Fisher Scientific, USA) was used to process the raw data obtained from the LC-S analysis. Each sample's data was normalized to total area.

The sample number, normalized peak intensities, and all variate data (including retention time (rt) and charge-to-mass ratio (m/z)) were uploaded to SIMCA-P+ 12.0 software (Umetrics, Umea, Sweden). Multivariate analyses were performed to categorize the lipid samples; this included orthogonal partial least squares discriminant analysis (OPLS-DA) and principal component analysis (PCA). A permutation test with the permutation number of 200 was used to validate the OPLS-DA models [22].

Using Lipid Search software (Thermo Fisher Scientific, USA), a qualitative analysis of the lipid metabolites was

$R^2X(1) = 0.413$ $R^2X(2) = 0.202$ Ellipse: Hotelling's T^2 (95%)

● plv-NC

■ ATP9a-KO

● R^2

■ O^2

(a)

$R^2X(1) = 0.489$ $R^2X(2) = 0.295$ Ellipse: Hotelling's T^2 (95%)

● plv-NC

▲ ATP9a-OV

● R^2

■ O^2

(b)

FIGURE 4: Continued.

$R^2X(1) = 0.263$ $R^2X(2) = 0.276$ Ellipse: Hotelling's T^2 (95%)

■ ATP-9a-KO
▲ ATP9a-OV

● R^2
■ O^2

(c)
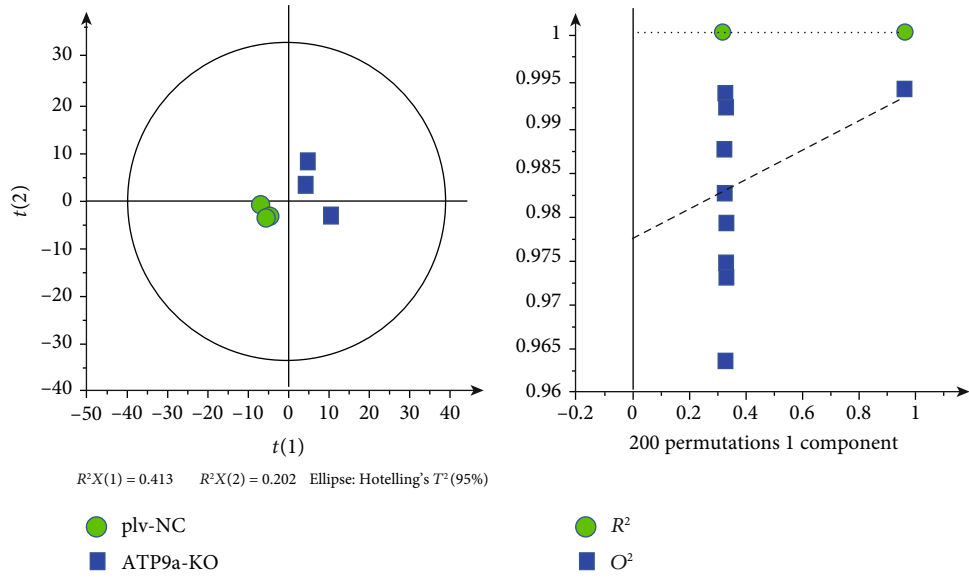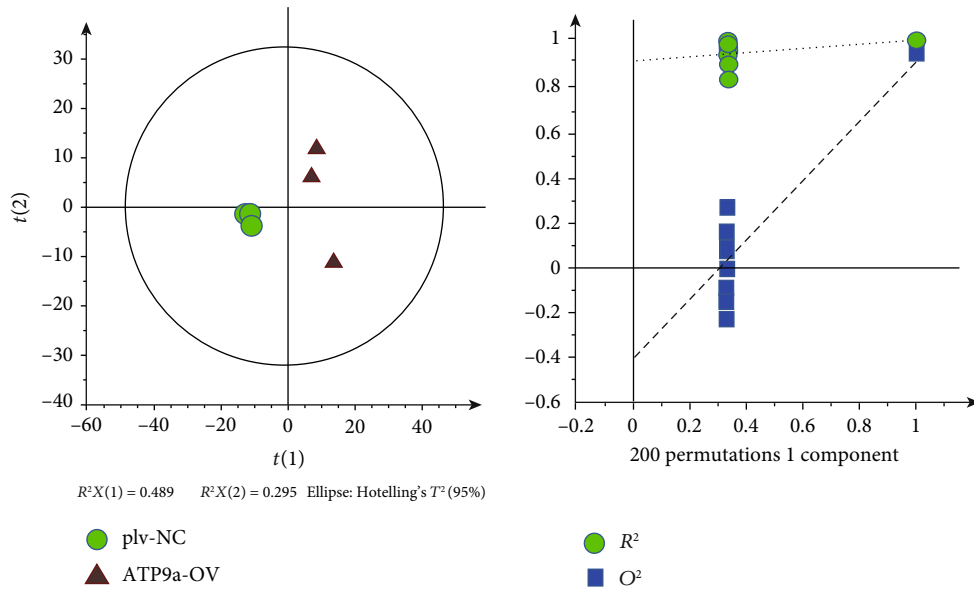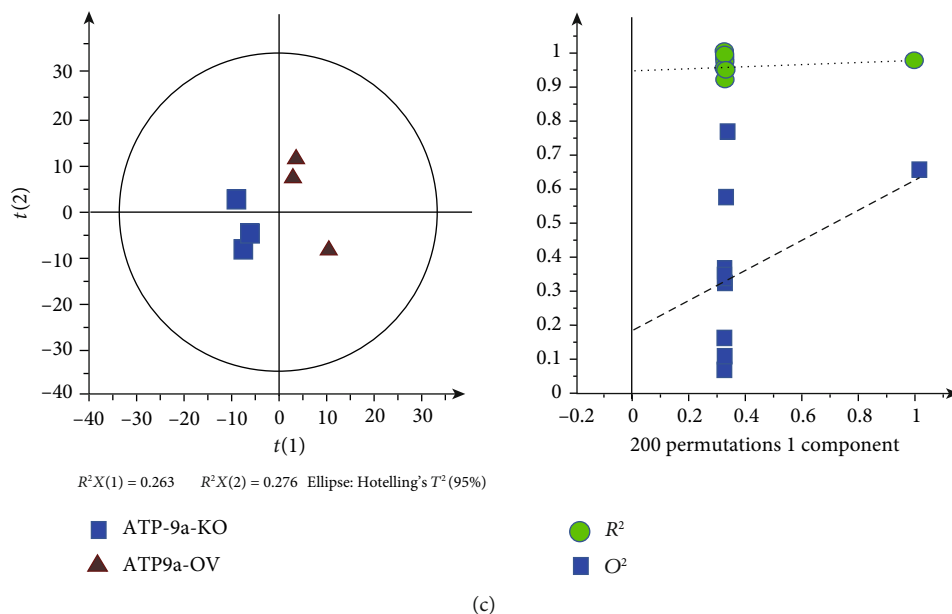
FIGURE 4: The OPLS-DA score plots of the plv-NC, ATP9A-OV, and ATP9A-KO groups. (a) OPLS-DA score between the plv-NC and ATP9A-KO groups. (b) OPLS-DA score between the plv-NC and ATP9A-OV groups. (c) OPLS-DA score between the ATP9A-KO and ATP9A-OV groups.

performed. The information collected included the type of lipids, chain length, and number of saturated bonds. The screening conditions for the potential lipid biomarkers were determined by the lipid metabolites in the OPLS-DA model having variable importance in the projection (VIP) scores > 1 and P values obtained from the t – test < 0.05.

2.8. Statistical Analysis. GraphPad Prism 7.0 was used to determine whether differences between groups were significantly different. For differences between two groups, an unpaired, two-sided Student's t-test was conducted, whereas, for three or more groups, a one-way ANOVA was used. Statistical significance is set as $P < 0.05$.

3. Results

To explore ATP9A's role in EV release in HEK293 cells, the location of ATP9A in the cells was examined. Using red fluorescent protein- (RFP-) tagged ATP9A (ATP9A-OV), it was noted that the location of ATP9A in the cells was accumulated primarily in intracellular vesicles (Figure 1).

As ATP9A was detected at the plasma membrane and intracellular vesicles, reduced expression of ATP9A could affect ectosome or exosome release. Figure 2 demonstrates that the number of EVs emitted in ATP9A-KO (ATP9A knockout cells) was significantly greater than the number of EVs released by the ATP9A-OV and plv-NC groups. The ATP9A-OV group released the fewest EVs. These findings suggest that the observed increase in the number of EVs from ATP9A knockout cells is mainly caused by elevated secretion of exosomes.

Lipidomics were performed for plv-NC, ATP9A-OV, and ATP9A-KO cells to better characterize the effects of ATP9A

■ plv-NC
■ ATP9a-KO
■ ATP9a-OV
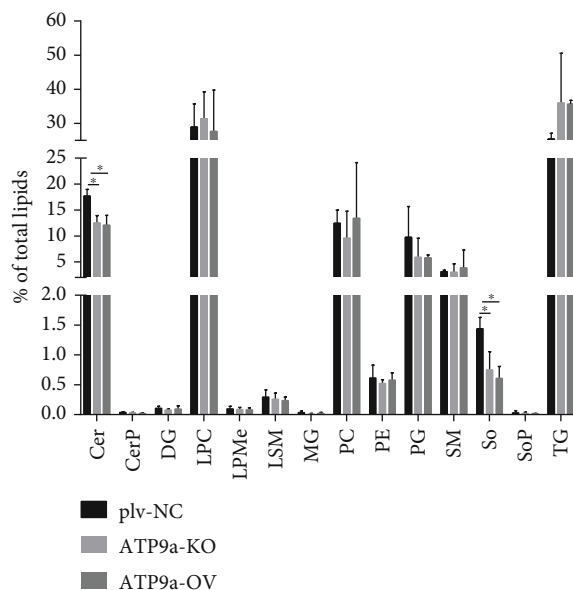
FIGURE 5: Percentage of all classes of lipids detected in the plv-NC, ATP9A-OV, and ATP9A-KO groups. Ceramides, lysophosphatidylcholine, phosphatidylglycerol, sphingomyelin, and triglycerides were the most common types of lipids. The percentage of ceramides (Cer), diacylglycerol (DG), lysophosphatidylcholine (LPC), lysophosphatidylmethanol (LPMe), monoglyceride (MG), phosphatidylcholine (PC), phosphatidylethanolamine (PE), phosphatidylglycerol (PG), sphingomyelin (SM), sphingoshine (So), and triglyceride (TG) are shown.

TABLE 1: The different lipid metabolites between the plv-NC, ATP9A-KO, and ATP9A-OV groups.

Lipid class	ATP9A-KO and plv-NC			ATP9A-OV and plv-NC			ATP9A-KO and ATP9A-OV		
	Positive mode	Negative mode	Total	Positive mode	Negative mode	Total	Positive mode	Negative mode	Total
Phosphatidylcholine (PC)	6	—	6	16	4	20	—	—	0
Phosphatidylethanolamine (PE)	2	—	2	3	—	3	2	—	2
Phosphatidylglycerol (PG)	1	—	1	—	—	0	—	—	0
Lysophosphatidylcholine (LPC)	8	—	8	12	1	13	4	—	4
Phosphatidylinositol (Pl)	—	—	0	—	—	0	2	—	2
Triglyceride (TG)	21	—	21	87	—	87	—	—	0
Diacylglycerol (DG)	—	—	0	1	—	1	1	—	1
Monogalactosylmonoacylglycerol (MGDG)	—	—	0	—	1	1	—	—	0
Sphingoshine (So)	1	—	1	2	—	2	—	—	0
Ceramides (Cer)	10	—	10	10	—	10	1	—	1
Total	49	—	49	131	6	137	10	—	10

on exosome biosynthesis. Principal component analysis (PCA) showed that in the positive mode, the R^2X and Q^2 between the ATP9A-KO and plv-NC groups were 0.659 and -0.00879, respectively. Between the ATP9A-OV and plv-NC groups, the R^2X and Q^2 were 0.79 and 0.477, respectively. Finally, between the ATP9A-KO and ATP9A-OV groups, the R^2X and Q^2 values were 0.689 and 0.0479, respectively (Figure 3). As the R^2X values all exceeded 0.4, the models were considered reliable. The PCA score plots obtained by comparing the three groups revealed that three clusters were separated in the positive mode by the first two components.

Figure 4 presents the PLS-DA score plots for the comparison of the three groups. This clearly shows separation in positive mode. The respective R^2X, R^2Y, and Q^2 between the ATP9A-KO and plv-NC groups were 0.615, 0.983, and 0.851. Similarly, the respective R^2X, R^2Y, and Q^2 values between the ATP9A-OV and plv-NC groups were 0.783, 0.99, and 0.951. Finally, the same respective values between the ATP9A-KO and ATP9A-OV groups were 0.539, 0.98, and 0.676.

Figure 5 presents the amount of different lipids as a percentage of the total. The percentage of Cer was significantly greater in the plv-NC group than in the ATP9A-OV and ATP9A-KO groups ($P < 0.05$). The level of sphingosine (So) was greatest in the plv-NC group ($P < 0.05$).

In total, there was a difference of 7 lipid classes, comprising 49 significantly different lipid metabolites, between the ATP9A-KO and plv-NC groups. This difference increased to 8 lipid classes and 137 significantly different lipid metabolites between the ATP9A-OV and plv-NC groups. The ATP9A-KO and ATP9A-OV groups differed by 5 lipid classes and 10 significantly different lipid metabolites (Table 1). The detailed differences in lipid metabolites between the plv-NC, ATP9A-KO, and ATP9A-OV groups in the positive mode are shown in Tables 2, 3, and 4. Table 5 shows the detailed differences in lipid metabolites between the ATP9A-OV and plv-NC groups in negative mode.

4. Discussion

ATP9A, a trafficking protein, plays a key role in the initiation of vesicle biogenesis [7, 23]. In this study, we found that the release of EVs from HEK293 cells was modulated by P4-ATPase ATP9A. The percentage of ceramides and sphingosine was significantly greater in the normal control cells than in the ATP9A overexpression and ATP9A knockout cells. The subcellular localization of mammalian P4-ATPases was observed using fluorescently labeled phospholipids to visualize the transport of phospholipids into cells. ATP9A was detected in the plasma membrane and intracellular compartments. This suggests that the presence of ATP9A in the plasma membrane is important for the purpose of assisting in the recycling of plasma membrane proteins through endocytosis [23]. EV release was increased in cell lines when ATP9A was knocked out; this implies that ATP9A plays an inhibitory role in EV release.

Many biological processes, such as angiogenesis, blood clotting, and immune response, are modulated by proteins, DNA, miRNA, and mRNAs, which could be controlled via EV-instigated intercellular communication. In this study, we demonstrated that exosome secretion was inhibited by ATP9A and this could be achieved through glucose transporter 1 (GLUT1) and transferrin receptor, as they are recycled to the plasma membrane through ATP9A endocytic recycling [17]. The knockdown expression of ATP9A in human hepatoma cells shows that the elevated release of EVs is independent of the activation of caspase-3 [23]. The quantity of EVs was significantly reduced in ATP9A knockdown cells in which exosome release had been pharmacologically blocked [23].

It is also possible that the elevated secretion of EVs is secondary to disrupting other key processes. ATP9A deficiency may be associated with cell death, proliferation, and survival pathways. Indeed, in HepG2 cells in which ATP9A was minimal, the cells underwent massive cell death approximately two weeks after ATP9A had been exhausted. As mentioned

TABLE 2: Detailed differences in lipid metabolites between the ATP9A-KO and plv-NC groups in positive mode.

No.	Lipid ion	Lipid group	Class	Fatty acid	Ion formula	VIP	T-test	Log_FC (ATP9a-KO/plv-NC)
1	Cer(d20:0/18:0) + H	Cer(d38:0) + H	Cer	(d20:0/18:0)	C38 H78 O3 N1	1.2604	0.030618969	-3.831098851
2	Cer(d22:0/18:0) + H	Cer(d40:0) + H	Cer	(d22:0/18:0)	C40 H82 O3 N1	1.24235	0.025143001	-4.328152705
3	Cer(d28:0) + H	Cer(d28:0) + H	Cer	(d28:0)	C28 H58 O3 N1	1.28102	0.0294742	-4.24959194
4	Cer(d30:0) + H	Cer(d30:0) + H	Cer	(d30:0)	C30 H62 O3 N1	1.275	0.025176996	-3.979850415
5	Cer(d32:0) + H	Cer(d32:0) + H	Cer	(d32:0)	C32 H66 O3 N1	1.26661	0.023622931	-4.490550701
6	Cer(d34:0) + H	Cer(d34:0) + H	Cer	(d34:0)	C34 H70 O3 N1	1.25672	0.029461839	-4.056379416
7	Cer(d34:0) + H	Cer(d34:0) + H	Cer	(d34:0)	C34 H70 O3 N1	1.23012	0.04426622	-3.117818449
8	Cer(d36:0) + H	Cer(d36:0) + H	Cer	(d36:0)	C36 H74 O3 N1	1.34994	0.008080528	-4.472595341
9	Cer(d36:3) + H	Cer(d36:3) + H	Cer	(d36:3)	C36 H68 O3 N1	1.29906	0.015827678	-4.504241793
10	Cer(d38:1) + H	Cer(d38:1) + H	Cer	(d38:1)	C38 H76 O3 N1	1.3665	0.004044369	-4.339760529
11	LPC(16:0) + H	LPC(16:0) + H	LPC	(16:0)	C24 H51 O7 N1 P1	1.19626	0.044904373	-3.965795361
12	LPC(16:0) + Na	LPC(16:0) + Na	LPC	(16:0)	C24 H50 O7 N1 P1 Na1	1.2719	0.019244897	-4.12685101
13	LPC(16:1) + H	LPC(16:1) + H	LPC	(16:1)	C24 H49 O7 N1 P1	1.37999	0.002239195	-4.666120577
14	LPC(18:1) + H	LPC(18:1) + H	LPC	(18:1)	C26 H53 O7 N1 P1	1.27108	0.019255048	-3.993299768
15	LPC(18:1) + H	LPC(18:1) + H	LPC	(18:1)	C26 H53 O7 N1 P1	1.27193	0.022622097	-5.420039555
16	LPC(18:3) + H	LPC(18:3) + H	LPC	(18:3)	C26 H49 O7 N1 P1	1.21783	0.033842529	-3.871958979
17	LPC(20:4) + H	LPC(20:4) + H	LPC	(20:4)	C28 H51 O7 N1 P1	1.3028	0.013961964	-5.206227559
18	LPC(22:6) + H	LPC(22:6) + H	LPC	(22:6)	C30 H51 O7 N1 P1	1.26602	0.021855354	-4.887480292
19	PC(31:0) + H	PC(31:0) + H	PC	(31:0)	C39 H79 O8 N1 P1	1.25034	0.043489185	-2.736580322
20	PC(33:0e) + H	PC(33:0e) + H	PC	(33:0e)	C41 H85 O7 N1 P1	1.24296	0.034649083	-4.296299639
21	PC(36:3) + H	PC(36:3) + H	PC	(36:3)	C44 H83 O8 N1 P1	1.25828	0.026138449	-2.824548745
22	PC(36:3) + H	PC(36:3) + H	PC	(36:3)	C44 H83 O8 N1 P1	1.22197	0.043015998	-2.834383398
23	PC(38:5) + H	PC(38:5) + H	PC	(38:5)	C46 H83 O8 N1 P1	1.26417	0.032636589	-2.865997476
24	PC(38:6) + H	PC(38:6) + H	PC	(38:6)	C46 H81 O8 N1 P1	1.2539	0.034802661	-2.826696561
25	PE(34:1e) + Na	PE(34:1e) + Na	PE	(34:1e)	C39 H78 O7 N1 P1 Na1	1.24296	0.034649083	-4.296299639
26	PE(38:6) + H	PE(38:6) + H	PE	(38:6)	C43 H75 O8 N1 P1	1.31751	0.016479104	-4.448539426

Table 2: Continued.

No.	Lipid ion	Lipid group	Class	Fatty acid	Ion formula	VIP	T-test	Log_FC (ATP9a-KO/plv-NC)
27	PG(45:6) + NH$_4$	PG(45:6) + NH$_4$	PG	(45:6)	C51 H93 O10 N1 P1	1.24296	0.034649083	-4.296299639
28	So(d16:0) + H	So(d16:0) + H	So	(d16:0)	C16 H36 O2 N1	1.25709	0.02502734	-2.937662223
29	TG(15:0/14:0/14:1) + NH$_4$	TG(43:1) + NH$_4$	TG	(15:0/14:0/14:1)	C46 H90 O6 N1	1.28754	0.026596333	-0.398603466
30	TG(15:0/17:0/17:0) + NH$_4$	TG(49:0) + NH$_4$	TG	(15:0/17:0/17:0)	C52 H104 O6 N1	1.3776	0.0031683	-2.264427759
31	TG(16:0/16:1/16:1) + NH$_4$	TG(48:2) + NH$_4$	TG	(16:0/16:1/16:1)	C51 H98 O6 N1	1.24966	0.034179356	-4.494068391
32	TG(16:0/18:1/18:1) + NH$_4$	TG(52:2) + NH$_4$	TG	(16:0/18:1/18:1)	C55 H106 O6 N1	1.27119	0.024617268	-2.876897982
33	TG(16:0/18:1/18:1) + NH$_4$	TG(52:2) + NH$_4$	TG	(16:0/18:1/18:1)	C55 H106 O6 N1	1.24273	0.029055366	-5.502551812
34	TG(16:1/16:1/16:1) + NH$_4$	TG(48:3) + NH$_4$	TG	(16:1/16:1/16:1)	C51 H96 O6 N1	1.25074	0.037153469	-2.820151763
35	TG(16:1/16:1/18:1) + Na	TG(50:3) + Na	TG	(16:1/16:1/18:1)	C53 H96 O6 Na1	1.38231	0.001565792	-4.888822805
36	TG(16:1/16:1/18:1) + NH$_4$	TG(50:3) + NH$_4$	TG	(16:1/16:1/18:1)	C53 H100 O6 N1	1.29488	0.013430777	-4.189332374
37	TG(16:1/18:1/18:1) + Na	TG(52:3) + Na	TG	(16:1/18:1/18:1)	C55 H100 O6 Na1	1.31766	0.013435952	-3.30410743
38	TG(16:1/18:1/18:1) + NH$_4$	TG(52:3) + NH$_4$	TG	(16:1/18:1/18:1)	C55 H104 O6 N1	1.30996	0.013226079	-3.528809232
39	TG(18:0/17:0/18:1) + NH$_4$	TG(53:1) + NH$_4$	TG	(18:0/17:0/18:1)	C56 H110 O6 N1	1.29598	0.022872573	0.90918934
40	TG(18:1/18:1/18:2) + NH$_4$	TG(54:4) + NH$_4$	TG	(18:1/18:1/18:2)	C57 H106 O6 N1	1.2432	0.044586752	-5.336667642
41	TG(18:1/18:2/18:2) + NH$_4$	TG(54:5) + NH$_4$	TG	(18:1/18:2/18:2)	C57 H104 O6 N1	1.2438	0.043561191	-2.874871415
42	TG(18:2/18:2/18:2) + Na	TG(54:6) + Na	TG	(18:2/18:2/18:2)	C57 H98 O6 Na1	1.28903	0.026337165	-4.660675027
43	TG(18:2/18:2/18:2) + NH$_4$	TG(54:6) + NH$_4$	TG	(18:2/18:2/18:2)	C57 H102 O6 N1	1.22084	0.039362783	-4.36954712
44	TG(18:4/18:1/18:1) + H	TG(54:6) + H	TG	(18:4/18:1/18:1)	C57 H99 O6	1.21603	0.04656314	-3.727194618
45	TG(20:5/18:2/18:2) + H	TG(56:9) + H	TG	(20:5/18:2/18:2)	C59 H97 O6	1.34412	0.00940743	-5.064000583
46	TG(4:0/16:0/18:0) + NH$_4$	TG(38:0) + NH$_4$	TG	(4:0/16:0/18:0)	C41 H82 O6 N1	1.30211	0.020072444	-0.008648167
47	TG(4:0/18:0/18:0) + NH$_4$	TG(40:0) + NH$_4$	TG	(4:0/18:0/18:0)	C43 H86 O6 N1	1.39232	0.001247294	-1.058028038
48	TG(6:0/16:0/20:4) + H	TG(42:4) + H	TG	(6:0/16:0/20:4)	C45 H79 O6	1.36281	0.005419013	4.422086595
49	TG(6:0/18:1/18:1) + NH$_4$	TG(42:2) + NH$_4$	TG	(6:0/18:1/18:1)	C45 H86 O6 N1	1.24028	0.047259192	18.15651265

previously, ATP9A is a member of subclass 2 in P4-ATPases [11]; Neo1 (*Saccharomyces cerevisiae*) and TAT-5 (*C. elegans*) are orthologs of ATP9A. While it is recognized that P4-ATPase deficiency can result in lethal consequences, it is not yet known what molecular mechanisms are responsible for this phenomenon [24]. Hela cells containing CRISPR-mediated knockout of ATP9A did not die; however, it is noted that data for long-term culture were omitted [17]. This suggests that some cell types can withstand ATP9A depletion; the pathway in which the protein is involved may determine the outcome.

P4-ATPases are important to many plasma and intracellular membrane-associated processes. One of these enzymes' primary functions is to institute and maintain a state of phospholipid asymmetry of cell membranes [7]. Increased exposure of PS in the exoplasmic leaflet of ATP9A-depleted

TABLE 3: Detailed differences in lipid metabolites between the ATP9A-KO and plv-NC groups in positive mode.

No.	Lipid ion	Lipid group	Class	Fatty acid	Ion formula	VIP	T-test	Log_FC(ATP9a-OV/plv-NC)
1	Cer(d20:0/18:0) + H	Cer(d38:0) + H	Cer	(d20:0/18:0)	C38 H78 O3 N1	1.18056	0.011353875	-0.412362667
2	Cer(d22:0/18:0) + H	Cer(d40:0) + H	Cer	(d22:0/18:0)	C40 H82 O3 N1	1.15478	0.017086722	-0.595999589
3	Cer(d22:1/2:0) + H	Cer(d24:1) + H	Cer	(d22:1/2:0)	C24 H48 O3 N1	1.11826	0.043499783	-0.570814243
4	Cer(d30:0) + H	Cer(d30:0) + H	Cer	(d30:0)	C30 H62 O3 N1	1.15035	0.025673707	-0.586615549
5	Cer(d32:0) + H	Cer(d32:0) + H	Cer	(d32:0)	C32 H66 O3 N1	1.10775	0.043725597	-0.631568883
6	Cer(d32:0) + H	Cer(d32:0) + H	Cer	(d32:0)	C32 H66 O3 N1	1.11214	0.048398875	-0.841046781
7	Cer(d32:0) + H	Cer(d32:0) + H	Cer	(d32:0)	C32 H66 O3 N1	1.13423	0.041166313	-0.537395468
8	Cer(d34:0) + H	Cer(d34:0) + H	Cer	(d34:0)	C34 H70 O3 N1	1.15175	0.021192786	-0.739156196
9	Cer(d36:0) + H	Cer(d36:0) + H	Cer	(d36:0)	C36 H74 O3 N1	1.1546	0.028080187	-0.343491384
10	Cer(d38:1) + H	Cer(d38:1) + H	Cer	(d38:1)	C38 H76 O3 N1	1.25148	0.000869044	-0.708510594
11	DG(18:1/18:1) + NH₄	DG(36:2) + NH₄	DG	(18:1/18:1)	C39 H76 O5 N1	1.14775	0.032034195	-1.170941291
12	LPC(14:0) + H	LPC(14:0) + H	LPC	(14:0)	C22 H47 O7 N1 P1	1.17492	0.011401697	-2.037925913
13	LPC(16:0) + H	LPC(16:0) + H	LPC	(16:0)	C24 H51 O7 N1 P1	1.18361	0.015200139	-1.185399006
14	LPC(16:0) + H	LPC(16:0) + H	LPC	(16:0)	C24 H51 O7 N1 P1	1.16722	0.016014207	-1.586333123
15	LPC(16:0) + Na	LPC(16:0) + Na	LPC	(16:0)	C24 H50 O7 N1 P1 Na1	1.2007	0.006996003	-1.69267157
16	LPC(16:1) + H	LPC(16:1) + H	LPC	(16:1)	C24 H49 O7 N1 P1	1.25501	0.000734215	-1.973182318
17	LPC(18:0) + H	LPC(18:0) + H	LPC	(18:0)	C26 H55 O7 N1 P1	1.17629	0.009004989	-1.955935386
18	LPC(18:1) + H	LPC(18:1) + H	LPC	(18:1)	C26 H53 O7 N1 P1	1.19239	0.008904148	-1.722036886
19	LPC(18:1) + H	LPC(18:1) + H	LPC	(18:1)	C26 H53 O7 N1 P1	1.17863	0.013931838	-1.295055719
20	LPC(18:2) + H	LPC(18:2) + H	LPC	(18:2)	C26 H51 O7 N1 P1	1.09975	0.033368835	-1.836675727
21	LPC(18:3) + H	LPC(18:3) + H	LPC	(18:3)	C26 H49 O7 N1 P1	1.17536	0.011863232	-1.692803017
22	LPC(20:4) + H	LPC(20:4) + H	LPC	(20:4)	C28 H51 O7 N1 P1	1.20989	0.006643335	-1.601519506
23	LPC(22:6) + H	LPC(22:6) + H	LPC	(22:6)	C30 H51 O7 N1 P1	1.18109	0.012416167	-1.660861569
24	PC(16:0/20:4) + Na	PC(36:4) + Na	PC	(16:0/20:4)	C44 H80 O8 N1 P1 Na1	1.18728	0.009695918	-1.197287937
25	PC(18:0/20:4) + Na	PC(38:4) + Na	PC	(18:0/20:4)	C46 H84 O8 N1 P1 Na1	1.19373	0.01387346	-1.252308071
26	PC(34:2) + H	PC(34:2) + H	PC	(34:2)	C42 H81 O8 N1 P1	1.13145	0.021697615	-1.645003452

Table 3: Continued.

No.	Lipid ion	Lipid group	Class	Fatty acid	Ion formula	VIP	T-test	Log_FC(ATP9a-OV/plv-NC)
27	PC(34:2) + Na	PC(34:2) + Na	PC	(34:2)	C42 H80 O8 N1 P1 Na1	1.14273	0.022076089	-2.192884674
28	PC(36:2) + H	PC(36:2) + H	PC	(36:2)	C44 H85 O8 N1 P1	1.18637	0.009290191	-1.520413569
29	PC(36:3) + H	PC(36:3) + H	PC	(36:3)	C44 H83 O8 N1 P1	1.2034	0.00592586	-1.534810921
30	PC(36:3) + H	PC(36:3) + H	PC	(36:3)	C44 H83 O8 N1 P1	1.091	0.063303852	-0.584433881
31	PC(36:3) + H	PC(36:3) + H	PC	(36:3)	C44 H83 O8 N1 P1	1.17719	0.013773598	-1.530770278
32	PC(36:4) + H	PC(36:4) + H	PC	(36:4)	C44 H81 O8 N1 P1	1.15291	0.019974882	-1.409087872
33	PC(36:4) + H	PC(36:4) + H	PC	(16:0/20:4)	C44 H81 O8 N1 P1	1.15056	0.024222573	-1.151908928
34	PC(36:4p) + H	PC(36:4p) + H	PC	(36:4p)	C44 H81 O7 N1 P1	1.09667	0.056620135	-1.032394903
35	PC(38:4) + H	PC(38:4) + H	PC	(18:0/20:4)	C46 H85 O8 N1 P1	1.01835	0.138748412	-0.52148975
36	PC(38:5) + H	PC(38:5) + H	PC	(38:5)	C46 H83 O8 N1 P1	1.10915	0.058086289	-0.647388207
37	PC(38:6) + H	PC(38:6) + H	PC	(38:6)	C46 H81 O8 N1 P1	1.22093	0.004912756	-1.089933633
38	PC(38:6) + Na	PC(38:6) + Na	PC	(38:6)	C46 H80 O8 N1 P1 Na1	1.16989	0.018637803	-1.222573329
39	PC(40:7) + H	PC(40:7) + H	PC	(40:7)	C48 H83 O8 N1 P1	1.11113	0.053579975	-0.945260739
40	PE(16:0p/18:1) + H	PE(34:1p) + H	PE	(16:0p/18:1)	C39 H77 O7 N1 P1	1.11038	0.055327279	0.456373702
41	PE(38:6) + H	PE(38:6) + H	PE	(38:6)	C43 H75 O8 N1 P1	1.22639	0.004954273	-2.282070421
42	PE(39:5) + H	PE(39:5) + H	PE	(39:5)	C44 H79 O8 N1 P1	1.1443	0.017276536	-1.751279845
43	So(d14:1) + H	So(d14:1) + H	So	(d14:1)	C14 H30 O2 N1	1.17166	0.01993559	-2.081806693
44	So(d16:0) + H	So(d16:0) + H	So	(d16:0)	C16 H36 O2 N1	1.09733	0.046617899	-1.916789565
45	TG(12:0/12:0/18:3) + H	TG(42:3) + H	TG	(12:0/12:0/18:3)	C45 H81 O6	1.2558	0.000676947	1.943382457
46	TG(15:0/14:0/14:1) + NH4	TG(43:1) + NH4	TG	(15:0/14:0/14:1)	C46 H90 O6 N1	1.19099	0.014229158	1.640598605
47	TG(15:0/16:0/16:0) + Na	TG(47:0) + Na	TG	(15:0/16:0/16:0)	C50 H96 O6 Na1	1.1358	0.02142449	1.159764763
48	TG(15:0/16:0/16:1) + NH4	TG(47:1) + NH4	TG	(15:0/16:0/16:1)	C50 H98 O6 N1	1.03827	0.099079456	-0.913642961
49	TG(15:0/16:0/18:1) + NH4	TG(49:1) + NH4	TG	(15:0/16:0/18:1)	C52 H102 O6 N1	1.17672	0.017013743	0.731184335
50	TG(15:0/17:0/17:0) + NH4	TG(49:0) + NH4	TG	(15:0/17:0/17:0)	C52 H104 O6 N1	1.16807	0.022219937	1.500799668
51	TG(15:1/14:0/16:1) + NH4	TG(45:2) + NH4	TG	(15:1/14:0/16:1)	C48 H92 O6 N1	1.12638	0.046410662	1.228411695
52	TG(16:0/10:0/18:1) + NH4	TG(44:1) + NH4	TG	(16:0/10:0/18:1)	C47 H92 O6 N1	1.21473	0.006570563	1.270938382

Table 3: Continued.

No.	Lipid ion	Lipid group	Class	Fatty acid	Ion formula	VIP	T-test	Log_FC(ATP9a-OV/plv-NC)
53	$TG(16:0/12:0/13:0) + NH_4$	$TG(41:0) + NH_4$	TG	$(16:0/12:0/13:0)$	$C44\ H88\ O6\ N1$	1.21837	0.006165409	1.937202801
54	$TG(16:0/12:0/14:0) + Na$	$TG(42:0) + Na$	TG	$(16:0/12:0/14:0)$	$C45\ H86\ O6\ Na1$	1.20558	0.00933199	1.253529015
55	$TG(16:0/12:0/14:0) + NH_4$	$TG(42:0) + NH_4$	TG	$(16:0/12:0/14:0)$	$C45\ H90\ O6\ N1$	1.12469	0.041448684	0.995570056
56	$TG(16:0/12:0/18:1) + NH_4$	$TG(46:1) + NH_4$	TG	$(16:0/12:0/18:1)$	$C49\ H96\ O6\ N1$	1.21927	0.006268795	0.851464834
57	$TG(16:0/13:0/14:0) + NH_4$	$TG(43:0) + NH_4$	TG	$(16:0/13:0/14:0)$	$C46\ H92\ O6\ N1$	1.11757	0.045489213	1.347749132
58	$TG(16:0/14:0/14:0) + Na$	$TG(44:0) + Na$	TG	$(16:0/14:0/14:0)$	$C47\ H90\ O6\ Na1$	1.24805	0.001498992	1.376050197
59	$TG(16:0/14:0/14:0) + NH_4$	$TG(44:0) + NH_4$	TG	$(16:0/14:0/14:0)$	$C47\ H94\ O6\ N1$	1.26237	0.000353143	0.962131291
60	$TG(16:0/14:0/16:0) + Na$	$TG(46:0) + Na$	TG	$(16:0/14:0/16:0)$	$C49\ H94\ O6\ Na1$	1.26857	8.80516E-05	1.565797115
61	$TG(16:0/14:0/16:0) + NH_4$	$TG(46:0) + NH_4$	TG	$(16:0/14:0/16:0)$	$C49\ H98\ O6\ N1$	1.21901	0.00635889	1.450016601
62	$TG(16:0/14:0/20:4) + H$	$TG(50:4) + H$	TG	$(16:0/14:0/20:4)$	$C53\ H95\ O6$	1.26854	9.83824E-05	1.326744372
63	$TG(16:0/16:0/16:0) + Na$	$TG(48:0) + Na$	TG	$(16:0/16:0/16:0)$	$C51\ H98\ O6\ Na1$	1.26708	0.000130539	1.471325066
64	$TG(16:0/16:0/16:0) + NH_4$	$TG(48:0) + NH_4$	TG	$(16:0/16:0/16:0)$	$C51\ H102\ O6\ N1$	1.25972	0.000420793	1.491554693
65	$TG(16:0/16:0/16:1) + Na$	$TG(48:1) + Na$	TG	$(16:0/16:0/16:1)$	$C51\ H96\ O6\ Na1$	1.26997	6.14983E-05	1.144805299
66	$TG(16:0/16:0/16:1) + NH_4$	$TG(48:1) + NH_4$	TG	$(16:0/16:0/16:1)$	$C51\ H100\ O6\ N1$	1.25463	0.000897787	1.053045297
67	$TG(16:0/16:0/18:1) + Na$	$TG(50:1) + Na$	TG	$(16:0/16:0/18:1)$	$C53\ H100\ O6\ Na1$	1.25028	0.00106583	1.831200518
68	$TG(16:0/16:0/18:1) + NH_4$	$TG(50:1) + NH_4$	TG	$(16:0/16:0/18:1)$	$C53\ H104\ O6\ N1$	1.25192	0.000771575	1.773752236
69	$TG(16:0/16:0/20:3) + H$	$TG(52:3) + H$	TG	$(16:0/16:0/20:3)$	$C55\ H101\ O6$	1.26734	0.000120746	2.280590338
70	$TG(16:0/16:0/20:4) + H$	$TG(52:4) + H$	TG	$(16:0/16:0/20:4)$	$C55\ H99\ O6$	1.25001	0.001163477	1.849719348
71	$TG(16:0/16:1/18:1) + Na$	$TG(50:2) + Na$	TG	$(16:0/16:1/18:1)$	$C53\ H98\ O6\ Na1$	1.03902	0.051199679	-0.248516244
72	$TG(16:0/17:0/18:1) + NH_4$	$TG(51:1) + NH_4$	TG	$(16:0/17:0/18:1)$	$C54\ H106\ O6\ N1$	1.12884	0.042802734	2.648612904
73	$TG(16:0/18:1/18:1) + NH_4$	$TG(52:2) + NH_4$	TG	$(16:0/18:1/18:1)$	$C55\ H106\ O6\ N1$	1.04551	0.102202776	-1.220332232
74	$TG(16:0/18:2/18:2) + Na$	$TG(52:4) + Na$	TG	$(16:0/18:2/18:2)$	$C55\ H98\ O6\ Na1$	1.01276	0.072197269	-0.233717192
75	$TG(16:0/18:2/18:2) + NH_4$	$TG(52:4) + NH_4$	TG	$(16:0/18:2/18:2)$	$C55\ H102\ O6\ N1$	1.1579	0.015560565	-0.777716804
76	$TG(16:0/8:0/18:1) + NH_4$	$TG(42:1) + NH_4$	TG	$(16:0/8:0/18:1)$	$C45\ H88\ O6\ N1$	1.27372	5.23657E-06	2.89136082
77	$TG(16:1/16:1/18:1) + Na$	$TG(50:3) + Na$	TG	$(16:1/16:1/18:1)$	$C53\ H96\ O6\ Na1$	1.24888	0.000976709	-0.791307191
78	$TG(16:1/16:1/18:1) + NH_4$	$TG(50:3) + NH_4$	TG	$(16:1/16:1/18:1)$	$C53\ H100\ O6\ N1$	1.16996	0.013073421	-0.641262818
79	$TG(16:1/18:1/18:1) + Na$	$TG(52:3) + Na$	TG	$(16:1/18:1/18:1)$	$C55\ H100\ O6\ Na1$	1.22748	0.002533394	-0.763755159

Table 3: Continued.

No.	Lipid ion	Lipid group	Class	Fatty acid	Ion formula	VIP	T-test	Log_FC(ATP9a-OV/plv-NC)
80	TG(16:1/18:1/18:1) + NH$_4$	TG(52:3) + NH$_4$	TG	(16:1/18:1/18:1)	C55 H104 O6 N1	1.20162	0.005474227	-0.786386257
81	TG(18:0/16:0/16:0) + Na	TG(50:0) + Na	TG	(18:0/16:0/16:0)	C53 H102 O6 Na1	1.26614	0.000158837	2.275169817
82	TG(18:0/16:0/16:0) + NH$_4$	TG(50:0) + NH$_4$	TG	(18:0/16:0/16:0)	C53 H106 O6 N1	1.26293	0.000281314	2.032336625
83	TG(18:0/16:0/18:0) + Na	TG(52:0) + Na	TG	(18:0/16:0/18:0)	C55 H106 O6 Na1	1.25922	0.000520621	2.41337606
84	TG(18:0/16:0/18:0) + NH$_4$	TG(52:0) + NH$_4$	TG	(18:0/16:0/18:0)	C55 H110 O6 N1	1.26597	0.000180915	2.667777604
85	TG(18:0/16:0/18:1) + Na	TG(52:1) + Na	TG	(18:0/16:0/18:1)	C55 H104 O6 Na1	1.26724	0.000138532	2.887231449
86	TG(18:0/16:0/18:1) + NH$_4$	TG(52:1) + NH$_4$	TG	(18:0/16:0/18:1)	C55 H108 O6 N1	1.26045	0.000462091	3.231733656
87	TG(18:0/16:0/20:4) + H	TG(54:4) + H	TG	(18:0/16:0/20:4)	C57 H103 O6	1.26769	0.000124179	3.110340992
88	TG(18:0/16:0/22:0) + NH$_4$	TG(56:0) + NH$_4$	TG	(18:0/16:0/22:0)	C59 H118 O6 N1	1.22968	0.004316666	2.187805394
89	TG(18:0/17:0/18:0) + NH$_4$	TG(53:0) + NH$_4$	TG	(18:0/17:0/18:0)	C56 H112 O6 N1	1.26138	0.000396904	2.424298519
90	TG(18:0/17:0/18:1) + NH$_4$	TG(53:1) + NH$_4$	TG	(18:0/17:0/18:1)	C56 H110 O6 N1	1.18602	0.016664437	2.713496047
91	TG(18:0/18:0/18:0) + Na	TG(54:0) + Na	TG	(18:0/18:0/18:0)	C57 H110 O6 Na1	1.26827	0.000105223	5.230250311
92	TG(18:0/18:0/18:0) + NH$_4$	TG(54:0) + NH$_4$	TG	(18:0/18:0/18:0)	C57 H114 O6 N1	1.26949	5.7205E-05	2.285459979
93	TG(18:0/18:0/18:1) + Na	TG(54:1) + Na	TG	(18:0/18:0/18:1)	C57 H108 O6 Na1	1.26278	0.000305486	4.481228399
94	TG(18:0/18:0/18:1) + NH$_4$	TG(54:1) + NH$_4$	TG	(18:0/18:0/18:1)	C57 H112 O6 N1	1.27143	3.13706E-05	4.649314869
95	TG(18:0/18:0/18:3) + H	TG(54:3) + H	TG	(18:0/18:0/18:3)	C57 H105 O6	1.26198	0.000356975	2.416341259
96	TG(18:0/18:0/20:4) + H	TG(56:4) + H	TG	(18:0/18:0/20:4)	C59 H107 O6	1.26273	0.000307805	4.483895814
97	TG(18:0/18:1/18:1) + Na	TG(54:2) + Na	TG	(18:0/18:1/18:1)	C57 H106 O6 Na1	1.22634	0.002728095	1.662501
98	TG(18:0/18:1/18:1) + NH$_4$	TG(54:2) + NH$_4$	TG	(18:0/18:1/18:1)	C57 H110 O6 N1	1.19634	0.010041025	1.513228258
99	TG(18:1/18:1/18:2) + NH$_4$	TG(54:4) + NH$_4$	TG	(18:1/18:1/18:2)	C57 H106 O6 N1	1.15588	0.023234959	-0.351349117
100	TG(18:1/18:1/20:4) + H	TG(56:6) + H	TG	(18:1/18:1/20:4)	C59 H103 O6	1.04017	0.05964527	-0.182813869
101	TG(18:1/18:2/18:2) + NH$_4$	TG(54:5) + NH$_4$	TG	(18:1/18:2/18:2)	C57 H104 O6 N1	1.22517	0.004865563	-0.471280945
102	TG(18:2/18:2/18:2) + Na	TG(54:6) + Na	TG	(18:2/18:2/18:2)	C57 H98 O6 Na1	1.01999	0.138715238	-0.381333699
103	TG(18:2/18:2/18:2) + NH$_4$	TG(54:6) + NH$_4$	TG	(18:2/18:2/18:2)	C57 H102 O6 N1	1.14238	0.030646745	-0.792226116
104	TG(18:3/18:2/18:2) + H	TG(54:7) + H	TG	(18:3/18:2/18:2)	C57 H97 O6	1.0853	0.053095571	-0.233717192
105	TG(18:3/18:2/18:2) + NH$_4$	TG(54:7) + NH$_4$	TG	(18:3/18:2/18:2)	C57 H100 O6 N1	1.04634	0.083166907	-0.934006022
106	TG(18:4/18:1/18:1) + H	TG(54:6) + H	TG	(18:4/18:1/18:1)	C57 H99 O6	1.17609	0.009589781	-0.65252347
107	TG(20:0e/18:2/18:3) + H	TG(56:5e) + H	TG	(20:0e/18:2/18:3)	C59 H107 O5	1.20462	0.010060286	3.325380766
108	TG(20:5/18:2/18:2) + H	TG(56:9) + H	TG	(20:5/18:2/18:2)	C59 H97 O6	1.01499	0.144587695	-0.440537678
109	TG(4:0/12:0/18:1) + NH$_4$	TG(34:1) + NH$_4$	TG	(4:0/12:0/18:1)		1.20296	0.01036702	4.04828539

Table 3: Continued.

No.	Lipid ion	Lipid group	Class	Fatty acid	Ion formula	VIP	T-test	Log_FC(ATP9a-OV/plv-NC)
					C37 H72 O6 N1			
110	TG(4 : 0/12 : 0/18 : 3) + H	TG(34 : 3) + H	TG	(4 : 0/12 : 0/18 : 3)	C37 H65 O6	1.06475	0.062064921	0.316304726
111	TG(4 : 0/14 : 0/18 : 1) + NH₄	TG(36 : 1) + NH₄	TG	(4 : 0/14 : 0/18 : 1)	C39 H76 O6 N1	1.24976	0.001350972	23.88325332
112	TG(4 : 0/14 : 0/18 : 3) + H	TG(36 : 3) + H	TG	(4 : 0/14 : 0/18 : 3)	C39 H69 O6	1.14385	0.035066923	2.573454618
113	TG(4 : 0/15 : 0/16 : 0) + NH₄	TG(35 : 0) + NH₄	TG	(4 : 0/15 : 0/16 : 0)	C38 H76 O6 N1	1.26752	0.000121981	5.017537183
114	TG(4 : 0/15 : 0/18 : 1) + NH₄	TG(37 : 1) + NH₄	TG	(4 : 0/15 : 0/18 : 1)	C40 H78 O6 N1	1.2024	0.010822476	3.978439339
115	TG(4 : 0/16 : 0/17 : 0) + NH₄	TG(37 : 0) + NH₄	TG	(4 : 0/16 : 0/17 : 0)	C40 H80 O6 N1	1.26052	0.000457105	3.907668532
116	TG(4 : 0/16 : 0/18 : 0) + Na	TG(38 : 0) + Na	TG	(4 : 0/16 : 0/18 : 0)	C41 H78 O6 Na1	1.22345	0.005085456	2.38625847
117	TG(4 : 0/16 : 0/18 : 0) + NH₄	TG(38 : 0) + NH₄	TG	(4 : 0/16 : 0/18 : 0)	C41 H82 O6 N1	1.10835	0.058570888	1.040201462
118	TG(4 : 0/16 : 0/18 : 1) + Na	TG(38 : 1) + Na	TG	(4 : 0/16 : 0/18 : 1)	C41 H76 O6 Na1	1.25375	0.000949516	6.971333525
119	TG(4 : 0/16 : 0/18 : 1) + NH₄	TG(38 : 1) + NH₄	TG	(4 : 0/16 : 0/18 : 1)	C41 H80 O6 N1	1.25057	0.001235431	6.528128518
120	TG(4 : 0/16 : 0/20 : 3) + H	TG(40 : 3) + H	TG	(4 : 0/16 : 0/20 : 3)	C43 H77 O6	1.23489	0.003249599	3.288156904
121	TG(4 : 0/17 : 0/18 : 1) + NH₄	TG(39 : 1) + NH₄	TG	(4 : 0/17 : 0/18 : 1)	C42 H82 O6 N1	1.2527	0.001062263	4.151115681
122	TG(4 : 0/18 : 0/18 : 0) + NH₄	TG(40 : 0) + NH₄	TG	(4 : 0/18 : 0/18 : 0)	C43 H86 O6 N1	1.13529	0.036323412	1.926228297
123	TG(4 : 0/18 : 1/18 : 1) + Na	TG(40 : 2) + Na	TG	(4 : 0/18 : 1/18 : 1)	C43 H78 O6 Na1	1.22707	0.004439594	1.831811125
124	TG(4 : 0/18 : 1/18 : 1) + NH₄	TG(40 : 2) + NH₄	TG	(4 : 0/18 : 1/18 : 1)	C43 H82 O6 N1	1.22764	0.004258607	1.648333529
125	TG(4 : 0/18 : 1/18 : 3) + H	TG(40 : 4) + H	TG	(4 : 0/18 : 1/18 : 3)	C43 H75 O6	1.25375	0.000949516	6.971333525
126	TG(46 : 1) + Na	TG(46 : 1) + Na	TG	(16 : 0/12 : 0/18 : 1)	C49 H92 O6 Na1	1.23901	0.002745257	0.902280507
127	TG(6 : 0/16 : 0/17 : 0) + NH₄	TG(39 : 0) + NH₄	TG	(6 : 0/16 : 0/17 : 0)	C42 H84 O6 N1	1.25624	0.000728265	2.333598845
128	TG(6 : 0/16 : 0/18 : 1) + NH₄	TG(40 : 1) + NH₄	TG	(6 : 0/16 : 0/18 : 1)	C43 H84 O6 N1	1.26874	8.63677E-05	4.581376753
129	TG(6 : 0/16 : 0/20 : 4) + H	TG(42 : 4) + H	TG	(6 : 0/16 : 0/20 : 4)	C45 H79 O6	1.26166	0.000379843	7.405154525
130	TG(6 : 0/18 : 1/18 : 1) + NH₄	TG(42 : 2) + NH₄	TG	(6 : 0/18 : 1/18 : 1)	C45 H86 O6 N1	1.24437	0.001939902	19.65297904
131	TG(8 : 0/12 : 0/18 : 3) + H	TG(38 : 3) + H	TG	(8 : 0/12 : 0/18 : 3)	C41 H73 O6	1.19976	0.011885245	2.272770506

HepG2 cells resulted in partial loss of plasma membrane asymmetry [23]. In *S. cerevisiae*, the asymmetry of the plasma membrane is lost as PE and PS become exposed as a consequence of NEO1 deficiency [24]. Similarly, the exposure of PE in the exoplasmic leaflet of *C. elegans* increases with TAT-5 deficiency; however, no external PS was detected [16]. In this study, ATP9A-depleted HEK293 cells did not exhibit an increase in PS, but ceramides (Cer) and sphingosine were decreased in cells in which ATP9A was overex-pressed or knocked out. A number of pathologies are associated with dysregulated sphingolipid metabolism; these include cancer, cardiovascular disease, hepatic steatosis, metabolic disorders, neurological disease, and type 2 diabetes [25, 26]. Exosomes were exchanged between the tumor cells and other tissues; however, few studies have examined the functional roles of these exosomal lipids [27]. Cer is enriched in the exosomes, and it is also an important lipid in exosomal formation. As the center in the sphingolipid metabolism, Cer

TABLE 4: Detailed differences in lipid metabolites between the ATP9A-OV and ATP9A-KO groups in positive mode.

No.	Lipid ion	Lipid group	Class	Fatty acid	Ion formula	VIP	T-test	Log_FC(ATP9a-OV/ATP9a-KO)
1	Cer(d32:0) + H	Cer(d32:0) + H	Cer	(d32:0)	C32 H66 O3 N1	1.53407	0.046202984	-1.221196739
2	DG(18:1/18:1) + NH$_4$	DG(36:2) + NH$_4$	DG	(18:1/18:1)	C39 H76 O5 N1	1.57489	0.033527384	-0.844934869
3	LPC(16:0) + H	LPC(16:0) + H	LPC	(16:0)	C24 H51 O7 N1 P1	1.55693	0.038858829	-0.646114065
4	LPC(16:1) + H	LPC(16:1) + H	LPC	(16:1)	C24 H49 O7 N1 P1	1.67884	0.010297907	-0.870328703
5	LPC(18:0) + H	LPC(18:0) + H	LPC	(18:0)	C26 H55 O7 N1 P1	1.57303	0.034060664	-1.147680261
6	LPC(20:4) + H	LPC(20:4) + H	LPC	(20:4)	C28 H51 O7 N1 P1	1.61395	0.023265476	-0.549852755
7	PE(16:0p/18:1) + H	PE(34:1p) + H	PE	(16:0p/18:1)	C39 H77 O7 N1 P1	1.64662	0.016093919	1.531453663
8	PE(38:6) + H	PE(38:6) + H	PE	(38:6)	C43 H75 O8 N1 P1	1.65057	0.015315495	-0.898920166
9	TG(15:0/16:0/16:0) + Na	TG(47:0) + Na	TG	(15:0/16:0/16:0)	C50 H96 O6 Na1	1.59647	0.027631258	0.747616493
10	TG(16:0/12:0/13:0) + NH$_4$	TG(41:0) + NH$_4$	TG	(16:0/12:0/13:0)	C44 H88 O6 N1	1.56416	0.036667833	1.376598918

TABLE 5: Detailed differences in lipid metabolites between the ATP9A-OV and plv-NC groups in negative mode.

No.	Lipid ion	Lipid group	Class	Fatty acid	Ion formula	VIP	T-test	Log_FC(ATP9A-OV/plv-NC)
1	LPC(16:0) + HCOO	LPC(16:0) + HCOO	LPC	(16:0)	C25 H51 O9 N1 P1	1.42619	0.02839175	-0.956682794
2	PC(16:0/18:2) + HCOO	PC(34:2) + HCOO	PC	(16:0/18:2)	C43 H81 O10 N1 P1	1.40826	0.033403463	-0.777315557
3	PC(16:0/20:4) + HCOO	PC(36:4) + HCOO	PC	(16:0/20:4)	C45 H81 O10 N1 P1	1.45251	0.020556433	-0.64073783
4	PC(18:0/18:2) + HCOO	PC(36:2) + HCOO	PC	(18:0/18:2)	C45 H85 O10 N1 P1	1.4845	0.011801161	-0.732314818
5	PC(16:0/22:6) + HCOO	PC(38:6) + HCOO	PC	(16:0/22:6)	C47 H81 O10 N1 P1	1.38346	0.030681364	-0.753866237
6	MGDG(47:12) + HCOO	MGDG(47:12) + HCOO	MGDG	(47:12)	C57 H85 O12	1.52892	0.004986124	-0.722153703

is predominantly produced via acid sphingomyelinase-mediated hydrolysis of sphingomyelin and then metabolized to sphingosine by acid ceramidase [28]. Cosker and Segal suggested that the exosomal lipids can transmit "mobile rafts" that can activate cell signaling pathways in oncogenesis and metastasis [29]. Cer can modulate the roles of these mobile rafts and their effects on the signaling pathways [29]. Sphingosine may increase the activation of the TRPML1 channel in the presence of ML-SA1. ATP9A may regulate sphingosine production and, thus, decrease TRPML1 channel activity [30]. It was previously postulated that the translocation undertaken by P4-ATPases was selective, favoring glycerophospholipids and excluding sphingolipids. Thus, the molecular relationship between *ATP9A* and ceramides and sphingosine are mysterious [31].

Data Availability

The datasets generated and analyzed during the current study are available from the corresponding authors on reasonable request.

Conflicts of Interest

The authors declare that they have no conflicts of interest.

Authors' Contributions

Xiao Xu and Limei Xu contributed equally to this work.

Acknowledgments

References

[1] K. B. Beer and A. M. Wehman, "Mechanisms and functions of extracellular vesicle release *in vivo*—what we can learn from flies and worms," *Cell Adhesion & Migration*, vol. 11, no. 2, pp. 135–150, 2017.

[2] M. Colombo, G. Raposo, and C. Thery, "Biogenesis, secretion, and intercellular interactions of exosomes and other extracellular vesicles," *Annual Review of Cell and Developmental Biology*, vol. 30, no. 1, pp. 255–289, 2014.

[3] E. Cocucci and J. Meldolesi, "Ectosomes and exosomes: shedding the confusion between extracellular vesicles," *Trends in Cell Biology*, vol. 25, no. 6, pp. 364–372, 2015.

[4] J. M. Stein and J. P. Luzio, "Ectocytosis caused by sublytic autologous complement attack on human neutrophils. The sorting of endogenous plasma-membrane proteins and lipids into shed vesicles," *Biochemical Journal*, vol. 274, no. 2, pp. 381–386, 1991.

[5] Y. N. Gong, C. Guy, H. Olauson et al., "ESCRT-III acts downstream of MLKL to regulate necroptotic cell death and its consequences," *Cell*, vol. 169, no. 2, pp. 286–300.e16, 2017.

[6] M. Murate and T. Kobayashi, "Revisiting transbilayer distribution of lipids in the plasma membrane," *Chemistry and Physics of Lipids*, vol. 194, pp. 58–71, 2016.

[7] J. P. Andersen, A. L. Vestergaard, S. A. Mikkelsen, L. S. Mogensen, M. Chalat, and R. S. Molday, "P4-ATPases as phospholipid flippases—structure, function, and enigmas," *Frontiers in Physiology*, vol. 7, 2016.

[8] E. M. Bevers and P. L. Williamson, "Getting to the outer leaflet: physiology of phosphatidylserine exposure at the plasma membrane," *Physiological Reviews*, vol. 96, no. 2, pp. 605–645, 2016.

[9] R. B. Birge, S. Boeltz, S. Kumar et al., "Phosphatidylserine is a global immunosuppressive signal in efferocytosis, infectious disease, and cancer," *Cell Death & Differentiation*, vol. 23, no. 6, pp. 962–978, 2016.

[10] H. M. Hankins, R. D. Baldridge, P. Xu, and T. R. Graham, "Role of flippases, scramblases and transfer Proteins in phosphatidylserine subcellular distribution," *Traffic*, vol. 16, no. 1, pp. 35–47, 2015.

[11] V. A. van der Mark, R. P. Elferink, and C. C. Paulusma, "P4 ATPases: flippases in health and Disease," *International Journal of Molecular Sciences*, vol. 14, no. 4, pp. 7897–7922, 2013.

[12] B. P. Roland and T. R. Graham, "Decoding P4-ATPase substrate interactions," *Critical Reviews in Biochemistry and Molecular Biology*, vol. 51, no. 6, pp. 513–527, 2016.

[13] M. S. Jensen, S. R. Costa, A. S. Duelli et al., "Phospholipid flipping involves a central cavity in P4 ATPases," *Scientific Reports*, vol. 7, no. 1, article 17621, 2017.

[14] A. L. Vestergaard, J. A. Coleman, T. Lemmin et al., "Critical roles of isoleucine-364 and adjacent residues in a hydrophobic gate control of phospholipid transport by the mammalian P4-ATPase ATP8A2," *Proceedings of the National Academy of Sciences*, vol. 111, no. 14, pp. E1334–E1343, 2014.

[15] A. M. Wehman, C. Poggioli, P. Schweinsberg, B. D. Grant, and J. Nance, "The P4-ATPase TAT-5 inhibits the budding of extracellular vesicles in *C. elegans* embryos," *Current Biology*, vol. 21, no. 23, pp. 1951–1959, 2011.

[16] H. Takatsu, K. Baba, T. Shima et al., "ATP9B, a P4-ATPase (a putative aminophospholipid translocase), localizes to the *trans*-Golgi network in a CDC50 protein-independent manner," *Journal of Biological Chemistry*, vol. 286, no. 44, pp. 38159–38167, 2011.

[17] Y. Tanaka, N. Ono, T. Shima et al., "The phospholipid flippase ATP9A is required for the recycling pathway from the endosomes to the plasma membrane," *Molecular Biology of the Cell*, vol. 27, no. 24, pp. 3883–3893, 2016.

[18] A. Irie, K. Yamamoto, Y. Miki, and M. Murakami, "Phosphatidylethanolamine dynamics are required for osteoclast fusion," *Scientific Reports*, vol. 7, no. 1, article 46715, 2017.

[19] Y. Ophinni, M. Inoue, T. Kotaki, and M. Kameoka, "CRISPR/Cas9 system targeting regulatory genes of HIV-1 inhibits viral replication in infected T-cell cultures," *Scientific Reports*, vol. 8, no. 1, p. 7784, 2018.

[20] A. N. Böing, J. Stap, C. M. Hau et al., "Active caspase-3 is removed from cells by release of caspase-3-enriched vesicles," *Biochimica et Biophysica Acta (BBA) - Molecular Cell Research*, vol. 1833, no. 8, pp. 1844–1852, 2013.

[21] Y. Xu, Y. Wu, Y. Xiong et al., "Ascorbate protects liver from metabolic disorder through inhibition of lipogenesis and suppressor of cytokine signaling 3 (SOCS3)," *Nutrition & Metabolism*, vol. 17, no. 1, p. 17, 2020.

[22] M. Huang, Y. Dong, Y. Zhang et al., "Growth and lipidomic responses of juvenile Pacific white shrimp *Litopenaeus vannamei* to low salinity," *Frontiers in Physiology*, vol. 10, p. 1087, 2019.

[23] J. Naik, C. M. Hau, L. ten Bloemendaal et al., "The P4-ATPase ATP9A is a novel determinant of exosome release," *PLoS One*, vol. 14, no. 4, article e0213069, 2019.

[24] M. Takar, Y. Wu, and T. R. Graham, "The essential Neo1 protein from budding yeast plays a role in establishing aminophospholipid asymmetry of the plasma membrane," *Journal of Biological Chemistry*, vol. 291, no. 30, pp. 15727–15739, 2016.

[25] Y. A. Hannun and L. M. Obeid, "Sphingolipids and their metabolism in physiology and disease," *Nature Reviews Molecular Cell Biology*, vol. 19, no. 3, pp. 175–191, 2018.

[26] M. Mrad, C. Imbert, V. Garcia et al., "Downregulation of sphingosine kinase-1 induces protective tumor immunity by promoting M1 macrophage response in melanoma," *Oncotarget*, vol. 7, no. 44, pp. 71873–71886, 2016.

[27] A. Elsherbini and E. Bieberich, "Ceramide and exosomes: a novel target in cancer biology and therapy," *Advances in Cancer Research*, vol. 140, pp. 121–154, 2018.

[28] D. Shen, X. Wang, X. Li et al., "Lipid storage disorders block lysosomal trafficking by inhibiting a TRP channel and

lysosomal calcium release," *Nature Communications*, vol. 3, no. 1, article 731, 2012.

[29] K. E. Cosker and R. A. Segal, "Neuronal signaling through endocytosis," *Cold Spring Harbor Perspectives in Biology*, vol. 6, no. 2, 2014.

[30] G. Li, D. Huang, J. Hong, O. M. Bhat, X. Yuan, and P. L. Li, "Control of lysosomal TRPML1 channel activity and exosome release by acid ceramidase in mouse podocytes," *American Journal of Physiology-Cell Physiology*, vol. 317, no. 3, pp. C481–C491, 2019.

[31] B. P. Roland, T. Naito, J. T. Best et al., "Yeast and human P4-ATPases transport glycosphingolipids using conserved structural motifs," *Journal of Biological Chemistry*, vol. 294, no. 6, pp. 1794–1806, 2019.

Research Article

NFE2L2 Is a Potential Prognostic Biomarker and Is Correlated with Immune Infiltration in Brain Lower Grade Glioma: A Pan-Cancer Analysis

Qiang Ju [ID],[1] **Xinmei Li**,[2] **Heng Zhang**,[2] **Songxia Yan**,[1] **Ying Li**,[1] and **Yanjie Zhao** [ID][2]

[1]*Department of Blood Transfusion, The Affiliated Hospital of Qingdao University, Qingdao University, Qingdao, China*
[2]*School of Public Health, Qingdao University, Qingdao, China*

Correspondence should be addressed to Yanjie Zhao; zhaoyj@qdu.edu.cn

Nuclear factor, erythroid 2 like 2 (NFE2L2, NRF2) is a transcription factor that regulates various antioxidant enzymes. It plays a vital physiological role in regulating oxidative stress and inflammatory response. However, the roles of NFE2L2 in human cancers are still unclear. Our study is aimed at analyzing the prognostic value of NFE2L2 in pan-cancer and at revealing the relationship between NFE2L2 expression and tumor immunity. The present study revealed that NFE2L2 was abnormally expressed and significantly correlated with mismatch repair (MMR) gene mutation levels and DNA methyltransferase expression in human pan-cancer. In particular, pan-cancer survival analysis indicated that NFE2L2 expression was associated with adverse outcomes—overall survival (OS), disease-specific survival (DSS), and progression-free interval (PFI)—in adrenocortical carcinoma (ACC), brain lower grade glioma (LGG), and pancreatic adenocarcinoma (PAAD) patients. A positive relationship was also found between NFE2L2 expression and immune infiltration, including B cells, CD4+ T cells, CD8+ T cells, neutrophils, macrophages, and dendritic cells, especially in breast invasive carcinoma (BRCA), colon adenocarcinoma (COAD), kidney renal clear cell carcinoma (KIRC), LGG, liver hepatocellular carcinoma (LIHC), and prostate adenocarcinoma (PRAD). Additionally, NFE2L2 expression was positively correlated with the immune score and the expression of immune checkpoint markers in LGG. In conclusion, these results indicate that transcription factor NFE2L2 is a potential prognostic biomarker and is correlated with immune infiltration in LGG.

1. Introduction

Nuclear factor, erythroid 2 like 2 (NFE2L2) is a redox-sensitive transcription factor localized mainly in the cytoplasm. It is ubiquitously expressed in the esophagus, thyroid, and other tissues [1, 2]. NFE2L2-mediated oxidative stress is a prominent feature of cervical cancer [3], promoting the proliferation, inhibiting the apoptosis, and enhancing the migration and invasion of cervical cancer cells [4, 5], as well as increasing the tumor chemoresistance [6, 7], suggesting that NFE2L2 may be a marker of poor prognosis in cervical cancer patients [8]. In addition, the redox subtype of lung squamous cell carcinoma (LUSC) is driven by genomic mutations in the NFE2L2/KEAP1 complex [9]. Although

cervical cancer and LUSC have been studied, many research gaps remain across the cancer spectrum.

The tumor microenvironment (TME) is very complex and contains both the cellular and noncellular components. On the one hand, inflammatory cells, including neutrophils and myeloid-derived suppressor cells (MDSCs), suppress beneficial immune functions in the TME, preventing normal immune cells from attacking tumor cells and promoting tumor growth [10, 11]. On the other hand, immune cell infiltration of the TME constitutes a strategy used by tumor cells to evade immune-mediated killing [12–14]. Tumor-associated macrophages (TAMs) mediate immune escape and then play important roles in tumorigenesis and development [15–18]. Currently, immunotherapy is a trending topic

in tumor therapy. For example, programmed death-1 (PD-1) and programmed death-ligand-1 (PD-L1) inhibitors have been found to induce tumor cell apoptosis by blocking the PD-1/PD-L1 signaling pathway, thus playing an effective antitumor role in lung cancer and melanoma [13, 19–21]. However, the role and underlying mechanisms of NFE2L2 in tumor immunity are unknown.

In the current study, we comprehensively analyzed the association between NFE2L2 expression and patients' prognosis in 33 cancer types. In addition, we explored the correlation between NFE2L2 expression and tumor immunity. Our findings revealed the possible role of NFE2L2 across cancers, suggesting that NFE2L2 is a potential prognostic biomarker and is correlated with immune infiltration in many cancers, especially in LGG.

2. Materials and Methods

2.1. Sample Information and NFE2L2 Expression Analysis in Human Pan-Cancer. NFE2L2 gene expression data in 31 normal tissues and 21 tumor cell lines were obtained from the Genotype-Tissue Expression (GTEx) portal (https://gtexport.org/home/) and Cancer Cell Line Encyclopedia (CCLE) database (https://portals.broadinstitute.org/ccle/about). The difference in NFE2L2 expression between cancer and normal tissues was analyzed by combining the data for normal tissues from the GTEx database with the data from The Cancer Genome Atlas (TCGA). Level 3 RNA sequencing data and clinical follow-up information for patients with 33 types of cancers (ACC: adrenocortical carcinoma; BLCA: bladder urothelial carcinoma; BRCA: breast invasive carcinoma; CESC: cervical squamous cell carcinoma; CHOL: cholangiocarcinoma; COAD: colon adenocarcinoma; DLBC: lymphoid neoplasm diffuse large B cell lymphoma; ESCA: esophageal carcinoma; GBM: glioblastoma multiforme; LGG: brain lower grade glioma; HNSC: head and neck squamous cell carcinoma; KICH: kidney chromophobe; KIRC: kidney renal clear cell carcinoma; KIRP: kidney renal papillary cell carcinoma; LAML: acute myeloid leukemia; LIHC: liver hepatocellular carcinoma; LUAD: lung adenocarcinoma; LUSC: lung squamous cell carcinoma; MESO: mesothelioma; OV: ovarian serous cystadenocarcinoma; PAAD: pancreatic adenocarcinoma; PCPG: pheochromocytoma and paraganglioma; PRAD: prostate adenocarcinoma; READ: rectum adenocarcinoma; SARC: sarcoma; SKCM: skin cutaneous melanoma; STAD: stomach adenocarcinoma; TGCT: testicular germ cell tumors; THCA: thyroid carcinoma; THYM: thymoma; UCEC: uterine corpus endometrial carcinoma; UCS: uterine carcinosarcoma; and UVM: uveal melanoma) were obtained from TCGA database. All expression data were normalized through log2 conversion.

2.2. MMR Gene Mutation and DNA Methyltransferase Analysis. Abnormalities in the DNA mismatch repair system (MMRs) can lead to tumorigenesis [22]. The mutation levels of 5 MMR genes (MLH1, MSH2, MSH6, PMS2, and EPCAM) were obtained from TCGA database. Pearson correlation analysis was used to evaluate the relationship between NFE2L2 expression and MMR gene mutation levels.

In addition, DNA methyltransferases play an important role in altering chromatin structure and gene expression [23]. The relationship between the expression level of NFE2L2 and that of 4 methyltransferases (DNMT1, DNMT2, DNMT3A, and DNMT3B) was evaluated by Pearson correlation analysis.

2.3. Survival and Prognosis Analysis. The relationship between NFE2L2 gene expression and patients' prognosis (OS: overall survival; DSS: disease-specific survival; DFI: disease-free interval; and PFI: progression-free interval) in 33 cancers was visualized with forest plots and Kaplan-Meier curves. The hazard ratio (HR) and 95% confidence intervals were calculated via univariate survival analysis.

2.4. Correlations between NFE2L2 Expression and Immune Characteristics in the TIMER Database. The Tumor Immune Estimation Resource (TIMER) database contains 10,897 samples from TCGA (https://cistrome.shinyapps.io/timer/). RNA-seq expression profile data were used to evaluate the infiltration of 6 immune cells (B cells, CD4+ T cells, CD8+ T cells, neutrophils, macrophages, and dendritic cells) in tumor tissues. The scores of these 6 infiltrating immune cells in 33 cancers were downloaded from the TIMER database. Spearman correlation analysis was used to evaluate the correlation between NFE2L2 expression and immune infiltration. In addition, we evaluated the relationship between NFE2L2 expression and the immune/stromal scores (ImmuneScore and StromalScore) and immune checkpoint marker expression levels by Spearman and Pearson correlation analyses, respectively. Gene expression levels are shown as log2 RSEM values.

2.5. Statistical Analysis. The Kruskal-Wallis test was adopted to analyze NFE2L2 expression levels in different tissues and cancer cell lines. Differences in NFE2L2 expression levels in tumor tissues and normal tissues were evaluated by a *t*-test. In survival analysis, the HRs and *P* value were calculated by univariate Cox regression analysis. Kaplan-Meier curves were used to compare the survival of patients stratified according to different levels of NFE2L2 expression. $P < 0.05$ was set as the significance threshold for all statistical analyses.

3. Results

3.1. The mRNA Expression Level of NFE2L2 in Human Pan-Cancer. First, we analyzed NFE2L2 expression in 31 types of tissues using the GTEx dataset. As shown in Figure 1(a), NFE2L2 was generally highly expressed in the bladder, ovary, vagina, and thyroid tissues. Furthermore, we downloaded the data of tumor cell lines from the CCLE database and analyzed NFE2L2 expression in these tumor cell lines. Results showed that NFE2L2 was expressed in all 21 kinds of tumor cell lines (Figure 1(b)). To further determine the differences in NFE2L2 expression between the tumor and normal tissues, we obtained NFE2L2 expression data from TCGA database. As shown in Figure 1(c), NFE2L2 expression was significantly higher in CHOL and LUSC tissues than in normal tissues. However, it was significantly lower in BLCA, BRCA, COAD, KICH, KIRC, KIRP, LIHC, LUAD, PRAD, READ,
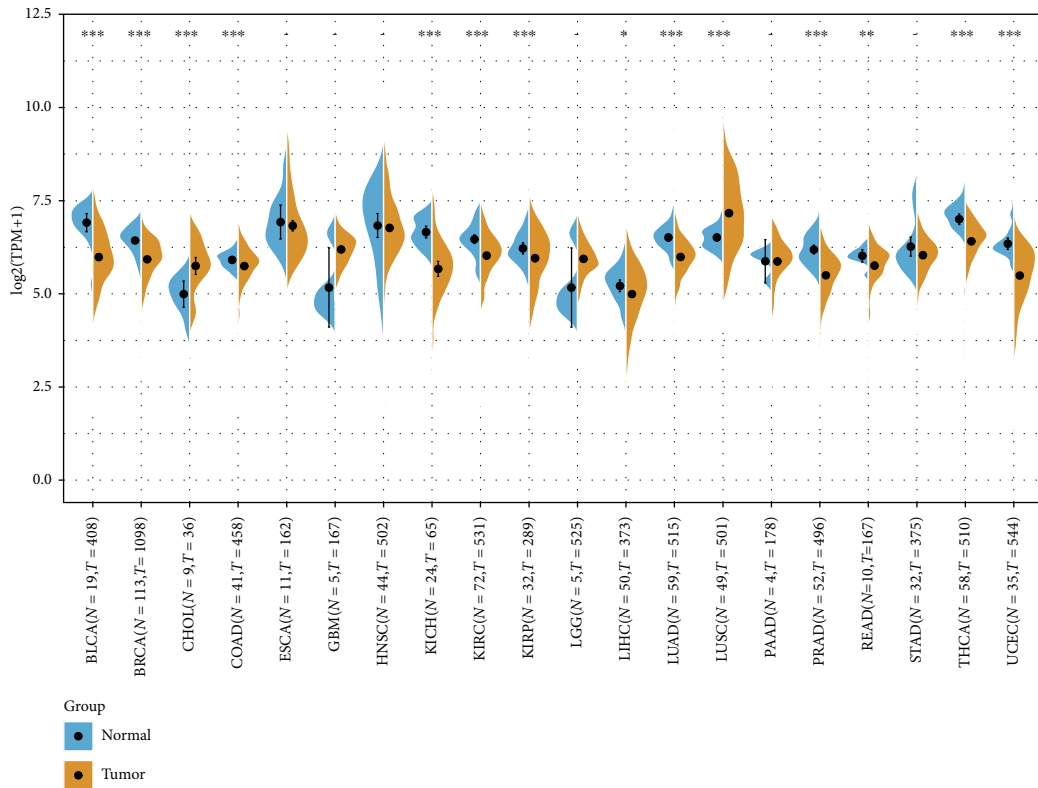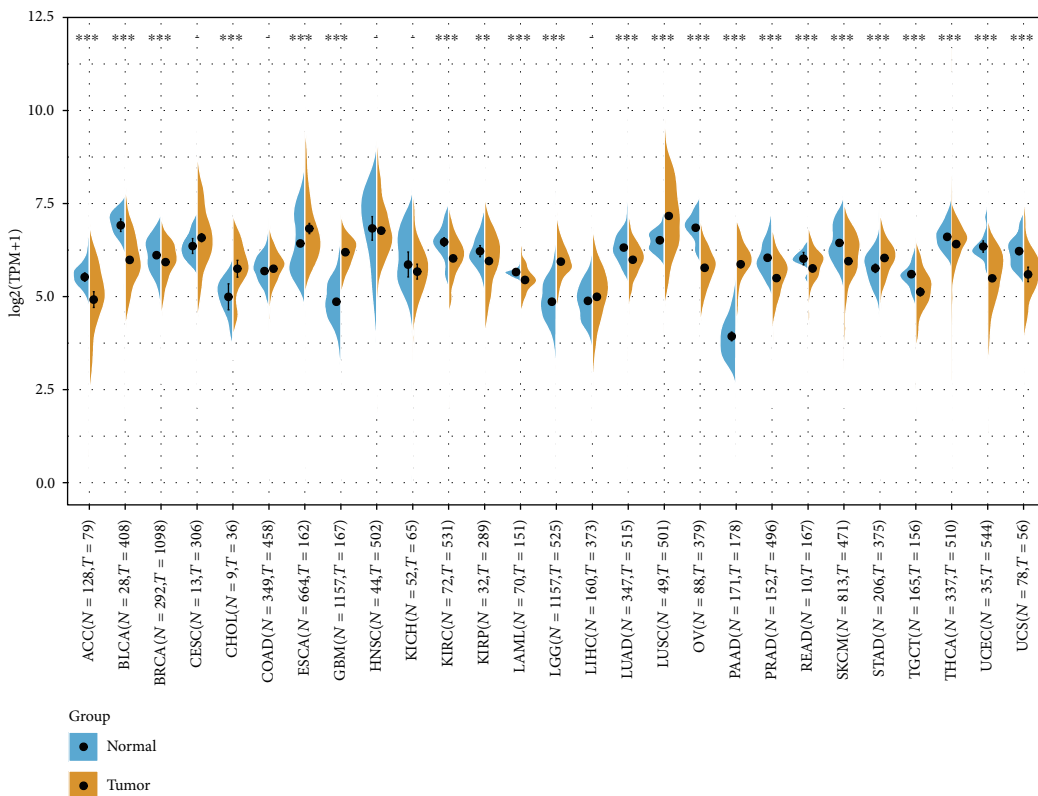
(a)

(b)
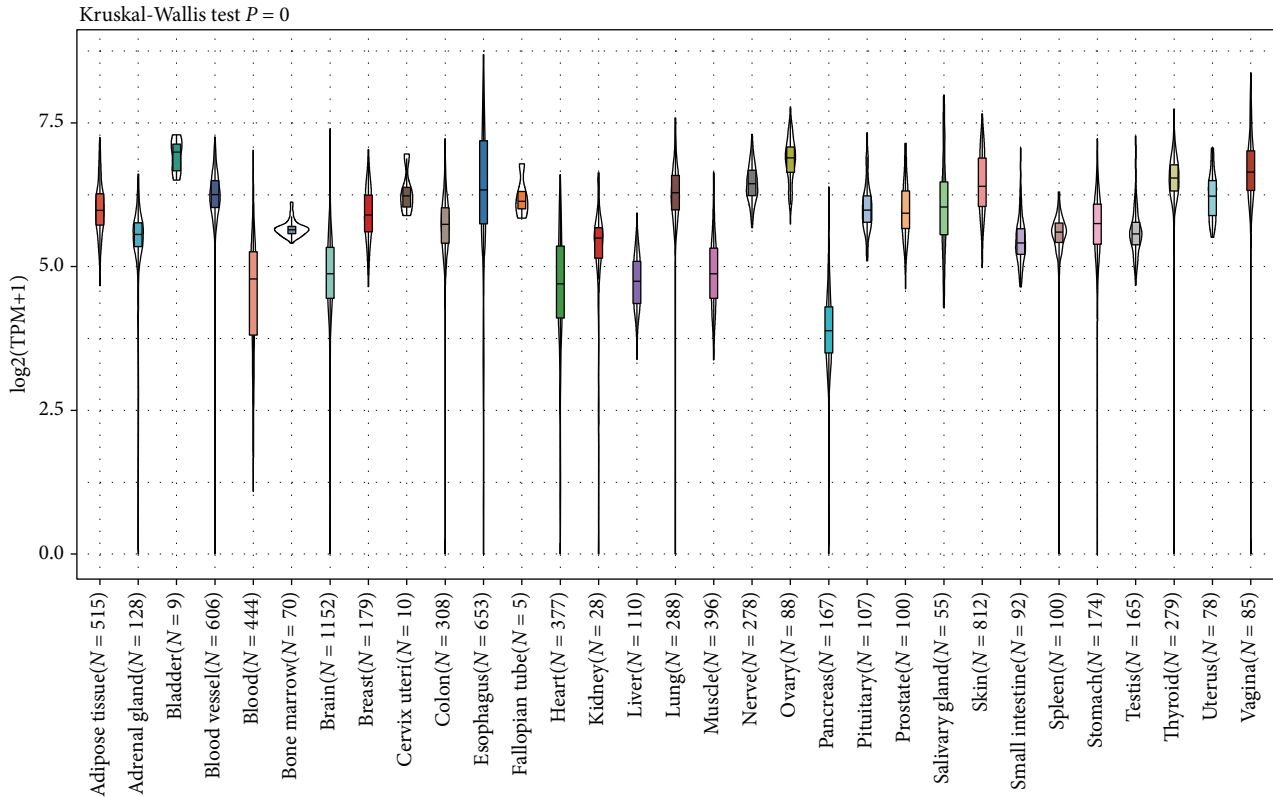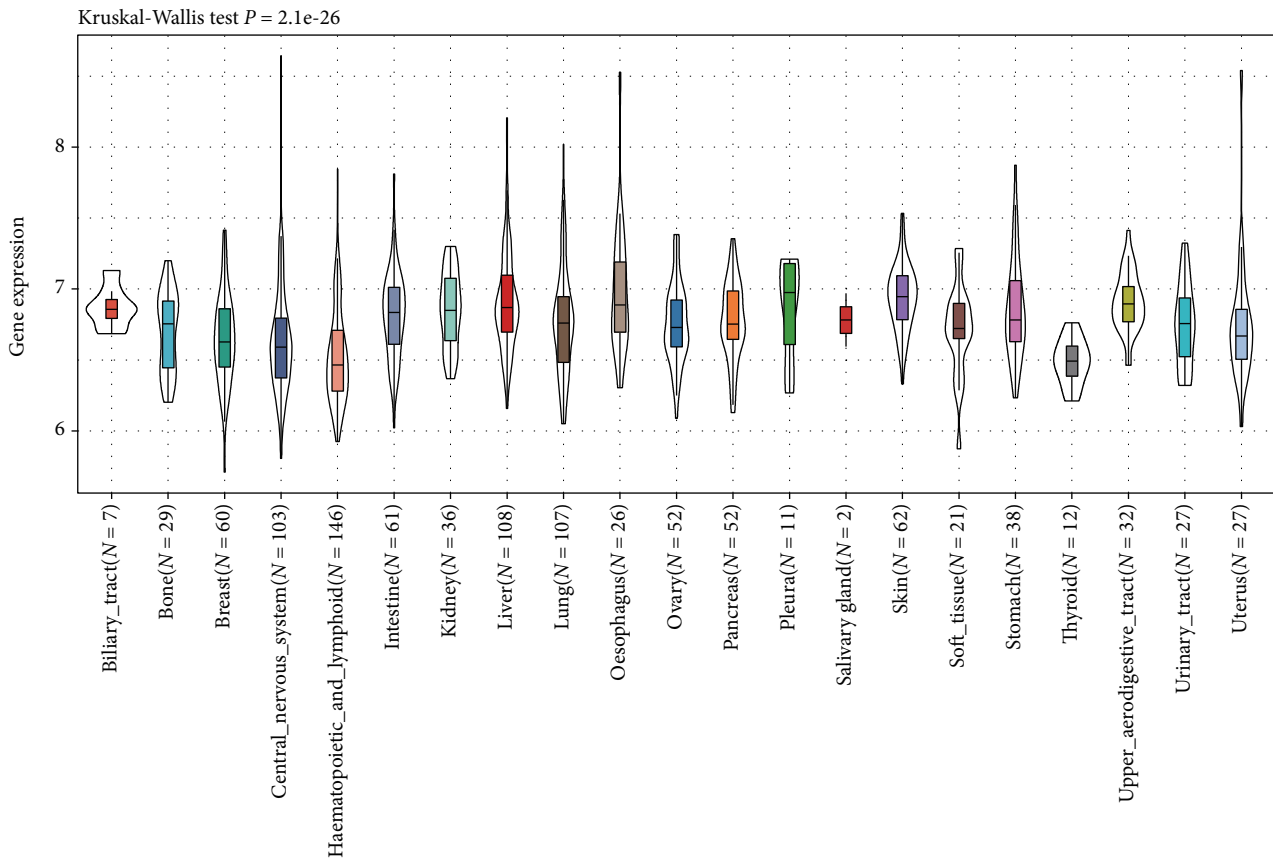
Figure 1: Continued.

(c)

(d)

Figure 1: NFE2L2 is abnormally expressed in pan-cancer. (a) NFE2L2 expression in 31 normal tissues from the GTEx database. (b) NFE2L2 expression in 21 tumor cells from the CCLE database. (c) Differential expression of NFE2L2 in cancers and normal tissues from TCGA database. (d) NFE2L2 expression in 27 cancer types from the GTEx database and TCGA database ($^*P < 0.05$, $^{**}P < 0.01$, and $^{***}P < 0.001$).
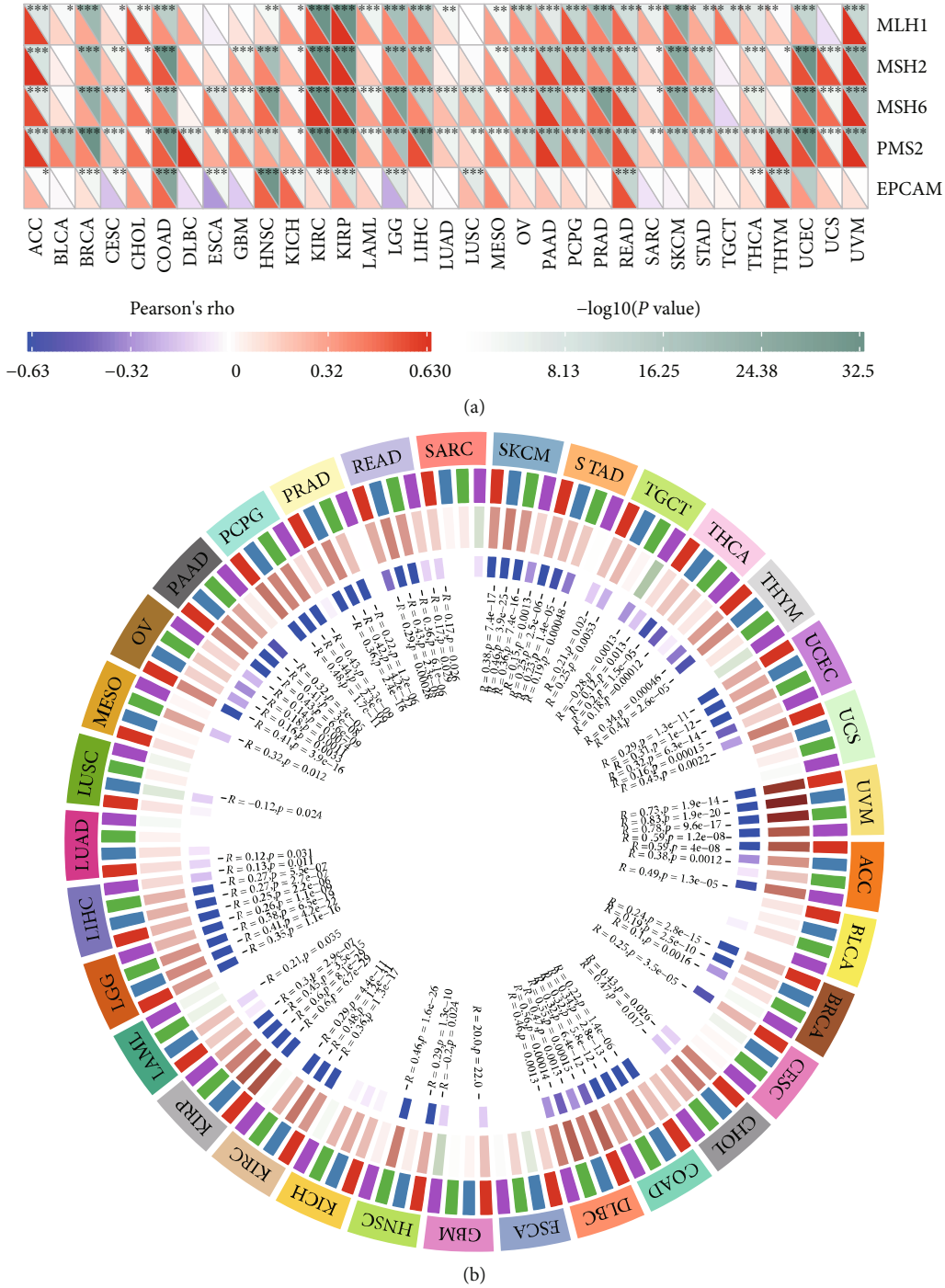
(a)

(b)

FIGURE 2: NFE2L2 expression is correlated with MMR gene mutation levels and DNA methyltransferase expression in pan-cancer. (a) Pearson correlation analysis of NFE2L2 expression with the mutation levels of 5 MMR genes (MLH1, MSH2, MSH6, PMS2, and EPCAM) in pan-cancer ($^*P < 0.05$, $^{**}P < 0.01$, and $^{***}P < 0.001$). (b) Pearson correlation analysis of NFE2L2 expression with that of 4 DNA methyltransferases (DNMT1, DNMT2, DNMT3A, and DNMT3B) in pan-cancer.

THCA, and UCEC compared with normal tissues. Due to the small number of normal tissue samples in TCGA database, we further integrated the normal tissue data from the GTEx database and the tumor tissue data from TCGA database to analyze the differences in NFE2L2 expression in 27 cancer types. Results revealed that NFE2L2 was abnormally expressed in 22 of these cancers. Specifically, NFE2L2 expres-sion was higher in tissues from 7 cancers (CHOL, ESCA, GBM, LGG, LUSC, PAAD, and STAD) and lower in tissues from 15 cancers (ACC, BLCA, BRCA, KIRC, KIRP, LAML, LUAD, OV, PRAD, READ, SKCM, TGCT, THCA, UCEC, and UCS) than in the normal tissues (Figure 1(d)). Taken together, these results reveal that NFE2L2 is abnormally expressed in different cancers.
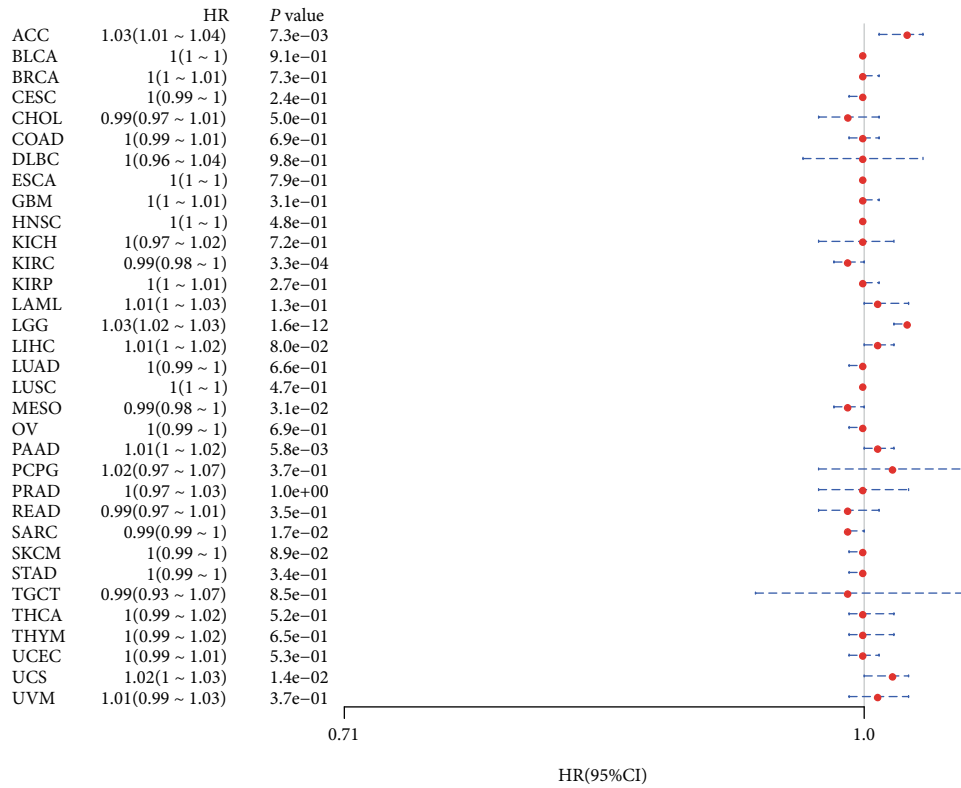
(a)
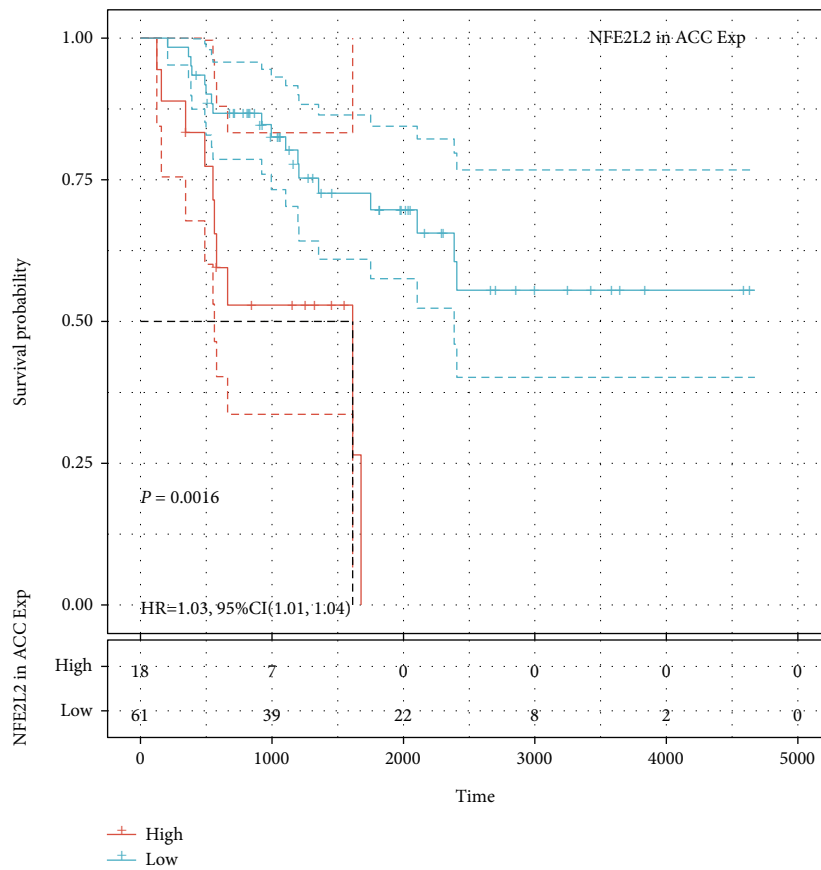
(b)

Figure 3: Continued.

(c)

(d)
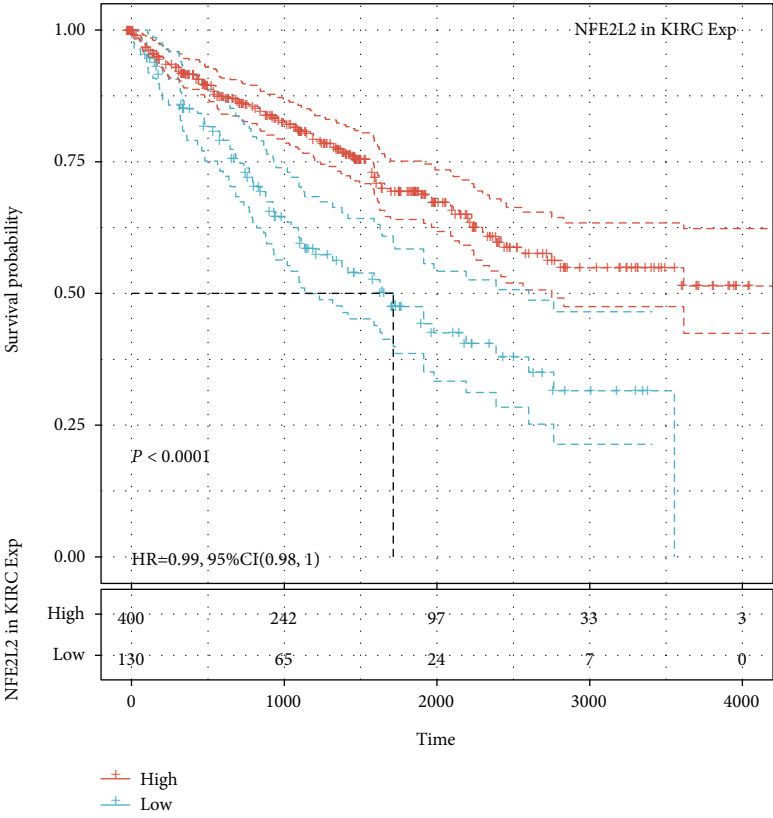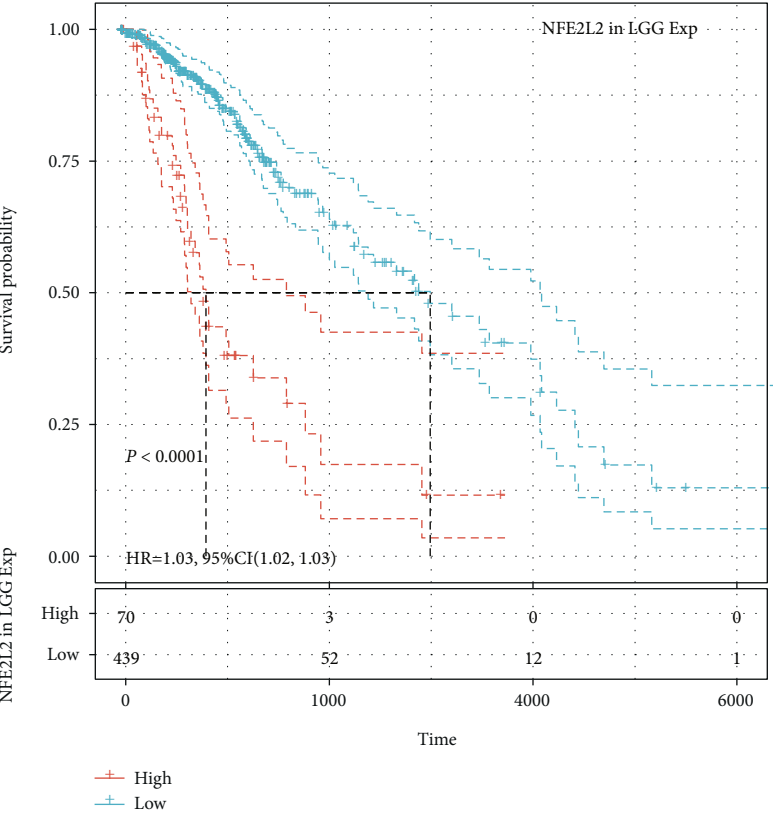
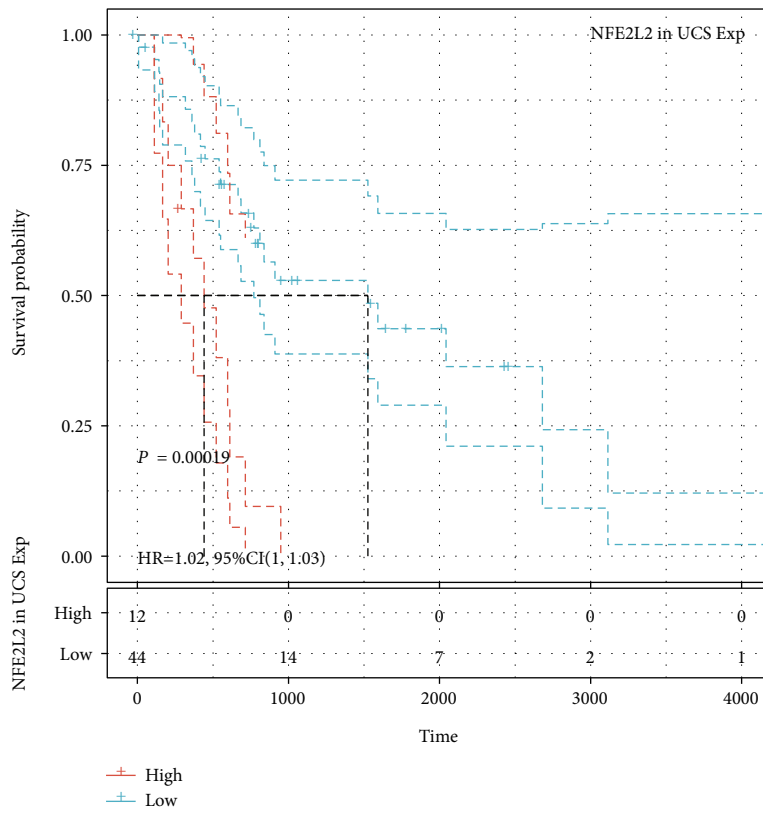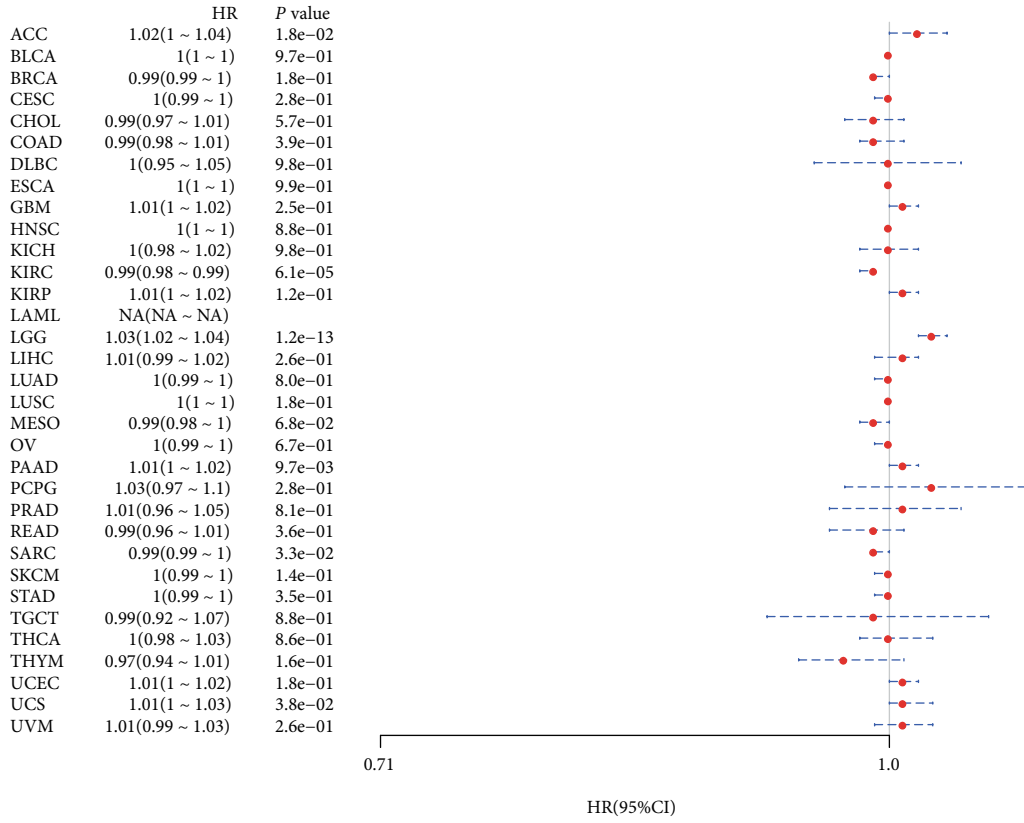Figure 3: Continued.

(e)

(f)
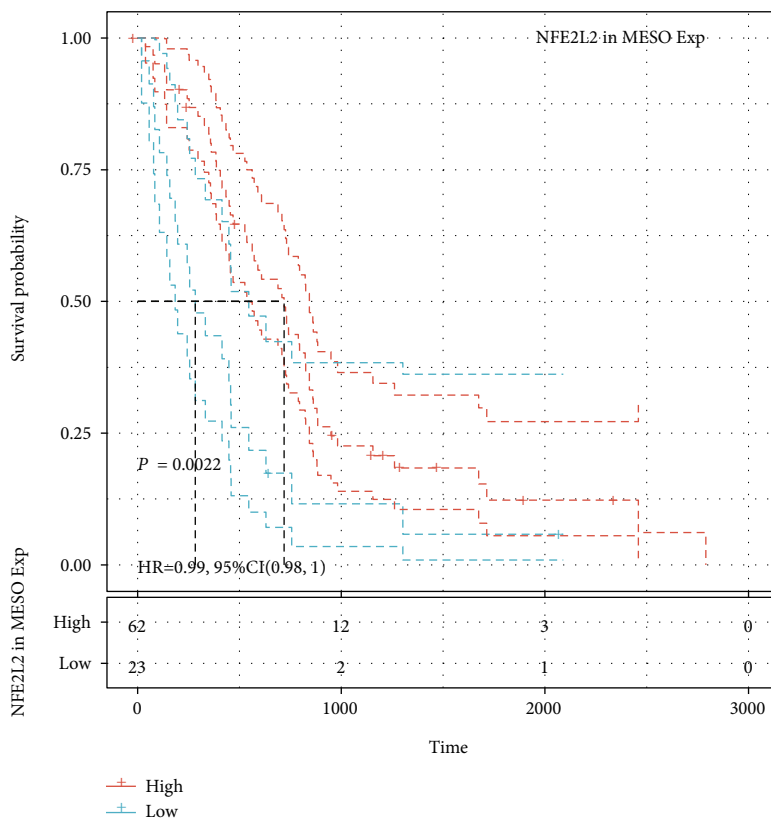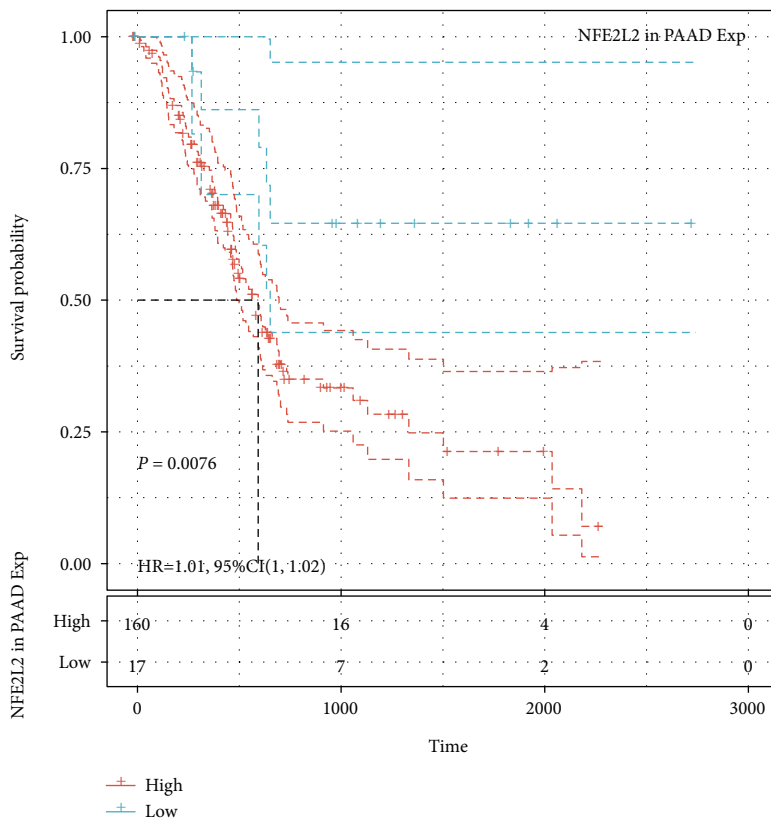
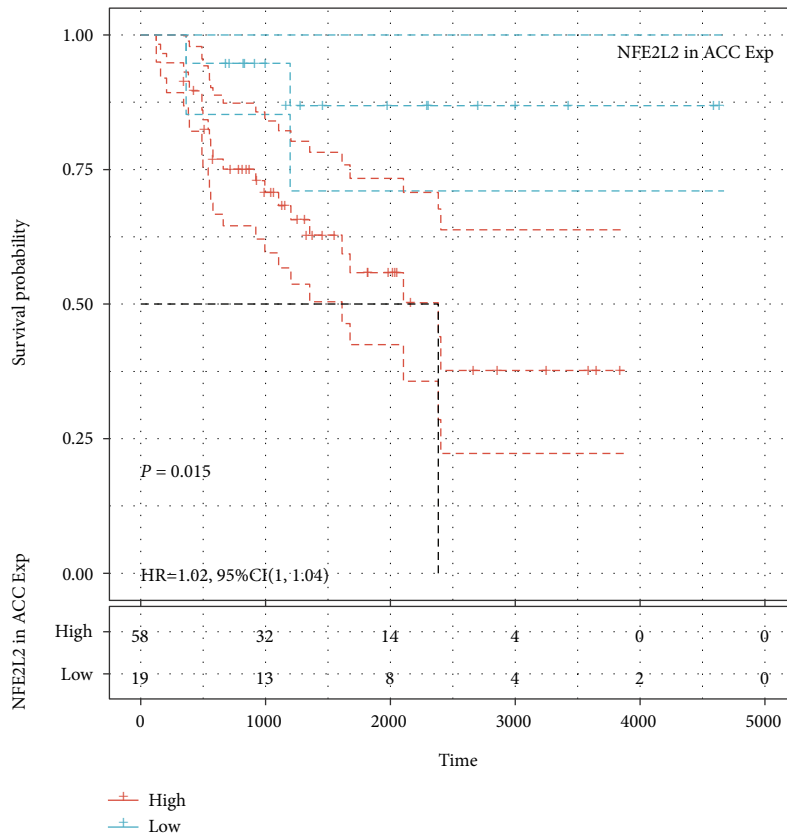Figure 3: Continued.
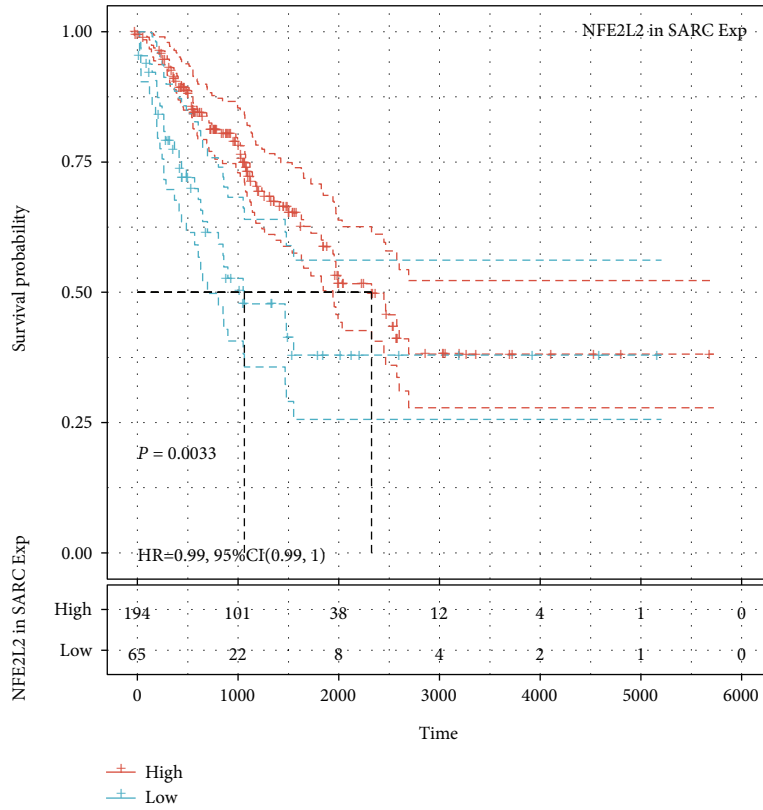
(g)

(h)

FIGURE 3: Relationship of NFE2L2 expression with patients' OS. (a) Forest plots showing the HRs related to NFE2L2 expression in 33 cancer types. (b–h) Kaplan-Meier OS curves for patients stratified by different expression levels of NFE2L2 in 7 cancer types.
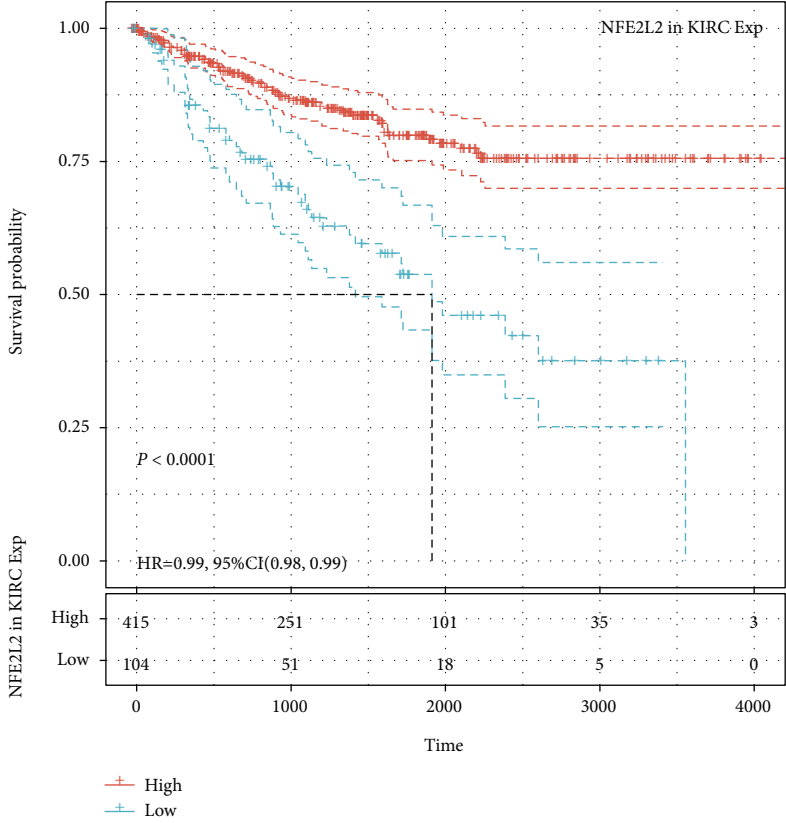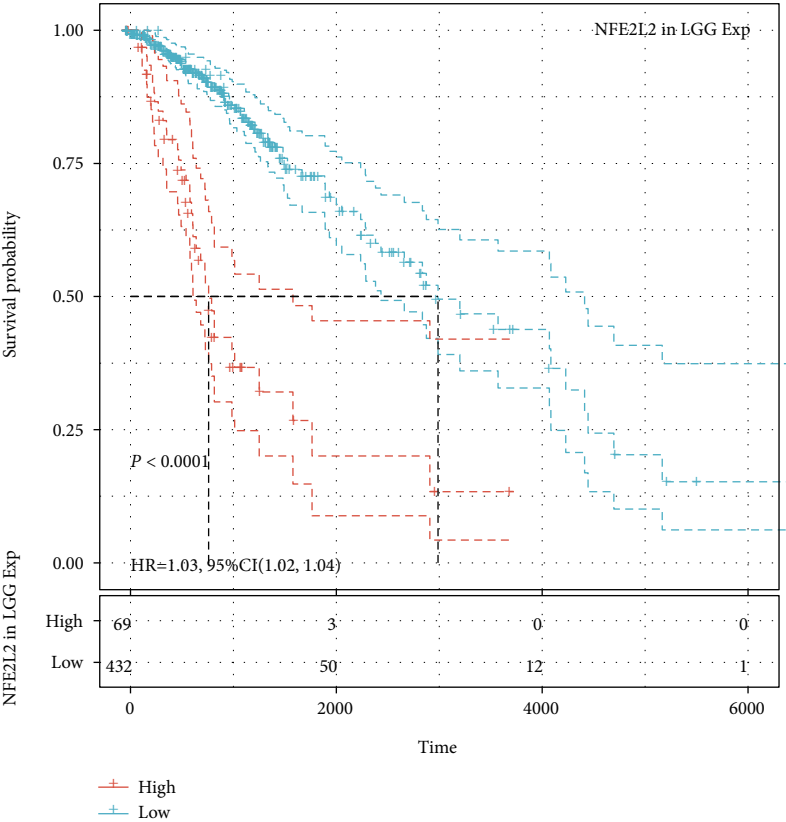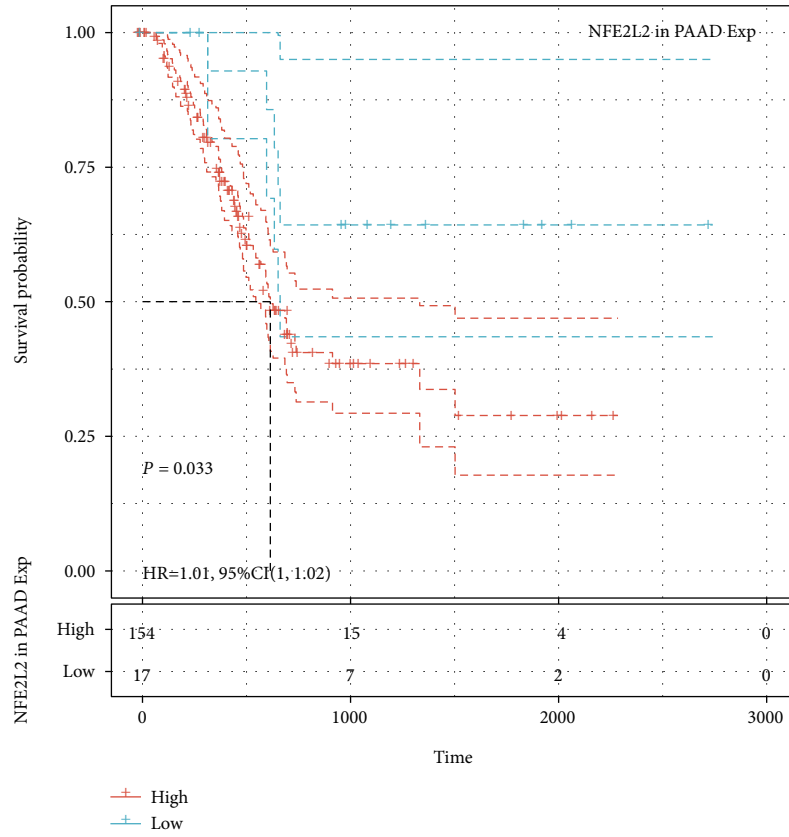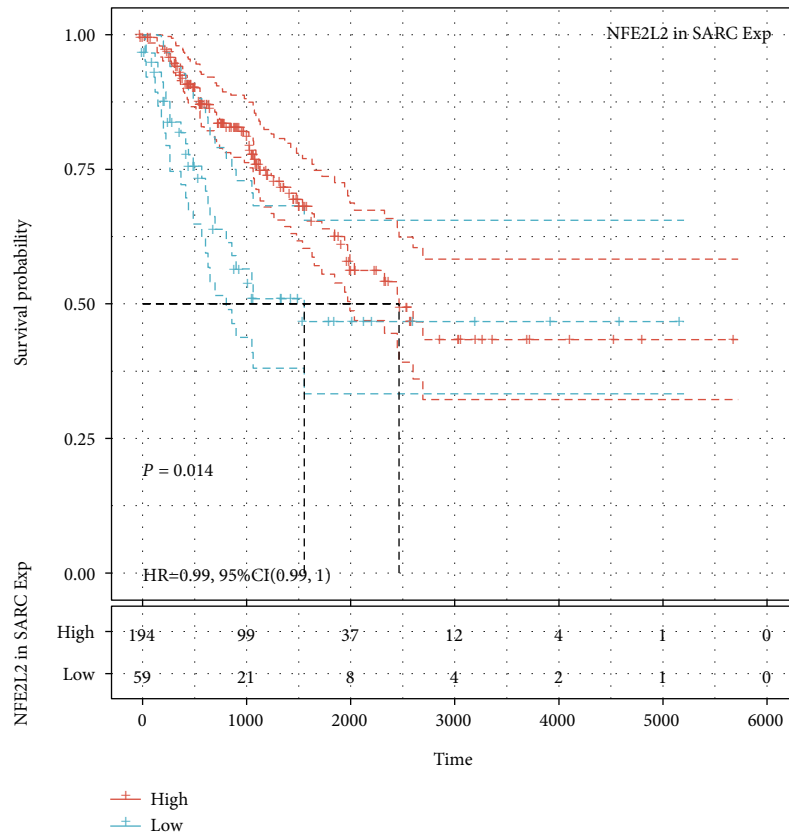
(a)

(b)

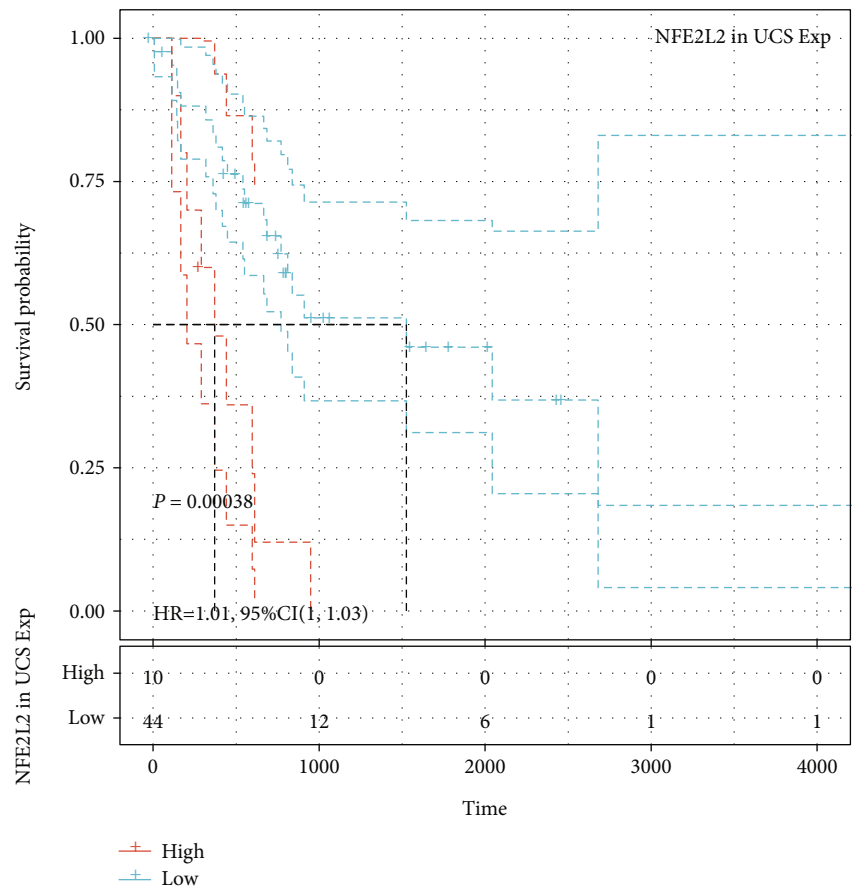FIGURE 4: Continued.

(c)

(d)

Figure 4: Continued.
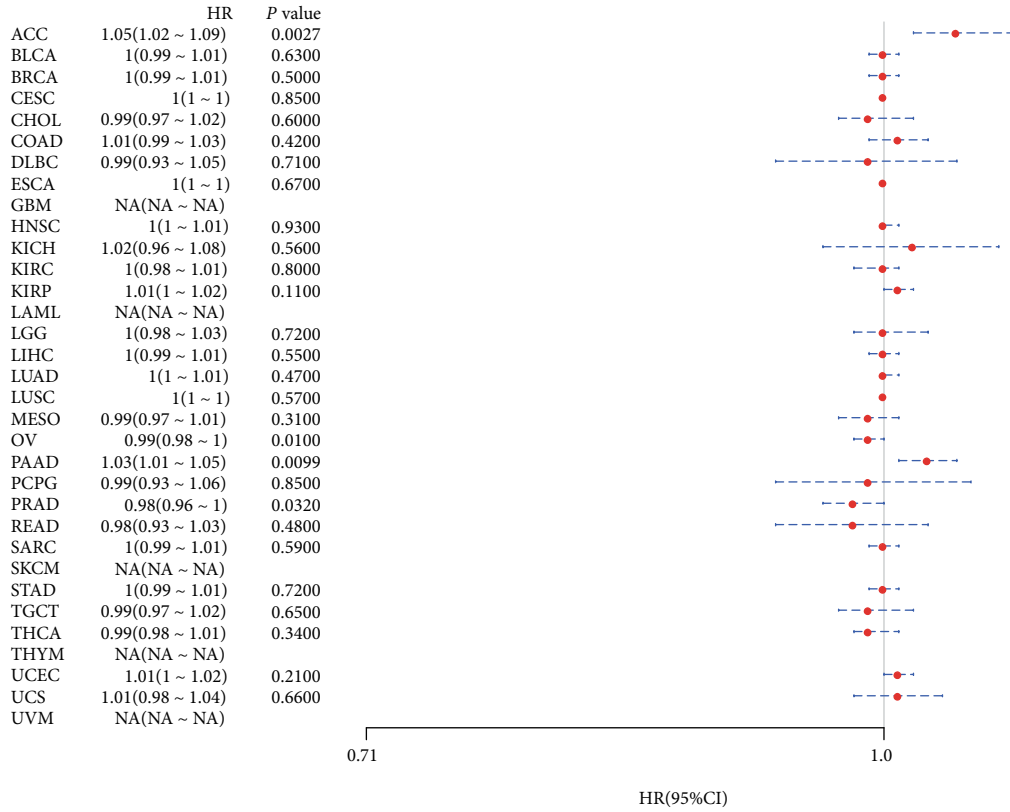
(e)

(f)

FIGURE 4: Continued.

(g)

FIGURE 4: Relationship of NFE2L2 expression with patients' DSS. (a) Forest plots showing the HRs related to NFE2L2 expression in 33 cancer types. (b–g) Kaplan-Meier DSS curves for patients stratified by different expression levels of NFE2L2 in 6 cancer types.

3.2. NFE2L2 Is Correlated with MMR Gene Mutation Levels and DNA Methyltransferase Gene Expression in Human Pan-Cancer. MMRs is a DNA damage repair mechanism. Functional loss of key genes in this mechanism leads to DNA replication errors [24], higher somatic mutations, and tumorigenesis [22, 25]. To evaluate the role of NFE2L2 in tumorigenesis, we analyzed the correlation between NFE2L2 expression and MMR gene mutation levels. Results showed that NFE2L2 expression was positively related to the mutation levels of 5 MMR genes (MLH1, MSH2, MSH6, PMS2, and EPCAM) in human cancers (Figure 2(a)).
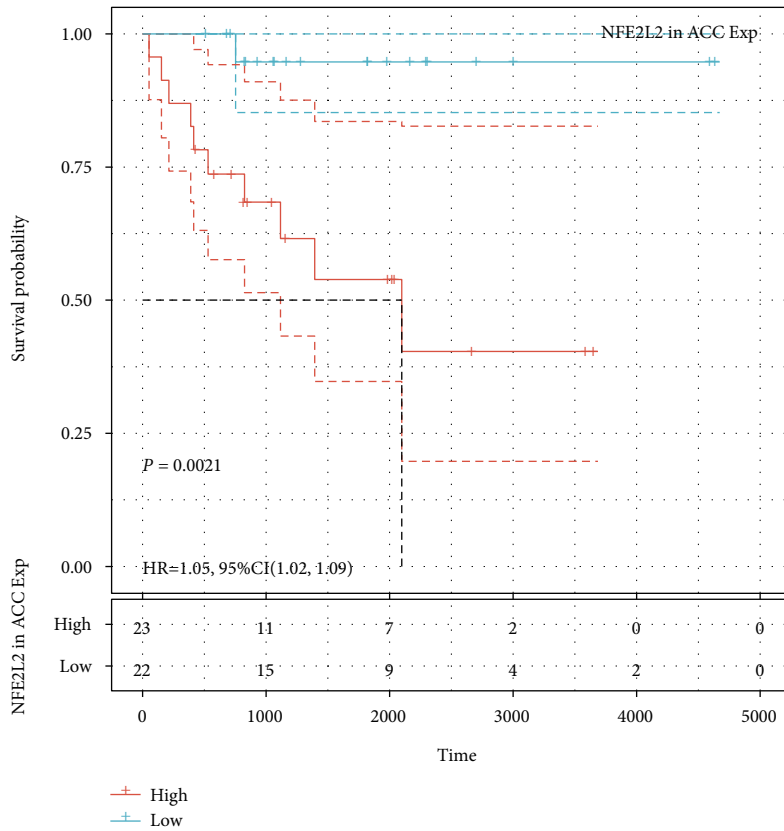
DNA methylation is an epigenetic modification that can alter gene expression [26]. Alteration of the DNA methylation status is an important factor in tumorigenesis [27]. Next, we further evaluated the correlation between NFE2L2 expression and that of 4 DNA methyltransferases. Evidently, NFE2L2 expression is closely related to the expression of DNMT1, DNMT2, DNMT3A, and DNMT3B across human cancers, especially in COAD, KIRP, LGG, and UVM (Figure 2(b)). In summary, these results indicate that NFE2L2 may mediate tumorigenesis by regulating DNA damage or methylation.

3.3. Prognostic Value of NFE2L2 in Human Pan-Cancer. Next, we investigated the relationship between NFE2L2 expression and the prognosis of patients in pan-cancer. Notably, NFE2L2

expression was significantly correlated with patients' OS in 7 types of cancer (ACC, KIRC, LGG, MESO, PAAD, SARC, and UCS) (Figure 3(a)). Specifically, NFE2L2 appeared to be a risk factor in 4 cancer types: ACC ($P = 0.0016$, HR = 1.03), LGG ($P < 0.0001$, HR = 1.03), PAAD ($P = 0.0076$, HR = 1.01), and UCS ($P = 0.00019$, HR = 1.02). In addition, NFE2L2 was a protective factor in 3 other types of cancer: KIRC ($P < 0.0001$, HR = 0.99), MESO ($P = 0.0022$, HR = 0.99), and SARC ($P = 0.0033$, HR = 0.99) (Figures 3(b)–3(h)). Since non-tumor-related factors may cause death during follow-up, we then analyzed the relationship between NFE2L2 expression and DSS in 33 cancers. Results showed NFE2L2 expression impacted patients' DSS in 6 cancer types (ACC, KIRC, LGG, PAAD, SARC, and UCS) (Figure 4(a)). Specifically, Kaplan-Meier curves showed that high expression of NFE2L2 was significantly correlated with poor prognosis of patients in ACC ($P = 0.015$, HR = 1.02), LGG ($P < 0.0001$, HR = 1.03), PAAD ($P = 0.033$, HR = 1.01), and UCS ($P = 0.00038$, HR = 1.01) and reversely in KIRC ($P < 0.0001$, HR = 0.99) and SARC ($P = 0.014$, HR = 0.99) (Figures 4(b)–4(g)). Subsequently, we investigated the relationship between NFE2L2 expression and DFI and found that increased NFE2L2 expression was correlated with poor prognosis in ACC ($P = 0.0021$, HR = 1.05) and PAAD ($P = 0.026$, HR = 1.03) but with favorable prognosis in OV ($P = 0.0099$, HR =
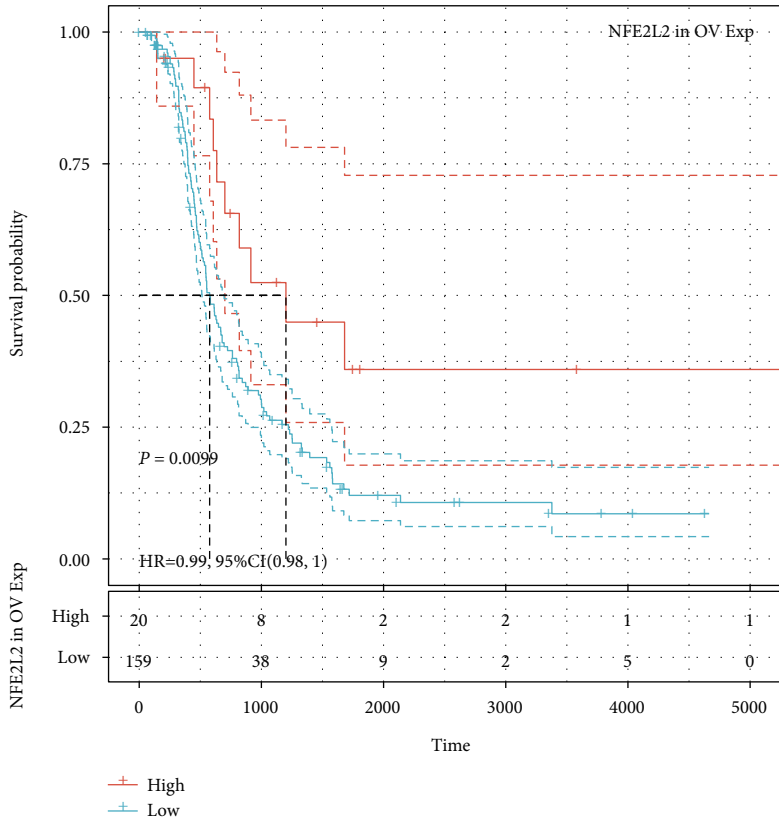
	HR	*P* value
ACC	1.05(1.02 ~ 1.09)	0.0027
BLCA	1(0.99 ~ 1.01)	0.6300
BRCA	1(0.99 ~ 1.01)	0.5000
CESC	1(1 ~ 1)	0.8500
CHOL	0.99(0.97 ~ 1.02)	0.6000
COAD	1.01(0.99 ~ 1.03)	0.4200
DLBC	0.99(0.93 ~ 1.05)	0.7100
ESCA	1(1 ~ 1)	0.6700
GBM	NA(NA ~ NA)	
HNSC	1(1 ~ 1.01)	0.9300
KICH	1.02(0.96 ~ 1.08)	0.5600
KIRC	1(0.98 ~ 1.01)	0.8000
KIRP	1.01(1 ~ 1.02)	0.1100
LAML	NA(NA ~ NA)	
LGG	1(0.98 ~ 1.03)	0.7200
LIHC	1(0.99 ~ 1.01)	0.5500
LUAD	1(1 ~ 1.01)	0.4700
LUSC	1(1 ~ 1)	0.5700
MESO	0.99(0.97 ~ 1.01)	0.3100
OV	0.99(0.98 ~ 1)	0.0100
PAAD	1.03(1.01 ~ 1.05)	0.0099
PCPG	0.99(0.93 ~ 1.06)	0.8500
PRAD	0.98(0.96 ~ 1)	0.0320
READ	0.98(0.93 ~ 1.03)	0.4800
SARC	1(0.99 ~ 1.01)	0.5900
SKCM	NA(NA ~ NA)	
STAD	1(0.99 ~ 1.01)	0.7200
TGCT	0.99(0.97 ~ 1.02)	0.6500
THCA	0.99(0.98 ~ 1.01)	0.3400
THYM	NA(NA ~ NA)	
UCEC	1.01(1 ~ 1.02)	0.2100
UCS	1.01(0.98 ~ 1.04)	0.6600
UVM	NA(NA ~ NA)	

0.71   1.0

HR(95%CI)

(a)

NFE2L2 in ACC Exp

P = 0.0021

HR=1.05, 95%CI(1.02, 1.09)

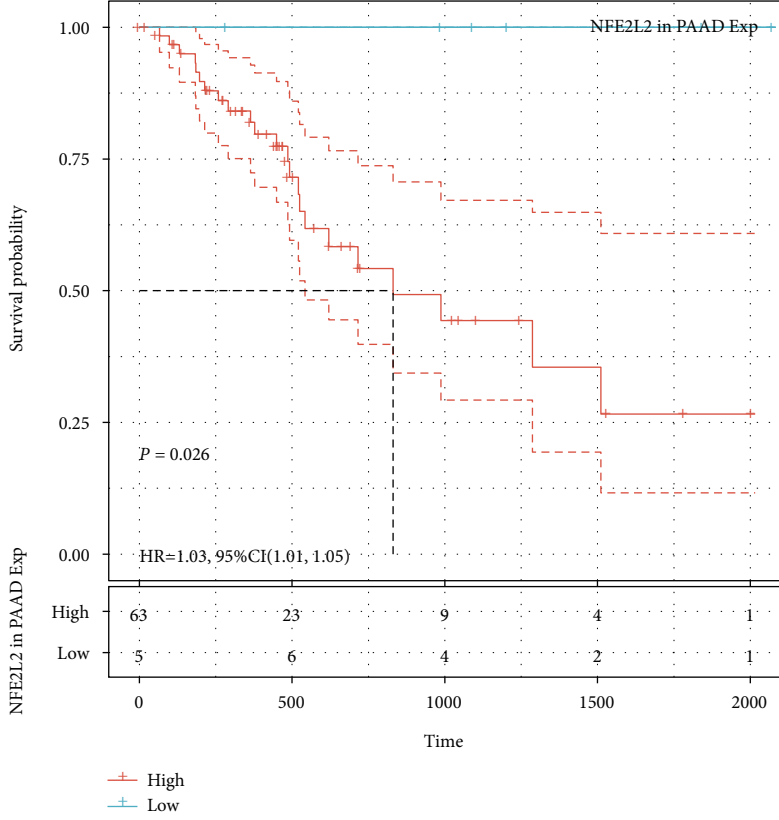| NFE2L2 in ACC Exp					
High	23	11	7	2	0	0
Low	22	15	9	4	2	0

Time

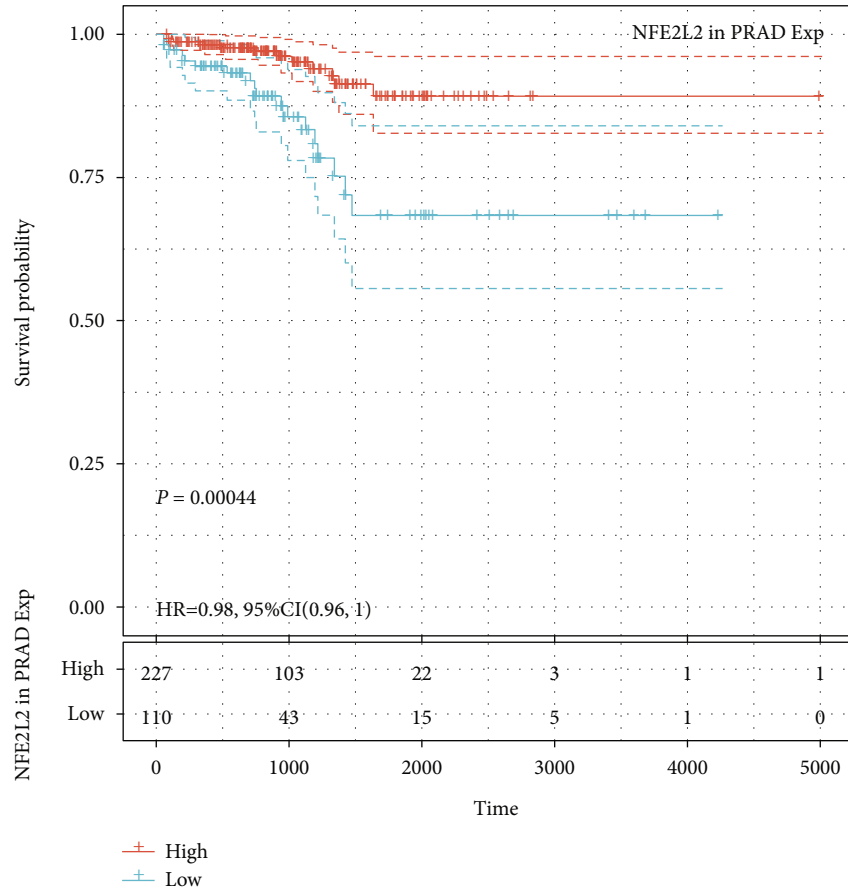—+— High
—+— Low

(b)

Figure 5: Continued.

(c)

(d)

FIGURE 5: Continued.

(e)

FIGURE 5: Relationship of NFE2L2 expression with patients' DFI. (a) Forest plots showing the HRs related to NFE2L2 expression in 33 cancer types. (b–e) Kaplan-Meier DFI curves for patients stratified by different expression levels of NFE2L2 in ACC, OV, PAAD, and PRAD.

0.99) and PRAD ($P = 0.00044$, HR = 0.98) (Figure 5). Moreover, we assessed the relationship between NFE2L2 expression and PFI. The results showed that high expression of NFE2L2 affected PFI unfavorably in ACC ($P < 0.0001$, HR = 1.03), LGG ($P < 0.0001$, HR = 1.02), PAAD ($P = 0.013$, HR = 1.01), and UVM ($P = 0.0062$, HR = 1.03) but favorably in KIRC ($P < 0.0001$, HR = 0.99) and MESO ($P = 8e - 04$, HR = 0.99) (Figure 6). In conclusion, these results suggest that NFE2L2 expression is significantly correlated with the prognosis of patients, especially those with ACC, LGG, and PAAD.

3.4. NFE2L2 Expression Is Correlated with Immune Infiltration Levels and Immune Checkpoint Marker Expression across Cancers. Immune cells in the TME affect patients' survival [28]. Therefore, the correlation between NFE2L2 expression and immune infiltration in human pan-cancer was further studied. First, we downloaded the scores of 6 types of infiltrating immune cells in 33 types of cancer from the TIMER database and then analyzed the correlation between the NFE2L2 expression level and immune infiltration levels. Results showed that NFE2L2 expression was appreciably positively correlated with the infiltration levels of 6 immune cells, including B cells, CD4+ T cells, CD8+ T cells, neutrophils, macrophages, and dendritic cells in LGG, PRAD, KIRC, COAD, and BRCA (Figure 7).

The immune score (i.e., ImmuneScore) and matrix score (i.e., StromalScore) were used to quantify the immune and matrix components in pan-cancer. NFE2L2 expression was positively correlated with the ImmuneScore in DLBC, LGG, PAAD, PRAD, LAML, and negatively correlated with the ImmuneScore in ESCA, LUSC, THYM, THCA, and MESO (Figure 8(a)). In addition, NFE2L2 expression was positively correlated with the StromalScore in LAML, LGG, BRCA, TGCT, DLBC, PAAD, PCPG, PRAD, and THYM and negatively correlated with the StromalScore in LUSC (Figure 8(b)).

Immune checkpoint inhibitors (ICIs), as novel tumor immunotherapy agents, play an important role in tumor immunotherapy [29]. Subsequently, we analyzed the correlation between NFE2L2 expression and that of 40 common immune checkpoint genes. Interestingly, in LGG and PRAD, NFE2L2 expression was correlated with more than 30 immune checkpoint markers, such as TNFSF4, CD48, and CD28 (Figure 9). Collectively, these results strongly suggest that NFE2L2 plays a vital role in tumor immunity.

4. Discussion

Pan-cancer analysis can reveal similarities and differences in tumors, providing insights into cancer prevention and the design of therapeutic targets [30]. Recently, many studies
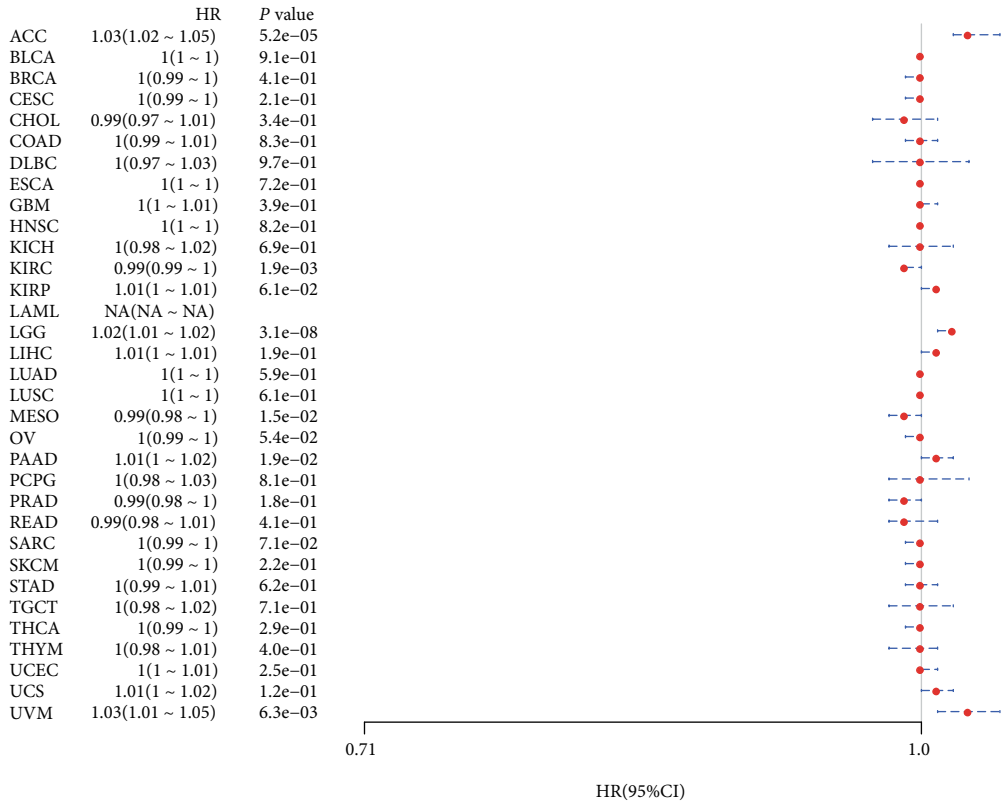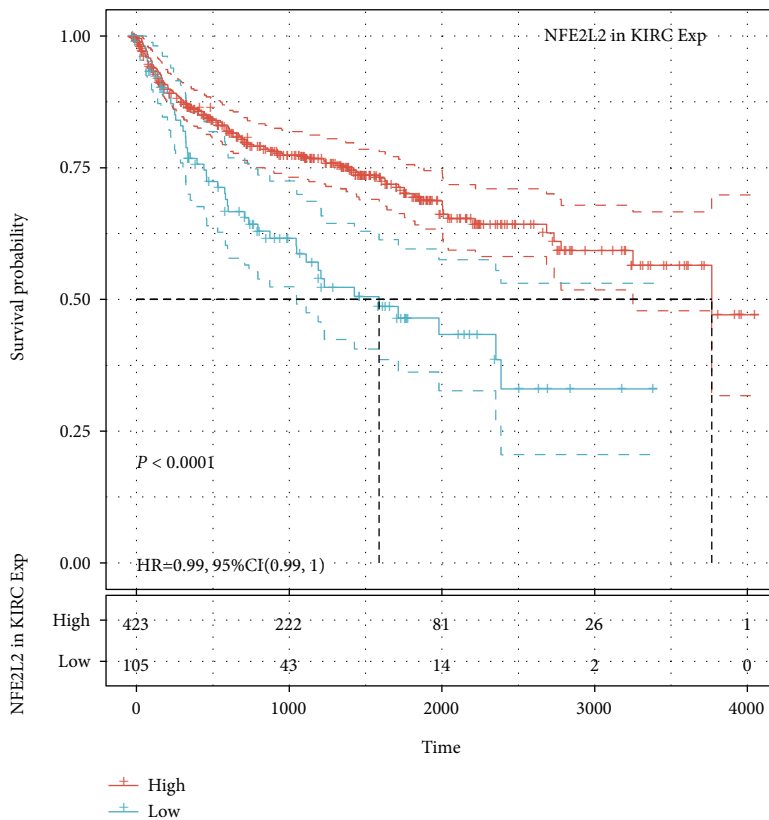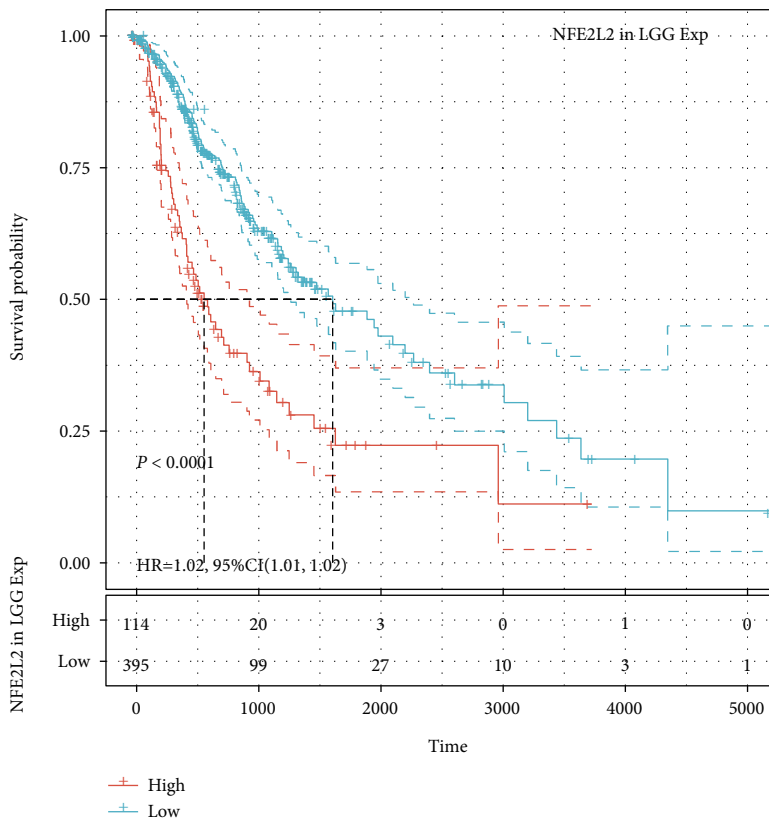
(a)
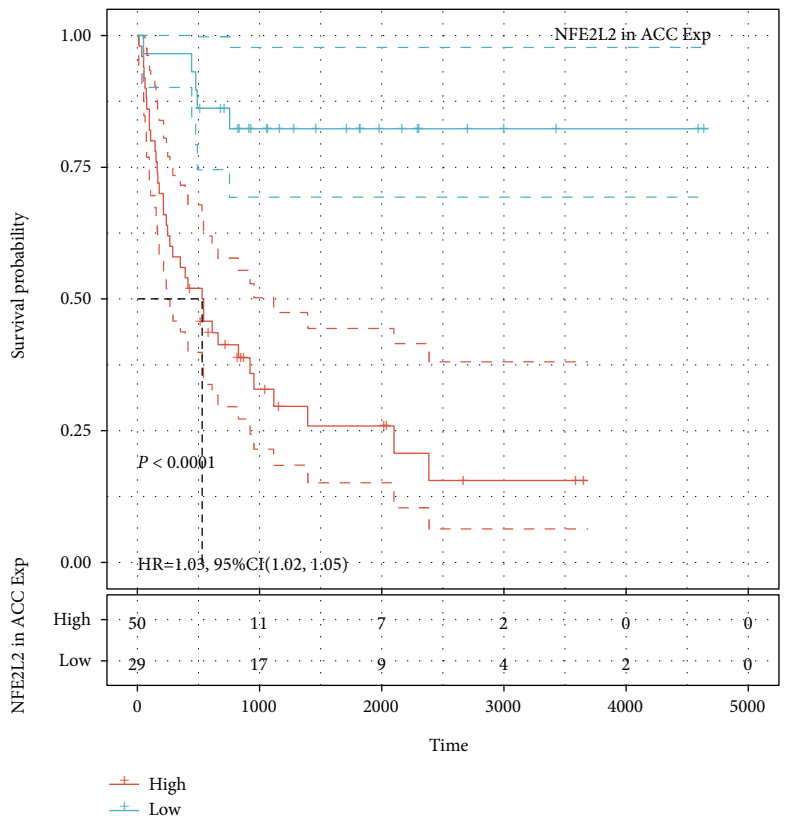
(b)
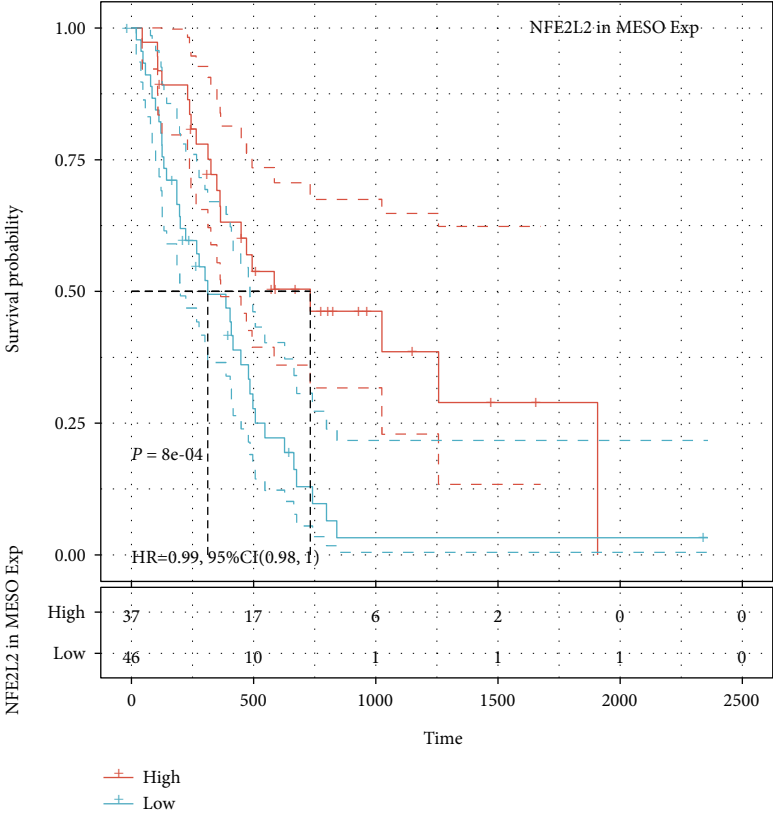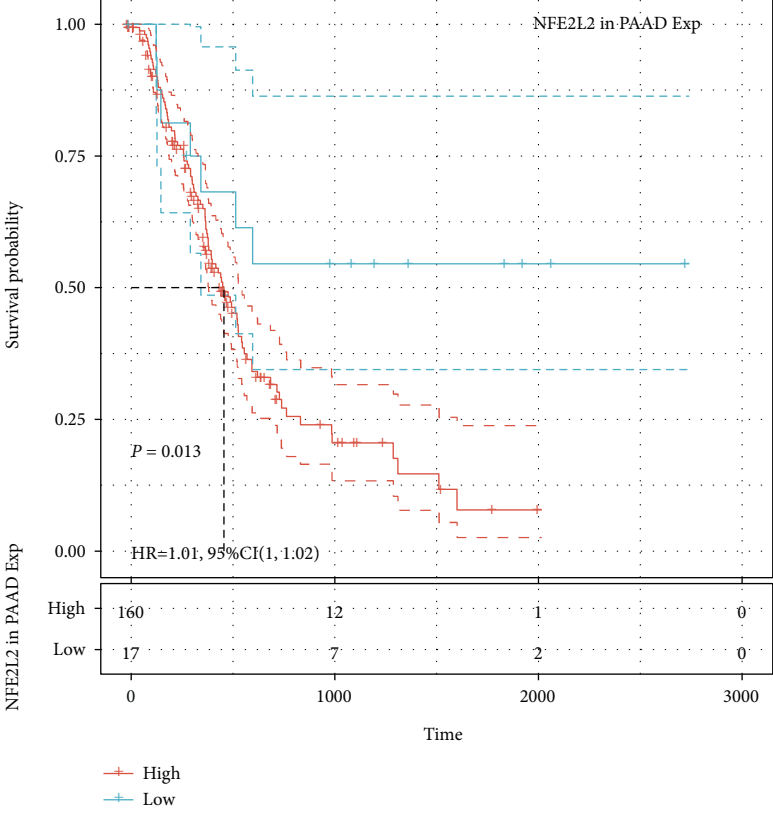
FIGURE 6: Continued.
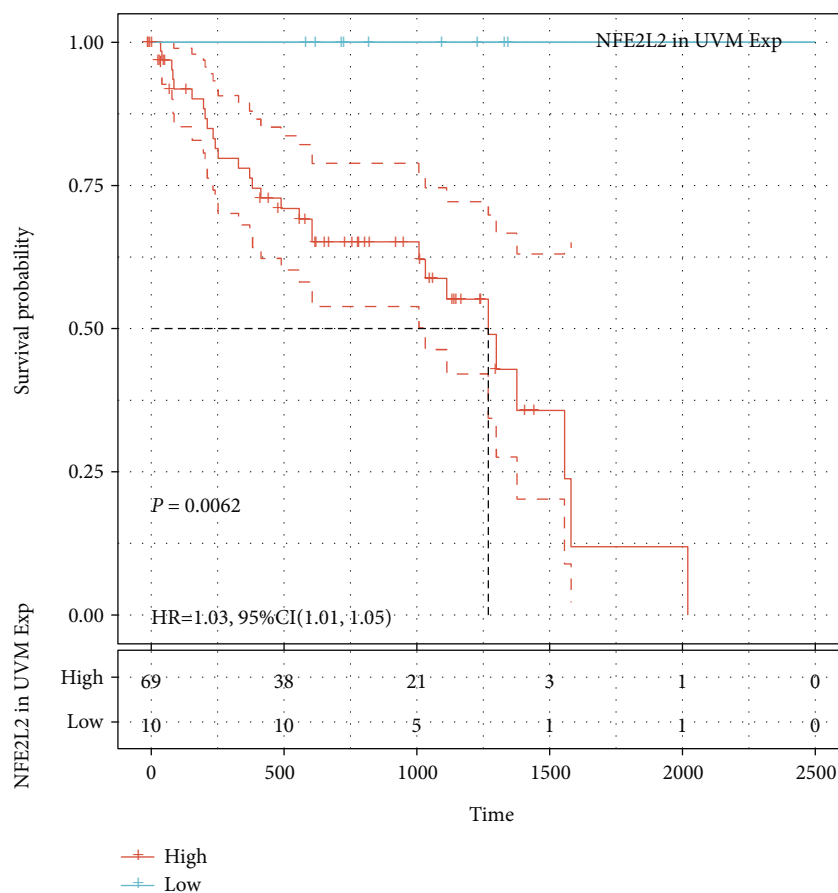
(c)

(d)

Figure 6: Continued.

(e)

(f)

FIGURE 6: Continued.

(g)

FIGURE 6: Relationship of NFE2L2 expression with patients' PFI. (a) Forest plots showing the HRs related to NFE2L2 expression in 33 cancer types. (b–g) Kaplan-Meier PFI curves for patients stratified by different expression levels of NFE2L2 in 6 cancer types.

have focused on pan-cancer analysis of the whole genome, revealing mutations, RNA alterations, and driver genes that are related to the occurrence and development of cancer, which is of importance for early diagnosis of cancer and development of biomarkers [31–35]. NFE2L2 is a transcription factor with alkaline lysine zipper structure, which plays a role in resisting oxidative stress and maintaining the body's redox homeostasis [36]. However, the roles of NFE2L2 in human pan-cancer have not been identified, and whether it can be used as a biomarker is still unknown. In the current study, we found that NFE2L2 is abnormally expressed in 22 cancer types and is significantly correlated with MMR gene mutation levels and DNA methylation. In addition, NFE2L2 expression was associated with poor prognosis (OS, DSS, and PFI) of patients, especially those with ACC, LGG, and PAAD. Furthermore, we observed that NFE2L2 expression was positively correlated with immune infiltration levels and the expression of immune checkpoint markers, especially in LGG. The above results strongly suggested that NFE2L2 may be used as a potential biomarker of LGG and play an indispensable role in tumor immunity.

Studies have shown that NFE2L2 could bind to KEAP1, which acts as a redox sensor to dissociate NFE2L2 from its cytoplasmic complex for translocation into the nucleus [37, 38]. In the nucleus, NFE2L2 binds to the antioxidant

response element (ARE) to activate the expression of detoxification, antioxidant, and anti-inflammatory genes, establishing the NFE2L2/KEAP1/ARE signaling pathway [37]. Disrupting the balance of this pathway can lead to aging, inflammation, and tumor chemoresistance [39, 40]. In addition, several studies have indicated that NFE2L2 is upregulated in different types of cancers and correlates with tumor progression, aggressiveness, and poor prognosis [41]. Another study showed that cytoplasmic NFE2L2 expression was associated with patients' poor prognosis, while the nuclear NFE2L2 expression was associated with a more favorable prognosis [42]. Moreover, NFE2L2 is abnormally overexpressed in lung cancer cell line A549 [43]. These previous findings indicate NFE2L2 may be abnormally expressed in various cancers and play important roles in cancer progression and patients' prognosis. In this study, we found for the first time that abnormal expression of NFE2L2 exists in human pan-cancer including ACC, LGG, and PAAD. Survival analysis showed NFE2L2 expression was associated with poor prognosis in multiple cancers, especially in ACC, LGG, and PAAD. These results strongly indicate NFE2L2 is a potential prognostic biomarker in ACC, LGG, and PAAD.

Under normal conditions, MMRs ensures the stability of DNA replication. MMRs consists of multiple heterodimers, including MLH1/PMS2, MSH2/MSH6, and EPCAM,
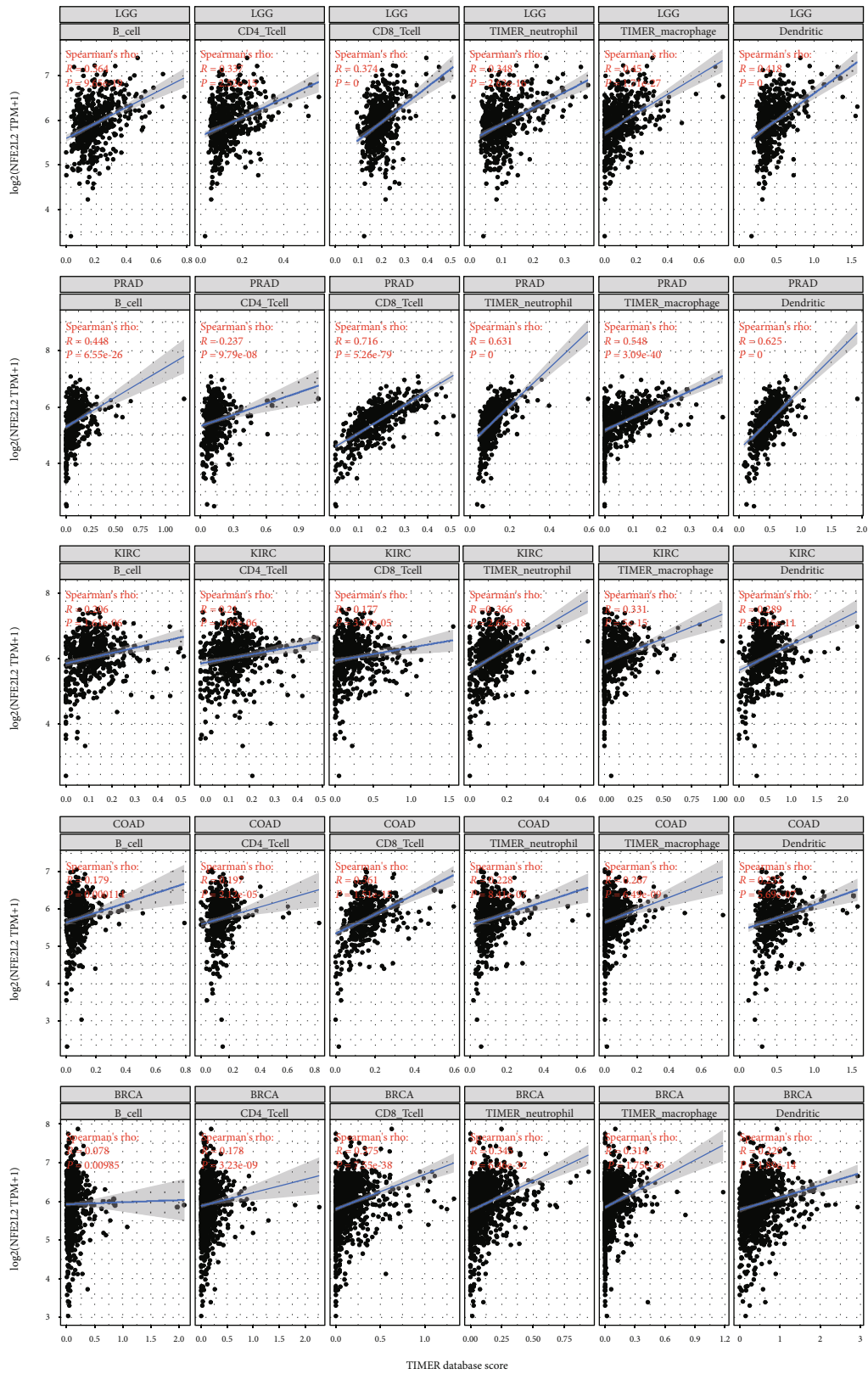
Figure 7: Correlation of NFE2L2 expression with immune infiltration levels of B cells, CD4+ T cells, CD8+ T cells, neutrophil cells, macrophage cells, and dendritic cells.
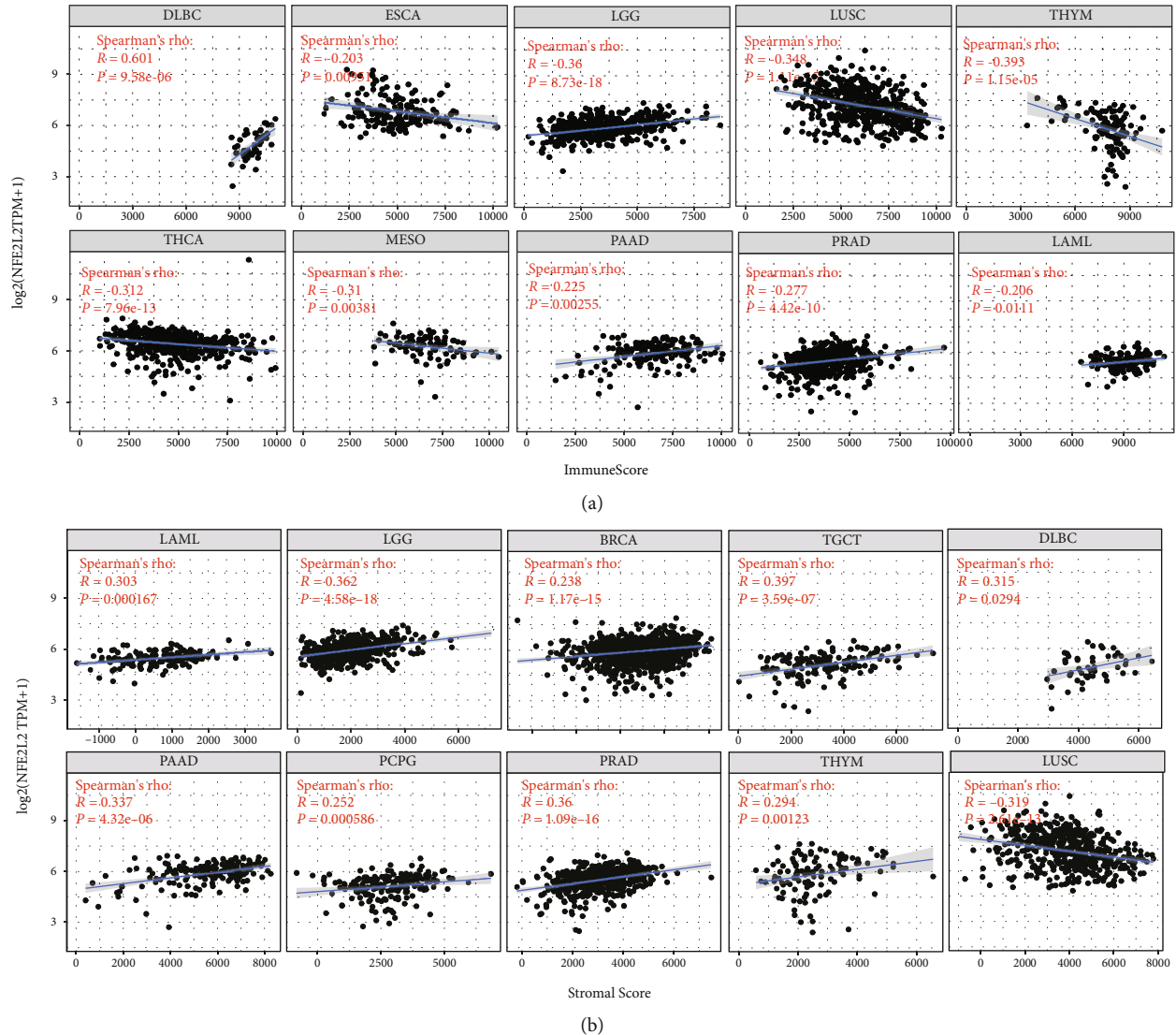
(a)

(b)

FIGURE 8: Correlation analysis between NFE2L2 expression and ImmuneScore/Stromal Score in cancers. (a) Correlation between NFE2L2 expression and ImmuneScore in DLBC, ESCA, LGG, LUSC, THYM, THCA, MESO, PAAD, PRAD, and LAML. (b) Correlation between NFE2L2 expression and StromalScore in LAML, LGG, BRCA, TGCT, DLBC, PAAD, PCPG, PRAD, THYM, and LUSC.

which can identify and correct gene mutations including base substitutions, insertions, deletions, or mismatches during DNA replication [44]. Mutations or defects in the MMR gene can lead to the accumulation of genetic errors, resulting in genomic or microsatellite instability, which contribute to the occurrence of tumors [45]. These indicate MMR gene mutation is a predictor of tumorigenesis. In this study, through correlation analysis, we found NFE2L2 expression was closely associated with the mutation levels of 5 MMR genes (MLH1, MSH2, MSH6, PMS2, and EPCAM) in human pan-cancer. In addition, alterations in DNA methylation status contribute to the development of cancer [46]. Recent research has shown that hypermethylation of the gene promoter is a common epigenetic feature of cancer [47, 48]. In our study, we also found that NFE2L2 expression was closely correlated with that of 4 DNA methyltransferases (DNMT1, DNMT2, DNMT3A, and DNMT3B) in human cancers, especially in

COAD, KIRP, LGG, and UVM. These results strongly support our conclusion that abnormal expression of NFE2L2 may play an important role in tumorigenesis by regulating MMR gene mutation levels and DNA methylation.

The TME has been a recent focus of tumor research. The immune microenvironment composed of tumor-infiltrating lymphocytes (TILs; B cells and T cells) and other immune cells (dendritic cells, neutrophils, and macrophages) is an important part of the TME [49, 50]. Studies have shown that immune cells play an indispensable role as a double-edged sword in tumors to promote or inhibit tumor progression [51–53]. Under normal conditions, immune cells play an antitumor role by monitoring and destroying cancer cells [54]. On the other hand, studies have shown that cancer cells can evade the surveillance of immune cells through a variety of mechanisms [55–58]. TILs have been shown to be an independent predictor of patients' prognosis in cancers [59]. CD4+ and CD8+ T cells are crucial members of the
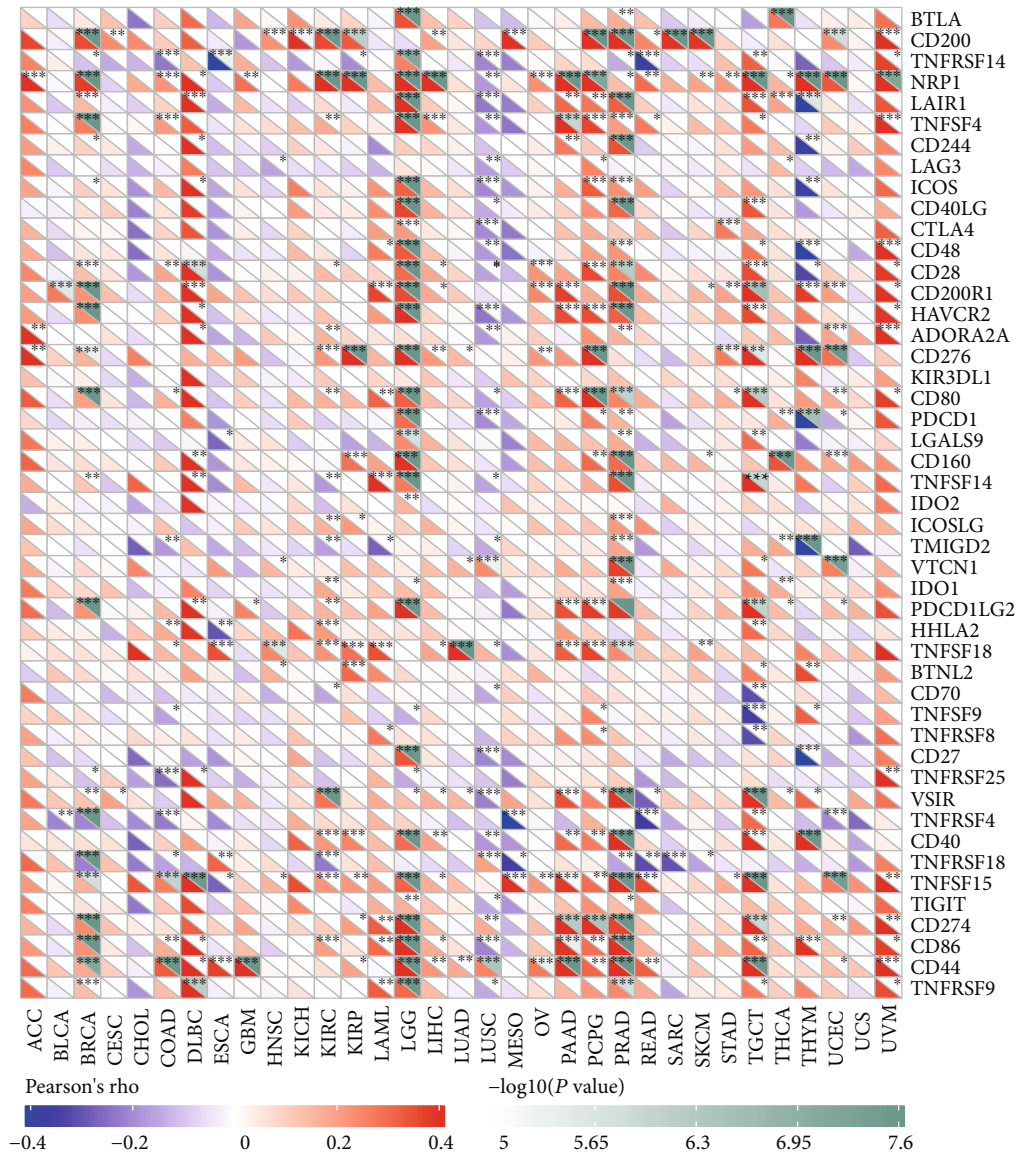
FIGURE 9: Correlation analysis of NFE2L2 expression levels with 40 common immune checkpoint gene levels in pan-cancer.

TME that participate in specific antitumor immune responses [60]. Neutrophils secrete MMP9 into the TME, which contributes to angiogenesis, tumor progression, and metastasis in mouse transplantation models [61]. Macrophages are the first line of defense against tumor immunity. Instead of killing tumor cells, TAMs mediate tumor development [62]. These observations indicate that TILs play a crucial part in tumor progression. However, there are few studies about the roles of NFE2L2 in the immune microenvironment. In this study, we found that NFE2L2 expression was significantly correlated with the levels of 6 types of infiltrating immune cells (B cells, CD4+ T cells, CD8+ T cells, dendritic cells, macrophages, and neutrophils) in BRCA, COAD, KIRC, LGG, and PRAD. These results indicate that NFE2L2 may lead to tumorigenesis or inhibit tumor progression by changing the TIL status. These novel findings constitute substantial progress in identifying the important role of NFE2L2 in immune infiltration.

Immune scoring is an approach to evaluate the infiltrating CD3+/CD45RO+, CD3+/CD8+, or CD8+/CD45RO+ lymphocyte population at the center and edges of a tumor [63]. In the TME, a higher ImmuneScore or StromalScore indicates a larger number of immune or matrix components [64]. Our results revealed that NFE2L2 expression was positively correlated with the ImmuneScore in DLBC, LGG, LAML, PAAD, and PRAD and negatively correlated with the ImmuneScore in ESCA, LUSC, THYM, THCA, and MESO. In addition, NFE2L2 expression was positively correlated with the StromalScore in BRCA, DLBC, LAML, LGG, PAAD, PCPG, PRAD, TGCT, and THYM and negatively correlated with the StromalScore in LUSC. Moreover, the correlation between NFE2L2 expression and immune checkpoint markers implies the role of NFE2L2 in regulating tumor immunology in cancers, especially in LGG. These results further strongly indicate NFE2L2's important roles in tumor immunity.

5. Conclusions

In conclusion, the results of the present study indicated that NFE2L2 overexpression correlates with poor prognosis of patients and increases the infiltration levels of B cells, CD8+ T cells, CD4+ T cells, macrophages, neutrophils, and dendritic cells in many cancers, especially in LGG. In addition, NFE2L2 expression was found to be significantly correlated with the expression of immune checkpoint markers in LGG. Therefore, NFE2L2 may play a vital role in immune infiltration and be a potential prognostic biomarker for LGG.

Data Availability

The data used to support the findings of this study are available from the corresponding author upon request.

Conflicts of Interest

The authors declare no conflicts.

Authors' Contributions

Qiang Ju and Xinmei Li contributed equally to this article.

Acknowledgments

References

[1] M. Hämäläinen, H.-R. Teppo, S. Skarp et al., "NRF1 and NRF2 mRNA and protein expression decrease early during melanoma carcinogenesis: an insight into survival and microRNAs," *Oxidative Medicine and Cellular Longevity*, vol. 2019, Article ID 2647068, 15 pages, 2019.

[2] S. Ma, C. Paiboonrungruan, T. Yan, K. P. Williams, M. B. Major, and X. L. Chen, "Targeted therapy of esophageal squamous cell carcinoma: the NRF2 signaling pathway as target," *Annals of the New York Academy of Sciences*, vol. 1434, no. 1, pp. 164–172, 2018.

[3] G. Kontostathi, J. Zoidakis, M. Makridakis et al., "Cervical cancer cell line secretome highlights the roles of transforming growth factor-beta-induced protein ig-h3, peroxiredoxin-2, and NRF2 on cervical carcinogenesis," *BioMed Research International*, vol. 2017, Article ID 4180703, 15 pages, 2017.

[4] L. Zhang, N. Wang, S. Zhou, W. Ye, G. Jing, and M. Zhang, "Propofol induces proliferation and invasion of gallbladder cancer cells through activation of Nrf2," *Journal of Experimental & Clinical Cancer Research*, vol. 31, no. 1, p. 66, 2012.

[5] Y. Mitsuishi, K. Taguchi, Y. Kawatani et al., "Nrf2 redirects glucose and glutamine into anabolic pathways in metabolic reprogramming," *Cancer Cell*, vol. 22, no. 1, pp. 66–79, 2012.

[6] T. W. Kensler and N. Wakabayashi, "Nrf2: friend or foe for chemoprevention?," *Carcinogenesis*, vol. 31, no. 1, pp. 90–99, 2010.

[7] A. Singh, S. Boldin-Adamsky, R. K. Thimmulappa et al., "RNAi-mediated silencing of nuclear factor erythroid-2-related factor 2 gene expression in non-small cell lung cancer inhibits tumor growth and increases efficacy of chemotherapy," *Cancer Research*, vol. 68, no. 19, pp. 7975–7984, 2008.

[8] J. Q. Ma, H. Tuersun, S. J. Jiao, J. H. Zheng, J. B. Xiao, and A. Hasim, "Functional role of NRF2 in cervical carcinogenesis," *PLoS One*, vol. 10, no. 8, article e0133876, 2015.

[9] P. A. Stewart, E. A. Welsh, R. J. C. Slebos et al., "Proteogenomic landscape of squamous cell lung cancer," *Nature Communications*, vol. 10, no. 1, p. 3578, 2019.

[10] D. R. Powell and A. Huttenlocher, "Neutrophils in the tumor microenvironment," *Trends in Immunology*, vol. 37, no. 1, pp. 41–52, 2016.

[11] M. Dysthe and R. Parihar, "Myeloid-derived suppressor cells in the tumor microenvironment," *Advances in Experimental Medicine and Biology*, vol. 1224, pp. 117–140, 2020.

[12] T. F. Gajewski, H. Schreiber, and Y. X. Fu, "Innate and adaptive immune cells in the tumor microenvironment," *Nature Immunology*, vol. 14, no. 10, pp. 1014–1022, 2013.

[13] S. L. Topalian, C. G. Drake, and D. M. Pardoll, "Immune checkpoint blockade: a common denominator approach to cancer therapy," *Cancer Cell*, vol. 27, no. 4, pp. 450–461, 2015.

[14] D. F. Quail and J. A. Joyce, "Microenvironmental regulation of tumor progression and metastasis," *Nature Medicine*, vol. 19, no. 11, pp. 1423–1437, 2013.

[15] Y. Zhu, J. Yang, D. Xu et al., "Disruption of tumour-associated macrophage trafficking by the osteopontin-induced colony-stimulating factor-1 signalling sensitises hepatocellular carcinoma to anti-PD-L1 blockade," *Gut*, vol. 68, no. 9, pp. 1653–1666, 2019.

[16] M. De Palma, D. Biziato, and T. V. Petrova, "Microenvironmental regulation of tumour angiogenesis," *Nature Reviews. Cancer*, vol. 17, no. 8, pp. 457–474, 2017.

[17] X. Li, W. Yao, Y. Yuan et al., "Targeting of tumour-infiltrating macrophages via CCL2/CCR2 signalling as a therapeutic strategy against hepatocellular carcinoma," *Gut*, vol. 66, no. 1, pp. 157–167, 2016.

[18] M. Cully, "Cancer: re-educating tumour-associated macrophages with nanoparticles," *Nature Reviews. Drug Discovery*, vol. 17, no. 7, p. 468, 2018.

[19] S. R. Gordon, R. L. Maute, B. W. Dulken et al., "PD-1 expression by tumour-associated macrophages inhibits phagocytosis and tumour immunity," *Nature*, vol. 545, no. 7655, pp. 495–499, 2017.

[20] D. Pardoll, "Cancer and the immune system: basic concepts and targets for intervention," *Seminars in Oncology*, vol. 42, no. 4, pp. 523–538, 2015.

[21] L. C. de Erauso, M. Zuazo, H. Arasanz et al., "Resistance to PD-L1/PD-1 blockade immunotherapy. A tumor-intrinsic or tumor-extrinsic phenomenon?," *Frontiers in Pharmacology*, vol. 11, p. 441, 2020.

[22] G. Cerretelli, A. Ager, M. J. Arends, and I. M. Frayling, "Molecular pathology of Lynch syndrome," *The Journal of Pathology*, vol. 250, no. 5, pp. 518–531, 2020.

[23] I. M. Krzyzewska, S. M. Maas, P. Henneman et al., "A genome-wide DNA methylation signature for *SETD1B*-related syndrome," *Clinical Epigenetics*, vol. 11, no. 1, p. 156, 2019.

[24] I. Georgakopoulos-Soares, G. Koh, S. E. Momen, J. Jiricny, M. Hemberg, and S. Nik-Zainal, "Transcription-coupled repair and mismatch repair contribute towards preserving genome integrity at mononucleotide repeat tracts," *Nature Communications*, vol. 11, no. 1, p. 1980, 2020.

[25] N. K. Porkka, A. Olkinuora, T. Kuopio et al., "Does breast carcinoma belong to the Lynch syndrome tumor spectrum? Somatic mutational profiles vs. ovarian and colorectal carcinomas," *Oncotarget*, vol. 11, no. 14, pp. 1244–1256, 2020.

[26] J. Tiffen, S. J. Gallagher, F. Filipp et al., "EZH2 cooperates with DNA methylation to downregulate key tumor suppressors and IFN gene signatures in melanoma," *The Journal of Investigative Dermatology*, 2020.

[27] M. Butler, L. Pongor, Y. T. Su et al., "*MGMT* status as a clinical biomarker in glioblastoma," *Trends Cancer.*, vol. 6, no. 5, pp. 380–391, 2020.

[28] L. Bonanno, A. Pavan, M. V. Dieci et al., "The role of immune microenvironment in small-cell lung cancer: distribution of PD-L1 expression and prognostic role of FOXP3-positive tumour infiltrating lymphocytes," *European Journal of Cancer*, vol. 101, pp. 191–200, 2018.

[29] J. S. J. Lim and R. A. Soo, "Nivolumab in the treatment of metastatic squamous non-small cell lung cancer: a review of the evidence," *Therapeutic Advances in Respiratory Disease*, vol. 10, no. 5, pp. 444–454, 2016.

[30] F. X. Schaub, V. Dhankani, A. C. Berger et al., "Pan-cancer alterations of the MYC oncogene and its proximal network across the Cancer Genome Atlas," *Cell Systems*, vol. 6, no. 3, pp. 282–300.e2, 2018.

[31] ICGC/TCGA pan-cancer analysis of whole genomes consortium, "Pan-cancer analysis of whole genomes," *Nature*, vol. 578, no. 7793, pp. 82–93, 2020.

[32] C. Calabrese, PCAWG Transcriptome Core Group, N. R. Davidson et al., "Genomic basis for RNA alterations in cancer," *Nature*, vol. 578, no. 7793, pp. 129–136, 2020.

[33] B. Rodriguez-Martin, PCAWG Structural Variation Working Group, E. G. Alvarez et al., "Pan-cancer analysis of whole genomes identifies driver rearrangements promoted by LINE-1 retrotransposition," *Nature Genetics*, vol. 52, no. 3, pp. 306–319, 2020.

[34] E. Rheinbay, P. C. A. W. G. Drivers, Functional Interpretation Working Group et al., "Analyses of non-coding somatic drivers in 2,658 cancer whole genomes," *Nature*, vol. 578, no. 7793, pp. 102–111, 2020.

[35] M. H. Bailey, C. Tokheim, E. Porta-Pardo et al., "Comprehensive characterization of cancer driver genes and mutations," *Cell*, vol. 173, no. 2, pp. 371–385.e18, 2018.

[36] Q. Liu, Y. Gao, and X. Ci, "Role of Nrf2 and its activators in respiratory diseases," *Oxidative Medicine and Cellular Longevity*, vol. 2019, 17 pages, 2019.

[37] M. de Freitas Silva, L. Pruccoli, F. Morroni et al., "The Keap1/Nrf2-ARE pathway as a pharmacological target for chalcones," *Molecules*, vol. 23, no. 7, p. 1803, 2018.

[38] V. Krajka-Kuźniak, J. Paluszczak, and W. Baer-Dubowska, "The Nrf2-ARE signaling pathway: an update on its regulation and possible role in cancer prevention and treatment," *Pharmacological Reports*, vol. 69, no. 3, pp. 393–402, 2017.

[39] P. Shaw and A. Chattopadhyay, "Nrf2-ARE signaling in cellular protection: mechanism of action and the regulatory mechanisms," *Journal of Cellular Physiology*, vol. 235, no. 4, pp. 3119–3130, 2019.

[40] E. Kubo, B. Chhunchha, P. Singh, H. Sasaki, and D. P. Singh, "Sulforaphane reactivates cellular antioxidant defense by inducing Nrf2/ARE/Prdx6 activity during aging and oxidative stress," *Scientific Reports*, vol. 7, no. 1, article 14130, 2017.

[41] A. L. Furfaro, N. Traverso, C. Domenicotti et al., "The Nrf2/HO-1 axis in cancer cell growth and chemoresistance," *Oxidative Medicine and Cellular Longevity*, vol. 2016, Article ID 1958174, 14 pages, 2016.

[42] J. Haapasalo, K. Nordfors, K. J. Granberg et al., "NRF2, DJ1 and SNRX1 and their prognostic impact in astrocytic gliomas," *Histol Histopathology*, vol. 33, no. 8, pp. 791–801, 2018.

[43] T. Ohnuma, K. Sakamoto, A. Shinoda et al., "Procyanidins from Cinnamomi cortex promote proteasome-independent degradation of nuclear Nrf2 through phosphorylation of insulin-like growth factor-1 receptor in A549 cells," *Archives of Biochemistry and Biophysics*, vol. 635, pp. 66–73, 2017.

[44] C. R. Boland and A. Goel, "Microsatellite instability in colorectal cancer," *Gastroenterology*, vol. 138, no. 6, pp. 2073–2087.e3, 2010.

[45] T. Armaghany, J. D. Wilson, Q. Chu, and G. Mills, "Genetic alterations in colorectal cancer," *Gastrointest Cancer Research*, vol. 5, no. 1, 2012.

[46] K. A. Szigeti, O. Galamb, A. Kalmár et al., "Role and alterations of DNA methylation during the aging and cancer," *Orvosi Hetilap*, vol. 159, no. 1, pp. 3–15, 2018.

[47] Y. Yin, K. Che, J. Hu et al., "Hypermethylation of the RSK4 promoter associated with BRAF V600E promotes papillary thyroid carcinoma," *International Journal of Oncology*, vol. 56, no. 5, pp. 1284–1293, 2020.

[48] M. Manoochehri, Y. Wu, N. A. Giese et al., "SST gene hypermethylation acts as a pan-cancer marker for pancreatic ductal adenocarcinoma and multiple other tumors: toward its use for blood-based diagnosis," *Molecular Oncology*, vol. 14, no. 6, pp. 1252–1267, 2020.

[49] M. R. Junttila and F. J. de Sauvage, "Influence of tumour micro-environment heterogeneity on therapeutic response," *Nature*, vol. 501, no. 7467, pp. 346–354, 2013.

[50] Z. Wang, K. Song, W. Zhao, and Z. Zhao, "Dendritic cells in tumor microenvironment promoted the neuropathic pain via paracrine inflammatory and growth factors," *Bioengineered*, vol. 11, no. 1, pp. 661–678, 2020.

[51] J. Berntsson, B. Nodin, J. Eberhard, P. Micke, and K. Jirström, "Prognostic impact of tumour-infiltrating B cells and plasma cells in colorectal cancer," *International Journal of Cancer*, vol. 139, no. 5, pp. 1129–1139, 2016.

[52] Y. Zhang, G. Yu, H. Chu et al., "Macrophage-associated PGK1 phosphorylation promotes aerobic glycolysis and tumorigenesis," *Molecular Cell*, vol. 71, no. 2, pp. 201–215.e7, 2018.

[53] T. Lianyuan, X. Dianrong, Y. Chunhui, M. Zhaolai, and J. Bin, "The predictive value and role of stromal tumor-infiltrating lymphocytes in pancreatic ductal adenocarcinoma (PDAC)," *Cancer Biology & Therapy*, vol. 19, no. 4, pp. 296–305, 2018.

[54] M. G. Morvan and L. L. Lanier, "NK cells and cancer: you can teach innate cells new tricks," *Nature Reviews. Cancer*, vol. 16, no. 1, pp. 7–19, 2016.

[55] P. Sharma, S. Hu-Lieskovan, J. A. Wargo, and A. Ribas, "Primary, adaptive, and acquired resistance to cancer immunotherapy," *Cell*, vol. 168, no. 4, pp. 707–723, 2017.

[56] G. P. Dunn, A. T. Bruce, H. Ikeda, L. J. Old, and R. D. Schreiber, "Cancer immunoediting: from immunosurveillance to

tumor escape," *Nature Immunology*, vol. 3, no. 11, pp. 991–998, 2002.

[57] Z. Wang, G. Li, S. Dou et al., "Tim-3 promotes *listeria monocytogenes* immune evasion by suppressing major histocompatibility complex class I," *The Journal of Infectious Diseases*, vol. 221, pp. 830–840, 2019.

[58] F. Tang, Y. Xu, and B. Zhao, "NLRC5: new cancer buster?," *Molecular Biology Reports*, vol. 47, no. 3, pp. 2265–2277, 2020.

[59] H. Ohtani, "Focus on TILs: prognostic significance of tumor infiltrating lymphocytes in human colorectal cancer," *Cancer Immunity*, vol. 7, p. 4, 2007.

[60] S. Hadrup, M. Donia, and P. thor Straten, "Effector CD_4 and CD8 T cells and their role in the tumor microenvironment," *Cancer Microenvironment*, vol. 6, no. 2, pp. 123–133, 2013.

[61] E. M. Bekes, B. Schweighofer, T. A. Kupriyanova et al., "Tumor-recruited neutrophils and neutrophil TIMP-free MMP-9 regulate coordinately the levels of tumor angiogenesis and efficiency of malignant cell intravasation," *The American Journal of Pathology*, vol. 179, no. 3, pp. 1455–1470, 2011.

[62] X. Shan, C. Zhang, Z. Wang et al., "Prognostic value of a nine-gene signature in glioma patients based on tumor-associated macrophages expression profiling," *Clinical Immunology*, vol. 216, article 108430, 2020.

[63] J. Galon, H. K. Angell, D. Bedognetti, and F. M. Marincola, "The continuum of cancer immunosurveillance: prognostic, predictive, and mechanistic signatures," *Immunity*, vol. 39, no. 1, pp. 11–26, 2013.

[64] K.-W. Bi, X.-G. Wei, X.-X. Qin, and B. Li, "BTK has potential to be a prognostic factor for lung adenocarcinoma and an Indicator for tumor microenvironment remodeling: a study based on TCGA data mining," *Frontiers in Oncology*, vol. 10, p. 424, 2020.